WHOI-2008-05

2007 Program of Study: Boundary Layers

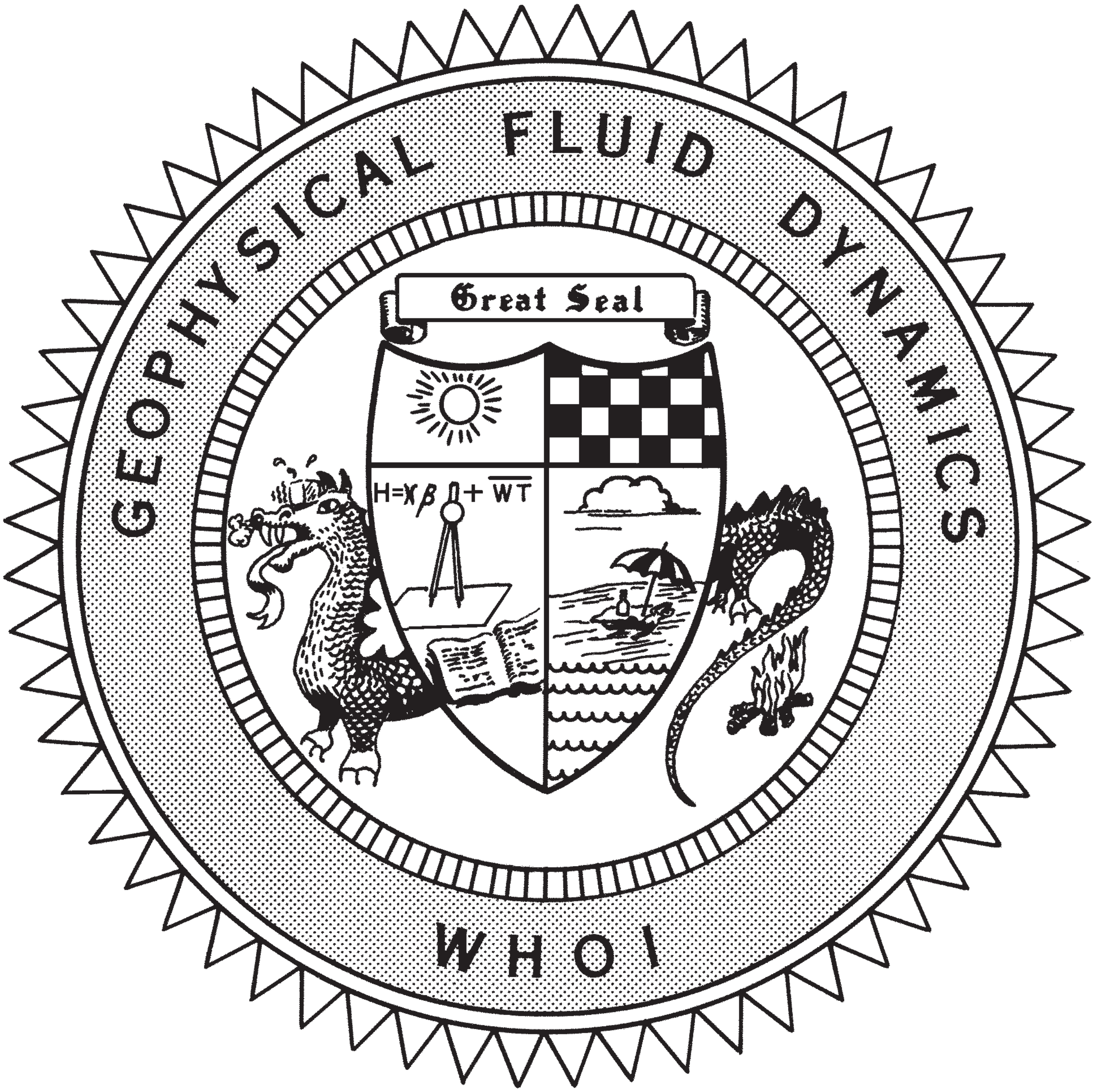
GEOPHYSICAL FLUID DYNAMICS
Great Seal
H=ϒβ ∫+ W̄T̄
WHOI

Course Lectures
Fellows Project Reports

WHOI-2008-05

2007 Program of Studies: Boundary Layers

by

Claudia Cenedese and John A. Whitehead, Co-Directors;
Joseph Pedlosky and Steven Lentz, Co-Principal Lecturers

June 2008

Technical Report

Funding was provided by the National Science Foundation under grant OCE-0325296 and by the Office of Naval Research, Processes and Prediction Division, Physical Oceanography Program under grant N00014-07-10776.

Reproduction in whole or in part is permitted for any purpose of the United States Government. This report should be cited as Woods Hole Oceanog. Inst. Tech. Rept., WHOI-2008-05.

Approved for public release; distribution unlimited.

Approved for Distribution:

Robert A Weller

Robert A. Weller, Chair

Department of Physical Oceanography

PREFACE

The topic of the Principal Lectures for the forty-ninth year of the program was "Boundary Layers". The subject centers around those problems in which the boundary conditions lead to a large gradient near the boundary. Nine of this year's principal lectures were given by Joe Pedlosky and the tenth was given by Steve Lentz. The fluid mechanics of boundary layers was reviewed, first starting from its classical roots and then extending the concepts to the sides, bottoms, and tops of the oceans. During week four, a mini-symposium on "Ocean Bottom and Surface Boundary Layers" gathered a number of oceanographers and meteorologists together to report recent advances. And, finally, Kerry Emanuel of MIT delivered the Sears Public Lecture to a packed hall in Clark 507. The title was "Divine Wind: The History and Sciences of Hurricanes."

The ten student projects continue to constitute the heart of the summer GFD experience. These are studies of new, original, and tractable problems by our fellows, who are in the midst of their graduate work. Some of the studies are already continuing to grow to full projects to be published in due course. Whatever the results of this summer's experience are for each fellow, be it a fully finished work, new ideas, fearless and honest inquiry, or simply experience working with a staff member in our craft, we wish our fellows well in their future studies and research.

Special thanks go to a number of people who served to make the program flow smoothly. Jeanne Fleming and Penny Foster ran the office and performed administrative work for the many visits and lectures. Their work in preparation during the "slack" season (completely misnamed) is especially appreciated. Janet Fields helps with all aspects of the academic programs for the fellows and, as usual, did a superb job. Keith Bradley created apparatus for a number of laboratory experiments, plus helped with odd tasks such as repairing old bicycles. George Veronis ran the world-class softball team that counted a number of wins in the season, including a victory over the staff, who, although ever wiser, never seem to age.

We extend our sincere thanks to the National Science Foundation for support for this program under OCE-0325296. Support was also provided by the Office of Naval Research, Processes and Prediction Division, Physical Oceanography Program, under grant N00014-07-10776.

Jack Whitehead and Claudia Cenedese,
Co-Directors

TABLE OF CONTENTS

PREFACE.. i

TABLE OF CONTENTS ii

PARTICIPANTS iv

LECTURE SCHEDULE viii

PRINCIPAL LECTURES
Joseph Pedlosky and Steven Lentz, Woods Hole Oceanographic Institution

Lecture 1
Boundary Layers
Joseph Pedlosky..1

Lecture 2
Boundary Layers
Joseph Pedlosky 12

Lecture 3
Boundary Layers: Stratified fluids
Joseph Pedlosky..22

Lecture 4
Observational evidence for the Ekman layer
Steven Lentz 28

Lecture 5
Boundary Layers: Sloping bottoms in a stratified, rotating fluid
Joseph Pedlosky..37

Lecture 6
Stress driven flow with a sloping bottom
Joseph Pedlosky..46

Lecture 7
Boundary Layers: Homogeneous ocean circulation
Joseph Pedlosky..63

Lecture 8
Boundary Layers: Homogeneous ocean circulation
Joseph Pedlosky..73

Lecture 9:
Internal boundary layers in the ocean circulation
Joseph Pedlosky...78

Lecture 10
Internal boundary layers in the ocean circulation
Joseph Pedlosky...90

FELLOWS' REPORTS

Internal wave radiation from gravity current down a slope in a stratified fluid
Jeroen Hazewinkel, Amsterdam University..108

Variations in sea surface temperature due to near surface straining flow
Andrew Wells, University of Cambridge..119

The stability of boundary layer flows
Jan Zika, University of New South Wales..143

Double diffusive effects in a dam break experiment
Frederic Laliberte, New York University..171

Convection of a van der Waals fluid near the critical point
Henrik van Lengerich, Cornell University..195

Instability theory of swirling flows with suction
Basile Gallet, Ecole Normale Superieure..210

Nonlinear Ekman dynamics for an advective flow
Rebecca W. Dell, Massachusetts Institute of Technology..230

An experimental study of the circular internal hydraulic jump
Iva Kavcic, University of Zagreb..244

Length and shape of a lava tube
Miranda Holmes, Courant Institute of Mathematics...264

Simultaneous differential diffusion under weak turbulence
Angel Ruiz-Angulo, Caltech...291

2007 GFD FELLOWS, STAFF AND VISITORS

Fellows

Rebecca Dell	Massachusetts Institute of Technology
Basile Gallett	Ecole Normale Supérieure
Jeroen Hazewinkel	Amsterdam University
Miranda Holmes	Courant Institute of Mathematical Science
Iva Kavcic	University of Zagreb
Frederic Laliberte	New York University
Angel Ruiz-Angulo	Caltech
Henrik van Lengerich	Cornell University
Andrew Wells	University of Cambridge
Jan Zika	University of New South Wales

Staff and Visitors

Benjamin Akers	University of Wisconsin, Madison
Erik Anderson	Grove City College
James Anderson	Stevens Institute of Technology
Andrew Belmonte	Pennsylvania State University
Onno Bokhove	University of Twente
Gregory Buck	Saint Anselm College
Claudia Cenedese	Woods Hole Oceanographic Institution
Eric Chassignet	Florida State University
Greg Chini	University of New Hampshire
Predrag Cvitanovic	Georgia Institute of Technology
William Dewar	Florida State University
Charles Doering	University of Michigan
Robert Ecke	Los Alamos National Laboratory
James Edson	University of Connecticut
Kerry Emanuel	Massachusetts Institute of Technology
Thomas Farrar	Woods Hole Oceanographic Institution
Stephan Fauve	Ecole Normale Supérieure
H. Joseph Fernando	Arizona State University
Glenn Flierl	Massachusetts Institute of Technology
Rockwell Geyer	Woods Hole Oceanographic Institution
John Gibson	Georgia Institute of Technology
Karl Helfrich	Woods Hole Oceanographic Institution
Louis Howard	Massachusetts Institute of Technology
Edward Johnson	University College
Shane Keating	University of California, San Diego
Joseph Keller	Stanford University
Joseph Kuehl	University of Rhode Island
Joseph LaCasce	The Norwegian Meteorological Institute
Norman Lebovitz	University of Chicago

Steven Lentz	Woods Hole Oceanographic Institution
Amala Mahadevan	Boston University
Willem Malkus	Massachusetts Institute of Technology
John Marshall	Massachusetts Institute of Technology
Brad Marston	Brown University
John McHugh	University of New Hampshire
W. Kendall Melville	University of California, San Diego
Philip Morrison	University of Texas, Austin
Takahide Okabe	University of Texas, Austin
Thomas Peacock	Massachusetts Institute of Technology
Joseph Pedlosky	Woods Hole Oceanographic Institution
Lawrence Pratt	Woods Hole Oceanographic Institution
James Price	Woods Hole Oceanographic Institution
Antonello Provenzale	Istituto di Scienze Dell'Atmosfera
Vitalii Sheremet	University of Rhode Island
Alexander Soloviev	Nova Southeastern University
Michael Spall	Woods Hole Oceanographic Institution
Edward Spiegel	Columbia University
Fiamma Straneo	Woods Hole Oceanographic Institution
Georgi Sutyrin	University of Rhode Island
Nobuhiro Suzuki	University of Rhode Island
Leif Thomas	Woods Hole Oceanographic Institution
Steve Thorpe	University of Wales, Bangor
Andreas Thurnherr	Lamont Doherty Earth Observatory
Mary-Louise Timmermanns	Woods Hole Oceanographic Institution
Peter Traykovski	Woods Hole Oceanographic Institution
John Trowbridge	Woods Hole Oceanographic Institution
Eli Tziperman	Harvard University
Lars Umlauf	Baltic Sea Research Institute
George Veronis	Yale University
Andrew Wells	University of Cambridge
John Whitehead	Woods Hole Oceanographic Institution
Carl Wunsch	Massachusetts Institute of Technology
Jiayan Yang	Woods Hole Oceanographic Institution
Philip Yecko	Montclair State University
Chris Zappa	Columbia University

2007 Participants

First row, seated (L/R): Rebecca Dell, Andrew Wells, Jeroen Hazewinkel, Angel Ruiz-Angulo, Miranda Holmes, Basile Gallet, Frederic Laliberte, Henrik van Lengerich, Jan Zika, Iva Kavcic.

Second row (L/R): Ed Spiegel (standing), Charles Doering, Willem Malkus, Vitalii Sheremet, Joe Keller, Antonello Provenzale, George Veronis, Erik Anderson, Claudia Cenedese, Eric Chassignet, Onno Bokhove.

Back row (L/R): Penny Foster, Steve Thorpe, Gregory Buck, Ted Johnson, Joe Pedlosky, Jim Anderson, Lou Howard, Bill Dewar, Jack Whitehead, Norm Lebovitz.

2007 Co-Principal Lecturers

Joe Pedlosky

Steve Lentz

2007 GFD Lecture Series Schedule

Monday, June 18

10:00 - Greetings (Dean James Yoder) and Lecture 1

Principal lectures (Weekdays at 10:00 AM through June 29)

Joseph Pedlosky, Woods Hole Oceanographic Institution

1. "Linear boundary Ekman layers"
    a) Boundary layers in density stratified fluids
    b) Control of interior
    c) An experimental application
    d) An extremely simple model for later use

2. "Coastal dynamics"
    a) Bottom boundary layer on shelf. The problem of the bottom velocity

3. "Oceanic boundary layers" (Pedlosky)
    a) Sverdrup theory and Munk, Stommel boundary layers
    b) Inertial boundary layers
    c) Inertial "runaway" and its repair
    d) The thermocline and its boundary layer structure

"Observation of the bottom boundary layer"
Steven Lentz, Woods Hole Oceanographic Institution

Staff lectures, June 20-29, 2:00 PM

June 20 - 2:00 PM
Representation of overflows in ocean models
Eric Chassignet, Florida State University

June 21 - 2:00 PM
Vortices, filaments and cascades in two-dimensional turbulence
Antonello Provenzale, Istituto di Scienze Dell'Atmosfera

June 22 – 2:00 PM – Informal seminar
Ferrofluids for fun and profit
Philip Yecko, Montclair State University

June 25 - 2:00 PM
Shallow two-dimensional transcritical flow over orography
Ted Johnson, University College, London

June 27 - 2:00 PM
Modulation of the cool skin of the ocean by internal waves
Tom Farrar, WHOI, Chris Zappa, Columbia University and
Claudia Cenedese, WHOI

June 28 - 2:00 PM
Hydraulic flow through a contraction: multiple steady states
Ben Akers, University of Wisconsin, Madison and
Onno Bokhove, University of Twente, with a demo by Jack Whitehead

June 29 – 2:00 PM – Informal lecture
Internal wave attractors
Jeroen Hazewinkel, Royal Netherlands Institute for Sea Research

Staff Lectures, July 2-6

July 2 - 10:00 AM
Heat transport in Rayleigh-Benard convection: 2007 update
Charles Doering, University of Michigan
July 2 - 2:00 PM
Decay and return of internal solitary waves with rotation
Karl Helfrich, WHOI

July 3 - 10:00 AM
Mathematics of games and sports
Joseph Keller, Stanford University

July 5 - 10:00 AM
Possible effects on climate of double diffusive Convection in the ocean
George Veronis, Yale University

July 5 - 2:00 PM
The dynamical-systems approach to transition in shear flows
Norman Lebovitz, University of Chicago

July 6 - 10:00 AM
On first looking into Chapman and Cowling
Ed Spiegel, Columbia University

July 6 - 2:00 PM - Informal seminar
Estimating mixing and subduction rates in inverse models
Jan Zika, CSIRO Marine and Atmospheric Research

Week 4 - July 9-13

Mini-Symposium on "Ocean bottom and surface boundary layers"

July 9 - 10:00 AM
Momentum, heat, & mass exchange in the marine atmospheric surface layer
Jim Edson, University of Connecticut

July 9 - 2:00 PM
Atmospheric boundary layer and its oceanic counterparts
Joe Fernando, Arizona State University

July 10 - 10:00 AM
Upper ocean response to a hurricane
Jim Price

July 11 - 10:00 AM
Surface wave processes in marine boundary layers
Ken Melville, University of California, San Diego

July 11 - 2:00 PM
Boundary layer effects in topographically constrained bottom gravity currents
Lars Umlauf, Baltic Sea Research Institute

July 12 - 10:00 AM
The ocean's diurnal boundary layer: observations and models
Tom Farrar, WHOI

July 12 - 2:00 PM Open Discussion

July 13 - 10:00 AM
A different kind of turbidity flow: wave supported turbidity flows on relatively flat shelves
Peter Traykovski, WHOI

Week 5 - July 16-20

July 16 – 10:30 AM
Roll vortices in the PBL (Planetary Boundary Layer)
Georgi Sutyrin, University of Rhode Island

July 17 - 10:30 AM
Laboratory experiments of oceanic overflows
Robert Ecke, Los Alamos National Laboratory

July 18 - 10:00 AM – Please note change of time from 10:30 to 10:00!
Kuroshio forcing in the East Asian marginal seas
Jiayan Yang, WHOI

July 19 - 10:30 AM
Does the marine biosphere mix the ocean?
Bill Dewar, Florida State University

July 20 - 10:30 AM
Chaotic dynamos generated by turbulent flows of liquid sodium
Stephan Fauve, Ecole Normale Superieure

July 20 - 2:00 PM - Informal seminar
The melting of icebergs and ice shelves
Andrew Wells, University of Cambridge

Week 6 - July 23-27

July 23 - 10:30 AM
Viscous, thermal, and diffusive sublayers at the air-sea interface
Alexander Soloviev, NOVA Southeastern University

July 23 - 2:00 PM
The stability of deep overflows
Larry Pratt, Physical Oceanography Department, WHOI

July 24 - 10:30 AM
The boundary layer of swimming fish
Erik Anderson, Grove City College

July 24 - 2:00 PM
Interpreting color imagery of the sea surface
Amala Mahadevan, Boston University

July 25 - 10:30 AM
The vortex merger rate in freely-decaying 2-D turbulence
Joseph LaCasce, University of Oslo

July 25 - 2:00 PM
Lateral coupling in baroclinically unstable flows
Mike Spall, Physical Oceanography Department, WHOI

July 26 - 10:30 AM
Interaction of a Western Boundary Current with a marginal sea: Kuroshio in Luzon Strait
Vitalii Sheremet, University of Rhode Island

July 26 – 2:00 PM
A thermodynamically exact temperature equation for a compressible fluid
George Veronis, Yale University

July 27 - 10:30 AM
Barefoot oceanic convection: twelve years later
Fiamma Straneo, Physical Oceanography Department, WHOI

Week 7 - July 30 - August 3

July 30 - 10:30 AM
Baroclinic instability in the upper ocean
Glenn Flierl, M.I.T.

July 31 - 10:30 AM
Are cascading flows stable?
Steve Thorpe, University of Wales

August 1 - 10:30 AM
Particles, propulsion and pertinent topography
Tom Peacock, M.I.T.

August 1 - 2:00 PM
Eddies in the Arctic Ocean
Mary-Louise Timmermans, WHOI

August 2 - 10:30 AM
Modification of the potential vorticity in frictional boundary layers
Leif Thomas, WHOI

August 3 - 10:30 AM
Overflows on the Mid-Atlantic Ridge
Andreas Thurnherr, Lamont Doherty Earth Observatory

Week 8 - August 6-10

August 6 – 10:30 AM
Global warming and hurricanes
Kerry Emanuel, M.I.T.

Public Lecture - August 6 - 3:00 PM - Clark 507
Divine Wind: The History and Sciences of Hurricanes
Kerry Emanuel, M.I.T.

August 7 - 10:30 AM
Geometry of boundary shear turbulence: a stroll through 61,506 dimensions
John Gibson, Georgia Tech University

August 8 - 10:00 AM – NOTE CHANGE OF TIME
Mixing in the Southern Ocean
John Marshall, M.I.T.

August 8 – 2:00 PM
Coalescence of charged water droplets
Andrew Belmonte, Pennsylvania State University

August 9 - 10:30 AM
Multiscale analysis of strongly nonlinear convection in the ocean surface
Boundary Layer
Greg Chini, University of New Hampshire

August 10 - 10:30 AM
Dinosaur forecast: cloudy; (or: a high latitude atmospheric convection mechanism for equable climate dynamics)
Eli Tziperman, Harvard University

Week 9 - August 13 – 17 NO TALKS THIS WEEKS

Week 10 - August 20 – 23 FELLOWS' PRESENTATIONS

Monday, August 20
10:00 AM

Jeroen Hazewinkel, Amsterdam University
Internal wave radiation by gravity currents down a slope

11:00 AM

Andrew Wells, University of Cambridge
Skinny dipping in Woods Hole: Investigating near surface variations in sea temperature

Tuesday, August 21
10:00 AM

Jan Zika, University of New South Wales
The stability of cascading flows

11:00 AM

Frederic Laliberte, New York University
Double diffusive effects in a dam break experiment

Wednesday, August 22

10:00 AM

Henrik van Lengerich, Cornell University
Convection of a van der Waals Fluid near the critical point

11:00 AM

Basile Gallet, Ecole Normale Superieure
Instability theory of swirling flows with suction

2:00 PM

Rebecca Dell, MIT/WHOI Joint Program
Nonlinear modifications to the Ekman Layer by an advecting geostrophic flow

3:00 PM

Iva Kavcic, University of Zagreb
Circular internal hydraulic jump

Thursday, August 23

10:00 AM

Miranda Holmes, Courant Institute of Mathematical Science
Length and shape of a lava tube

11:00 AM

Angel Ruiz-Angulo, Caltech
Differential diffusion paradox for turbulent flow

Boundary Layers

Lecture 1 by Rebecca Dell

The idea of a 'boundary layer' dates back at least to the time of Ludwig Prandtl. In 1904, he said:

> I have set myself the task of investigating systematically the motion of a fluid of which the internal resistance can be assumed very small. In fact, the resistance is supposed to be so small that it can be neglected wherever great velocity differences or cumulative effects of the resistance do not exist. This plan has proved to be very fruitful, for one arrives thereby at mathematical formulations which not only permit problems to be solved but also give promise of providing very satisfactory agreement with observations.
>
> ...the investigation of a particular flow phenomenon is thus divided into two interdependent parts: there is on the one hand the *free fluid*, which can be treated as inviscid according to the vorticity principles of Helmholtz, and on the other hand the transition layers at the fixed boundaries, the movement of which is controlled by the free fluid, yet which in turn give the free movement its characteristic stamp by the emission of vortex sheets. (H. Rouse and S. Ince. *History of Hydrodynamics.* New York: Dover, 1957, p269.)

Prandtl's central observation was that the the motion of a fluid of small viscosity could be separated into two *interdependent* parts: the free fluid and the boundary layer. The mathematical description of each would be quite different, but each would affect the other by the necessity of matching the two flows together. Physically, the free fluid forces the outer edge of the boundary layer, while the boundary layer diffuses vorticity into the free fluid. For more information about Prandtl, see the article in *Physics Today*, 2005, v.58, no.12, 42-48.

To get an idea of how this interplay between the boundary layer and the free fluid manifests itself mathematically, let's consider a couple of governing equations for geophysical fluid flow. Consider the Navier–Stokes equation

$$\rho\frac{\partial u_i}{\partial t}+\rho u_j\frac{\partial u_i}{\partial x_j}=-\frac{\partial p}{\partial x_i}+\rho F_i+\mu\frac{\partial^2 u_i}{\partial x_j\partial x_j}.$$

The final term expresses the effects of friction. If μ is small, as in most geophysical flows, the standard approximation is to neglect the final term. However, it is also the highest order term in the Navier–Stokes equation; neglecting it reduces the order of the equation and so reduces the number of boundary conditions that can be satisfied simultaneously. This is called a *singular perturbation.* We need to simplify our equation to make it mathematically tractable, but we must still satisfy our boundary conditions. To do this, it is necessary to find a way to retain the higher order derivatives *only where necessary.* The method for doing this is called boundary layer theory, which is a form of singular perturbation theory. In physical terms rather than mathematical terms, we apply boundary layer theory to understand the interplay between the localized viscous regions and the inviscid bulk of the fluid outside these regions.

To build intuition, let us consider another example. As we will learn in later chapters, the streamfunction of the steady, wind–driven ocean circulation is given by

$$\underbrace{\epsilon J(\Psi, \nabla^2\Psi)}_{\text{Nonlinear Advection of Vorticity}} \quad + \quad \underbrace{\frac{\partial \Psi}{\partial x}}_{\text{Planetary Vorticity Gradient}} \quad = \quad \underbrace{-r\nabla^2\Psi}_{\text{Bottom Friction}} \quad + \quad \underbrace{\nu\nabla^4\Psi}_{\text{Lateral Friction}} \quad + \quad \underbrace{T(x,y)}_{\text{Wind Forcing}} \quad .$$

In this equation, $\epsilon = \frac{U}{\beta L^2}$ is the Rossby number, and r and ν are nondimensional forms of the coefficients of bottom and lateral friction. Far from continental margins, in the free fluid, the dominant balance is between the advection of planetary vorticity and the wind forcing. The retention of only these two terms lowers the order of the equation. Any of the higher order terms—bottom friction, lateral friction, or advection— could be important in a restricted region of the flow along the boundaries. Generally, we think of boundary layers as a frictional effect, but it is important to realize that friction is not the sole source of boundary layers; inviscid nonlinear advection can create a boundary layer as well. This equation will be discussed in future lectures in great detail. For now, it is sufficient to recognize that boundary layer effects, such as the Gulf Stream, are clearly possible.

Looking ahead, the remaining lectures will adhere roughly to the following outline:

Linear Boundary Layer Theory : Ekman layers; boundary layers in a density–stratified fluid; boundary layer control of the interior; experimental applications

Coastal Bottom Boundary Layers : Boundary layers on the coastal shelf in cases of upwelling and downwelling; Observations (by S. Lentz)

Boundary Layers in the General Oceanic Circulation : Sverdrup theory; Stommel, Munk, and intertial boundary layers; inertial runaway; the thermocline and its boundary layer structure

1 Ekman Layers

Starting right in on linear boundary layer theory, let us derive the Ekman layer of a homogeneous fluid. The Ekman layer, described by Walfrid Ekman in 1902 in his doctoral dissertation, is a horizontal boundary layer in a rotating fluid. Such layers exist at the top and bottom of the ocean and at the bottom of the atmosphere. First, let's consider the steady equations of motion for an unstratified geophysical flow of uniform depth in a rotating coordinate frame

$$\begin{aligned}
u\frac{\partial u}{\partial x} + v\frac{\partial u}{\partial y} + w\frac{\partial u}{\partial z} - 2\Omega v &= -\frac{1}{\rho}\frac{\partial p}{\partial x} + \nu\left(\frac{\partial^2 u}{\partial x^2} + \frac{\partial^2 u}{\partial y^2} + \frac{\partial^2 u}{\partial z^2}\right)\\
u\frac{\partial v}{\partial x} + v\frac{\partial v}{\partial y} + w\frac{\partial v}{\partial z} + 2\Omega u &= -\frac{1}{\rho}\frac{\partial p}{\partial y} + \nu\left(\frac{\partial^2 v}{\partial x^2} + \frac{\partial^2 v}{\partial y^2} + \frac{\partial^2 v}{\partial z^2}\right)\\
u\frac{\partial w}{\partial x} + v\frac{\partial w}{\partial y} + w\frac{\partial w}{\partial z} &= -\frac{1}{\rho}\frac{\partial p}{\partial z} + \nu\left(\frac{\partial^2 w}{\partial x^2} + \frac{\partial^2 w}{\partial y^2} + \frac{\partial^2 w}{\partial z^2}\right) + g\\
\frac{\partial u}{\partial x} + \frac{\partial v}{\partial y} + \frac{\partial w}{\partial z} &= 0.
\end{aligned}$$

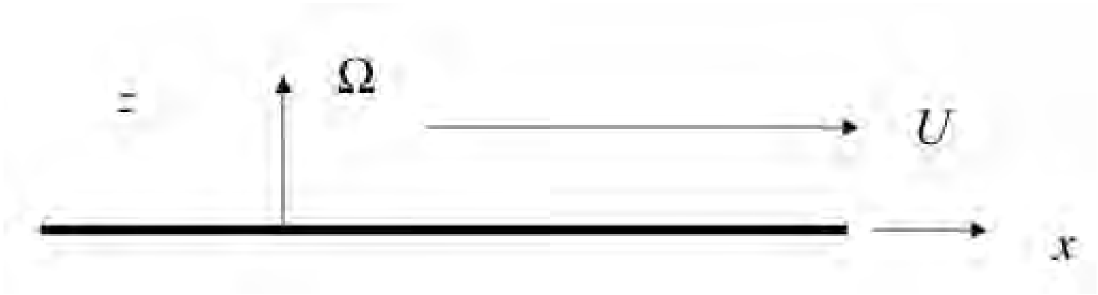

Figure 1: Ekman Layer Problem Setup

By omitting the energy equation, we implicitly assume that $\rho = \text{constant}$.

To derive the Ekman layer, we assume the fluid is flowing over an infinite flat plate, and far from the plate the fluid has velocity U, as shown in Figure 1. For simplicity, we assume that the far field velocity is constant in the down–stream direction, though it may vary in the cross–stream direction. We align our x–coordinate with the flow, so that $U = U(y)$, and we expect all quantities to be unvarying with x, $(\frac{\partial}{\partial x} = 0)$. Additionally, we rescale all lengths by some typical length scale L and all velocities by some typical velocity U_0. We assume that a natural length scale can be found, for example from some boundary far away or from the lateral scale of variations in $U(y)$. The above system of equations then becomes

$$\begin{aligned}
\epsilon\left(v\frac{\partial u}{\partial y} + w\frac{\partial u}{\partial z}\right) - v &= \frac{E}{2}\left(\frac{\partial^2 u}{\partial y^2} + \frac{\partial^2 u}{\partial z^2}\right) && (1)\\
\epsilon\left(v\frac{\partial v}{\partial y} + w\frac{\partial v}{\partial z}\right) + u &= -\frac{\partial p}{\partial y} + \frac{E}{2}\left(\frac{\partial^2 v}{\partial y^2} + \frac{\partial^2 v}{\partial z^2}\right) && (2)\\
\epsilon\left(v\frac{\partial w}{\partial y} + w\frac{\partial w}{\partial z}\right) &= -\frac{\partial p}{\partial z} + \frac{E}{2}\left(\frac{\partial^2 w}{\partial y^2} + \frac{\partial^2 w}{\partial z^2}\right) && (3)\\
\frac{\partial v}{\partial y} + \frac{\partial w}{\partial z} &= 0. && (4)
\end{aligned}$$

In these equations, our dimensionless parameters are the Rossby number, $\epsilon = \frac{U_0}{2\Omega L}$, and the Ekman number, $E = \frac{\nu}{\Omega L^2}$. Note that we have rescaled p by $\rho 2\Omega U_0$, and we have removed the hydrostatic component of the pressure, $-\rho g z$. We will also enforce two conditions at the lower boundary $z = 0$: no slip, that is $u = v = 0$; and no normal flow, that is $w = 0$.

We know that far from the boundary in the interior of the fluid, the velocity u_I must be given by

$$u_I = U(y).$$

If we assume that both ϵ and E are in some sense 'small', equation (2) tells us that in the interior

$$p_I = -\int^y U(y')\mathrm{y}'. \qquad (5)$$

This is a statement of geostrophy—the pressure and the rotation are the dominant balance. Equations (1) and (4) then imply $v_I = 0$ and $w_I = 0$. This solution satisfies all of the governing equations, but it does not satisfy a no–slip condition applied at $z = 0$. In order to satisfy this condition, we turn to a boundary layer. The boundary layer is expected to be very thin, so it is more convenient to examine it in a 'stretched' coordinate—a coordinate in which the boundary layer thickness is $O(1)$. In the boundary layer, the dominant physical process will be a balance between rotation and viscosity. In equations (1) to (4) the rotational terms are already $O(1)$, and to make the viscosity terms the same order, each vertical derivative must be $O(\frac{1}{\sqrt{E}})$. Therefore, we rescale z as

$$z = \sqrt{E}\zeta.$$

This corresponds to rescaling heights by δ, where:

$$\delta = \sqrt{\frac{\nu}{\Omega}} \tag{6}$$

is the thickness of the boundary layer, and it arises, as we said, from the balance of viscosity ν and rotation Ω. Since we are rescaling our vertical coordinate, we must similarly rescale our vertical velocity; let us define $W(y,\zeta) \equiv \frac{w}{\sqrt{E}}$. The chain rule tells us

$$\frac{\partial}{\partial z} = \frac{1}{\sqrt{E}}\frac{\partial}{\partial \zeta} \qquad ; \qquad \frac{\partial^2}{\partial z^2} = \frac{1}{E}\frac{\partial^2}{\partial \zeta^2}.$$

Our governing equations (1) – (4) now become

$$\begin{aligned}
\epsilon\left(v\frac{\partial u}{\partial y} + W\frac{\partial u}{\partial \zeta}\right) - v &= \frac{1}{2}\left(E\frac{\partial^2 u}{\partial y^2} + \frac{\partial^2 u}{\partial \zeta^2}\right) && (7)\\
\epsilon\left(v\frac{\partial v}{\partial y} + W\frac{\partial v}{\partial \zeta}\right) + u &= -\frac{\partial p}{\partial y} + \frac{1}{2}\left(E\frac{\partial^2 v}{\partial y^2} + \frac{\partial^2 v}{\partial \zeta^2}\right) && (8)\\
\epsilon E\left(v\frac{\partial W}{\partial y} + W\frac{\partial W}{\partial \zeta}\right) &= -\frac{\partial p}{\partial \zeta} + \frac{E}{2}\left(E\frac{\partial^2 W}{\partial y^2} + \frac{\partial^2 W}{\partial \zeta^2}\right) && (9)\\
\frac{\partial v}{\partial y} + \frac{\partial W}{\partial \zeta} &= 0. && (10)
\end{aligned}$$

Since we have included E in the scaling of ζ, in the limit where $E \to 0$ we remain in the boundary layer and friction remains important. If we again consider the Rossby number ϵ and the Ekman number E small with respect to one, these become:

$$\begin{aligned}
-v &= \frac{1}{2}\frac{\partial^2 u}{\partial \zeta^2} && (11)\\
+u &= -\frac{\partial p}{\partial y} + \frac{1}{2}\frac{\partial^2 v}{\partial \zeta^2} && (12)\\
0 &= -\frac{\partial p}{\partial \zeta} && (13)\\
\frac{\partial v}{\partial y} + \frac{\partial W}{\partial \zeta} &= 0. && (14)
\end{aligned}$$

Equation (13) tells us that we expect the pressure to be constant throughout the depth of the boundary layer, and so to be equal to its value in the inviscid interior, given by equation (5). The y–momentum equation (12) then becomes

$$u - U = \frac{1}{2}\frac{\partial^2 v}{\partial \zeta^2}. \tag{15}$$

The easiest way to solve the coupled equations (11) and (15) is to define a complex variable $\Lambda = (u - U) + iv$. The two equations can then be expressed as a single complex equation

$$\frac{\partial^2 \Lambda}{\partial \zeta^2} = 2i\Lambda.$$

This second–order equation has two solutions, but we discard the unbounded solution, leaving $\Lambda = \Lambda_0 e^{-(1+i)\zeta}$. Retaining only the real part of this, we find

$$\begin{aligned} u &= U + e^{-\zeta}\left(-A\cos\zeta + B\sin\zeta\right) \\ v &= e^{-\zeta}\left(A\sin\zeta + B\cos\zeta\right). \end{aligned}$$

Our no–slip boundary condition gives $A = U(y)$ and $B = 0$, so our final solution is

$$u = U(y)\left(1 - e^{-\zeta}\cos\zeta\right) \qquad (16)$$

$$v = U(y)e^{-\zeta}\sin\zeta. \qquad (17)$$

These solutions, normalized by $U(y)$, are plotted in Figure 2. They have the satisfying characteristic that as you move far from the boundary (as $\zeta \to \infty$), they approach the far–field solution of $u = U$ and $v = 0$. These same solutions are shown in Figure 3 as a hodograph, which traces out the direction of the total horizontal velocity vector. At the boundary $z = \zeta = 0$, the flow is at an angle of 45° to the far–field flow, and as ζ increases the velocity traces out a spiral, known as the Ekman spiral. It is interesting to note that Ekman began his investigations into boundary layers in rotating frames because Fridtjof Nansen observed from the deck of the *Fram* that icebergs in the Nordic Seas tend to move at an angle of 45° to the wind. Here we see that same observation arise in the mathematics.

At this point it is worth pausing briefly to consider physically what is happening. As fluid flows over the frictional plate, vorticity is generated at the boundary. This vorticity diffuses upward into the bulk of the fluid, tilting lines of planetary vorticity, 2Ω. At the same time, this diffusion is balanced and cancelled by the tilting of lines of constant vorticity caused by the rotation of the frame. Far from the plate, these two effects balance completely. The thickness of the boundary layer δ is the distance over which the vorticity shed from the bottom boundary moves before being balanced and cancelled by the tilting of planetary vorticity. It is a diffusive and inertial scale.

Now let us return to our calculated solution for velocity in the boundary layer, equations (16) and (17). As we are in a rotating frame, we generally expect flow to be along lines of constant pressure, called isobars. In the far field, pressure and velocity are both purely functions of y, and we see flow in the x–direction. However, in the boundary layer $v \neq 0$; we get flow *across* isobars. The combination of bottom friction and a rotating frame creates flow down the pressure gradient and perpendicular to the free fluid velocity. The total transport of this perpendicular velocity is given by

$$\int_0^\infty v \mathrm{d}z = \delta \int_0^\infty v \mathrm{d}\zeta = \frac{\delta}{2} U(y).$$

This perpendicular transport is known as the Ekman flux. If $U(y)$ is not constant, then our Ekman layer solution is horizontally divergent or convergent. By continuity (equation 14), this induces vertical motion, forcing fluid out of or into the boundary layer. This induced vertical motion is also referred to as the Ekman pumping. We find

$$W = -\frac{1}{2}\frac{\partial U}{\partial y}\left[1 - e^{-\zeta}\left(\cos\zeta + \sin\zeta\right)\right].$$

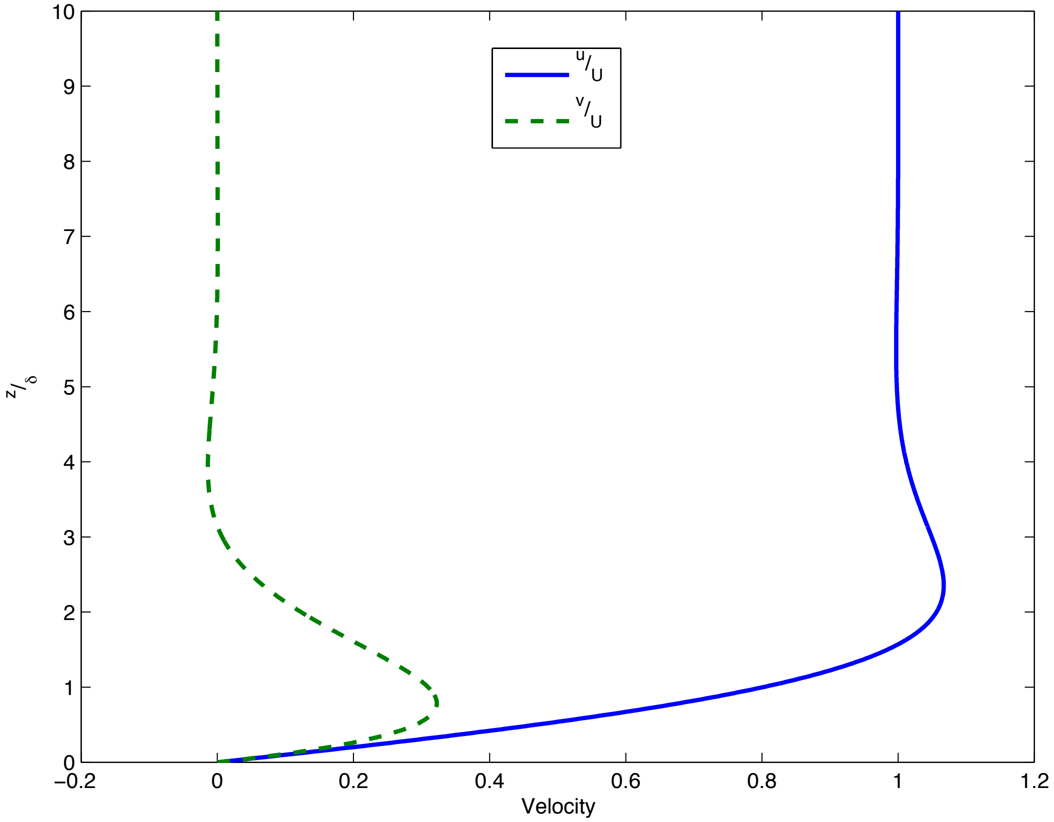

Figure 2: Velocity components in the boundary layer. Note the overshoot of the velocity profile at $u \approx 2$ and the oscillatory nature of the profile. This reflects the underlying inertial wave dynamics.

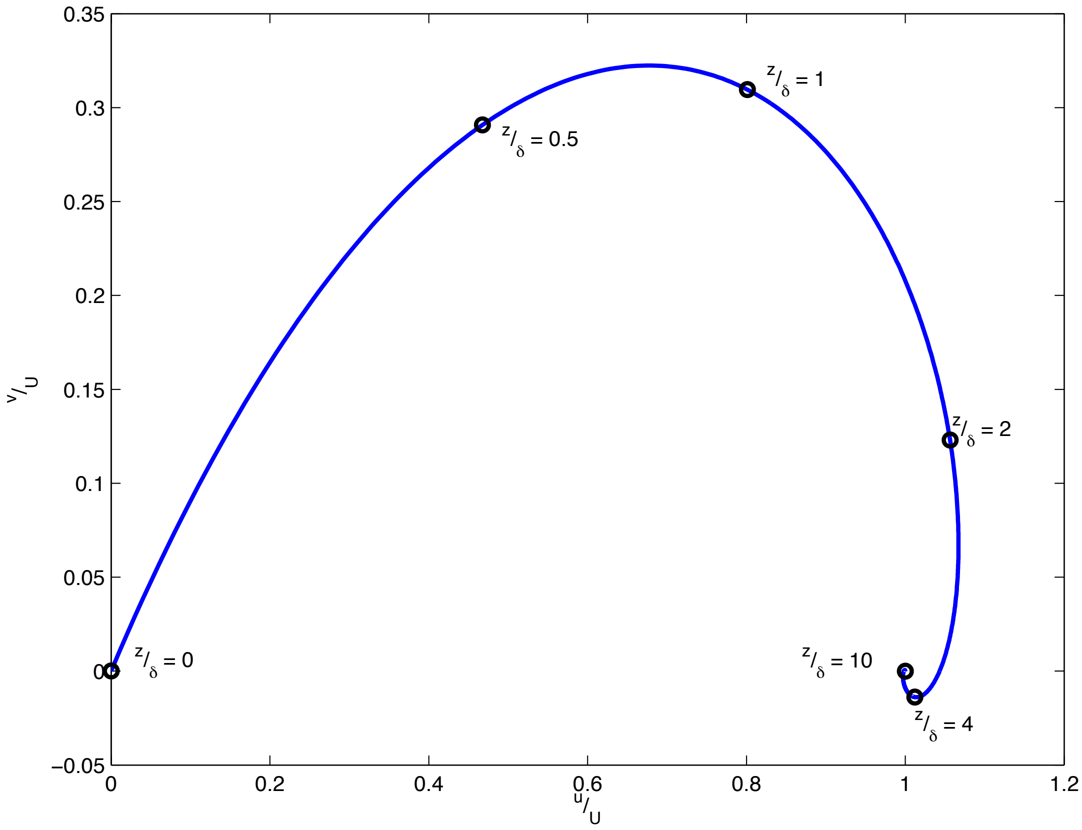

Figure 3: Ekman layer hodograph. This shows the line traced by the velocity vector as distance from the plate increases. Note that at the plate the fluid starts with a velocity at 45° to the forcing.

To derive this, we used the boundary condition that $W(\zeta = 0) = 0$. As we move far away from the bottom boundary, the lower boundary condition on the interior flow is

$$w_I(y, 0) = \sqrt{E} W(y, \zeta \to \infty) = -\frac{1}{2}\sqrt{E} U_y.$$

The combination of rotation and dissipation forces convergence in the boundary layer, which in turn creates a vertical velocity throughout the interior of the fluid. This vertical velocity is proportional to the vorticity of the interior flow. In the ocean, Ekman pumping is driven by layers at the surface and bottom. The surface Ekman pumping is on the order of 10^{-6}ms^{-1}, but it is enough to force the large–scale circulation of the entire ocean.

2 Spin Down

The vertical velocity we just calculated can have many substantial effects, including spinning down the fluid through vorticity conservation. If Ekman pumping forces fluid out of the boundary layer and into the overlying fluid, it will vertically compress the vortex tube of that fluid, an effect sometimes referred to as 'vortex squashing'. Conservation of circulation requires that the radial velocity in a vortex tube declines as the radius of the tube expands. This is described by the vorticity equation

$$\frac{d\omega}{dt} = \omega \cdot \nabla u + \text{Dissipation}.$$

For small ϵ in the interior, this reduces to

$$\epsilon \frac{d\omega}{dt} = \frac{\partial w}{\partial z}. \tag{18}$$

ω is the vertical component of the vorticity, given by

$$\omega = \frac{\partial v}{\partial x} - \frac{\partial u}{\partial y} = -\frac{\partial U}{\partial y}.$$

Equation (18) comes from taking the full vorticity equation, expanding in ϵ, and throwing out the higher order terms. We can integrate this equation over the depth of the fluid from the top of the boundary layer up. We know that ω is independent of z by the Taylor–Proudman effect for homogeneous fluids. Therefore, the left hand side is unchanged by integration. The right hand side simply gives us the difference between the vertical velocity at the bottom of our domain—which we know—and the vertical velocity at the top of our domain—which we assume is zero. We get

$$\begin{aligned} \epsilon \frac{d\omega}{dt} &= -\sqrt{E} \times w(z = 0) \\ &= \sqrt{E} \frac{1}{2} \frac{dU}{dy} = -\frac{\omega}{2}\sqrt{E}. \end{aligned}$$

The solution to this ODE is just an exponential decay, with non–dimensional decay time

$$T = \frac{2\epsilon}{\sqrt{E}}.$$

In dimensional units, this is

$$T = \frac{L}{U_0}\frac{2U_0}{2\Omega L}\sqrt{\frac{\Omega L^2}{\nu}} = \frac{L}{\sqrt{\Omega\nu}}.$$

This is the 'spin–down time' of the system, the characteristic time it takes for the vorticity from the bottom boundary to diffuse into the free fluid. It is so–called because it is the time scale over which the fluid would come to rest with respect to the bottom boundary. It is long compared with the rotation period of the system Ω, but it is *short* compared with the diffusion time of the system, $\frac{L^2}{\nu}$. This scale tells us that the larger the rotation rate, the less important viscosity becomes. However, the larger the rotation rate, the more rapidly the fluid is expected to spin down. This is because the coupling between the boundary layer and the interior is *inertial*, not viscous. The coupling of the inviscid vorticity dynamics of the interior and the viscous dynamics of the boundary layer is through vortex stretching.

3 Nonlinear Modifications of Ekman Layer

So far we have discussed only the linear theory of rotating boundary layers, however we can expect that introducing nonlinearity will both add terms and potentially change the structure of the solution. As we saw in equation (6), the thickness of the boundary layer is roughly given by the ratio of the effect of viscosity and rotation

$$\delta \sim \sqrt{\frac{\text{viscosity}}{\text{rotation}}}.$$

When we consider nonlinearity, we add the effects of advection, manifest as local vorticity. We therefore might guess that the thickness of the nonlinear boundary layer is given by something like

$$\delta = \sqrt{\frac{2\nu}{f+\omega}}.$$

In this $f = 2\Omega$ is the so–called Coriolis parameter and ω is the local or relative vorticity as before. However, the addition of relative vorticity has two competing effects. It causes the boundary layer to be thinner by the above equation, but at the same time it induces positive vertical velocity in the interior. This vertical velocity carries vorticity from the lower boundary upward, thickening the region affected by the presence of the boundary—that is thickening the boundary layer. A priori it is not obvious which of these effects is stronger and if the BL will get thicker or thinner. An exercise to develop intuition about problems of this type is to calculate the boundary layer flow over a non-rotating plate which has a uniform downward velocity through its surface.

To gain a quantitative insight into the net effect of this nonlinearity, we want to concentrate our attention on the scale at which it is most relevant, in the transition region between the Ekman layer and the free fluid interior. In this transitional region, we expect inertial effects—and therefore relative vorticity—to be as important as viscosity. In order for viscous and inertial effects to both be $O(1)$ in equations (7) – (10), we must again rescale our vertical coordinate, this time by the Rossby number ϵ

$$Z = \epsilon\zeta = \frac{\epsilon}{\sqrt{E}}z.$$

We now have three scales: the Ekman scale, where viscosity and rotation balance; the transitional scale, where viscosity and inertia balance; and the large scale of the free fluid, which we treat as invsicid. We assume that these scales are so well separated that we can treat Z and ζ as independent variables. By the chain rule, we then find

$$\frac{\partial}{\partial z} = \sqrt{\frac{1}{E}}\frac{\partial}{\partial \zeta} + \epsilon\sqrt{\frac{1}{E}}\frac{\partial}{\partial Z}.$$

Our equations of motion (1)–(4) become

$$\begin{aligned}
\epsilon\left(v\frac{\partial u}{\partial y} + W\frac{\partial u}{\partial \zeta}\right) - v &= \frac{1}{2}\left(E\frac{\partial^2 u}{\partial y^2} + \frac{\partial^2 u}{\partial \zeta^2} + 2\epsilon\frac{\partial^2 u}{\partial \zeta \partial Z}\right)\\
\epsilon\left(v\frac{\partial v}{\partial y} + W\frac{\partial v}{\partial \zeta}\right) + u &= -\frac{\partial p}{\partial y} + \frac{1}{2}\left(E\frac{\partial^2 v}{\partial y^2} + \frac{\partial^2 v}{\partial \zeta^2} + 2\epsilon\frac{\partial^2 v}{\partial \zeta \partial Z}\right)\\
\epsilon E\left(v\frac{\partial W}{\partial y} + W\frac{\partial W}{\partial \zeta}\right) &= -\frac{\partial p}{\partial \zeta} - \epsilon\frac{\partial p}{\partial Z} + \frac{E}{2}\left(E\frac{\partial^2 W}{\partial y^2} + \frac{\partial^2 W}{\partial \zeta^2} + 2\epsilon\frac{\partial^2 W}{\partial \zeta \partial Z}\right)\\
.\frac{\partial v}{\partial y} + \frac{\partial W}{\partial \zeta} + \epsilon\frac{\partial W}{\partial Z} &= 0
\end{aligned}$$

We now expand every variable in powers of ϵ, for example

$$\begin{aligned}
u &= u_0 + \epsilon u_1 + \ldots\\
p &= p_0 + \epsilon p_1 + \ldots\\
&\vdots \quad .
\end{aligned}$$

To lowest order, the problem we find is the linear problem we have already solved. If we repeat the solution procedure from the first section of this lecture, we find

$$\begin{aligned}
u_0 &= U(y) - A(y,Z)e^{-\zeta}\cos\zeta + B(y,Z)e^{-\zeta}\sin\zeta \qquad (19)\\
v_0 &= A(y,Z)e^{-\zeta}\sin\zeta + B(y,Z)e^{-\zeta}\cos\zeta. \qquad (20)
\end{aligned}$$

Note that we now allow our coefficients A and B to vary with Z. Mathematically, this is a consequence of treating Z and ζ as independent variables. Physically, this is possible because changes with Z are so slow on the ζ scale that the coefficients still act as though they were constant. From the no–slip condition, we have the conditions on the coefficients that $A(Z=0) = U$ and $B(Z=0) = 0$. Again as in the first section, we can use the convergence of u_0 and v_0 to calculate the induced vertical velocity

$$W_0 = C(Z) + \frac{1}{2}\frac{\partial A}{\partial y}e^{-\zeta}(\cos\zeta + \sin\zeta) + \frac{1}{2}\frac{\partial B}{\partial y}e^{-\zeta}(\cos\zeta - \sin\zeta).$$

$C(Z)$ is a constant of integration. To find $C(Z)$, we must consider the far–field flow that the vertical velocity matches to. By vorticity conservation, $\frac{\partial w}{\partial z} = 0$ to order ϵ in the interior from equation (18), so $w =$ constant. This means that $C(Z) = C(0) = -\frac{1}{2}\frac{\partial U}{\partial y}$ in order that the vertical velocity at the bottom of the interior flow matches that at the top of the boundary layer. This gives

$$W_0 = \frac{1}{2}\frac{\partial U}{\partial y} + \frac{1}{2}\frac{\partial A}{\partial y}e^{-\zeta}\left(\cos\zeta + \sin\zeta\right) + \frac{1}{2}\frac{\partial B}{\partial y}e^{-\zeta}\left(\cos\zeta - \sin\zeta\right).$$

However, to find A and B we must move on to the next higher order problem. As before, we can express it most compactly using complex notation

$$\frac{\partial^2 \Lambda_1}{\partial \zeta^2} - 2i\Lambda_1 = Ru + iRv. \tag{21}$$

where $\Lambda_1 = u_1 + iv_1$, and Ru and Rv are the nonlinear terms from the governing equations

$$\begin{aligned} Ru &\equiv 2\left(v_0 \frac{\partial u_0}{\partial y} + W_0 \frac{\partial u_0}{\partial \zeta}\right) - 2\frac{\partial^2 u_0}{\partial \zeta \partial Z} \\ Rv &\equiv 2\left(v_0 \frac{\partial v_0}{\partial y} + W_0 \frac{\partial v_0}{\partial \zeta}\right) - 2\frac{\partial^2 v_0}{\partial \zeta \partial Z}. \end{aligned}$$

We can see that some of the terms of Ru and Rv have the same form as the homogeneous solution of the left–hand side of equation (21), proportional to $e^{-(1+i)\zeta}$. This is a kind of resonance between the homogeneous solutions and the forcing functions. Forcing functions like these are called secular terms, and they give rise to terms of the form $\zeta e^{-(1+i)\zeta}$ in these solutions. They will grow linearly, and eventually lead to u_1 and v_1 to become the same size as u_0 and v_0, when $\epsilon\zeta = Z$ is $O(1)$. At this point, our expansion in powers of ϵ would be invalid. Therefore, we must eliminate these terms by setting their coefficients to zero.

Boundary Layers

Lecture 2 by Basile Gallet

continued from lecture 1

This leads to a differential equation in Z

$$\frac{\partial}{\partial Z}(A-iB)+(A-iB)[-C+\frac{U_y}{2i(1+i)}]=0 \text{ with } C=-\frac{U_y}{2}.$$

The solution to this equation with the boundary conditions $A(0)=U$ and $B(0)=0$ is

$$A(Z) = Ue^{-U_yZ/4}cos(U_yZ/4) \quad (1)$$

$$B(Z) = -Ue^{-U_yZ/4}sin(U_yZ/4). \quad (2)$$

Hence the corrected velocity field is

$$u_0 = U[1-e^{-\zeta(1+\epsilon U_y/4)}cos(\zeta(1-\epsilon U_y/4))] \quad (3)$$

$$v_0 = U[e^{-\zeta(1+\epsilon U_y/4)}sin(\zeta(1-\epsilon U_y/4))]. \quad (4)$$

If $U_y<0$, ω_z is positive, but the boundary layer is bigger than without the nonlinear correction : sacrebleu! Our guess on the size of the boundary layer $\delta=\sqrt{\frac{2\nu}{f+\omega_z}}$ was wrong. The main nonlinear effect is not that local vorticity should be added to the global rotation. There is a stronger effect which is that the vorticity in the boundary layer is advected in the z direction by the pumping velocity w ($w>0$ for $U_y<0$).

The equation for Λ_1 can then be solved to get the first order correction to u and v, and finally to w using the mass conservation equation

$$w_1=-E^{1/2}[\frac{1}{2}U_y+\frac{7\epsilon}{40}(U_y^2+UU_{yy})]. \quad (5)$$

The effects of the nonlinear terms on the pumping depend on the structure of the function $U(y)$, e.g. Uyy.

Boundary Layers: Stratified Fluids

1 Nansen's problem

1.1 Effect of the wind on the oceanic currents

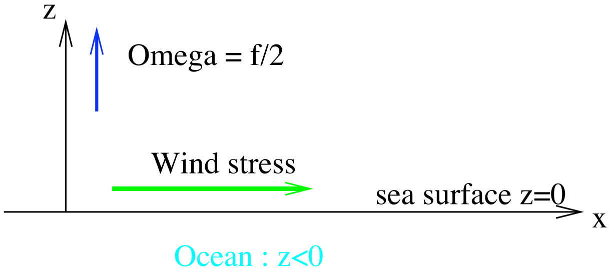

The problem in which the wind is applying a constant stress $\tau(y)$ in the x direction to the surface of the ocean is known as Nansen's problem. If the ocean is at rest, the velocity vanishes at great depth. The stress applied by the wind will induce a current in a boundary layer near the surface. If the Rossby number ϵ is small and the flow is steady, the Coriolis force will counterbalance the stress imposed by the wind. Since the velocity is significantly non-zero only inside the boundary layer, one can get an order of magnitude, U_0, of the velocity of the current from the equilibrium of these two terms

$$\tau \sim 2\rho\Omega U_0\delta_e \text{ which gives } U_0 = \tfrac{2\tau}{\rho f\delta_e} \text{ with } f = 2\Omega.$$

The velocities can be rescaled by U_0, the horizontal coordinates by L and the altitude by the height of the boundary layer δ_e. This leads to the variable $\zeta = \frac{z}{L}E^{-1/2}$. If we consider $\epsilon << 1$ we can rewrite the Navier-Stokes equation in terms of these non-dimensional variables

$$\begin{aligned} -v &= -p_x + u_{\zeta\zeta} && (6)\\ u &= -p_y + v_{\zeta\zeta} && (7)\\ 0 &= -p_\zeta. && (8) \end{aligned}$$

The pressure is independent of z (we included the gravity term in it) and is equal to its value outside the ocean, which does not depend on x and y. The system of equations reduces to

$$\begin{aligned} -v &= u_{\zeta\zeta} && (9)\\ u &= v_{\zeta\zeta}. && (10) \end{aligned}$$

This can be written in terms of the complex variable $\Lambda = u + iv$ and leads to

$$\Lambda\zeta\zeta - i\Lambda = 0. \qquad (11)$$

This problem is the same as the Ekman layer problem except for the boundary conditions on the velocity, which are $v_z = 0$ and $u_z = \tau$ at $z = 0$ and $u = v = 0$ at $z = -\inf$. The velocity field that satisfies these boundary conditions is

$$\begin{aligned} u &= \frac{\tau}{\sqrt(2)} e^{\zeta} cos(\zeta - \frac{\pi}{4}) \qquad (12) \\ v &= \frac{\tau}{\sqrt(2)} e^{\zeta} sin(\zeta - \frac{\pi}{4}). \qquad (13) \end{aligned}$$

One should note that the velocity at the surface makes a 45° angle on the right of the surface stress vector (for $\Omega > 0$) : the current induced by the wind does not drive the objects floating in the ocean exactly in the direction of the wind. They are deviated to the right in the North hemisphere and to the left in the South hemisphere. The hodograph shows that the velocities are very close to zero as soon as ζ is under -1. The vertical velocity is rescaled like the altitude and leads to the new variable $W = E^{-1/2} w$ which can be computed from the mass conservation equation

$$v_y + W_\zeta = 0 \text{ gives } W = -\tfrac{1}{2}\tau_y (1 - e^{\zeta} cos(\zeta)).$$

It has a non-zero limit at great depths, so

$$W(-\inf) = -\frac{1}{2}\tau_y. \qquad (14)$$

For a wind stress of $1 dyne/cm^2$ this is a velocity of $10 cm/day$. This phenomenon is responsible for a major part of the ocean circulation.

1.2 Role of non-linearities

We can now try to figure out what the effects of the nonlinear terms are. We consider the situation in which the velocity in the x direction is not zero in the deep ocean, but has a finite limit $u_g(y)$.

If the Rossby number is smaller than one but “not so small”, one may want to calculate the effect of non-linearities on the solution we found, which requires a new depth scale and a new variable $Z = \epsilon\zeta$. The velocity components are developed in powers of ϵ : $u = u_0 + \epsilon u_1, v = v_0 + \epsilon v_1$. As we did in the previous section, the zero order equation gives the solution we have just calculated but with constants of integration which depend on the variable Z. The first order equation in the equation of an oscillator with a “forcing” on the right hand side. For the development to be consistent there must not be any component of this forcing at the resonant frequency of the oscillator. This condition leads to a differential equation in Z for the integration constants of the zero order solution. We can solve this equation and get the corrected velocity

$$\begin{aligned} u_0 &= u_g + \frac{\tau}{\sqrt(2)} e^{\zeta(1-\epsilon(\frac{\tau_y}{2}+\frac{u_{gy}}{4}))} cos(\zeta(1 - \epsilon u_{gy}/4) - \frac{\pi}{4}) \qquad (15) \\ v_0 &= \frac{\tau}{\sqrt(2)} e^{\zeta(1-\epsilon(\frac{\tau_y}{2}+\frac{u_{gy}}{4}))} sin(\zeta(1 - \epsilon u_{gy}/4) - \frac{\pi}{4}). \qquad (16) \end{aligned}$$

The boundary layer thickness in dimensional form is

$$\delta_* = \sqrt{\frac{2\nu}{f - \frac{2\tau_{*y}}{\rho f \delta} - \frac{u_{*gy}}{2}}}. \qquad (17)$$

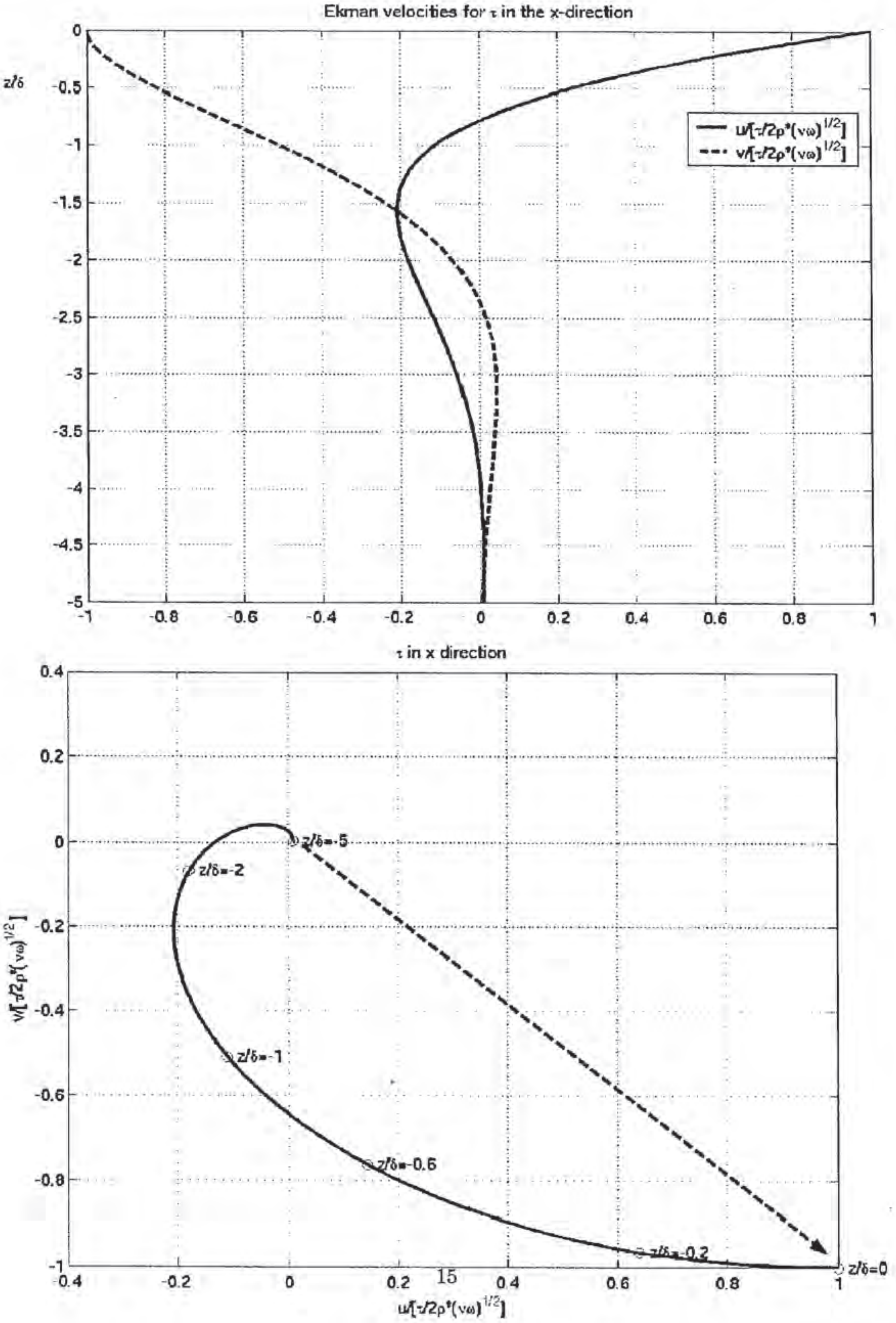

Figure 1: Top : Horizontal components of the Velocity field as a function of z/δ. Bottom : Hodograph of the horizontal components of the velocity field.

We see that in this case the boundary layer is thinner if $u_{gy} < 0$. It's not u_{gy} which create the vertical flow but the curl of the stress $-\tau_y$. The vertical advection is then independent of u_{gy} and the only effect of the vertical vorticity is to add to the global rotation to make a thinner boundary layer.

We can also compute the order one correction to the velocity field and the correction to the vertical flow

$$W(-\infty) = -\frac{1}{2}\frac{\partial}{\partial y}[\frac{\tau}{1-\epsilon(u_{gy}+\frac{\tau_y}{4})}]. \tag{18}$$

This vertical flow depends on the horizontal velocity gradients in the deep ocean only at the first order.

One may wonder if a linearization of the nonlinear terms around u_e is still possible in the case $u_g >> u_e$. For more information on this subject one can look at Thomas and Rhines (2002).

Stratified Fluids

In an ocean there are changes in the density of the water due to variations both in the salinity and the temperature of the water. The presence of density stratification introduces new and very interesting elements to the boundary layer picture and the control of the interior flow by the boundary layers. The control of the boundary layer on the interior flow is mediated by vertical inertial waves. The stratification allows information to propagate horizontally through internal gravity waves. There will be some kind of competition between the top and bottom boundary conditions on the one hand, which propagate through inertial waves, and the side walls boundary conditions, which propagate through internal gravity waves.

2 The cylinder problem

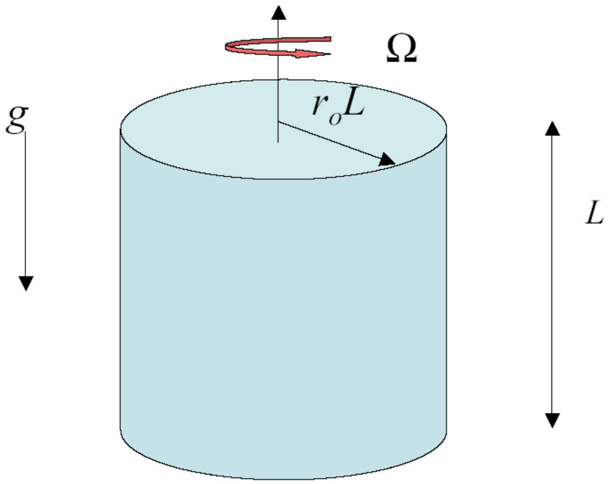

An interesting problem is to study the motion of a stratified fluid inside a rotating cylinder. The cylinder's axis is vertical. The height of the cylinder is L and its radius is $r_0 L$. We can use the following scalings:

$$\overrightarrow{u_*} = U\overrightarrow{u}, \tag{19}$$

$$\overrightarrow{x_*} = L\overrightarrow{x}, \tag{20}$$

$$T_* = \Delta T_v(z_*/L) + \Delta T_h T(x,y,z). \tag{21}$$

In these equations, the variables with a star are dimensional. ΔT_v and ΔT_h are the vertical and horizontal temperature variations over the size of the cylinder. The density is supposed to be linear in the temperature variations

$$\rho_* = \rho_0[1 - \alpha T_*]. \tag{22}$$

We define p as the non-dimensional pressure difference to the hydrostatic pressure

$$p_* = \rho_0 g\alpha\Delta T_v(z_*^2/(2L)) + \rho_0 fULp(x,y,z), \text{ with } f = 2\Omega.$$

The scaling velocity is given by a thermal wind balance : $U = \frac{\alpha g\Delta T_h}{f}$. The motion is supposed to be steady, incompressible and to follow the Boussinesq approximation. The equations are :

- Navier-Stokes $\epsilon(\overrightarrow{u}.\overrightarrow{\nabla})\overrightarrow{u} + \overrightarrow{k}\Lambda\overrightarrow{u} = -\overrightarrow{\nabla}(p) + T\overrightarrow{k} + \frac{E}{2}\nabla^2\overrightarrow{u}$
- Incompressibility $\overrightarrow{\nabla}.\overrightarrow{u} = 0$
- Temperature advection-diffusion $\epsilon(\overrightarrow{u}.\overrightarrow{\nabla})T + wS = \frac{E}{2\sigma}\nabla^2 T$

These 3 equations involve 4 dimensionless numbers :

- The Rossby number $\epsilon = \frac{U}{fL}$
- The Ekman number $E = \frac{2\nu}{fL^2}$
- The Prandtl number $\sigma = \frac{\nu}{\kappa}$, where κ is the thermal diffusivity of the fluid.
- A characteristic number of the vertical stratification $S = \frac{\alpha g\Delta T_v}{f^2 L} = \frac{N^2}{f^2}$, where N is the oscillation frequency of inertial waves inside the cylinder.

We consider that the ratio $\frac{\epsilon}{S} = \frac{\Delta T_h}{\Delta T_v}$ is small, so that the temperature equation can be linearized. We can impose different boundary conditions to the flow :

- We assume a no-slip boundary condition. There must also be no flow perpendicular to the boundary.
- One or more boundaries may be moving in their own plane.
- The cylinder walls may either be insulating or at a fixed given temperature.

We use polar coordinates, with u being the radial velocity, v the azimuthal one, and w the vertical one. We assume that the Rossby number is small so that the equations of motion are linear. For an axially symmetric motion we get

$$\begin{aligned}
-v &= -p_r + \frac{E}{2}[\nabla^2 u - \frac{u}{r^2}] && (23)\\
u &= \frac{E}{2}[\nabla^2 v - \frac{v}{r^2}] && (24)\\
0 &= -p_z + T + \frac{E}{2}\nabla^2 w && (25)\\
\frac{1}{r}(ru)_r + w_z &= 0 && (26)\\
w\sigma S &= \frac{E}{2}\nabla^2 T. && (27)
\end{aligned}$$

We see in the last equation that the perturbation due to vertical motion is balanced in the steady state by diffusion. The interior vertical velocity "tolerated" by the system is $w_I \sim \frac{E}{\sigma S}$. However, an Ekman boundary layer induces a vertical pumping which velocity is of order $E^{1/2}$. This means that for a low Ekman number the vertical pumping can be much stronger than the vertical velocity tolerated by the interior. We may wonder how the system is going to respond to such a perturbation. The Ekman layers are found using $z = \zeta E^{1/2}$ and $w = WE^{1/2}$

$$\begin{aligned}
-v &= -p_r + \frac{1}{2}u_{\zeta\zeta} && (28)\\
u &= \frac{1}{2}v_{\zeta\zeta} && (29)\\
0 &= -p_\zeta + E^{1/2}T + \frac{1}{2}EW_{\zeta\zeta} && (30)\\
(ru)_r + rW_\zeta &= 0 && (31)\\
\sigma S E^{1/2} W &= \frac{1}{2}T_{\zeta\zeta}. && (32)
\end{aligned}$$

We see in the last equation that if $\sigma S << E^{-1/2}$ we can ignore the buoyancy forces in the Ekman layer. The temperature is the same as in a purely diffusive state. The boundary layer is so thin that it remains unchanged. One should remember however that this is true only for a horizontal bottom boundary.

We can adapt the previous results for the Ekman layer to polar coordinates and get the compatibility condition between the boundary layer flow and the flow in the interior of the cylinder (variables with a subscript I)

$$\int_0^{+\infty} u(\zeta)d\zeta = \frac{v_I}{2} \text{ and } w_I(r,0) = E^{1/2}W(r,+\infty)$$

.

An integration with respect to ζ of the mass conservation equation leads to

$$w_I(r,0) = E^{1/2}W(r,+\infty) = \frac{E^{1/2}}{2r}(rv_I)_r. \quad (33)$$

If the upper boundary is rotating with differential speed $v_T(r)$, the same analysis yields

$$w_I(r,1) = \frac{E^{1/2}}{2r}\frac{\partial}{\partial r}(r(v_T - v_I(r,1))). \quad (34)$$

In the limit $E << 1$ the equations governing the interior flow are

$$\begin{aligned}
v_I &= p_{Ir} && (35)\\
T_I &= -p_{Iz} && (36)\\
u_I &= \frac{E}{2}[\nabla^2 v - \frac{v}{r^2}] && (37)\\
\frac{1}{r}(ru_I)_r + w_{Iz} &= 0 && (38)\\
w_I &= \frac{E}{2\sigma S}\nabla^2 T_I. && (39)
\end{aligned}$$

u_I is of order E, which means that if $\sigma S << 1$ then $w_I >> u_I$, so that the mass conservation equation becomes $\frac{\partial}{\partial z} w_I = 0$. The interior vertical velocity is independent of z and may be written as the mean of its values at $z = 0$ and $z = 1$

$$w_I = \frac{1}{2}(w_I(r,1) + w_I(r,0)) = \frac{E^{1/2}}{4r}\frac{\partial}{\partial r}[r(v_T - (v_I(r,1) - v_I(r,0)))]. \tag{40}$$

If we differentiate the azimuthal component of the Navier-Stokes equation in the interior with z and its vertical part with r we get the thermal wind equation

$$\frac{\partial}{\partial z} v_I = \frac{\partial}{\partial r} T_I. \tag{41}$$

This equation can be integrated with respect to z

$$v_I(r,1) - v_I(r,0) = \frac{\partial}{\partial r}\int_0^1 T_I(r,z')dz'. \tag{42}$$

The vertical velocity of the interior can then be written in terms of the temperature and of the forcing velocity

$$w_I = \frac{E^{1/2}}{4r}\frac{\partial}{\partial r}(rv_T) - \frac{E^{1/2}}{4r}\frac{\partial}{\partial r}(r\frac{\partial}{\partial r}(\int_0^1 T_I(r,z')dz')). \tag{43}$$

References

L. N. Thomas and Peter B. Rhines. Nonlinear stratified spin-up. *Journal of Fluid Mechanics*, (473):211–244, 2002.

Boundary Layers: Stratified Fluids

Lecture 3 by Jeroen Hazewinkel

continued from lecture 2

Using $w_I = E/(2\sigma S)\nabla^2 T_I$, the interior of the cylinder is be described by

$$\frac{E}{2\sigma S}\nabla^2 T_I + \frac{E^{1/2}}{4}\nabla^2 \int_0^1 T_I(r, z')dz' = \frac{E^{1/2}}{4}\frac{1}{r}(rv_T)_r. \tag{1}$$

This result can be rewritten as a Poisson equation

$$\nabla^2\Theta = \lambda\frac{1}{r}(rv_T)_r, \tag{2}$$

where we introduced the new temperature

$$\Theta = T_I + \lambda\int_0^1 T_I dz', \tag{3}$$

with

$$\lambda = \frac{\sigma S}{2E^{1/2}}. \tag{4}$$

This λ will be the determining parameter to the problem. Remember that, although being small, the term σS in λ is as yet undefined relatively to $E^{1/2}$. When λ is relatively small stratification is of little importance and the problem reduces to the unstratified Ekman problem. In the other limit, i.e. $\lambda \gg 1$, stratification suppresses most of the vertical motion.

In order to solve the Poisson equation 3 we need boundary conditions at all sides of the domain. At the top and bottom of the cylinder, we simply have to match the interior temperature with the forced exterior temperature. At the side walls we have to find solutions for $\Theta(r \to r_0)$. As we anticipate side wall boundary layers, we introduce a boundary layer correction to all variables, e.g. $u = u_I(r) + u_{bl}(\zeta) \to u_{bl} = 0, \zeta \to \infty$. As before we will use a boundary layer coordinate ζ. Note that the boundary layer scale has to be determined as yet, i.e. $r = \delta\zeta$ with δ unknown. In order to find this scale we turn back to the same balance equations that hold in the interior. However, the full Laplacian is replaced by its first approximation in the rapidly changing coordinate ζ, i.e. $\nabla \to \partial_{\zeta\zeta}$. This gives

$$v = p_\zeta, \tag{5}$$

$$u = \frac{E}{2} v_{\zeta\zeta}, \tag{6}$$

$$0 = p_z + T + \frac{E}{2} w_{\zeta\zeta}, \tag{7}$$

$$u_\zeta + w_z = 0, \tag{8}$$

$$\sigma S w = \frac{E}{2} T_{\zeta\zeta}. \tag{9}$$

Combination of the above equations results in $w_z = -E/2p_{4\zeta}$ and $T_z = -\sigma S p_{\zeta\zeta}$. Taking the z-derivative of 7 and using the above found relations gives one equation for pressure p,

$$\frac{E^2}{4} p_{6\zeta} + \sigma S p_{\zeta\zeta} + p_{zz} = 0. \tag{10}$$

Recall that we assume all derivatives to z are $O(1)$ and those to ζ are $O(1/\delta)$. This means that for example the first term of 10 is $O(E^2/\delta^6)$.

There are several balances that satisfy 10. We will examine the options. Firstly, there could be a balance between the first term and the last term. This implies that $E^2/\delta^6 = O(1), -> \delta = E^{1/3}$, the so called Stewardson layer. This layer exists for a homogeneous, rotating fluid. In order for the second term of 10 to be negligible we also find that $\sigma S \ll E^{2/3}$.

Considering $\sigma S \gg E^{2/3}$ there are two possible balances. For $\delta = E^{1/2}/(\sigma S)^{1/4}$ the first and second term balance. This boundary layer only depends on the stratification and is therefore called the buoyancy layer. For $\delta = (\sigma S)^{1/2}$ we find a balance between the second and third term of 10. This layer is the hydrostatic layer. As both boundary and hydrostatic layers are found in the limit $\sigma S \gg E^{2/3}$ they coexist. In the larger hydrostatic layer, close to the side wall the buoyancy layer is found. With decreasing stratification these two combine in the Stewardson layer. In both limits, σS small and large compared to $E^{2/3}$, the full sixth order of 10 is preserved. As we considered the cylinder with a stratification we will have to see the impact of both hydrostatic and buoyancy layers on the interior, or how they set the boundary condition for 3.

0.1 Hydrostatic boundary layer

Turning to the hydrostatic layer we introduce a stretched coordinate

$$\eta = \frac{r_0 - r}{\delta_{hydrostatic}} = \frac{r_0 - r}{(\sigma S)^{1/2}}. \tag{11}$$

We rewrite the azimuthal velocity as $v = \widetilde{v}(r, \eta)$. This indicates, from the governing equations, that $u = E/(\sigma S)\tilde{u}$ and $p = (\sigma S)^{1/2}$. The governing equations, accurate to terms of order larger than $E^{2/3}$, become

$$
\begin{aligned}
\widetilde{v} &= \widetilde{p}_{\eta}, \\
\widetilde{u} &= \frac{1}{2}\widetilde{v}_{\eta\eta}, && (12) \\
\widetilde{T} &= \widetilde{p}_{z}, && (13) \\
\widetilde{u}_{\eta} + \widetilde{w}_{z} &= 0, && (14) \\
\widetilde{w} &= \frac{1}{2}\widetilde{T}_{\eta\eta}. && (15)
\end{aligned}
$$

Friction is in this layer not of importance, as we balanced the second and third term in 10. Combining all terms we find an equation for v. These can be combined to give, (with the assumption) that v vanishes at $r = r_0$

$$\widetilde{v}_{\eta\eta} + \widetilde{v}_{zz} = 0. \tag{16}$$

To solve this we notice that the thickness of the hydrostatic layer, in the case of $\sigma S \gg E$, is much greater than that of the Ekman layer at the top and bottom. This means that for these Ekman layers the dynamics of the hydrostatic layer is part of the interior. The vertical velocity shows that

$$w_h = \frac{E}{(\sigma)^{3/2}}\widetilde{w} = \frac{E}{(\sigma)^{3/2}}\widetilde{T}_{\eta\eta} = \frac{E}{(\sigma)^{3/2}}\widetilde{v}_{z\eta}. \tag{17}$$

From the Ekman transport we find that this vertical velocity is

$$\frac{E}{2}\widetilde{v}_{hr} = \frac{E^{1/2}}{(\sigma)^{1/2}}\widetilde{v}_{\eta}, \tag{18}$$

indicating that $\widetilde{v}_{z\eta} = \sigma S/E^{1/2} v_{\eta}$ or $\widetilde{v}_{z} = \lambda\widetilde{v}$ at top and bottom of the hydrostatic layer. Complimentary to this we will assume that $\tilde{v} = V(z)e^{-a\eta}$, so that 16 results in

$$(\lambda^2 + a^2)\tilde{v} = 0. \tag{19}$$

This shows that the hydrostatic boundary layer has a characteristic scale of $a = (2\sigma S)^{1/2}/E^{1/4}$.

0.2 Buoyancy layer

In the very thin buoyancy layer we found the thickness to be $\delta_b = E^{1/2}/(\sigma S)^{1/4}$. Introducing the boundary layer coordinate $\xi = (r - r_0)/\delta_b$ and $v = \hat{v}$ etc., we rewrite the governing equations again to find

$$
\begin{aligned}
\hat{v} &= \hat{p}_{\xi}, && (20) \\
\hat{u} &= \frac{1}{2}\hat{v}_{\xi\xi}, && (21) \\
\hat{T} &= \frac{1}{2}\hat{w}_{\xi\xi}, && (22) \\
\hat{u}_{\xi} + \hat{w}_{z} &= 0, && (23) \\
\hat{w} &= \frac{1}{2}\hat{T}_{\xi\xi}. && (24)
\end{aligned}
$$

Note that, as we derived the buoyancy layer being the balance between buoyancy and the friction we also see this in the third equation above. We see that combining the equations implies that

$$\hat{T}_{4\xi} + 4\hat{T} = 0, \tag{25}$$

indicating an Ekman like boundary layer. Using the Ekman solution we find

$$\hat{T} = Ae^{-\xi}\cos\xi + Be^{-\xi}\sin\xi. \tag{26}$$

As $\hat{\psi} = \hat{T}_\xi$ we find that

$$\hat{\psi} = \frac{r_0}{2}[-Ae^{-\xi}(cos\xi + sin\xi) + Be^{-\xi}(cos\xi + sin\xi)]. \tag{27}$$

Now we have expressions for both hydrostatic and buoyancy layers. The sum of the solutions has to meet the outer boundary conditions.

0.3 Matching at $r = r_0$

At the outer rim, $r = r_0$, there is no slip which means that

$$v_I(r_0, z) + \tilde{v}(0, z) + \frac{E}{(\sigma S)^{3/2}}\hat{v}(0, z) = 0. \tag{28}$$

The last term on the lhs is negligible so we find that interior velocity is balanced by the velocity from the hydrostatic layer. Taking the z-derivative and using the thermal wind relation, **??**, leads to

$$(T_I)_r - \tilde{T}_\eta = 0. \tag{29}$$

In case of an insulating side wall at $r = r_0$ the radial derivative of total temperature should be zero, i.e. $(T_I)_r - \tilde{T}_\eta - T_\xi = 0$. Combining these two results we see that $T_\xi = 0$. Also the total stream function should be zero. Combining previously found expressions for ψ we find

$$0 = \psi_I + \frac{E}{(\sigma S)}\hat{\psi} + \frac{E}{\sigma S}\tilde{\psi} = \psi_I - \frac{Er_0}{2\sigma S}\tilde{T}_\eta - \frac{Er_0}{2\sigma S}\hat{T}_\xi. \tag{30}$$

Noting that we found an expression for $\tilde{T}(r_0)_\eta$ and $\hat{T}(r_0)_\xi = 0$, we see that

$$\psi_I = \frac{Er_0}{2\sigma S}(T_I)_r. \tag{31}$$

By definition $\psi_r = rw$ and we recall the interior balance between vertical flux and temperature and forcing velocity. We recast this at position $r = r_0$ so that we can use 31, and find

$$\frac{E^{1/2}}{4}r_0 v_T - \frac{E^{1/2}}{4}r_0\int_0^1 \partial_r T_I dz - \frac{r_0 E}{2\sigma S}r_0\int_0^1 \partial_r T_I dz = 0. \tag{32}$$

Assuming that there is no z dependence for the interior temperature, the integrals give us the integrants so we have

$$\partial_r T_I = \frac{\lambda}{1+\lambda}v_T(r_0). \tag{33}$$

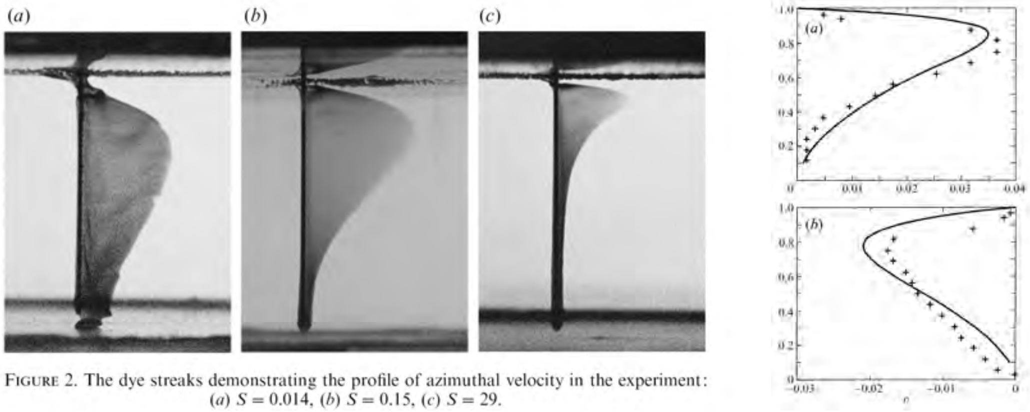

FIGURE 2. The dye streaks demonstrating the profile of azimuthal velocity in the experiment: (a) $S = 0.014$, (b) $S = 0.15$, (c) $S = 29$.

Figure 1: Observations by Pedlosky et al. (1997) in a rotating cylinder with a temperature profile on top. Shown are three different experiments in which the azimuthal velocity is visualized by dye. Note that the profiles changes for different stratification. On the right their comparison between observations (+) and theoretical predicted profile (line)

The z independence of T also means that $\Theta(r_0)_r \equiv T_r(r_0)+\lambda\int_0^1 T_r(r_0)dz = (1+\lambda)T_r(r_0) = \lambda v_T(r_0)$. This means that we finally found the boundary condition for 3 being

$$\Theta_r(r_0) = \lambda v_t(r_0). \tag{34}$$

1 Two experiments

We will briefly discuss two experiments that can be seen as confirmation of the above theory for a rotating, stratified fluid. In their experiment **?** considered a cylinder, having a temperature on top in the varying in the radial direction and bottom at a fixed temperature. The boundary on top did not rotate differentially from the rotation of the whole tank. In this special set-up it turns out that on the side walls both hydrostatic and buoyancy layers are inactive but a layer of the scale $(\sigma S)^{1/2}$ exists in the vicinity of the upper boundary. For sufficiently large stratification, the Ekman pumping into the interior is completely suppressed. The nearly inviscid interior velocity field has to match the no-slip in a layer that decreases with decreasing stratification. Beneath this layer, a smooth transition of the azimuthal velocity towards null at the bottom is found. In a comparison between theory and experiments the velocity profiles were found to be in good agreement, as shown in Figure 1.

In a second study Whitehead and Pedlosky (2000), again a stratified fluid in a rotating cylinder was considered. However, in this case not the top, but a coil around the cylinder heated the fluid. The heating was placed in the middle of the height of the cylinder. This sidewall warming forces a vertical mass flux in the sidewall boundary layer. The divergence of this flux effects the interior flow and drives a azimuthal velocity. Again, the theoretical predictions and observations were in close agreement. In Figure 2 both theory and experimental velocity profiles at several radii are shown. As the stratification increased, Whitehead and Pedlosky (2000) observed that the velocity profile got a sharper peak.

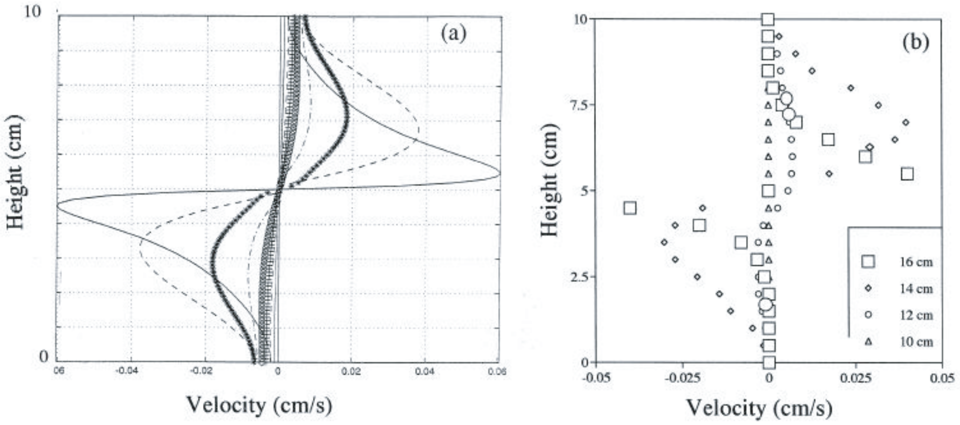

Figure 2: Comparison between a) theoretical prediction for the velocity profiles and b) the observations. The various lines and dots correspond to different sampling radii. in Whitehead and Pedlosky (2000).

References

J. Pedlosky, J. A. Whitehead, and G. Veitch. Thermally driven motions in a rotating stratified fluid. theory and experiment. *Journal of Fluid Mechanics*, 339:391–411, 1997.

J. A. Whitehead and J. Pedlosky. Circulation and boundary layers in differentially heated rotating stratified fluid. *Dynamics of Atmosphere and Oceans*, 31:1–21, 2000.

Observational evidence for the Ekman layer
lecture by Steve Lentz

Lecture 4 by Miranda Holmes

This lecture focuses on observations that test the Ekman dynamics developed so far and to come.

Eddy viscosity Recalling that the size of the Ekman layer is $\delta_E = \sqrt{2\nu/f}$ and using typical values of $\nu = 10^{-6} m^2/s$, $f = 10^{-4} s^{-1}$ gives $\delta_E = 10$cm. However, in the ocean δ_E is on the order of 10m, suggesting that we should use a much higher viscosity coefficient of $\nu^{\text{ocean}} = 10^{-2} m^2/s$. This can be achieved by a suitable parameterization of an eddy viscosity.

We define a turbulent eddy-viscosity coefficient A such that

$$Au_z \approx -\langle u'w' \rangle \ .$$

Unlike the molecular viscosity ν, A depends on the flow and the stratification.

Madsen (Madsen (1977)) found that a suitable form for A in a turbulent Ekman layer is

$$A = \kappa u_* z \ , \qquad u_* = \sqrt{\tau^s/\rho_0} \ , \tag{1}$$

where z is the distance from the boundary, τ^s is the applied stress, and $\kappa = 0.4$ is Von Karman's constant. This form can also be derived through dimensional arguments. If we define $u_* = \sqrt{\tau^s/\rho_0}$, then the stress at the surface is $\tau^s/\rho_0 = A\frac{\partial u}{\partial z}$. From dimensional analysis, we have that $\frac{\partial u}{\partial z} \propto u_*/z$. Letting the constant of proportionality be $1/\kappa$ gives (1).

This is the parameterization most often used to test Ekman theory. It can be used to derive the frequently-cited Law of the Wall. Integrating $\frac{\partial u}{\partial z} = \frac{1}{\kappa}\frac{u_*}{z}$ gives the Law of the Wall:

$$\sqrt{u^2+v^2} = \frac{u_*}{\kappa}\ln(z) - \frac{u_*}{\kappa}\ln(z_0) \ , \qquad u_* = \tau^b/\rho_0 \tag{2}$$

Reminder Ekman Dynamics Recall that in a steady wind-driven flow with no horizontal variations in the flow field or density field, the Ekman transport is

$$\int_{-\infty}^{0}(v - v^g)dz = 0 \qquad \int_{-\infty}^{0}(u - u^g)dz = \frac{\tau_y^s}{\rho_0 f} \ ,$$

where τ_y^s is the y-component of the surface stress. (The x-component is assumed to be 0.) (Note that the roles of u and v have been interchanged from the previous lectures.) This depth-integrated result is independent of the vertical viscosity, provided there is a depth where the internal stress is small compared to the surface stress. This feature allows us to test the Ekman transport predictions even though we don't have a full understanding of the details of the mixing processes.

Testing the Theory To test the theory, we need the following:

1. Velocity profiles $(u(z), v(z))$ to sufficient accuracy and vertical resolution.
2. Surface stress τ^s. This is typically found from a bulk formula using wind velocity measurements.
3. Geostrophic velocity, or a way to determine where $\tau = 0$, to separate the boundary layer from the interior flow.
4. Filtering out of high frequency $(1/f)$ velocity variability, since we usually neglect accelerations in the calculation of the Ekman transport.

Observational Tests of the Ekman Transport Relationship The following two studies have been important in verifying the Ekman transport relationship:

- Price, Weller, Schudlich, Science 1987
- Chereskin, JGR 1995

Both took measurements for about 160 days, and integrated down to a boundary layer thickness of about 50m. The plots of measured average transport, compared to theoretical Ekman transport, show excellent agreement (see figures 1, 2).

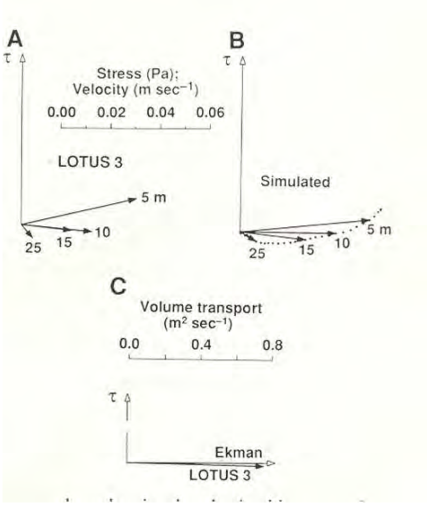

Figure 1: Observed and simulated Ekman spiral (A,B). Measured transport versus theoretical transport (C). (Price and Schudlich (1987))

They also showed the qualitative characteristics of the Ekman spiral, with the mean velocity turning to the right (in the northern hemisphere) and decreasing as depth increases. (Figures 1, 2).

Observations of the Ekman spiral under ice Hunkins (K.Hunkins (1966)) dropped a drogue under ice and measured the drag on it. The drag was used in a force balance to infer the velocity. From this, he obtained a picture of an Ekman spiral below the ice (Figure 3).

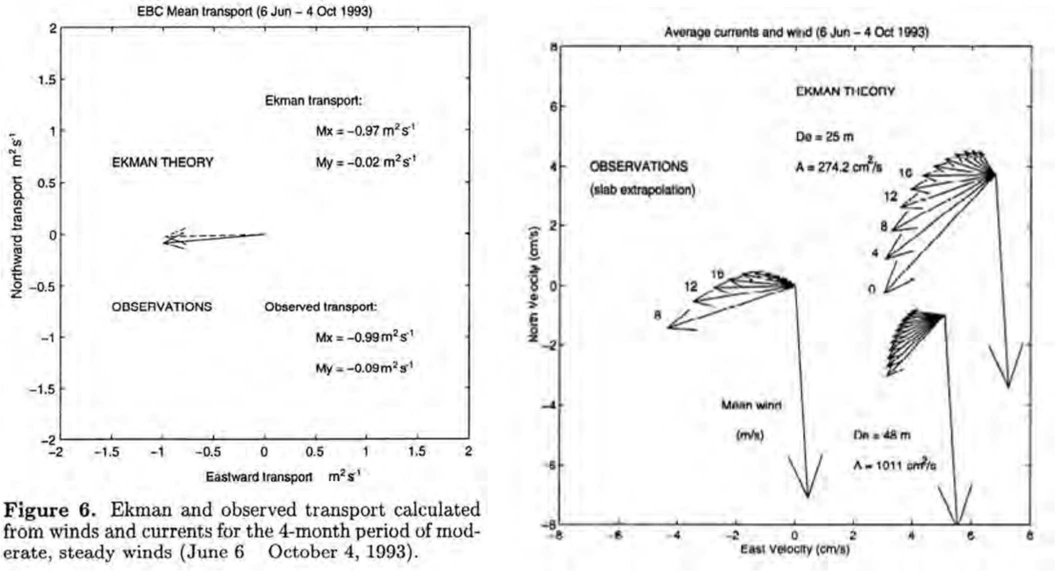

Figure 6. Ekman and observed transport calculated from winds and currents for the 4-month period of moderate, steady winds (June 6 October 4, 1993).

Figure 2: (Chereskin (1995))

Surface Mixed Layer Lentz (Lentz (1992)) measured the depth of the mixed layer and compared it to the wind stress and the depth of the wind-driven flow. He found there was a good correlation between the wind stress and the depth of the mixed layer. The depth of the wind-driven flow also depended on the wind stress, but tended to exceed the mixed-layer depth.

Summary of surface Ekman layer There is convincing evidence of wind-driven transport with the right magnitude and direction, which extends beyond the mixed layer. Note that it is only the *mean* profiles that veer clockwise - the profiles at any instant of time show large fluctuations on storm timescales (1 day) and diurnal timescales. Present research is focused on (a) the character of turbulent mixing in the boundary layer; and (b) the role of surface waves in determining the vertical structure of the flow - these have the additional complication of introducing a non-rigid boundary and wave momentum transfer.

Bottom boundary layer Ekman theory is essentially the same if the bottom is flat, or if the flow is unstratified and the slope is small. However, for stratified flow over a sloping bottom, a buoyancy force comes into play that may dominate the dynamics. Here we give a brief, qualitative description of this buoyancy force - it will be described with more rigor in the next lecture.

Suppose we have a stably stratified flow along a bottom of slope α. Stress on the bottom results in vertical mixing and up- or down-slope Ekman transport (figure 4 left). This flow displaces the isopycnals, and a buoyancy force develops that may oppose the interior pressure gradient (figure 4 center). This buoyancy force reduces v in the bottom boundary layer through the thermal wind balance, $-fv_z = g\rho^b_x/\rho_o$, so the stress on the bottom is reduced. As the boundary layer continues to grow, v decreases at the bottom (figure 4 right). Eventually a steady-state is reached where the bottom stress, and hence the Ekman transport, are both zero, so the isopycnals are displaced no further. At the bottom, the pressure gradient of the interior flow is balanced by the buoyancy force in the boundary layer. The end result is geostrophic flow that just happens to be zero at the

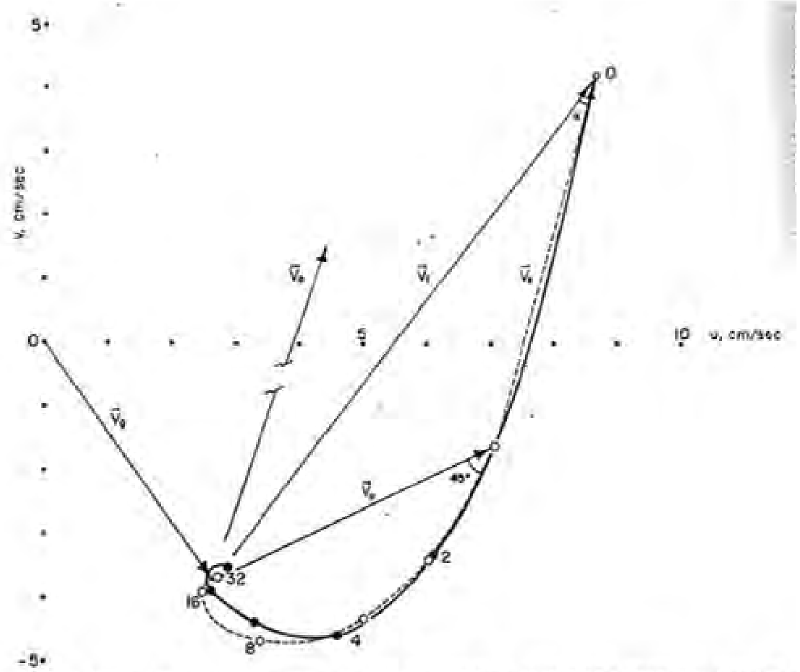

Fig. 7. Comparison between mean observed hodograph for periods 8–13 (solid line and circles) and theoretical curve for surface boundary layer and Ekman layer with $D = 18$ m (dotted line and open circles). Numbers refer to depths in meters below the base of the ice.

Figure 3: (K.Hunkins (1966))

bottom.

If the flow is out of the page and the slope is as in Figure 5, then the Ekman transport is initially down the slope. This advects light fluid under heavy, creating convective instabilities, which enhance mixing, so we expect a thicker boundary layer. If the flow is into the page, then the Ekman transport is initially upslope, advecting heavy fluid under lighter, so we expect a thinner boundary layer because this configuration is convectively stable.

Observations of the bottom boundary layer There are relatively few observational studies of the bottom boundary layer. References (Weatherly and Martin (1978)), (Trowbridge and Lentz (1991)), (MacCready and Rhines (1991)), (MacCready and Rhines (1993)), (Garrett and Rhines (1993)) are some of the main ones. Here we summarize results from a small number of studies.

Lentz and Trowbridge (Lentz and Trowbridge (1991)) tested the hypothesis that the thickness of the boundary layer across a sloping bottom should depend on the direction of the flow, using data taken from the Northern California shelf. Because of the turbulence created by the strong shear near the sea floor, the bottom boundary layer tends to be well-mixed, with nearly homogeneous temperature and density profiles. This allowed them to characterize the height of the bottom boundary layer as the place where the temperature deviated from the temperature at the sea floor by more than a given amount. In their experiment, they characterized the height of the boundary layer as the place where $|T - T_b| < 0.05$°C. They found a good correlation between the direction of the flow and the thickness of the boundary layer. Figure 6 (left) shows that the estimated boundary layer height is larger when the flow is downwelling, and smaller when the flow is upwelling. Figure

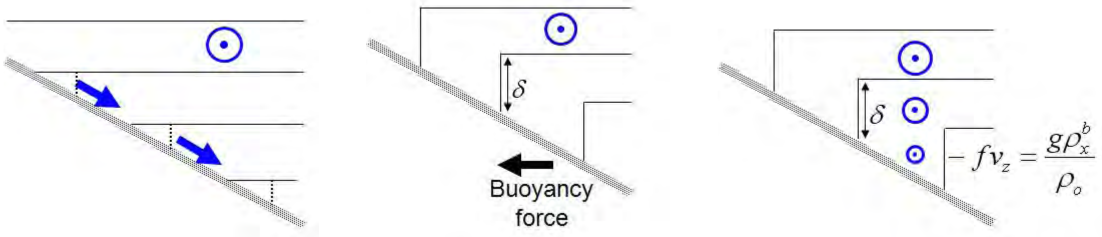

Figure 4: A bottom that is sloping with respect to the isopycnals introduces a buoyancy force in the boundary layer that may be important to the dynamics.

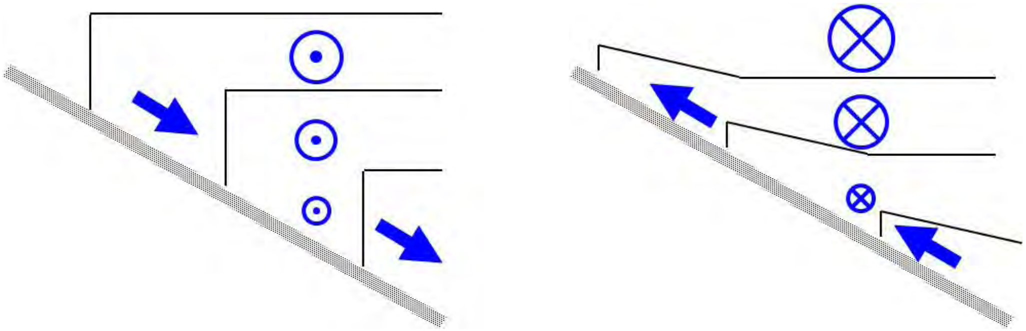

Figure 5: Downslope Ekman transport produces a thick boundary layer (left), while upslope Ekman transport produces a thinner layer (right).

6 (right) plots this correlation.

Moum et al (Moum and Kosro (2004)) looked for convectively driven mixing in the bottom boundary layer, which should be present if the flow is downwelling. Their measurements showed an unstable density gradient near the bottom, typical of convection. The slope was in good agreement with the Law of the Wall scaling (equation (2)).

Many previous observational studies have noted a qualitative 'Ekman-like' veering of the velocity field near the bottom. However, this needs to be looked at more quantitatively. Two questions of interest are: (1) Does the Ekman balance hold? (2) If not, are the cross-isobath buoyancy forces significant in the cross-isobath momentum balance? The bottom boundary layer momentum balance has been tested in two observational studies.

(Trowbridge and Lentz (1998)) looked at 2 years of data off the Northern California shelf. They measured the transport with current meters, and estimated the stress using the Law of the Wall (2). The buoyancy force was estimated from temperature measurements. As in other studies, the boundary layer was defined to be the place where $|T - T_b| < 0.05$.

Because they had the appropriate data, they included acceleration terms in their calculations of the terms in the momentum balances. The equations they used are

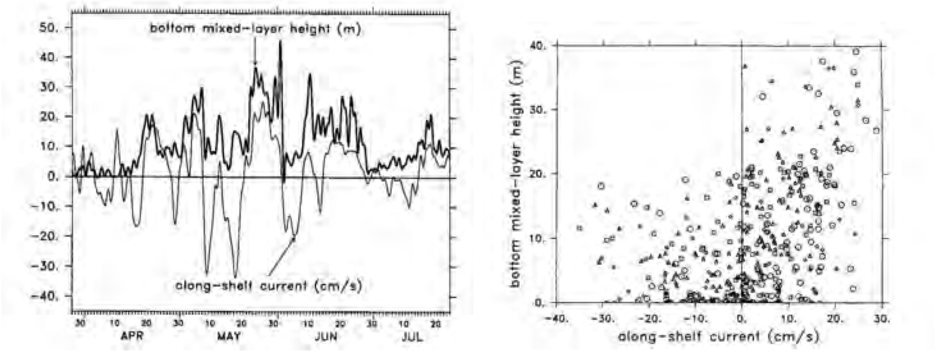

Figure 6: Left: The thickness of the bottom boundary layer (the bottom mixed-layer height) is greater when the along-shelf current is positive, inducing a downwelling Ekman flux, than when it is negative, with an induced upwelling flux. Right: Bottom mixed-layer height versus along-shelf current. (Lentz and Trowbridge (1991))

$$\rho_0 \int_0^\delta \left[\frac{\partial u}{\partial t} - \left(\frac{\partial u}{\partial t} \right)_\delta \right] dz - \underbrace{\rho_0 f \int_0^\delta (v - v_\delta) dz}_{\text{Ekman transport}} = \underbrace{\beta g \left[\frac{\delta^2}{2} \frac{\partial T}{\partial x} + \alpha \int_0^\delta (T - T_\delta) dz \right]}_{\text{buoyancy force}} - \tau_x^b$$

$$\rho_0 \int_0^\delta \left[\frac{\partial v}{\partial t} - \left(\frac{\partial v}{\partial t} \right)_\delta \right] dz + \underbrace{\rho_0 f \int_0^\delta (u - u_\delta) dz}_{\text{Ekman transport}} = \underbrace{\beta g \frac{\delta^2}{2} \frac{\partial T}{\partial y}}_{\text{buoyancy force}} - \tau_y^b$$

If they neglected the buoyancy term, they found a poor agreement between the wind stress and Ekman transport (Figure 7 top), particularly during large boundary layer transport events. If the buoyancy force was included, the agreement was better (Figure 7 middle), showing that the buoyancy term is as large as the bottom stress, particularly during downwelling when the bottom mixed layer is thick.

(Perlin and Klymak (2005)) looked at the momentum balance in transects of the Oregon shelf. They measured the cross-shelf bottom boundary layer velocity u_b and compared it to the Ekman velocity estimated from Ekman balance: $u_{EK} = \frac{\tau^{by}}{\rho_0 f \delta^E}$. Although they neglected the buoyancy force, they found a good agreement between these velocities in the moored observations (Figure 8)

These two studies show that the current observational evidence supporting either Ekman balance, or the importance of the buoyancy force in the bottom boundary layer, is very limited.

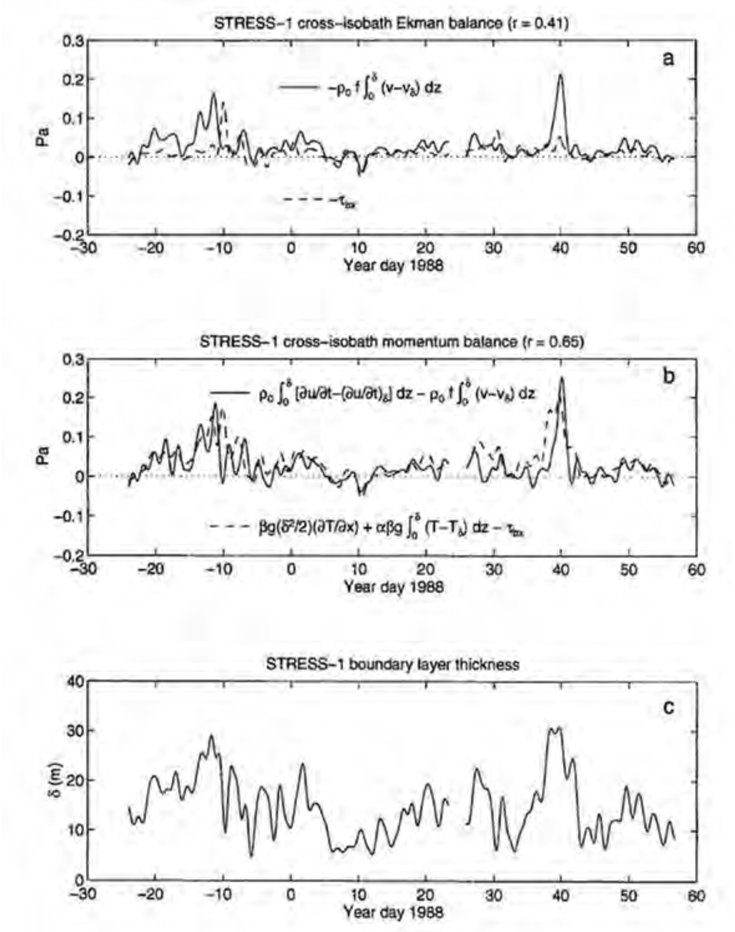

Figure 7: Wind stress (dotted) and Ekman transport (solid), neglecting the buoyancy term (top) and including the buoyancy term (middle) (Trowbridge and Lentz (1998))

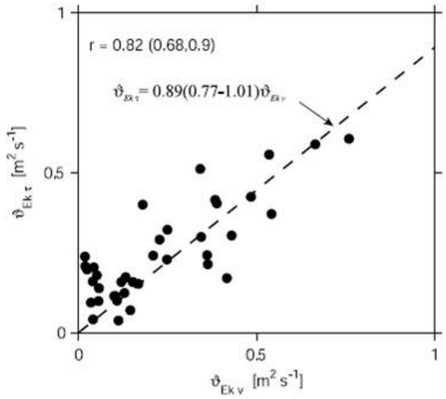

Figure 14. Comparison of the transport computed by vertical integration of the velocity perpendicular to that at height D_{Ek} using moored velocity data (3 month time series), and the Ekman transport computed from bottom stress using a drag coefficient and the current speed at 20 m.

Figure 8: (Perlin and Klymak (2005))

References

T. K. Chereskin. Direct evidence for an ekman balance in the california current. *J. Geophys. Res.*, 13:18,261 –18,269, 1995.

P. MacCready Garrett, C. and P. Rhines. Boundary mixing and arrested ekman layers: rotating stratified flow near a sloping boundary. *Ann. Rev. Fluid Mech.*, 25:291–323, 1993.

K.Hunkins. Ekman drift currents in the arctic ocean. *Deep Sea Res.*, 13:607–620, 1966.

S. J. Lentz. The surface boundary layer in coastal upwelling regions. *J. Phys. Oceanogr.*, 22: 1517–1539, 1992.

S. J. Lentz and J. H. Trowbridge. The bottom boundary layer over the northern california shelf. *J. Phys. Oceanogr.*, 21:1186–1201, 1991.

P. MacCready and P. B. Rhines. Buoyant inhibition of ekman transport on a slope and its effect on stratified spin-up. *J. Fluid Mech.*, 223:631–661, 1991.

P. MacCready and P. B. Rhines. Slippery bottom boundary layers on a slope. *J. Phys. Oceanogr.*, 23:5–22, 1993.

O. S. Madsen. A realistic model of the wind-induced ekman boundary layer. *J. Phys. Oceanogr.*, 7:248–255, 1977.

A. Perlin J. M. Klymak M. D. Levine T. Boyd Moum, J. N. and P. M. Kosro. Convectively driven mixing in the bottom boundary layer. *J. Phys. Oceanogr.*, 34:2189–2202, 2004.

J. N. Moum Perlin, A. and J. M. Klymak. Response of the bottom boundary layer over a sloping shelf to variations in alongshore wind. *J. Geophys. Res.*, 110:C10S09,doi:10.1029/2004JC002,500, 2005.

R. A. Weller Price, J. F. and R. R. Schudlich. Wind-driven ocean currents and ekman transport. *Science*, 238:1534–1538, 1987.

J. H. Trowbridge and S. J. Lentz. Asymmetric behavior of an oceanic boundary layer above a sloping bottom. *J. Phys. Oceanogr.*, 21:1171–1185, 1991.

J. H. Trowbridge and S. J. Lentz. Dynamics of the bottom boundary layer on the northern california shelf. *J. Phys. Oceanogr.*, 28:2075–2093, 1998.

G. L. Weatherly and P. J. Martin. On the structure and dynamics of the oceanic bottom boundary layer. *J. Phys. Oceanogr.*, 8:557–570, 1978.

Boundary Layers: Sloping bottoms in a stratified, rotating fluid

Lecture 5 by Iva Kavčič

In oceanic coastal regions, e.g. on the shelf regions between the coast and the deep ocean, the bottom generally slopes and the fluid is stratified.
We have already seen the way the thermal boundary layers on vertical walls can control the interior flow and how the Ekman layers on horizontal boundaries can do the same for rotating fluids. Sloping boundaries are a type of a hybrid of these two.

1 The model

We begin with the schematic of the bottom boundary layer (hereafter: BL), shown in Fig. 1. Fluid is stratified with the density gradient $\partial\rho/\partial z'$. Here z' denotes the direction of the true vertical (Fig. 2), aligned with the direction of gravity, g, and planetary rotation, Ω. The bottom is in direction y of the slant coordinate frame (y, z), rotated counterclockwise with the angle θ with respect to the reference coordinate frame (y', z'), (Fig. 2). The density gradient, $\partial\rho/\partial z'$, produces the buoyancy

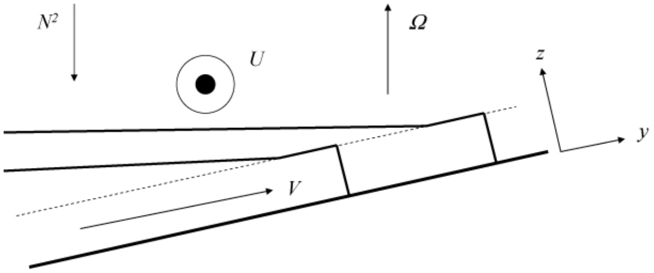

Figure 1: A schematic of the bottom BL, upwelling case

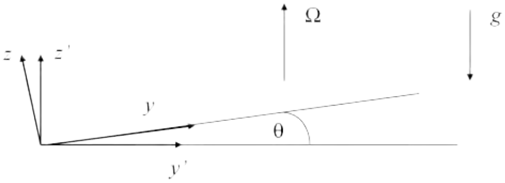

Figure 2: The reference, (y', z'), and the slant coordinate frame, (y, z)

force in the true vertical, with the frequency, (Fig. 1),

$$N^2 = -\frac{g}{\rho}\frac{\partial \rho}{\partial z'}. \tag{1}$$

As in the linear Ekman layer problem, the flux is to the left (from high to low pressure) of the along isobar flow component U (Fig. 1). Here this results in canceling of the density gradient component perpendicular to the bottom ($\partial\rho/\partial z$) due to the upslope transport of the heavier fluid by the cross isobar flow component V, and formation of the mixed BL (Fig. 1). The density gradient component along the slope ($\partial\rho/\partial y$) can be derived as

$$\frac{\triangle\rho}{\triangle z'} = \frac{\triangle\rho}{\triangle y \sin\theta}, \tag{2}$$

$$g\frac{\partial\rho}{\partial y} = -\rho N^2 \sin\theta. \tag{3}$$

From (3) we see that fluid moving up the slope a distance $\triangle y = \triangle z'/\sin\theta$, (Fig. 3), will produce a density anomaly

$$\triangle\rho = -\frac{1}{g}N^2\rho_0 \sin\theta\triangle y. \tag{4}$$

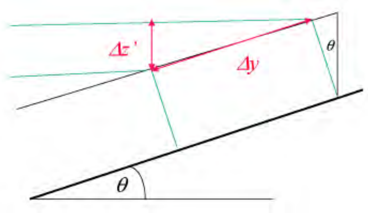

Figure 3: The distances in reference and slant coordinate frame

From (3) and the thermal wind relation

$$f\frac{\partial U}{\partial z} = \frac{g}{\rho}\frac{\partial\rho}{\partial y}, \tag{5}$$

we see that over a depth of the bottom BL of the order

$$H = -\frac{fU}{N^2\sin\theta} \tag{6}$$

it would be possible to adjust the speed of the current to zero without Ekman layers and their dissipation, i.e. currents could flow long distances without decay. Here f is the Coriolis parameter, $f = 2\Omega\cos\theta \approx 2\Omega$, for θ small.

Following MacCready and Rhines, MacCready and Rhines (1993), we write the equations in the slant coordinate frame (Fig. 2):

$$v = v'\cos\theta + w'\sin\theta \tag{7}$$

$$w = -v'\sin\theta + w'\cos\theta \tag{8}$$

Far from the lower boundary the temperature is:

$$T_\infty = \triangle T_v z'/D, \tag{9}$$

with $\triangle T_v$ being the mean temperature difference in the true vertical, z' (Fig. 2). The buoyancy frequency now can be defined as:

$$N = \left(\frac{g\alpha\triangle T_v}{D}\right)^{1/2}. \tag{10}$$

The temperature equation is then:

$$\begin{aligned} T &= \triangle T_v z'/D + \vartheta(y,z) && (11)\\ &= \triangle T_v (z\cos\theta + y\sin\theta)/D + \vartheta(y,z), && (12)\end{aligned}$$

where the $\vartheta(y,z)$ is the temperature perturbation. We assume that $\vartheta \to 0$ as $z \to \infty$.

2 The steady-state solution

As in the case of stratified fluid, we investigate the steady-state behavior of the flow in the BL and interior. Here we simplify the problem by searching for the solutions independent of y, i.e. only functions of z. As $z \to \infty$, $u \to U$, and a constant v is independent of y. The above, together with the assumption of incompressibility, gives $w \equiv 0$. Furthermore, nonlinear terms in equations vanish identically.

The governing equations of motions then are:

$$\begin{aligned} 2\Omega\cos\theta u &= -\frac{1}{\rho_0}\frac{\partial\tilde{p}}{\partial y} + Av_{zz} + b\sin\theta, && (13)\\ -2\Omega\cos\theta v &= Au_{zz}, && (14)\\ 2\Omega\sin\theta u &= -\frac{1}{\rho_0}\frac{\partial\tilde{p}}{\partial z} + b\cos\theta, && (15)\\ vN^2\sin\theta &= \kappa b_{zz}. && (16)\end{aligned}$$

Here A is the momentum mixing coefficient, κ is the thermal diffusivity and $\tilde{p}(y,z)$ is the pressure perturbation. Buoyancy perturbation, b, is given by

$$b = \alpha g\vartheta, \tag{17}$$

where α is the coefficient of thermal expansion, and Coriolis parameter is $f = 2\Omega\cos\theta$.

The boundary conditions (hereafter: BC) at the lower boundary $(z = 0)$ are:

$$\begin{aligned} u(z=0) &= 0, && (18)\\ v(z=0) &= 0, && (19)\\ b_z(z=0) &= -N^2\cos\theta. && (20)\end{aligned}$$

Here (20) represents the insulating BC at $z = 0$.

Since u, v and b are independent of y, derivation of (15) with respect to y gives:

$$\partial^2\tilde{p}/\partial y\partial z = 0. \tag{21}$$

Then, from (13) and (14) we derive the boundary layer equation:

$$-\frac{f^2}{A}v = Av_{zzzz} + b_{zz}\sin\theta. \tag{22}$$

If the fluid were homogeneous ($\partial\rho/\partial z' = 0$) or if the bottom were flat ($\theta = 0$) we would recover the Ekman layer problem. Using the thermal equation (16) to eliminate b in favor of v yields:

$$\begin{aligned} v_{zzzz} + 4q^4 v &= 0, & (23)\\ q^4 &= \frac{1}{4}\left[\frac{f^2}{A^2} + \frac{N^2}{A\kappa}\sin^2\theta\right]. & (24)\end{aligned}$$

The general form of the solution of (23) is $v \sim \exp(rz)$, which gives

$$r_{1,\dots,4} = \pm(1 \pm i)\,q. \tag{25}$$

Since it is not physical for the solutions to grow exponentially in space, we keep the ones with $Re\,(r) < 0$. Their linear combination is also the solution of (23):

$$v = C\exp(-qz)\cos(qz) + B\exp(-qz)\sin(qz) \tag{26}$$

From (24) we can see that if the bottom is flat ($\theta = 0$) the BL scale is the Ekman layer thickness. If the bottom is vertical, i.e. if $\theta = \pi/2$, the scale is the buoyancy layer thickness. Applying the BC (19) gives $C = 0$. Then, from the thermal equation (16) follows

$$b_z = -B\frac{N^2\sin\theta}{2q\kappa}\exp(-qz)\left(\cos(qz) + \sin(qz)\right), \tag{27}$$

and from (14)

$$u = -\frac{f}{2Aq^2}B\exp(qz)\cos(qz) + U_\infty. \tag{28}$$

The insulating BC, (20), gives $B = 2q\kappa\cot\theta$, while the non slip condition on u, (18), yields

$$U_\infty = -\frac{f}{Aq}\kappa\cot\theta, \tag{29}$$

giving the solution for u

$$u = U_\infty\left[1 - \exp(-qz)\cos(qz)\right]. \tag{30}$$

Therefore, we see that the flow at infinity is not arbitrary - it is the part of the solution. Moreover, equation (29) gives the two limiting cases for u on horizontal (for $\theta = 0$, $U_\infty \to \infty$) and vertical ($U_\infty = 0$ for $\theta = \pi/2$) bottom.

Similarly to the linear Ekman problem, only the frictionally driven flow up the slope (v component) contributes to the total flux (stream function)

$$\Psi(z) = \int_0^z v\,dz = \kappa\cot\theta\left\{1 - \exp(qz)\left[\cos(qz) + \sin(qz)\right]\right\}. \tag{31}$$

The total, as $z \to \infty$, is:

$$\Psi(\infty) = \kappa\cot\theta = \frac{Aq}{f}U_\infty. \tag{32}$$

This also follows directly from the integral of the thermal equation (16), together with the insulating BC (20).
Now, we see that the boundary layer controls the interior through the dependence of the U_∞ on the thermal diffusion and the slope (29). This result, while at first glance non intuitive, is really just a manifestation of the control mechanisms we have already met in our discussion of the linear flow in the cylinder, although here in a more extreme form.
Unlike in the linear Ekman layer case, now we are not any more able to drive the system as we would like and establish some arbitrary equilibrium velocity along the isobaths. We continue our presentation by investigating the possibility of initially specifying a different far field along shore flow, and monitor its evolution in time. Further reference can be found in the work of MacCready, Rhines and Garrett, Garrett and Rhines (1993).

3 The slow diffusion equation

We now derive the "slow diffusion equation" (hereafter: SDE) from the time-dependant system of driving equations (13)-(16):

$$\begin{aligned} \frac{\partial v}{\partial t} + 2\Omega\cos\theta u &= -\frac{1}{\rho_0}\frac{\partial \tilde{p}}{\partial y} + Av_{zz} + b\sin\theta, && (33)\\ \frac{\partial u}{\partial t} - 2\Omega\cos\theta v &= Au_{zz}, && (34)\\ 2\Omega\sin\theta u &= -\frac{1}{\rho_0}\frac{\partial \tilde{p}}{\partial z} + b\cos\theta, && (35)\\ \frac{\partial b}{\partial t} + vN^2\sin\theta &= \kappa b_{zz}. && (36) \end{aligned}$$

As in the case of Ekman layer in a stratified fluid, we apply the scaling: $y = Ly',\ z = Dz',\ t = \frac{D^2}{\kappa}t'$, where L, D and D^2/κ are the characteristic length, depth ant time scales, respectively, and y', z' and t' are the non-dimensional variables. The velocity components are scaled with $(u, v) = U(u', v')$, pressure is scaled with respect to the geostrophic balance, $\tilde{p} = \rho_0 fUL\tilde{p}'$, and buoyancy with $b = \frac{fUL}{D}b'$.
After defining the BL thickness as $\delta = D/L$ and dropping the primes, the dimensional system (33)-(36) can be written in the non-dimensional form:

$$\begin{aligned} \frac{E}{2\sigma}\frac{\partial v}{\partial t} + u &= -\frac{\partial \tilde{p}}{\partial y} + \frac{E}{2}v_{zz} + b\frac{\sin\theta}{\delta}, && (37)\\ \frac{E}{2\sigma}\frac{\partial u}{\partial t} - v &= \frac{E}{2}u_{zz}, && (38)\\ -\delta\tan\theta u &= -\frac{\partial \tilde{p}}{\partial z} + b\cos\theta, && (39)\\ \frac{E}{2\sigma}\frac{\partial b}{\partial t} + \frac{\sin\theta}{\delta}Sv &= \frac{E}{2\sigma}b_{zz}, && (40) \end{aligned}$$

where $f = 2\Omega\cos\theta$ is the Coriolis parameter, $E = \frac{2A}{fD^2}$ is the Ekman number, and $S = \frac{N^2\delta^2}{f^2}$ is the stability parameter.

In the interior (as in the case of stratified fluid before) it is reasonable to neglect friction and to assume stationarity. Also, $\tan\theta$ is small. Therefore, the system (37)-(40) reduces to:

$$\begin{aligned} u_I &= -\frac{\partial p_I}{\partial y} + b_I \frac{\sin\theta}{\delta}, \qquad (41) \\ b_I \cos\theta &= \frac{\partial p_I}{\partial z}. \qquad (42) \end{aligned}$$

Eliminating v between (38) and (40) yields:

$$\frac{1}{\sigma}\frac{\partial}{\partial t}\left[u_I + \frac{\delta}{S\sin\theta} b_I\right] = \frac{1}{2}\frac{\partial^2}{\partial z^2}\left[u_I + \frac{\delta}{\sigma S\sin\theta} b_I\right]. \qquad (43)$$

Eliminating the pressure in (41) and (42) and noting that b is independent of y gives:

$$\frac{\partial u_I}{\partial t} = \frac{\partial b_I}{\partial z}\left[\frac{\sin\theta}{\delta}\right], \qquad (44)$$

and the SDE is then:

$$\frac{\partial}{\partial t}\left(\frac{\partial u_I}{\partial z}\right) = \sigma \frac{1 + \frac{\delta^2}{\sigma S \sin^2\theta}}{1 + \frac{\delta^2}{S\sin^2\theta}} \frac{\partial^2}{\partial z^2}\left(\frac{\partial u_I}{\partial z}\right). \qquad (45)$$

We introduce the modified stability parameter, S_*, as:

$$S_* \equiv S\frac{\sin^2\theta}{\delta^2} = \frac{N^2}{f^2} sin^2\theta. \qquad (46)$$

The effective diffusion coefficient then becomes:

$$\mu_{diff} = \sigma\left(\frac{\frac{1}{\sigma} + S_*}{1 + S_*}\right), \qquad (47)$$

in the non-dimensional form, whereas its dimensional form is given with:

$$(\mu_{diff})_{dimensional} = A\left(\frac{\frac{1}{\sigma} + S_*}{1 + S_*}\right). \qquad (48)$$

From both (47) and (48) we can see that if $\sigma > 1$, the diffusion coefficient would be smaller than in the absence of stratification.

Now, if u is independent of z and t as $z \to \infty$, we obtain the final form of the SDE:

$$\frac{\partial u_I}{\partial t} = mu_{diff}\frac{\partial^2 u_I}{\partial z^2}. \qquad (49)$$

To obtain the BC for SDE we need to consider the BL at sloping bottom, i.e. find BC such as to match the boundary.

We introduce the BL coordinate:

$$\zeta = zE^{-1/2}, \ \lim_{z\to 0}\zeta = 0. \qquad (50)$$

Then (labeling correction variables with "e") the BL equations for correction functions are:

$$\begin{aligned} u_e &= -\frac{\partial p_e}{\partial y} + \frac{1}{2} v_{z\zeta\zeta} + b_e \frac{\sin\theta}{\delta}, && (51) \\ -v_e &= \frac{1}{2} u_{e\zeta\zeta}, && (52) \\ -\delta \tan\theta u_e &= -\frac{1}{E^{1/2}} \frac{\partial p_e}{\partial \zeta} + b_e \cos\theta, && (53) \\ \frac{\sin\theta}{\delta} v_e &= \frac{1}{2\sigma S} b_{e\zeta\zeta}. && (54) \end{aligned}$$

These are the same steady equations, (13)-(16), and BC, (18)-(20) we dealt with before, yielding the equation for v_e:

$$\begin{aligned} \frac{\partial^4 v_e}{\partial \zeta^4} + 4 q_e^4 v_e &= 0, && (55) \\ q_e^4 &= \left[1 + \sigma S \frac{\sin^2\theta}{\delta^2}\right]. && (56) \end{aligned}$$

Like for the steady-state case, the BL solution is then:

$$\begin{aligned} v_e &= C \exp(-q_e\zeta) \cos(q_e\zeta) + B \exp(-q_e\zeta) \sin(q_e\zeta) && (57) \\ b_e &= \sigma S \frac{\sin\theta}{\delta} \left\{\exp(-q_e\zeta)\left[(C-B)\sin(q_e\zeta) - (C+B)\cos(q_e\zeta)\right]\right\} && (58) \\ u_e &= \frac{1}{q_e^2}\left[C \exp(-q_e\zeta)\sin(q_e\zeta) - B\exp(-q_e\zeta)\cos(q_e\zeta)\right] && (59) \\ & && (60) \end{aligned}$$

Matching conditons between BL and the interior:

$$\begin{aligned} u_I + u_e &= 0 && (61) \\ v_I + v_e &= 0 && (62) \end{aligned}$$

Here: $v_I \sim O(E) \rightarrow B = 0$, and

$$\frac{\partial b_I}{\partial z} + E^{-1/2} \frac{\partial b_e}{\partial \zeta} = -\frac{S}{\varepsilon} \cos\theta \rightarrow A = 0, \tag{63}$$

where $\varepsilon = \frac{U}{fL}$.
The frictional BL vanishes to the lowest order. Also, u_I must satisfy the no-slip BC at $z = 0$, giving us the solution for u_I:

$$u_I = U_\infty \frac{2}{\sqrt{\pi}} \int_0^{\zeta/\sqrt{\mu_{diff} t}} \exp\left(-\varphi^2\right) d\varphi \tag{64}$$

Next order BL solution still has $V_e = 0 \Rightarrow A = 0$.
BL contribution to buoyancy flux yields:

$$B = -\frac{\delta\alpha}{2\sigma S \sin\theta} \left[\frac{S}{\varepsilon}\cos\theta + \frac{\delta U_\infty}{\sin\theta\sqrt{\pi\mu_{diff} t}}\right] \tag{65}$$

The long time solution in BL is obtained as $t \to \infty$:

$$b_e = -E^{1/2} \frac{S}{\varepsilon\alpha} \cos\theta \exp\left(-\alpha\zeta\right) \cos\left(\alpha\zeta\right), \tag{66}$$

which is the steady state solution (in non-dimensional form) already attained.
Hence it is possible to consider arbitrary interior flows but, at least with the simple physics here, the boundary layer control eventually expunges the along isobath flow and yields an asymptotically weak frictional boundary layer. This, in one sense resolves the conundrum posed by the steady boundary layer solution in which the interior flow and the cross-shelf flow depended only on the stratification and the vertical thermal diffusion coefficient. Nevertheless, the solution presented here eventually approaches that very constrained solution.

References

P. MacCready Garrett, C. and P. B. Rhines. Boundary mixing and arrested ekman layers: Rotating stratified flow near a sloping boundary. *Annu. Rev. Fluid Mech.*, 25:291–323, 1993.

P. MacCready and P. B. Rhines. Slippery bottom boundary layers on a slope. *J. Phys. Ocean.*, 23: 5–22, 1993.

Stress Driven Flow with a Sloping Bottom

Lecture 6 by Frédéric Laliberté

In the preceding chapter, we investigated an isolated Ekman boundary layer for a sloping bottom in a stratified, rotating fluid. In this chapter, we intend to reconnect both the surface, stress driven boundary layer with a gently sloping bottom boundary layer.

1 Upwelling

The most physically stable case is without doubt the one leading to upwelling, a displacement that does not lead to a local inversion in the stratification. Indeed, if a volume of fluid is pushed upward along a sloping bottom, the only result in a hydrostatic point of view is a local increase in stratification, which negatively feedbacks on the ability of this volume to continue to move upward. So, one can easily argue that such a water movement must be relatively slow and strongly stratified near the bottom boundary. A flow with both of these qualities, one can argue, can only have (and will probably have) limited turbulence. Assuming that it is the case, one can thus start with the hypothesis that the flow will be laminar and smooth everywhere, including close to the boundary. This is a very desirable simplification that makes the upwelling case more physically tractable and intuitive, a path we will pursue first.

Oceanographically speaking, the problem we want to model is the upwelling on the continental shelf due an along shore wind stress resulting in a surface mass divergence. However, for our treatment to remain valid we must be sufficiently far from the shore so that we do not have to worry about our laminar bottom boundary layer merging with the surface Ekman layer. The schematic of the problem can be found in fig. 1. In this figure, the surface boundary layer transport results in a Coriolis force balancing the along shore wind stress τ. Again, we will be working in a rotated coordinate system so that the bottom slope corresponds to $z = 0$, i.e. the z axis is not parallel to the gradient of the geopotential (the gravitational force) but is instead perpendicular to the bottom.

1.1 Boussinesq equations

In order to study this problem without being systematically confusing which coordinate system is used, we will carefully restate the dimensional incompressible Boussinesq equations. If we use the usual cartesian coordinates with the z-coordinate parallel to the gravity, we have (for a reference see, for example, Vallis (2006)):

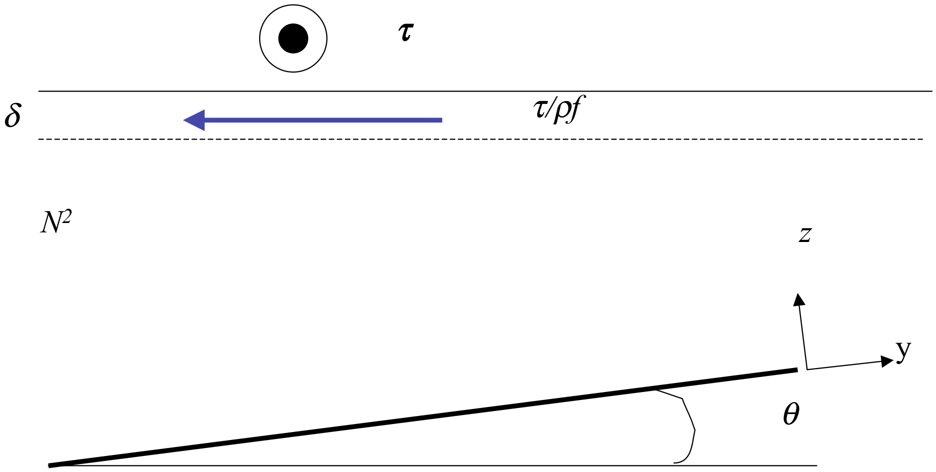

Figure 1: Idealized upwelling schematics on a sloping shelf away from shore. Notice the rotated coordinates

$$\partial_t \vec{u}' + \vec{u}' \cdot \nabla' \vec{u}' + f\hat{k}' \times \vec{u}' = -\frac{1}{\rho_0}\nabla' p + b\hat{k}' + \nabla' \cdot (\mathbf{A}'\nabla\vec{u}'), \tag{1}$$

$$\nabla' \cdot \vec{u}' = 0, \tag{2}$$

$$\partial_t b + \vec{u}' \cdot (\nabla' b + N^2\hat{k}') = \nabla' \cdot (\boldsymbol{\kappa}'\nabla' b). \tag{3}$$

where $b = -g\tilde{\rho}/\rho_0$ and $N^2 = -g\partial_{z'}\bar{\rho}/\rho_0$, with $\rho = \rho_0 + \bar{\rho}'(z') + \tilde{\rho}'(\mathbf{x}', t)$.

1.2 Approximation for the sloping bottom

In the previous equations we have allowed the *eddy viscosity* $\mathbf{A}'$ and the *eddy diffusivity*, $\boldsymbol{\kappa}'$ to be anisotropic.

The next step is to apply these three approximations:

1. The flow is stationary, all the time derivatives vanish.
2. We linearize the flow about $\vec{u}' = 0$.
3. We rotate the axis in order to have the y axis parallel to the bottom slope, assuming the slope is extremely gentle. We will clarify later what it means for a slope to be small.

The resulting system of equations is

$$f\hat{n} \times \vec{u} = -\frac{1}{\rho_0}\nabla p + b\hat{n} + \nabla \cdot (\tilde{\mathbf{A}}\nabla\vec{u}), \tag{4}$$

$$\nabla \cdot \vec{u} = 0, \tag{5}$$

$$\vec{u} \cdot (\nabla b + N^2\hat{n}) = \nabla \cdot (\tilde{\boldsymbol{\kappa}}\nabla b). \tag{6}$$

where all the quantities are now considered in the tilted frame and $\hat{n} = R\hat{k}'$, $\mathbf{A} = R\mathbf{A}'R^T$ and $\boldsymbol{\kappa} = R\boldsymbol{\kappa}'R^T$. These are simply the rotated values for the anisotropy vectors/tensors.

$$R = \begin{pmatrix} 1 & 0 & 0 \\ 0 & \cos\theta & \sin\theta \\ 0 & -\sin\theta & \cos\theta \end{pmatrix}, \quad \hat{n} = \begin{pmatrix} 0 \\ \sin\theta \\ \cos\theta \end{pmatrix}. \tag{7}$$

The anisotropic mixing coefficients will be assumed to be diagonal in the flow interior:

$$\mathbf{A}' = \begin{pmatrix} A_h & 0 & 0 \\ 0 & A_h & 0 \\ 0 & 0 & A_v \end{pmatrix}, \quad \boldsymbol{\kappa}' = \begin{pmatrix} \kappa_h & 0 & 0 \\ 0 & \kappa_h & 0 \\ 0 & 0 & \kappa_v \end{pmatrix}. \tag{8}$$

To obtain these tensors in the tilted frame we just have to apply the transformation, yielding:

$$\mathbf{A} = \mathbf{A}' + (A_v - A_h)\sin\theta\mathbf{O}, \quad \boldsymbol{\kappa} = \boldsymbol{\kappa}' + (\kappa_v - \kappa_h)\sin\theta\mathbf{O}. \tag{9}$$

where the matrix $\mathbf{O}$ is given by:

$$\mathbf{O} = \begin{pmatrix} 0 & 0 & 0 \\ 0 & \sin\theta & \cos\theta \\ 0 & \cos\theta & -\sin\theta \end{pmatrix} \tag{10}$$

We will further assume that the motion is *mostly independent of the x-x' coordinates* so that we can neglect all the x derivatives.

The final set of equations reduces to

$$-fv\cos\theta + fw\sin\theta = \nabla\cdot(\mathbf{A}\nabla u), \tag{11}$$

$$fu\cos\theta = -\frac{1}{\rho_0}\partial_y p + b\sin\theta + \nabla\cdot(\mathbf{A}\nabla v), \tag{12}$$

$$-fu\sin\theta = -\frac{1}{\rho_0}\partial_z p + b\cos\theta + \nabla\cdot(\mathbf{A}\nabla w), \tag{13}$$

$$\partial_y v + \partial_z w = 0, \tag{14}$$

$$v(N^2\sin\theta + \partial_y b) + w(N^2\cos\theta + \partial_z b) = \nabla\cdot(\boldsymbol{\kappa}\nabla b). \tag{15}$$

in the tilted frame.

1.3 Top boundary layer

In the gravitational frame, there will be a top boundary layer with pumping vertical velocity given by:

$$w' = w'_e = -\frac{1}{\rho_0 f}\partial_{y'}\tau \tag{16}$$

1.4 The interior solution

Vertical velocity Using the zonal momentum equation in the gravitational frame and non-dimensionalizing it with vertical scale D (of the ocean depth order), horizontal scale L, vertical velocity scale W and horizontal velocity scale U, we obtain,

$$-v'_I = \frac{A_v}{fD^2}(\partial^2_{z'} u'_I + \frac{A_h}{A_v}\left(\frac{D}{L}\right)^2 \partial^2_{y'} u'_I). \tag{17}$$

For geophysical flows, the aspect ratio $\frac{D}{L} \ll 1$ and we can expect, generally, that $A_v > A_h$ (intensified mixing in the vertical, a result of the possibility of isopycnals overturning). Labeling $E := \frac{A_v}{fD^2}$, we see that v'_I is $O(E)$.

With this result, we get from the continuity equation that $\partial_{z'} w'$ must be of $O(E\frac{D}{L}\frac{U}{W})$, implying that $w'_I \equiv w'_e$.

Buoyancy In order to find a suitable expression for the interior buoyancy, we can find a solution such that b is independent of z'. Neglecting v'_I comparatively to w'_I, we obtain the following equation for b:

$$\kappa_h \partial^2_{y'} b_I = w'_I N^2 \tag{18}$$

$$= -\frac{1}{\rho_0 f}\partial_{y'}\tau. \tag{19}$$

Assuming the wind stress disappears far from the shelf region, we obtain

$$\partial_{y'} b_I = -\frac{1}{\rho_0 f}\frac{N^2}{\kappa_h}\tau. \tag{20}$$

Zonal velocity Using the thermal wind balance, $f\partial_{z'} u'_I = -\partial_{y'} b_I$, we get

$$u'_I = \frac{N^2}{\kappa_h}\frac{\tau}{\rho_0 f^2} z' + u'_{I0}(y'). \tag{21}$$

Bottom buoyancy diffusive flux The flux perpendicular to the bottom boundary can be written as

$$\mathcal{F}_z = -\hat{k}\cdot(\boldsymbol{\kappa}\nabla b) = -\hat{k}\cdot(\tilde{\boldsymbol{\kappa}}\nabla' b). \tag{22}$$

What we want to do is to recast the insulated boundary condition, $b_{z'} = -N^2\cos\theta$ as a boundary condition on the perpendicular flux, $\mathcal{F}_z$. This yields,

$$(\mathcal{F}_z)_{\text{ins}} = (\kappa_v \cos^2\theta - \kappa_h \sin^2\theta)N^2 \approx \kappa_v \cos\theta N^2. \tag{23}$$

to $O(\theta^2)$, where we have assumed that $\kappa_v \gg \kappa_h \cot^2(\theta)$. This is the condition of smallness required for θ.

Next, we want to find the contribution to the perpendicular flux by the interior solution:

$$(\mathcal{F}_z)_I = -\frac{\tau}{\rho_0 f}\sin\theta N^2. \tag{24}$$

The boundary condition should be

$$(\mathcal{F}_z)_{\text{tot}} = (\mathcal{F}_z)_{\text{ins}}. \tag{25}$$

which can only be satisfied, in general, with the boundary layer contribution.

1.5 Bottom boundary layer

As seen previously, when we had only a bottom layer, we can reduce the problem to

$$\partial_z^4 v_b + \frac{4}{l^4} v_b = 0, \tag{26}$$

where $l^{-4} = \frac{f^2}{4A_v^2}\left[1 + \frac{N^2 \sin^2\theta}{f^2 \kappa_v / A_v}\right]$.

Thus,

$$v_b = e^{-\frac{z}{l}}[A\cos(\frac{z}{l}) + B\sin(\frac{z}{l}], \tag{27}$$

$$u_b = \frac{f}{A_v}\frac{l^2}{2}e^{-\frac{z}{l}}[A\sin(\frac{z}{l}) - B\cos(\frac{z}{l}], \tag{28}$$

$$\partial_z b_b = -\frac{N^2}{2\kappa_v}\delta\sin\theta e^{-\frac{z}{l}}[A(\cos(\frac{z}{l}) - \sin(\frac{z}{l})) + B(\cos(\frac{z}{l}) + \sin(\frac{z}{l}))], \tag{29}$$

$$w_b = \frac{l}{2}e^{-\frac{z}{l}}[\partial_y A(\cos(\frac{z}{l}) - \sin(\frac{z}{l})) + \partial_y B(\cos(\frac{z}{l}) + \sin(\frac{z}{l})) + \sin(\frac{z}{l}))]. \tag{30}$$

1.6 Matching Solutions

In order to determine the integration constants, we need the interior solutions plus the boundary corrections to add up and satisfy the no-slip boundary condition. The interior fields at the bottom boundary yields

$$u_I = u_0'(y') = u_0', \tag{31}$$

$$v_I = \sin\theta w_I' = -\sin\theta\frac{1}{\rho_0 f}\partial_{y'}\tau', \tag{32}$$

$$w_I = \cos\theta w_I' = -\cos\theta\frac{1}{\rho_0 f}\partial_{y'}\tau', \tag{33}$$

$$\mathcal{F}_z = N^2(\kappa_v\cos\theta + \frac{\tau'}{\rho_0 f}\sin\theta). \tag{34}$$

It remains to match the solutions in order to satisfy the no-slip boundary condition:

$$u_{\text{tot}} = 0, \qquad u_0(y) - \frac{f}{A_v}\frac{l^2}{2}B = 0, \tag{35}$$

$$v_{\text{tot}} = 0, \qquad -\frac{1}{\rho_0 f}\partial_y\tau\sin\theta + A = 0, \tag{36}$$

$$w_{\text{tot}} = 0, \qquad -\frac{1}{\rho_0 f}\partial_y\tau + \frac{l}{2}(A+B) = 0, \tag{37}$$

$$(\mathcal{F}_z)_{\text{tot}} = (\mathcal{F}_z)_{\text{ins}}, \qquad \kappa_v\cos\theta N^2 + N^2\frac{\tau}{\rho_0 f}\sin\theta - N^2\frac{l}{2}\sin\theta(A+B) = 0. \tag{38}$$

Using the last equation we can recover

$$\frac{l}{2}(A+B) = \frac{\tau}{\rho_0 f} + \kappa_v\cot\theta, \tag{39}$$

the boundary layer mass flux.

The first term on the RHS corresponds to the surface offshore flux balancing the onshore bottom Ekman flux. The second term is the transport in bottom boundary layer induced by stratification and diffusion as in the previous solution.

Using the remaining equations, we obtain

$$A = \frac{1}{\rho_0 f}\partial_y \tau \sin\theta, \tag{40}$$

$$B = -A + \frac{2}{l}\left(\frac{\tau}{\rho_0 f} + \kappa_v \cot\theta\right), \tag{41}$$

$$u_0 = -\frac{f}{A_v}\frac{l^2}{2}B. \tag{42}$$

From now on, we will assume that $\frac{fl^2}{2A_v} = O(1)$.

The controlled interior along shore velocity is

$$u_I = \frac{fl^2}{2A_v}\left(\frac{\tau}{\rho_0 f}\left(\left[\frac{2N^2 A_v}{\kappa_h f^2 l^2}\right] z + \frac{2}{l}\right) - \frac{1}{\rho_0 f}\partial_y \tau \sin\theta + 2\kappa_v \cot\theta\right) \tag{43}$$

Of the three terms independent of z, the second one, the one of $O(\frac{1}{l})$, must be the dominant of these terms since l is a small length scale. Therefore, we have a good idea of how the boundary control affects the interior flow by comparing this term with the first term, the one dependent on z. Assuming z is of order D in the interior, we obtain the ratio:

$$r_{1/2} \approx \frac{N^2}{f^2}\frac{f}{\kappa_h} Dl \tag{44}$$

$$= \frac{N^2 D^2}{f^2 L^2}\frac{fL^2}{A_h(\kappa_h A_h)}\frac{l}{D} \tag{45}$$

$$= \frac{\sigma_h S}{E_h} E_v^{\frac{1}{2}} = \left[\frac{\sigma_h S}{E_v^{1/2}}\right]\left(\frac{E_v}{E_h}\right). \tag{46}$$

If $E_v/E_h = O(1)$ then if $\sigma_h S \gg E_v^{1/2}$, *the interior velocity is only marginally controlled by the boundary layer* and, hence, it must nearly satisfy the no slip boundary condition on $z = 0$ without the boundary layer.

The reader might remember that this has also been observed in the cylinder problem with strong stratification.

2 Turbulent bottom boundary layer

In figure 2 we show the schematics for an upwelling bottom boundary layer. During the process, denser water is brought up, under lighter water, hence enhancing the static stability. The situation for *downwelling* is fundamentally different in that it reduces the hydrostatic stability by forcing lighter fluid under a heavier fluid. This leads to local overturning and convective instability. We thus expect the presence of a thicker turbulent boundary layer as in the upwelling case. The schematics for the problem, usually referred to as the Chapman-LentzChapman and Lentz (1997) (CL) model, are shown in figure 3. In this figure, we have illustrated the physics of the boundary layer, where one expect the fluid to be well-mixed, with isopycnals normal to the bottom boundary.

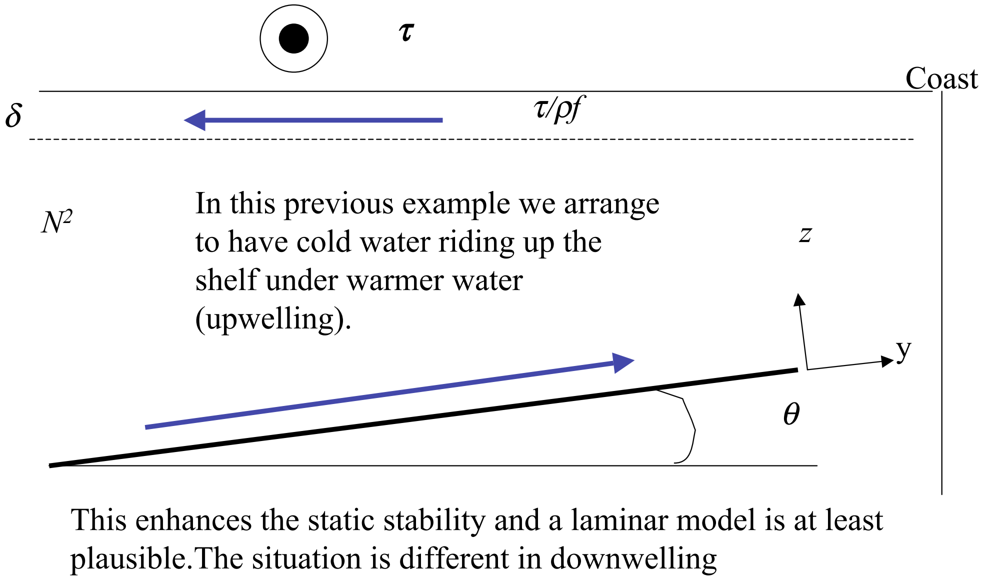
τ
Coast
δ
$\tau/\rho f$
N^2
z
y
θ

In this previous example we arrange to have cold water riding up the shelf under warmer water (upwelling).

This enhances the static stability and a laminar model is at least plausible.The situation is different in downwelling

Figure 2: Idealized *upwelling* schematics on a sloping shelf away from shore. Notice the rotated coordinates

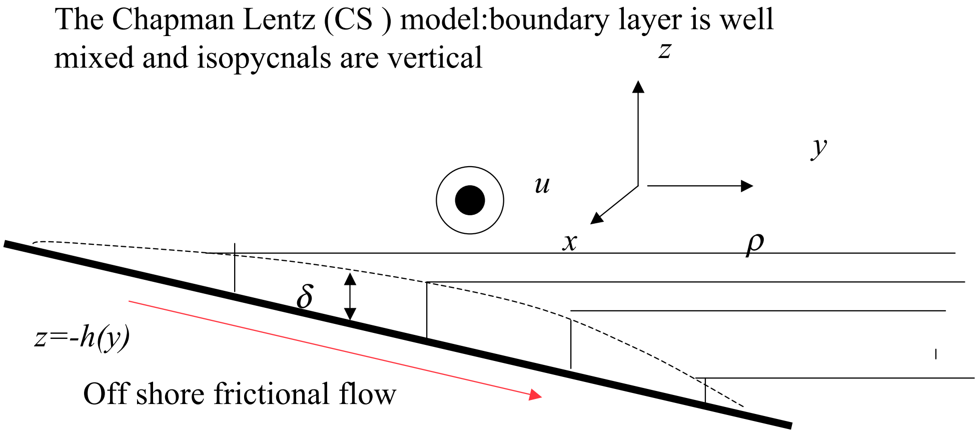

The Chapman Lentz (CS) model:boundary layer is well mixed and isopycnals are vertical

z
y
u
x
ρ
δ
z=-h(y)
Off shore frictional flow

Figure 3: Schematics for the Chapman Lentz model for turbulent boundary layer

2.1 Model Equations

In this section, we return to the usual coordinates with unprimed variables corresponding to the frame where the z axis is parallel to the gravitational force. The model considers an hydrostatic flow and it neglects momentum advection. The equations read:

$$-fv = -\frac{1}{\rho_0}\partial_x p + \frac{1}{\rho_0}\partial_z \tau^x \tag{47}$$

$$fu = -\frac{1}{\rho_0}\partial_y p - g\rho \tag{48}$$

$$0 = -\partial_z p - g\rho \tag{49}$$

$$\partial_x u + \partial_y v + \partial_z w = 0 \tag{50}$$

$$u\partial_x \rho + v\partial_y \rho + w\partial_z \rho = \partial_y\left(\kappa_h \partial_y \rho\right) + \partial_z\left(\kappa_v \partial_z \rho\right). \tag{51}$$

where ρ is the perturbation density and B is the vertical turbulent density flux.

The interior flow is considered vertically uniform, therefore, all the partial derivatives in z vanish. All the turbulent effects including mixing, are assumed to be taking place in the bottom boundary layer that lies between $z = -h(y)$ and $z = -h(y) + \delta(x, y)$. Here, δ represent the boundary layer depth.

In the boundary layer, the mixing is assumed so intense that the fluid is vertically well-mixed, making the isopycnals perpendicular to the boundary. The boundary layer is also considered to be of sufficient extent that the intra boundary layer shears are not affected by the bottom friction. Instead, it is assumed that the horizontal variation in the density field are solely responsible for such shears.

2.1.1 Primary results

In their paper, Chapman & Lentz use slightly different equations and use them to derive a relation between p and δ, the thickness of the layer, where p decays like a one-dimensional diffusion equation, with x acting as time. This particular analysis is relevant for the problem of a coastal current, which definitely requires all three dimensions.

The current is thought to be narrow at the start and spread laterally due to friction, with the boundary layer thickening as the current flows downstream. One of the results of their model is that the boundary layer thickness evolves until the thermal winds brings u to zero, thus eliminating the bottom stresses. A schematic of this result is shown in figure 4. In figure 5, one will find one solution as computed by CL. It shows both the solution for a fixed stratification and for no stratification. The two leads to qualitatively very different results.

2.1.2 Further simplifications

Unlike in the previously mentioned reference, in order to carry tractable analysis further, we must make more simplifications. First, we assume that the forcing is independent of x, the along-shore coordinate. As a consequence, the boundary layer must transport mass offshore and the whole flow

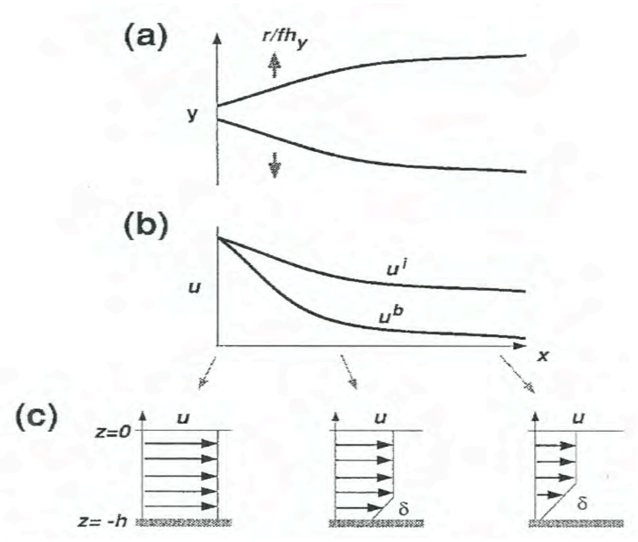

Figure 4: Schematic depicting the adjustment and evolution of a narrow inflow starting at $x = 0$. (a) Plan view of the current boundaries that initially spread, owing to bottom friction, at a rate set by $\frac{r}{fh_y}$, (b) Evolution of the interior velocity u^i and bottom velocity u^b with downstream distance. (c) Along-isobath velocity profiles at various stages downstream The bottom boundary layer grows, while the interior and bottom velocities both decrease, eventually reaching an equilibrium where the bottom velocity vanishes.

must be two-dimensional, resulting in the equations:

$$fu = -\frac{1}{\rho_0}\partial_y p, \tag{52}$$

$$-fv = \frac{1}{\rho_0}\partial_z \tau, \tag{53}$$

$$\frac{\rho}{\rho_0}g = -\frac{1}{\rho_0}\partial_z p, \tag{54}$$

$$\partial_y v + \partial_z w = 0, \tag{55}$$

$$v\partial_y \rho + w\partial_z \rho = \partial_y\left(\kappa_h \partial_y \rho\right) + \partial_z\left(\kappa_v \partial_z \rho\right). \tag{56}$$

2.1.3 Interior Flow

As before, the interior is to first order affected by the wind stress, τ^w, which produces an Ekman pumping

$$w = w_e = -\frac{1}{\rho_0 f}\partial_y \tau^w. \tag{57}$$

The bottom is assumed to lie at $z = -h(y) = -\alpha y + \delta$. with α a specified constant. At this boundary, we demand that the buoyancy flux normal to the bottom vanishes and all perturbations resulting from the boundary layer go to zero for large y. Moreover, we require that the density be continuous at the bottom since it is being mixed by the local turbulence.

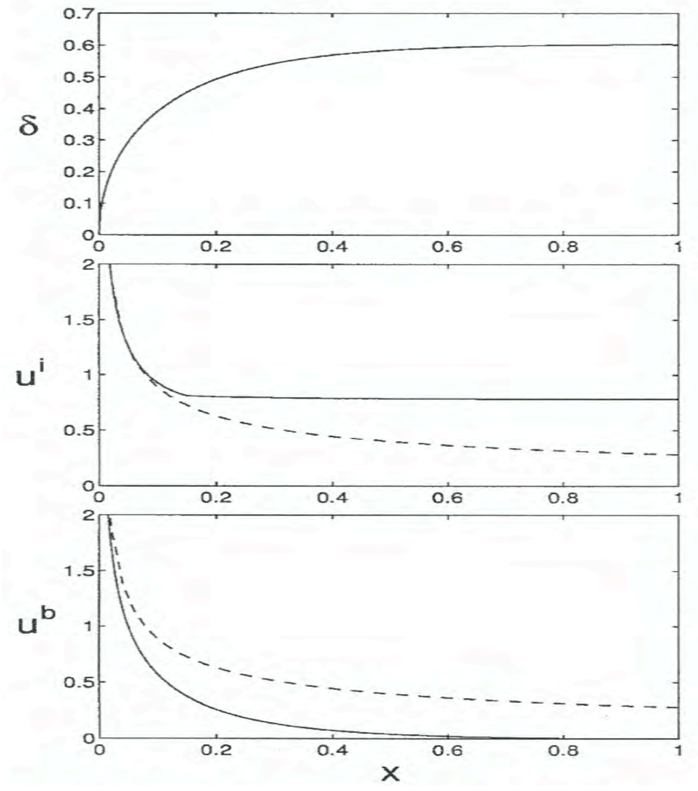

Figure 5: Maximum values of (upper) bottom boundary layer thickness, (middle) interior along-isobath velocity, and (lower) bottom velocity at each downstream (x) location. Dashed curves correspond to an unstratified flow.

Below the surface Ekman layer and above the bottom boundary layer, the turbulent stress in the fluid interior is zero, thus the interior velocity, v_I, must vanish as it is not affected by either of the boundary layers. This, as previously in this work, implies $w_I = w_e(y) = -\frac{1}{\rho_0 f}\partial_y \tau^w$.

Interior density equation With the results of the previous section, the density equation greatly simplifies in the interior:

$$w_e \partial_z \rho_I = \partial_y \left(\kappa_{h_I} \partial_y \rho_I\right) + \partial_z \left(\kappa_{v_I} \partial_z \rho_I\right). \tag{58}$$

The vertical density gradient is assumed to be constant, $\frac{g}{\rho_0}\partial_z \rho_I = -N^2$, which constrains the density to be

$$\frac{\rho_I}{\rho_0} = -z\frac{N^2}{g} - \int_y^\infty \frac{\tau^w}{\rho_0 f}\frac{N^2}{g\kappa_{h_I}} dy' + 1 \tag{59}$$

where we have chosen ρ_0 to be the surface density away from all perturbations.

Interior along shore velocity Using the thermal wind equation, we can recover the along shore interior velocity

$$\partial_z u_I = \frac{g}{f\rho_0}\partial_y \rho_I = \frac{\tau^w}{\rho_0 f^2}\frac{N^2}{\kappa_{h_I}}, \tag{60}$$

which yields

$$u_I = \frac{z}{\kappa_{h_I}}\frac{N^2}{f^2}\frac{\tau^w}{\rho_0} - \frac{1}{\rho_0 f}\partial_y p_s \tag{61}$$

where p_s, the barotropic pressure, is an unknown function.

2.1.4 Inside the bottom boundary layer

The model time scale is so large that the hydrostatically unstable region are assumed to overturn instantaneously, which is equivalent to assume a very intense mixing. This implies that $\rho_b(y) = \rho_I(y, z = -h(y) + \delta(y))$, i.e. the density in the boundary layer is independent of z and continuous with ρ_I at the separation interface, so density obeys.

$$\frac{\rho_b}{\rho_0} = (h-\delta)\frac{N^2}{g} - \int_y^\infty \frac{\tau^w}{\rho_0 f}\frac{N^2}{f\kappa_{h_I}} dy' + 1. \tag{62}$$

Pressure must be hydrostatic and continuous with the interior:

$$\frac{p_b}{\rho_0} = -(h-\delta)[z + \frac{h-\delta}{2}]N^2 + z\int_y^\infty \frac{\tau^w}{\rho_0 f}\frac{N^2}{f\kappa_{h_I}} dy' - gz + \frac{p_s}{\rho_0}. \tag{63}$$

Using the geostrophic balance for u, we can recover u_b,

$$u_b = \frac{N^2}{f}\partial_y((h-\delta)[z + \frac{h-\delta}{2}]) + z\frac{\tau^w}{\rho_0 f}\frac{N^2}{f\kappa_{h_I}} + \frac{1}{\rho_0 f}\partial_y p_s. \tag{64}$$

2.1.5 Finding the barotropic pressure

One unknown quantity that is left to be determined is the barotropic pressure p_s, used to define the along-shore velocities. In order to prescribe it, we use an Ekman bottom drag parameterization of the form

$$v_b\delta = \frac{ru_b(-h)}{f} \tag{65}$$

which enables us to write

$$-\frac{1}{\rho_0 f}\partial_y p_s = \frac{N^2}{f}\delta\partial_y(h-\delta) + h\frac{\tau^w}{\rho_0 f^2 \kappa_{h_I}} + \frac{\tau^w}{\rho_0 r}. \tag{66}$$

in terms $\delta(y)$, a still undetermined quantity.

Boundary Layers velocities Having the barotropic pressure p_s, we can find the along-shore velocities,

$$u_b = \frac{N^2}{f}(z+h)\left[\partial_y(h-\delta) + \frac{\tau^w}{\rho_0 f \kappa_{h_I}}\right] + \frac{\tau^w}{\rho_0 r}, \tag{67}$$

$$u_I = \frac{N^2}{f}(z+h)\left[\frac{\tau^w}{\rho_0 f \kappa_{h_I}}\right] + \frac{N^2}{f}\delta\partial_y(h-\delta) + \frac{\tau^w}{\rho_0 r} \tag{68}$$

We observe that they are continuous at $z=-h+\delta$. We also observe that in the absence of stress the bottom velocity in the bottom boundary layer is zero as in MacCready and Rhines MacCready and Rhines (1993)

2.2 Budgets

In this section, we want to derive precise budgets for the different quantities of importance. In fig. 6 we show what the bottom boundary layer should look like.

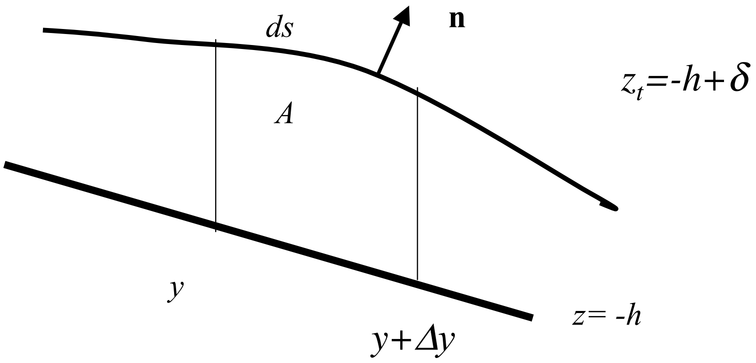

Figure 6: Schematics for the bottom boundary layer

2.2.1 Mass budget

In this problem, the Ekman flux from along-shore winds induce a shoreward mass flux that must be balanced by the bottom boundary transport. In order to make this intuitive idea more rigorous, we consider the vertical integral of the continuity equation, over the depth of the bottom boundary layer:

$$\int_{-h}^{-h+\delta} \partial_y v_b dz = 0. \tag{69}$$

where the part corresponding to the internal flow vanishes since the interior onshore velocity vanishes, $v_I = 0$.

If one integrates by parts,

$$0 = \partial_y \int_{-h}^{-h+\delta} v_b dz + [w_b(-h+\delta) - v_b(-h+\delta)\partial_y(-h+\delta)] + [w_b(-h) - v_b(-h)\partial_y(-h)], \tag{70}$$

$$= \partial_y(v_b\delta) + w_*, \tag{71}$$

where the first bracket corresponds to the flux across the boundary layer surface and the second bracket corresponds to the flux through the sea floor, a term that must vanish.

Since $v_I = 0$ and the problem has no x-dependence, the continuity equation implies that $w_* = w_e$. This mean that the mass budget is fully determined,

$$\partial_y(v_b\delta) - \frac{1}{\rho_0 f}\partial_y \tau^w = 0, \tag{72}$$

$$\Rightarrow \quad v_b\delta = \frac{\tau^w}{\rho_0 f}. \tag{73}$$

as expected.

2.2.2 Buoyancy budget

In this section we want to use the buoyancy equation, eq. 56,

$$v\partial_y\rho + w\partial_z\rho = \partial_y\left(\kappa_h\partial_y\rho\right) + \partial_z\left(\kappa_v\partial_z\rho\right). \tag{74}$$

First, we integrate it, making the vertical transport term disappear, leaving us with

$$v_b\delta\partial_y\rho_b dy = \mathcal{T}_b \cdot \hat{n} ds + \partial_y(\kappa_{h_b}\delta\partial_y\rho_b)dy, \tag{75}$$

where the first term on the rhs corresponds to the diffusive mass flux at the upper boundary of the bottom boundary layer. We have also used the fact that ρ_b is independent of z (the bottom layer is well-mixed).

Using a pill-box argument, one can show that the diffusive flux $\mathcal{T}_b$ must be continuous and, hence, it must be equal to the interior diffusive flux at the top of the bottom boundary layer $\mathcal{T}_b = \mathcal{T}_I$.

Thus, one can write

$$\mathcal{T}_b \cdot \hat{n}\frac{ds}{dy} = \mathcal{T}_I \cdot \hat{n}\frac{ds}{dy} = \kappa_{v_I}\partial_z\rho_I - \kappa_{h_I}\partial_y\rho_I\partial_y(-h+\delta). \tag{76}$$

Using the expressions for ρ_I and ρ_b in eq. 59 and in eq. 62, one can write an equation for δ:

$$\partial_y\left[\kappa_{h_b}\delta\partial_y(h-\delta) + \kappa_{h_b}\delta\frac{\tau^w}{\rho_0 f\kappa_{h_I}}\right] = \kappa_{v_I} + \frac{1}{\kappa_{h_I}}\left(\frac{\tau^w}{\rho_0 f}\right)^2 \tag{77}$$

2.2.3 Investigation of a special case

In this section, we want to investigate the solutions for a special case of bottom bathymetry and wind stress. As before, we use $h = -\alpha y$ and impose a stress of the form $\tau^w = \tau_0 e^{-a(y/L)}$.

The equation for δ becomes

$$\frac{d}{dy}\left[\delta\frac{d\delta}{dy} - (1 + Fe^{-ay})\delta\right] = -\Sigma_v - F^2\Sigma_h e^{-2ay} \tag{78}$$

where $F = \frac{\tau_0}{\alpha\rho_0 f\kappa_{h_I}}$, $\Sigma_v = \frac{\kappa_{v_I}}{\kappa_{h_b}\alpha^2}$ and $\Sigma_h = \frac{\kappa_{h_I}}{\kappa_{h_b}}$.

If one integrate this equation once,

$$\delta\partial_y\delta - (1 + Fe^{-ay})\delta = -\Sigma_v(y - y_0) - \frac{F^2}{2a}[e^{-2ay} - e^{-2ay_0}]\Sigma_h + C \tag{79}$$

where y_0 is the starting point of integration (we cannot deal with the singularity linked with the apex) and C is a constant of integration.

$$C = \left\{\delta\left[\frac{d\delta}{dy} - (1 + Fe^{-ay_0})\right]\right\}_{y=y_0} = \left\{\delta\left[-\frac{g}{\alpha N^2\rho_0}\partial_y\rho_b\right]\right\}_{y=y_0} < 0 \tag{80}$$

using the definition of ρ_b.

When δ goes to zero Knowing the internal velocity, given by eq. 68,

$$u_I = \frac{N^2}{f}(z + h)\left[\frac{\tau^w}{\rho_0 f\kappa_{h_I}}\right] + \frac{N^2}{f}\delta\partial_y(h - \delta) + \frac{\tau^w}{\rho_0 f} \tag{81}$$

we can observe that the ratio of the last term to the first term is

$$\frac{N^2H^2}{f^2L^2}\frac{fL^2}{\kappa_{h_I}}\frac{r}{Hf} \approx \frac{\sigma S}{E_h}E_v^{\frac{1}{2}} = \frac{\sigma S}{E_v^{\frac{1}{2}}}\frac{E_v}{E_h}. \tag{82}$$

So, as in the rotating cylinder case, when $\frac{\sigma S}{E_v^{\frac{1}{2}}} >> 1$, the interior velocity nearly satisfy the boundary condition.

2.2.4 Results

The results for this special case are shown in figure 7 and 8.

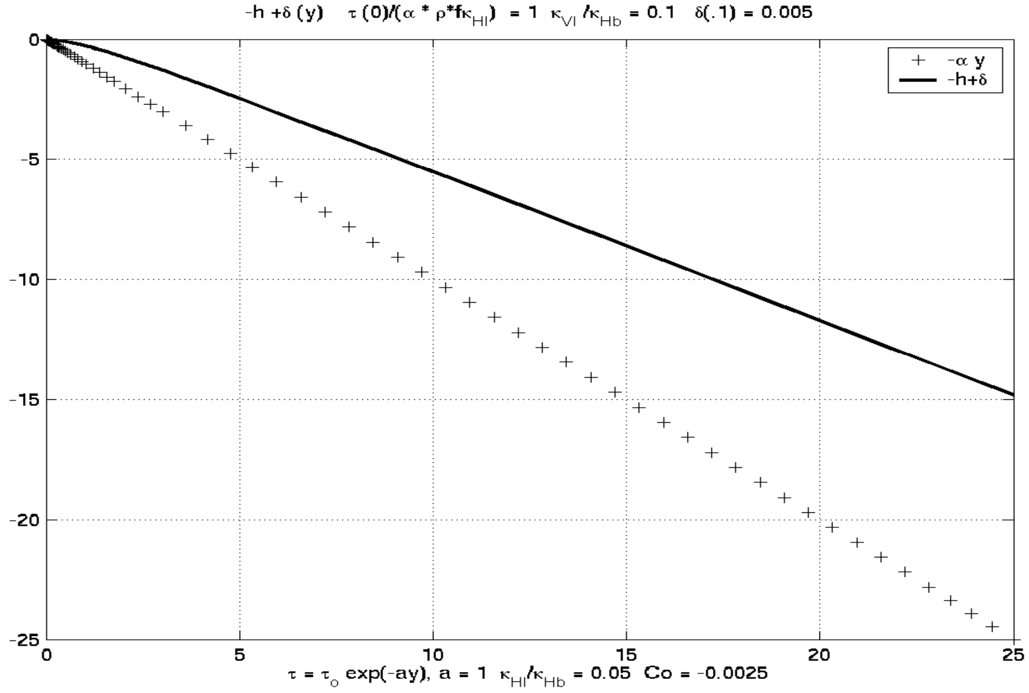

Figure 7: The boundary layer thickness with respect to the sloping bottom for $a = 1$, $\Sigma_v = 0.1$, $\Sigma_h = 0.05$. A starting value of δ of the depth at $y = y_0 = 0.01$ is chosen and C is -0.0025. $F = 1$ has been used.

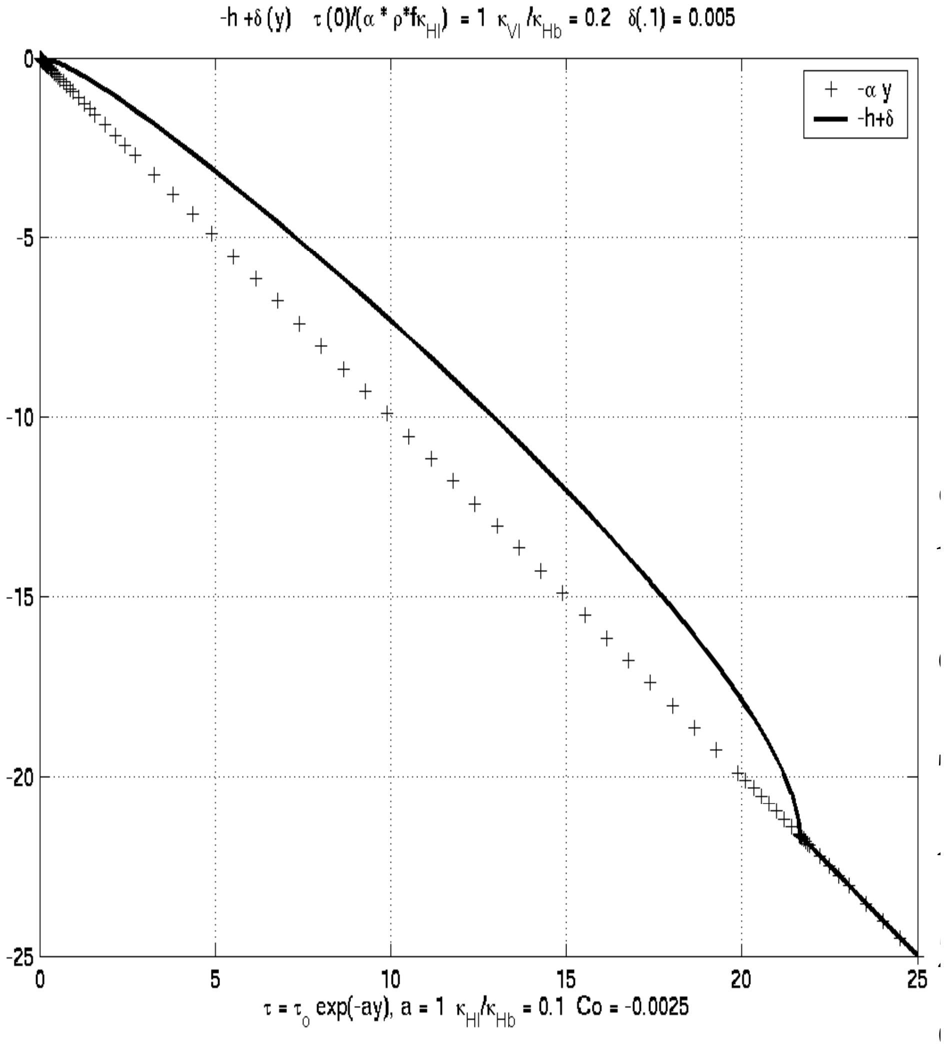

Figure 8: For larger coefficients in the interior, $\Sigma_v = 0.2$, $\Sigma_h = 0.1$, δ goes to zero well beyond the region of wind stress. The interior velocity then satisfies the zero velocity condition.

References

David C. Chapman and Steven J. Lentz. Adjustment of stratified flow over a sloping bottom*. *Journal of Physical Oceanography*, 27(2):340–356, 1997. URL `http://dx.doi.org/10.1175%2F1520-0485%281997%29027%3C0340%3AAOSFOA%3E2.0.CO%3B2`.

Parker MacCready and Peter B. Rhines. Slippery bottom boundary layers on a slope. *Journal of Physical Oceanography*, 23(1):5–22, 1993. URL `http://dx.doi.org/10.1175%2F1520-0485%281993%29023%3C0005%3ASBBLOA%3E2.0.CO%3B2`.

G. K. Vallis. *Atmospheric and Oceanic Fluid Dynamics: Fundamentals and Large-Scale Circulation*. Cambridge University Press, Cambridge, U.K., 2006.

Boundary Layers: Homogeneous Ocean Circulation

Lecture 7 by Angel Ruiz-Angulo

The first explanation for the western intensification of the wind-driven ocean circulation was provided by Henry Stommel (1948). The following chapter considers that work and subsequent developments in the context of boundary layer theory.

1 The homogeneous model

Midlatitude ocean circulation can be approached by using *boundary layer theory.* We begin by idealizing the ocean basin as a box with irregular bottom and filled up with homogeneous water. At the top of the box, the ocean surface, the wind flows only on the zonal direction, x, but varies on the meridional direction, y. This imposed wind stress results in the surface Ekman layer, which drives subsurface ocean waters via vertical *Ekman pumping.* Figure 1 shows the idealized ocean basin for this model.

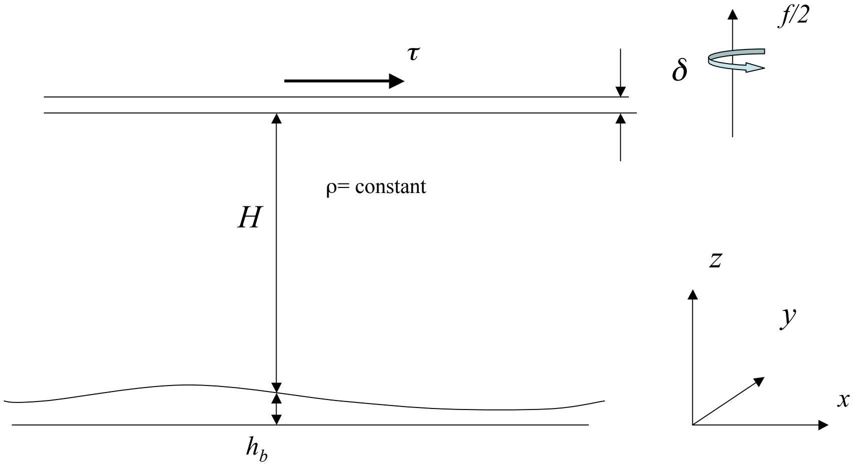

Figure 1: Proposed model for wind driven flows, allowing the bottom to have some variations on the topography

The Ekman pumping results in a vertical velocity, w_e, which is proportional to the curl of the wind stress (See lecture 1)

$$w_{top} = w_e = \hat{k} \cdot \nabla \times \left(\frac{\vec{\tau}}{\rho f} \right), \text{ at } \quad z = H + h_b \tag{1}$$

The contribution from the bottom Ekman pumping is given by

$$w_{bottom} = \frac{\delta}{2}\zeta + \vec{u}\cdot\nabla h_b = \frac{\delta}{2}\left[v_x - u_y\right] + uh_{bx} + vh_{by}, \quad \text{at} \quad z = h_b \tag{2}$$

In addition to the component due to the interior relative vorticity, ζ, the magnitude of w_{bottom} is affected by the interaction of the velocity with the topography. Note that the first term on the RHS corresponds to the classical *flat bottom solution*.

Assume that the interior (the fluid away from the bottom and top Ekman layers) is a homogeneous geostrophic flow over a non-uniform bottom. We now introduce the *beta approximation*. On a spherical planet, the Coriolis parameter is $f = 2\Omega sin\theta$. By expanding around a reference latitude, θ_0, and keeping the first order term we find the parameters for a Cartesian framework called $\beta-plane$:

$$f = \underbrace{2\ \Omega\ sin\theta_0}_{\text{reference Coriolis parameter}} + \underbrace{\frac{2\ \Omega\ cos\theta_0}{R}}_{\beta \text{ parameter}}\ y \ + \ .... \tag{3}$$

Thus,

$$f = f_0 + \beta_0 y$$

In general, β is expressed as:

$$\beta = \frac{\partial f}{\partial y} = \frac{2\Omega cos\theta}{R}$$

We assume $\beta_0\ y\ << f_0$, which is called he $\beta-$plane approximation. Physically we are working on a cartesian plane tangent to the sphere at the reference latitude θ_0.

1.1 Equations of motion

By taking the curl of the N-S equations we can writhe the governing equations for the model in terms of vorticity

$$\left(\frac{\partial}{\partial t} + u\frac{\partial}{\partial x} + v\frac{\partial}{\partial y}\right)\zeta + \beta v = f\frac{\partial w}{\partial z} + A\left(\frac{\partial^2}{\partial x^2} + \frac{\partial^2}{\partial y^2}\right)\zeta \tag{4}$$

If u and v are independent of z (thermal wind and constant density) then w must be a linear combination of z. The upper and lower limits of the vertical velocity are given by the top Ekman layer (Eq. 1) and the bottom Ekman layer (Eq. 2), therefore:

$$\frac{\partial w}{\partial z} = \frac{w_{top} - w_{bottom}}{H}$$

Applying this approximation and integrating vertically Eq. 4 then becomes

$$\left(\frac{\partial}{\partial t} + u\frac{\partial}{\partial x} + v\frac{\partial}{\partial y}\right)\zeta + \beta v + \frac{f_0\vec{u}}{H} = \frac{f_0 w_e}{H} - \frac{f_0\delta}{2H}\zeta + A\left(\frac{\partial^2}{\partial x^2} + \frac{\partial^2}{\partial y^2}\right)\zeta \tag{5}$$

Since the interior remains in geostrophic balance horizontally we can introduce the *geostrophic stream function*:

$$\psi = \frac{p}{\rho f_0} \quad \text{where} \quad u = -\frac{\partial\psi}{\partial y} \quad \text{and} \quad v = \frac{\partial\psi}{\partial x}$$

The global variables are scaled with:

Velocity:	U
Length:	L
Potential, ψ:	UL
Time:	$(\beta_0 L)^{-1}$

Let us choose U such that it balances the input of vorticity by the wind with the advection of planetary vorticity

$$U = \frac{\tau_0}{\rho H_0 L \beta_0}$$

Similarly, the Ekman pumping scales as,

$$W_e = \frac{\tau_0}{\rho f_0 L}$$

Finally, scaling Eq. 5 results in:

$$\frac{\partial}{\partial t}\nabla^2\psi + \delta_I^2 J(\psi, \nabla^2\psi + \psi_x + \eta J(\psi, h_b) = w_e - \delta_s \nabla^2\psi + \delta_m^3 \nabla^4 \psi \tag{6}$$

$$\delta_I = \frac{(U/\beta_0)^{1/2}}{L}, \quad \eta = \frac{f_0 \Delta h_b}{H_0 \beta_0 L}, \quad \delta_s = \frac{f_0 \delta}{2 H_0 \beta L}, \quad \delta_m = \frac{(A/\beta)^{1/3}}{L}$$

Where, δ_I is the inertial scale , η is the relative strength of the bottom topography to $\beta-$effect, δ_s is the Stommel boundary layer scale and δ_m corresponds to the Munk's boundary layer scale.

2 The singular perturbation problem

Assume that all the boundary layers are small compared to the length of the basin, L, i.e. $\delta_i/L << 1, \quad \delta_s/L << 1 \quad \text{and} \quad \delta_m/L << 1$. Considering that the bottom is flat in the interior and ignoring the inertial and friction terms, the governing equation is:

$$\psi_x = w_e(x, y) \tag{7}$$

This is the Sverdrup relation. The solution to this equation cannot satisfy no-normal flow at both boundaries.There are two solutions based on the boundary conditions, either $\psi(x = 0) = 0$ at the western boundary or $\psi(x = x_e) = 0$ at the eastern boundary, where $x = x_e$ corresponds to the eastern boundary. Hence, the two possible interior solutions are:

1) Satisfying $\psi(x = 0) = 0$, no normal flow on the western boundary:

$$\psi = \int_0^x w_e(x', y) dx' \tag{8}$$

Using a similar wind stress distribution as Stommel Stommel (1948), the solution to Eq. 8 in the basin is shown in Figure 2. The solutions are:

$$\psi_1 = -x sin(\pi y), \quad u_1 = -\frac{\partial \psi_1}{\partial y} = x\pi cos(\pi y) \quad \text{and} \quad v_1 = -sin(\pi y)$$

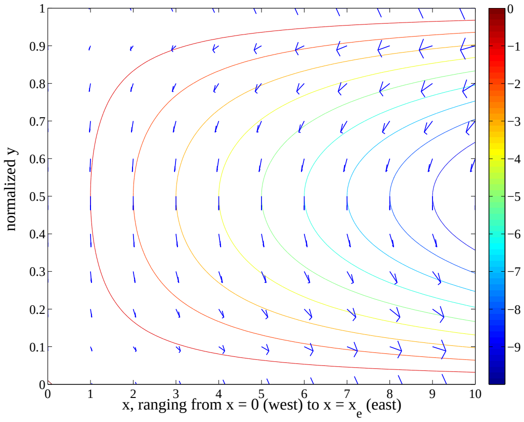

Figure 2: Streamlines and the velocity field inside the basin model corresponding to the solution of the Eq. 8.

2) The other potential solution is no normal flow on the eastern boundary, $\psi(x = x_e) = 0$.

$$\psi = -\int_{x}^{x_e} w_e(x', y)dx' \tag{9}$$

Using the same wind stress as before, the following geostrophic potential satisfies the boundary conditions for Eq. 9. The corresponding solution in the basin model domain is shown in Figure 3.

$$\psi_2 = (x_e - x)sin(\pi y), \quad u_2 = -\frac{\partial \psi_1}{\partial y} = -(x_e - x)\pi cos(\pi y) \quad \text{and} \quad v_2 = -sin(\pi y)$$

2.1 An Integral constraint

By taking a steady and closed streamline from the interior of the basin and integrating over the closed contour, C, the Eq. 6 results in

$$\cancelto{0}{\oint_C \frac{\partial \vec{u}}{\partial t} \cdot d\vec{s} + \oint_C \vec{u}\left[\delta_I^2\zeta + y + \eta h_b\right] \cdot \hat{n}ds} = \oint_C \vec{\tau} \cdot d\vec{s} - \delta_s \oint_C \vec{u} \cdot d\vec{s} + \delta_m^3 \oint_C \nabla\zeta \cdot \hat{n}ds \tag{10}$$

The left hand side of the Eq. 10 is equal to zero for a steady closed streamline, the temporal term vanishes and since there is no flux across any steady closed streamline, the second term vanishes as well, therefore

$$0 = \oint_C \vec{\tau} \cdot d\vec{s} - \delta_s \oint_C \vec{u} \cdot d\vec{s} + \delta_m^3 \oint_C \nabla\zeta \cdot \hat{n}ds \tag{11}$$

From Eq. 11 it is possible to observe that the circulation (net input of vorticity) on each streamline should be balanced by either diffusion in the interior or friction at the bottom. The

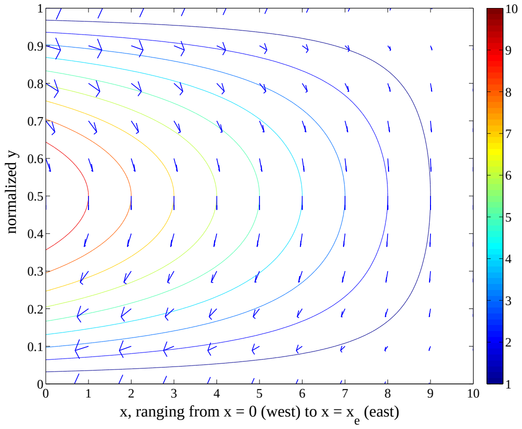

Figure 3: Streamlines and velocity field inside the basin model corresponding to the solution of the Eq. 9, i.e., $\psi(x = xe) = 0$.

Munk layer δ_m includes, in principle, the unresolved eddies within A_H. The explicit flux from eddies, if known, is included in the flux vorticity integral by an additional flux term, i.e.

$$0 = \oint_C \vec{\tau} \cdot d\vec{s} - \delta_s \oint_C \vec{u} \cdot d\vec{s} + \delta_m^3 \oint_C \nabla\zeta \cdot \hat{n} ds - \delta_I^2 \oint_C \overline{\vec{u}'\zeta'} \cdot \hat{n} ds \tag{12}$$

Since the basin model is itself a streamline, this last term should be zero for the streamline coincident with the boundary (no normal flow through the boundaries).

2.2 The Energy constraint

Intuitively, by looking at wind stress distribution shown in Figure 4, the natural (comfortable) solution to the Sverdrup expression, Eq. 7, corresponds to the one that satisfies no flow at the eastern boundary, Eq. 9. Additionally, this solution compares well with the observations. In order to prove the validity of this intuitive choice we look at the energetics of the fluid flow for a steady circulation in a rectangular ocean basin on the $\beta-$plane. The system of equations needed to solve the energetics is governed by the simplified vorticity equation (Eq. 4) and the following boundary conditions for the given domain **D**. It is

$$\psi\Big|_{\partial D} = 0, \qquad \text{and} \qquad \nabla\psi\Big|_{\partial D} = 0 \qquad if \quad \delta_m \neq 0$$

where,

$$D = [0 \ \leq \ x \ \leq x_e] \ \times \ [0 \ \leq \ y \ \leq 1].$$

The energy equation is obtained by multiplying Equation 4 by ψ, integrating over the whole basin, **D**, and applying the boundary conditions. Finally, the result is:

$$\langle w_e \ \psi\rangle = -\delta_s \ \langle|\nabla\psi|^2\rangle - \delta_m^3 \ \langle|\nabla^2\psi|^2\rangle \tag{13}$$

where,

$$\langle \mathrm{f} \rangle \equiv \int\int_D \mathrm{f}\, dxdy$$

The equilibrium has been reached, the forcing term, $\langle w_e \psi \rangle$ is balanced by the dissipation terms. The condition to satisfy this balance is that w_e and ψ must be negatively correlated, and this favors the circulation of Figure 3

3 The linear boundary layer problem

We now explore another simplification of the governing equation (Eq. 6) where the amplitudes of the relative motion are small, i.e.

$$\delta_I << \delta_s \quad \text{and} \quad \delta_I << \delta_m.$$

The resulting equation is a the linear boundary layer problem:

$$\psi_x = w_e - \delta_s \nabla^2 \psi + \delta_m^3 \nabla^4 \psi \tag{14}$$

The proposed *interior solution* for this problem is ψ_I.

$$\psi_I(x, y) = -\int_x^{x_e} w_e(x', y) dx' + \Psi(y). \tag{15}$$

Note that the limits of integration make no distinction between the eastern and western boundaries, so no intensification is expected in the interior (temporary ignorance!!).

3.1 The Stommel Model

For the interior of the linear boundary layer we need to manipulate Equation 14. By assuming small variations in the flow along the boundary layer and large variations across the boundary layer flow, we can now keep only the x derivatives. Furthermore, scaling by $x = \delta\xi$ results in $\delta w_e << 1$, which can be neglected. We now integrate once over η so that

$$\underbrace{\phi}_{a} = -\underbrace{\left(\frac{\delta_s}{\delta}\right)\frac{\partial \phi}{\partial \xi}}_{b} + \underbrace{\left(\frac{\delta_m^3}{\delta^3}\right)\frac{\partial^3 \phi}{\partial \xi^3}}_{c}. \tag{16}$$

Assuming that $\delta_s >> \delta_m$ and $\delta \sim \delta_s$ allows us to ignore the term c. Since this is the highest-order derivative in the equation this becomes a singular perturbation problem. Stommel's model for the boundary layer problem is recovered (Stommel (1948)).

$$\frac{\partial \phi}{\partial \xi} + \phi = 0. \tag{17}$$

It has the following solution,

$$\phi = A(y)e^{-\xi}.$$

No normal flow condition is necessary at one of the boundaries; as before, we can apply this condition on either the eastern boundary or the western boundary. For the western boundary, $x = 0$,

$$A = -\psi_I(0, y).$$

Let us define a new boundary layer coordinate, ξ', for the eastern boundary

$$\xi' = \frac{(x_e - x)}{\delta_s} \quad \text{then,} \quad \frac{\partial \phi}{\partial \xi'} - \phi = 0.$$

Then, our new boundary layer equation is:

$$\frac{\partial \phi}{\partial \xi'} - \phi = 0.$$

The corresponding solution is:

$$\phi = A(y) e^{\xi'}.$$

This solution has exponential growth of the BL on the eastern boundary, which is physically not possible since the BL should be finite and should be absorbed smoothly by the interior. Therefore, we keep the first solution, which actually corresponds to the *western intensification* (our temporary ignorance has been removed!). Looking at the general solution for the interior, $\Psi(y) = 0$ on the boundary. Finally, combining our equations for the linear BL (Eqns. 14 and 15) with the valid solution results in

$$\psi(x, y) = \psi_I(x, y) - \psi_I(0, y) e^{-(x/\delta_s)}$$

with,

$$\psi_I(x, y) = -\int_x^{x_e} w_e(x', y) dx'.$$

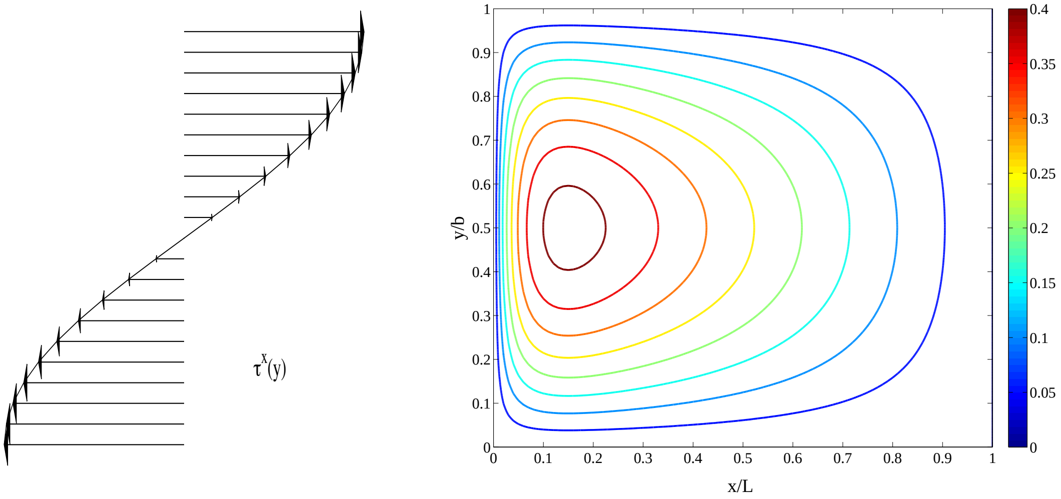

Figure 4: Streamlines corresponding to wind driven circulation in the ocean basin based on Stommel's model. The dimensions of the basin is **L** (west to east) by **b** (south to north), the size of the boundary layer respect to the basin length is $\delta_s/L = 0.05$. Henry Stommel proposed $\tau = -F cos(\pi y/b)$ (Stommel (1948))

.

The western intensification represented in Figure 4 is controlled by the boundary layer and the β−effect.

So far, Stommel's model neglects the **no slip** condition on the western boundary. Figure 5 shows the meridional velocity v. Note that the velocity is northward close to the boundary layer and then turns southward as Sverdrup flow for most of the ocean basin extent.

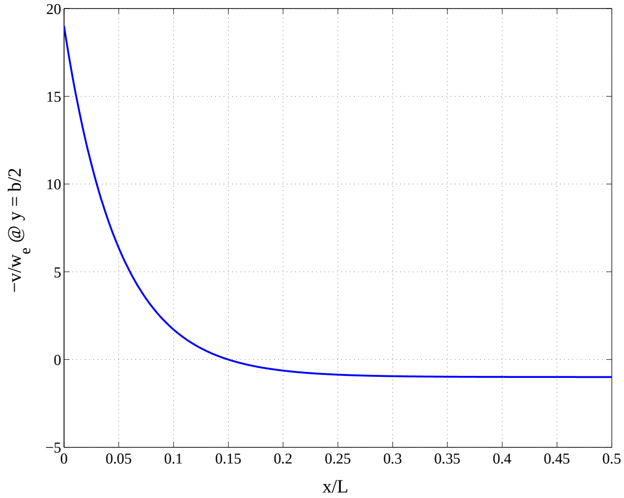

Figure 5: Meridional velocity in the middle of the basin as predicted by Stommel's model (normalized by $w_e(y = b/2)$). Note that the only boundary condition satisfied is zero flow through the western boundary, i.e., $v(x = 0) \neq 0$. As before $\delta_s/L = 0.05$

3.2 The no slip condition and the sublayer

Stommel's model assumption that $\delta_m/\delta \sim 0$ leaves no room to satisfy a *no slip* condition, as a natural consequence the vorticity balance of the whole basin depends on the lateral diffusion term.

In order to satisfy the no slip boundary condition, we now rewrite the Equation 16 with a slightly different scaling, $x = \delta_s \xi$.

$$\underbrace{\phi}_{a} = -\underbrace{\frac{\partial \phi}{\partial \xi}}_{b} + \underbrace{\left(\frac{\delta_m^3}{\delta_s^3}\right)\frac{\partial^3 \phi}{\partial \xi^3}}_{c}. \tag{18}$$

It is necessary now to keep both of the terms; **b** and **c** that we are adding to Stommel's model as an additional sublayer. Defining $\xi = l\ \eta$ as the sublayer scale and balancing the terms **b** and **c** we find

$$l = \left(\frac{\delta_m}{\delta_s}\right)^{3/2}.$$

The thickness of the sublayer inside the Stommel boundary layer is given by,

$$\delta_{sub} = \delta_s\ l \quad = \frac{\delta_m^{3/2}}{\delta_s^{1/2}} \quad = \quad \left[\frac{A}{L^2}\frac{H_0}{\sqrt{2vf}}\right]^{1/2}$$

After scaling Eq. 18 and integrating it once over η, we find the correction function for the sublayer:

$$\chi_{\eta\eta} - \chi = 0, \quad \text{where,} \quad \chi(\eta) = C(y)\ e^{-\eta}.$$

The solution should be bounded, therefore the term proportional to $exp(+\eta)$ automatically goes to zero. Hence, we could rewrite Stommel's solution with the additional sublayer correction function

$$\psi(x, y) = \psi_I(x, y) + A(y)e^{-(x/\delta_s)} + C(y)e^{-(x/\delta_{sub})}.$$

Applying the boundary conditions of no slip, $\psi_x(0, y) = 0$, and no flow at the western boundary, $\psi(0, y) = 0$ allows us to find the function *C(y)* since *A(y)* is already known

$$C = -\frac{\delta_{sub}}{\delta_s}\ A \quad \text{and,} \quad A = -\psi_I(0, y).$$

Finally, the **total solution** for the ocean basin including no slip at the western boundary is given by,

$$\psi(x, y) = \psi_I(x, y) - \psi_I(0, y)\left[e^{-(x/\delta_s)} - \left(\frac{\delta_{sub}}{\delta_s}\right) e^{-(x/\delta_{sub})}\right]. \tag{19}$$

Figure 6 shows the resulting profile for the meridional velocity. Note that the magnitude of v, approaches to zero near the western boundary.

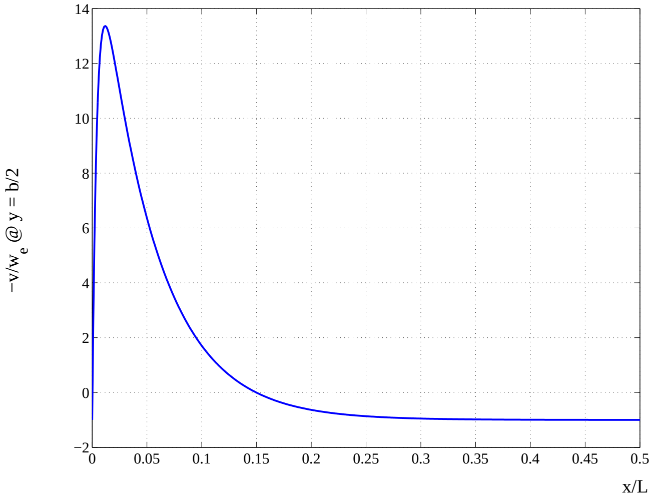

Figure 6: Meridional velocity in the middle of the basin adding no slip condition at the western boundary, i.e., $v(x = 0) = 0$. $\delta_s/L = 0.05$ and $\delta_{sub} = 0.0045$

References

H. Stommel. The westward intensification of wind-driven ocean currents. *Trans. Amer. Geophys. Union*, 29:202–206, 1948.

Boundary Layers: Homogeneous Ocean Circulation

Lecture 8 by Henrik van Lengerich

1 Vorticity Balance

Vorticity is conserved along streamlines and this allows us to extract information from the governing equations without the use of the solution.

1.1 Balance along x - direction

We perform an integral from $x = 0$ to $x = x_e$ about the vorticity equation (Eq. **??**), this is also known as the dissipation balance. We neglect u_y because it is small compared to v_x in the boundary layer and we ignore all inertial and viscous terms in the interior, as well as use the no slip condition on v at $x = 0$, to obtain

$$\int_0^{x_e} [\psi_x = w_e - \delta_s \nabla^2 \psi + \delta_M^3 \nabla^4 \psi] dx. \tag{1}$$

ψ is conserved so the left hand side of Eq. 1 is zero. The stream function multiplied by the boundary layer thickness is negligible close to the right hand side. This gives, for $w_e = w_e(y)$,

$$0 = x_e w_e + \delta_s \psi_x(0) - \delta_m^3 \psi_{xxx}(0). \tag{2}$$

The first derivative of ψ is zero at the left boundary due to the no slip condition. This gives

$$0 = x_e w_e + \delta_m^3 \psi_{xxx}(0), \tag{3}$$

which means that the vorticity inserted by the Ekman pumping must be dissipated by the sublayer. We verify that (1.20) is a solution to Eq. 3

$$x_e w_e = x_e w_e \delta_m^3 (\frac{\delta_m}{\delta_s})^{3/2} \frac{1}{\delta_s^3 (\delta_m/\delta_s)^{9/2}}. \tag{4}$$

We can also look at the streamlines that go through the Stommel layer. Performing an integral around the vorticity from the Stommel layer at 0_+ to the right edge at x_e of the Stommel solution (ϕ) similar to Eq. 1, gives

$$0 = x_e w_e(0_+) + \delta_s \phi_x(0_+). \tag{5}$$

We can verify that the solution previously obtained matches this condition

$$0 = x_e w_e(0_+) - \delta_s x_e w_e(0_+)/\delta_S. \tag{6}$$

This means that for the total solution of the stream function obtained the vorticity of the streamlines that pass through the Stommel layer are balanced by bottom friction.

1.2 Vorticity Balance along y - direction

We perform an integral of the vorticity equation (Eq. **??**) for an area R of the boundary layer from two arbitrary latitudes y_1 to y_2.

$$\int_R \delta_I^2 \nabla \cdot \overrightarrow{u} \zeta dA + \int_R v dA + \int_R \nabla \cdot \overrightarrow{u} h_b dA = -\delta_s \int_R \zeta dA + \int_R \delta_m^3 \nabla^2 \zeta dA. \tag{7}$$

Because the velocity in the x-direction does not vary much with y, the local vorticity can be approximated as

$$\zeta \approx v_x. \tag{8}$$

We assume that the bottom is flat, so that the term with h_b is zero, then Eq. 7 becomes

$$\frac{1}{2}\delta_I^2[v^2(0,y_1) - v^2(0,y_2)] + \int_{y_1}^{y_2} \psi_l(0,y)dy = \delta_s \int_{y_1}^{y_2} v(0,y)dy - \delta_m^3 \int_{y_1}^{y_2} \zeta_x(0,y)dy. \tag{9}$$

Using the no-slip condition at $x = 0$, this simplifies to

$$\int_{y_1}^{y_2} \psi_I(0,y)dy = -\delta_m^3 \int_{y_1}^{y_2} \zeta_x(0,y)dy. \tag{10}$$

The term on the left is the vorticity added due to the wind and the term on the right is the dissipation of vorticity due to viscosity in the viscous sublayer. Because we have not fixed the bounds on y, the vorticity added on any latitude is dissipated in the boundary layer at that latitude. It should be noted that this interpretation is only valid under the assumption that $v_x \gg u_y$ as stated at the onset.

2 Inertial Boundary Layers

Previously we have assumed the δ_I term was small, but this is pretty unrealistic considering the Reynolds number of ocean flows. We focus on a parameter region where inertial effects become important, that is $1 \gg \delta_I \gg \delta_m \gg \delta_s$. To retain the inertial terms of highest order we re-scale the x variable such that

$$\xi = x/\delta_I. \tag{11}$$

To order $1/\delta_I$ the vorticity equation (Eq. **??**) governs the inertial boundary layer, and is given by

$$\psi_\xi \psi_{\xi\xi y} - \psi_y \psi_{\xi\xi\xi} + \psi_\xi = 0. \tag{12}$$

Note that the left hand side is the same as the substantial derivative, so we write

$$\frac{D}{Dt}(\psi_{\xi\xi} + y) = 0 \tag{13}$$

$$\psi_{\xi\xi} + y = Q(\psi). \tag{14}$$

$$\tag{15}$$

This means that the vorticity is conserved along streamlines.

2.1 Example

Assume that the velocity u is constant and ψ is independent of x far from the boundary. Then $\psi_{\xi\xi}$=0 and we can solve Eq. 14 far from the boundary to get

$$y = Q(\psi). \tag{16}$$

Using the definition of the stream function we find that

$$\psi = -uy \tag{17}$$

far from the boundary. Here the integration constant is arbitrary and set to zero.

Now we apply Eq. 17 for ψ in the boundary region to obtain

$$\begin{aligned} Q(\psi) &= -\psi/u & (18)\\ \psi_{\xi\xi} + y &= -\psi/u & (19)\\ \psi &= A(y)e^{\psi/\sqrt{-u}} + B(y)e^{-\psi/\sqrt{-u}} + uy. & (20) \end{aligned}$$

We eliminate the $A(y)$ term because we need ψ to be bounded in x in order to match it to an inner solution where ξ goes to infinity. We use the no penetration condition on u, but allow the fluid to slip along the $x = 0$ edge. Again, setting the integration constant to zero gives

$$\psi = uy(1 - e^{-\xi/\sqrt{-u}}). \tag{21}$$

We know that the interior flow needs to be westward, so this expression cannot close the circulation; it also does not satisfy the no slip condition at $x = 0$.

2.2 Inertial Sub-layer Thickness

Looking at the balance of vorticity of an inertial sub-layer solution it can be seen that the vorticity input by the wind needs to be balanced by the viscous sub-layer; however, most streamlines do not go through the viscous sub-layer, therefore there is an accumulation of vorticity. We define a re-scaled Reynolds number as $Re = UL/A{*}\delta_I = \delta_I^3/\delta_m^3$, then numerical simulations by Fox-Kemper Fox-Kemper (2003) show that for Re = 1.95 the solution is stable, but at Re = 4.29 there is an inertial runaway.

3 Enhanced Sub-layer

Fox-Kemper and Pedlosky's Fox-Kemper and Pedlosky (2004) solution to the inertial runaway is to modify the momentum mixing viscosity such that it captures two dissipation mechanisms. The first is the effect of unresolved eddies in the interior and the boundary layers. The second is the interaction of the fluid with the boundary. These effects were incorporated into the Munk layer as

$$\delta_m^3 = \frac{\delta_I^3}{Re_i} + (\frac{\delta_I^3}{Re_b} - \frac{\delta_I^3}{Re_i})(e^{-x/\delta_d} + e^{-(1-x)/\delta_d}) \tag{22}$$

such that the effect is continuous as x is varied. The first term in the summation represents the unresolved eddies, the second term is the interaction with the boundary (which is at x=1). The two Reynolds numbers and the thickness of the region where the boundary viscosity is enhanced are given by

$$Re_i = (\frac{\delta_I}{\delta_m})^3_{interior} \tag{23}$$

$$Re_b = (\frac{\delta_I}{\delta_m})^3_{boundary} \tag{24}$$

$$\delta_d = \frac{\delta_I}{\sqrt{Re_I}}. \tag{25}$$

The effect of this enhanced dissipation mechanism can be seen in Figure 1. As the boundary layer Reynolds number is decreased the vorticity decreases due to dissipation in the boundary layer. The same is true of the interior Reynolds number. The energy of the system also decreases as either of the Reynolds numbers are decreased. Shown in the lower right hand corner of Figure 1 is a situation with a large internal vorticity (larger than what was unstable in section 2.2), but this vorticity is dissipated to the boundary region.

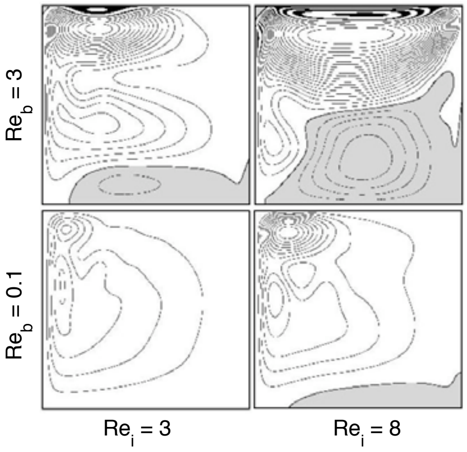

Figure 1: Streamlines for various Re_i and Re_b. Shaded regions are of negative vorticity. Figure taken from Fox-Kemper (2003).

References

B Fox-Kemper. *Eddies and Friction: Removal of vorticity from the Eddies and Friction: Removal of vorticity from the wind-driven gyre.* PhD thesis, MIT/WHOI Joint Program, 2003.

B Fox-Kemper and J. Pedlosky. Wind-driven barotropic gyre i: Circulation control by eddy vorticity fluxes to an enhanced removal region. *Journal of Marine Research*, 62:169–193, 2004.

Internal boundary layers in the ocean circulation

Lecture 9 by Andrew Wells

We have so far considered boundary layers adjacent to physical boundaries. However, it is also possible to find boundary layers in the interior of the fluid domain. Two specific examples which we will discuss later are the oceanic thermocline and the equatorial undercurrent.

1 A simple example of an internal boundary layer: heat flow in a pipe

To demonstrate some of the characteristics of internal boundary layers we first consider a simple problem. Consider one-dimensional flow in a cylindrical pipe as shown in figure 1. The fluid is initially at a uniform temperature T_0 throughout the pipe, with flow at a constant velocity U along the length of the pipe. For time $t \geq 0$ the opening of the pipe is heated and maintained at a constant temperature T_1. The transfer of heat down the pipe can be described by the one dimensional advection-diffusion equation

$$\frac{\partial T}{\partial t} + U\frac{\partial T}{\partial x} = \kappa \frac{\partial^2 T}{\partial x^2}. \tag{1}$$

The thermal diffusivity κ is typically small, and so as a first approximation we might neglect the diffusion term on the right hand side of (1). This yields the solution

$$T = T_1 \qquad x - Ut \leq 0, \tag{2}$$
$$T = T_0 \qquad x - Ut > 0, \tag{3}$$

corresponding to a discontinuous jump in temperature propagating down the pipe at velocity U, as shown in figure 2(a). Clearly the discontinuity is unphysical, and we need an internal boundary layer

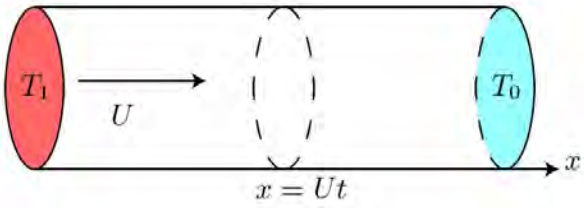

Figure 1: Fluid is pumped down a cylindrical pipe at a constant velocity U parallel to the pipe axis. The temperature is maintained at the constant value T_1 at the opening of the pipe at $x = 0$, with the remainder of the fluid initially at a temperature T_0.

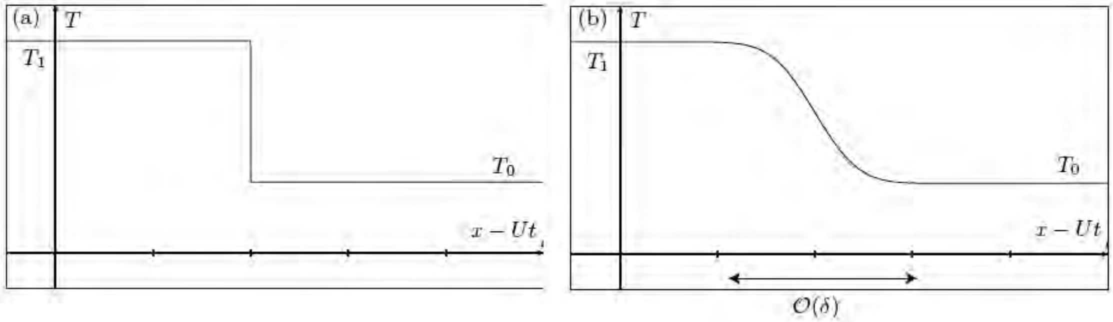

Figure 2: Snapshots of the temperature variation along the pipe, taken at a fixed value of t. (a) The solution in the absence of diffusion, showing a discontinuous jump in temperature. (b) The solution of the full advection diffusion equation. Diffusion acts to smooth the jump across an internal boundary layer of width $\delta = \mathcal{O}(\sqrt{\kappa t})$.

to smooth it out. The discontinuity arises due to the neglect of the diffusion term, mathematically giving a singular perturbation.

In this case we can obtain a solution of the full heat equation with the diffusion term included. We introduce a new system of co-ordinates moving with the shock, $\xi = x - Ut$ and $\tau = t$, so that (1) yields

$$\frac{\partial T}{\partial \tau} = \kappa \frac{\partial^2 T}{\partial \xi^2}. \tag{4}$$

In this reference frame, there are no imposed horizontal lengthscales and so we obtain the similarity solution

$$T = \frac{T_0 + T_1}{2} + \frac{T_0 - T_1}{2} \operatorname{erf}\left(\frac{\xi}{2\sqrt{\kappa\tau}}\right), \tag{5}$$

where the error function is defined as

$$\operatorname{erf}(x) = \int_0^x \exp\left(-u^2\right)\, du. \tag{6}$$

The full solution is plotted in figure 2(b), where we see that the jump in temperature has been smoothed out by diffusion over an internal boundary layer of width $\delta = \mathcal{O}(\sqrt{\kappa t})$. In the following discussion we will see that several structures of the ocean circulation are explained by the presence of internal boundary layers within the ocean.

2 The ventilated thermocline

The sub-tropical oceans have an interesting density profile, with a rapid variation in density over the upper kilometer of depth and a much weaker density gradient in the abyss at depths of 1 to 5.5 km. Typical density profiles in the Pacific Ocean are plotted in figure 3. The upper region of rapid variation, or *thermocline*, shows a distinct bowl-like shape in each hemisphere with the isopycnals sloping upward as we approach both poles and also as we approach the equator.

We outline a qualitative description of the dynamics here to motivate the detailed mathematical model presented in §2.1. The abyssal deep water beneath the thermocline is of polar origin and

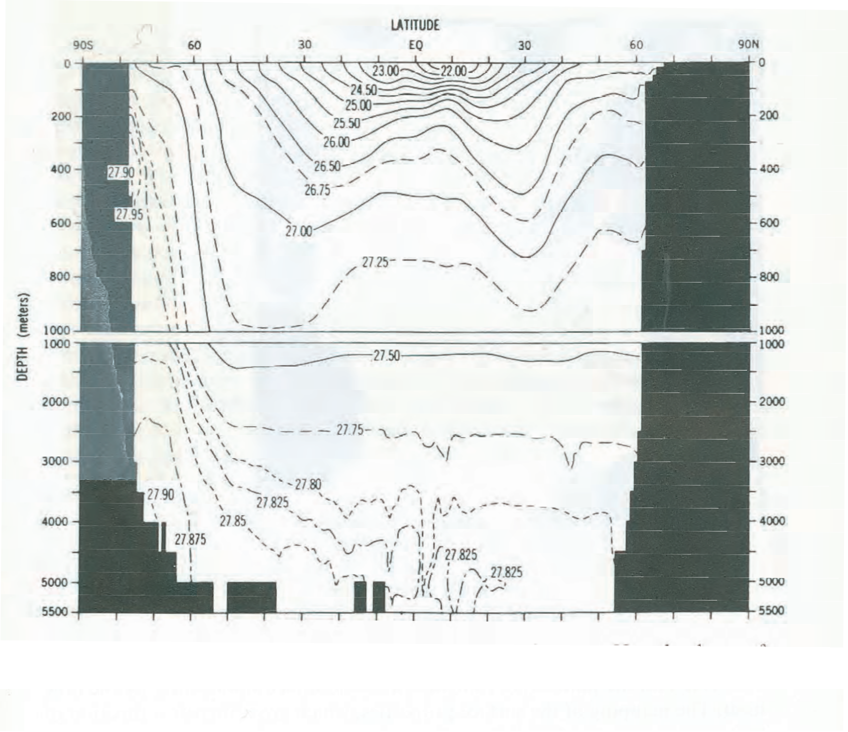

Figure 3: The zonally averaged potential density field for the Pacific Ocean. Note the change of vertical scale below 1000km reflecting the decrease in stratification below this depth. Image from Pedlosky (1998).

is thought to slowly upwell at mid-latitudes, establishing a temperature contrast with the warmer waters of the thermocline. The atmosphere imposes a temperature distribution on the surface of the ocean. This generates a decrease in surface density from the poles to the equator and hence the ispoycnals must intersect the surface. The surface wind stress in the sub-tropical gyres produces a downward Ekman pumping, carrying the surface density distribution downwards to generate a vertical density stratification. However, it is not immediately clear why we have an upwelling of the density distribution at low latitudes, creating a strongly stratified upper ocean close to the equator. By analogy with our pipe flow example, we might think of the downward pumping of the density distribution being interrupted in an internal boundary layer close to the equator, where a different dynamical balance takes over.

In the following section we develop a model of the ventilated thermocline, and use it to answer two principal questions:

1. Why does the isopycnal bowl become shallow at low latitudes?
2. Why does the surface forcing only penetrate to 1km?

2.1 The LPS model of the ventilated thermocline

Luyten et al. (1983) developed a model of the thermocline by considering the upper ocean as consisting of a series of layers of constant density. The entire wind driven circulation in the sub-tropical gyre is driven by a downward Ekman pumping of typical magnitude $w_e \approx 10^{-4}\mathrm{cm\,s^{-1}}$, generated by the wind shear stress exerted on the ocean surface. This is incorporated into the model by imposing an Ekman flux

$$w_e = \hat{\mathbf{k}} \cdot \nabla \times \frac{\tau}{\rho f}, \tag{7}$$

at the upper ocean surface as derived in a previous lecture (we do not resolve the upper mixed layer here.) We will consider a model with steady motion in two layers with thicknesses $h_1(x, y)$ and $h_2(x, y)$, lying above a deep abyss that is at rest. The structure and notation is illustrated schematically in figure 4. Note that the isopycnal at $z = -h_1$, marking the lower boundary of layer 1, outcrops at the latitude $y = y_2$ so that layer 2 is in contact with the surface forcing for $y > y_2$. This model is rather simplistic, but it describes the key characteristics of the circulation and it is possible to use it to construct a continuum model by resolving further layers.

2.1.1 Governing equations

We assume that the fluid flow is steady and effectively inviscid in the interior, with frictional effects confined to the surface Ekman layers and described by the imposed Ekman flux w_e. We treat the flow in each layer using inviscid shallow water theory, so that there is negligible frictional stress between the layers and no normal flow across the density interfaces. Applying mass conservation to each layer we obtain

$$\begin{aligned} \frac{\partial}{\partial x}(u_2 h_2) + \frac{\partial}{\partial y}(v_2 h_2) &= -w_e \qquad y > y_2, \\ &= 0 \qquad y < y_2, \qquad (8) \\ \frac{\partial}{\partial x}(u_1 h_1) + \frac{\partial}{\partial y}(v_1 h_1) &= -w_e \qquad y < y_2. \qquad (9) \end{aligned}$$

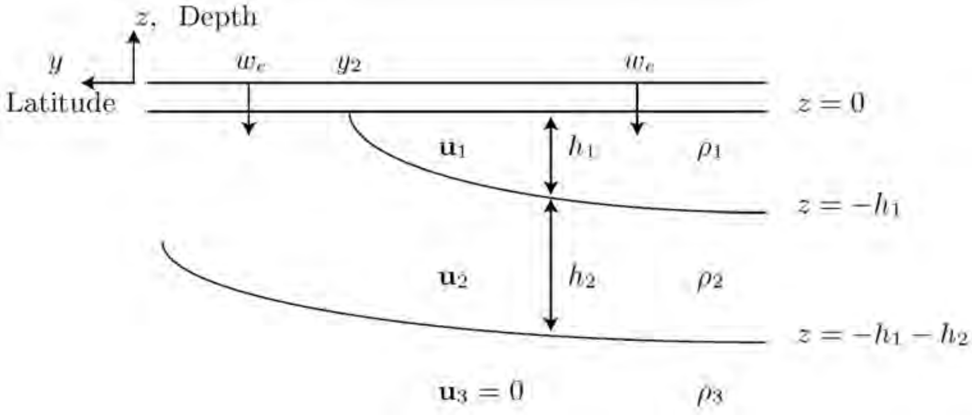

Figure 4: The two layer LPS model. The co-ordinates (x, y, z) vary with longitude, latitude and depth respectively. Fluid of density ρ_1 and pressure $p_1(x, y, z)$ flows with velocity $\mathbf{u}_1(x, y)$ in a layer $-h_1(x, y) < z < 0$. This overlies fluid of density ρ_2, pressure p_2 and velocity $\mathbf{u}_2$ in $-(h_1 + h_2) < z < -h_1$. The abyssal layer of density ρ_3 is at rest in $z < -(h_1 + h_2)$. The circulation is driven by an imposed Ekman downwelling velocity w_e.

In a steady state the horizontal mass flux in each layer changes only due to fluid input across the upper and lower interfaces. Hence each layer is fed by an Ekman pumping w_e while in contact with the free surface, and then after becoming submerged has no divergence of the horizontal mass flux because there is no normal flow across density interfaces.

In previous chapters we have seen that the dominant terms in the momentum balance will depend on the relevant scales for the problem. The Coriolis parameter is given by $f = 2\Omega \sin\theta$ where θ varies with latitude y. We let $\beta = \partial f/\partial y$ describe the variation of the Coriolis parameter with latitude. For a typical oceanic basin scale L and horizontal velocity U we have $U/\beta L^2 \ll 1$, so that the inertial scale is small relative to the basin scale. Alternatively we might think of this as implying that relative velocity gradients are small compared to planetary vorticity gradients. We can therefore neglect the non-linear advection terms, in addition to the viscous terms, so that the appropriate horizontal momentum equations are those of planetary geostrophic balance and hydrostatic balance in each layer. This gives

$$\rho_n f v_n = \frac{\partial p_n}{\partial x}, \tag{10}$$

$$\rho_n f u_n = -\frac{\partial p_n}{\partial y}, \tag{11}$$

$$\rho_n g = -\frac{\partial p_n}{\partial z}, \tag{12}$$

$$\frac{\partial u_n}{\partial x} + \frac{\partial v_n}{\partial y} + \frac{\partial w_n}{\partial z} = 0. \tag{13}$$

where the final equation describes incompressibility. We can combine (10), (11) and (13) to derive the Sverdrup balance in each layer

$$\beta v_n = f\frac{\partial w_n}{\partial z}. \tag{14}$$

Integrating vertically over all layers, and using continuity of w_n at each density interface we obtain

$$\beta \sum_n v_n h_n = f w_e. \tag{15}$$

It will also prove useful to consider the evolution of the *potential vorticity* in each layer, f/h_n. Using incompressibility (13) to eliminate $\partial w/\partial z$ from the Sverdrup balance (14) and combining with the mass conservation relations (8-9) we obtain, after some algebra,

$$\begin{aligned} u_2 \frac{\partial}{\partial x}\left(\frac{f}{h_2}\right) + v_2 \frac{\partial}{\partial y}\left(\frac{f}{h_2}\right) &= \frac{f}{h_2^2} w_e \Theta\left[y - y_2\right], & (16) \\ u_1 \frac{\partial}{\partial x}\left(\frac{f}{h_1}\right) + v_1 \frac{\partial}{\partial y}\left(\frac{f}{h_2}\right) &= \frac{f}{h_1^2} w_e \Theta\left[y_2 - y\right]. & (17) \end{aligned}$$

We use Θ to denote the Heaviside step function here,

$$\Theta\left[x\right] = \begin{cases} 1 & x > 0, \\ 0 & x < 0. \end{cases}$$

We note that potential vorticity is conserved in submerged layers, and it changes only due to Ekman pumping when the layer is in contact with the surface.

The horizontal pressure gradient in each layer can be related to the layer thicknesses. Vertically integrating the hydrostatic balance (12) and substituting into the geostrophic balance conditions (10-11) we obtain

$$f u_2 = -\frac{\partial}{\partial y}\left(\gamma_2 h\right), \qquad f v_2 = \frac{\partial}{\partial x}\left(\gamma_2 h\right), \tag{18}$$

$$f u_1 = -\frac{\partial}{\partial y}\left(\gamma_2 h + \gamma_1 h_1\right), \qquad f v_1 = \frac{\partial}{\partial x}\left(\gamma_2 h + \gamma_1 h_1\right), \tag{19}$$

where $h = h_1 + h_2$ and the relevant reduced gravities are

$$\gamma_1 = \frac{\rho_2 - \rho_1}{\rho_0} g, \qquad \gamma_2 = \frac{\rho_3 - \rho_2}{\rho_0} g. \tag{20}$$

2.1.2 Solution for the single moving layer

At large latitudes ($y > y_2$) layer 2 is in direct contact with the ocean surface and forms the only active layer, so that $h = h_2$. The depth-integrated Sverdrup balance (15) and geostrophic balance (18) then yield

$$\beta v_2 h_2 = f w_e, \qquad v_2 = \frac{\gamma_2}{f} \frac{\partial h_2}{\partial x}. \tag{21}$$

Eliminating v_2 we obtain a differential equation for h_2

$$\frac{\partial h_2^2}{\partial x} = 2 \frac{f^2}{\beta \gamma_2} w_e. \tag{22}$$

There is no normal flow across the eastern boundary of the basin, and so $u_2 = 0$ at $x = x_e$. In general we can satisfy this condition by taking h_2 as a constant - however for our purposes it is sufficient to assume $h_2 = 0$ at $x = x_e$, so that upper layer has zero depth at the boundary. We ignore the details of the boundary conditions on the western boundary here, and assume that these are satisfied by an appropriate western boundary current similar to that obtained in the previous chapter. Integrating (22) gives the layer depth

$$h_2^2 = -2\frac{f^2}{\beta\gamma_2}\int_x^{x_e} w_e(x', y)\, dx' \qquad \text{for} \qquad y \geq y_2. \tag{23}$$

The entire solution is uniquely specified in terms of h_2 for $y \geq y_2$, with the horizontal velocities given by the conditions of geostrophic balance (18).

2.1.3 Solution for two moving layers

As we move closer to the equator layer 2 is subducted under layer 1 for $y \leq y_2$. The Ekman pumping then transfers to layer 1, so that the subducted layer is no longer driven directly by the surface forcing. The potential vorticity equation (16) for layer 2 then yields

$$\mathbf{u}_2 \cdot \nabla \left(\frac{f}{h_2}\right) = 0 \tag{24}$$

so that the potential vorticity is conserved on each streamline. We define a geostrophic streamfunction ψ_2, such that $fv_2 = \gamma_2 \partial\psi_2/\partial x$ and $fu_2 = -\gamma_2\partial\psi_2/\partial y$. We can then satisfy geostrophic balance (18) in layer 2 by setting $\psi_2 = h$. Hence we can write

$$\frac{f}{h_2} = Q_2(h) \tag{25}$$

for an arbitrary function Q_2, so that the potential vorticity is a function of streamline.

In order to determine the form of Q_2, we consider matching of the two solutions at the subduction point $y = y_2$, where $h_1 = 0$, $h = h_2$ and $f = f_2$. The constant f_2 is defined by

$$f_2 \equiv f_0 + \beta y_2. \tag{26}$$

Substituting these values into (25) we determine

$$Q_2\left[h_2(x, y_2)\right] = \frac{f_2}{h_2(x, y_2)} = \frac{f_2}{h(x, y_2)}, \tag{27}$$

so that we can write the potential vorticity as

$$\frac{f}{h_2(x, y)} = \frac{f_2}{h(x, y)}, \tag{28}$$

at any point in layer 2 with $y \leq y_2$. We can use the potential vorticity relation (28) to express the individual layer thicknesses in terms of f and h, giving

$$h_1 = \left(1 - \frac{f}{f_2}\right) h, \qquad h_2 = \frac{f}{f_2} h. \tag{29}$$

In order to determine the evolution of h we again use the depth integrated Sverdrup balance (15). The geostrophic balance relations (18-19) can be used to eliminate v_1 and v_2, so that we obtain

$$\frac{\partial}{\partial x}\left(h^2 + \frac{\gamma_1}{\gamma_2} h_1^2\right) = 2\frac{f^2}{\beta\gamma_2} w_e. \tag{30}$$

The appropriate boundary conditions are $h = h_1 = h_2 = 0$ at $x = x_e$, required to enforce no normal flow at the Eastern boundary. Integrating (30) gives

$$h^2 + \frac{\gamma_1}{\gamma_2} h_1^2 = -2\frac{f^2}{\beta\gamma_2}\int_x^{x_e} w_e(x', y)\,dx' \qquad \text{for} \qquad y \le y_2. \tag{31}$$

We eliminate h_1 in favor of h using (29) and obtain a solution for h in $y < y_2$, given by

$$h = \frac{\left(D_0^2\right)^{1/2}}{\left[1 + \frac{\gamma_1}{\gamma_2}\left(1 - \frac{f}{f_2}\right)^2\right]^{1/2}}, \tag{32}$$

where

$$D_0^2 \equiv -2\frac{f^2}{\beta\gamma_2}\int_x^{x_e} w_e(x', y)\,dx' \ge 0. \tag{33}$$

The characteristic depth D_0 is a measure of the strength of the Ekman pumping which is forcing the circulation.

2.1.4 Structure of the full solution

We now look at the detailed structure of the solution for a particular example of Ekman pumping. Figure 5 shows calculated layer depths for an idealized Ekman pumping given by

$$w_e = \sin\left(\frac{\pi f}{f_0}\right). \tag{34}$$

The contours show the characteristic bowl structure as seen in field observations of the thermocline density structure (see figure 3.) The horizontal circulation is plotted in figure 6. The layer 1 circulation, confined to $y < y_2$, shows a similar qualitative circulation pattern to that given by the Sverdrup interior solution for a homogenous fluid. The layer 2 streamlines show the same

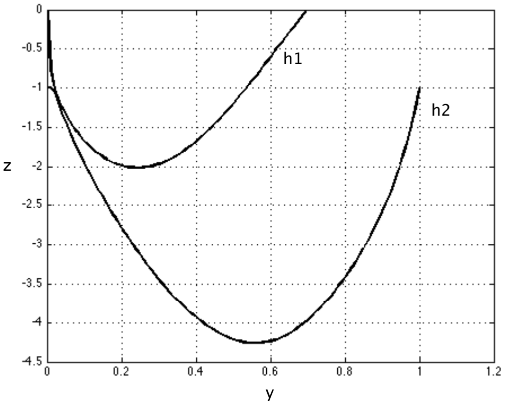

Figure 5: Plot of variation of the with latitude y of the density interfaces at $z = -h_1$ and z=$-h$ for $w_e = \sin(\pi f/f_0)$.

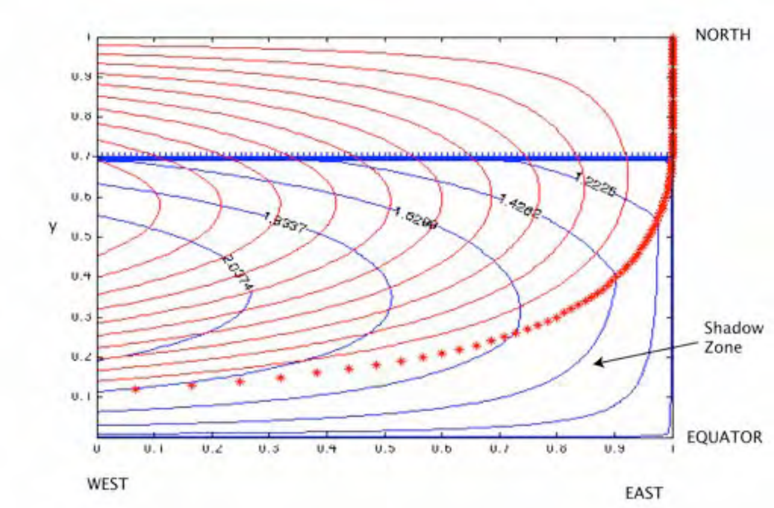

Figure 6: Plots of streamlines in layer 1 (blue curves) and layer 2 (red curves) in a square oceanic basin, for $w_e = \sin(\pi f/f_0)$. The blue dashed line shows the line $y = y_2$, where layer 2 subducts under the Northern most edge of layer 1. The red dotted curve marks the edge of a shadow zone in layer 2, with no flow to the South of this curve.

characteristic shape, except in a shadow zone towards the South-East of the basin. This shadow zone is an interesting prediction of the theory and can be explained as follows. The no normal flow boundary condition on the Eastern boundary requires that h_2 is constant on $x = x_e$. However, after layer 2 subducts and loses contact with the surface we have conservation of potential vorticity on streamlines ($\mathbf{u}_2 \cdot \nabla(f/h_2) = 0$ for $y < y_2$). Since f varies with y, we cannot satisfy the potential vorticity condition with constant h_2, unless $\mathbf{u}_2 = 0$ in a stagnant shadow zone adjacent to the boundary.

We now consider the behavior of the solution as we approach the equator at $y = 0$. If the wind stress τ is aligned in the x direction, we have

$$w_e = -\frac{\partial}{\partial y}\left(\frac{\tau}{\rho_0 f}\right) = -\frac{1}{\rho_0 f}\frac{\partial \tau}{\partial y} + \frac{\beta}{\rho_0 f^2}\tau, \tag{35}$$

and (33) becomes

$$D_0^2 = (x_e - x)\frac{2}{\rho_0 \gamma_2}\left(\frac{\partial \tau}{\partial y}\frac{f}{\beta} - \tau\right). \tag{36}$$

As $f \to 0$, D_0^2 approaches the finite value

$$D_0^2 = -\tau(x_e - x)\frac{2}{\rho_0 \gamma_2}. \tag{37}$$

At low latitudes the trade winds generate a negative shear stress $\tau < 0$, and so (32) implies that the layer thicknesses remain finite as $y \to 0$ and we approach the equator. However, if geostrophic balance is still to hold,

$$v_2 = \frac{\gamma_2}{f}\frac{\partial h}{\partial x}, \tag{38}$$

so that v_2 diverges as $f \to 0$. This singularity is clearly unphysical, and reflects the fact that a new physical balance must become important near the equator. We will resolve this problem in §2.1.6 by introducing an inertial boundary layer close to the equator, where the dynamical balances are modified.

2.1.5 Extensions and the continuous model

The simple model we have developed can be extended to improve the description of the physical processes at work. Rhines and Young (1982)considered how the wind driven circulation might impact directly on the lower layer and the ideas were developed further by Pedlosky and Young (1983) (see also Pedlosky, 1998). The extension towards a continuous model was considered by Huang (1989), who added a larger number of layers into the model. As the number of layers increases we approach a high resolution finite difference approximation to the continuous form of the solution. This solution also shows upwelling of isopycnals as we approach the equator.

2.1.6 The equatorial inertial boundary layer

Our current model of the thermocline breaks down as $y \to 0$ and we approach the equator, with geostrophic balance implying a divergence of the equator-ward velocity v_2 (we can also deduce a similar result for layer 1.) This singularity occurs due to the neglect of certain terms in the governing equations - in order to heal the singularity we must reintroduce the relevant terms to make sure we capture the correct physical balances. We return to the full non-linear inviscid governing equations in each layer, with mass conservation and horizontal momentum conservation in each layer yielding

$$\begin{aligned} \frac{\partial}{\partial x}\left(u_n h_n\right)+\frac{\partial}{\partial y}\left(v_n h_n\right) &= 0, && (39)\\ u_n \frac{\partial u_n}{\partial x}+v_n \frac{\partial u_n}{\partial y}-\beta y v_n &= -\frac{1}{\rho_0} \frac{\partial p_n}{\partial x}, && (40)\\ u_n \frac{\partial v_n}{\partial x}+v_n \frac{\partial v_n}{\partial y}+\beta y u_n &= -\frac{1}{\rho_0} \frac{\partial p_n}{\partial y}. && (41) \end{aligned}$$

We note that near to the equator the Coriolis parameter is approximately linear in y, so that $f = 2\Omega \sin\theta \approx \beta y$.

To determine the appropriate balances, we consider the scaling of all terms in the governing equations. We set

$$(x, y)=(L x', l y'), \quad h=H h', \quad (u, v)=U\left(u', \frac{l}{L} v'\right), \quad p=\rho_0 \beta l^2 U p', \tag{42}$$

where l, L and H are all lengthscales, and U is the appropriate velocity scale. Typically the basin width is $L \approx 1000$km and we will show that the width of the equatorial layer is $l \approx 100$km, so that $l \ll L$. Note that the scaling of the pressure has been chosen for a system where the pressure gradient will be of the same order as the coriolis acceleration. With these scalings in place, the non-dimensional forms of (39-41) are

$$\begin{aligned}
\frac{\partial}{\partial x'}\left(u'_n h'_n\right) + \frac{\partial}{\partial y'}\left(v'_n h'_n\right) &= 0, && (43)\\
\frac{U}{\beta l^2}\left(u'_n \frac{\partial u'_n}{\partial x'} + v'_n \frac{\partial u'_n}{\partial y'}\right) - y' v'_n &= -\frac{\partial p'_n}{\partial x'}, && (44)\\
\frac{U}{\beta l^2}\frac{l^2}{L^2}\left(u'_n \frac{\partial v'_n}{\partial x'} + v'_n \frac{\partial v'_n}{\partial y'}\right) + y' u'_n &= -\frac{\partial p'_n}{\partial y'}. && (45)
\end{aligned}$$

In order to avoid singular behavior of v as $y \to 0$, we need to include the non-linear inertia terms in the x-momentum balance (44). This requires that

$$U/\beta l^2 = \mathcal{O}(1). \tag{46}$$

The retention of some non-linearity reflects the fact that the relative component of vorticity becomes comparable to, and exceeds the planetary vorticity as we approach the equator. However, we can neglect the inertial terms in (45) due to the extra factor of $l/L \ll 1$, so that the y-momentum is in geostrophic balance. We have a loss of symmetry in a narrow region close to the equator, with only the x-component of inertia being important - this is sometimes called *semi-geostrophy*.

We require two further scaling relations in order to determine the depth scale H, boundary layer width l and velocity U uniquely in terms of the imposed physical scales. We assume the pressure will satisfy hydrostatic balance, so that

$$p \sim \rho_0 \gamma_2 H \sim \rho_0 U \beta l^2, \tag{47}$$

where the second balance is obtained from the direct scaling introduced for p. We determine a scale for H by assuming smooth matching of the depth of the thermocline outside of the internal boundary layer. This requires $H \sim D_0$, so that scaling of (36) yields

$$H^2 = \frac{\tau L}{\rho_0 \gamma_2}. \tag{48}$$

Combining (46-48) we obtain the lengthscales

$$l = \left(\frac{\gamma_2 \tau L}{\rho_0 \beta^4}\right)^{1/8}, \quad H = \left(\frac{\tau L}{\gamma_2 \rho_0}\right)^{1/2}, \quad U = \left(\frac{\gamma_2 \tau L}{\rho_0}\right)^{1/4}. \tag{49}$$

Using typical oceanic values of $\gamma \approx 0.01\mathrm{m\,s^{-2}}$, $L \approx 1000\mathrm{km}$ and $\tau \approx 0.01\mathrm{m^2\,s^{-2}}$, we find that $l \approx 200\mathrm{km}$, $H \approx 100\mathrm{m}$ and $U \approx 1\mathrm{ms^{-1}}$.

References

R. X. Huang. On the three dimensional structure of the wind-driven thermocline inthe North Atlantic. *Dyn. Atmos. and Oceans*, 15:117–159, 1989.

J. R. Luyten, J. Pedlosky, and H. Stommel. The ventilated thermocline. *J. Phys. Ocean.*, 13: 292–309, 1983.

J. Pedlosky. *Ocean Circulation Theory*, page 453. Springer Verlag, 1998.

J. Pedlosky and W. R. Young. Ventilation, potential vorticity homogenization and the structure of the ocean circulation. *J. Phys. Ocean.*, 13:2020–2037, 1983.

Internal boundary layers in the ocean circulation

Lecture 10 by Jan Zika

This section follows on from Andy's 'Internal boundary layers in the ocean circulation'.

1 Equations of motion in the equatorial region

We may now define the scaled boundary layer equations

$$-(y+\zeta_n)v_n = -\frac{\partial B_n}{\partial y} \quad , \quad \zeta_n = -\frac{\partial u_n}{\partial y}. \tag{1}$$

Here the Bernoulli potential is defined as

$$B_n = P_n + \frac{1}{2}u_n^2 \tag{2}$$

and close to the equator we assume the relative vorticity is dominated by its local component $-\frac{\partial u}{\partial y}$. Beneath the surface, the streamfunction (ψ) may be defined on each layer such that

$$h_n\vec{u}_n = \hat{k}\times\nabla\psi_n. \tag{3}$$

We also define the potential vorticity

$$q_n = \frac{y-\frac{\partial u_n}{\partial y}}{h_n}, \tag{4}$$

which is the combination of both the planetary and relative components of vorticity. By combining (3) and (5), the streamfunction and Bernoulli function may be related by

$$q_n\frac{\partial\psi_n}{\partial x} = \frac{\partial B_n}{\partial x}, \tag{5}$$

and combined with zonal geostrophy ($yu_n = -\frac{\partial P_n}{\partial y}$) equation (4) may be extended to

$$q_n\nabla\psi_n = \nabla B_n. \tag{6}$$

Here the gradient of the Bernoulli function is related to the motion of potential vorticity. Although B_n is a closely related to streamfunction in rotating flows, in areas of no rotation this is not so (i.e. consider a non rotating flow where $q_n = 0$ hence B_n is a constant whereas there can by a complicated function for the flow (ψ) but for a rotating fluid the functions are intimately linked). By taking the dot product of $\vec{u}_n$ on both sides of (6), we may derive the following relationships in the equatorial region

$$q_n\vec{u}_n\cdot\nabla\psi_n = \vec{u}_n\cdot\nabla B_n. \tag{7}$$

Above this region, $\vec{u}_n \cdot \nabla \psi_n = 0$ by definition. Also, the streamfunction and potential vorticity are related by $\nabla q_n \times \nabla \psi_n = 0$, and from this and (7)

$$\vec{u}_n \cdot \nabla q_n = o \quad \& \quad \vec{u}_n \cdot \nabla B_n = 0. \tag{8}$$

So, in this equatorial region both q_n and B_n are conserved on streamlines and hence they may be related to one and another on each layer by the function Q_n such that

$$q_n = Q_n(B_n) \tag{9}$$

i.e. when B_n is constant on a streamline (q_n must be also). Assuming the flow is once again hydrostatic the pressure p on layers 1 and 2 may be represented in terms of the depth h such that $p_2 = h, p_1 = h + \Gamma_{12} h_1$ for $\Gamma_{i,j} = \frac{\gamma_i}{\gamma_j}$. Writing the relationship between potential vorticity and B for layer 2 in full,

$$\frac{y - \frac{\partial u_2}{\partial y}}{h_2} \quad = \quad Q_n(h + \frac{1}{2}u_2^2). \tag{10}$$

For geostrophic balance of u_2, we must have $\frac{\partial h}{\partial y} = -y u_2$. We have defined systems of equations that describe both the large f midlatitude regions and those of small f close to the equator. It is now pertinent to merge the two solutions and derive a solution for the full system.

2 Linking the equatorial and mid-latitude regions

The physically important question now arises as to what Q_2 must be in order to link the equatorial regions to those of the multitudes in a consistent way. For large y (where y is a coordinate of the equatorial region), the solutions must merge. About the transition region on layer 2

$$q_2 \approx \frac{y}{h_2} \qquad B_2 \approx h. \tag{11}$$

Using (11) from the ventilated thermocline solution we have

$$Q_2(B_2) \quad = \quad \frac{y_2}{B_2} \tag{12}$$

and hence

$$\frac{y - \frac{\partial u_2}{\partial y}}{h_2} \quad = \quad \frac{y_2}{h + \frac{1}{2}u_2^2}. \tag{13}$$

As Joe pointed out in the principal lectures, equation (13) is the water parcel analogy to marriage. A girl with a lot of potential (y_2) is united with a boy of great thickness (h_2) at high latitudes. Together the flow of life takes them to lower latitudes and although the girl develops added spin ($\frac{\partial u_2}{\partial y}$) and the boy becomes more energetic ($\frac{1}{2}u_2^2$), the relationship between the now man and woman remains the same. However, as Antonello points out, there is a lot of turbulence in the world and such simple models are often not able to be generalized. It is left to the reader to derive a relationship incorporating turbulent terms (both theoretically and experimentally).We may now simply define the following set of ODEs in y only.

$$\frac{\partial u_2}{\partial y} = y - \frac{y_2}{h + \frac{1}{2}u_2^2}; \tag{14}$$

$$\frac{\partial h}{\partial y} = -yu_2; \tag{15}$$

$$h_2 = h - h_1. \tag{16}$$

In order for the system defined above to be solved we require a relationship between the depth h and thickness of layer 2 h_2. As the solution must hold for the equatorial regions, the Sverdrup relation breaks down and may not be applied here. We will thus attempt to match the solutions at the equatorial boundary. It is feasible to add additional layers, because it is simply the relationship between h_1 and h_2 that we desire. Indeed the inclusion of additional layers reduces the influence of our assumptions about h at the surface.

We will apply two closure techniques. In both cases we allow the solutions to merge at $y_n >> 1$. The first closure assumes that

$$h(x, y) = h(x, y_n) \tag{17}$$

for all y and the second assumes

$$h(x, y) = h_1(x, y_n) + \frac{h(x, y_n) - h(x, y)}{\Gamma_{12}}, \tag{18}$$

which implies that the upper layer *pressure gradient* is independent of y (a somewhat ‘sketchy’ assumption that should suffice for the present). In order to conserve potential vorticity we may allow no normal flow across the equator. So at $y = 0$ $B_2 = const. = B_0$ where $B_o = h(0, y_n)$. So B_0 will be the final value of h as it makes a transition from higher latitudes to y=0 (figure 1). Thus

$$u_2h_2 = \frac{1}{q_2}\frac{\partial B_2}{\partial y} = -\frac{\partial}{\partial y}\left(\frac{B_2^2}{2y_2}\right). \tag{19}$$

Thus integrating from $y = 0$ to y_n

$$\int_0^{y_n} u_2h_2dy = \left[-\left(\frac{B_2^2}{2y_2}\right)\right]_0^{y_n} = \frac{B_0^2 - h^2(0, y_n)}{2y_2}. \tag{20}$$

This integration may now be carried out for each x so that the closure is met at large y and $B_2 = B_0$ at $y = 0$ for all x. This is done by the ‘shooting’ method, where u_2 is guessed at $y = y_n$ in an attempt to ‘hit’ B_0, with the u_2 guess being adjusted at each attempt. The method is repeated iteratively until convergence to a solution for u and h. Figure 2 shows solutions, using the second closure, gained through this method for various points in the domain. An interesting result is the prediction of increased zonal velocity close to the equator. The feature is known as the Equatorial Undercurrent (EUC). Indeed the increase in deep flow is coincident with shallowing of the thermocline from west to east (Figure 3). The same essential result is gained using the alternative closure (Figure 4).

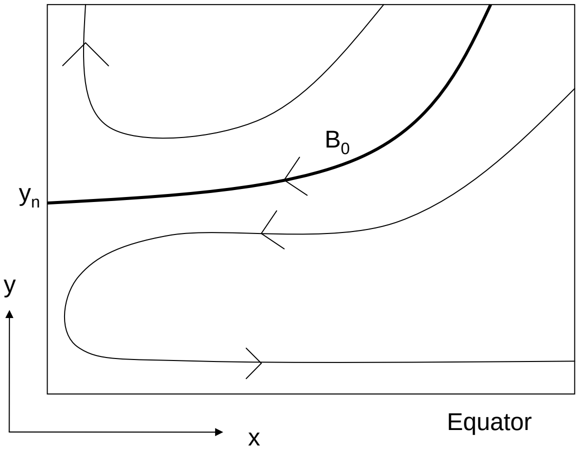
B0
yn
y
x
Equator

Figure 1: Image showing how B_o is defined at y_n as $h(0, y_n)$ defining a boundary higher and lower latitudes.

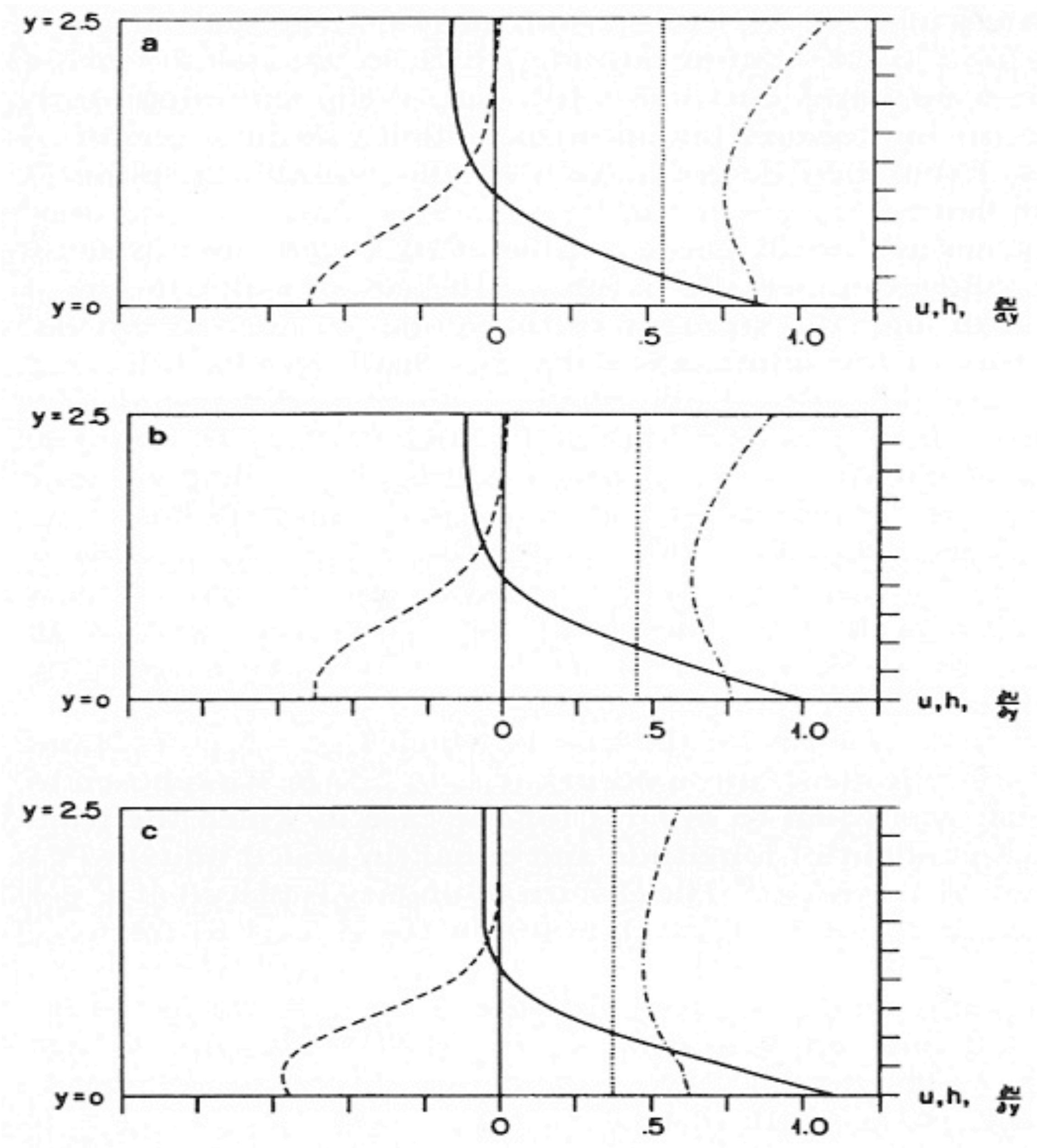

Figure 2: Solutions of (20) for u_2 (solid line), $\frac{\partial u_2}{\partial y}$ (dashed line) and h (dashed-dotted). In this case $\Gamma_{12} = 1$ (second closure). The three panels correspond to profiles at x=0.25, 0.50 and 0.75 respectively. $B_0 = 1.265$ and $y_2 = 5$. Pedlosky (1987)

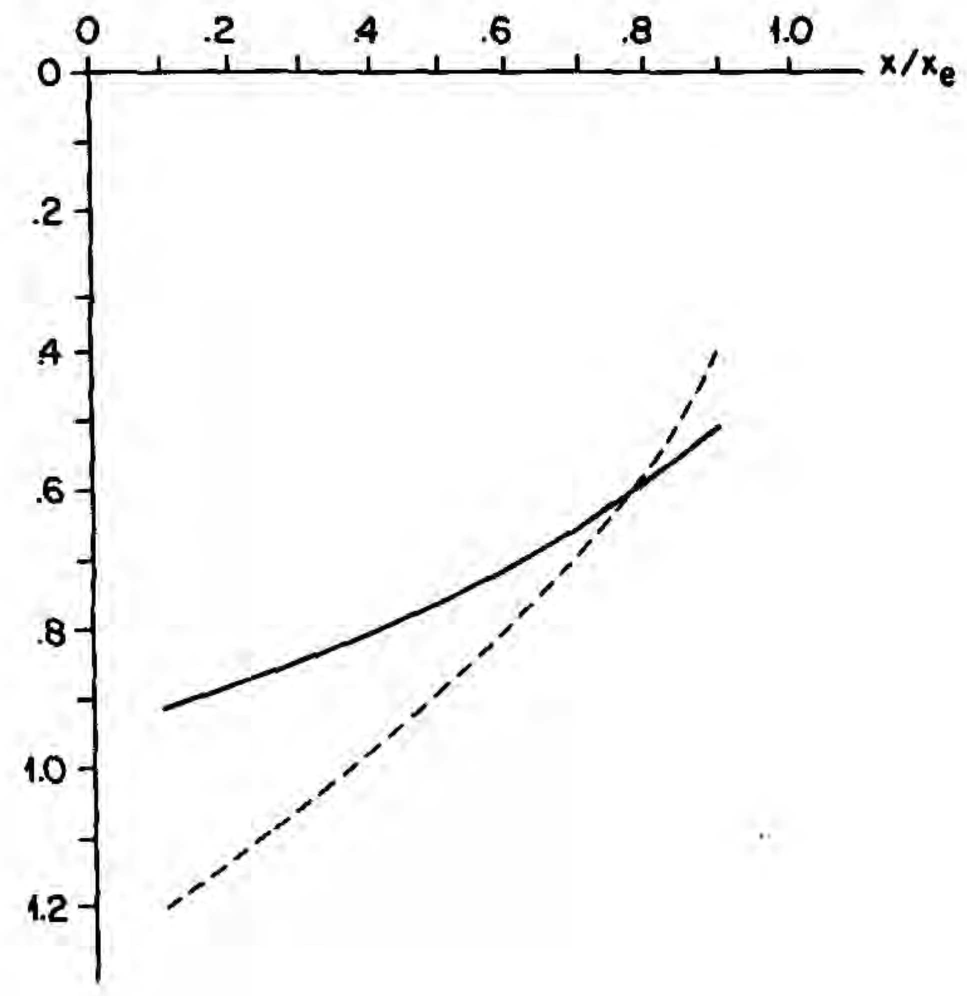

Figure 3: Depth of the base of the moving thermocline layer representing the core of the undercurrent shown as a *solid line* at the equator and as a *dashed line* in the matching region at $y = y_n$. Pedlosky (1987)

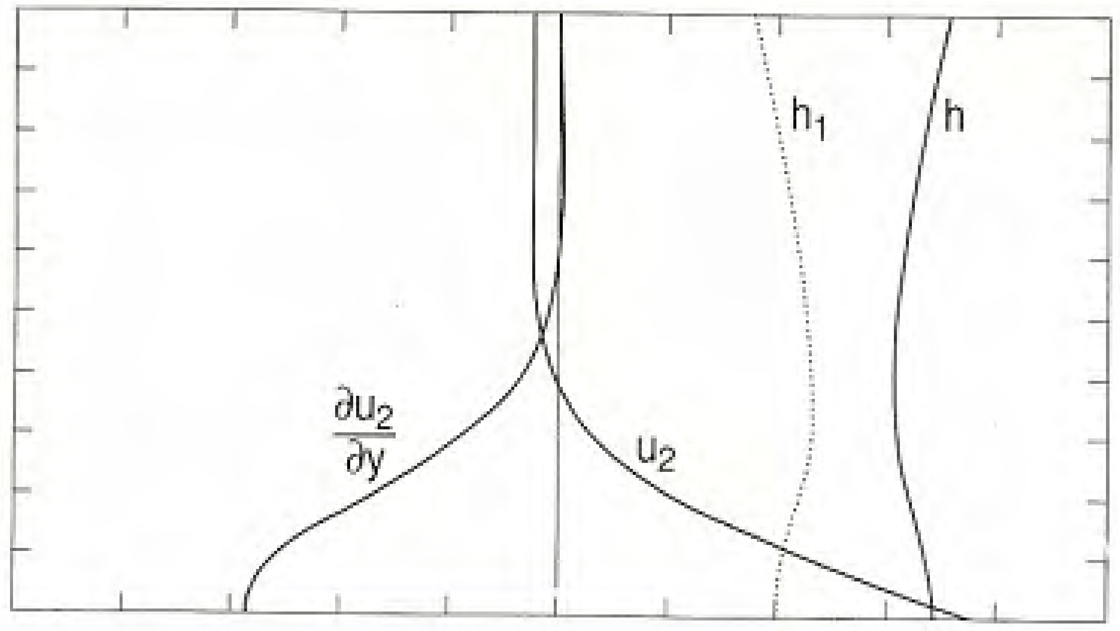

Figure 4: Profiles of u_2, $\frac{\partial u_2}{\partial y}$, h, and h_1 for the case in which (17) is satisfied. The parameters are otherwise as in Figure (2). The calculation is at $x = 0.5$. The maximum eastward velocity is now 0.910.

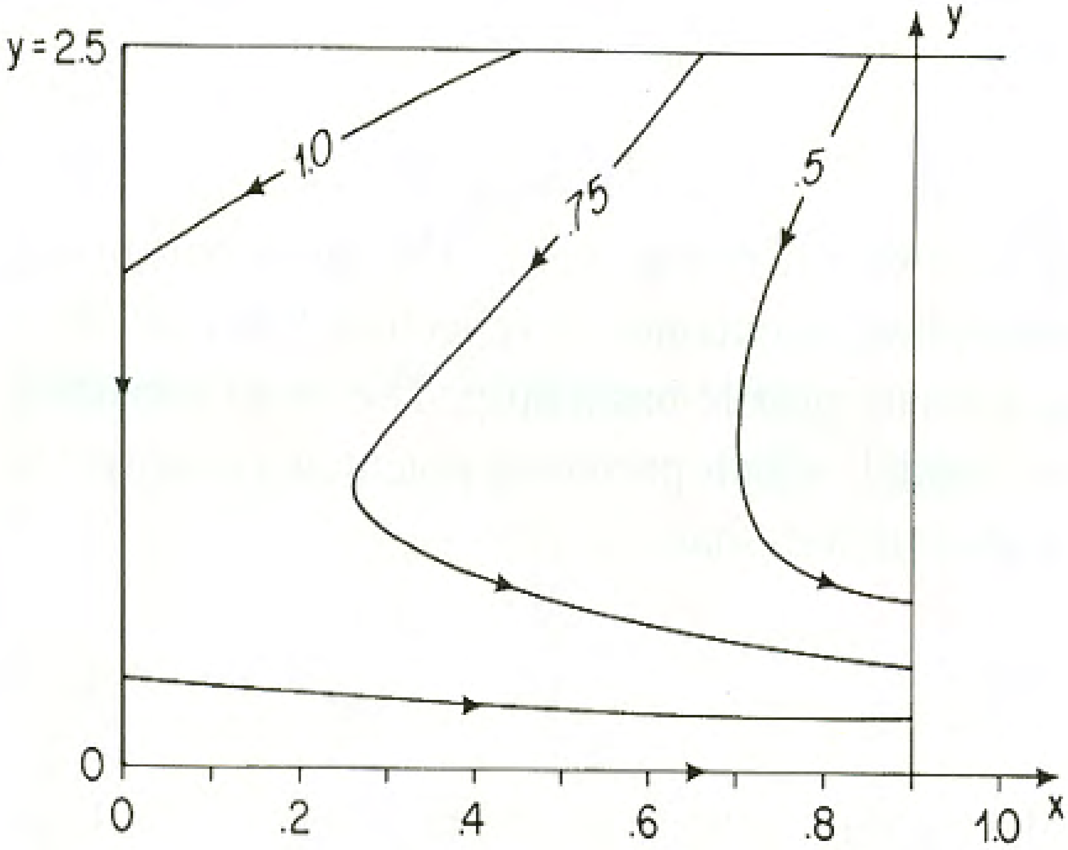

Figure 5: Lines of Constant B_2, which are surrogates for streamlines, calculated from results of 2nd matching (figure 2). Pedlosky (1987)

Analyzing the Bernoulli function B_2 on layer 2 reveals the structure of the undercurrent (Figure 4) as lines of constant B are surrogates of streamlines. The flow is largely southward from the matching region and steers towards the East as the equator is approached.

Modifications to this model, allowing for multiple layers, have been made and show that the undercurrent is still present on deeper layers and reduces in magnitude away from the surface (Figure 6). Indeed, this undercurrent is observed and known as the equatorial undercurrent (EUC) and has been observed as a clear zonal velocity maximum at around 120m depth in the Atlantic and observed also in the Pacific (Figures 7 and 8). Numerical studies also predict this inertially driven EUC (Figure 9).

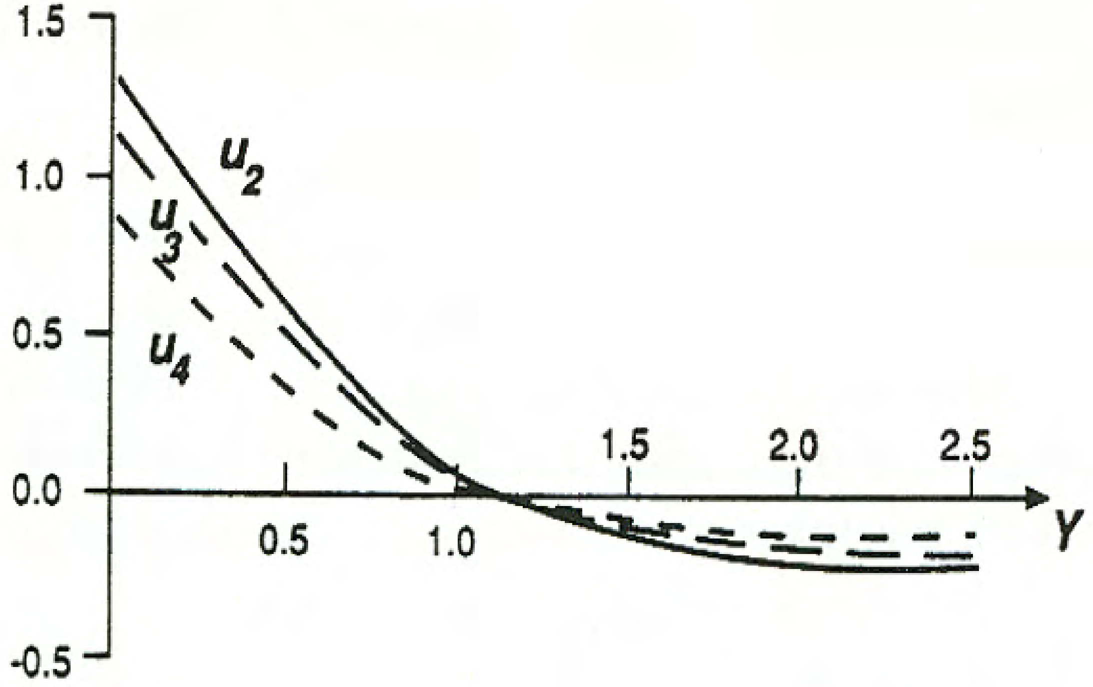

Figure 6: Results of a four-layer model showing the monotonic decrease of the velocity with depth in the undercurrent solution. (Courtesy of R Samelson, pers. comm.)

3 The Internal Boundary Layer in the Thermocline

We now turn our attention to the boundary between the warm surface waters of the thermocline and the dense abyssal waters derived from the poleward regions. We wish to consider the interaction between the coldest water in the subtropical thermocline downwelled from the equatorward boundary of a subpolar gyre and the denser waters below. In order to have a smooth transition between these two regions, it has been anticipated Welander (1971) that a diffusive 'internal' layer might exist. In order to explore this layer and its effect on the ocean and its sensitivity to the magnitude of vertical diffusivity, we follow the approach of Samelson and Vallis Samelson and Vallis (1990).

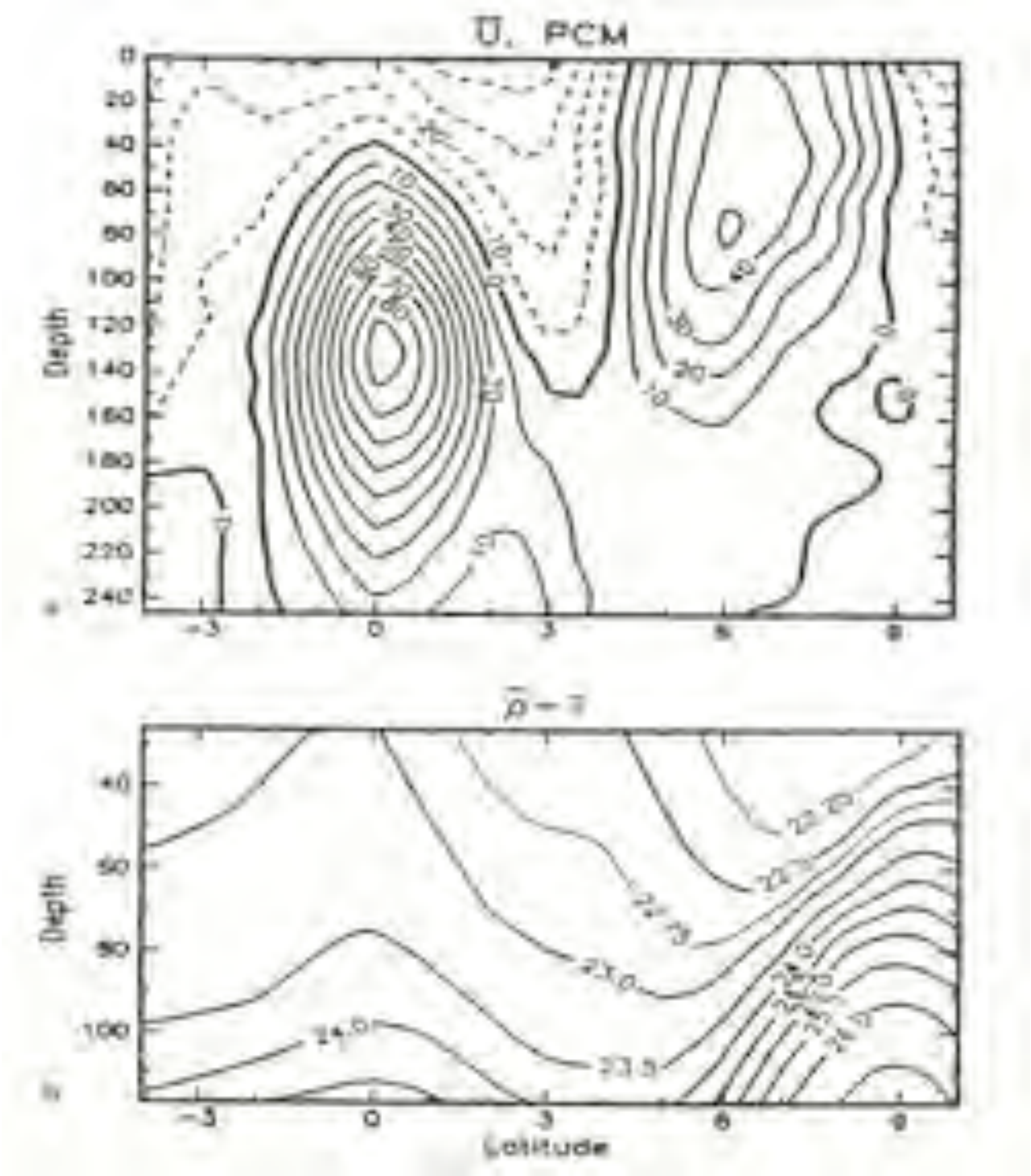

Figure 7: Panel **a** shows contours of zonal velocity measured using current meters in the Pacific. Panel **b** show the density field of the same region. It should be noted that the meridional density gradient vanishes at the equator. Johnson and Luther (1994)

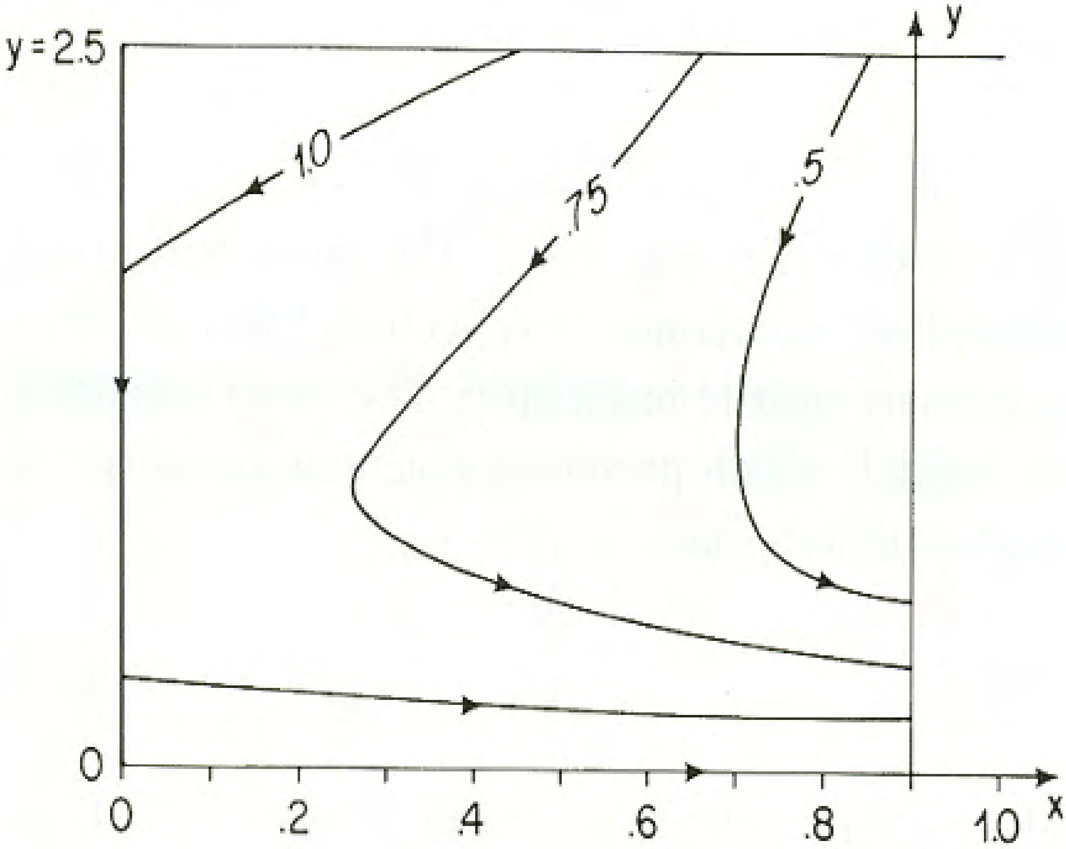

Figure 8: Evidence of the EUC from temperature and zonal velocity profiles from the Atlantic and Pacific Oceans. In each case measurements represent 2-year means. Halpern and Weisberg (1994)

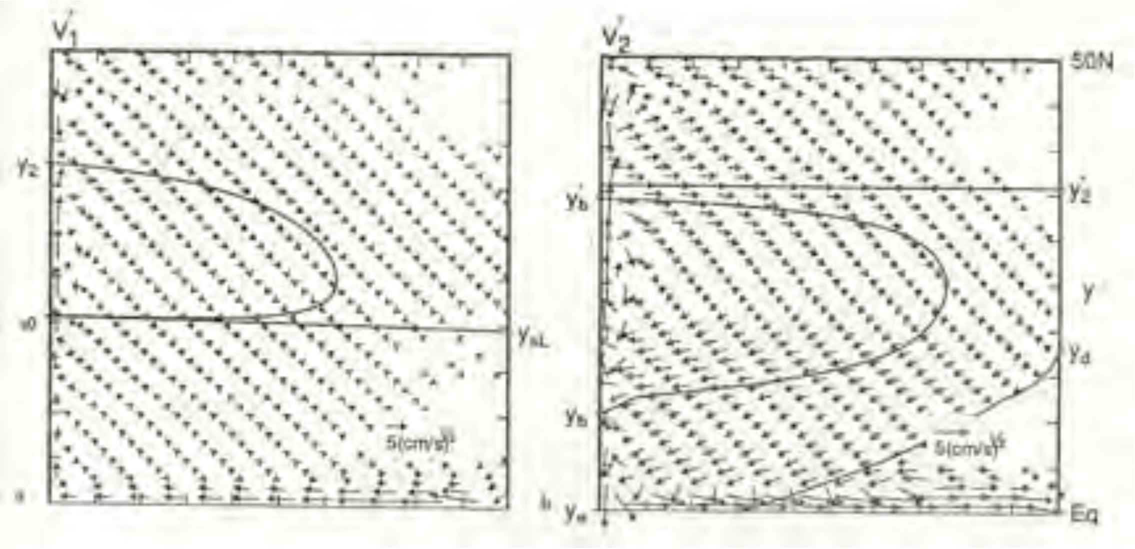

Figure 9: Numerical studies McCreary (1994) show a shadow zone which strikes the equator within the basin. In this case the EUC is fed from the subtropical gyre through the interior as well as the western boundary current.

By assuming a geostrophic and Boussinesq fluid we may define the following set of equations:

$$-fv = -\frac{\partial p}{\partial x} - \epsilon u \quad , \quad -fu = -\frac{\partial p}{\partial y} - \epsilon v, \tag{21}$$

$$\frac{\partial u}{\partial x} + \frac{\partial v}{\partial y} + \frac{\partial w}{\partial dz} = 0. \tag{22}$$

Here a traditional (and somewhat unsatisfying) friction term ϵ is included to avoid singularities in $\mathbf{u}$ when f=0. We shall assume that the fluid is hydrostatic and conserve buoyancy ($b = \frac{\rho - \rho_0}{\rho} g$) such that

$$b_t + ub_x + vb_y + wb_z = \kappa_v b_z z + \kappa_H \nabla^2 b - \lambda \nabla^4 b \quad \& \quad \frac{\partial p}{\partial z} = b, \tag{23}$$

and the Laplacian is defined only in the horizontal ($\nabla^2 = \frac{\partial^2}{\partial x^2} + \frac{\partial^2}{\partial y^2}$). Specifying the Ekman pumping and applying typical boundary conditions, a double structure of the thermocline is revealed (Figure 10). The temperature gradient in (10) reveals a local maxima at which point the vertical velocity switches from a downward pumping to a deep *positive* w, which reduces with depth. Since w is zero at the base of the adiabatic thermocline and the horizontal gradient of buoyancy is determined by the slope of the isopycnals in the ventilated thermocline solution we may use the scalings

$$\frac{\partial w}{\partial z} = \frac{\beta}{f} v \quad \Rightarrow \quad W = \frac{\beta}{f} U \delta \tag{24}$$

$$u_z = -b_y/f \quad \Rightarrow \quad \frac{\Delta b}{L} = \frac{fU}{D_a}, \tag{25}$$

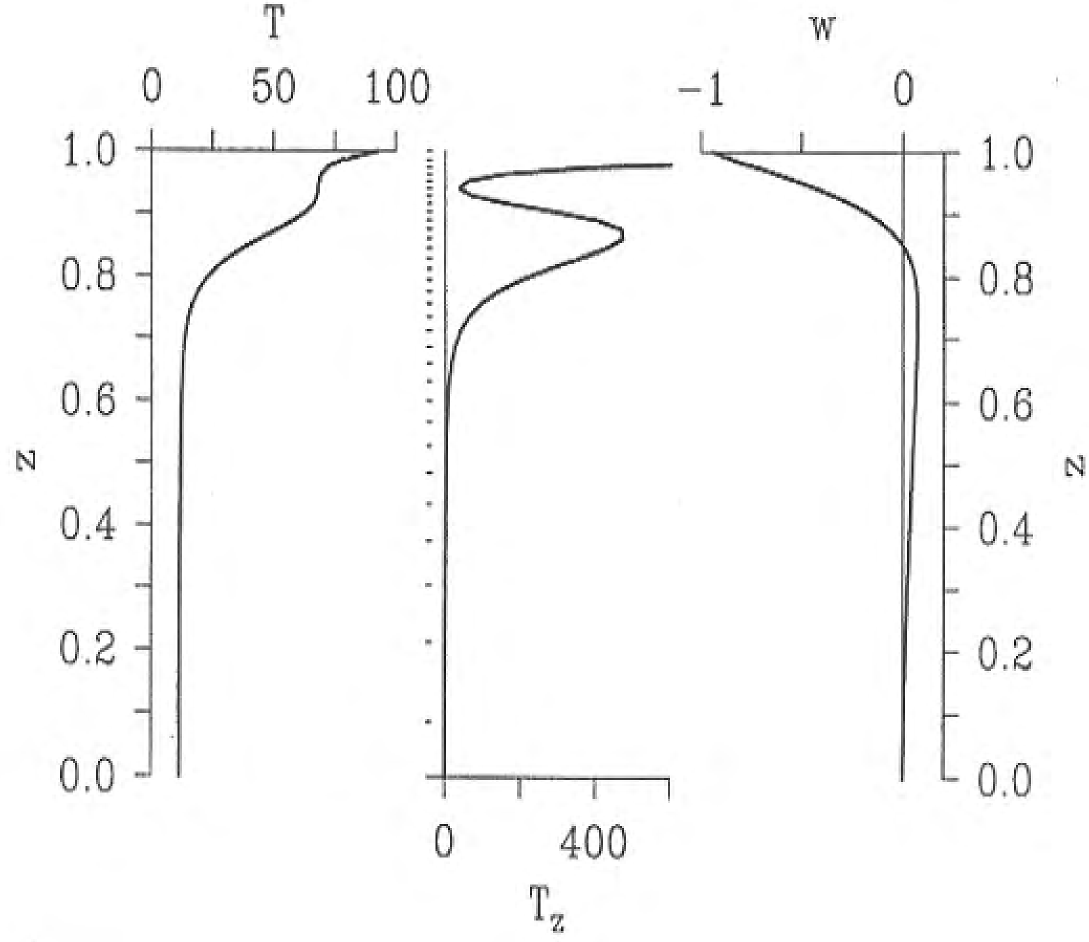

Figure 10: Vertical profiles of T (left panel), T_z (centre), and w (right) at the centre of the domain, (x,y)=(0.5,0.5)

and hence we define the vertical scale of the adiabatic thermocline D_a as

$$D_a^2 \, \frac{f^2 W_e L}{\beta \Delta b}. \tag{26}$$

We see that in the region of the internal thermocline, vertical diffusion balances vertical advection (Figure 11) such that $wT_z \approx \kappa T_{zz}$ (in this model T is a proxy for b) and such that the vertical velocity scales by $W/\delta \;\kappa_v \delta^2$. Again using scalings (24) and (25) we have

$$W_e = \frac{\beta}{f}\frac{\Delta b}{L} D_a \delta = \frac{\kappa_v}{\delta} \quad \& \quad \delta = \left(\frac{\kappa f L}{\beta \Delta b D_a} \right) \tag{27}$$

$$\Rightarrow \delta = \kappa_v^{1/2} \left(\frac{\kappa f^2 L}{\beta \Delta b W_e} \right)^{1/4} \tag{28}$$

Here we have uncovered a $\kappa_v^{1/2}$ relationship by using the scaling height δ which is the scale over which the velocities u and w vary rather than the scale of the thermocline D_a which yields a 1/3 power law. Analysis of the model of Samelson and Vallis indeed reveals the 1/2 power law as shown in figure (12). So Samelson and Vallis, with their simple thermocline model, establish that the flux through the internal boundary is intrinsically diffusive, scaling as $\kappa_z^{1/2}$. Indeed others have treated the internal boundary layer problem in a different way, looking at the entirety of the Thermocline as a diffusive boundary layer. Salmon (1990) looks at this problem and combines the geostrophic balance relationships

$$fv = \frac{1}{\rho_0}\frac{\partial P}{\partial x} \quad \& \quad \beta v = f \frac{\partial w}{\partial z} \tag{29}$$

to get

$$\frac{1}{\rho_0}\frac{\partial P}{\partial x} \quad = \quad \frac{f^2}{\beta}\frac{\partial w}{\partial z}. \tag{30}$$

It is implied from the above that there exists some function M such that

$$\frac{1}{\rho_0} P = M_z \quad \& \quad \frac{f^2 w}{\beta} = M_x \tag{31}$$

and therefore

$$u = -\frac{M_{zy}}{f}, \quad v = \tfrac{M_{zx}}{f}, \quad \frac{g\rho}{\rho_0} = M_z z. \tag{32}$$

From density conservation ($\mathbf{u} \cdot \nabla \rho = \kappa_v \rho_z z$) the following relationship for M results

$$\frac{1}{f}\left[M_{zx} M_{zzy} - M_{zy} M_{zzx} \right] + \frac{\beta}{f^2} M_x M_{zzz} = \kappa_v M_z zzz. \tag{33}$$

If we take the simple case where $M = M(x, z)$, using the scaling factors L, U, d, g' and W and writing (29) and the one dimensional density equation ($w\rho_z = \kappa_v \rho_z z$) in terms of these gives

$$\frac{U}{d} = \frac{g'}{fL}, \quad U = \tfrac{fW}{\beta d}, \quad W = \frac{\kappa_v}{d} \tag{34}$$

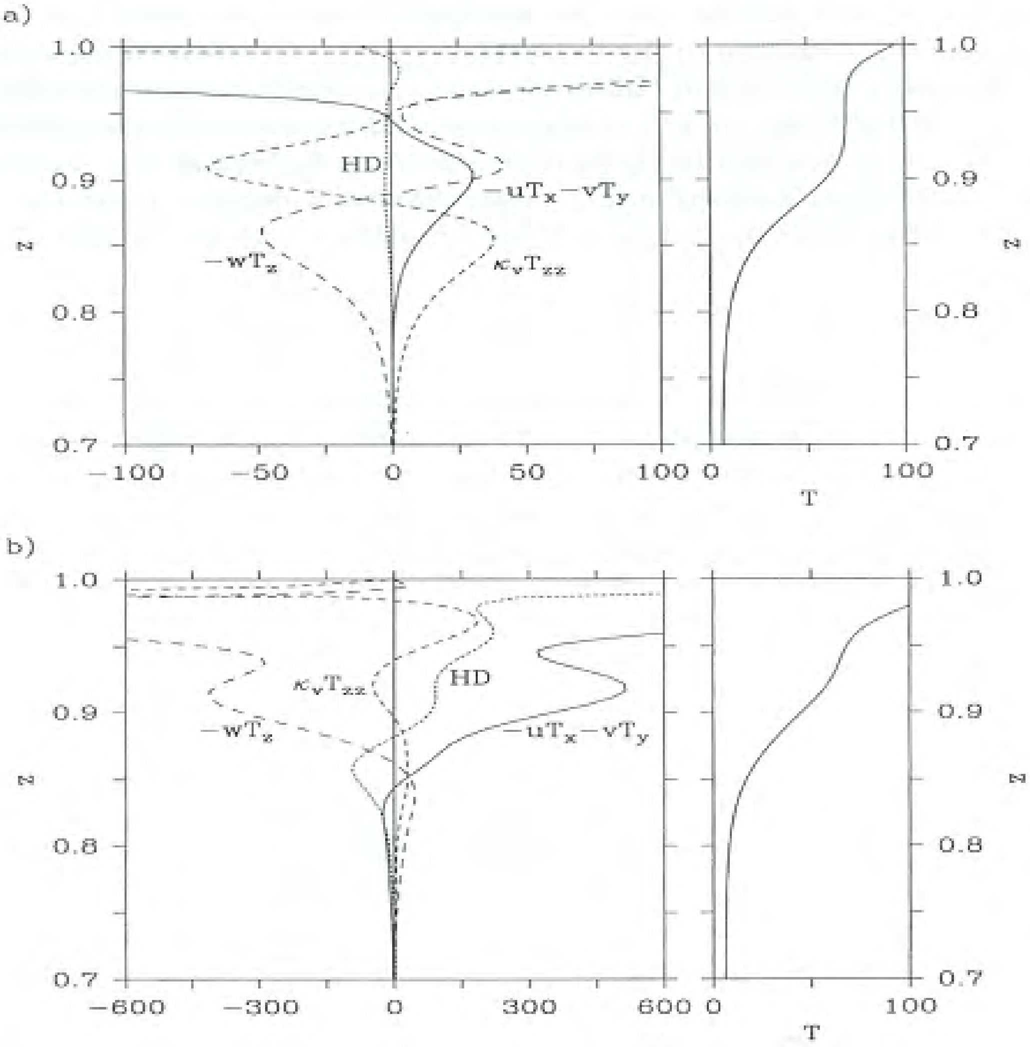

Figure 11: Vertical profiles of terms in the thermodynamic equation for $K_h = 0.002$ with $K_v = 0.003$ at (a) the centre of the domain, (x,y)=(0.5,0.5), and (b) near the western boundary, (x,y)=(0.024,0.5). The profiles for horizontal advection ($-uT_x - vT_y$), vertical advection ($-wT_z$), vertical diffusion ($\kappa_v T_z z$) and the horizontal (Laplacian plus biharmonic) diffusion (HD) are labeled accordingly. The corresponding profiles of T are also shown (right panels). The units are $T_*/t_* = 5.4 \times 10^{-4}\mathrm{Kyr}^{-1}$.

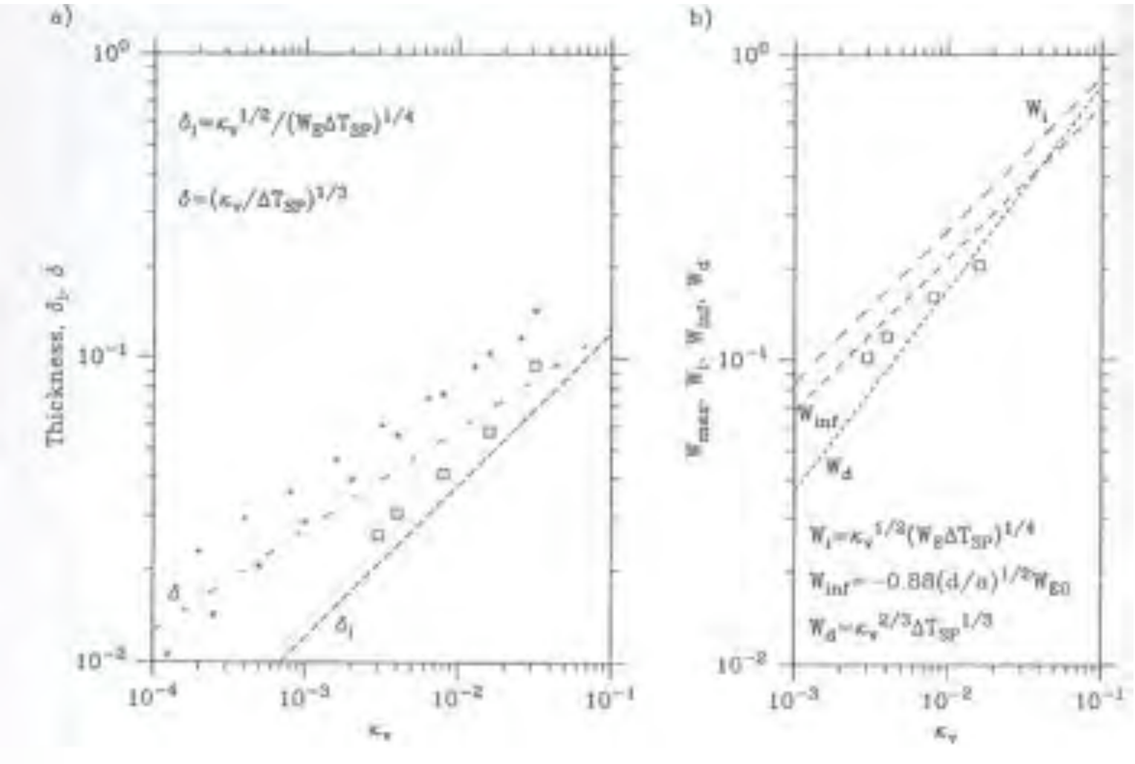

Figure 12: (a) Thickness of the internal peak of T_z versus κ_v, from the profiles in Figure 11. The internal boundary layer scale δ_i and the advective-diffusive scale δ are also shown (dashed lines), along with the corresponding thickness from solutions of the similarity equations (...) and (...). (b) Maximum upward vertical velocity at (x,y)=(0.5,0.5) versus κ_v, from solutions in Figure 11. The internal boundary layer scale W_i, the asymptotic estimate $W_{inf} = W_{\mathrm{inf}}$ and the advective-diffusive scale W_d are also shown (dashed lines).

and hence

$$d = \left(\frac{\kappa_v f^2 L}{\beta g'}\right)^{1/3} \quad \& \quad W = \kappa_v^{2/3}\left(\frac{\beta g'}{f^2 L}\right). \tag{35}$$

So, by this simple scaling argument we have found evidence for a thicker boundary layer and a weaker vertical flow w below the thermocline. Solutions of the one-dimensional version of equation (33) with appropriate boundary conditions applied at the surface and ocean bottom are shown in figure (13). These indeed show a deeper boundary layer and small vertical velocity in the interior.

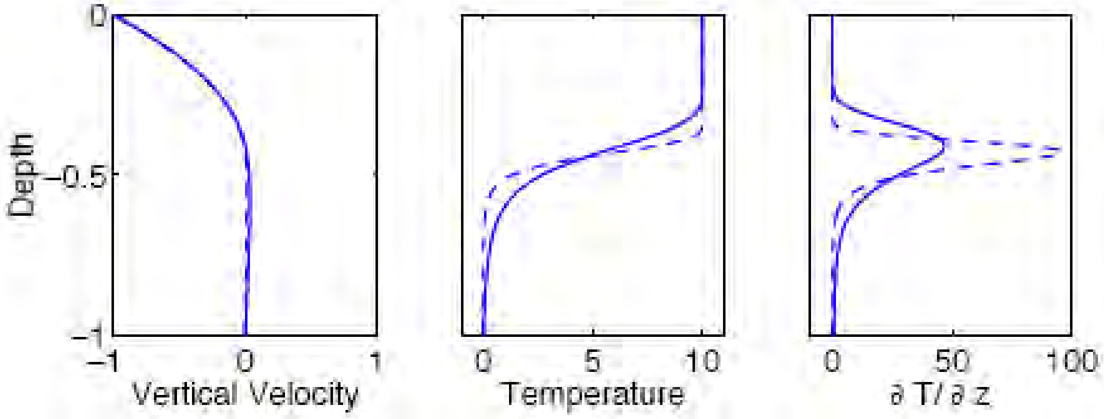

Figure 13: Solution of the one dimensional version of thermocline equation (33) for two different values of the diffusivity: $\hat{\kappa} = 3.2 \times 10^{-3}$ (solid line) and $\hat{\kappa} = 0.4 \times 10^{-3}$ (dashed line), in the domain $0 \leq \hat{z} \leq -1$.'Vertical velocity' is W, 'temperature' is $-W_{\hat{z}\hat{z}}$, and all units are the non-dimensional ones of the equation itself. A negative vertical velocity, $\hat{W}_E = -1$, is imposed at the surface (representing Ekman pumping) B_0=10. The inertial boundary layer thickness increases as $\hat{\kappa}^{1/3}$, so doubling in thickness requires an eightfold increase in $\hat{\kappa}$. The upwelling velocity above the internal boundary layer is much larger and almost independent of $\hat{\kappa}$. The depth of the boundary layer increases as $\hat{W}_E^{1/2}$, so if $\hat{W}_E = 0$ the boundary layer is at the surface. Vallis (2006)

Somewhat different one-dimensional thermocline models have been described, and these have slightly different scaling properties. However, their qualitative features are very similar. For example, in both cases the thickness of the internal thermocline increases with increasing diffusivity (κ_v), and the thickness gets smaller with increasing temperature difference across it. The strength of the vertical velocity increases with increasing diffusivity also. This has an obvious implication for the overturning circulation as the upwelling velocity is an integral component of it.

References

D. Halpern and R. H. Weisberg. Upper Ocean thermal and flow fields at 0°, 28^oW (Atlantic) and 0°, 140^oW (Pacific). 10:7651–7664, 1994.

E. S. Johnson and D. S. Luther. Mean zonal momentum balance in the upper and central equatorial Pacific Ocean. 10:7651–7664, 1994.

J.P. Jr. Lu P. McCreary. The interaction between the subtropical and equatorial circulations: The subtropical cell. 24:466–497, 1994.

J. Pedlosky. An Inertial Theory of the Equatorial Undercurrent. 17:1978–1985, 1987.

R.M. Samelson and G.K. Vallis. Large-scale circulation with small diapycnal diffusion: the two thermocline limit. 55:223–275, 1990.

G. K. Vallis. *Atmospheric and Oceanic Fluid Dynamics: Fundamentals and Large-Scale Circulation.* Cambridge University Press, Cambridge, U.K., 2006.

P. Welander. The Thermocline Problem. *Phil. Trans. R. Soc. Lond. A*, 270:415–421, 1971.

Internal wave radiation from gravity current down a slope in a stratified fluid

J. Hazewinkel
Supervisor: C. Cenedese

Abstract

Experiments with gravity currents in stratified domains thus far ignored the possible radiation of internal waves. The main focus in those experiments has been on entrainment of ambient fluid into the current. Here, we focus on a dense current streaming down a gentle slope with very little entrainment of the ambient fluid. In a linearly stratified ambient, we observe internal waves being radiated from the nose of the dense current. The nose clearly slows down along the slope as its buoyancy difference with the ambient reduces. A simple model for the nose position in time compared well with the observations. In none of the experiments the internal waves emitted show a dominant frequency or wavelength. Rather, a whole spectrum of frequencies and wavelengths are found. We observe three different internal wave regimes, one in which the internal waves are observed close to the nose of the dense current, one in which the internal waves radiate freely out from the nose and one in which we do not find internal waves at all. In order to summarize the results we define an ambient (or bulk) Froude number, $Fr_b = U/(Nh_c)$, based on the stratification N, measured velocity U and the height of the current nose h_c. Using this Froude number we find the free internal waves for $1 < Fr_b <\approx 5$. This range indicates that internal wave emission from gravity currents is very dependent on ambient and local conditions of the flow. In the broader range of currents observed in the ocean it is expected that only a small part will meet these conditions.

1 Gravity currents

Gravity driven currents are naturally occurring flows that are found in atmosphere and ocean. In the atmospheric boundary layer, the so called katabatic winds are driven by dense air, formed by cooling, that flows downwards along the local topography. In the ocean there are currents that are similarly driven by their density anomaly. For example, at high latitudes brine rejection or extreme cooling at the surface increases the total density of the water column. In the Arctic, this dense water eventually spills in overflows through the Faroe Bank Channel and the Denmark Strait. These dense currents flow down the topography into the stratified ocean until they come to their level of neutral buoyancy.

The dynamics of these dense overflow currents has been considered in both theoretical and experimental studies. Some included the effect of rotation, others mainly considered the effect of stratification. Cenedese *et al.* (2004) and Adduce & Cenedese (submitted) included the effect of rotation in experiments with a dense current flowing down a slope in a homogeneous ambient. Different flow regimes were observed that varied from laminar flow, via a flow with roll waves, to a turbulent flow featuring breaking waves. Adduce & Cenedese (submitted) considered the resulting mixing in these different regimes. Mixing in dense currents in non-rotating but stratified environments has been quantified by Baines (2001) and Baines (2005) for slopes with several angles. Also in these studies different regimes were identified, a gravity current regime and a plume regime. In the gravity current regime a balance is reached between the buoyancy force and drag, the current has a distinct upper interface. Mixing occurs only at this upper interface. In the plume regime the current is detached from the topography.

Not on a slope but on a flat bottom, Maxworthy *et al.* (2002) considered the propagation of a dense current in a stratified fluid, both experimentally and numerically. The dense fluid was initially behind a lock and was then released into the ambient stratified fluid. They used dye lines at regular heights to visualize the motion in the interior of the tank. When the gravity current moved at a velocity larger than the internal waves sustain (current faster than the fastest linear wave), the only waves seen were locked to the nose of the current. In this, so called, supercritical regime their Froude number, $Fr = U/(Nh)$ was larger than 0.318, where U is the velocity of the nose of the dense current, h is the initial (before release) height of the dense fluid and N the buoyancy frequency. For lower, or sub critical, velocities the waves propagated out ahead of the nose of the current. However, due to their method of visualization, they could not obtain a more detailed picture of the internal waves, e.g. frequency or wavelength information, other than a sinusoidal raise and fall of the dye lines.

Internal waves, as found in linearly stratified fluids, are distinctly different from interfacial (internal) waves. Internal waves in linear stratifications will only propagate away from a disturbance if the frequency of the disturbance is less than the buoyancy frequency, $N = \sqrt{g/\bar{\rho}\,\partial\rho'(z)/\partial z}$. These internal waves will have the same frequency ω as the disturbance. Also, the energy will propagate under an angle θ with the vertical, or gravitational direction, following the dispersion relation $\omega = N\cos\theta$, Phillips (1977) and Mowbray & Rarity (1967). Surprising at first, the dispersion relation also predicts that the crest and troughs, i.e. the phase lines, travel perpendicular to the energy. Internal waves in the ocean are usually described as vertical modes. However, due to the above curious dispersion relation, near the generation areas this modal description breaks down while a ray-like description becomes more appropriate. Sources of internal wave rays in the ocean are predominantly the interaction of tides and topography as investigated in many studies.

In the experimental study of Aguilar *et al.* (2006) internal waves were generated by dragging a sinusoidal 'topography' through a linearly stratified fluid. They observed different regimes in which waves could propagate freely into the ambient fluid or were evanescent and beyond which turbulence took over.

The motivation of this study came from the combination of the roll waves on the dense current observed by Cenedese *et al.* (2004) with the internal wave generation by a wave pattern by Aguilar *et al.* (2006). We intended to investigate whether the roll waves could be a source for internal wave generation. Since a dense current flowing down a slope can be seen as a disturbance of the stratified ambience, it can be expected that internal waves are found near a gravity current in a stratified fluid. The question is whether these waves can take out energy from the flow and transport it over a long distance. Also the investigation of a Froude number range for the existence of internal waves, as in previous studies, will be of interest.

The remainder of this paper is as follows. Section 2 describes the experimental apparatus used in this study. In Section 3 we present results from the experiments done followed by some analysis in Section 4. In Section 5 we summarize and discuss these results.

2 Method

To study the generation of internal waves by dense currents we use a perspex tank having dimensions 770 × 210 × 250 mm (length, width, height). The well known double bucket method and salt are used to fill the tank with a stratification that linearly increases with depth. The water depth in the tank will be denoted by H. The maximum salinity, and thus the density, varied in each experiment. We present results from experiments where the maximum salinity varies between the salinity of the sea water from the tap, $\rho \approx 1.02\text{g/cm}^3$, to a very salty brine, $\rho \approx 1.1\text{g/cm}^3$. For the latter we use Morton's

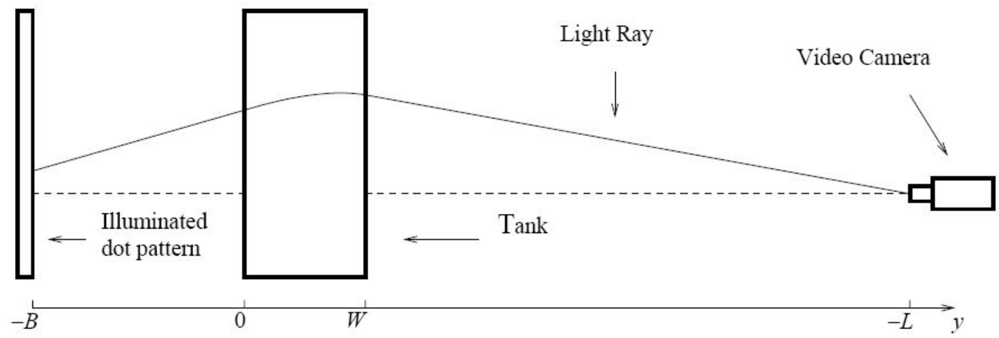

Figure 1: Schematic of the experimental set up.

Kosher salt which does not contain supplements that affect the visibility of the water. After filling the tank, we subtract samples from the fluid at several, typically six, vertical positions. The density of these samples is measured by a Anton Paar densiometer with a accuracy of 10^{-5} g/cm^3.
In the earlier experiments, we would put the slope in after filling the tank. In this case, the slope runs from the upper left side of the tank under an angle α down to the right side of the tank. The source for the dense water is on top of the slope just below the surface. In the second set of experiments (presented in this report) the slope was already in the tank during the filling. In these experiments the lower side of the slope was at the bottom of the tank. In both cases the source, on top of the slope, was connected via a pump with a reservoir of water of density ρ_c, usually the same density as the fluid at the bottom of the tank. In some experiments this dense water was dyed.
To measure the motions in the fluid non-intrusively, we use the synthetic schlieren technique (Dalziel *et al.* (2000)). Synthetic schlieren measures the refractive index changes of a medium resulting from density perturbations. The principle is as follows. When a light-ray propagates through the fluid, the direction of propagation of this ray will be altered by the local value of the gradient of the index of refraction, see schematic in Figure 1. A random dot pattern on a light bank at $B = 0.2$ m behind the tank is monitored through the fluid. Density perturbations alter the refractive index and hence the direction of the light and are observed as apparent movement of the dots. Unfortunately, the refractive index of the air, between the tank and the point of observation, is also altered by unavoidable temperature fluctuations in the laboratory. This leads to some ‘thermal noise’ contaminating the observations and to minimize the effect we had curtains extending from the camera to the tank. To record the apparent movements, we use a Hitachi digital camera positioned at L=3.2 m from the tank. We try to zoom in as much as possible on the region of interest in the tank. Also, we minimize the aperture as much as possible in order the reduce the errors resulting from light coming under an angle. As the buffer memory of the pc used is limited, we could only take 320 frames per experiment. However, we varied the amount of frames taken per second. Regarding an unperturbed reference image, the perturbed position of the dots is translated into corresponding density gradient variations. For this comparison and data processing we use the DigiFlow software. As we observe the changes in the density gradient field, the stronger the undisturbed gradient field is, the more the dots appear to move. For this reason the results of experiments with large N give better results. Also, as the current ’lifts’ the whole stratification slightly in the vertical, we observe in most experiments a constant mean change in the stratification. Thereby, when the currents has passed the ambient fluid diffusive processes will smooth out the perturbed stratification. We will call this process re-stratification. We will present the observations as components of $\mathbf{b} = (b_x, b_z) = \nabla\rho'/(d\bar{\rho}/dz)$, i.e. the perturbation density gradient relative to the gradient of the unperturbed background stratification, $(d\bar{\rho}/dz)$.

Experiment	γ	N s^{-1}	ρ_c g/cm^3	ρ_{bot} g/cm^3	ρ_{top} g/cm^3
030807	0.1	1.4	1.061	1.061	1.003
110807	0.05	1.7	1.071	1.073	1.009
130807	0.2	1.6	1.069	1.068	1.018
150807	0.1	0.9	1.022	1.022	1.004
160807 (default exp)	0.1	1.6	1.069	1.062	1.016

Table 1: Parameters of the experiments presented

Before the start of a typical experiment, we would leave the stratified tank undisturbed for some time after connecting the source and reservoir. We do this, to let re-stratification overcome small perturbations. At the start of the experiment there would be no flow down the slope. Then, the pump will pump the dense water with a fixed flow rate Q, given in cm^3/s, into the source from where it enters the stratified fluid through a sponge. The pump was left running for the time that frames were taken.

3 Results

Several experiments with different slopes and stratifications were performed. We present results from the experiments listed in Table 1. In this table are listed the tangent of the slope $\gamma = \tan \alpha$, the buoyancy frequency N, the density of the current ρ_c and the density at the bottom/top of the tank $\rho_{bot,top}$. All experiments had a discharge $Q = 2.1\mathrm{cm}^3\mathrm{s}^{-1}$ and the slope ended at the bottom of the tank. We consider experiment 160807 as a default experiment with a slope of $\gamma = 0.1$ and a stratification $N = 1.6\ \mathrm{s}^{-1}$ and we will discuss the differences observed in the other experiments. Note that in these experiments the density of the current matches the density at the bottom of the tank.

3.1 Default experiment

Our default experiment has slope $\gamma = 0.1$ and a stratification $N = 1.6\ \mathrm{s}^{-1}$. The descent of the dense current is shown by three snapshots of b_x and b_z in Figures 2. The colour indicates the positive or negative gradients of the perturbation density field. We observe the descent of the dense current, shown by the darkest blue and red colour, Figures 2 a) and b), going over the slope in Figures 2 c) and d) and Figures 2 e) and f). When the nose is at intermediate depth, Figures 2 c) and d), internal waves are radiated from the nose of the current. However, in the first snapshot, Figures 2 a) and b), the waves observed are close to the nose of the current, whereas in Figures 2 c) and d) the waves are found much further away. It is worth noticing that there is no clear defined angle under which the waves propagate. Finally, in the third snapshot, Figures 2 e) and f), the nose does not radiate any waves anymore although there is a remnant of the waves still visible from the nose of the dense current.

In order to find the position of the nose in time along the slope, we take a section parallel to the slope of b_x in time a few pixels above the slope. This section is shown in Figure 3. In the first 20 seconds of the experiment the nose is not in the camera field of view and no apparent movement is resolved. Figure 3 shows flat grey and changes gradation as soon as the nose comes in and shows clearly the position of the nose (vertical axis) in time (horizontal axis). Note that the velocity, or better displacement per time, of the

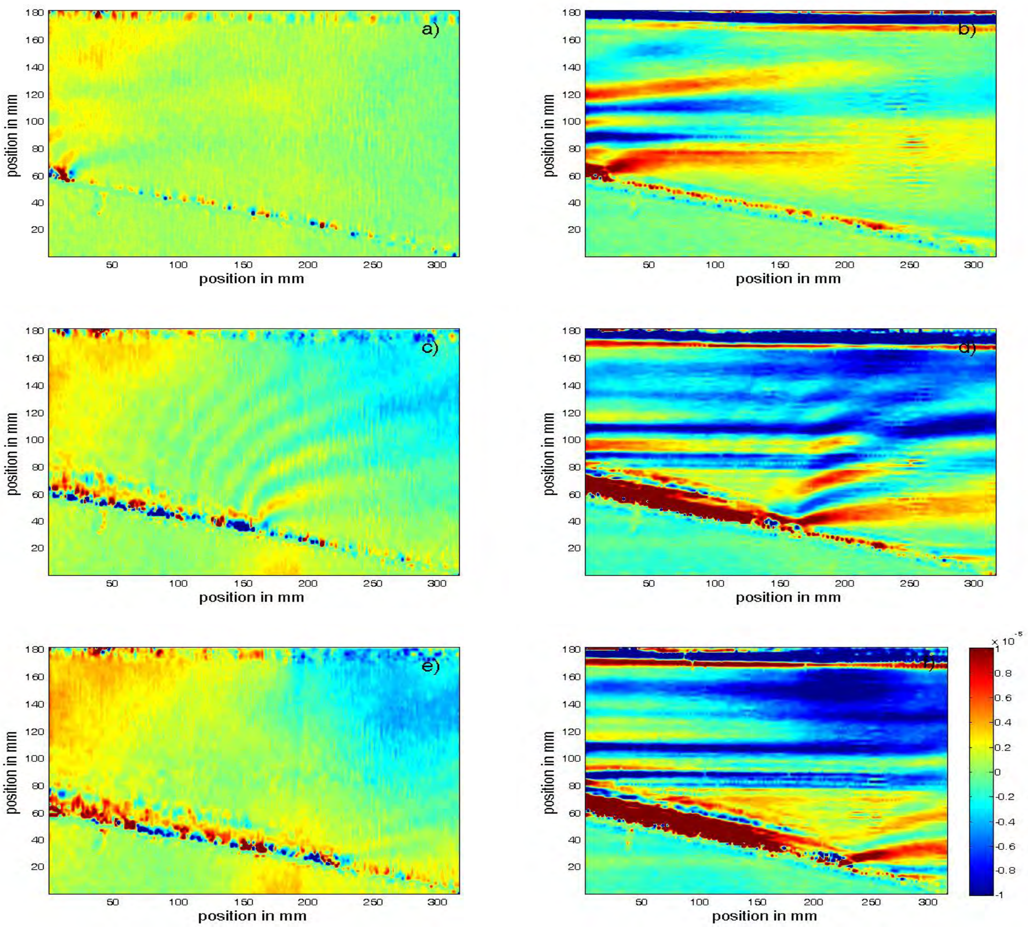

Figure 2: Experiment 160807, three snapshots of b_x (left) and b_z (right), colour indicates value as in colour bar f). Shown are times t=20 s a) and b), 45 s c) and d) and 70 s e) and f) after the start of the experiment. Note that in the vertical gradient the re-stratification causes horizontal lines in the b_z data.

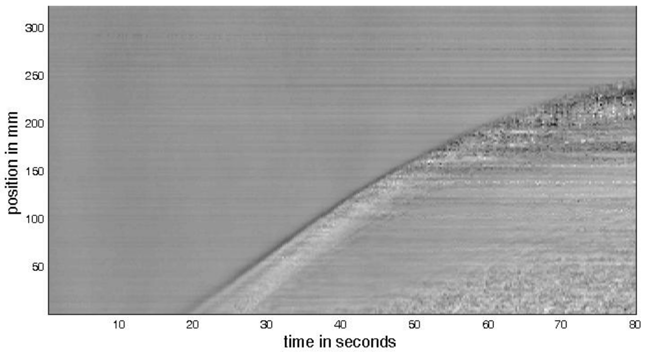

Figure 3: Section of b_x of Experiment 160807 parallel to the slope in time. The colour changes indicates the position of the nose. Note the decrease in displacement in time

current nose clearly decreases along the slope. Obtaining an accurate velocity proved to be problematic as the data of the positions in time is not a smooth/differentiable curve. For later use, we take 10 cm bins and find the different times needed for the nose to travel them. From this we get average velocities along the slope.

3.2 Changing N

The results for the experiments with the same slope angle but different stratification, Experiments 030807 and 150807, show very similar qualitative results as observed in the default experiment. However, the waves are observed to radiate out from the nose starting from a point higher up on the slope. In Experiment 150807, after a short phase of bounded waves, the whole recorded descent of the current shows that the waves radiated are comparable with the default experiment as in Figures 2 c) and d). In experiment 030807 the waves disappear when the current slows down, similar as observed in Figures 2 e) and f). The position of the nose in time, in the same section just above the slope as in the default experiment, shows a lower velocities down slope. The positions in time of the current nose for both experiments are presented in Figure 8 as the noisy lines. Time is off set for clarity. Experiment 150807 (black line) shows very little slowdown while the velocity in experiment 030807 (green line) shows a stronger change in velocity as the nose flows down the slope.

3.3 Changing γ

We also carried out experiments with the same stratification as in the default experiment, i.e. $N = 1.6\ \mathrm{s}^{-1}$ but in which the slope angle is changed. For a steeper slope, $\gamma = 0.2$, we observe the radiation of steep internal waves that remain close to the nose of the current, as shown in Figure 4a). Down slope the current slows down and the internal wave field resembles that of the default experiment (Figures 2 c and d). The position of the nose is shown in Figure 8 by the blue line. In the experiment with a smaller slope, $\gamma = 0.05$, it is difficult to observe anything at all. First, the current is difficult to distinguish from the noise level and second, there are no internal waves generated by the dense current. Our algorithm to detect the position of the nose failed for this experiment and we do not plot it in Figure 8.

4 Analysis

In our default experiment we observe that the radiated internal waves do not seem to have a clear angle of propagation or wave length. This observation seems generic for all

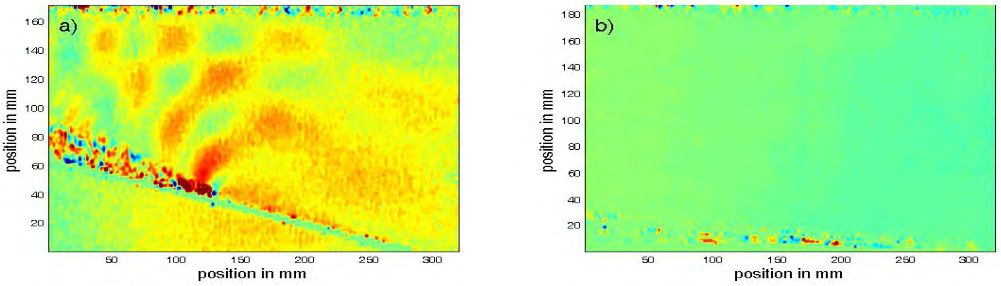

Figure 4: b_x for two different slopes a) $\gamma = 0.2$ and b) $\gamma = 0.05$. Colour as in Figure 2

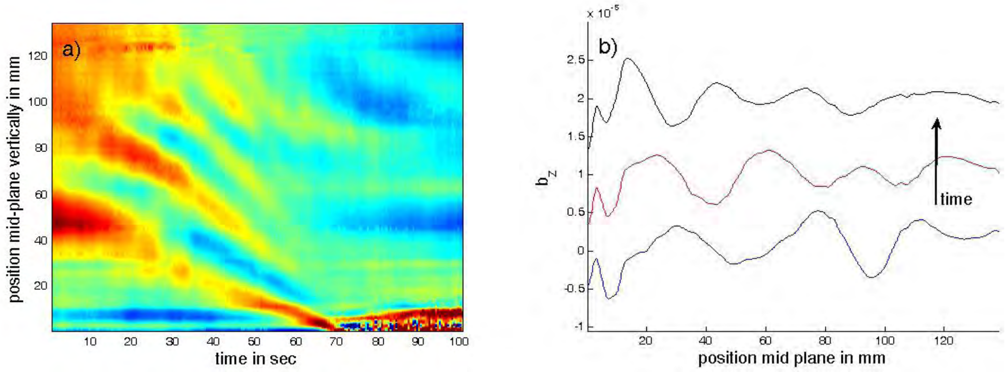

Figure 5: Vertical section mid-slope of b_z of the default experiment. a) shows the amplitude of b_z along this line in the vertical vs time in the horizontal, colour as in Figure 2. b) shows three profiles from a).

experiments in which internal wave radiation is observed. This means that the following, although only presented for the default experiment, applies to the other experiments. In order to investigate whether there are dominant wave lengths or frequencies we take a vertical section mid-slope of b_z of the default experiment. This section runs from the slope up to the surface, vertical axis in Figure 5 a). Presented is the amplitude of b_z in colour and the development in time (horizontal axis). As this section is mid-slope the nose has not passed though it until $t = 70$s, clearly seen in Figure 5 a). The wavelength in this section is observed to decrease as time increases, i.e. towards the nose, furthermore waves are absent after $t = 70$s. Note that for $t > 70$s some horizontal lines appear, this is the result of some re-stratification. We plot three individual sections at $t = 30, 40$ and 50s in Figure 5b), to show that indeed no dominant wavelength is observed and that there is a clear decrease in wavelength in time. This result suggests that a whole range of wave lengths in generated by the dense current flowing down a slope in a stratified ambient.

In order to investigate whether there are dominant frequencies of the waves emitted by the dense current we take a second section. This section of b_z (default experiment), is taken parallel to the slope and 5 cm above it, Figure 6 a). The section is on the horizontal axis and the time on the vertical, the colour is the amplitude of b_z. Figure 6 a) shows a wave pattern moving obliquely in time (vertical axis), which is expected as we have a section parallel to the slope and the current nose is below it. Also, following the waves obliquely, the intensity of the colour, and thus b_z, diminishes along the slope. Time series of three points along the section, are shown in Figure 6 b). All three the sections show that a whole range of frequencies is generated, note the decreasing period of the sinusoidal oscillations. This confirms the observation that a whole range of angles of propagation

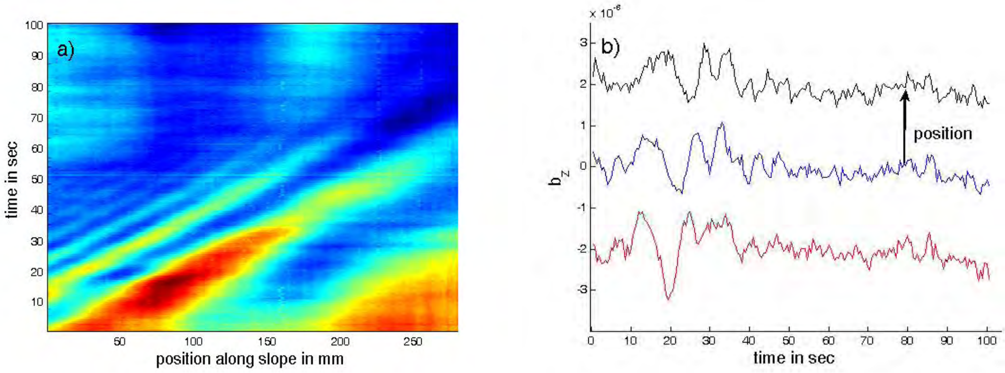

Figure 6: Section parallel to the slope of b_z of the default experiment. a) shows the amplitude of b_z along this line in the horizontal vs time in the vertical, colour as in Figure 2 f). b) shows three profiles from a).

(dispersion relation) is found.

4.1 Simple model for nose position

The current nose is observed to slow down along the slope. The first cause for this is the increasing of the density of the surrounding fluid and the subsequent loss of buoyancy of the current. We will describe the nose speed in terms of the reduced gravity and current height h_c

$$U_f = \sqrt{g'(z) h_c \cos(\alpha)}, \qquad g'(z) = g\frac{\rho_c - \rho(z)}{\bar{\rho}}, \tag{1}$$

based on Simpson & Britter (1979) but including the slope angle α. The vertical dependence of the reduced gravity $g'(z)$ is due to the decreasing difference in density between the local ambient fluid, $\rho(z)$, and the density of the current, ρ_c, as the current runs down the slope. The vertical coordinate is antiparallel with unprimed g, the acceleration due to gravity. We define $z = 0$ at the surface and $\rho(0) = \rho_{top}$. Similarly, at the bottom, $z = -H$, we will denote $\rho(-H) = \rho_{bot}$. We will assume that the stratification is linear over the tank depth H, i.e. $N^2 = g\ (\rho_{bot} - \rho_{top})/H\bar{\rho}$ with $\bar{\rho}$ the characteristic density of water. This means that we can express the density as a function of the depth, i.e. $\rho(z) = \rho_{top} - N^2\bar{\rho}z/g$. We also assume that the entrainment of ambient fluid into the dense current, which would cause a change in ρ_c, is negligible. The above assumptions combine in

$$U(z) = \sqrt{\left(\frac{g(\rho_c - \rho_{top})}{\bar{\rho}} + N^2 z\right) h_c \cos(\alpha)}. \tag{2}$$

This expression for $U(z)$ shows that for decreasing z the velocity decreases and comes to rest at the bottom, $z = -H$, for values of $\rho_c = \rho_{bot}$. From $U(z)$ we find an expression for $U(s)$, where $s = zsin(\alpha)$ is the along slope coordinate. Integrating U(s) in time results in the position on the slope of the current nose in time. Of the variables in Equation (2), only the current thickness $h_c = O(1mm)$ is unknown, for the others see Table 1. As an example we plot the position of the nose in experiment 160708 and two predictions in red for the positions of the nose based on $h_c = 1$mm and 0.5 mm. The two red curves show similar positions for the nose in time as the observations, suggesting that our estimate for the thickness of the current, $h_c = 1$ mm, is reasonable.

Similarly, we find that the positions of the nose for all the experiments listed in Table 1 can be predicted by Equation (2) by using a thickness of h_c =1mm for the current. A

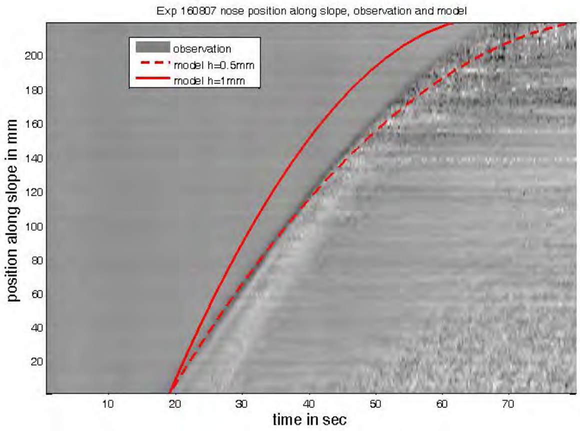

Figure 7: Position of the nose in experiment 160708 and two predictions in red for the positions based on $h_c = 1$mm and 0.5 mm.

combined plot of these nose positions (noisy lines) and theoretical curves (solid lines: h_c=1mm and dashed line h_c=0.5mm) for the experiments listed in Table 1 are shown in Figure 8. Profiles of different experiments are offset for clarity. We observe that of the experiments with γ =0.1 and varying N (black, red and green curves) only the prediction for experiment 030807 (green) is not accurate. Also for the nose position for the experiment with the steeper slope (experiment 130807, blue) the prediction works, remember that we did not have good data for experiment 110807. The fact that our observed and predicted positions of the nose on the slope agree so well, suggests that little to no loss of velocity is caused by internal wave radiation. After all, if there would be any loss this would show up as a discrepancy from velocity loss due to buoyancy effects, i.e. our prediction.
As our observed nose velocities have values that are of order $\sqrt{g'(z)h_c\cos(\alpha)}$, the local Froude number will always be

$$Fr = \frac{U}{\sqrt{g'(z)h_c\cos(\alpha)}} \approx 1. \tag{3}$$

Hence, the different regimes observed can not be related to the local Froude number. However, we can make that distinction when we consider a bulk $Fr_b = U/(Nh_c)$, similar to e.g. Aguilar & Sutherland (2006) and Maxworthy *et al.* (2002). It is worth remarking that the relevant height is h_c, since the slope or height of the free surface could in principle be extended without influencing the internal waves regimes. The height of the current however, plays a crucial role in determining the velocity of the nose and thus the radiation of waves. This definition of Fr_b requires an estimate for the velocity of the nose. We estimate these velocities by taking the displacements of the nose over several seconds and subsequently calculate the average velocities. Assuming that $h_c = 1$mm we find that the Fr_b varies from 6 to 1, as shown in Table 2. Although it seems that bounded waves are found from $Fr_b > 4.3$ in experiment 160807 we observe radiating waves in experiment 150807 with a Fr_b=5. This indicates that perhaps our definition of bounded and radiating waves is not correct. Alternatively it might be argued that the thickness of the current is assumed to be the same in all experiments, i.e. 1mm, and that this thickness could vary between experiment and change the Froude numbers. In any case, Table 2 indicates that a dense current flowing down a slope in a stratified ambiance radiates internal waves $Fr_b < 5$.

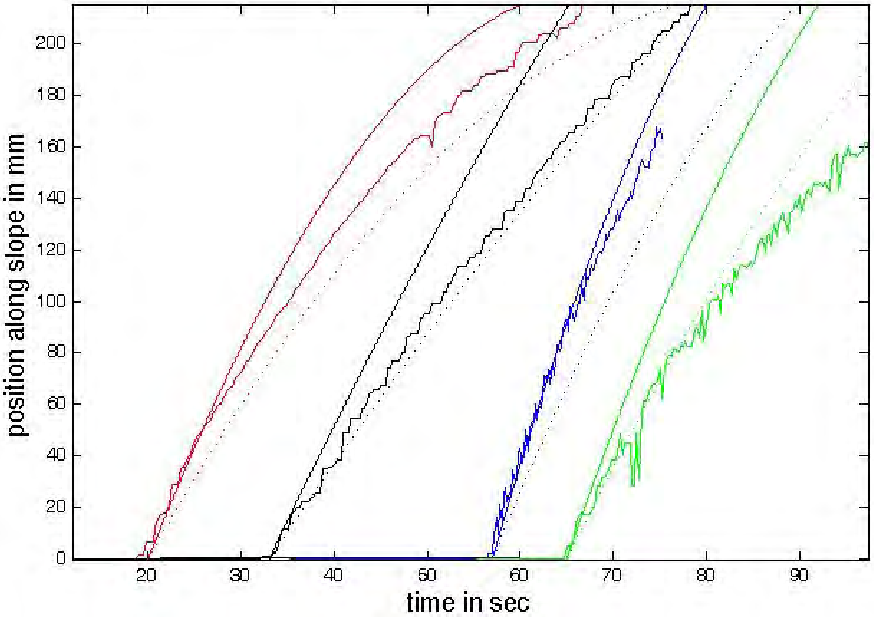

Figure 8: Comparison between observed position of current nose along the slope (noisy line) and the model (solid ($h_c = 1$ mm) and dashed lines($h_c = 0.5$ mm)). For clarity the profiles are set off. Colour correspond to Experiment 030807(green), 130807(blue), 150807(black) and 160807 (red).

Experiment	displacement (mm)	$\triangle t$ (s)	average velocity (mm/s)	Fr_b	regime
030807	80	15	5.3	3.8	radiating waves
030807	28	20	1.4	1	horizontal waves
110807	-	-	<0.2	<0.1	no waves
130807	36	5	7.2	4.5	bounded waves
150807	55	10	5.5	6	bounded waves
150807	45	10	4.5	5	radiating waves
160807	34.5	5	6.9	4.3	bounded waves
160807	39	10	3.9	2.4	radiating waves
160807	14	5	1.8	1.1	horizontal waves

Table 2: Estimated values for Fr_b and the observed internal waves

5 Discussion and Conclusions

In this report experiments are presented investigating internal wave generation from a gravity current. We conclusively show that the nose of a gravity current does emit internal waves. Originally, we intended to investigate whether or not the roll waves, observed by Cenedese *et al.* (2004), would be a suitable generating mechanism for internal waves comparable with the generation of internal wave by a sinusoidal topography (Aguilar & Sutherland, 2006). However, the presented experiments were not in the roll wave regime. For the highest Froude numbers investigated, the internal waves were bounded and the current was still in the laminar regime. This suggests that the roll wave regime might be outside the internal wave radiation regime and if occurring will not radiate internal waves. However, at the lower Froude numbers we did observe internal waves radiating from the nose of the dense current and found a clear dependence of the internal waves radiation on the nose velocity. The nose velocity was well described by the local gravity wave velocity and consequently depends on the unknown/unmeasurable height of the current. Using a reasonable guess for the current height made it possible to compare the measured and predicted position of the nose on the slope in time with good agreement for h_c between 1 and 0.5 mm.

I thank Keith Bradley for his expertise in the laboratory, Steve Thorpe for useful suggestions and the GFD staff and fellows for the summer. JH obtained a GFD Fellowship.

References

ADDUCE, C. & CENEDESE, C. submitted Mixing in a density driven current flowing down a slope in a rotating fluid. *Journal of Fluid Mechanics* .

AGUILAR, D. A. & SUTHERLAND, B. R. 2006 Internal wave generation from rough topography. *Physics of Fluids* **18**, online.

AGUILAR, D. A., SUTHERLAND, B. R. & MURAKI, D. J. 2006 Laboratory generation of internal waves from sinusoidal topogaphy. *Deep-Sea research II* **53**, 96–115.

BAINES, P. G. 2001 Mixing in flows down gentle slopes into stratified environments. *Journal of Fluid Mechanics* **443**, 237–270.

BAINES, P. G. 2005 Mixing regimes for the flow of dense fluid down slopes into stratified environments. *Journal of Fluid Mechanics* **538**, 245–267.

CENEDESE, C., WHITEHEAD, J. A., ASCARELLI, T. A. & OHIWA, M. 2004 A dense current flowing down a sloping bottom in a rotating fluid. *Journal of Physical Oceanography* **34**, 188–203.

DALZIEL, S. B., HUGHES, G. O. & SUTHERLAND, B. R. 2000 Whole field density measurements by 'synthetic schlieren'. *Experiments in Fluids* **28**, 322–335.

MAXWORTHY, T., LEILICH, J., SIMPSON, J. E. & MEIBURG, E. H. 2002 The propagation of a gravity current into a linearly stratified fluid. *Journal of Fluid Mechanics* **453**, 371–394.

MOWBRAY, D. E. & RARITY, B. S. H. 1967 A theoretical and experimental investigation of te phase configuration of internal waves of small amplitude in a density stratified liquid. *Journal of Fluid Mechanics* **28**, 1–16.

PHILLIPS, O. M. 1977 *The Dynamics of the Upper Ocean, 2nd ed.*. Cambridge University Press.

SIMPSON, J. E. & BRITTER, R. E. 1979 The dynamics of the head of a gravity current advancing over a horizontal surface. *Journal of Fluid Mechanics* **94**, 477–495.

Variations in sea surface temperature due to near surface straining flow

Andrew Wells

March 26, 2008

Abstract

The dynamics of the thermal boundary layer below the free surface of the ocean can be influenced by flows generated in the fluid interior, resulting in changes in sea surface temperature. These thermal boundary layer dynamics are studied using laboratory experiments with upwelling flows. The measured surface temperature is well described by a non-dimensional formulation of previous theoretical results. This non-dimensional formulation allows us to predict that internal waves are unlikely to be responsible for large changes in sea surface temperature, but could have an important effect on the transfer of gases between the ocean and atmosphere.

1 Introduction

Detailed modelling of the atmosphere and ocean requires knowledge of the sea surface temperature, which influences the exchange of heat and mass across the air–water interface. Small changes in sea surface temperature can significantly effect the air–sea heat exchange and also change evaporation rates at the interface, leading to modifications in near surface salinity. As a result, the thermal boundary layer near to the ocean surface, or *skin layer*, has recently been an area of active research interest (e.g. Castro *et al.*, 2003; Soloviev, 2007). The thermal boundary layer plays an important role in controlling the sea surface temperature, yet it lies at too small a scale to be resolved in global climate models or field observations. The influence of the thermal boundary layer on sea surface temperature must therefore be parameterised, and so a detailed understanding of the boundary layer dynamics is required in order to provide an accurate parameterisation of the unresolved physics (Fairall *et al.*, 1996). We present a discussion of the effects of upwelling and downwelling flow on sea surface temperature and experimentally investigate the resulting dynamics of the thermal boundary layer.

Some of the pioneering measurements of the ocean skin layer were conducted by Woodcock & Stommel (1947), who observed colder temperatures close to the surface than in the interior of salt and fresh water ponds. This has been followed by numerous field, laboratory, theoretical and numerical studies. For low wind speeds a free convective boundary layer develops, as summarised by Katsaros (1980). The dynamics are modified slightly in the presence of strong winds (see Saunders, 1967; Castro *et al.*, 2003, for example), with additional shear generated turbulence acting to thin the thermal boundary layer. The near-surface boundary layer may also be modified by the presence of surface waves (see Katsaros, 1980, for a review), or surfactants (McKenna & McGillis, 2004). The dynamically similar problem of air-sea gas transfer has also received considerable attention (Soloviev & Schlüssel, 1994; Soloviev *et al.*, 2007).

There have been comparatively fewer studies of the effect of sub-surface flows on the free surface temperature. Infrared observations of the sea surface temperature have shown banded thermal signatures consistent with the scales of internal waves (Walsh *et al.*, 1998; Marmorino *et al.*, 2004; Zappa & Jessup, 2005; Farrar *et al.*, 2007). This suggests that flow structures generated within the ocean interior may be responsible for modifying the properties of the near surface thermal boundary layer. An increase in surface temperature had also qualitatively been observed above an upwelling jet flow in the experiments of Ewing & McAlister (1960). Osborne (1965) presented a theory to describe the modulation of surface temperature by waves and other flows, and Leighton *et al.* (2003) used direct numerical simulation to consider the effect of the local straining flow generated by convection cells. However, there has been no detailed investigation of the dynamics described by the Osborne (1965) theory.

We present a quantitative experimental investigation of the dynamics of the thermal boundary layer in the presence of a local upwelling flow. In §2 we review the details of previous theoretical treatments of the free convective boundary layer and the modifications resulting from a straining flow applied near to the surface. A non-dimensional formulation is presented that identifies different dynamical regimes for the thermal boundary layer, with a corresponding difference in the resulting sea surface temperature. The non-dimensional formulation allows us to identify the relevant regime for flows in the laboratory, and also in the ocean. The experimental procedure and results are described in §3 and §4, respectively. We observe a local increase in surface temperature above regions of upwelling flow, and show that the Osborne (1965) and Leighton *et al.* (2003) theories both provide an accurate description of the observed difference between the free surface and bulk temperatures. We conclude with a discussion of implications for climate modelling in §5. A simple application of the Osborne (1965) theory suggests that internal waves produce only a small effect on sea surface temperature via the skin layer straining mechanism, but could be responsible for significant change in ocean-atmosphere gas transfer.

2 Theoretical Background

The cool skin of the ocean can be considered as a laminar thermal boundary layer occurring where oceanic turbulence is suppressed close to the free surface. The surface of the ocean is cooled by radiative, evaporative and sensible heat fluxes from the ocean to the atmosphere. The transfer of heat is purely by molecular conduction just below the ocean surface. Conservation of enthalpy across the air–water interface requires that the sub-surface conducted heat flux must balance Q, the loss of heat to the atmosphere, so that

$$-\rho c_p \kappa \left.\frac{\partial T}{\partial z}\right|_{z=0} = Q = Q_{\mathrm{rad}} + Q_{\mathrm{evap}} + Q_{\mathrm{sens}}. \tag{1}$$

The radiative component of ocean to atmosphere heat flux is denoted by Q_{rad}, with Q_{evap} and Q_{sens} the corresponding evaporative and sensible heat flux components, respectively. Typically $Q \approx 200\,\mathrm{W\,m^{-2}}$ for a daytime ocean to atmosphere heat flux (see Wick *et al.*,

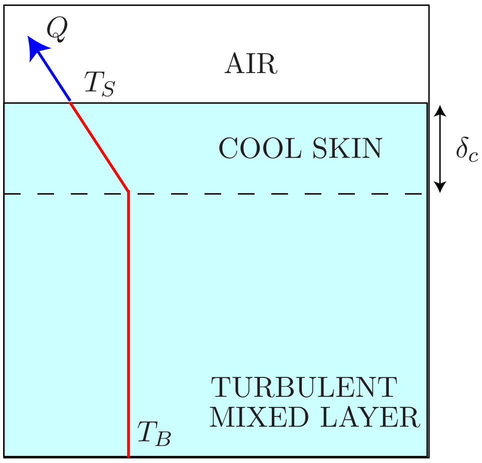

Figure 1: Schematic model of the surface thermal boundary layer of the ocean. A cold, laminar conductive boundary layer overlies a turbulent well mixed interior.

1996, for example.).[1] The ocean is confined to $z < 0$ and has temperature T, with density ρ, specific heat capacity c_p and thermal diffusivity κ. The removal of heat at the upper surface leads to the formation of a thermal conductive boundary layer just below the surface of the ocean. As we move deeper into the fluid the laminar surface layer breaks down due to turbulent velocity and temperature fluctuations and we have a fully turbulent mixed layer, as shown schematically in figure 1. Oceanic turbulence can be generated by buoyant convection or by a surface wind stress, and acts to maintain a relatively uniform temperature down to depths of metres or more.

2.1 Convective boundary layer in absence of imposed flow

For relatively calm conditions with negligible imposed wind shear, the dominant source of mixed layer turbulence is from the buoyancy supplied by cooling at the ocean surface. The dynamics of the resulting convective flow is well described by surface renewal models (Soloviev & Schlüssel, 1994) which build on the analysis of Howard (1966) for convection below a cooled surface. The ocean surface acts as an effectively impermeable upper boundary, so that turbulence is suppressed in a laminar layer immediately below the surface. The removal of heat into the atmosphere leads to a cooling of this surface layer, with the thickness increasing in time as the cold layer grows downward by diffusion. The thickness of the cold layer grows until a critical value of the Rayleigh number is exceeded. The layer then becomes unstable and sheds filaments of cold fluid into the interior. This flux of buoyancy helps to maintain the turbulence in the well mixed interior. Howard (1966) derived an expression for the time-averaged temperature profile generated by this diffusive growth mechanism, which can be expressed as

$$\frac{T(z) - T_B}{T_S - T_B} = \left(1 + 2\zeta^2\right) \operatorname{erfc}\zeta - 2\pi^{-1/2}\zeta \exp(-\zeta^2). \tag{2}$$

---

[1] A positive Q corresponds to a net heat flux from the ocean to the atmosphere in our notation. Note that the opposite sign convention is used in some of the previous literature.

The surface temperature is denoted T_S, and T_B is the temperature in the bulk, deep in the mixed layer. The non-dimensional co-ordinate

$$\zeta = -\frac{\sqrt{\pi}}{4}\frac{z}{\delta_c} \tag{3}$$

represents the depth scaled by the conductive lengthscale δ_c. One possibility is to identify the diffusive lengthscale δ_c as the laminar layer thickness in the simplified model shown in figure 1. If the temperature gradient is linear across the surface laminar layer we have

$$T_B - T_S = \frac{Q\delta_c}{\rho c_p \kappa}, \tag{4}$$

so that the bulk-skin temperature difference is determined by the heat flux Q and conductive layer depth δ_c.

In the case of free convection, Saunders (1967) suggested that the conductive lengthscale δ_c and bulk-skin temperature difference, $T_B - T_S$, can be uniquely determined in terms of the heat flux Q by applying the '4/3rds' convection heat transfer law for turbulent Rayleigh-Bénard convection. Scaling theories suggest that

$$\frac{Q}{\rho c_p} = A\kappa \left(\frac{\beta g}{\kappa \nu}\right)^{1/3} \Delta T^{4/3}, \tag{5}$$

for thermal convection of fluid between two isothermal horizontal plates, with the upper surface cooled. The coefficient of thermal expansion is denoted by β, g is the acceleration due to gravity, ν is the kinematic viscosity, $\Delta T = T_B - T_S$ is the temperature difference between the plates and $A = 0.20$ is a constant of proportionality. We can combine (4) and (5) to give

$$\Delta T = A^{-3/4}\left(\frac{Q}{\rho c_p \kappa}\right)^{3/4}\left(\frac{\kappa\nu}{\beta g}\right)^{1/4}, \tag{6}$$

$$\delta_c = A^{-3/4}\left(\frac{Q}{\rho c_p \kappa}\right)^{-1/4}\left(\frac{\kappa\nu}{\beta g}\right)^{1/4}. \tag{7}$$

so that the bulk–skin temperature difference and thermal boundary layer thickness are determined uniquely by the heat flux applied at the surface. In section 4 we will consider how (6) and (7) compare to the corresponding values observed in experiments.

In the ocean, the above picture of the thermal boundary layer is modified due to forced convection generated by wind. Additional shear turbulence is generated by the applied wind stress, acting to reduce the thickness of the laminar-thermal-boundary layer to $\delta_c = \mathcal{O}(1\text{mm})$.

2.2 Modification of surface thermal boundary by straining flow

Osborne (1965) considered the structure of the thermal boundary layer near to the surface in the presence of an applied flow and inferred variations in sea surface temperature due to ocean waves. We discuss this modification to the surface renewal model below and its implication for regions of local upwelling in the ocean.

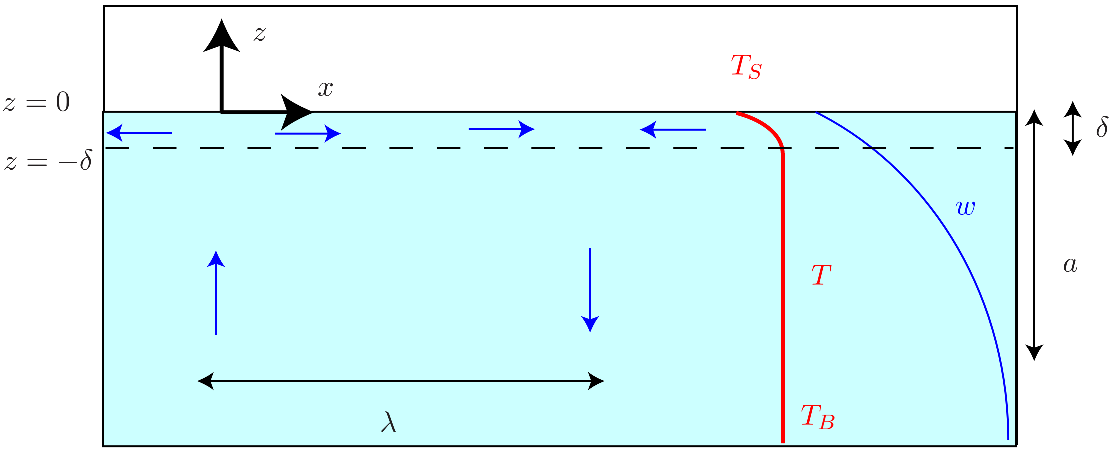

Figure 2: Geometry of the thermal boundary layer in the presence of an imposed internal wave motion. The thermal boundary layer evolves quasi-statically below the free surface, with the internal waves generating diverging and converging flow near to the surface. Typical vertical velocity and temperature profiles are plotted on the right hand side of the figure, with the temperature field varying over a much shorter lengthscale than the velocity field.

Conservation of heat within the fluid is described by the Reynolds-averaged advection-diffusion equation

$$\frac{\partial T}{\partial t} + \mathbf{u} \cdot \nabla T = \kappa \nabla^2 T - \nabla \cdot \left(\overline{\mathbf{u}' T'}\right), \tag{8}$$

where $\overline{(\xi)}$ represents an ensemble average of a variable ξ over a time-scale longer than the typical eddy turnover time-scale but shorter than any time-scale of variation of the bulk flow (see Tennekes & Lumley, 1972, for example.) The ensemble averaged fluid velocity and temperature are denoted by $\mathbf{u}$ and T, while $\mathbf{u}'$ and T' are the corresponding turbulent fluctuations about the mean. We motivate our scalings by considering typical two dimensional ocean internal waves, but the analysis can also be applied to any other system with the same ordering of length-scales (including the axisymmetric flow observed in the laboratory experiments discussed in §3-4). Non-linear internal waves are typically observed to have horizontal wavelengths $\lambda \approx 10 - 100\,\mathrm{m}$, vertical amplitudes $a \approx 1 - 10\,\mathrm{m}$ and frequencies $\omega = \mathcal{O}(0.005)\,\mathrm{Hz}$. The length-scales of variation of the internal wave flow are much larger than the thermal boundary layer thickness (typically $\delta = 0.1 - 1\,\mathrm{cm}$ in the ocean) and so we can make some simplifications to our model under the assumption that $\delta \ll a, \lambda$. Working in a reference frame where the air-water interface is fixed (see figure 2), we expect no normal flow at the free surface so that the vertical velocity $w = 0$ at $z = 0$. We can then approximate the near surface vertical velocity by the leading term in a Taylor expansion

$$w = z \left.\frac{\partial w}{\partial z}\right|_{z=0} + \mathcal{O}\left(a\omega \frac{\delta^2}{a^2}\right). \tag{9}$$

Continuity requires that the local upwelling be accompanied by a horizontally diverging flow. We can think of the internal waves generating a local straining flow about some point within the thermal boundary layer, so that

$$w = -\alpha z, \qquad u = \alpha_1 x, \qquad v = \alpha_2 y, \qquad \alpha = \alpha_1 + \alpha_2 \tag{10}$$

where $\alpha = \mathcal{O}(\omega)$ is the vertical strain rate, (x, y) are the horizontal co-ordinates relative to the centre of the divergence, and (u, v) are the corresponding horizontal components of velocity. We expect horizontal variations to scale with the flow wavelength λ and vertical variations to scale with the boundary layer thickness δ, so that $\partial_x, \partial_y \ll \partial_z$ and we can neglect horizontal diffusion compared to vertical diffusion across the boundary layer. If Q is independent of x and y, we expect horizontal variations in temperature to be small compared to the bulk skin temperature difference, so that $\mathbf{u} \cdot \nabla T \approx w\partial_z T$. Finally, we assume that turbulence is suppressed near to the surface, so that $\overline{\mathbf{u}'T'} \approx 0$ in the upper laminar layer $-\delta < z < 0$. The heat equation (8) then simplifies to give

$$\frac{\partial T}{\partial t} - \alpha z \frac{\partial T}{\partial z} = \kappa \frac{\partial^2 T}{\partial z^2}. \tag{11}$$

For near surface flow generated by internal waves we expect the time dependent term to be comparable to the vertical advection (since $\alpha < \omega$ for linear internal waves). This possibility was discussed in more detail by Osborne (1965), with the resulting solutions exhibiting a wave-like propagation of the temperature signal through the boundary layer. We will focus on the quasi-steady case relevant to our laboratory experiments, so that (11) reduces to the ordinary differential equation

$$-\alpha z \frac{\partial T}{\partial z} = \kappa \frac{\partial^2 T}{\partial z^2}. \tag{12}$$

This is subject to boundary conditions

$$T = T_B \quad \text{at} \quad z = -\delta, \qquad -\rho c_p \kappa \frac{\partial T}{\partial z} = Q \quad \text{at} \quad z = 0, \tag{13}$$

so that the temperature matches the bulk temperature at the top of the mixed layer and is subject to an imposed heat flux at the atmosphere-ocean interface. The system (12–13) has solution

$$T(z) - T_B = \frac{Q}{\rho c_p \kappa} \int_{-\delta}^{z} \exp\left(-\frac{\alpha \xi^2}{2\kappa}\right) d\xi, \tag{14}$$

so that we observe a bulk–skin temperature difference

$$T_S - T_B = \frac{Q}{\rho c_p \kappa} \int_{-\delta}^{0} \exp\left(-\frac{\alpha \xi^2}{2\kappa}\right) d\xi. \tag{15}$$

As α varies we obtain different asymptotic limits. In the limit of no imposed flow ($\alpha = 0$) we recover the linear conduction temperature difference

$$T_S - T_B = \frac{Q\delta}{\rho c_p \kappa}. \tag{16}$$

For flows with large strain rate,

$$\frac{\alpha \delta^2}{\kappa} \gg 1, \tag{17}$$

we obtain a temperature difference

$$T_S - T_B = \frac{Q}{\rho c_p}\sqrt{\frac{\pi}{2\kappa\alpha}}. \tag{18}$$

We note that the equation (18) closely resembles the prediction of Leighton *et al.* (2003), who used a surface straining model to describe the static free convection boundary layer (with $\alpha = 0$ in our notation.) The Leighton *et al.* (2003) model assumes that, for free convection, the thermal boundary layer is set up by a balance between vertical diffusion and a flow with strain rate γ, generated by turbulence in the interior. Leighton *et al.* (2003) suggest that their result can also be generalised for other sources of turbulence by a suitable choice of the effective strain rate γ. It is interesting to note that the large strain rate limit (18) of the Osborne (1965) theory agrees with the Leighton *et al.* (2003) result if we take $\gamma = \alpha$, corresponding to the imposed vertical advection dominating that generated by convective turbulence.

2.3 Non-dimensional formulation

We can also describe the bulk-skin temperature difference in non-dimensional form, in order to identify the different dynamical balances that can be observed in the thermal boundary layer, and ascertain when each balance can be applied. Scaling vertical lengths with δ, temperature differences with the conductive temperature difference $Q\delta/\rho c_p\kappa$, and time with $1/\omega$, we define non-dimensional variables $\hat{z} = z/\delta$, $\theta = \rho c_p\kappa(T - T_B)/Q\delta$ and $\hat{t} = \omega t$. The governing equation (11) becomes

$$\mathrm{St}\,\mathrm{Pe}\,\frac{\partial\theta}{\partial\hat{t}} - \mathrm{Pe}\,\hat{z}\frac{\partial\theta}{\partial\hat{z}} = \frac{\partial^2\theta}{\partial\hat{z}^2}, \tag{19}$$

where the *Péclet number*

$$\mathrm{Pe} = \frac{\alpha\delta^2}{\kappa}, \tag{20}$$

measures the importance of advection of heat relative to diffusion, and the *Strouhal* number,

$$\mathrm{St} = \frac{\omega}{\alpha}, \tag{21}$$

is the dimensionless frequency of the wave motion. The non-dimensional forms of the boundary conditions (13) are

$$\theta = 0 \quad \text{at} \quad \hat{z} = -1, \qquad \text{and} \qquad \frac{\partial\theta}{\partial\hat{z}} = -1 \quad \text{at} \quad \hat{z} = 0. \tag{22}$$

We immediately see from (19) that we can only neglect the unsteady term if $\mathrm{St} \ll 1$ and we have a low frequency motion. Linear internal and surface waves have $\alpha < \omega$, so that $\mathrm{St} > 1$ and the unsteady term must be retained.

For steady flows, the Osborne (1965) prediction (15) can be rewritten as

$$\frac{1}{\mathrm{Nu}} = \sqrt{\frac{\pi}{2}}\frac{\mathrm{erf}\left[(\mathrm{Pe}/2)^{1/2}\right]}{\mathrm{Pe}^{1/2}}, \tag{23}$$

where the *Nusselt number*

$$\mathrm{Nu} = \frac{Q\delta}{\rho c_p \kappa \left(T_S - T_B\right)}, \tag{24}$$

represents the ratio of total heat flux compared to the conducted heat flux for the static ($\alpha = 0$) boundary layer. We have used the error function

$$\operatorname{erf}[x] = \frac{2}{\sqrt{\pi}} \int_0^x \exp\left(-u^2\right) \, du \tag{25}$$

here. For large Péclet number (23) reduces to

$$\frac{1}{\mathrm{Nu}} \sim \sqrt{\frac{\pi}{2\,\mathrm{Pe}}} \quad \text{as} \quad \mathrm{Pe} \to \infty, \tag{26}$$

so that the limit (18) is valid whenever $\mathrm{Pe} = \alpha\delta^2/\kappa \gg 1$. For small Péclet number ($\mathrm{Pe} \ll 1$) we have

$$\frac{1}{\mathrm{Nu}} = 1 - \frac{\mathrm{Pe}}{6} + \mathcal{O}\left(\mathrm{Pe}^2\right). \tag{27}$$

We will see that this limit has important consequences later on.

In §3 and §4 we discuss an experimental investigation of the dynamics described by this theory.

3 Experimental Procedure

A laboratory experiment was used to investigate the structure of the thermal boundary layer below a free surface. The experimental set up is shown in figures 3 and 4 A laminar jet was created at the base of an inner tank by pumping fluid through a vertical nozzle. The nozzle was covered by a sponge to generate a diffuse source of momentum, thus allowing the generation of small strain rates close to the free surface. The pump flow rate was varied between $0.12\,\mathrm{cm}^3\,\mathrm{s}^{-1} \le F \le 1.14\,\mathrm{cm}^3\,\mathrm{s}^{-1}$, in order to alter the input momentum flux and hence the strain rate close to the surface. The jet decelerates as it approaches the free surface, so that there is an axisymmetric straining flow close to the surface (indicated by the blue arrows in figure 4). The fluid then spreads radially, creating a surface divergence, before overflowing into an outer tank where fluid is returned to the pump via a sink. The outer tank has insulated side walls and bottom so that the dominant heat loss is across the air–water interface.

The bulk temperature was measured with a resolution of 0.02°C by a digital HOBO data logging thermometer placed deep in the tank. A PME microscale temperature–conductivity (T-C) probe (incorporating a Thermometrics FP07 thermistor) was lowered into the tank from above in order to measure the variation of temperature with depth and enable estimation of the skin layer thickness δ. The probe tip was aligned to pierce the interface close to the centre of the upwelling jet. Temperature profile measurements were taken over the upper 5 cm of the tank interior, with one sample taken every 0.001 cm. Downward sampling was used so that the probe tip could take measurements before the probe casing influenced the upwelling flow. Several measurements were also made with an upward moving U–shaped probe for the static thermal boundary layer case ($\alpha = 0$), and no qualitative

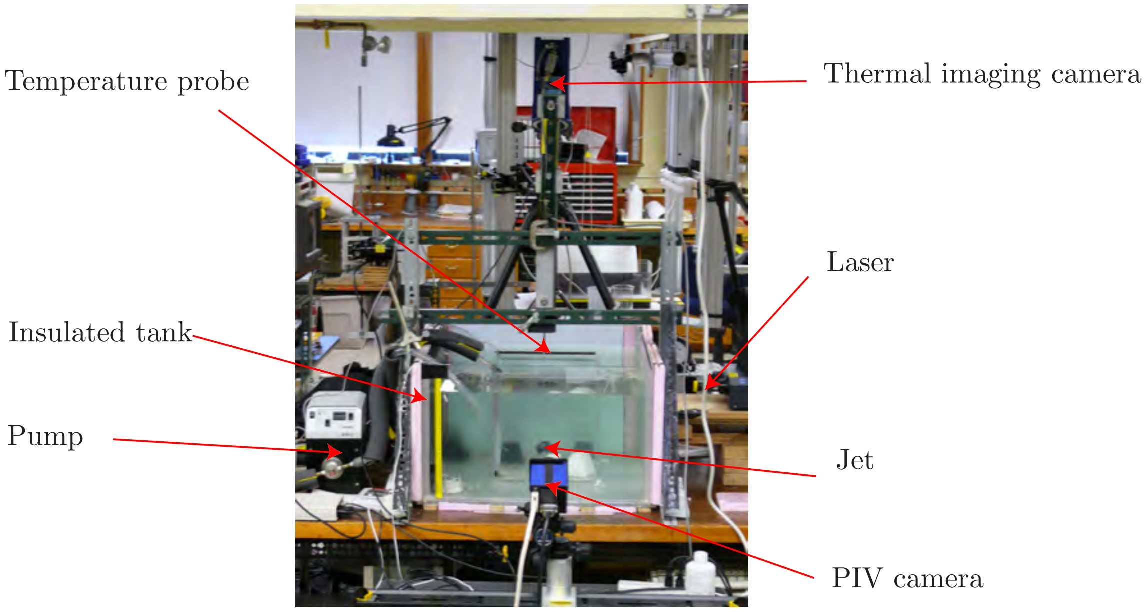
Temperature probe
Thermal imaging camera
Laser
Insulated tank
Pump
Jet
PIV camera

Figure 3: Photograph of the experimental apparatus.

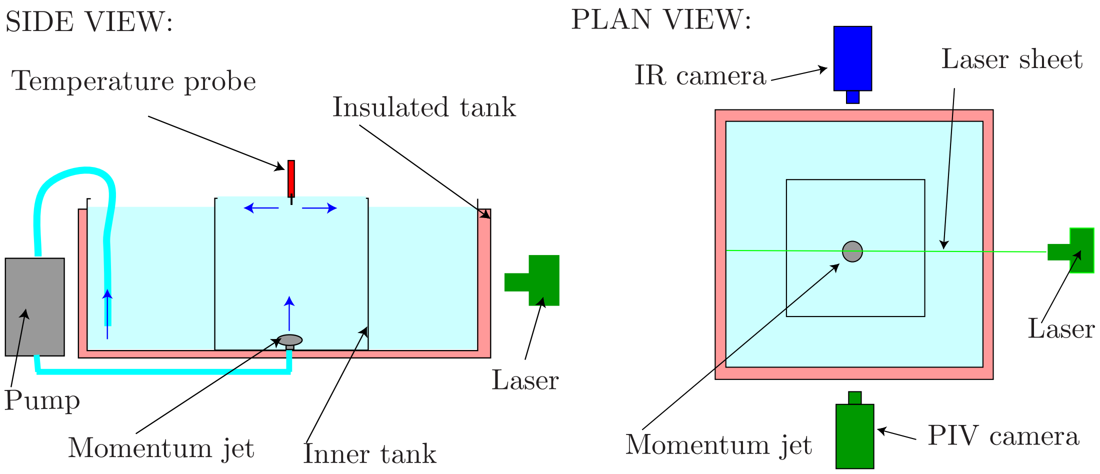
SIDE VIEW:
Temperature probe
Insulated tank
Pump
Laser
Momentum jet
Inner tank
PLAN VIEW:
IR camera
Laser sheet
Laser
Momentum jet
PIV camera

Figure 4: Schematic diagram illustrating the experimental set-up. Fluid is injected via a jet at the base of the inner tank to create a near surface flow divergence, as indicated by the blue arrows.

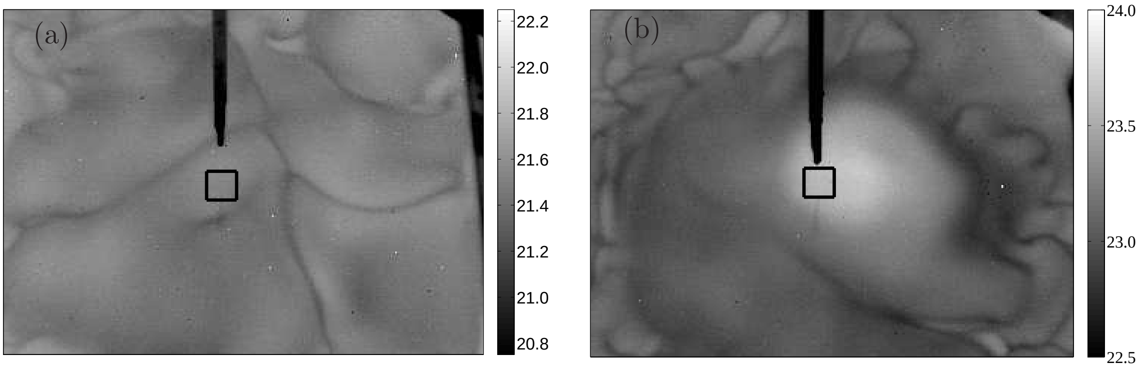

Figure 5: Instantaneous images of the measured temperature, in °C, at the free surface, for (a) pure free convection and (b) an upwelling jet of volume flux $F = 1.14\,\mathrm{cm}^3\,\mathrm{s}^{-1}$. Each image shows a region of the surface 15 cm × 12 cm, with the 1 cm × 1 cm averaging region indicated by a black outline. The microscale-temperature probe shows in black at the centre of the image, shortly before it is lowered into the water. Convection roll structures are observed in the free convective case (a) with cold regions above local regions of downwelling. The relatively warm patch in the centre of frame (b) corresponds to the thermal signature of the upwelling jet. Note that the temperature scales differ for each image, since the bulk temperature T_B differs between the images.

difference in temperature profiles was observed. This suggests that the vertical motion of the probe tip does not have a strong influence on the thermal boundary layer, as similar profiles are observed for both an upward and downward moving probe. The analogue output of the microscale conductivity probes was subject to some contamination by electrical noise generated within the laboratory. This noise implies an accuracy of only 0.1°C in the temperature profile measurements.

The free surface temperature was measured to an accuracy of 0.001°C and at a sample rate of 20 Hz with an infra-red thermal imaging camera, mounted 60cm above the water surface with a viewing angle of 26° to the vertical. In particular, the free surface temperature was determined by a spatial average over a $1\,\mathrm{cm}^2$ square box centred on the T-C probe tip, and then a further time average over 5 seconds worth of images. Single images of the free surface temperature variation are shown in figure 5, both with and without an imposed flow, with the measurement region marked by a black outline.

The velocity field was measured using a particle image velocimetry technique, which is briefly described below. The tank was seeded with $10\,\mu$m diameter glass beads of near neutral buoyancy, which were illuminated by a vertical laser sheet passing through the centre-plane of the jet. The particles effectively behave as passive tracers for the flow speeds of $\mathcal{O}(1\,\mathrm{cm/s})$ observed in the jet. The particle displacements between a pair of consecutive camera frames are then correlated to estimate the velocity components in the plane of illumination. An interval of 0.06 s between frames was found to give best resolution of the flow. For each flow rate, a sequence of 155 image pairs was taken at a sampling rate of 4 Hz. This sequence was then time averaged and a subsequent mean vertical velocity profile $w(z)$ was then calculated for the centre of the jet. For each value of z a horizontal average of w was taken across a cross-section of width 2 cm about the centreline of the jet.

An integral heat budget was used to estimate the total heat flux across the air-water interface. If we assume negligible heat loss across the well insulated side walls and bottom of the tank then most of the heat loss has to occur across the free surface. Turbulent convection maintains the interior of the tank at a uniform temperature, except in the small thermal boundary layer over the upper centimetre of depth. The order 1 cm surface boundary layer comprises less than 5% of the 30 cm depth of the tank, and so we neglect the small effect of departure from the bulk temperature in this thermal boundary layer. Balancing the rate of change of heat within the tank to the heat flux across the free surface, we obtain

$$\rho c_p \frac{d}{dt}\left(\mathcal{V} T_B\right) = \mathcal{A} Q, \tag{28}$$

where $\mathcal{V}$ is the volume of water in the tank, and $\mathcal{A}$ is the area of the free surface. Note that we have assumed that the water-air heat flux Q is relatively uniformly distributed across the free surface. The integral heat budget (28) gives an estimate of the water–air heat flux Q from the temporal variation of the bulk temperature measured with the HOBO digital thermometer. The time rate of change of T_B was calculated by applying a 600 second box filter to the temperature record to remove noise, and then using the difference in smoothed temperature 300 seconds before and 300 seconds after each measurement to calculate the derivative. This provided a smooth variation of heat flux in time.

The above measurements were taken for different strain rates (i.e different flow rates F) and also different bulk temperatures. For each experiment, the following procedure was adopted. One hundred thermal camera images were taken over a period of 5 seconds, before a temperature–depth profile was taken with the T-C probe moving downward through the free surface. The heat flux and bulk temperature values were recorded continuously during several experiments. Particle image velocimetry measurements were taken for each flow rate for a range of bulk temperatures. It was found that there was negligible change in the near surface strain rate α with bulk temperature, suggesting that the dynamical effect of convection is relatively weak compared to that of the imposed flow of the jet. A single average value of α was therefore used for each flow rate in the subsequent calculations.

4 Experimental results

A series of measurements were taken to assess the accuracy of the method and explore how an applied upwelling flow alters the thermal boundary layer structure. In §4.1 we present measurements of the thermal boundary layer for pure convection with no imposed flow in order to provide a consistency check on our results. We then move on to consider the effects of an imposed upwelling flow in §4.2, before giving a qualitative discussion of the effects of downwelling flow and the presence of surfactants in §4.3.

4.1 Convective boundary layer with no imposed flow

The experimental procedure was first tested by taking measurements of a purely convective thermal boundary layer as a consistency check with previous studies (Howard, 1966; Katsaros *et al.*, 1977). Figure 6 shows the raw output from a typical measured sub-surface temperature profile. The persistent variation of 0.1°C might be explained in part by elec-

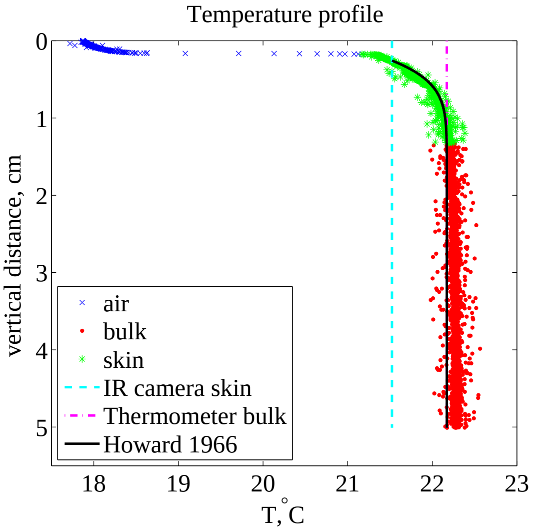

Figure 6: Variation in sub-surface temperature in °C with depth in cm. The measured temperature signal at each point is shown by symbols, with blue cross symbols denoting measurements in air, green star symbols denoting measurements in the skin layer and red dot symbols denoting measurements in the interior as determined by an automated algorithm (see text). The independent thermal camera measurement of the surface temperature is shown by a dashed blue line and the thermometer measurement of the bulk temperature is shown by a dash-dotted pink line. The solid black curve shows the profile predicted by the Howard (1966) convective boundary layer theory using $\zeta = -\sqrt{\pi}z/4\delta_c$.

trical noise in the laboratory contaminating the signal.

An automated algorithm was used to determine the vertical position of the air–water interface and also to determine the depth of the skin layer. Measurements in approximately the upper 0.3 cm have been taken in air (blue cross symbols) and are shown purely to illustrate the surface detection algorithm (the instrument does not measure temperature accurately in air.) The transition from readings taken in air to readings taken in water was characterised by a region of large vertical gradient in the temperature signal, as the probe pierced the interface. The position of the air-water interface was therefore estimated by taking the vertical co-ordinate of the tenth data point after the maximum value of dT/dz was attained. This algorithm systematically under-predicts the surface temperature compared to the thermal camera measurement, due in part to the effects of partial immersion of the probe tip and surface tension dominated deformation of the interface. However, the temperature profile reaches the same value as the thermal camera estimate of surface temperature within 0.05 cm (which is, perhaps not coincidentally, about the diameter of the glass encased thermistor). Hence, the disagreement in surface temperature between the temperature profile and the thermal camera has only a small effect on the inferred values of the thermal boundary layer thickness $\delta = \mathcal{O}(1\,\mathrm{cm})$. The remaining data points in the temperature profile were then inferred to be in the skin layer (green star symbols) if the observed temperature deviated from the average bulk temperature by more than 5% of the bulk–skin temperature difference (where the bulk temperature was taken from the temperature profile at 4 cm depth.) The data points from the remainder of the profile in the interior are plotted using red circles. This algorithm enabled an estimate of the thermal boundary layer thickness δ by computing the depth of the inferred skin layer. Typically observed values lie in the range $0.4\,\mathrm{cm} \le \delta \le 1.5\,\mathrm{cm}$, as expected, with thinner boundary layers observed for a larger surface heat flux. The theoretical solution (2) due to Howard (1966) is also plotted in figure 6 (solid black curve), and shows good agreement with the observed shape of the temperature profile. Note that we have estimated the conductive lengthscale δ_c using (7) here.

Figure 7 shows a comparison of the observed bulk–skin temperature difference $T_B - T_S$ with the prediction (6) made by applying the '4/3rds' heat flux law. We observe a linear relationship between the observed and predicted bulk-skin temperature differences, with equation (6) under-predicting the observed bulk-skin temperature difference by approximately 0.3°C. The cause of this offset was not immediately clear, but is of a consistent order of magnitude to the bulk-skin temperature differences that can be generated by Marangoni convection (Katsaros, 1980). The surface may also be affected by contamination with surfactants either contained within the tap water used, or those that have settled onto the surface from the atmosphere. We note that some intrinsic scatter in the data is to be expected due to turbulent flow fluctuations. The convection theory described in §2.1 is based on a statistically steady state approximation, with the governing equations averaged both in time and horizontal space. This means that some time-dependent and spatial variation is expected between individual temperature profiles (in particular we expect some horizontal variation in temperature due to the structure of the convection cells). The above results and their agreement with previous theories give us confidence that our experimental techniques are adequate before moving on to consider the effect of an upwelling flow on the thermal boundary layer dynamics.

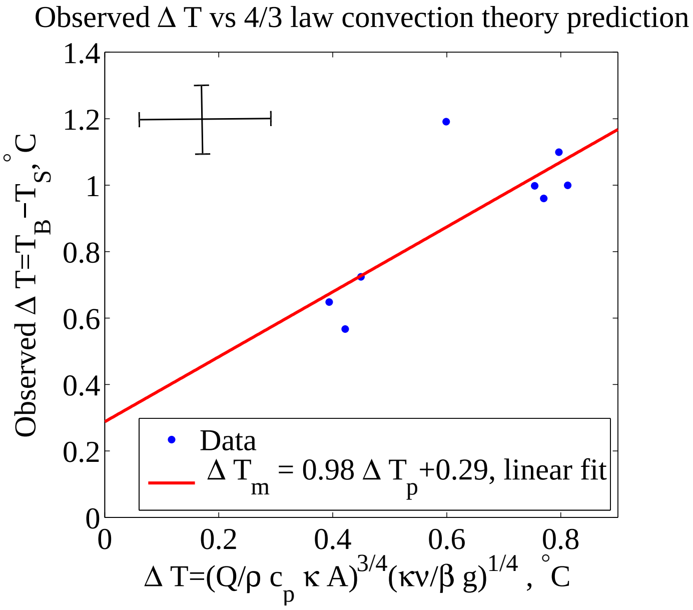

Figure 7: Comparison of the observed bulk–skin temperature (measured using thermal camera and digital thermometer) with the theoretical prediction $T_B - T_S = A^{-3/4}\left(Q/\rho c_p \kappa\right)^{3/4}\left(\kappa\nu/\beta g\right)^{1/4}$ given by (6). The red curve shows a linear fit to the relationship between measured values ΔT_m and predicted values ΔT_p. Typical error bars are shown by the cross in the top left corner.

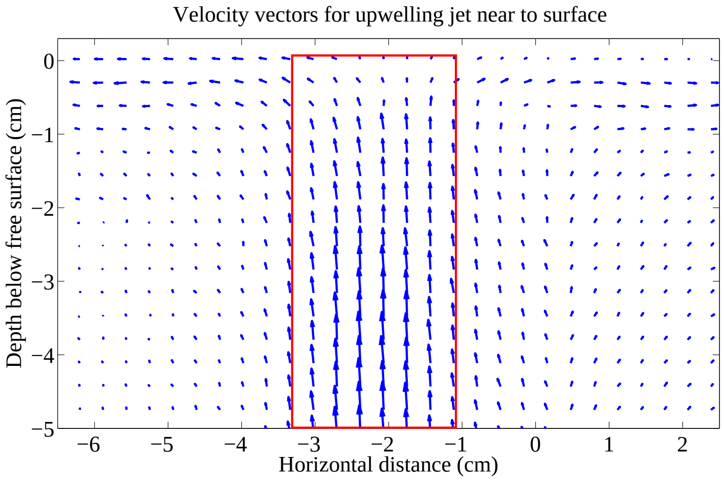

Figure 8: Time-averaged velocity vectors calculated from particle image velocimetry measurements for a laminar momentum jet with volume flux $F = 1.14\,\mathrm{cm}^3\,\mathrm{s}^{-1}$. The vertical jet exerts a local upwelling between $x = -3.2\,\mathrm{cm}$ and $x = -1.2\,\mathrm{cm}$, generating a diverging flow near to the surface. The mean vertical velocity is determined by taking a cross sectional average at each height z within the red rectangle.

4.2 Convective boundary layer with imposed near surface divergence

A near surface divergence was generated by the local upwelling flow produced by the diffuse vertical jet described in §3. The jet was of laminar character, and remained relatively steady over the period of an experiment, with occasional intermittent bursts of unsteadiness. Figure 8 shows a plot of the time averaged flow vectors measured using particle image velocimetry for a jet with volume flux $F = 1.14\,\mathrm{cm}^3\,\mathrm{s}^{-1}$. The jet has a confined core flowing upwards with weak entrainment of the exterior fluid. The flow diverges radially as the free surface is approached. Figure 9 shows a plot of the average vertical velocity $w(z)$ near the centre of the jet, calculated using the methods described in §3. Directly above the source ($z \sim -20\,\mathrm{cm}$) we observe an increase in vertical velocity - this effect is a consequence of the plane of measurement not coinciding precisely with the centre of the jet. Closer to the surface we observe the expected vertical deceleration, with the vertical velocity tending to zero as we approach the free surface. The variation of vertical velocity w is approximately linear in z over the upper 2.5 cm of the profile. This lengthscale exceeds the typical thickness of the thermal boundary layer $\delta = \mathcal{O}(1\,\mathrm{cm})$, so that we are in a regime of constant strain rate within the thermal boundary layer. We estimate the constant strain rate α by applying a linear finite difference across the upper 2 cm of the profile, so that

$$\alpha = \frac{w(z = 0\,\mathrm{cm}) - w(z = -2\,\mathrm{cm})}{2\,\mathrm{cm}}. \tag{29}$$

Different values of α were obtained by varying the jet flow rate - these are are summarised in table 1.

The imposed diverging flow field has a significant effect on the temperatures observed both at and below the free surface. Figure 5 shows an example of the instantaneous free surface temperature measured with the infra-red thermal camera, for cases with and without

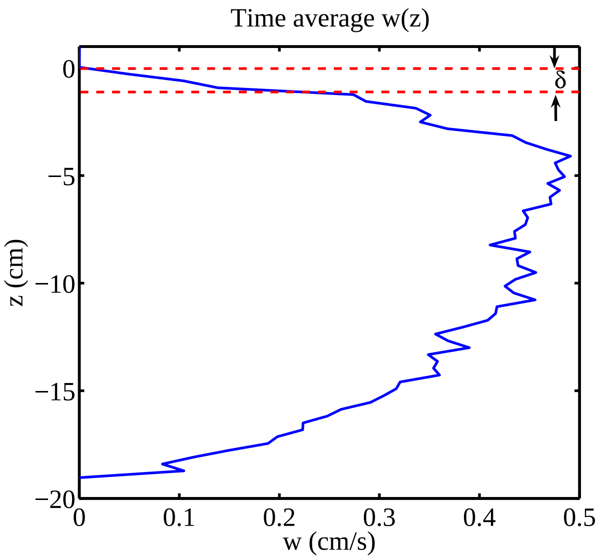

Figure 9: Typical variation of mean vertical velocity w with depth z, for a jet with volume flux $F = 1.14\,\mathrm{cm}^3\,\mathrm{s}^{-1}$. The velocity variation is linear close to the surface, so that the strain rate is approximately constant over the width of the thermal boundary layer δ. A typical reference value of δ is marked by red dashed lines for comparison.

Flow rate F ($\mathrm{cm}^3\,\mathrm{s}^{-1}$)	0.12	0.19	0.60	1.14
Strain rate α (s^{-1})	0.043	0.057	0.118	0.158

Table 1: Values of near surface strain rate $\alpha = \partial w/\partial z$ estimated from particle image velocimetry measurements.

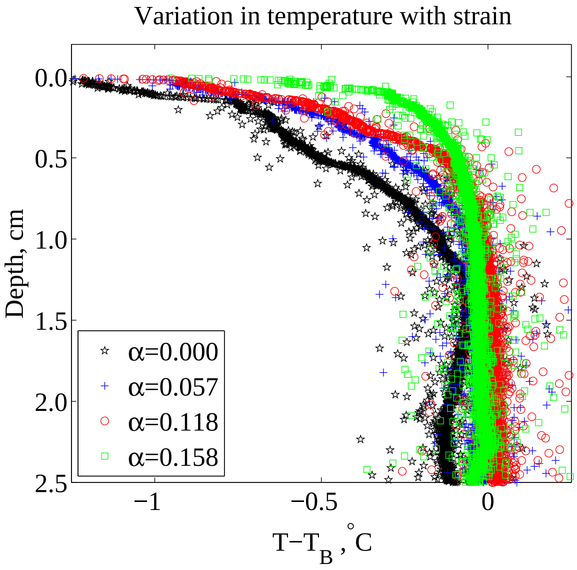

Figure 10: Variation of sub-surface temperature from bulk temperature, $T - T_B$, with depth z, for different values of the applied strain rate $\alpha = \partial w/\partial z$. As α, and hence the vertical advection, increases the boundary layer becomes thinner, and the bulk skin temperature difference is reduced.

an imposed flow. With no imposed flow (figure 5(a)) we observe regions of warm temperature bounded by bands of colder fluid. These patches are due to convection cells, with upwelling creating a warm region at their centre and downwelling at the cell boundaries creating a colder surface temperature. These structures bear a striking resemblance with those observed in the DNS of Leighton *et al.* (2003) (see their figure 2), and provide a qualitative indication that vertical sub-surface flow influences the surface temperature.

The addition of a vertical jet flow produces an obvious change in the free surface temperature pattern, as seen in figure 5(b). Upwelling of heat from the interior leads to a localised patch of warmer surface temperature above the centre of the jet, as compared to the surface temperature in the far field. The convection cell structure appears to be suppressed within this patch. This may reflect the fact that the jet creates a relatively large Péclet number in the boundary layer (Pe $= \alpha\delta^2/\kappa \approx 10 - 100$). The convection cell structures are set up by a diffusive balance across an upper conductive layer. For large Péclet number the advection of heat by the jet dominates over diffusion and so the convection cell structures are suppressed. A quantitative analysis of the thermal boundary layer is discussed below.

The variation in surface temperature is accompanied by a corresponding change to the sub-surface thermal boundary layer. Figure 10 shows the measured temperature variation with depth for four different applied strain rates. The measurements suggest that the bulk-skin temperature difference is reduced as the strain rate increases. This is qualitatively consistent with the Osborne (1965) theory, with the surface temperature being locally larger due to vertical advection of warm fluid from the interior. We also note a reduction in the measured boundary layer thickness δ as we increase the strain rate α, with the temperature variation confined to a narrower region close to the surface.

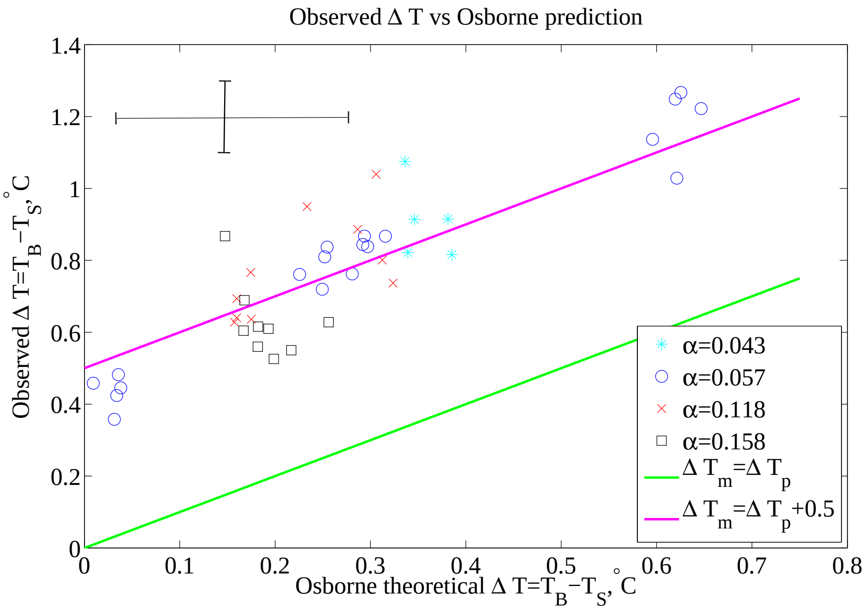

Figure 11: Comparison of observed bulk-skin temperature difference in °C, to the Osborne (1965) theoretical prediction (15). The observed surface temperature is measured using the thermal imaging camera, and the bulk temperature is measured by the digital thermometer. Also shown are the lines $\Delta T_{measured} = \Delta T_{predicted}$ and $\Delta T_{measured} = \Delta T_{predicted} + 0.5°\mathrm{C}$ for reference. The cross in the top left corner shows the typical scale of errors inferred from experimental measurement precision.

In order to provide a quantitative comparison with the Osborne (1965) theory, the measured values of α, δ and Q were used to predict a value of the bulk-skin temperature difference for each experiment according to (15). Figure 11 shows the predicted bulk-skin temperature difference compared to the value measured using the infra-red camera and digital thermometer readings for each individual experiment. The results follow a linear trend, with the Osborne (1965) prediction (15) producing a consistent under-estimate of the observed bulk-skin temperature difference by approximately 0.5°C. We again note that we expect some intrinsic scatter in the data as a result of time dependent turbulent flow fluctuations. The Osborne (1965) theory is derived for a statistically steady state, described by a surface renewal type theory for the convective boundary layer. This means that some time-dependent variation is expected between individual temperature profiles as filaments of cold fluid detach from the boundary layer and mix downwards. The level of scatter is also of a similar magnitude to the error estimates provided by a compound of the measurement precision of each of the instruments, as shown by the error bars in figure 11. The cause of the consistent offset of 0.5°C was again undetermined, but may also be consistent with the effects of Marangoni convection or surface contamination.

An alternative comparison with the Osborne (1965) theory is to consider the measured variation of the non-dimensional Nusselt number Nu with the Péclet number Pe, as shown on logarithmic scales in figure 12. The data appear to follow the scaling of the large Péclet

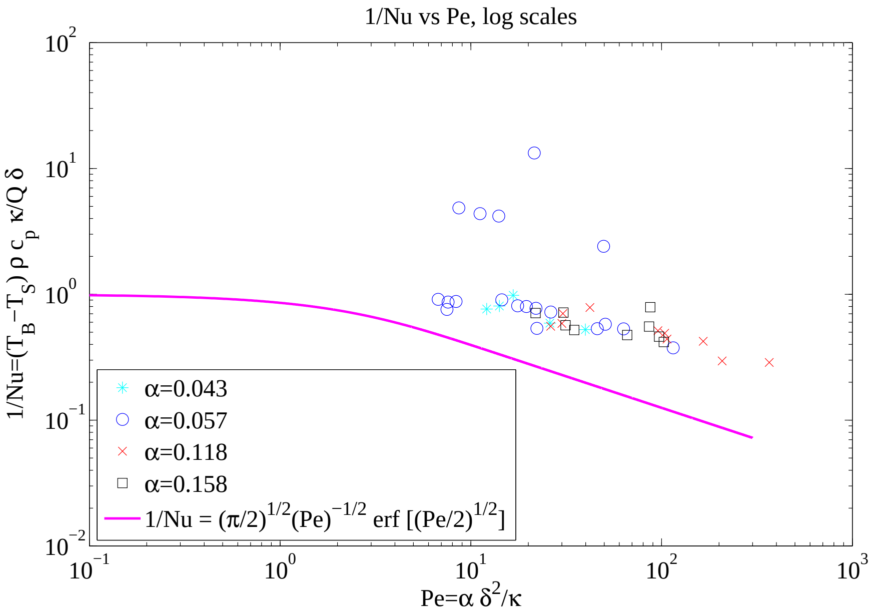

Figure 12: Variation of inverse Nusselt number $1/\mathrm{Nu} = (T_B - T_S)\rho c_p \kappa / Q\delta$ with Péclet number $\mathrm{Pe} = \alpha\delta^2/\kappa$, plotted on logarithmic scales. The non-dimensional form of the Osborne (1965) prediction (23) is plotted with a solid line for comparison.

number limit, with

$$\frac{1}{\mathrm{Nu}} \sim \sqrt{\frac{\pi}{2}}\mathrm{Pe}^{-1/2}, \qquad \text{as} \qquad \mathrm{Pe} \to \infty. \tag{30}$$

This suggests that the Osborne (1965) theory provides an effective description of large Péclet number flow in the laboratory.

4.3 Discussion of surface convergence and surfactant effects

Attempts were made to perform experiments with a converging flow generated close to the surface. In order to generate a converging flow the direction of the pump was reversed so as to create a sink flow in the inner tank. In addition the sink nozzle was moved to within 3 cm of the surface to allow large strain rates to be observed close to the interface. Figure 13 shows the surface temperature measured for a strong sink flow of volume flux $F = 90\,\mathrm{cm}^3\,\mathrm{s}^{-1}$. This set up did not allow detailed quantitative measurements, as we could not obtain a constant strain rate α over the entire width of the thermal boundary layer. However, a reduction in surface temperature of approximately 0.2°C was observed in the neighbourhood of the draining sink flow.

Ten experiments were also performed with an insoluble surfactant added to the water in order to investigate the effects of contamination by a surface film. 250μl of cholesterol was added to the surface of the tank, the tank was stirred and left to settle for 30 minutes. Figure 14 shows a comparison of predicted and observed values of the bulk-skin temperature difference both without and with the addition of artificial surfactant. The addition of surfactant generates a reduction in the observed bulk-skin temperature difference, so that

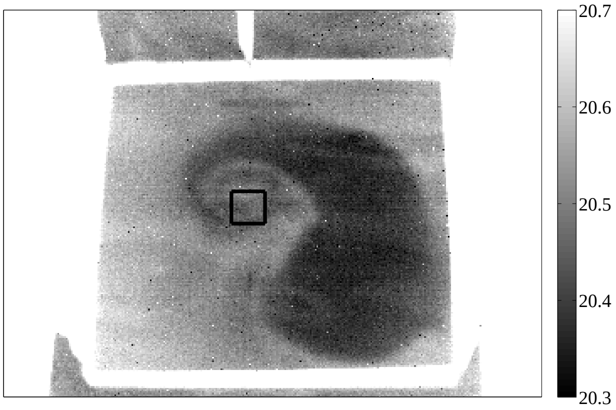

Figure 13: Surface temperature measured in the presence of a strong sink flow of volume flux $F = 90\,\mathrm{cm}^3\,\mathrm{s}^{-1}$. The cold (dark) region is observed above regions of near-surface convergence generated by the sink flow draining the container. The cause of the warm patch close to the sink is undetermined, but suggests that horizontal advection may be important in this flow.

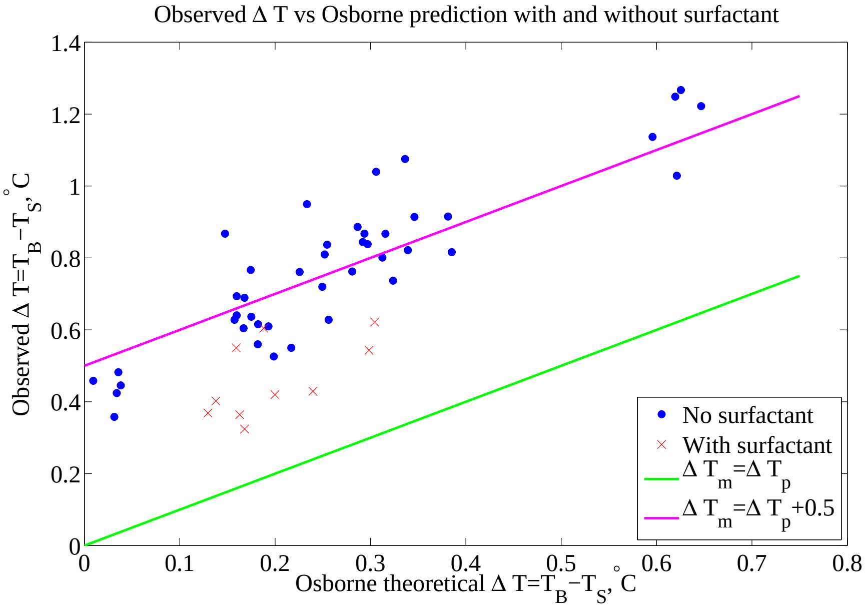

Figure 14: Comparison of observed bulk-skin temperature difference in °C, to the Osborne (1965) theoretical prediction (15). Data without the addition of artificial surfactant are plotted with blue points and measurements with the addition of surfactant are plotted with red crosses.

the skin temperature is warmer than we would find without the presence of surfactant. This increase in surface temperature is somewhat surprising, appearing to oppose the usually quoted effect of a surface film (e.g. McKenna & McGillis, 2004). The observed strain rate appears to be significantly reduced by the addition of surfactant, with a change in strain rate from $\alpha = 0.43\,\mathrm{s}^{-1}$ to $\alpha = 0.27\,\mathrm{s}^{-1}$. This is consistent with the expected effect of adding surfactant, as the increase in interfacial tension generates a stress acting to oppose the radially diverging flow and hence reduce near surface fluid velocity (McKenna & McGillis, 2004).

5 Discussion

The laboratory results presented above demonstrate that an imposed near surface diverging flow can generate local variations in the temperature at the free surface. The Osborne (1965) model effectively describes the trends observed in the laboratory experiments at large Péclet number, although it appears to under-predict the observed bulk-skin temperature difference by an offset of approximately 0.5°C. In a large Péclet number regime, the Osborne (1965) theoretical prediction (15) reduces to the limit (18). This limit has the interesting feature that the bulk-skin temperature difference is independent of the boundary layer thickness. The vertical heat transport from the interior is dominated by advection, and so the free surface temperature is controlled by a steady-state balance between vertical advection of heat into the boundary layer and loss of heat into the atmosphere. The thermal boundary layer then adjusts its thickness so that it supplies the necessary conducted heat flux at the air-water interface.

The cause of the 0.5°C offset is undetermined, but could be due to processes such as Marangoni-Bénard convection. Further investigation is required in order to explain this behaviour.

We conclude with a discussion of the application to oceanic flows. The laboratory experiments principally explored a regime of large Péclet number, where the advection of heat dominates diffusion over most of the thermal boundary layer. We expect ocean internal waves to produce flows with much smaller Péclet numbers, since oceanic turbulence generated by a surface wind stress acts to reduce the thermal boundary layer thickness. If we take a typical strain rate of $\alpha = 0.002\,\mathrm{s}^{-1}$ (Gasparovic *et al.*, 1988), a thermal conductivity $\kappa \approx 0.001\,\mathrm{cm}^2\,\mathrm{s}^{-1}$ and an ocean skin layer thickness of $\delta \approx 0.1\,\mathrm{cm}$ (Saunders, 1967) we obtain $\mathrm{Pe} = 0.02$. In the small Péclet number regime we can no longer apply the limit (18), with diffusion playing a more important role in the thermodynamical balance close to the air-water interface. We then expect the bulk-skin temperature difference to have a strong dependence on the thermal boundary layer thickness. Attaining a small Péclet number regime was beyond the scope of the current experimental set up, and so further experimental work is needed in order to explore this limit. In addition, internal waves are an inherently unsteady phenomenon. As previously discussed, the Strouhal number $\mathrm{St} = \omega/\alpha > 1$, and so we cannot use asymptotic arguments to neglect time-dependent variation in the heat equation (8). Osborne (1965) treats linearised time-dependent solutions in three different scenarios, corresponding to different hypotheses as to how the skin layer thickness and bulk temperature respond to the action of waves. Further work is required to determine which, if any, of these cases is appropriate for application to internal wave modulation of the sea surface temperature.

Having determined that localised flow structures can influence temperature at an air-water interface, it is natural to ask whether such flows have significant impact on ocean to atmosphere heat and gas exchange. For the case of internal waves we present a simplified model calculation, under the (slightly unrealistic) assumption that the steady Osborne (1965) result can be applied in a quasi-steady fashion. We expect internal waves to generate alternating periods of diverging and converging flow near to the free surface. As a simplified model, we pose that the internal waves generate a time-dependent strain $\alpha = \alpha_0 \cos \omega t$ near to the ocean free surface. If we assume that the boundary layer evolves in a quasi-steady fashion, with constant skin layer thickness δ, we can apply the Osborne (1965) result (15) to predict the bulk-skin temperature difference at each time t. The equation (15) is highly asymmetric as we vary α between positive and negative values, and so we might expect a significant difference between the time averaged skin temperature in the presence of waves, and that obtained in a calm ocean with $\alpha = 0$. Using a typical ocean skin layer thickness of $\delta = 0.1\,\mathrm{cm}$, ocean–atmosphere heat flux of $Q = 100\,\mathrm{W\,m^{-2}}$ and internal wave strain rate of $\alpha_0 = 0.002\,\mathrm{s^{-1}}$ we obtain a time averaged bulk-skin temperature difference of $\overline{\Delta T} = 0.1671°\mathrm{C}$. Interestingly, this does not differ significantly from the static bulk-skin temperature difference of $\Delta T = 0.1667°\mathrm{C}$ for $\alpha = 0$. This result is initially surprising, but can be reconciled by considering the small Pe expansion of the non-dimensional result (23). Recall, that for $\mathrm{Pe} \ll 1$, (27) gives

$$\frac{1}{\mathrm{Nu}} = 1 - \frac{\mathrm{Pe}}{6} + \mathcal{O}\left(\mathrm{Pe}^2\right). \tag{31}$$

This implies that small Péclet number flows can only induce small changes in the bulk-skin temperature difference, with the change from the static bulk-skin temperature difference only at $\mathcal{O}(\mathrm{Pe})$. The Péclet number relevant to our internal wave example is $\mathrm{Pe} = 0.02$, and so the percentage change to the bulk-skin temperature difference is correspondingly small (in fact the time average temperature difference is $\mathcal{O}\left(\mathrm{Pe}^2\right)$ in our case, as the linear term time averages to zero.) The small Péclet number expansion (31) may also have important consequences for the parameterisation of the skin temperature in climate models. We can use (31) to asymptotically bound the change in skin temperature induced by any small Péclet number flow satisfying the assumptions of the steady Osborne (1965) theory. This suggests that small Péclet number flows will not generate significant changes in the skin temperature via the skin layer straining mechanism, and as a result will not have a significant impact on the ocean-atmosphere heat transfer. In particular, internal waves cannot generate large changes in sea surface temperature, as compared to the static bulk-skin temperature difference. This may also explain our difficulties in quantifying the effects of small Péclet number flows in the laboratory, as the resulting change in bulk-skin temperature difference is smaller than the resolution of our experimental equipment.

We can also use our results to infer consequences for transfer of dissolved gases between ocean and atmosphere. The non-dimensional representation presented in §2.3 immediately generalises to transport of any other scalar quantity by replacing temperature with gas concentration, thermal diffusivity κ with a gas diffusivity D and defining a corresponding gas flux to replace the heat flux Q. The behaviour of the surface gas concentration is then determined by a Péclet number based on gas diffusivity, $\mathrm{Pe}_D = \alpha\delta^2/D$. If gas diffusion is significantly slower than thermal diffusion, $D \ll \kappa$, this raises the interesting possibility of having a small thermal Péclet number at the same time as a large gas Péclet number. This is the case for diffusion of dissolved carbon dioxide, with $D/\kappa \approx 0.01$ (Wanninkhof, 1992). Hence, although internal waves have a small effect on sea surface temperature, they may have important consequences for gas transfer. Solutions of the time dependent advection-diffusion equation (19) therefore warrant further consideration so that we can accurately quantify the effects of internal waves on ocean-atmosphere gas transfer.

Acknowledgments I would like to thank all the staff and fellows for providing an excellent working atmosphere and a rewarding summer. In particular, I am grateful to Keith Bradley and Karl Helfrich for their technical assistance and patience in the laboratory. I am also indebted to Claudia Cenedese, Tom Farrar and Chris Zappa for their support, guidance and numerous stimulating discussions throughout the summer.

References

Castro, S. L., Wick, G. A. & Emery, W. J. 2003 Further refinements to models for the bulk-skin sea surface temperature difference. *Journal of Geophysical Research* **108** (C12), doi:10.1029/2002JC001641.

Ewing, G. C. & McAlister, E. D. 1960 On the thermal boundary layer of the ocean. *Science* **131**, 1374–1376.

Fairall, C. W., Bradley, E. F., Rogers, D. P., Edson, J. B. & Young, G. S. 1996 Bulk parameterisation of air-sea fluxes for Tropical Ocean-Global Atmosphere Coupled Ocean-Atmosphere Response Experiment. *Journal of Geophysical Research* **101** (C2), 3747–3764.

Farrar, J. T., Zappa, C. J., Weller, R. A. & Jessup, A. T. 2007 Sea surface temperature signatures of oceanic internal waves in low winds. *Journal of Geophysical Research* **112** (C06014), doi:10.1029/2006JC003947.

Gasparovic, R. F., Apel, J. R. & S., K. E. 1988 An overview of the SAR internal wave signature experiment. *Journal of Geophysical Research* **93** (C10), 12304–12316.

Howard, L. N. 1966 Convection at high Rayleigh number. In *Proceedings of the eleventh international congress of applied mechanics* (ed. H. Görtler), pp. 1109–1115. Springer-Verlag.

Katsaros, K. B. 1980 The aqueous thermal boundary layer. *Boundary-Layer Meteorology* **18**, 107–127.

Katsaros, K. B., Liu, W. T., Businger, J. A. & Tillman, J. E. 1977 Heat transport and thermal structure in the interfacial boundary layer measured in an open tank of water in turbulent free convection. *Journal of Fluid Mechanics* **83**, 311–335.

Leighton, R. I., Smith, G. B. & Handlerb, R. A. 2003 Direct numerical simulations of free convection beneath an air-water interface at low Rayleigh numbers. *Physics of Fluids* **15**, 3181–3193.

Marmorino, G. O., Smith, G. B. & Lindemann, G. J. 2004 Infrared imagery of ocean internal waves. *Geophysical Research Letters* **31** (L11309), doi:10.1029/2004GL020152.

McKenna, S. P. & McGillis, W. R. 2004 The role of free-surface trubulence and surfactants in air-water gas transfer. *International Journal of Heat and Mass Transfer* **47**, 539–553.

Osborne, M. F. M. 1965 The effect of convergent and divergent flow patterns on infrared and optical radiation from the sea. *Deutsche Hydrographische Zeitschrift* **18** (1), 1–25.

Saunders, P. 1967 The temperature at the ocean-air interface. *Journal of Atmospheric Science* **24**, 269–273.

Soloviev, A., Donelan, M., Graber, H., Haus, B. & Schlüssel, P. 2007 An approach to estimation of near-surface turbulence and CO_2 transfer velocity from remote sensing data. *Journal of Marine Systems* **66**, 182–194.

Soloviev, A. V. 2007 Coupled renewal model of ocean viscous sublayer, thermal skin effect and interfacial gas transfer velocity. *Journal of Marine Systems* **66**, 19–27.

Soloviev, A. V. & Schlüssel, P. 1994 Parameterisation of the cool skin of the ocean and of the air-ocean gas transfer on the basis of modeling surface renewal. *Journal of Physical Oceanography* **24**, 1339–1346.

Tennekes, H. & Lumley, J. L. 1972 *A first course in turbulence*, chap. 1, pp. 27–34. MIT.

Walsh, E. J., Pinkel, R., Hagan, D. E., Weller, R. A., Fairall, C. W., Rodgers, D. P., Burns, S. P. & Baumgartner, M. 1998 Coupling of internal waves on the main thermocline to the diurnal surface layer and sea surface temperature during the Tropical Ocean-Global Atmosphere Coupled Ocean-Atmosphere Response Experiment. *Journal of Geophysical Research* **103**, 12613–12628.

Wanninkhof, R. 1992 Relationship between wind speed and gas exchange over the ocean. *Journal of Geophysical Research* **97**, 7373–7382.

Wick, G. A., J., E. W., Kantha, L. H. & Schlüssel, P. 1996 The behaviour of the bulk-skin sea surface temperature difference under varying wind speed and heat flux. *Journal of Physical Oceanography* **26** (10), 1969–1987.

Woodcock, A. H. & Stommel, H. 1947 Temperatures observed near the surface of a fresh-water pond at night. *Journal of Meteorology* **4**, 102–103.

Zappa, C. J. & Jessup, A. T. 2005 High-resolution airborne infrared measurements of ocean skin temperature. *IEEE Geoscience and Remote Sensing Letters* **2** (2), 146–150.

The Stability of Boundary Layer Flows

Summer Fellow: J.D. Zika

Advisor: S.A. Thorpe

Produced as part of the 49th Summer Program in Geophysical Fluid Dynamics at the Woods Hole Oceanographic Institution, Massachusetts 2007

Abstract

This study aims to answer the question: Are stably stratified boundary layer flows marginally unstable? Using the Taylor Goldstein equation, we analyse the linear stability of a number of observed mean flows in stably stratified boundary layers. We find that although Kelvin Helmholtz instability may occur the growth rates of unstable modes are small compared to the time scales of fluctuation in the flow and in all cases where unstable or stable modes are found a change in velocity shear of no more than 20% is required to stabilise or destabilise the flow, respectively. The implications of these results and potential for further studies are discussed.

1 Introduction

In his book *Buoyancy Effect in Fluids* J.S. Turner (1973) makes the following conjecture regarding gravity driven flows down a uniform slope: 'While turbulence is present the drag on the layers increases and the velocity falls, but when it is suppressed the flow is accelerated again by gravity'. The mean flow is consequently self-controlled close to a state at which turbulence sets in and is one of marginal stability. This study presents evidence in support of Turner's conjecture that boundary layer flows are maintained in a marginal state of stability, which we shall assume is that in which small disturbances to the mean flow have zero growth rate.

Our method for analysing the stability of such flows shall be to use the Taylor-Goldstein equation

$$\frac{\partial^2 \phi}{\partial \hat{z}^2} + \left(\frac{\hat{N}^2}{(U-C)^2} - k^2 - \frac{\frac{\partial^2 U}{\partial \hat{z}^2}}{U-C} \right) \phi = 0 \tag{1}$$

where the perturbation streamfunction is $\psi(\hat{x}, \hat{z}, \hat{t}) = \phi(\hat{z}) e^{[ik(\hat{x} - C\hat{t})]}$ with wave number k, phase speed $C = C_r + iC_i$ and mean velocity U and the bouncy frequency $\hat{N}^2 = -g\rho_z/\rho$ (variables with a hat are in their dimensional form and will later be nondimensionalised). The Taylor-Goldstein equation is derived from the mass and momentum conservation equations for a stratified fluid without rotation and describes the evolution of an initial disturbance to the steady, inviscid and unidirectional stratified flow under a velocity shear. In using (1) we implicitly disregard the stresses and eddy diffusivities associated with turbulent motion. The common dimensionless number used to characterise the flow is the Richardson number $Ri = \hat{N}^2/(U_z)^2$.

The canonical theorem of Miles and Howard (Miles, 1961) (Howard, 1961) shows, using 1, that steady, inviscid and unidirectional flows with Richardson numbers above a quarter everywhere in the flow are *stable* to small perturbations (Drazin and Reid, 1981). Although it is commonly espoused that flows are unstable below this critical value it is in fact (theoretically at least) not the case. For particular flows with U and ρ prescribed, Hazel (1972) has shown that when the boundary of a stratified flow is not at infinity the instability can be inhibited and the critical value of minimum Richardson number (called J) is reduced. As is shown in figure (1) as the distance from the boundary increases the region where growing waves exist and perturbations can grow decreases. Indeed where the boundaries are within 1.5 H (H being the typical height scale) of the shear the flow is stable for Richardson numbers above 0.125 and almost always for 1.25H. Indeed, even if the stratification is increased (increasing Ri) the stability is not necessarily increased, Thorpe (1969) and Miles (1963) both show cases where the presence or increase in stratification can reduce the stability of a flow. Such examples suggest that the stability of a shear flow can not accurately be described by the Richardson number at an isolated point alone but solutions to the Taylor-Goldstein equation involving representation of U and $\hat{\rho}$ as functions of $\hat{z}$ over the entire flow should be considered.

The body of evidence in support of Turner's conjecture is small and not yet convincing. Indeed the original statements are made with reference to the laboratory studies of Mittendorf (1961) who showed how the Kelvin-Helmholtz mechanism reduces the shear leading to a maintenance of a gravity driven flow in a state of marginal stability. Thorpe and Hall discussed such a concept in their study of a wind driven flow in Loch Ness, Scotland (1977). Small perturbations were shown to be likely to grow if the Richardson number were increased from that observed by only 10% (i.e. an increase in the mean shear of only 5%). Merrill (1977) examined the linear stability of an airflow near the ground and although he did not estimate whether the flow was 'marginally' unstable he found that for a boundary flow with $J = 0.15$, the growth rates of the most unstable modes were small. Nielsen (1991) looked at instability on a frontal inversion in the Atmosphere and although unstable modes where not found for the observed profiles, he was able to extrapolate

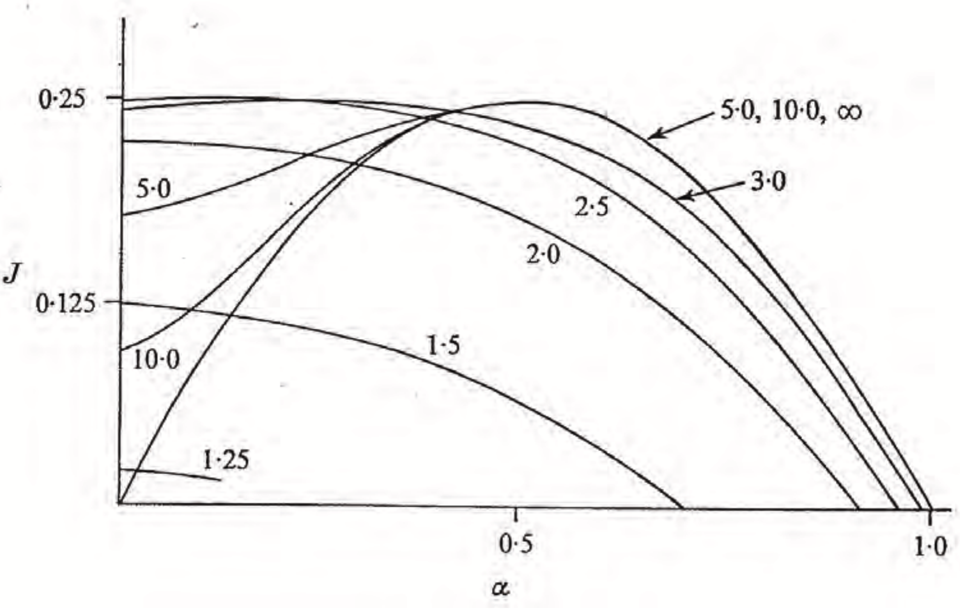

Figure 1: Stability boundaries for 'tanh' profiles at nondimensional distances marked. The vertical axis J represents the minimum Richardson number (found at $z = 0$) and the dimensionless wavenumber $\alpha = kH$ for some typical length H. (Taken from Hazel (1972)).

from unstable modes found by reducing the Richardson number of the flow and found that the observed profiles were at or very near a state of marginal stability. As in this study numerical problem often arise when such stability analysis is conducted on actual profiles of velocity and density. A recent study by Thorpe and Ozen (2007) (hereafter TO07) has asked the question of whether boundary flows are marginally stable. They look at a cascading flow in Lake Geneva and find that both a functional fit to the data and the data itself in a canonical case, are unstable but only marginally so.

Boundary currents and how they influence the dynamics of the Ocean and Atmosphere is currently the subject of great interest in geophysical research. Two examples of stably stratified boundary currents were mixing and turbulence are known to be of great importance in the Ocean are wind driven flows in the presence of surface heating and gravity driven boundary currents that feed dense water into the major ocean basins. Correctly describing such flows and the instabilities that can arise from them is extremely important for numerical models of the Climate System.

The consequences of boundary flows being generally in a state of marginal stability (if that can be shown) is important from the point of view of numerical models. It is customary in many numerical models, to mix and entrain fluid in a stratified flow when the Richardson number drops below the canonical 1/4 value or to adopt an empirical entrainment coefficient. As we have discussed, boundaries may act to stabilise the flow despite such a shear existing. It would preferential to use linear stability analysis, rather than simply the *Ri* condition to assess the accuracy, and thus constrain, a numerical model and test whether numerically predicted flows are, like those observed, close to marginal stability.

The following section of this report, Section (2), establishes the theoretical framework under which we will conduct our stability analysis. Section (3) discusses the data collected from a cascading flow in Lake Geneva and section (4) describes the results of our linear stability theory. A discussion of the implications of these results and ongoing research are discussed in section (5).

2 Nondimensionalisation and Boundary Conditions

We follow the same nondimensionalisation as that of TO07 where h is defined by the thickness of the current, $z = \hat{z}/h$, $u = U/U_{max}$, $c = \hat{C}/U_{max}$, $g\Delta$ is the reduced gravity ($\Delta = (\rho(z = 0) - \rho(z = 1))/(\rho(z = 0) + \rho(z = 1))$) and U_{max} is the maximum velocity difference in the flow (see Figure (2)) and $N^2 = g\Delta\hat{N}^2/h$ and the Taylor-Goldstein equation (1) becomes

$$\frac{\partial^2\phi}{\partial z^2} + \left(\frac{N^2}{Fr^2(u-c)^2} - \alpha^2 - \frac{\frac{\partial^2 u}{\partial z^2}}{u-c}\right)\phi = 0. \tag{2}$$

where the Froude number $Fr = U_{max}/\sqrt{g\Delta h}$

The data we will use to assess the linear stability of boundary layer flows will, in the majority of cases, be limited to the region of the boundary flow itself. In previous treatments of flow using the Taylor-Goldstein equation it is assumed that there is some point in the flow where a solid boundary exists such that $\phi = 0$. In cases where we have only data in the flow region it is more preferable to assign some mean stratification and flow to the region distant from the flow or interior (i.e. for $z > 1$). For our purposes we will assume the interior has the following properties: the mean flow ($\overline{u}$,$\overline{v}$) and density ($\overline{\rho}$) are constant in x, y, z and t, the mean flow is hydrostatic such that $\frac{\partial \overline{p}}{\partial z} = -\overline{\rho} g$ and

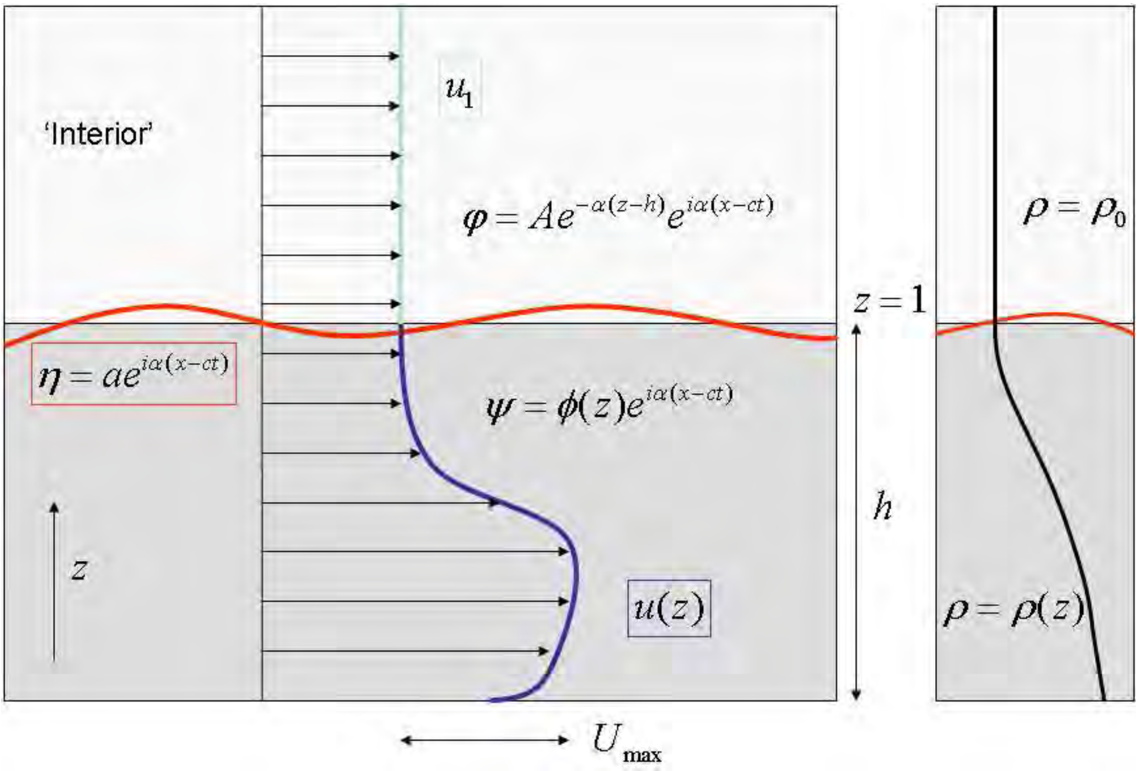
u_1
'Interior'
$\varphi = Ae^{-\alpha(z-h)}e^{i\alpha(x-ct)}$
$\rho = \rho_0$
$z = 1$
$\eta = ae^{i\alpha(x-ct)}$
$\psi = \phi(z)e^{i\alpha(x-ct)}$
h
z
$u(z)$
$\rho = \rho(z)$
U_{max}

Figure 2: A schematic showing how the scales U_{max}, h, the perturbation streamfunction Ψ, potential flow φ and free surface displacement in the matching region η are defined for a typical flow profile.

it is irrotational. In the upper region ($z > 1$) there exists a potential flow $\varphi = Ae^{k(z-1)}e^{i\alpha(x-ct)}$ which will be matched to the perturbation streamfunction close to $z = 1$ where the free surface displacement is $\eta = ae^{i\alpha(x-ct)}$. Here A and a are unknown constants. Assuming the flow is two dimensional (for the time being) we write a linearized equation for η (eliminating $u'\frac{\partial\eta}{\partial x}$ terms) at the interface between the two regions ($\hat{z} = 1 + \eta$)

$$\frac{\partial\eta}{\partial t} + \overline{u}\frac{\partial\eta}{\partial x} = w \tag{3}$$

where $w = w' = \frac{\partial\varphi}{\partial z} = -\frac{\partial\Psi}{\partial x}$ and $\overline{u}$ is at the interface. Substituting our potential φ into the above equation we get $a = \varphi/(c - \overline{u})$ and $A = i\varphi$. Below $z = 1 + \eta$ and we may describe the pressure as having a mean and wave component such that $p = P(z) + p(z)e^{i\alpha(x-ct)}$ and we may invoke the hydrostatic approximation also ($P(z) = P_0 + g\int_z^1 \rho dz$). The momentum equation for the perturbation in this region is

$$\frac{\partial u}{\partial t} + \overline{u}\frac{\partial u}{\partial x} + w\frac{\partial\overline{u}}{\partial z} = -\frac{1}{\overline{\rho}}\frac{\partial p}{\partial x}. \tag{4}$$

Recalling that $\frac{\partial\Psi}{\partial z} = u$ and $\frac{\partial\Psi}{\partial x} = -w$ we have

$$p = \overline{\rho}\left[(c - \overline{u})\frac{\partial\phi}{\partial z} + \phi\frac{\partial\overline{u}}{\partial z}\right] \tag{5}$$

and therefore the total pressure at $z = 1$ is

$$P = P_0 + \left\{-ga\rho(h) + \overline{\rho}\left[(c - \overline{u})\frac{\partial\phi}{\partial z} + \phi\frac{\partial u}{\partial z}\right]e^{i\alpha(x-ct)}\right\}. \tag{6}$$

Bernoulli's equation for the upper region is

$$\frac{P}{\overline{\rho}} + \frac{\partial\varphi}{\partial t} + \frac{1}{2}(u + \overline{u})^2 + \frac{1}{2}(w + \overline{w})^2 + gz = B \tag{7}$$

where B is a constant and thus the pressure at $z = 1$ (determined from the upper side) is also

$$P = \overline{\rho}\left\{C - \frac{1}{2}\overline{u}^2 - gh + [ik(c - \overline{u})A - ga]e^{i\alpha(x-ct)}\right\}. \qquad (8)$$

Matching the pressure described by (5) and (8) and assuming the velocity and density are continuous at $z = 1+\eta$ it follows that the boundary condition at $z = 1$ is

$$(c - \overline{u})\frac{\partial \phi}{\partial z} + \frac{\partial u}{\partial z}\phi + \alpha(c - \overline{u})\phi = 0. \qquad (9)$$

3 Boundary Flow Data from Lake Geneva

The data we shall use to investigate the stability of cascading boundary flows comes primarily from Lake Geneva. In winter, during cold nights, shallow regions of the Lake are cooled and these form cascading gravity currents which flow down the boundaries of Lake Geneva (Fer *et al.*, 2001). Profiles of density ($\overline{\rho}$), downslope velocity (U) and across slope velocity (V) have been collected from the bottom to 25m above equating to about a third of the overall water column. An example of such a flow is shown in Figure (3) with a density section taken down the slope.

The flow displays hallmarks of many forms of instability. The flows are punctuated by pulses of water consistent with roll waves in steep open channel flows (Fer *et al.*, 2001). Hydraulic jumps can occur in the fluid and the stability of such events is discussed in Thorpe and Ozen's Study. A time series of both U and V along with temperature is shown in figure (4). The flow is clearly unsteady, and probably turbulent, although data are not presently available to characterise the variability at frequencies less than about 0.01Hz. The data we shall consider in this study are 2hr averages taken of both the

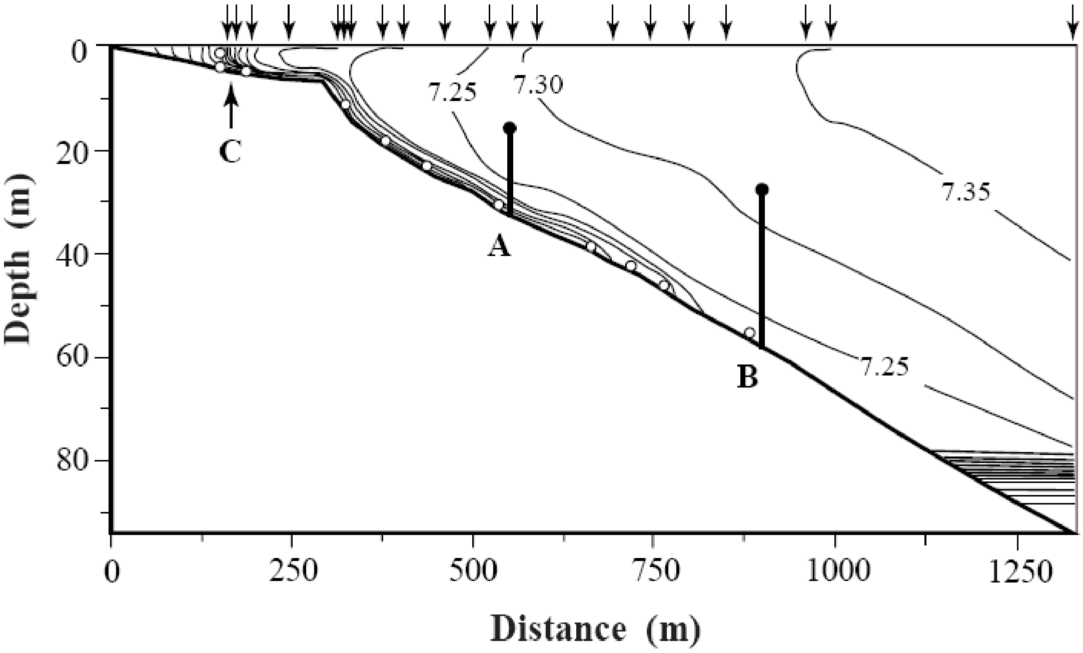

Figure 3: Cold water spilling down the sloping side of Lake Geneva from shallow water. Temperature contours at 0.05°C from a CTD section made on the northern side of Lake Geneva between 1030-1330 hrs local time, 23 December 1998 after a period of nocturnal cooling with positive surface buoyancy flux. Station positions are marked by arrows at the top. Circles show the positions of temperature miniloggers .A and B mark positions of vertical arrays and C marks a warm front in shallow water. Taken from Fer *et. al* (2001).

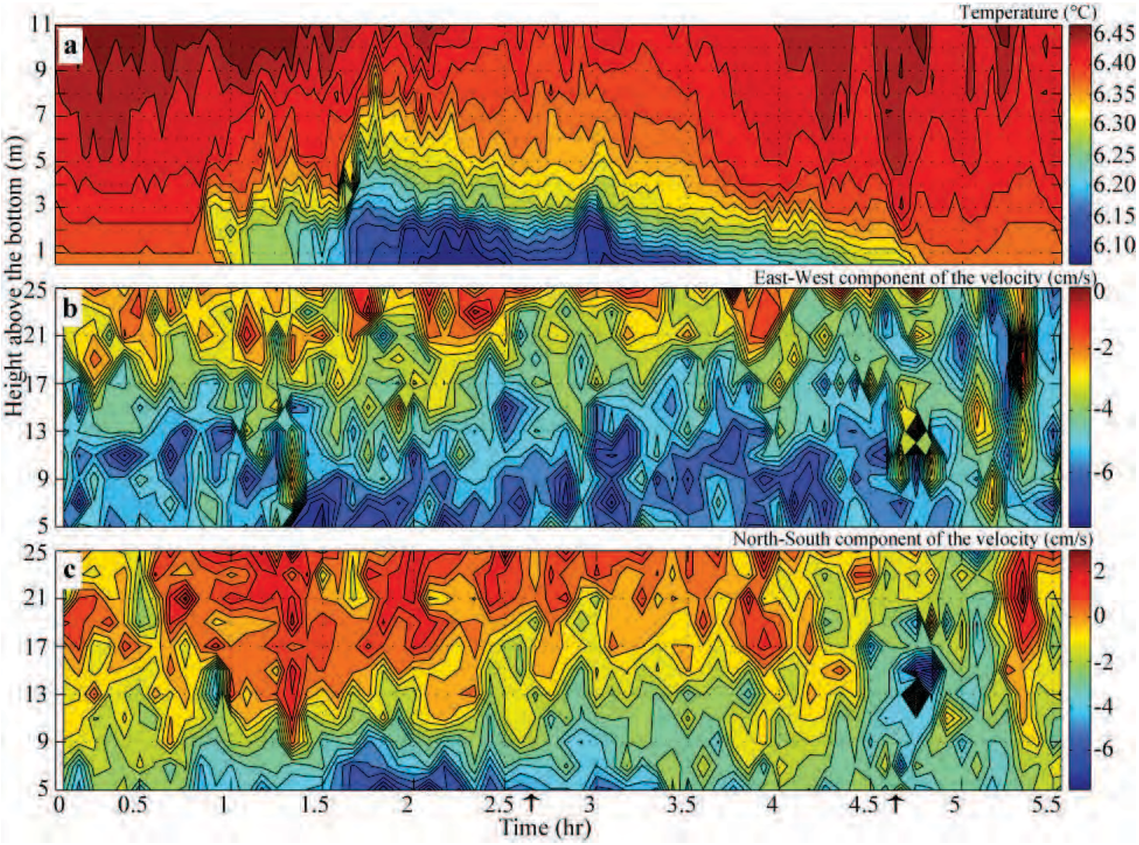

Figure 4: Contour plots of the recorded temperature and velocity data during an interval of 5.5, starting from 22 January 2004, 09:00 PM. Panel (a) shows temperatures, (b) East-West and (c) North-South components of the velocity. Data for case one is a 2 hour average taken between times marked on panel (c) (Ozin private communication).

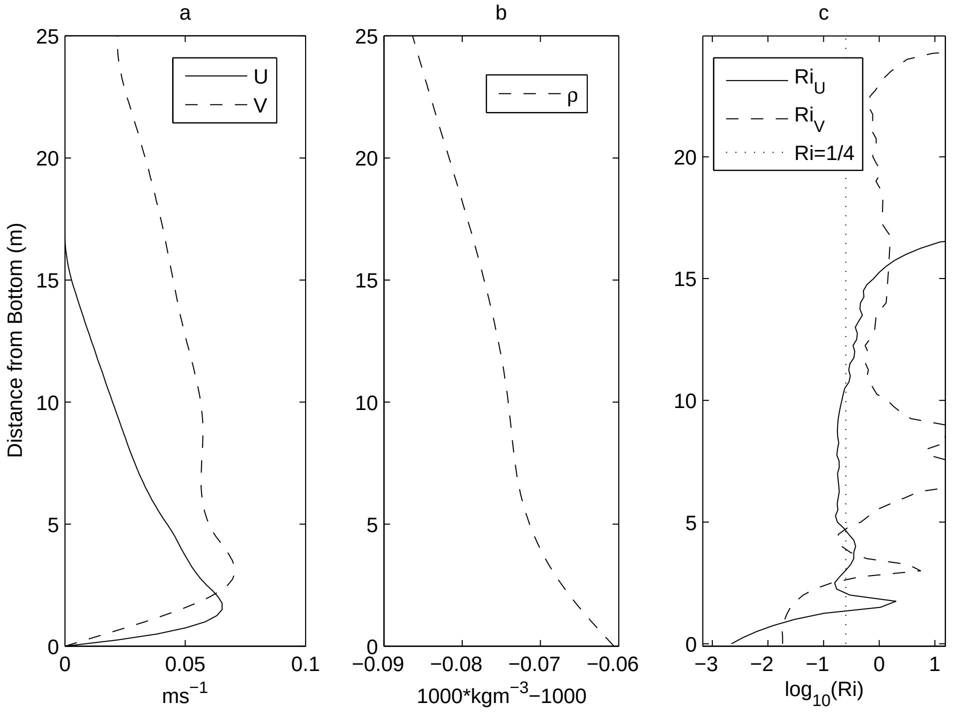

Figure 5: Density (panel a), down-slope (solid) and along-slope (dashed) velocity (panel b) and Richardson number (panel c) for case 1.

down slope and along slope components of the velocity. Measurements are taken on an incline which is typically of similar order to that shown in figure (2) and are chosen specifically to be those with steady slopes. The quality of the data reduces close to 25m from the bottom and the shear becomes weak. We thus match the data smoothly to constant profiles of density and velocity close to this height taken as $z = 1$.

The two examples we shall consider are characterised as follows: Case 1, shown in figure (5), the flow has a canonical shape in the down-slope direction, similar to those discussed in TO07 but there exists a significant mean flow in the along-slope direction. The flow around Lake Geneva is often cyclonic, the along-slope flow in this case being toward the West (the

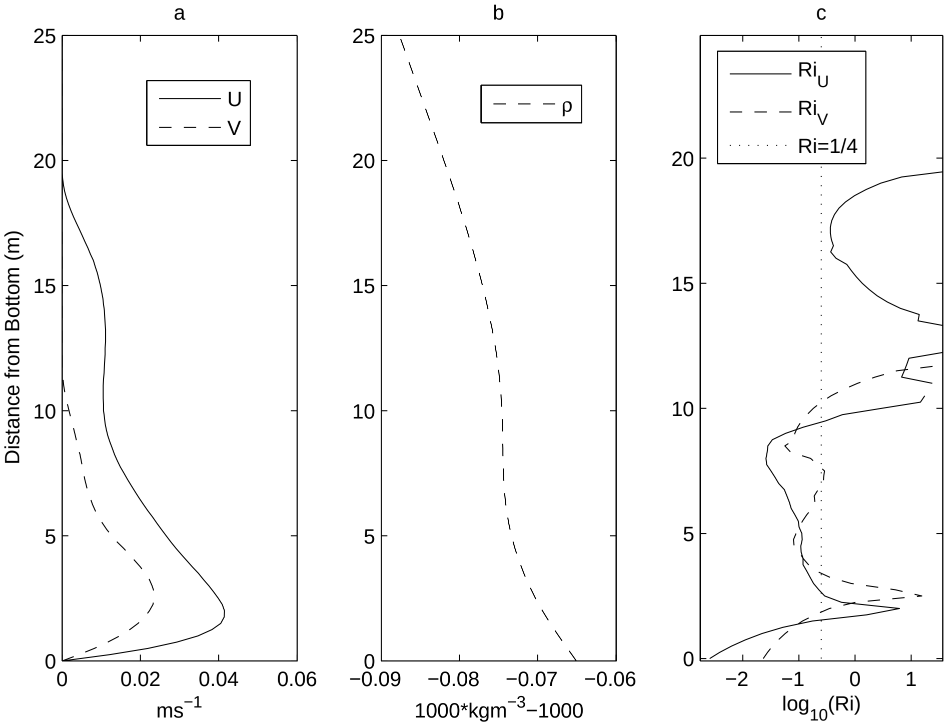

Figure 6: Density (panel a), down-slope (solid) and along-slope (dashed) velocity (panel b) and Richardson number (panel c) for case 2.

measurements are taken on the northern side of the lake). It is possible that Ekman effects are occurring in the boundary layer driving flow up the slope (i.e. to the right of the along slope flow) competing with the gravity driven cascade. We do not consider such effects in this study. The flow in case 2 (figure 6) is largely down-slope but displays a curious double hump structure perhaps due to the fluid mixing in various layers as it moves down the slope. The presence of two inflection points may allow the development of multiple modes of instability. In both case 1 and case 2 the Richardson number falls well below the 'critical' value of 1/4 and so the Miles-Howard theorem tells us that instabilities 'may' occur and linear stability to the K-H mechanism is not assured.

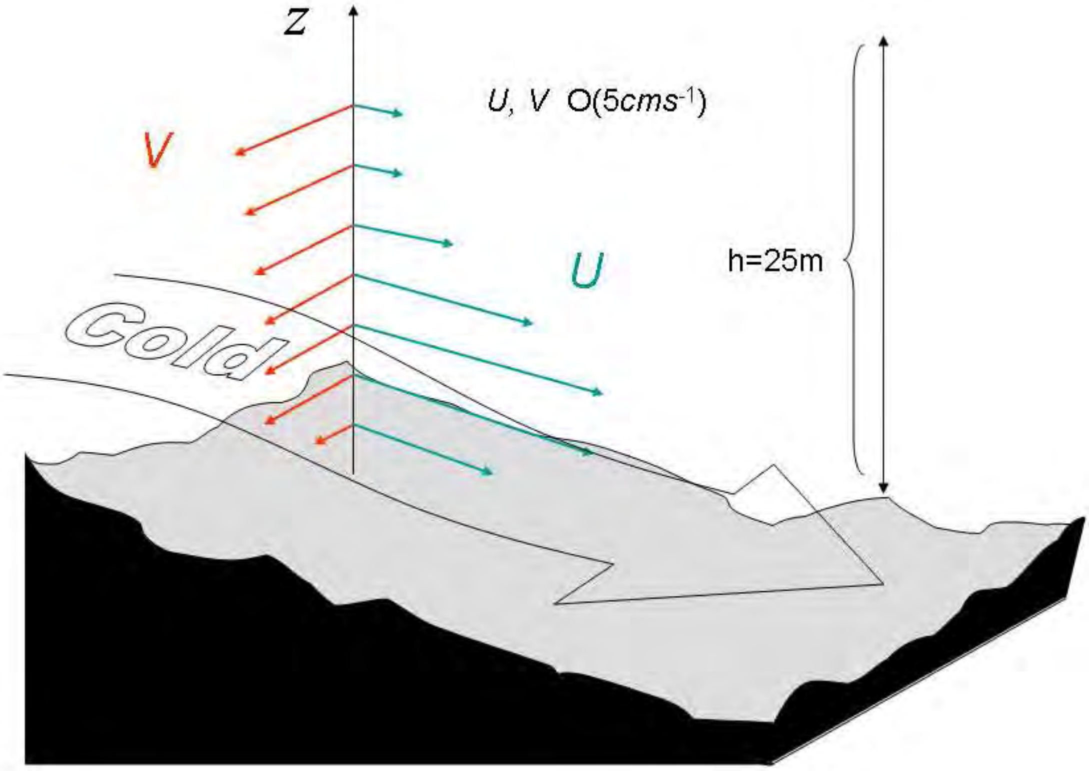
Z
V
U, V O(5cms-1)
U
h=25m
Cold

Figure 7: Image showing typical flow of cold water down slope (U) along slope mean flow (V) both of order $5cms^{-1}$ and measured over a vertical scale of 25m

4 Stability analysis of stratified shear flow

We wish to solve the Taylor Goldstein equation (2) searching for the Eigenvalue c of the fastest growing modes. As well as the condition on the upper boundary of the flow described in section (2), the solid boundary beneath the flow allows us to impose a no normal flow condition ($\phi(z = 0) = 0$). The Howard semicircle theorem states that $[C_r - 1/2(U_{max} + U_{min})^2] + C_i^2 \leq [1/2(U_{max} - U_{min})]^2$, where U_{max} and U_{min} are the maximum and minimum values of the velocity. Initial attempts to solve (2) were made using a shooting method similar to those of Merrill (1977), and TO07. For the measured values of U and ρ, coherent solutions to the Eigenvalue problem are not found and the solution is dominated by modes associated with numerical instabilities. Many techniques are attempted to abate such difficulties including, changing the grid resolution, constraining the modes possible and fitting the data with smoother cubic spline functions but no method yields coherent results for the observed velocity and density profiles. The scheme (which we will call M1), despite being checked against 'synthetic cases' generated from the hyperbolic tan profiles used by Hazel (see figure 1), is only able to resolve stability curves for the observed velocity and density profiles for increased Fr (discussed later) .

In order to avoid stability problems at small c_i and to allow more efficient search for eigenvalues, a second method (M2) is developed. In M2 we write (2) in the following form

$$(D^2 + F(c))\psi = 0 \tag{10}$$

where D^2 is the second derivative operator and $F(c)$ is function of the known mean velocity and density profiles and c. Eigenvalues c exist when the determinant of $D^2 + F(c)$ is zero. An advanced nonlinear root finder is used to find the roots of this expression and far more accuracy is found close to the observed Froude number than M2 but the same results are yielded for the cases shown in this report.

Our aim is to determine how far from being at the margin between stability and instability the observed profiles are or more precisely, how much would we need to increase or decrease the mean velocity (or change the stratification) to have a flow regime where infitesimal disturbances grow. In order to do this we introduce a factor ϵ by which we shall divide the Froude number. A value of $\epsilon = 0$ translates to an infinite mean velocity, no stratification or some combination of the two extremes while $\epsilon = 1$ translates to the observed velocity and density profiles. By starting at $\epsilon = 0$ and iterating toward $\epsilon = 1$ we can observe the trend in the maximum growth rates of the most unstable modes. This technique is similar to that used by Nielsen (1991) and TO07 increasing the bulk Froude number of the flow by the factor $1/\epsilon$ and extrapolating to a value of the Froude number such that the flow becomes marginally stable. Figure (8) shows such curves for case 1 for epsilon=0 to 0.5 in steps of 0.1.

As we have both components of the velocity we may continue this 2 dimensional analysis, but as in (Thorpe, 1999) we may orient the 2d disturbance in each direction θ where the velocity in that direction is $u_\theta = usin(\theta) - vcos(\theta)$ and $\psi(x, z, t)$ has the same meaning but the x direction is that of θ (see figure 9). We plot the maximum growth rates for each angle θ, again for $\epsilon = 0$ to 0.5 in figure (12). Focusing on angles between $\Theta = -90^o$ and $\theta = 0^o$ rotating between the along slope and down slope direction we estimate the critical values of the bulk Froude number and the critical value of the maximum Ri of the profile. We do this by extrapolating from the approximately linear re-

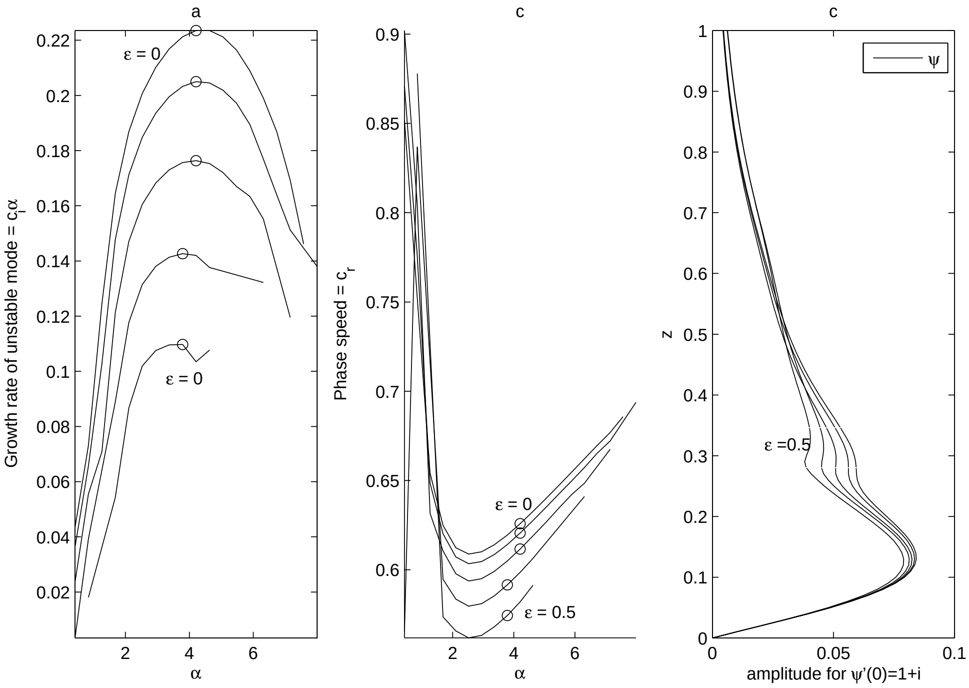

Figure 8: Nonsimensionalised Growth Rate (panel a), Phase Speed (panel b) and (panel c) for various values of ϵ for case 1.

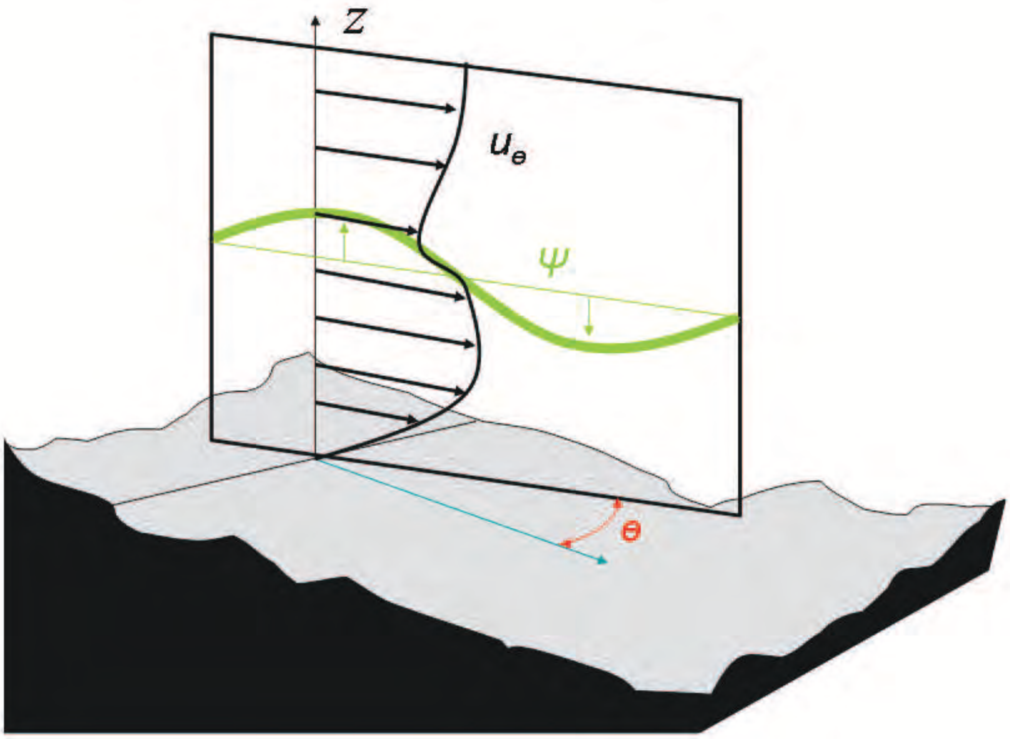

Figure 9: A cartoon showing how we may orient disturbances ψ angle θ to the down slope flow and use the velocity in that direction to conduct the stability analysis.

lationship between ϵ and $C_i\alpha$ to a point where the growth rate would change sign. An example of this linear relationship for the down slope flow of case 1 is shown in figure (10).

The manner in which such extrapolation is conducted is highly subjective and such a method is only used to give an estimate of whether the observed flow is 'close' (i.e. within some range of 10%-20%) to being stable/unstable.

We may follow the same process for case 2. Figure (13) shows the stability curves, phase speeds and growing modes for different values of ϵ for disturbances oriented in the down slope direction. Figure (14) again shows the result of rotating the 2d analysis over various angles θ. We see in figure (14)

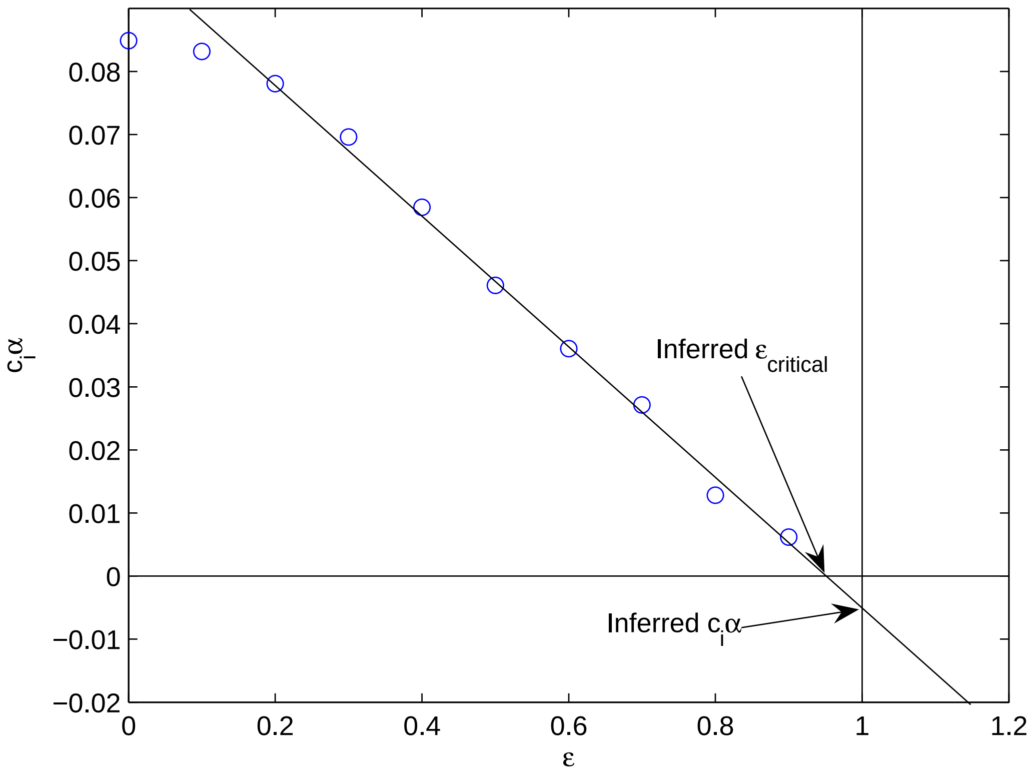

Figure 10: Case 1: Example of inference of $\epsilon_{critical}$ at which the flow is likely to become stable. In this case $\epsilon_{critical}$ is less than 1 and disturbances to the mean flow are not predicted to grow.

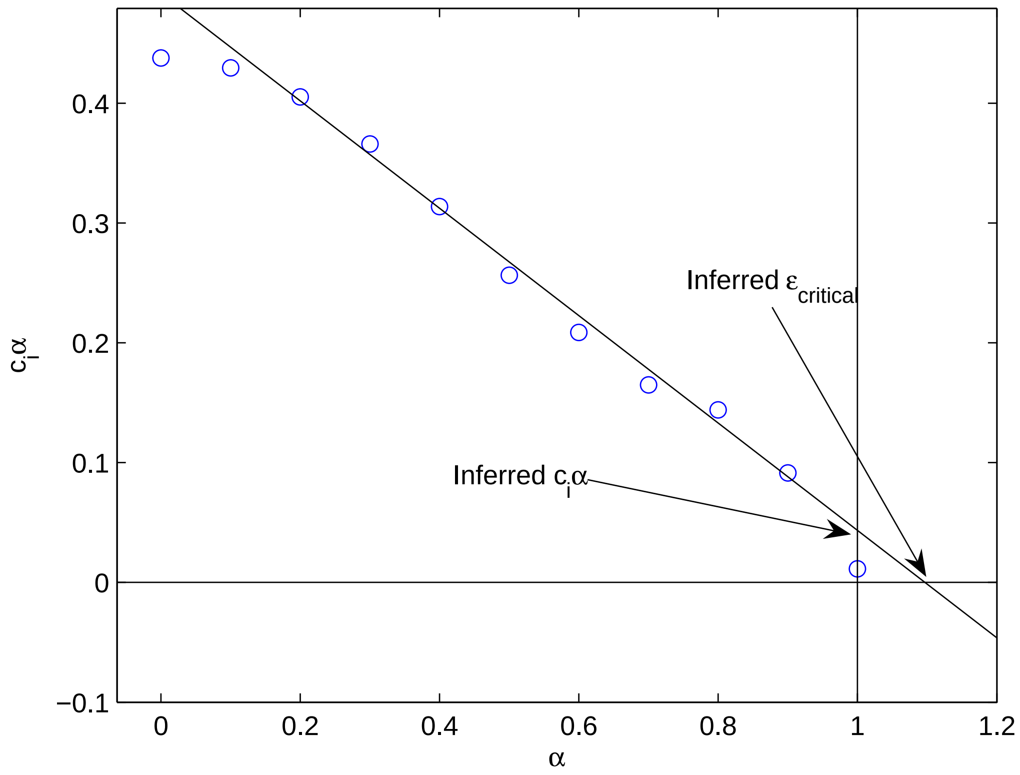

Figure 11: Case 2: Example of inference of $\epsilon_{critical}$ at which the flow marginally stable. In this case $\epsilon_{critical}$ is greater than 1 and disturbances to the mean flow are not predicted to grow at a rate $c_i\alpha$.

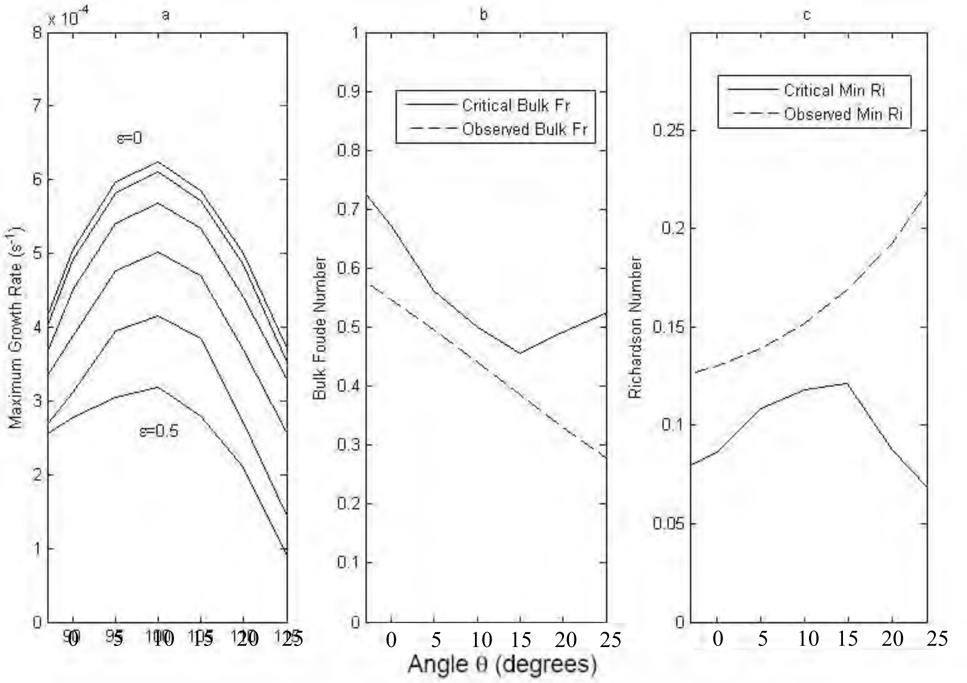

Figure 12: Case 1: Greatest Growth Rate at each angle (panel a) and for increasing $\epsilon * Fr$. Panel b shows a comparison between the observed bulk Froude number of the flow and the critical value inferred from extrapolating with increasing ϵ while panel c shows the same but for the peak Richardson number in that direction.

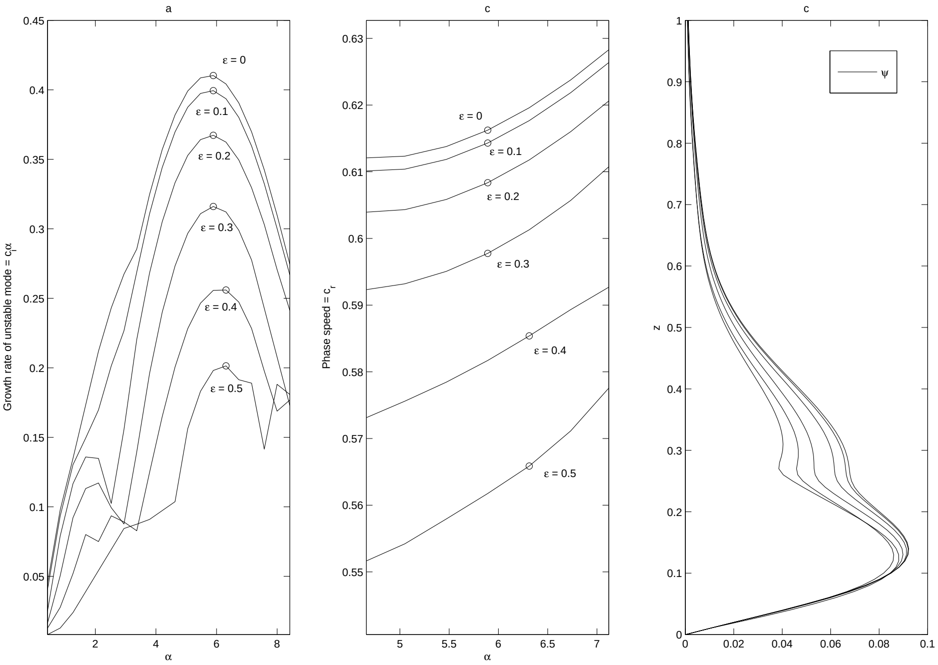

Figure 13: Nonsimensionalised Growth Rate (panel a), Phase Speed (panel b) and (panel c) for various values of ϵ for case 2.

that a decrease in the mean velocity of case 2 reducing the bulk Froude number from the observed 0.44 to only 0.38, a reduction in the maximum velocity of only 10-15%, would be enough to prevent perturbations from growing for all wavenumbers. The stability analysis of case 1 suggests the flow is stable as the extrapolation predicts a critical Froude number above that of the profile, however an increase in the maximum velocity difference of only 10% in the down stream direction would bring the flow into the estimated critical region.

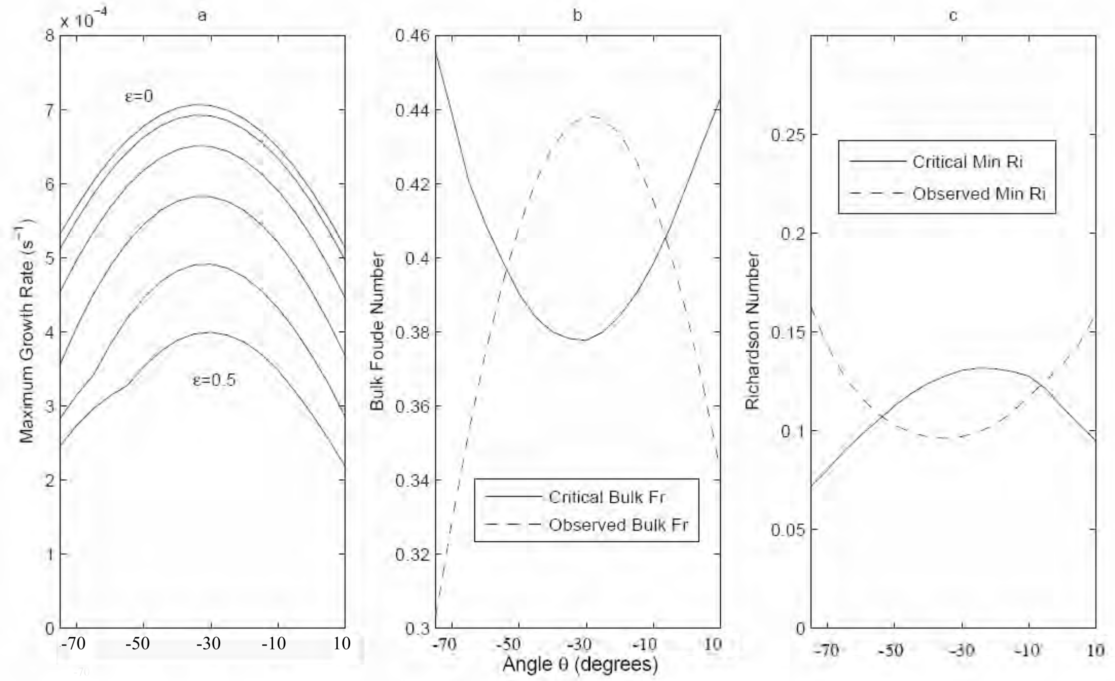

Figure 14: Case 2: Panel a shows the greatest growth rate at each angle and for increasing $\epsilon * Fr$. Panel b shows a comparison between the observed bulk Froude number of the flow and the critical value inferred from extrapolating with increasing ϵ while panel c shows the same but for the peak Richardson number in that direction.

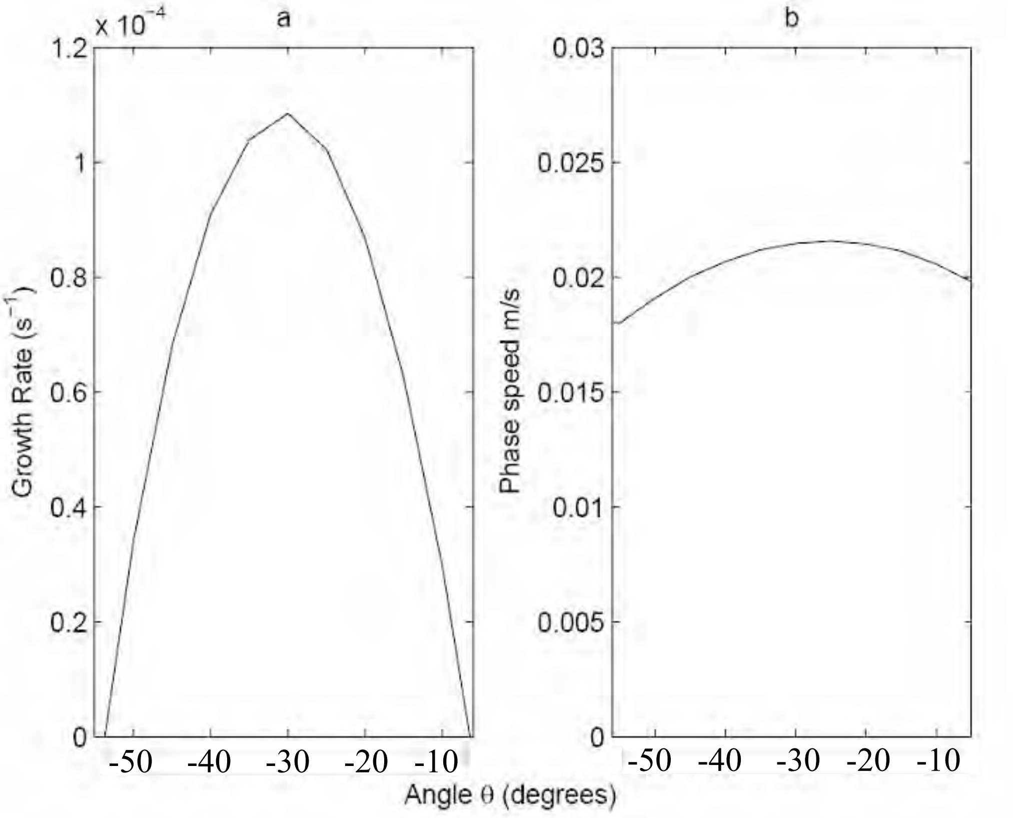

Figure 15: Predicted growth rates (panel a) and phase speeds (b) of most unstable modes at given orientations θ, of the perturbation. For all values shown the wavenumber k is approximately $0.24 m^{-1}$ ($\lambda \approx 4.17 m$)

5 Discussion and ongoing work

In this study we have looked at two stratified boundary flows and find them both to be close to marginally stable to Kelvin-Helmholtz instability. We define the flows as marginal if an increase or decrease of the observed mean velocity of around 10% would render the flow unstable or stable (respectively) to linear (infinitesimally small) perturbations.

We observe, in case 2 of the cascading flows from Lake Geneva, that instabilities are likely to occur in an orientation 60° downslope of the along slope direction and with growth rates of order $10^{-4}s^{-1}$ (i.e. the perturbations would grow by a factor of $e = 2.71$ over a period of 2.5-3hr) phase speeds of order 0.02ms^{-1}, and a wavelength of approximately 4.2m. The velocity and Richardson number profile for this angle θ are shown in figure (16). Case 1 is predicted to be stable to K-H instability but an increase in flow velocity of approximately 10% would be likely, according to our analysis, to allow waves of lengths of order 6m and phase speeds around 4cms^{-1} to grow in a direction down the slope.

As was discussed in section (1) the presence of a boundary can greatly inhibit the growth of unstable modes and allow smaller Richardson numbers (i.e. larger shears) to exist without instabilities occurring. In the observed mean profiles, only when the minimum Richardson number is below 0.1 for 6-7m of the profile is it unstable. This may seem surprising to those who take $Ri = 1/4$ to be the critical point below which instability occurs but there exist analytical examples such as those of exponential u and ρ against a rigid boundary, where the flow is stable to all Richardson numbers. Reinforcing the assertion that the entire profile should be considered when conducting such stability analysis.

In the two cases discussed the along slope component of the flow had

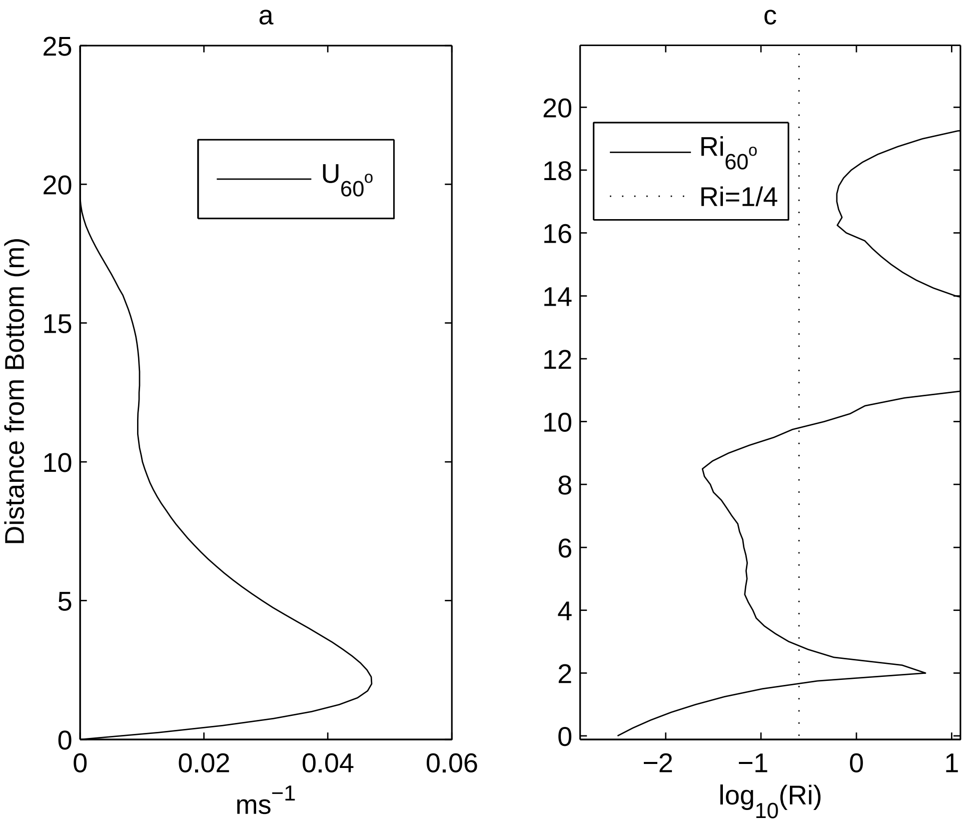

Figure 16: Velocity and Richardson number of flow oriented 30° to the down slope direction, the orientation in which fastest growing disturbances are found.

a nontrivial influence on the stability. Indeed, although in case 2 the along slope component of the flow was much smaller than the down slope, the effect on the Richardson number was significant in both profiles displaying different minimum Ris at different depths (figure (6)) leading to a slightly different, and apparently more unstable profile at the angle of 30° to the right of the down slope direction.

Although many cases remain to be explored, this work has presented evidence in support of Turner's conjecture that the mean state of stably stratified boundary flows is maintained in a state of marginal stability. It remains to be seen if deep ocean overflows and wind driven surface flows, can be shown to be stable in a similar way and whether simple techniques can then be applied to the output of numerical model data to asses its stability and constrain such a model.

6 Acknowledgements

I am grateful to Dr U. Lemmin (EPFL, Switzerland) for the use of his data and to B. Ozen for supplying it. B. Ozen was funded by the Swiss Science Foundation grant 200020-109349. I would also like to thank Steve Thorpe for his support and supervision over the summer and the organisers, Claudia Cenedese and Jack Whitehead, and faculty and fellows of the 2007 GFD program for their guidance and stimulation throughout the Summer.

References

Drazin, P. G. and Reid, W. H.: 1981, *Hydrodynamic Stability*, Cambridge University Press, Fer, I., Lemmin, U., and Thorpe, S.: 2001, *Geophysical Research Letters* **28**, 2093–2096

Hazel, P.: 1972, *Journal of Fluid Mechanics* **51**, 39–61

Howard, L.: 1961, *Journal of Fluid Mechanics* **17**, 509–512

Merrill, J. T.: 1977, *Journal of Atmospheric Sciences* **34**, 911–920

Miles, J.: 1961, *Journal of Fluid Mechanics* **17**, 496–508

Mittendorf, G.: 1961, *The instability of stratified flow.*, MSc. Thesis, State University of Iowa.

Nielsen, J.: 1991, *Journal of Atmospheric Sciences* **34**, 911–920

Thorpe, S. A.: 1977, *Nature* **265**, 719–722

Thorpe, S. A.: 1999, *Journal of Physical Oceanography* **29**, 2433–2441

Thorpe, S. A. and Ozen, B.: 2007, *Journal of Fluid Mechanics* **589**, 411–432

Turner, J. S.: 1973, *Buoyancy Effects in Fluids*, Cambridge University Press.

Double-Diffusive effects in a Dam Break Experiment

Frédéric Laliberté

March 11, 2008

Abstract

A rotating dam break experiment was conducted with a vertical barrier at the midpoint separating a salt solution in one half of the channel and a sugar solution in the other half. Sugar diffuses slower than salt so that it plays a role equivalent to oceanic salt which diffuses slower than heat. In simpler experiments with fresh water in one half and a slightly denser saline solution in the other, a tongue of fresh water flows along the surface on the right side of the channel and the interface at the surface dividing the two fluids becomes unstable and sheds fresh vortices into the salt solution. When the less dense fluid contains salt and the heavier fluid contains sugar, with a small initial density difference, much weaker instabilities occur and vertical diffusion of salt into the sugar solution reduces the density of the saline solution and therefore increase the density differences. This local increase in reduced gravity, resulting in spatial variations of the deformation scale, widens the boundary current, suppresses the instabilities and enhance the rightward flux of mass.

1 Introduction

Previous works on gravity currents are numerous with early results dating as far back as Benjamin [1], who mentions even earlier work by von Kármán (1940). In his paper, Benjamin describes non-rotating gravity currents in a two-layer system and derives some of the first rigorous results, including an asymptotic expression for the velocity of propagation of a gravity current over a deep layer. This result, which assumes that away from the head of the current the depth attains a constant value H, states that the head's velocity should be $c = \sqrt{2g\frac{\Delta\rho}{\rho}H}$. This system has been extensively studied in the laboratory with results that vary depending on the flow regime. In most flows, viscosity as well as mixing tend to remove the factor $\sqrt{2}$, and other effects, such as the interaction with a wall perpendicular to the motion, tends to affect the velocity dramatically.

In a rotating environment, the dynamics may be expected to be quite different with the current being constrained to propagate along a wall due to Coriolis deflection [3]. However, apart from an initial adjustment, it has been shown by Stern, Whitehead and Hua [5] both theoretically and experimentally that the the gravity current nose speed should be essentially the same as for the non-rotating case, with similar dependence on viscous, mixing and boundary interaction effects. In another set of experiments, Stern [4] investigated the evolution of a coastal gravity current and observed strong instabilities. These instabilities often develop filaments and smaller eddies, impacting on the entrainment (and detrainment) capabilities of the jet.

As described by Stern and Chassignet [2], several laboratory experiments in a rotating basin have been carried out in which a lighter fluid (fresh water) flows as a boundary current over a denser environment (salty water). In these experiments, detachment of eddies is common and is thought to reduce significantly the downstream transport of fresh water. The impact on the jet is observed to be important in comparison with the theoretical laminar flow with a large amount of detrainment occurring due to small scale eddies separating from the jet. Depending on the nature of these small scale turbulent features, the current can be observed to effectively widen or actually "eject" mass to its surroundings.

In double diffusive experiments, where one of the fluids is a sugar solution and the other is a salt solution, it has been observed [6] that these instabilities disappear, that the gravity current propagates faster and that the boundary current is wider. The exact mechanism on how the instabilities are damped was not clarified nor how this influences the effectiveness of the flow to transport lighter fluid over heavier fluid.

The goal of this report is to demonstrate, for the range of parameters investigated, that the flow is primarily driven by double diffusion and that it increases the transport of lighter fluid over heavier fluid. We also show that the rate at which the boundary current widens is higher in the regions where a non-diffusive current would shed eddies, leading us to propose that it is the local increase in the deformation radius by double diffusion that suppresses the interfacial instabilities. In section 2 we describe the experimental setup and in section 3 how we processed our photographic data. In section 4 we discuss our results, always comparing double-diffusive experiments with their non-diffusive counterparts. We finally conclude in section 5 and we propose a theoretical model in appendix A for future work.

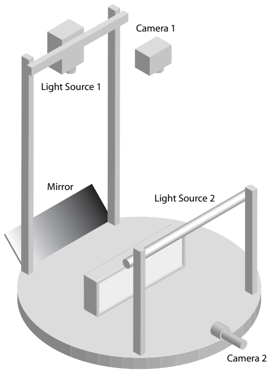

Figure 1: Our experimental setup, where camera 2 was not used. Taken from [6].

2 The Experiment

2.1 Experimental Setting

The experiment was conducted in a 60 cm ×10 cm tank with a removable barrier in the middle. The tank was on a table rotating with angular velocity Ω where $f = 2\Omega = 1.25\ \mathrm{s}^{-1}$. A co-rotating digital still camera was placed directly above the tank and a mirror inclined at 45° to the horizontal was used in order to obtain a side view. The lighter fluid, placed on the left, was dyed blue and we used approximately 1 liter of each fluid, leading to a depth of $\approx 3.3cm$. The experiments were carried through in two distinct sessions, one during the summer of 2007 and the other during the month of October 2007. The setup changed slightly between these two sessions, with the major difference being the introduction of a motor to lift the gate. The motor has the advantage of lifting slowly enough that only limited turbulence is produced by the removal of the gate but with the drawback that it takes several rotations before the gate is lifted, thus impacting on the initial evolution of the flow. The experimental schematics are depicted in figure 1.

2.2 Experimental Parameters

The environment was maintained at a constant temperature, 20°C, and the atmospheric pressure was assumed to be constant. The rotation frequency was kept constant at a value of $f = 1.25\ \mathrm{s}^{-1}$. This choice was to some extent arbitrary and was mainly dictated by experimental manipulations. A faster rotation would have made manipulations more intricate without having a profound impact on the physics of the experiment. This frequency, corresponding to a rotation period of 10.25 s, was conveniently in phase with our digital camera's highest shooting rate, at 11 s. This

Table 1: Experimental parameters and the number of experiments conducted

(a) Summer 2007

ρ_0 (g cm^{-3}) $\Delta\rho$ (g cm^{-3})	0.99823	1.0100	1.0400
2.0×10^{-4}	1	1	1
3.5×10^{-4}	1	1	1
5.0×10^{-4}	1	1	1

(b) October 2007

ρ_0(g cm^{-3}) $\Delta\rho$(g cm^{-3})	0.99823	1.0050	1.0100	1.0150
0.8×10^{-4}	2	3	3	3
2.0×10^{-4}	3	3	3	4
3.5×10^{-4}	3	3	3	3

The experiments with $\rho_0 = 0.99823$ g cm^3 were carried with fresh water on top and salty water on the bottom so that in these situations $\Delta\rho = \rho_T - \rho_f$. For all other experiments, the salty solution was on top and $\Delta\rho = \rho_S - \rho_T$.

slight out-of-phase leads to a slow phase change, reducing possible biases due to position.

In order to describe our experiments, we use two parameters, $\Delta\rho = \rho_S - \rho_T$ and $\rho_0 = \rho_S$, where ρ_S and ρ_T are the density of sweet water and salty water, respectively. The first quantity indicates how fast the boundary current should propagate initially ($v_i \approx \sqrt{g(\Delta\rho/\rho_0)H}$) whereas the second quantity is a measure of how strong double diffusion is at the removal of the gate (the diffusive fluxes are proportional to $\rho_0 - \rho_f$, where ρ_f is the density of fresh water). Note that the sign of $\Delta\rho$ indicates which of the two layers is salty. These parameters have been investigated for the values shown in table 1.

Negative values of $\Delta\rho$ for $\rho_0 > \rho_f = 0.99823$ g cm^3 would lead to "sugar fingers", the salty-sweet system's counterpart of salt fingers in the warm-salty system, a situation we decided not to study because of its complicated layer structure.

3 Data Acquisition

The fluid in each experiment was calibrated with a 10^{-5} g cm^{-3} accurate densiometer. These values were assumed highly accurate with inconsequential associated errors since we were computing density differences of the order of 10^{-4} g cm^3. The rest of the data was acquired by two cameras, both top mounted with a side view provided by a 45° mirror. One of the cameras was a low-resolution analog camera, used mainly as a quick experiment assessment tool. The second camera, a still 10 megapixels digital camera (resolution of 2448 × 3264 pixels), was our reliable data acquisition apparatus. The camera was set to take a shot every 11 seconds (the shortest interval allowed by the equipment) with constant lighting and fixed exposure settings. The result is a sequence of high resolution photos. The main uncertainty remaining is the exact moment that the gate was pulled. This exact moment is in fact immaterial to our analysis since we will look mainly at time derivatives of quantities and never compare two quantities at a fixed time after the removal of the gate.

3.1 Image Processing

The image files produced by the camera, once loaded in Matlab, have three components for each pixel: one red, one green and one blue. If blue dye was used, one can infer the thickness of the blue layer by the intensity of blue color, after having removed the constant signal coming from shadows and other constant variations in spatial light intensity. In figure 2, we show a photo that includes the side view. For $y > 0$, we see the fluid from directly above and for $y < 0$, we see the side view through the 45° mirror. This means that one can recover the z-coordinates by simply writing $z = -y$ for $y < 0$. In the figure, the side view shows a linearly decreasing depth in x from 10 cm to 20 cm to the right of the barrier (located at $x = 0$ in the graph). Since during the experiment we could easily assess that the most blue dye was located at $y = 0$ cm, we know that along this line the thickness decreases linearly.

Next, we show in figure 3 the adjusted color intensity for the three color components along the line $y = 0$ in the photo. The adjustment refers to the removal of white noise from the blue color, by using the empty tank as a reference point. In this figure, we see clearly that the intensity increases linearly (the line is a linear fit) over the same region over which the thickness decreases linearly. From this, we concluded that there is a linear correspondence between thickness and adjusted blue color intensity. This linear relation is computed independently for each experiment, in order to remove systematic errors.

One of the remaining problems is to filter out the noise when the intensity of blue color reaches saturation. Even though the intensity is on average constant in the no-dye region, the fluctuations can be quite large, hence a need to filter out this unnecessary noise. If one would simply demand that negative thicknesses be ignored, important noise would be left. Instead, we realized that the red color intensity was almost a step function at the nose (as can easily be seen from figures 2 and 3), and so we used the red component as a simple cutoff criterion (we cut off at $>$ 70 of intensity) to decide when the thickness was zero, regardless of the noise.

One could inquire why the green component of the image was not used instead of the blue. After all, in figure 3 the green intensity and the blue intensity seem to behave similarly. However, there is one major difference: the green color is everywhere less intense, making our thickness inference more susceptible to noise for thick regions, leading to a less accurate layer thickness analysis.

In the remaining part of this report, when we refer to the thickness we refer to the linearly inferred thickness plus the red-color filtering that we just discussed.

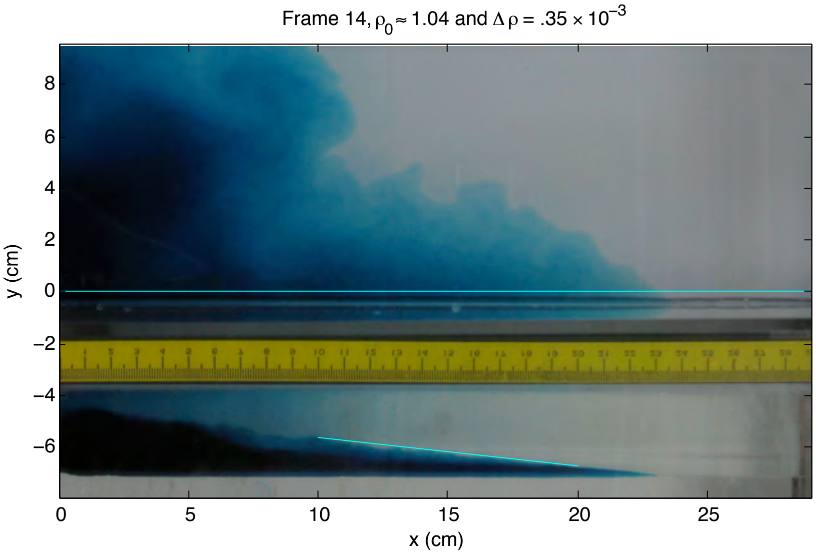

Figure 2: Picture taken during an experiment. In the upper part of the picture, the line shows the section along which figure 3 is plotting the color intensities. In the lower part, the line is there to show how linear the depth is in this region.

4 Results

4.1 Evolution of the jet

Non-Diffusive case, fresh water over salty water In the non-diffusive case, the jet starts off as a laminar boundary current of width determined by the radius of deformation [4] and is usually accompanied by an unstable interface that fluxes

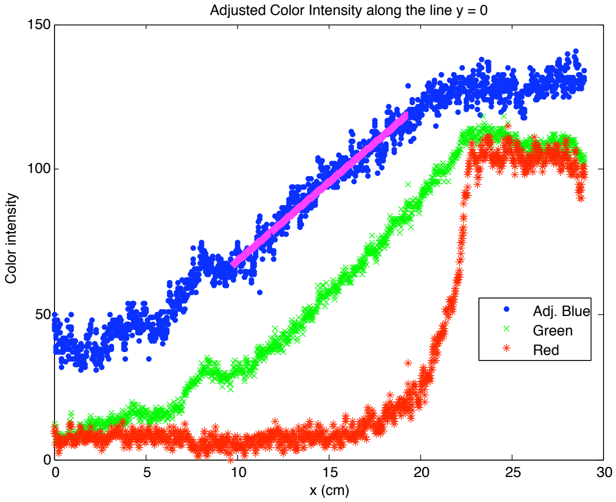

Figure 3: The color intensity along the line in figure 2. The line is a linear fit on the blue color. Note the sudden increase in red color at $x \approx 22$ cm in the transition zone between blue dye and no dye.

mass toward the center of the tank. Sometimes eddies are formed (for small density differences) and detach themselves from the right-flowing current.

In figure 4, we show the time-evolution of a non-diffusive dam break experiment. What is observed is typical of small reduced gravity experiments, with strong instabilities and numerous eddies. Note how most of the dye is restricted to a region close to the boundary, with the transition zone between this current and the interior flow being almost entirely populated with instabilities and their generated eddies. The evolution is constant with the first onset of instabilities appearing very shortly after the removal of the gate. Otherwise, most of the dye seems to be transported first by the boundary jet with a secondary transport towards the interior, by the deformation of the interface. Notice in figure 4 the big lump of blue dye that seems to be trapped left of $x = 5$ cm; this feature was observed systematically in all non-diffusive experiments.

Double Diffusive case, salty water over sweet water The double diffusive case has been extensively studied in non-rotating environments. The typical double diffusive jet evolution with rotation has not often been described and it still remains unclear how the instabilities observed in the non-diffusive case are suppressed.

In figure 5, we show the evolution of the jet for one of the double diffusive

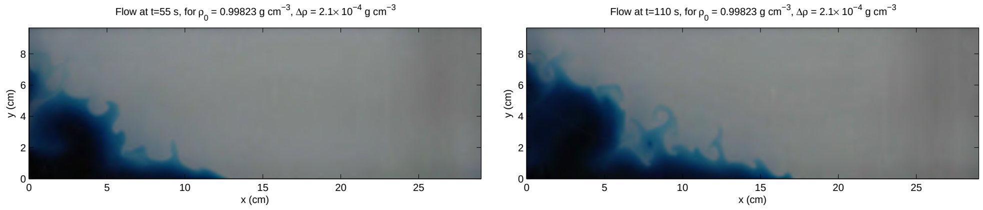
Flow at t=55 s, for ρ_0 = 0.99823 g cm^{-3}, $\Delta\rho$ = 2.1× 10^{-4} g cm^{-3}
Flow at t=110 s, for ρ_0 = 0.99823 g cm^{-3}, $\Delta\rho$ = 2.1× 10^{-4} g cm^{-3}
y (cm)
x (cm)
0
2
4
6
8
5
10
15
20
25

(a) t=55 s

(b) t=110 s

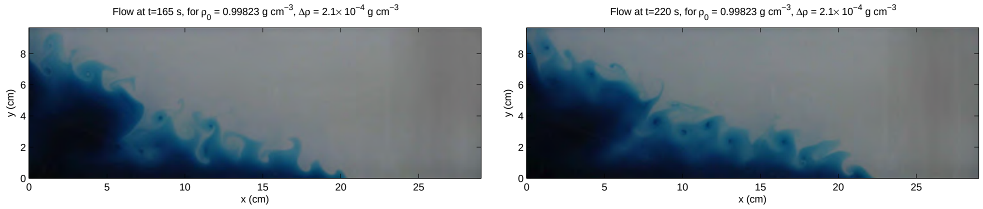
Flow at t=165 s, for ρ_0 = 0.99823 g cm^{-3}, $\Delta\rho$ = 2.1× 10^{-4} g cm^{-3}
Flow at t=220 s, for ρ_0 = 0.99823 g cm^{-3}, $\Delta\rho$ = 2.1× 10^{-4} g cm^{-3}
y (cm)
x (cm)
0
2
4
6
8
5
10
15
20
25

(c) t=165 s

(d) t=220 s

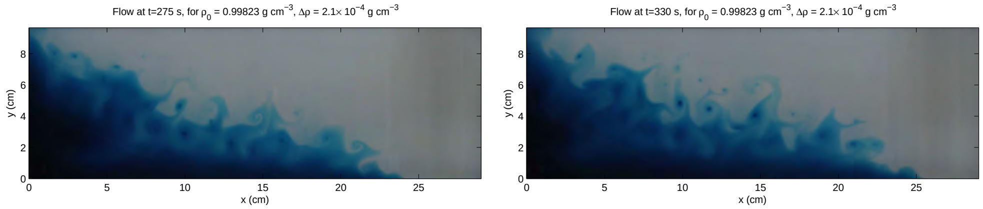
Flow at t=275 s, for ρ_0 = 0.99823 g cm^{-3}, $\Delta\rho$ = 2.1× 10^{-4} g cm^{-3}
Flow at t=330 s, for ρ_0 = 0.99823 g cm^{-3}, $\Delta\rho$ = 2.1× 10^{-4} g cm^{-3}
y (cm)
x (cm)
0
2
4
6
8
5
10
15
20
25

(e) t=275 s

(f) t=330 s

Figure 4: Time evolution of a non-diffusive front for $\rho_0 = 0.99823$ g cm^{-3} and $\Delta\rho = 2.1 \times 10^{-4}$ g cm^{-3}.

experiments with $\Delta\rho$ about the same as that in figure 4. One quickly notices that the boundary current is wider and has progressed farther than the one in figure 4. It is also relatively shallow away from the boundary. What is striking about these experiments is how they inhibit the development of the instabilities. One can see in figure 5(d), the interface growing filaments, in precisely the same manner as for the non-diffusive jet. However, for some reason, these are not sustainable in a double-diffusive environment and collapse soon after their first appearance. They usually simply evolve as to reform another interface, a bit further from the boundary.

Referring again to figure 5, one sees how a large part of the blue dye actually does not have to propagate first through the boundary current but instead is able to penetrate much further. This is in stark contrast with the non-diffusive experiment where most of the dye was confined to $x < 5$ cm or to the boundary current. In the double diffusive case, the bulk of the blue dye does not even seem to be confined, except that the interior circulation appears to be slower than the propagation speed of the jet. This gives a second way for double-diffusive experiments to flux mass rightward, a statement that will be clarified later.

4.2 Nose Displacement

The speed at which the tip of the gravity current propagates is directly affected by the gravitational forcing associated to $\Delta\rho$. This means that any change in $\Delta\rho$, through diffusion for example, will influence the speed at which the nose moves. In order to quantify how much, we computed the nose position as a function of time for each experiment. Then, we found the linear fit of the nose position over the time interval $[t_{15}, t_{25}]$, where the time t_{x_0} is the first time when the nose reaches x_0. The slope of the linear fit gives the nose speed over that interval. We have plotted these speeds as a function of ρ_0 in figure 6.

For the two smaller $\Delta\rho$, we observe a clear tendency of the flow to be accelerated with increasing ρ_0 but for the largest $\Delta\rho$, this tendency seems absent. One explanation is that as $\Delta\rho$ increases the initial velocity increases, which reduces the time scale, but for fixed ρ_0, the diffusive fluxes are kept constant. The compounded effect of diffusion over the course of an experiment will then be of the order of the time scale multiplied by the diffusive fluxes. Therefore, a smaller time-scale should lead to weaker total diffusive effects. One could imagine in the limit of very large $\Delta\rho$, for a fixed ρ_0, to observe no clear effects of double diffusion before the nose reaches the end of the tank. In figure 7, we plotted the relative gain of speed by double diffusion for each $\Delta\rho$. The bigger the $\Delta\rho$, the smaller the relative gain is, which justifies our explanation.

Alternatively, one could argue that the error bars being as large as they are, these results should be taken with some reserve. This is clearly true for the largest $\Delta\rho$

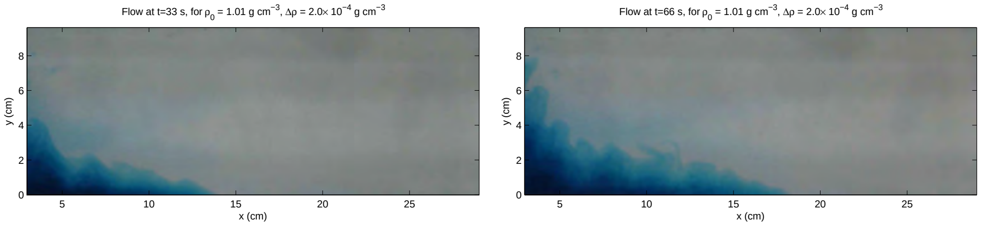
Flow at t=33 s, for ρ_0 = 1.01 g cm^{-3}, $\Delta\rho$ = 2.0× 10^{-4} g cm^{-3}
Flow at t=66 s, for ρ_0 = 1.01 g cm^{-3}, $\Delta\rho$ = 2.0× 10^{-4} g cm^{-3}
y (cm)
0
2
4
6
8
x (cm)
5
10
15
20
25

(a) t=33 s

(b) t=66 s

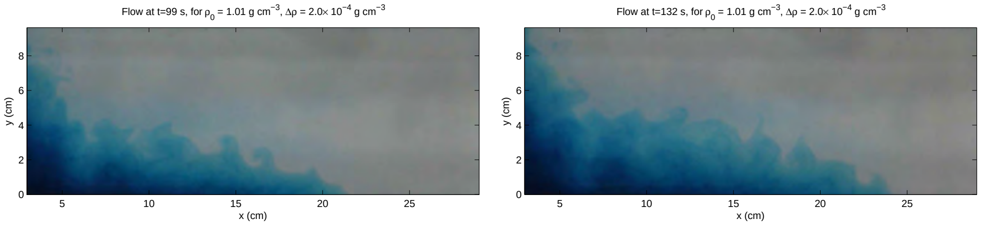
Flow at t=99 s, for ρ_0 = 1.01 g cm^{-3}, $\Delta\rho$ = 2.0× 10^{-4} g cm^{-3}
Flow at t=132 s, for ρ_0 = 1.01 g cm^{-3}, $\Delta\rho$ = 2.0× 10^{-4} g cm^{-3}
y (cm)
0
2
4
6
8
x (cm)
5
10
15
20
25

(c) t=99 s

(d) t=132 s

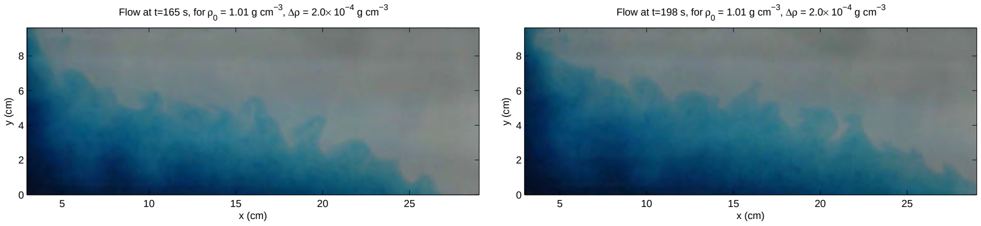
Flow at t=165 s, for ρ_0 = 1.01 g cm^{-3}, $\Delta\rho$ = 2.0× 10^{-4} g cm^{-3}
Flow at t=198 s, for ρ_0 = 1.01 g cm^{-3}, $\Delta\rho$ = 2.0× 10^{-4} g cm^{-3}
y (cm)
0
2
4
6
8
x (cm)
5
10
15
20
25

(e) t=165 s

(f) t=198 s

Figure 5: Time evolution of a double diffusive front for $\rho_0 = 1.01$ g cm^{-3} and $\Delta\rho = 2.0 \times 10^{-4}$ g cm^{-3}. Note that panel 5(f) occurs at a time between panels 4(c) and 4(d)

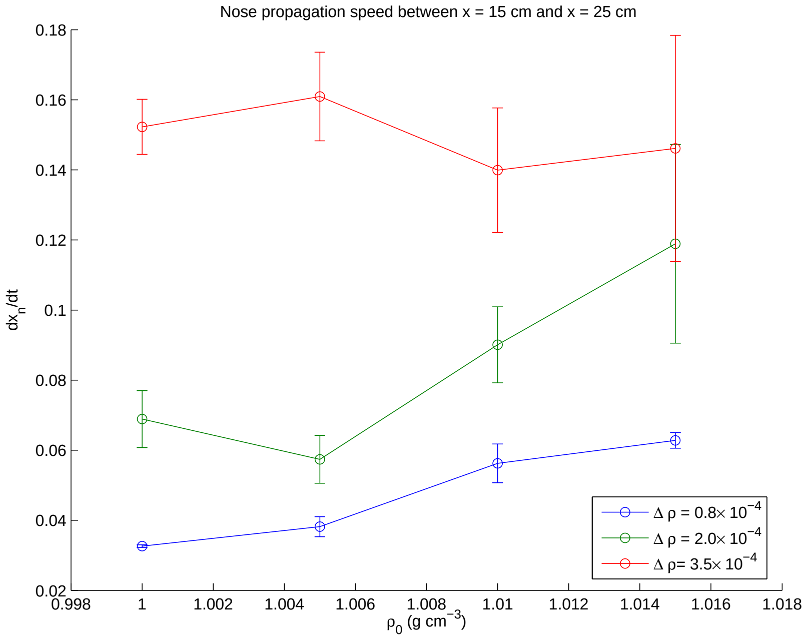

Figure 6: The linear fit velocity of the nose during its residence between $x = 15$ cm and $x = 25$ cm. Observe the dependence on ρ_0 for the two lower $\Delta\rho$ but no obvious dependence for $\Delta\rho = 3.5 \times 10^{-4}$ g cm^{-3}. The error bars are sampling standard deviations.

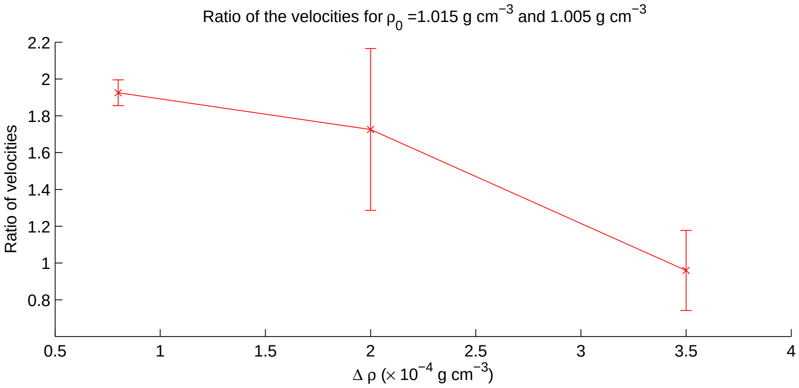

Figure 7: The ratio of the nose speed for $\rho_0 = 1.015$ g cm^{-3} to the velocity for $\rho_0 = 1.005$ g cm^{-3}. Observe the decrease in ratio with increasing $\Delta\rho$.

but not for the smallest. More experiments would be needed to solve this problem, ideally with a longer tank for higher $\Delta\rho$.

4.3 Mass transport

The nose speed is an important quantity because it gives us an idea of how fast the system is able to transport lighter fluid to the right. It is however limited in scope because it only tells us how fast the current close to the wall at $y = 0$ cm is going. In the situation where the bulk of the mass is transported close to the wall, this velocity multiplied by the cross-section of the boundary current would be equivalent to the mass transport. But if that is not the case and an important part of the transport is located far from the wall, this velocity does not give the whole picture. One could imagine a fast boundary current that releases an important quantity of slow moving fluid towards the interior. The effect would be a fast nose and a wide current that would not flux much more mass than a slower current that does not eject any mass towards increasing y. The mass transport thus appears to be an important feature of the flow worth investigating.

In order to compute the mass transport, we assume that the blue dye is a tracer and that each layer is shallow enough that it has a velocity uniform in z:

$$\partial_t h + \nabla \cdot (h\mathbf{u}) = 0 \tag{1}$$

where h is the thickness of the blue layer.

Since there is no flow normal to the side walls, if we integrate over the region to the right of a vertical line x, we get

$$\partial_t \Big[\int_x^{30} \int_0^{10} h \, dx \, dy \Big] = \int_0^{10} h(x,y) u(x,y) dy \tag{2}$$

where the term in the time derivative corresponds to the total amount of dye at the right of x, that will be denoted $\mathcal{H}(x,t)$, and where the right hand side corresponds to the total horizontal dye flux across the vertical line at x, that will be denoted $\mathcal{F}_h(x,t)$.

This means that from our data we can recover the horizontal flux through any vertical line. This can be done by fixing an x, $x = 15$ cm for example, computing $\mathcal{H}(15,t)$ for all time and then taking the time derivative. This way, we can observe how efficient our currents are at transporting mass rightward. Using the same approach as with the nose speed, we compute the derivative of $\mathcal{H}(15,t)$ by using a linear fit on the time interval when the nose is between $x = 25$ cm and $x = 30$ cm. We are using a different interval because as the nose crosses the line $x = 15$ cm, $\mathcal{H}(15,t)$ increases non-linearly until the nose is sufficiently far.

In figure 8, we plotted the fluxes at 15 cm as a function of ρ_0. The flux is seen to increase with ρ_0 but it is unclear why there so much variability. Clearly, higher density differences are leading to apparently smaller gains, which is coherent with our discussion about velocities.

4.4 Area Increase

Another striking feature of double diffusive gravity currents is how their width exceed that of non-diffusive currents. In order to get a measure of the width, we first tracked the evolution of the interface by using an uncommon technique. The technique uses the $h(x,y,t)$, the depth in space and time, and the function

$$y_p(x,t), \quad \text{such that} \int_0^{y_p(x,t)} h(x,y',t)\, dy' = p \int_0^{10} h(x,y',t)\, dy', \tag{3}$$

where we must have $p \leq 1$.

If one sets $p = 1$, $y_1(x,t)$ is simply the interface between the blue and the transparent fluid. By using $p < 1$, $y_p(x,t)$ is the curve below which lies a fraction p of the mass on the vertical line passing through x. It enables us to track the interface without really tracking it, thus reducing the noise, especially in non-diffusive experiments. Also, it emphasizes the fact that even though the interface has important physical properties, it is what happens to the *bulk* of the flow that interests us. We show an example of such a curve with $p = 0.75$ in figure 9.

Now, one can compute the area $A_p(t) = \int_0^{30} y_p(x,t) dx$, thus finding the area occupied by the fraction p of the mass closest to the boundary at $y = 0$ cm. Using

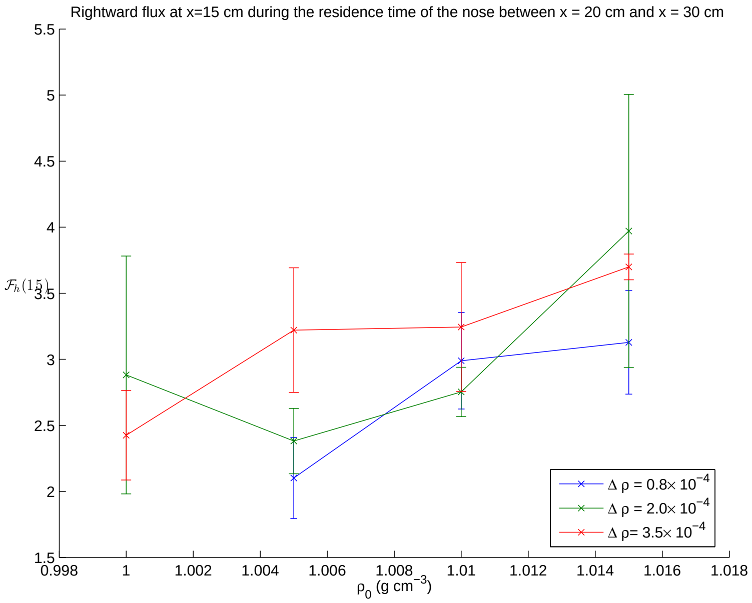

Figure 8: Flux at $x = 15$ cm. Generally the flux increases with ρ_0 except for $\rho_0 = 0.99823$ g cm^{-3} and $\Delta\rho = 2.0 \times 10^{-4}$ g cm^{-3}. Considering the high level of uncertainty associated with this point, we attribute this to statistical errors. The absence of data for the non-diffusive experiment with the lowest $\Delta\rho$ is due to the fact that the current did not propagate far enough in the tank.

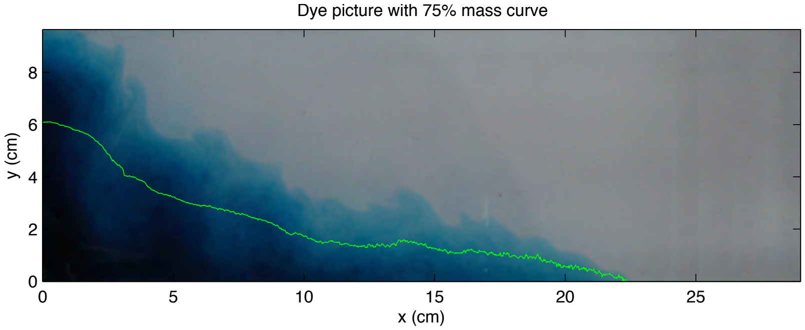

Figure 9: An example of the curve $y_{.75}(x)$ for a double diffusive experiment. For each x, $y = y_{.75}(x)$ corresponds to the point below which lies 75% of the mass on the vertical passing by x.

this technique on our data, we realized that on the time interval where the nose lies between $x = 15$ cm and $x = 25$ cm, $A_p(t)$ is almost a linear function of time. Computing a linear fit on this function over that time interval is thus justified and the slope of the fit is then a good approximation of the time derivative $\frac{dA_p(t)}{dt}$. This quantity is then giving us an idea how fast the bulk of the fluid is spreading.

Dilatation of the interior flow. The flow can be qualitatively split into two regions: the boundary current and the interior flow. The boundary current contains most of the mass, is concentrated close to the wall at $y = 0$ cm and its dynamic is to first order characterized by the nose velocity. The interior flows is defined as the slow moving, shallow and instabilities prone region that remains. When one is evaluating how the bulk of the flow is spreading using the previously described technique, both the evolution of the boundary current and of the interior flow contribute to the analysis. Since the two regions have qualitatively different dynamics, we should not expect to capture any feature particular to any one of these regions. We will therefore have to devise an analysis that enables us to observe each region separately.

In order to do so, we need to have a quantitative definition of each region. Any such definition will be to some extent arbitrary so here we decide to define the interior flow as the region that has 50% of the mass furthest from the boundary. Basically, it is the region contained between the curve $y_{.5}(x,t)$ and $y_{.95}(x,t)$. The rate of change of its area, $\frac{dA_{.95}}{dt} - \frac{dA_{.5}}{dt}$, indicates how the bulk of the interior spreads. The results are shown in figure 10.

It shows a clear increase in area with ρ_0, implying a general increase in deformation radius. One could compute the average widening, or the average increase in deformation radius, by dividing the rate of change by 20 cm, the average length of the boundary current when the derivative was taken. This would be a way to quantify the bulk diffusion but what interests us is where most of this diffusion occurs, not how much it occurs on average. To accomplish this, we have to develop another special technique.

Spatial distribution of area increase. We start by subdividing the interval $[0, x_N(t)]$, where $x_N(t)$ is the nose position, in n subintervals $[x_i, x_{i+1}]$. Then we define the area under the curve $y_p(x,t)$ in the ith subinterval by

$$a_p^{(i)}(t) = \int_{x_i}^{x_{i+1}} y_p(x,t)\,dx. \tag{4}$$

Summing up and taking the time derivative,

$$\frac{dA_p}{dt} = \sum_{i=1}^{N} \frac{da_p^{(i)}}{dt} \tag{5}$$

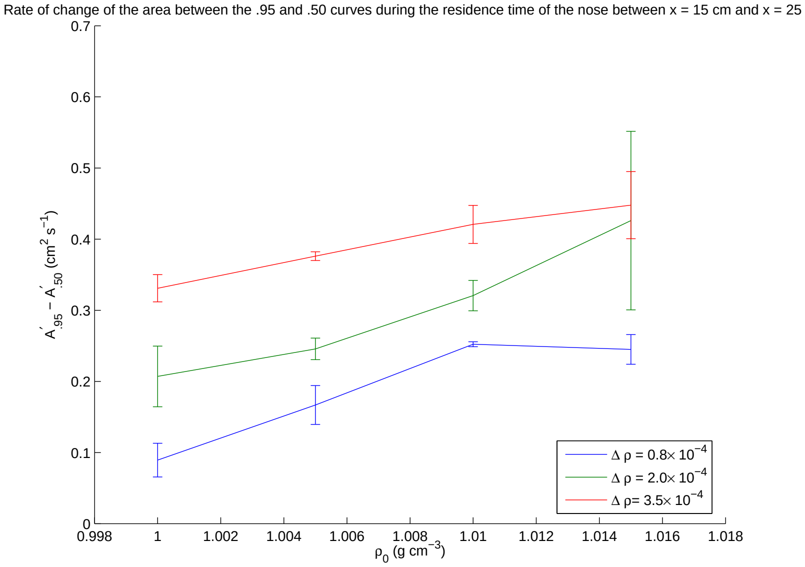

Figure 10: The linear fit rate of change of $\frac{dA_{.95}}{dt} - \frac{dA_{.5}}{dt}$ during the residence time of the nose between $x = 15$ cm and $x = 25$ cm. Observe a clear increase in the rate of change of the area for increasing ρ_0. Only the experiments with $\rho_0 = 1.015$ g cm^{-3} have higher uncertainties but not enough to make the previously mentioned tendency be questionable. The error bars are sampling standard deviations.

where A_p is as defined in section 4.4.

The functions $\frac{da_p^{(i)}}{dt}$, the rates of change of the area in the ith subinterval, are the quantities we would like to recover because they locally quantify how fast the flow spreads towards the interior. But what we have now is one equation for n unknowns, which is highly underdetermined. Thus, in order to make any progress, we have to make some assumptions. We assume that for any p_1, p_2 such that $.95 \geq p_2 > p_1 \geq .5$ we can write

$$\frac{da_{p_2}^{(i)}}{dt} - \frac{da_{p_1}^{(i)}}{dt} = \bar{a}_i' \left(\frac{a_{p_2}^{(i)}(t) - a_{p_1}^{(i)}(t)}{a_{.95}^{(i)}(t) - a_{.5}^{(i)}(t)} \right), \tag{6}$$

which means that every subinterval has an uniform rate of area increase $\bar{a}_i'$. The factor is the fraction of the area between y_{p_2} and y_{p_1} with the total area of the interior flow in the ith subinterval.

We then divide the interval $[.5, .95]$ in m subintervals $[p_j, p_{j+1}]$, yielding a system of m equations for $\bar{a}_i'$,

$$\frac{dA_{p_{j+1}}}{dt} - \frac{dA_{p_j}}{dt} = \sum_{i=1}^{n} \bar{a}_i'(t) \left(\frac{a_{p_{j+1}}^{(i)}(t) - a_{p_j}^{(i)}(t)}{a_{.95}^{(i)}(t) - a_{.5}^{(i)}(t)} \right), \tag{7}$$

which is of the form $M\xi = b$ with the columns of M summing to 1.

If $m = n$, this system has a unique solution. However, this solution will most likely result in negatives $\bar{a}_i'$, which would indicate a reduction of area in some interval $[x_i, x_{i+1}]$. Even if such a situation could be physically justified, we would like to avoid it for numerical stability purposes. So, instead, we solve the system in a least-squares sense demanding that the solution be everywhere positive and that the total change in area be conserved,

$$\frac{dA_{.95}}{dt} - \frac{dA_{.5}}{dt} = \sum_{i=1}^{n} \bar{a}_i'(t). \tag{8}$$

This is an optimization problem that depends on the initial guess, here chosen as a random vector, to reduce bias.

We can then convert the $\bar{a}_i'$ to local width increase by

$$\bar{l}'(x,t) = \bar{a}_i' \left(\frac{y_{.95}(x,t) - y_{.5}(x,t))}{a_{.95}^{(i)}(t) - a_{.5}^{(i)}(t)} \right), \qquad \text{for } x \in [x_i, x_{i+1}]. \tag{9}$$

Since by construction $\bar{l}'(x,t) \geq 0$, it can be transformed into a distribution and one can compute its moments. For example, one can compute $\bar{x} = \langle x_N - x \rangle_{\bar{l}'}$, its first moment with respect to the nose position. This value tells us where the average widening takes place. If it is close to 0, it means most of the widening happens

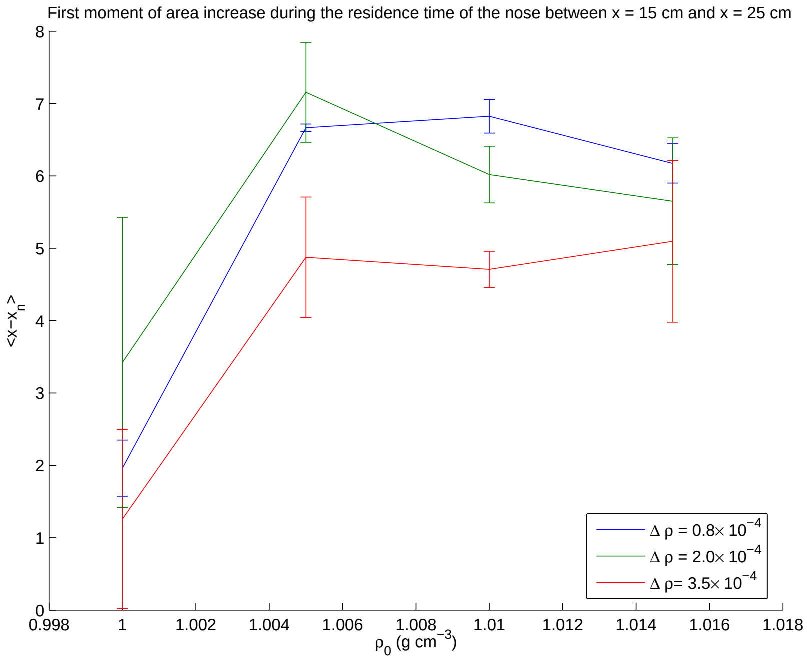

Figure 11: The average distance from the nose where the widening of the jet occurs. Note how much closer to the nose the non-diffusive experiments widen.The error bars are sampling standard deviations.

at the nose whereas, if it is non-zero, the widening occurs on average at $\bar{x}$ cm at the left of the nose. In figure 11, we show the results for our experiments. We observe that for non-diffusive experiments, the increase is close to the nose, which is not surprising considering that our technique does not correct for the increase in area due to the gravitational propagation of the boundary current. For diffusive experiments, however, most of the widening occurs away from the nose, at about 5 cm to the left, precisely where the unstable eddies would form in the non-diffusive case.

5 Conclusion

The double diffusive rotating dam break experiment shows significant qualitative differences from the non-diffusive one, with most instabilities suppressed. The resulting boundary currents are wider and transport mass more effectively. From our data, we are able to extract a clear trend that shows an increase in nose velocity with increasing ρ_0, mainly for smaller $\Delta\rho$. Moreover, our data suggest that the rightward flux of mass is enhanced with increasing values of ρ_0. This indicates that double diffusive systems should be more efficient at transporting mass than non-diffusive ones, with the effect of ρ_0 dominating that due to $\Delta\rho$ in diffusive experiments.

This means that over the course of the experiment, $\Delta\rho$ must acquire a significant spatial variation, in order to drive the system. Such a spatial variation, one can hypothesize, must increase the local radius of deformation, thereby widening the boundary current. Variations of radii of deformation should also influence the turbulent cascade and, hence, the energy spectrum distribution of the system since it is the scale at which eddies evolve. This means that major spatial variations in deformation scale would most likely distort and make unsustainable two-dimensional type turbulent eddies.

We have demonstrated that the width of the boundary current in diffusive experiments exceeds that in non-diffusive ones, and that the width increases with increasing values of ρ_0. In diffusive experiments, the first moment of this widening was shown to occur in the region where the turbulent eddies form in non-diffusive experiments. In contrast, in non-diffusive experiments it occurred close to the nose, which is consistent with the biases of our measurement method. This strongly suggests that the deformation radius in regions where instabilities would normally develop in non-diffusive experiments increases in double diffusive experiments. This leads us to conclude that this local inflation of the deformation radius destroys the instabilities.

This conclusion remains to be investigated using more theoretical models. In appendix A, we propose a simple toy model that could verify this explanation. It is based on a two-layer QG model with spatially varying radius of deformation. We expect that in such a model growth of instabilities will be slowed, if not removed, and that the width of the boundary current will be wider than in situations with a constant radius of deformation.

6 Acknowledgments

The success of this project must be entirely credited to George Veronis' enthusiasm and enlightening physical insights. Without the numerous hours spent in the lab debating about science and being amazed by the beautiful vortices created in our experiments this project would never have attained the same maturity. I am also grateful to Keith Bradley and his dedication at making things works. Finally, I would like to thank WHOI for this beautiful opportunity as well as Claudia Cenedese and Jack Whitehead for organizing such a memorable summer.

A Two-layer QG with non-uniform densities

To derive the shallow water equations for non-uniform densities, one makes the momentum budget in a test volume containing a whole layer:

$$\begin{aligned}
\partial_t\rho_1 h_1 + \nabla\cdot(\rho_1 h_1\mathbf{u}_1) &= 0,\\
\partial_t(\rho_1 h_1\mathbf{u}_1) + \nabla\cdot(\rho_1 h_1\mathbf{u}_1\otimes\mathbf{u}_1) + \mathbf{f}\times\rho_1 h_1\mathbf{u}_1 &= -g\nabla(\rho_1\frac{h_1^2}{2}) - g\rho_1 h_1\nabla h_2, \qquad (10)\\
\partial_t\rho_2 h_2 + \nabla\cdot(\rho_2 h_2\mathbf{u}_2) &= 0,\\
\partial_t(\rho_2 h_2\mathbf{u}_2) + \nabla\cdot(\rho_2 h_2\mathbf{u}_2\otimes\mathbf{u}_2) + \mathbf{f}\times\rho_2 h_2\mathbf{u}_2 &= -g\nabla(\rho_1 h_1 h_2 + \rho_2\frac{h_2^2}{2}) + g\rho_1 h_1\nabla h_2,
\end{aligned}$$

These equations characterize the system if ρ_i are constants. However, here we want to allow them to vary in both space and time. We assume that $\rho_i = \rho_0 + \rho_{Ti} + \rho Si$ where ρ_0 is the density of pure water at some fixed temperature. ρ_T and ρ_S are the densities of salt and sugar respectively.

We assume that the two layers don't mix but that they can exchange chemicals. This leads to

$$\begin{aligned}
\partial_t(\rho_{\alpha i}h_i) + \nabla\cdot(\rho_{\alpha i}h_i\mathbf{u}_i) &= (-1)^i S_\alpha + D_{\alpha i},\\
\partial_t\rho_0 h_i + \nabla\cdot(\rho_0 h_i\mathbf{u}_i) &= 0. \qquad (11)
\end{aligned}$$

where the last expression implies conservation of volume since ρ_0 is constant.

S_α is the exchange of mass between the two layers. A heuristic candidate would be:

$$S_\alpha = \kappa_\alpha\rho_i(m_{\alpha 1} - m_{\alpha 2})\sqrt{|\nabla h_2|^2 + 1}|\rho_{\alpha 1} - \rho_{\alpha 2}| \qquad (12)$$

where $m_{\alpha i} = \frac{\rho_{\alpha i}}{\rho_i}$ is the mass fraction and κ_α is a diffusivity constant.

From these equations, one can find advection equations:

$$\frac{Dm_{\alpha i}}{Dt} = (-1)^i\frac{S_\alpha}{\rho_i h_i} + \frac{D_{\alpha i}}{\rho_i h_i} \qquad (13)$$

Where the diffusion can be written as

$$\frac{D_{\alpha i}}{\rho_i h_i} = \bar{\kappa}_\alpha\nabla^2 m_{\alpha i}$$

or as any other mass-ratio diffusion.

From now on, we will drop the diffusion as it only add uninteresting complexity.

Equations After some manipulations, one gets the following equations:

$$\begin{aligned}
&\partial_t h_i + \nabla \cdot (h_i \mathbf{u}_i) = 0, \\
&\qquad \frac{Dm_{\alpha i}}{Dt} = (-1)^i \frac{S_\alpha}{\rho_i h_i}, \\
&\qquad \gamma_i = \frac{1}{\rho_i h_i} = \frac{1 - m_{Ti} - m_{Si}}{\rho_0 h_i}, \\
&\frac{D\mathbf{u}_1}{Dt} + f \times \mathbf{u}_1 = \mathbf{u}_1 \gamma_1 (S_T + S_S) - g\gamma_1 \nabla(\rho_1 \frac{h_1^2}{2}) - g\nabla h_2, \\
&\frac{D\mathbf{u}_2}{Dt} + f \times \mathbf{u}_2 = -\mathbf{u}_2 \gamma_2 (S_T + S_S) - g\gamma_2 \nabla(\rho_1 h_1 h_2 + \rho_2 \frac{h_2^2}{2}) + g\frac{\gamma_2}{\gamma_1} \nabla h_2.
\end{aligned} \tag{14}$$

March towards a QG formulation In order to find a QG formulation of the problem, one must first find the geostrophic winds. First, we assume a small Rossby number, leading to:

$$\begin{aligned}
f \times \mathbf{u}_1 &= \mathbf{u}_1 \gamma_1 (S_T + S_S) - g\nabla(h_1 + h_2) - g\frac{h_1}{2}\frac{\nabla \rho_1}{\rho_1}, \\
f \times \mathbf{u}_2 &= -\mathbf{u}_2 \gamma_2 (S_T + S_S) + g\frac{\rho_2 - \rho_1}{\rho_2} \nabla h_1 - g\nabla(h_1 + h_2) \\
&\qquad - g(h_1 \frac{\nabla \rho_1}{\rho_2} + \frac{h_2}{2}\frac{\nabla \rho_2}{\rho_2}).
\end{aligned} \tag{15}$$

We now assume the density variations in horizontal to be small and that the mass exchange between the layers is relatively weak. This leads to the following streamfunctions:

$$\begin{aligned}
\psi_1 &= \frac{g}{f}(h_1 + h_2), \\
\nabla^2(\psi_2 - \psi_1) &= -\nabla \cdot (\frac{g'}{f} \nabla h_1).
\end{aligned} \tag{16}$$

Advection of reduced gravity We now assume that the density difference is small between the two layers, so that $\rho_1 \approx \rho_2 = \bar{\rho}$. Subtracting the two advection equations, yields

$$\frac{D(\Delta m_\alpha)}{Dt} = \frac{S_\alpha}{\bar{\rho}}(\frac{1}{h_1} + \frac{1}{h_2})$$

and adding the two diffusers,

$$\frac{D\Delta m}{Dt} = \frac{S_T + S_S}{\bar{\rho}}(\frac{1}{h_1} + \frac{1}{h_2})$$

where $\Delta m = (m_{T2} + m_{S2}) - (m_{T1} + m_{S1})$.

Now, one can write

$$\frac{1}{\bar{\rho}}(S_T + S_S) = \sqrt{|\nabla h_2|^2 + 1}(\kappa_T \Delta m_T |\Delta m_T| + \kappa_S \Delta m_S |\Delta m_S|))$$

where we wrote $m_{\alpha i} \approx \frac{\rho_{\alpha i}}{\bar{\rho}}$.

Now, assuming $\frac{\kappa_S}{\kappa_T} \ll 1$, we obtain

$$\frac{D\Delta m}{Dt} \approx \kappa_T \Delta m_T |\Delta m_T| (\frac{1}{h_1} + \frac{1}{h_2})\sqrt{|\nabla h_2|^2 + 1} \tag{17}$$

which can be seen as a equation of reduced gravity since $g' \approx g\Delta m$.

PV advections By defining the PVs:

$$q_i = \frac{\omega_i + f}{\rho_i h_i}$$

One get the following advection equations:

$$\begin{aligned}
\frac{Dq_1}{Dt} &= -\gamma_1^2 f(S_T + S_S) + \gamma_1 J(\psi_1, \gamma_1(S_T + S_S)) - \frac{g}{2}J(\gamma_1, h_1), \\
\frac{Dq_2}{Dt} &= \gamma_2^2 f(S_T + S_S) + \gamma_2 J(\psi_2, \gamma_2(S_T + S_S)) + \gamma_2 J(g', h_1) - \\
&\qquad g\gamma_2 \left(J(\frac{h_1}{\rho_2}, \rho_1) + \frac{1}{2}J(\frac{h_2}{\rho_2}, \rho_2) \right).
\end{aligned}$$

Assuming a small Rossby number and high correlation between densities and constant heights, we can neglect most terms:

$$\begin{aligned}
\frac{Dq_1}{Dt} &= -\gamma_1^2 f(S_T + S_S), \\
\frac{Dq_2}{Dt} &= \gamma_2^2 f(S_T + S_S).
\end{aligned}$$

The last terms remaining are the ones relating the exchange of vorticity due to the exchange of mass, in order to conserve the total vorticity. One could not bother and assume that the mass exchange is not done in a PV preserving kind of way and neglect them, which is the approach we will take here.

PV inversion The PV perturbations can be written as:

$$q_i \approx \frac{1}{\bar{\rho}_i H_i}\left(f + \omega_i - \frac{f}{H_i}h_i' - \frac{f}{\bar{\rho}_i}\rho_i'\right)$$

The resulting set of simplified equations is:

$$\begin{aligned}
\psi_1 &= \frac{g}{f}(h_1' + h_2'), \\
\nabla^2(\psi_2 - \psi_1) &= -\nabla \cdot (\frac{g'}{f}\nabla h_1'), \\
q_i &= \nabla^2\psi_i - \frac{f}{H_i}h_i' - \frac{f}{\bar{\rho}_i}\rho_i', \\
\partial_t q_i + J(\psi_i, q_i) &= 0.
\end{aligned} \tag{18}$$

Looking more closely at the inversion equations:

$$\begin{aligned}
\xi_1 &= q_1 - \frac{f}{\bar{\rho}_1}\rho_1 = \nabla^2\psi_2 - \nabla \cdot (\frac{g'}{f}\nabla h_1') - \frac{f}{H_1}h_1', \\
\xi_2 &= q_2 - \frac{f}{\bar{\rho}_2}\rho_2 = \nabla^2\psi_2 + \frac{f}{H_2}h_1' - \frac{f^2}{gH_2}\psi_1.
\end{aligned}$$

We use the rigid lid approximation to neglect the last term in ξ_2, leading to:

$$\begin{aligned}
\xi_1 &= \nabla^2\psi_2 + \nabla \cdot (\frac{g'}{f}\nabla h_1) - \frac{f}{H_1}h_1', \\
\xi_2 &= \nabla^2\psi_2 + \frac{f}{H_2}h_1'.
\end{aligned} \tag{19}$$

One can solve the baroclinic equations for h_1:

$$\xi_2 - \xi_1 = -\nabla \cdot (\frac{g'}{f}\nabla h_1') + (\frac{1}{H_1} + \frac{1}{H_2})fh_1'. \tag{20}$$

with homogeneous dirichlet BCs.

Which enables to solve for ψ_i:

$$\begin{aligned}
\xi_1 + \frac{f}{H_1}h_1' &= \nabla^2\psi_1, \\
\xi_2 - \frac{f}{H_2}h_1' &= \nabla^2\psi_2.
\end{aligned} \tag{21}$$

This then gives us h_2:

$$h_2' = \frac{f}{g}\psi_1 - h_1'.$$

So this means that the system we are looking at consists of 6 advection equations, one helmhotz equation and 2 poisson's equation.

References

[1] T. Brooke Benjamin. Gravity currents and related phenomena. *Journal of Fluid Mechanics*, 31(02):209–248, 1968.

[2] Stern M. E. and Chassignet E. P. Mechanism of eddy separation from coastal currents. *Journal of Marine Research*, 58:269–295, 2000.

[3] A. E. Gill. Adjustment under gravity in a rotating channel. *Journal of Fluid Mechanics*, 77(03):603–621, 1976.

[4] Melvin E. Stern. Geostrophic fronts, bores, breaking and blocking waves. *Journal of Fluid Mechanics*, 99(04):687–703, 1980.

[5] Melvin E. Stern, John A. Whitehead, and Bach-Lien Hua. The intrusion of a density current along the coast of a rotating fluid. *Journal of Fluid Mechanics*, 123(-1):237–265, 1983.

[6] Marshall Ward. Experimental study of double diffusive gravity currents under rotation. In Woods Hole Oceanographic Institution, editor, *Proceedings of the GFD Program*, volume 46, 2004.

Convection of a van der Waals fluid near the critical point

Henrik B. van Lengerich

advised by E. A. Spiegel

Abstract

Convection in a van der Waals fluid, with no-stress and fixed flux boundary conditions is studied. The problem is scaled with the infinite horizontal wavelength of the convection cell. A criterion is found that predicts the onset of convection; it contains information from the Rayleigh and Schwarzschild criterion over the entire cell. The criterion is evaluated and compared with previous experiments on a similar experiment. Governing equations, boundary conditions, constitutive equation and convection mechanisms are explained.

1. Introduction

Past studies of laboratory convection have focused on incompressible or ideal gas fluids. The aim of this study is to approach a theory of convection for a fluid containing both a liquid and a gas phase. This is done by focusing on the conditions where the phase change originates, namely, the critical point of the substance.

Convection near the critical point is difficult both experimentally and theoretically because the fluctuation in properties becomes very large and many thermodynamic properties (such as the heat capacities and thermal conductivity) diverge. We model the fluid as an ideal van der Waals fluid, which a good qualitative (but not quantitative) model because it captures two phases, the critical point, and the divergence of thermodynamic properties. Because the thermal conductivity goes to infinity as the critical point is approached, we show that a fixed flux, rather than a fixed temperature boundary is sometimes appropriate. By doing this we can find the critical temperature difference by scaling the problem appropriately as done in [8].

This paper will first explain some of the previous research that has been done on convection near the critical point of the fluid. Background information is given to explain the properties of the van der Waals fluid and the onset of convection for both incompressible and compressible fluids. Finally, governing equations are derived for the situation to be studied, these equations are scaled, and then the criterion for the onset of convection is found.

2. Literature Review

The criterion for instability as well as the plan form function (the function which explains patterns and evolution) for an ideal gas with fixed flux and no-stress boundary conditions are described in [8]. Analysis of an incompressible fluid with fixed flux boundaries was done by

Chapman and Proctor [7]. A derivation of when to use the constant flux condition was given by Hurle et. al. [11], however, therein the thermal diffusivity and not thermal conductance was used to match the fluxes in the solid and fluid. This error is corrected in the boundary condition derivation in this report.

Experimental studies have been done by Kogan et. al. [12] to determine the onset of convection for ^3He near the critical point. These find that the onset can be understood using only the Rayleigh criteria and the adiabatic temperature gradient (aka Schwarzschild criterion), the same result was found by Carles and Ugurtas [6] using the full governing equations and real data to determine which terms can be ignored. Experimental studies by Assenheimer and Steinberg [2] show that close to the critical point hexagons, lines, roll patches, and target or spiral patterns can be seen. This motivates the current research because it may be possible that additional patterns can be formed, and a plan form function of a van der Waals fluid would help to find the proper parameter regime.

Previous studies of convection near the critical point have focused on the "piston effect" which is the heating up of fluid close to the boundary, then the boundary fluid expands and compresses the bulk fluid, and the compression of the bulk fluid raises the bulk temperature. This was explained using thermodynamic arguments by Onuki [13] and then later derived by Pierre Carles in a lengthy manner using all the governing equations [9], [5]. Further studies continue to look at this piston effect [1].

There have been some numerical simulations of van der Waals fluids close to the critical point [1], [15]. These focus on the piston effect and do little in the way of making new predictions.

Lastly, there is a very good review of hydrodynamics near the critical point by Gitterman [10], and the thermodynamics for phase changes and close to the critical point are concisely explained in the second edition of Callen's book on thermodynamics [4].

3. Gas Properties

A typical phase diagram is shown in Figure 1. The liquid and gas phases are separated by a phase transition line. When the phase transition line is crossed there is a discontinuous jump in the thermodynamic properties of the fluid (such as conductivity, density, and heat capacity). This jump becomes smaller and smaller as one moves to higher temperature and pressure, until the discontinuities disappear at the critical point, which is where the line ends. Incidentally, no critical point has been found for the liquid-solid phase transition.

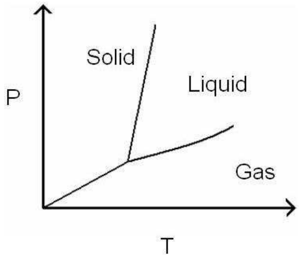

Fig. 1. Typical Phase Diagram

3.1. *Van der Waals Fluid*

A van der Waals fluid is a bunch of particles that are attracted to each other by some potential effects and repelled due to a hard spheres shell. We assume that the attraction force decays to the -6 power. The constitutive equation

$$P = \frac{\Re \rho T}{1 - b\rho} - a\rho^2 \tag{1}$$

can be derived from such a model. Here b contains the information of the finite size of the particles, and as the density of the particles goes to 1/b the space is completely packed with particles so the pressure goes to infinity. The $a\rho^2$ term represents the attraction of the particles, and this tends to decrease the pressure.

In figure 2 are shown several isotherms of the van der Waals equation. The bottom (green) curve has an isotherm temperature below the critical point, from the phase diagram this suggests that the fluid has two phases. Where are the two phases? Imagine a fluid that lies on the green isotherm that has a density of about one, so that the slope is positive. Imagine a fluid blob at this point in the surrounding fluid. If the volume of this blob is made to be slightly bigger, then the pressure increases, so the volume continues to increase until the slope of the curve is negative. Similarly, if the volume is perturbed to be slightly smaller, the blob will continue to decrease in size until it reaches a point where the slope of the curve is negative. So all of the liquid will break up into high density and low density blobs, and these are the two phases. Usually a straight line is drawn across such there are no unstable slopes in the isotherm pressures, when this is done, it is easy to see the discontinuity in density that occurs at the phase transition. When the temperature is well beyond the critical value the top (red) curve shown in Figure 2 applies. This fluid has no phase transition because there are no parts with positive slopes. The middle curve is the curve at the critical temperature, the critical point is where the first and second derivatives of the pressure with respect to volume occur at the same volumes ($\rho_c = \frac{1}{3b}$,$T_c = \frac{8a}{27b}$,$P_c = \frac{a}{27b^2}$).

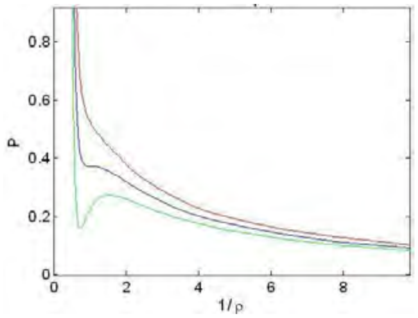

Fig. 2. Pressure for various isotherms

3.2. *Diverging Properties near the Critical Point*

By definition of an ideal van der Waals fluid the constant volume heat capacity is only a function of volume and does not diverge at the critical point. The constant pressure heat capacity can be found from the standard thermodynamic relation

$$C_P = C_V - \frac{T}{\rho^2}\left(\frac{\partial \rho}{\partial T}\right)_P \left(\frac{\partial P}{\partial T}\right)_\rho \tag{2}$$

$$C_P = C_V - \frac{T}{\rho^2}\frac{1}{\left(\frac{\partial T}{\partial \rho}\right)_P}\frac{\rho}{1 - b\rho} \tag{3}$$

$$C_P = C_V - \frac{\frac{8a}{27b}}{2a\frac{1}{3b}(1 - 1/3)^2 - \frac{8a}{27b}} \tag{4}$$

Where the last step was just inserting the critical values. The constant pressure heat capacity diverges as the -1 power as the critical point is approached. The thermal conductivity diverges to the roughly -1/2 power as shown in [14].

4. Convection Mechanisms

The criterion that determine the onset of convection can be derived from physical arguments. For an incompressible fluid the usual Rayleigh criteria is found. For a compressible fluid the adiabatic temperature gradient (or Schwarzschild criterion) is found.

4.1. *Incompressible Convection*

Consider a fluid blob of volume $V = a^3$ contained in the fluid. Perturb the blob upward slightly, so that it is less dense than its surroundings and experiences a force directed upward due to the buoyancy. When moving upward, the blob experiences a force directed downward due to the viscous drag. Write the buoyancy force as

$$F_B = gV\delta\rho \tag{5}$$

The change in density is assumed to be due to the gradient in temperature

$$\delta\rho = -\rho\alpha\delta T \tag{6}$$

$$\alpha = -\frac{1}{\rho}\left(\frac{\partial \rho}{\partial T}\right)_P \tag{7}$$

The change in temperature of the blob is due to the temperature of the surroundings changing at a rate proportional to the temperature gradient times the rate at which this temperature diffuses into the blob.

$$\delta T = \frac{\Delta T}{d} v_z C_2 \frac{a^2}{\kappa} \tag{8}$$

This makes the buoyancy force equal to

$$F_B = -g\rho\alpha a^5 C_2 \frac{\Delta T}{d\kappa} v_z \tag{9}$$

The drag force is given by

$$F_D = C_1 a\mu v_z \tag{10}$$

By Newton's second law, the particle is stationary if the drag force is greater than the buoyancy force.

$$F_D > F_B \tag{11}$$

$$C_1 a\mu v_z > g\rho\alpha a^5 C_2 \frac{\Delta T}{d\kappa} v_z \tag{12}$$

$$a = C_3 d \tag{13}$$

$$\frac{C_1}{C_2 C_3^4} > \frac{g\alpha d^3 \Delta T}{\nu\kappa} \tag{14}$$

$$Ra_c > \frac{g\alpha d^3 \Delta T}{\nu\kappa} \tag{15}$$

This means that the fluid is stable if the Rayleigh number is below some critical Rayleigh number value.

4.2. *Compressible Convection*

Consider again a blob of fluid in an inviscid and nonconducting surrounding fluid. The blob has a density ρ_{blob} and the bulk fluid has an equal density ρ. Perturb the fluid upward slightly, now the blob has a density $\rho_{blob} + \delta\rho_{blob}$ and the fluid has a density $\rho(z + \delta z)$. The force on the particle at its new hight is given by the buoyancy force

$$F_B = gV(\rho(z + \delta z) - (\rho_{blob} + \delta\rho_{blob})). \tag{16}$$

Expand the density of the fluid in terms of z

$$F_B = gV(\frac{\partial\rho}{\partial z}\delta z - \delta\rho_{blob}). \tag{17}$$

The fluid is neutrally stable if the force of buoyancy is zero.

$$\frac{\partial\rho}{\partial z}\delta z = \delta\rho_{blob} \tag{18}$$

The density is written as a function of T and P:

$$\rho = \rho(T, P) \tag{19}$$

$$\frac{\partial\rho}{\partial z} = \left(\frac{\partial\rho}{\partial T}\right)_P \frac{\partial T}{\partial z} + \left(\frac{\partial\rho}{\partial P}\right)_T \frac{\partial P}{\partial z} \tag{20}$$

Inserting this into Eq. 18 gives

$$\frac{\partial\rho_{blob}}{\partial z} = \left(\frac{\partial\rho}{\partial T}\right)_P \frac{\partial T}{\partial z} + \left(\frac{\partial\rho}{\partial P}\right)_T \frac{\partial P}{\partial z} \tag{21}$$

Using the momentum and adiabatic energy balance (heat transfer term is neglected) we obtain

$$\frac{\partial\rho_{blob}}{\partial z} = \frac{C_v \rho^2 \frac{\partial T}{\partial z}}{T\left(\frac{\partial P}{\partial T}\right)_\rho} \tag{22}$$

Simplifying and using some thermodynamic relations,

$$\left(\frac{\partial\rho}{\partial T}\right)_P \partial T z + \left(\frac{\partial\rho}{\partial P}\right)_T g\rho = \frac{C_v \rho^2 \frac{\partial T}{\partial z}}{T\left(\frac{\partial P}{\partial T}\right)_\rho} \tag{23}$$

$$\frac{\partial T}{\partial z} = \left(1 - \frac{C_v}{C_P}\right)\left(\frac{\partial T}{\partial P}\right)_\rho \rho g \tag{24}$$

which is an expression for the adiabatic temperature gradient in terms of experimentally accessible quantities.

5. Governing Equations

The mass balance for an incompressible fluid is

$$\frac{\partial \rho}{\partial t} + \nabla \cdot (\rho v) = 0. \tag{25}$$

The Navier-Stokes equations contain the effects of viscosity due to compressibility.

$$\rho(\frac{\partial v}{\partial t} + (v \cdot \nabla)v) + \nabla P = \mu[\nabla^2 v + \frac{1}{3}\nabla(\nabla \cdot v)] + \rho g \hat{k} \tag{26}$$

The conservation of energy is a bit tricky, so I will derive it.

$$d\hat{U} = Td\hat{S} - Pd\hat{V} \tag{27}$$

$$\hat{U} = \hat{U}(T, V) \tag{28}$$

$$d\hat{U} = \frac{\partial \hat{U}}{\partial T}_V dT + \frac{\partial \hat{U}}{\partial V}_T d\hat{V} \tag{29}$$

$$\frac{\partial \hat{U}}{\partial V}_T = T\frac{\partial \hat{S}}{\partial V}_T - P = T\frac{\partial P}{\partial T}_V - P \tag{30}$$

$$d\hat{U} = \hat{C_V} dT + (T\frac{\partial P}{\partial T}_V - P)d\hat{V} \tag{31}$$

$$\hat{C_V} dT = -T\frac{\partial P}{\partial T}_V d\hat{V} + Td\hat{S} \tag{32}$$

$$\rho C_V \frac{DT}{Dt} = -T\frac{\partial P}{\partial T}_V \nabla \cdot v + \nabla \cdot q + \mu\Phi \tag{33}$$

Recall the van der Waals equation of state

$$P = \frac{\mathfrak{R}\rho T}{1 - b\rho} - a\rho^2 \tag{34}$$

Inserting the van der Waals equation of state and the diverging thermal conductivity gives

$$C_v \rho(\frac{\partial T}{\partial t} + v \cdot \nabla T) = -(P + a\rho^2)\nabla \cdot v + k\nabla \cdot [(1 + \Lambda(T/T_c - 1)^{-1/2})\nabla T] + \mu\Phi \tag{35}$$

where Φ is given by:

$$\Phi = (\frac{\partial v_i}{\partial x_j} + \frac{\partial v_j}{\partial x_i} - \frac{2}{3}\delta_{ij}\nabla \cdot v)\frac{\partial v_i}{\partial x_j} \tag{36}$$

The parameters a and b are found from their values at the critical point, and Λ is given by [1]

$$a = \frac{9}{8}\frac{T_c \mathcal{R}}{\rho_c} \tag{37}$$

$$b = \frac{1}{3\rho_c} \tag{38}$$

$$\Lambda = 3/4 \tag{39}$$

5.1. *Boundary Conditions*

Unlike incompressible convection, the amount of particles put into the cell needs to be specified. In order to avoid ever calculating an infinite pressure at $\rho = 1/b$ set

$$max(\rho) = \rho_{max} \tag{40}$$

as the boundary condition on the density.

The temperature is specified as a combination of temperature and flux. I follow [11] to match the flux and temperature at the solid - fluid interface. Focus just the bottom solid, the only difference in the top is that the z coordinate is flipped.

The energy balance in the solid is

$$C_{solid}\rho_{solid}\frac{\partial T_{solid}}{\partial t} = k_{solid}\nabla^2 T_{solid}. \tag{41}$$

The boundary condition at the interface is:

$$T_{solid} = T_{fluid} \tag{42}$$

$$k_{solid}\frac{\partial T_{solid}}{\partial z} = k_{fluid}\frac{\partial T_{fluid}}{\partial z}. \tag{43}$$

Expand T_{solid} as a static solution plus a deviation:

$$T_{solid} = T'_{solid} + \theta \tag{44}$$

Static solution for solid:

$$T'_{solid} = T_{bottom} + \frac{k_{solid}}{k_{fluid}} z \tag{45}$$

Assume the solid plate is infinite and the disturbances decay at $-\inf$, then

$$C_{solid}\rho_{solid}\frac{\partial \theta}{\partial t} = k_{solid}\nabla^2\theta \tag{46}$$

$$\Theta = \theta^{il_x x + pt} \tag{47}$$

$$p\Theta = \frac{k_{solid}}{C_{solid}\rho_{solid}}\left(\frac{\partial^2}{\partial z^2} - l_x^2\right)\Theta \tag{48}$$

$$\Theta = A_0 exp\left[z\sqrt{l_x^2 + p\frac{C_{solid}\rho_{solid}}{k_{solid}}}\right] \tag{49}$$

Recall the boundary conditions

$$k_{solid}\frac{\partial \theta}{\partial z} = k_{fluid}\frac{\partial \theta_{fluid}}{\partial z} \tag{50}$$

$$\theta = \theta_{fluid} \tag{51}$$

This can solved for the fluid variables and rearranged to give

$$\frac{\frac{\partial \theta_{fluid}}{\partial z}}{\theta_{fluid}} = \frac{k_{solid}}{k_{fluid}}\sqrt{l_x^2 + p/\kappa} \tag{52}$$

$$\frac{\partial \theta_{fluid}}{\partial z} = \frac{k_{solid}}{k_{fluid}} l_x \theta_{fluid} \tag{53}$$

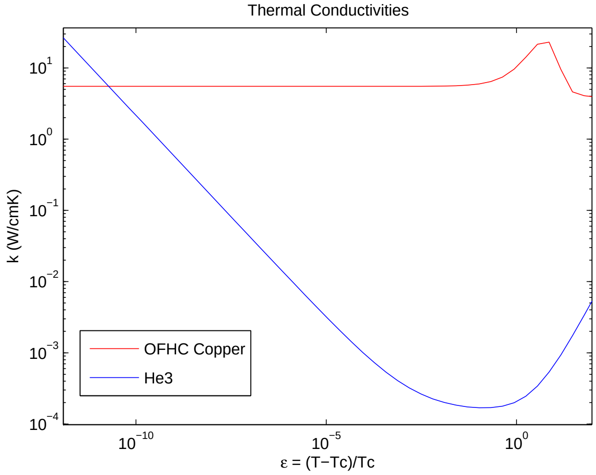

Fig. 3. Conductivity of ^3He close to the critical point

If the thermal conductivity of the solid is much greater than that of the fluid, then using a constant temperature is a reasonable approximation. If the reverse is true, then a constant flux should be imposed.

It was noted earlier that the conductivity of the fluid goes to infinity as the critical point is approached; this initially lead to the conclusion that all past theoretical work was incorrect. This was checked by looking up the conductivity of ^3He in [14], and this is displayed in figure 3

The conductivities of some common materials are

$$k_{Copper} = O(1-100)\frac{W}{cm^\circ K} \tag{54}$$

$$k_{Steel} = O(0.01)\frac{W}{cm^\circ K} \tag{55}$$

$$k_{Kevlar} = O(10^{-6})\frac{W}{cm^\circ K} \tag{56}$$

For experiments done by Kogan [12] copper was used, and for this the fixed temperature boundary (for which the critical Rayleigh number was found) is appropriate. It is assumed that the boundaries satisfy no-shear, whereas Kogan and others have used no-slip.

Boundary Conditions:

$$\frac{\partial T}{\partial z}_{(z=0)} = F_{bottom} \tag{57}$$

$$\frac{\partial T}{\partial z}_{(z=1)} = F_{top} \tag{58}$$

$$v_{z_{(z=0)}} = v_{z_{(z=1)}} = 0 \tag{59}$$

$$\frac{\partial v_x}{\partial z}_{(z=0)} = 0\frac{\partial v_x}{\partial z}_{(z=1)} = 0 \tag{60}$$

6. Dimensionless Equations

Because the Prandlt number goes to infinity, a thermal time scale is used. Let $\tilde{t} = \frac{tk}{C_v \rho_c d^2}$, $\tilde{T} = \frac{T}{T_c}$, $\tilde{x} = \frac{x}{d}$, $\tilde{\rho} = \frac{\rho}{\rho_c}$, $\tilde{a} = \frac{9}{8}$ and $\tilde{b} = 1/3$ where the tilde represents the dimensionless variables. Dropping the tilde we obtain the following dimensionless equations:

Mass Balance:

$$\frac{\partial \rho}{\partial t} + \nabla \cdot (\rho v) = 0 \tag{61}$$

Momentum Balance:

$$\rho(\frac{\partial v}{\partial t} + (v \cdot \nabla) v) + \nabla P = \sigma[\nabla^2 v + \frac{1}{3}\nabla(\nabla \cdot v)] + \sigma \lambda \rho \hat{k} \tag{62}$$

Energy:

$$\begin{aligned} &\lambda m \rho(\frac{\partial T}{\partial t} + v \cdot \nabla T) = \\ &-(P + \lambda m(\gamma - 1) a \rho^2) \nabla \cdot v + \lambda m \nabla \cdot [(1 + \Lambda (T-1)^{-1/2}) \nabla T] + \sigma \Phi \end{aligned} \tag{63}$$

where Φ is given by:

$$\Phi = (\frac{\partial v_i}{\partial x_j} + \frac{\partial v_j}{\partial x_i} - \frac{2}{3}\delta_{ij} \nabla \cdot v)\frac{\partial v_i}{\partial x_j} \tag{64}$$

Equation of state:

$$P = \lambda m (\gamma - 1)(\frac{\rho T}{1 - b\rho} - a\rho^2) \tag{65}$$

Boundary Conditions:

$$max(\rho) = \rho_{max} \tag{66}$$

$$\frac{\partial T}{\partial z}_{(z=0)} = F_{bottom} \tag{67}$$

$$\frac{\partial T}{\partial z}_{(z=1)} = F_{top} \tag{68}$$

$$v_{z_{(z=0)}} = v_{z_{(z=1)}} = 0 \tag{69}$$

$$\frac{\partial v_x}{\partial z}_{(z=0)} = \frac{\partial v_x}{\partial z}_{(z=1)} = 0 \tag{70}$$

where the dimensionless parameters are given by

$$\sigma = \frac{\mu C_v}{k} \tag{71}$$

$$\lambda = \frac{g C_v d^3 \rho_c^2}{\mu k} \tag{72}$$

$$m = \frac{C_v^2 T_c \mu}{kgd} \tag{73}$$

$$\gamma - 1 = \frac{\mathcal{R}}{C_v} \tag{74}$$

Notice that the right hand side of the equation of state could have used a much simpler expression, this one was chosen so that when a perturbation method solution is done such that λ was expanded then the first order deviation of λ would drop out of the first order equations.

7. Onset of Convection

7.1. *Scaling*

Hurle shows that as the thermal conductivity of the fluid over the conductivity of the solid goes to infinity, the wavenumber of the least unstable mode is zero. Because the convection cell is much wider than it is high, let

$$x = \epsilon^{-1/2}\zeta \tag{75}$$

$$t = \epsilon^{-2}\tau \tag{76}$$

where the time scaling is the standard one and I do not know what motivates it.

Because conservation of volume might dominate when convection starts, it is suggestive to scale the x and z velocities as

$$u = \epsilon^{1/2}U \tag{77}$$

$$w = \epsilon W \tag{78}$$

Expand the variables as follows:

$$\rho = \rho_s + \epsilon\rho_1 + \epsilon^2\rho_2 + ... \tag{79}$$

$$T = T_s + \epsilon T_1 + \epsilon^2 T_2 + ... \tag{80}$$

$$P = P_s + \epsilon P_1 + \epsilon^2 P_2 + ... \tag{81}$$

$$U = U_s + \epsilon U_1 + \epsilon^2 U_2 + ... \tag{82}$$

$$W = W_s + \epsilon W_1 + \epsilon^2 W_2 + ... \tag{83}$$

7.2. *Order 1 (Static Solution)*

$$\frac{\partial P_s}{\partial \zeta} = 0 \tag{84}$$

$$\frac{\partial P_s}{\partial z} = \sigma\lambda\rho_s \tag{85}$$

$$0 = \frac{\partial}{\partial z}[(1 + \Lambda(T_s - 1)^{-1/2})\frac{\partial T_s}{\partial z}] \tag{86}$$

$$P_s = \lambda m(\gamma - 1)(\frac{\rho_s T_s}{1 - b\rho_s} - a\rho_s^2) \tag{87}$$

Order one boundary conditions:

$$\frac{\partial T_s}{\partial z}_{(z=0)} = F_{bottom} \tag{88}$$

$$\frac{\partial T_s}{\partial z}_{(z=1)} = F_{top} \tag{89}$$

$$max(\rho_s) = \rho_{max} \tag{90}$$

The temperature profile has an analytic profile

$$T_s = c_1 z + c_2 + 2\Lambda^2 - 2\Lambda(c_1 z + c_2 + \Lambda^2 - 1)^{1/2} \tag{91}$$

The density and pressure profiles are solved numerically

$$\left(\frac{T_s}{1 - b\rho_s} + \frac{bT_s\rho_s}{(1 - b\rho_s)^2} - 2a\rho_s\right)\frac{d\rho_s}{dz} = \left(\frac{\sigma}{(\gamma - 1)m} - \frac{1}{1 - b\rho_s}\frac{dT_s}{dz}\right)\rho_s \tag{92}$$

$$P_s = \frac{\rho_s T_s}{1 - b\rho_s} - a\rho_s^2 \tag{93}$$

The temperature profile is shown in Figure 4 for an artificial case. $\Lambda = 0$ is what is used for ideal gases and far away from the critical point, and $\Lambda = 10$ is a fluid strongly effected by deviations close to the critical point.

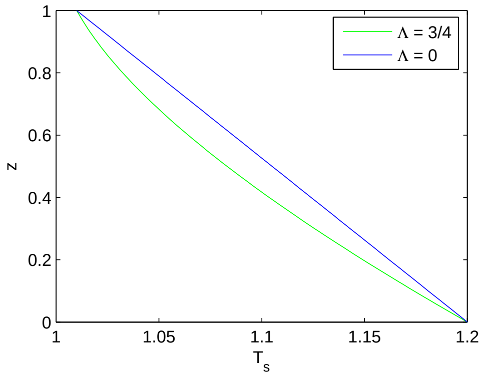

Fig. 4. Static Temperature Profile. The addition of the the Lambda effects cause the temperature profiles to be nonlinear

The pressure and the density profiles are shown in Figure 5 left and right, respectively. The effects of the van der Waals gas can easily seen from the pressure profiles. Increasing the attraction parameter decreases the pressure, whereas increasing the size of the hard spherical particles causes the pressure to increase. These effects cause the differences in the density profiles.

7.3. *Order ϵ*

The governing equations at order ϵ give:

$$0 = \rho_s\frac{\partial U_1}{\partial \zeta} + \rho_s\frac{\partial W_1}{\partial z} + W_1\frac{\partial \rho_s}{\partial z} \tag{94}$$

$$\frac{\partial P_1}{\partial \zeta} = \sigma\frac{\partial^2 U_1}{\partial z^2} \tag{95}$$

$$\frac{\partial P_1}{\partial z} = \sigma\lambda\rho_1 \tag{96}$$

$$0 = \frac{\partial}{\partial z}[(1 + \Lambda(T_s - 1)^{-1/2})\frac{\partial T_1}{\partial z} - \frac{1}{2}\Lambda(T_s - 1)^{-3/2}T_1\frac{\partial T_s}{\partial z}] \tag{97}$$

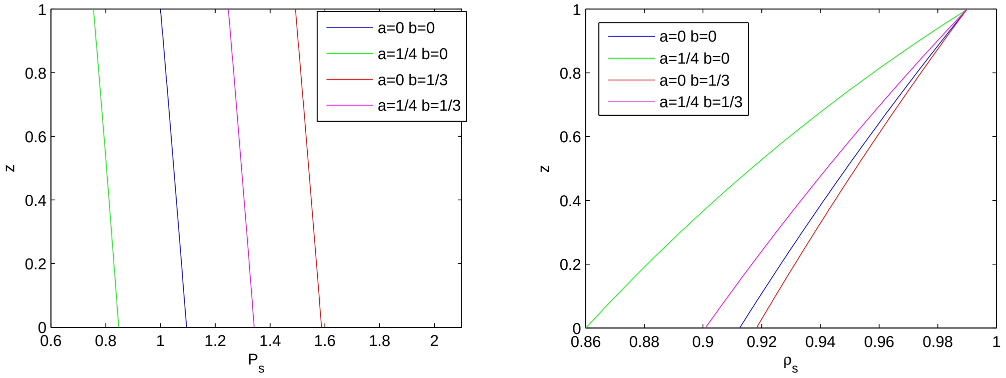

Fig. 5. Left: Static Pressure Profile. The addition of the attractive force a, reduces the pressure, whereas the repulsive forces b cause the pressure to increase. A combination of the two is the linear sum of the two effects. Right: Static Density Profile. The adverse temperature gradient causes the fluid at the bottom to be less dense than the fluid above it. Clearly this is an unstable situation.

$$P_1 = \lambda m(\gamma - 1)\left(\frac{\rho_1 T_s}{(1 - b\rho_s)^2} + \frac{\rho_s T_1}{1 - b\rho_s} - 2a\rho_s\rho_1\right) \tag{98}$$

The order ϵ boundary conditions are:

$$W_1(z = 0) = W_1(z = 1) = 0 \tag{99}$$

$$\left(\frac{\partial U_1}{\partial z}\right)_{(z=0)} = \left(\frac{\partial U_1}{\partial z}\right)_{(z=1)} = 0 \tag{100}$$

$$\left((1 + \Lambda(T_s - 1)^{-1/2})\frac{\partial T_s}{\partial z} - \frac{1}{2}\Lambda(T_s - 1)^{-3/2}T_1\frac{\partial T_1}{\partial z}\right)_{(z=0)} = 0 \tag{101}$$

$$\left((1 + \Lambda(T_s - 1)^{-1/2})\frac{\partial T_s}{\partial z} - \frac{1}{2}\Lambda(T_s - 1)^{-3/2}T_1\frac{\partial T_1}{\partial z}\right)_{(z=1)} = 0 \tag{102}$$

The solution to these equations is given by

$$T_1 = \frac{f(\zeta,\tau)}{1 + \Lambda(T_s - 1)^{-1/2}} = f(\zeta,\tau)g_1 \tag{103}$$

$$\rho_1 = f(\zeta,\tau)g_2 \tag{104}$$

$$P_1 = \lambda m(\gamma - 1)f(\zeta,\tau)g_3 \tag{105}$$

$$U_1 = \frac{\lambda m(\gamma - 1)}{\sigma}\frac{\partial f(\zeta,\tau)}{\partial \zeta}g_4 \tag{106}$$

$$W_1 = \frac{\lambda m(\gamma - 1)}{\sigma}\frac{\partial^2 f(\zeta,\tau)}{\partial \zeta^2}g_5 \tag{107}$$

where g_2 through g_5 are given by

$$\begin{aligned}\left(-\frac{\sigma}{m(\gamma - 1)} + \frac{d}{dz}\left(\frac{T_s}{(1 - b\rho_s)^2} - 2a\rho_s\right)\right)g_2 +& \\ \left(\frac{T_s}{(1 - b\rho_s)^2} - 2a\rho_s\right)\frac{dg_2}{dz} = -\frac{d}{dz}\left(\frac{\rho_s g_1}{1 - b\rho_s}\right)&\end{aligned} \tag{108}$$

$$g_3 = \frac{g_2 T_s}{1-b\rho_s} + \frac{\rho_s g_1}{1-b\rho_s} - 2a\rho_s g_2 \tag{109}$$

$$\frac{d^2 g_4}{dz^2} = g_3 \tag{110}$$

$$\frac{dg_5}{dz} + \frac{1}{\rho_s}\frac{d\rho_s}{dz} g_5 = -g_4 \tag{111}$$

with boundary conditions

$$g_5(z=0) = g_5(z=1) = 0 \tag{112}$$

$$\left(\frac{dg_4}{dz}\right)_{(z=0)} = \left(\frac{dg_4}{dz}\right)_{(z=1)} = 0 \tag{113}$$

where the functions g_2 through g_5 are found numerically. The boundary value problems are solved using the shooting method. Integrating across the z domain, the x-component momentum equation gives the condition that

$$\int_0^1 g_3 dz = 0. \tag{114}$$

This trick makes the problem substantially easier, instead of shooting in two directions at the same time, first an iterative method is used to find $g_2(z=0)$ and once this solution is obtained an independent shooting method is used to obtain the value of $g_4(z=0)=0$ that matches $g_5(z=1)=0$.

For $\frac{T-T_c}{T_c} = 0.01$ and $\rho_{max} = 0.99$ the horizontal and vertical velocities are shown in Figure 6 left and right.

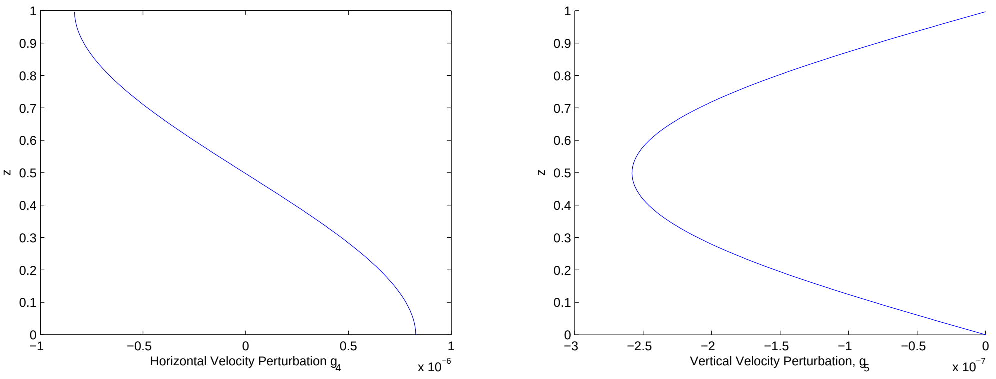

Fig. 6. Left: Horizontal Perturbation Velocity. Right: Vertical Perturbation Velocity.

7.4. *Order ϵ^2*

Only the heat equation is necessary, this is

$$\lambda m \rho_s W_1 \frac{\partial T_s}{\partial z} = -\left(P_s + \lambda m(\gamma-1)a\rho_s^2\right)\left(\frac{\partial U_1}{\partial \zeta} + \frac{\partial W_1}{\partial z}\right) +$$

$$\lambda m\left[1+\Lambda(T_s-1)^{-1/2}\right]\frac{\partial^2 T_1}{\partial \zeta^2}+\frac{\partial q}{\partial z} \tag{115}$$

Inserting the order ϵ solution and integrating from 0 to 1 eliminates the flux in the z-direction. It is seen that $\frac{\partial^2 f}{\partial \zeta^2}$ is in front of all the terms so this cancels.

$$0=\int_0^1\left[\frac{\lambda m(\gamma-1)}{\sigma}g_5\rho_s\frac{\partial T_s}{\partial z}+\frac{(\gamma-1)}{\sigma}\left(P_s+\lambda m(\gamma-1)a\rho_s^2\right)\left(g_4+\frac{\partial g_5}{\partial z}\right)-1\right]dz \tag{116}$$

The expression is then simplified using the order ϵ governing equations.

$$\frac{\lambda m(\gamma-1)}{\sigma}\int_0^1 g_5[\rho_s\frac{\partial T_s}{\partial z}-\frac{(\gamma-1)T_s}{1-b\rho_s}\frac{\partial \rho_s}{\partial z}]dz=1 \tag{117}$$

The equivalent expression

$$\frac{\lambda m(\gamma-1)}{\sigma}\int_0^1 g_5\rho_s[\frac{\partial T_s}{\partial z}-\frac{(\gamma-1)T_s}{1-b\rho_s}\frac{\partial ln(\rho_s)}{\partial z}]dz=1 \tag{118}$$

is sometimes preferred.

For an experimentalist, the difference in top and bottom temperatures was calculated for a given temperature of the bottom plate. For a fixed density of $\rho_{max}=0.99$, with heat conductivity from [14], heat capacity from [3], and viscosity from [16] this is shown in Figure 7

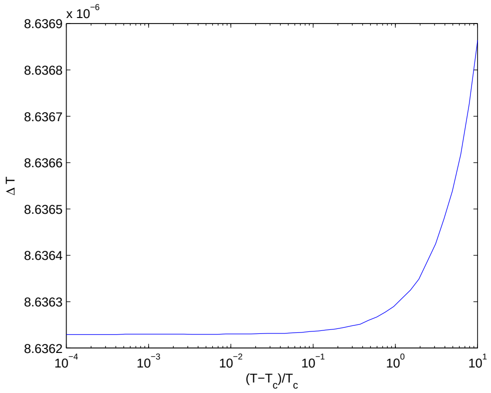

Fig. 7. Difference between top and bottom temperature of apparatus as T_c is approached.

Figure 7 can be compared with Figure 2 in Kogan et. al [12]. Kogan used He3 for constant temperature and no slip walls. The magnitude of the ΔT close to the critical point for the simulation is about $20\mu K$ whereas the experimental value is closer to $4\mu K$. The slope of the plot as curve further away from the critical point is also much shallower than that shown in [12], but this depends highly on the value of viscosity, heat capacity, and conductivity; none of which were divulged in the paper by Kogan.

8. Conclusion

A criterion for the onset of convection for a van der Waals fluid was found. It is an average over the cell of the Rayleigh and Schwarzschild criteria. Numerical solutions have some similarities with experimental data, but are far from quantitative. The boundary conditions used were constant flux, although most experiments done so far have been justified in their use of constant temperature, so this work predicts the onset of convection for a situation with walls made of a low conducting material, such as kevlar. Interesting aspects of this problem that require further work involve finding the evolution equation for this situation, to see if any patterns occur that are previously unknown. It would also be interesting to move away from the critical point and try to model two different phases.

Acknowledgements

I am appreciative of Ed Spiegel, who came up with this research topic and enthusiastically helped me along the way. I am also thankful for the WHOI GFD program for hosting me, as well as George Veronis, who helped me with much of the thermodynamics.

References

[1] Amiroudine, S., Bontoux, P., Larroude, P., Gilly, B., Zappoli,B. 2001 Direct numerical simulation of instabilities in a two-dimensional near-critical fluid layer heated from below. J. Fluid Mech. **442**, 119-140.

[2] Assenheimer, M. and Steinberg, V. 1993 Rayleigh Benard Convection near the Gas-Liquid Critical Point. Phys. Rev. Let. **70**, 3888-3891.

[3] Brown, G. R., and Meyer, H. 1972 Study of the Specific-Heat Singularity of He^3 near Its Critical Point. Phys. Rev. A. **6**, 364-377.

[4] Callen, H. B. 1985 Thermodynamics and an introduction to Thermostatistics, 2nd Ed. Wiley and Sons.

[5] Carles, P. 2000 The onset of free convection near the liquid-vapour critical point Part 2: Unsteady heating. Physica D. **147**, 36-58.

[6] Carles, P. and Ugurtas, B. 1999 The onset of free convection near the liquid-vapour critical point Part 1: Stationsary initial state. Physica D. **126**, 69-82.

[7] Chapman, C. J. and Proctor, M. R. E. 1980 Nonlinear Rayleigh-Benard convection between poorly conducting boundaries. J. Fluid Mech **101**, 759-782.

[8] Depassier, M. C. and Spiegel, E. A. 1981 The Large-scale structure of compressible convection. Astro. J. **86**, 496-512.

[9] 4 El Khouri, L. and Carles, P. 2002 Scenarios for the onset of convection close to the critical point. Phys. Rev. E. **66**, 066309 1-4.

[10] Gitterman, M. 1978 Hydrodynamics of fluids near a critical point. Rev. of Mod. Phys. **50**, 85-106.

[11] Hurle, D. T. J., Jakeman, E., and Pike, E. R. 1967 On the solution of the Benard problem with boundaries of finite conductivity. Proc. Roy. Soc. A **296**, 469-475.

[12] Kogan, A. B., Murphy, D., and Meyer, H. 1999 Rayleigh-Benard Convection Onset in a Compressible Fluid: ^3He near T_c. Phys. Rev. Let. **82**, 4635-4638.

[13] Onuki, A., Hao, H., and Ferrell, R. A. 1990 Fast adiabatic equilibration in a single-component fluid near the liquid-vapor critical point. Phys. Rev. A. **41**, 2256-2258.

[14] Pittman, C. E., Cohen, L. H., and Meyer, H. 1982 Transport Properties of Helium Near the Liquid-Vapor Critical Point. J. low Temp. Phys. **46**, 115-135.

[15] Polezhaev, V. I. and Soboleva, E. B. 2004 Rayleigh-Benard Convection in a Near-Critical Fluid in the Neighborhood of the Stability Threshold. Fluid Dynamivs. **40**, 209-220.

[16] Taylor, R. D. and Dash, J. G. 1957 Hydrodynamics of Oscillating Disks in Viscous Fluids: Viscosities of Liquids He^3 and He^4. Phys. Rev. **106**, 398-403.

Instability theory of swirling flows with suction

Basile GALLET, supervised by C.Doering and E.Spiegel

May 21, 2008

1 Introduction

Accretion disks radiate a tremendous amount of energy. In these systems the only source of energy is gravitational energy. Turbulence in the disk converts this gravitational energy into heat and finally radiation. During this process the angular momentum of the fluid is carried out by turbulent transport, which allows accretion of the fluid onto the central object. Without turbulence the angular momentum would not be carried out efficientely enough and the accretion rate would be extremely low. The velocity profile of an accretion disk is considered to be mostly Keplerian, and the accretion rate is quite low, which means that the motion of the fluid inside the disk is almost circular. However, circular Keplerian flows are known to be linearly stable and one may wonder how turbulence is generated in such a system.

If the magnetic field inside the disk is high enough, it has been shown that the magnetorotational instability (MRI) can destabilize the flow and produce turbulence [3]. This provides at least one mechanism to drive turbulence in accretion disks. However, it has been shown that the MRI may be suppressed if the magnetic Prandtl number (ratio of the viscosity over the magnetic viscosity) is not high enough. In cold proptoplanetary nebulas for instance, the ionization is too low and one has to find another way to destabilize the flow than the MRI.

This is one of our main motivations to study the combined effects of both rotation and accretion on a very simple flow : the Taylor-Couette flow with inward suction. Although the astrophysical relevance of such a flow as a model of an accretion disk is quite limited, it can be used to show that taking into account both accretion and rotation leads to very different stability propreties of the flow than considering only rotation (circular flows) or only accretion (accretion onto a central object with a spherical symmetry). Both the energy stability and the linear stability of the flow are discussed in this report.

In section 2 we describe the Taylor-Couette flow with suction. The energy stability technique is described in section 3. Some rigorous bounds on the energy stability limit of the flow are derived in section 4, and the actual energy stability limit is computed numerically in section 5. Finding bounds on the energy dissipation of this flow appears to be very challenging. This is discussed in section 6. Finally the linear stability of the problem is studied in section 7.

2 Formulation of the problem

2.1 Geometry of the problem and boundary conditions

We study the incompressible motion of a Newtonian fluid between two concentric porous cylinders. In the configuration we focus on, the inner cylinder is maintained in a static position while the outer cylinder is rotating with constant angular velocity Ω. Let us write R_1 and R_2 the radii of the inner and outer cylinders and use cylindrical coordinates (r, θ, z). We assume no slip boundary conditions : the azimuthal and vertical components of the velocity field vanish at the two cylinders.

To this classical Taylor-Couette flow is added a radial inward suction : the fluid is injected through the outer cylinder with a flux Φ (volume of fluid injected per unit time and per unit height of cylinder) and sucked at the inner cylinder. Incompressibility imposes the conservation of the radial flux of fluid so that the fluid is removed at $R1$ with the same flux Φ. We consider the simplest problem in which the fluid is uniformly injected at $R2$ and removed at $R1$, which means that Φ is independant of both time and θ. If the velocity field is designated as $\overrightarrow{u} = u\overrightarrow{e_r} + v\overrightarrow{e_\theta} + w\overrightarrow{e_z}$, the boundary conditions are :

$$\overrightarrow{u}(R_1, \theta, z) = -\frac{\Phi}{2\pi R_1}\overrightarrow{e_r} \qquad (1)$$

$$\overrightarrow{u}(R_2, \theta, z) = -\frac{\Phi}{2\pi R_2}\overrightarrow{e_r} + R_2\Omega\overrightarrow{e_\theta} \qquad (2)$$

The incompressibility constraint $\overrightarrow{\nabla}.\overrightarrow{u} = 0$ adds two other boundary conditions :

$$u_r(R_1) = 0 \text{ and } u_r(R_2) = 0 \qquad (3)$$

where the subscript r designate a derivative with respect to r. We assume periodic boundary conditions in the z direction with a period L_z.

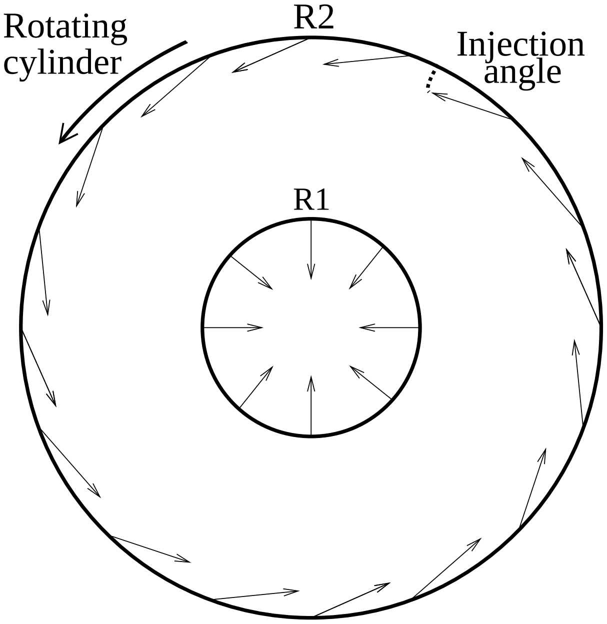

Figure 1: Schematic of the boundary conditions. The outer cylinder is rotating with an angular velocity Ω and the fluid is injected at the outer boundary with an entry angle Θ

2.2 Dimensionless numbers

The problem we are studying involves the 5 parameters : the two radii R_1 and R_2, the angular velocity of the outer cylinder Ω, the flux of injection Φ, and the viscosity of the fluid ν. These parameters can be expressed with one unit of time and one unit of length. We thus have in this problem $5 - 2 = 3$ dimensionless numbers in terms of which the physical results can be expressed :

- The geometrical factor $\eta = \frac{R_1}{R_2}$. When η goes to one we reach the narrow gap limit where $(R_2 - R_1) << R_1$. We expect to find results similar to the slab geometry (plane Couette flow with suction) in this limit. On the other hand, when η goes to zero, the outer radius R_2 goes to infinity if the inner radius remains constant. In this limit we expect to see some strong effects of the rotation on the stability of the flow, such as centrifugal effects.

- The injection angle at the outer cylinder, which we designate as Θ. This angle is linked to the radial and azimuthal components of the velocity field at the outer boundary :

  $$tan(\Theta) = \frac{|U(R_2)|}{V(R_2)} = \frac{\Phi}{2\pi R_2^2\Omega}$$

  If $tan(\Theta) = 0$ there is no suction and we recover the classical Taylor-Couette problem. When $tan(\Theta)$ goes to infinity we reach the limit in which there is mostly suction and almost no azimuthal velocity.

- The azimuthal Reynolds number :

  $$Re = \frac{R_2\Omega(R_2 - R_1)}{\nu}$$

  We choose this definition of the Reynolds number so that it matches the definition of the Reynolds number for the plane Couette flow when η goes to one.

Although only 3 dimensionless numbers are required to describe the physics of the system, it is useful to introduce also the radial Reynolds number $\alpha = \frac{\Phi}{2\pi\nu}$ to make the equations more compact. This number is linked to Re, η and $\tan(\Theta)$ by the relation :

$$\alpha = \frac{Re\tan(\Theta)}{1-\eta} \tag{4}$$

2.3 Laminar solution

The steady laminar solution of the problem $\overrightarrow{V_l} = (U(r), V(r), 0)$ is derived from the Navier-Stokes equations, together with the incompressibility condition $\overrightarrow{\nabla}.\overrightarrow{V_l} = 0$. The latter yields :

$$\begin{aligned} \frac{1}{r}(rU)_r &= 0 \\ U(r) = -\frac{\Phi}{2\pi r} \end{aligned}$$

The azimuthal component of the Navier-Stokes equation is then :

$$\nu V_{rr} + \frac{V_r}{r}(\nu + \Psi) + \frac{V}{r^2}(\Psi - \nu) = 0$$

with $\Psi = \frac{\Phi}{2\pi}$. One can look for solutions of this equation in the form $V(r) = Ar^p$. We find 2 acceptable values for p :

$$p = -1 \text{ or } p = 1 - \alpha$$

The solution for V which matches the boundary conditions is then :

$$V = Ar^{1-\alpha} + \tfrac{B}{r} \text{ with } \begin{cases} A = \frac{-R_2^2\Omega}{R_1^{2-\alpha} - R_2^{2-\alpha}} \\ B = \frac{R_1^{2-\alpha}R_2^2}{R_1^{2-\alpha} - R_2^{2-\alpha}}\Omega \end{cases}$$

This azimuthal velocity profile is represented in figure 2 for different values of α and η.

When α goes to zero we recover the classical velocity field of the Taylor-Couette flow (with a steady inner cylinder), which is independant of the viscosity ν. The azimuthal velocity monotonously increases when r goes from R_1 to R_2.

However, for nonzero values of the entry angle $\tan(\Theta)$ and large values of the Reynolds number ($Re\tan(\Theta) >> 1$), going outward from the inner cylinder the azimuthal velocity rapidly increases in a boundary layer of thickness δ near the inner cylinder and then decreases from $R_1 + \delta$ to R_2. The azimuthal velocity profile has a maximum for $r = R_1 + \delta$:

$$V_r(R_1 + \delta) = 0 \Leftrightarrow R_1 + \delta = \left(\frac{B}{A(1-\alpha)}\right)^{\frac{1}{2-\alpha}} = \frac{R_1}{(1-\alpha)^{\frac{1}{2-\alpha}}}$$

For large values of α, the boundary layer is very thin and :

$$\frac{\delta}{R_1} = (\alpha - 1)^{\frac{1}{\alpha-2}} - 1 \simeq \frac{ln(\alpha)}{\alpha}$$

The physical origin of this non monotonous velocity profile is easy to understand : at high Reynolds number, the motion of the fluid is nearly inviscid. A fluid element injected at the outer boundary with the azimuthal velocity $R_2\Omega$ will spiral towards the center. It has to conserve its azimuthal angular momentum $rV(r)$ during this quasi-inviscid motion :

$$rV(r) = constant \Rightarrow V(r) = \frac{R_2^2\Omega}{r}$$

The azimuthal velocity of the fluid element increases during this inward movement, but it has to vanish at the inner boundary. The role of the viscous boundary layer is to dissipate the angular momentum of the incoming fluid so that the azimuthal velocity goes from $V_{max} \simeq \frac{R_2^2\Omega}{R_1} = \frac{R_2\Omega}{\eta}$ to zero at the inner cylinder. The fact that the azimuthal velocity profile has a high maximum is strongly linked to the cylindrical geometry of the problem, and this effect disappears in the plane limit $\eta \to 1$ since $\frac{V_{max}}{R_2\Omega} = \frac{1}{\eta}$.

One should notice that the asymptotic velocity profile at $Re \to \infty$ is dramatically modified from $\tan(\Theta) = 0$ to $\tan(\Theta) \neq 0$: if $\tan(\Theta) = 0$ the azimuthal velocity profile is the classical Taylor-Couette profile which is independant of the Reynolds number. However, if $\tan(\Theta) \neq 0$ the azimuthal velocity profile goes like $\frac{1}{r}$ everywhere inside the gap and the boundary layer becomes infinetely thin in the limit $Re \to \infty$. This shows that even if the accretion rate is very low, one cannot neglect it and study the problem with rotation only. Mathematically this is due to the fact that the limits $Re \to \infty$ and $\tan(\Theta) \to 0$ do not commute.

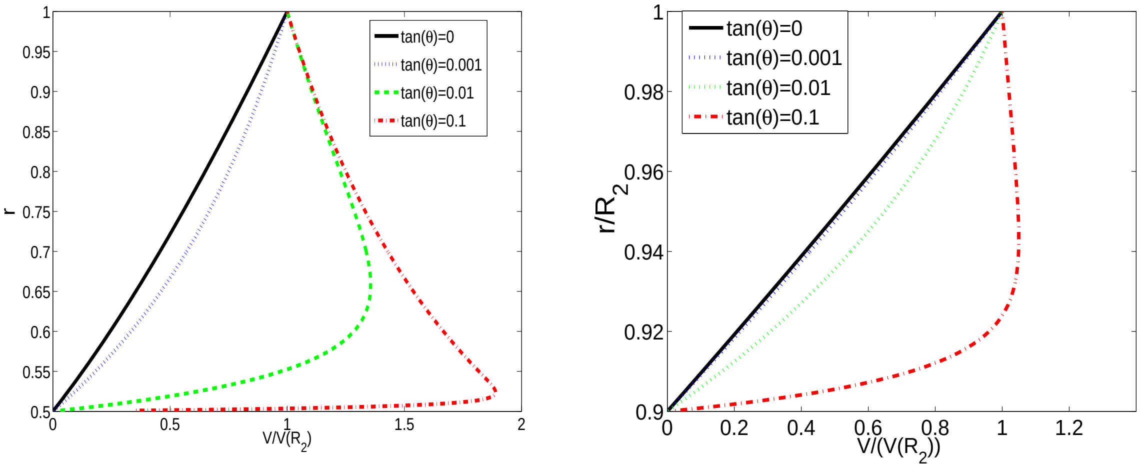

Figure 2: Azimuthal velocity profiles for different values of the entry angle. (Left : $\eta = 0.5$, right : $\eta = 0.9$)

3 Energy stability of the laminar solution

We study in this section the energy stability of the flow, a very strong form of stability in a sense which will be described precisely in paragraph 3.2. The energy stability technique provides sufficient conditions for a flow to be stable, but one should keep in mind that if a flow is not energy stable it can still be stable.

3.1 Decomposition of the velocity field

The starting point of this technique is to decompose the velocity field $\overrightarrow{u}$ into a steady background flow $\overrightarrow{V}$ and a time dependant field $\overrightarrow{v}$. We require both the background flow and the fluctuating field to be divergence free :

$$\overrightarrow{u}(\overrightarrow{r},t) = \overrightarrow{V}(\overrightarrow{r}) + \overrightarrow{v}(\overrightarrow{r},t) \text{ with } \left\{ \begin{array}{l} \overrightarrow{\nabla}.\overrightarrow{V} = 0 \\ \overrightarrow{\nabla}.\overrightarrow{v} = 0 \end{array} \right.$$

Moreover, the background flow has to verify the boundary conditions on $\overrightarrow{u}$ as they were specified in equations 1 and 2 , whereas the fluctuation field verifies the homogeneous boundary conditions $\overrightarrow{v} = \overrightarrow{0}$ at the two cylinders. Finally, both $\overrightarrow{V}$ and $\overrightarrow{v}$ are periodic in z with the same period L_z. We can introduce the decomposition of $\overrightarrow{u}$ into the Navier-Stokes equation to find :

$$\overrightarrow{v}_t + (\overrightarrow{v}.\overrightarrow{\nabla})\overrightarrow{v} + (\overrightarrow{V}.\overrightarrow{\nabla})\overrightarrow{v} + (\overrightarrow{v}.\overrightarrow{\nabla})\overrightarrow{V} + (\overrightarrow{V}.\overrightarrow{\nabla})\overrightarrow{V} + \overrightarrow{\nabla}(p) \quad = \quad \nu\Delta\overrightarrow{v} + \nu\Delta\overrightarrow{V} \tag{5}$$

To study the kinetic energy of the fluctuation field we need to take the dot product of this equation with $\overrightarrow{v}$ and integrate over one cell, i.e. over the domain $\tau = [R_1, R_2] \times [0, 2\pi] \times [0, L_z]$. Let us write $d\tau$ the volume element in this domain and define the standard N_2 norm as :

$$||\overrightarrow{f}||^2 = \int_\tau |\overrightarrow{f}|^2 d\tau$$

Then we perform a few integration by parts using the homogeneous boundary condition on $\overrightarrow{v}$ to find :

$$d_t\left(\frac{||\overrightarrow{v}||^2}{2}\right) + \int_\tau \overrightarrow{v}.[(\overrightarrow{V}.\overrightarrow{\nabla})\overrightarrow{V} - \nu\Delta\overrightarrow{V}]d\tau \quad = \quad -\int_\tau \nu|\overrightarrow{\nabla}\overrightarrow{v}|^2 + \overrightarrow{v}.(\overrightarrow{\nabla}\overrightarrow{V}).\overrightarrow{v}\,d\tau \tag{6}$$

3.2 Absolute stability

To study the energy stability of the laminar solution we let the background flow be this laminar solution $\overrightarrow{V_l}$. This makes the integral on the left hand side of equation 6 to vanish and leads to :

$$\left\{ \begin{array}{l} d_t\left(\frac{||\overrightarrow{v}||^2}{2}\right) = -\mathcal{H}\{\overrightarrow{v}\} \\ \text{with } \mathcal{H}\{\overrightarrow{v}\} = \int_\tau \nu|\overrightarrow{\nabla}\overrightarrow{v}|^2 + \overrightarrow{v}.(\overrightarrow{\nabla}\overrightarrow{V_l}).\overrightarrow{v}\,d\tau \end{array} \right.$$

$\mathcal{H}\{\overrightarrow{v}\}$ is a quadratic form in $\overrightarrow{v}$. If this quadratic form is strictly positive the kinetic energy of the perturbation $\overrightarrow{v}$ is a decreasing function of time. Moreover, we can prove thanks to Gronwall's inequality that it will decay at least like an exponential. We should emphasize the fact that we have not made any assumption on the size of the perturbation (as in linear theory for instance where the perturbation has to be infinitesimal), which means that any divergence-free perturbation of arbitrary amplitude which matches the homogeneous boundary conditions will be damped out : a flow for which $\mathcal{H}$ is a positive quadratic form has a very strong form of stability which is called energy stability or absolute stability.

Let us define the function $\mu(Re, \tan(\Theta))$ as :

$$\mu(Re, \tan(\Theta)) = \inf \frac{\mathcal{H}\{\overrightarrow{v}\}}{||\overrightarrow{v}||^2} \tag{7}$$

the infimum being taken over every divergence-free vector field satisfying the homogeneous boundary conditions. The absolute stability is achieved in the region of the $(Re, \tan(\Theta))$ plane where $\mu(Re, \tan(\Theta)) > 0$. The line $\mu(Re, \tan(\Theta)) = 0$ is the limit in this plane under which the flow is absolutely stable.

3.3 Euler-Lagrange equations

To the variational problem which defines μ corresponds a set of Euler-Lagrange equations. The quadratic form can be written $\mathcal{H}\{\overrightarrow{v}\} = \overrightarrow{v}.L\overrightarrow{v}$, L being a linear symmetric operator. This operator is thus diagonalizable in an orthonormal basis and has real eigenvalues. One can prove that the infimum in equation 7 is reached when $\overrightarrow{v}$ is an eigenvector of L for its lowest eigenvalue λ. The Euler-Lagrange equations for this problem are then the equations of the eigenvalue problem for the linear operator L. The divergence free constraint is introduced in $\mathcal{H}$ with a Lagrange multiplier as $p\overrightarrow{\nabla}.\overrightarrow{v}$ which turns into a pressure term in L after an integration by parts. The Euler-Lagrange equations are then :

$$\lambda\overrightarrow{v} = -\nu\Delta\overrightarrow{v} + \frac{1}{2}[(\overrightarrow{\nabla}\overrightarrow{V_l}).\overrightarrow{v} + \overrightarrow{v}.(\overrightarrow{\nabla}\overrightarrow{V_l})] + \overrightarrow{\nabla}(p) \tag{8}$$

together with the incompressibility constraint $\overrightarrow{\nabla}.\overrightarrow{v} = 0$.

Since this problem is linear and periodic in both θ and z one can decompose $\overrightarrow{v}$ into Fourier modes in these directions and look for the stability of each one of these modes independently. Let us write one of these modes:

$$\overrightarrow{v} = (u(r), v(r), w(r))_{\{r,\theta,z\}} e^{im\theta} e^{ikz}$$

Inserting this development in the Euler-Lagrange equations and developing $\overrightarrow{V_l}$ yields :

$$\begin{aligned}
(-\lambda + A(r) + \frac{\psi}{r^2})u + Z(r)v + p_r - \nu\frac{1}{r}(ru_r)_r &= 0 &(9)\\
Z^*(r)u + (-\lambda + A(r) - \frac{\psi}{r^2})v + \frac{im}{r}p - \nu\frac{1}{r}(rv_r)_r &= 0 &(10)\\
(-\lambda + A(r) - \frac{\nu}{r^2})w + ikp - \nu\frac{1}{r}(rw_r)_r &= 0 &(11)
\end{aligned}$$

where the two functions A and Z are :

$$\begin{aligned}
A(r) &= \nu\left(k^2 + \frac{m^2+1}{r^2}\right)\\
Z(r) &= \frac{1}{2}(r\Gamma_r) + 2im\frac{\nu}{r^2}
\end{aligned}$$

Z^* is the complex conjugate of Z, and we introduced the angular velocity of the laminar solution $\Gamma(r) = \frac{V(r)}{r}$. The last equation of the system is the incompressibility constraint :

$$\frac{1}{r}(ru)_r + im\frac{v}{r} + ikw = 0 \tag{12}$$

To determine wether the flow is energy stable or not, one should solve this system of equations together with the homogeneous boundary conditions on $\overrightarrow{v}$ to find the lowest eigenvalue λ. The flow is energy stable if $\lambda > 0$.

4 Bounds on the energy stability limit

Our strategy in this section is not to solve the variational problem explicitly, but to find some bounds on the location of the line $\mu(Re, \tan(\Theta)) = 0$ in the $(Re, \tan(\Theta))$ plane. Two different techniques are used :

- In paragraphs 4.1 and 4.2 we specify a mode for $\overrightarrow{v}$ and we study the energy stability limit of this particular mode. If any mode of perturbation can grow, then the flow is not energy stable. This means that the energy stability limit of one particular mode of perturbation is an upper bound on the energy stability limit of the flow for an arbitrary perturbation.

- In paragraph 4.3 we derive a lower bound on the quadratic form $\mathcal{H}$. As long as this lower bound remains positive, $\mathcal{H}$ is positive and the flow is energy stable. This gives a lower bound on the energy stability limit, and thus a rigorous sufficient condition for the flow to be absolutely stable.

4.1 Stability of the mode $m = 0$, $k = 0$

Let us study perturbations which are axisymmetric and translation invariant in the z direction. Such perturbations correspond to the mode $m = 0$ and $k = 0$. For this mode the mass conservation equation is simply :

$$(ru)_r = 0 \Rightarrow u = u(R_2)\frac{R_2}{r}$$

but since $\overrightarrow{v}$ satisfies the homogeneous boundary conditions, $u(R_2) = 0$ and $u = 0$. To find the marginal energy stability limit we impose $\lambda = 0$ in the Euler-Lagrange equations (remember that since $\mathcal{L}$ is a symmetric operator, its eigenvalues are real). The azimuthal component of these equations simplifies to :

$$\nu v_{rr} + \nu\frac{v_r}{r} + (\psi - \nu)\frac{v}{r^2} = 0 \tag{13}$$

We can look for power law solutions of this equation in the form $v(r) = Ar^p$. This leads to a second order equation in p :

$$p^2 = 1 - \alpha$$

We are interested in the case $\alpha > 1$ which corresponds to the most unstable situation. We obtain two values of p and the corresponding solution v:

$$\begin{aligned} p &= \pm i\sqrt{\alpha - 1} \\ v(r) &= A\cos(\sqrt{\alpha - 1}\ln(\frac{r}{R_2})) + B\sin(\sqrt{\alpha - 1}\ln(\frac{r}{R_2})) \end{aligned}$$

The first boundary condition $v(R_2) = 0$ imposes $A = 0$ while the second one imposes :

$$v(R_1) = 0 = B\sin(\sqrt{\alpha - 1}\ln(\eta)) \Rightarrow B = 0 \text{ or } \sqrt{\alpha - 1}\ln(\eta) = q\pi, q \in \mathbb{Z}^*$$

The first mode to become non energy stable as α increases is the mode $q = 1$, and the corresponding critical value of α is :

$$\alpha_c = 1 + \frac{\pi^2}{(\ln(\eta))^2}$$

We come back to the $(Re, \tan(\Theta))$ plane using equation 4 to find our first upper bound on the energy dissipation limit :

$$Re_1(\tan(\Theta)) = \left(1 + \frac{\pi^2}{(\ln(\eta))^2}\right)\frac{1 - \eta}{\tan(\Theta)} \tag{14}$$

The line $Re_1(\tan(\Theta))$ has been drawn on figure 4 for several values of the geometrical factor η. This upper bound shows that whatever the injection angle is, energy stability is lost when the Reynolds number becomes high enough.

We can explain why the mode $(m = 0, k = 0)$ will grow for large values of α : a small perturbation $v_0 = v(t = 0)$ in the azimuthal velocity field at an initial radius $R_0 = R(t = 0)$ will be advected towards the center by the suction. If α is large enough, the flow is nearly inviscid and the fluid conserves its angular momentum during the inward motion. Hence the velocity perturbation becomes :

$$v(R(t), t) = v_0\frac{R_0}{R(t)}, \text{ with } R(t) \leq R_0$$

which means that the kinetic energy of this perturbation increases : the mode is not energy stable. However, when the perturbation is advected all the way to the boundary layer near R_1, the viscous effects dissipate the angular momentum of the perturbation and the perturbation is swept away by the suction. For this reason we expect to see transient growth for this mode more than an actual instability.

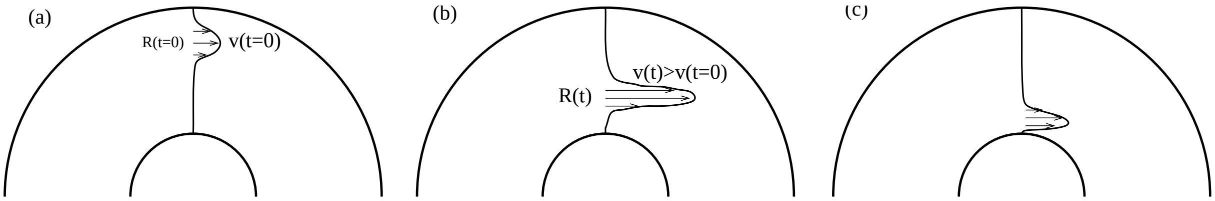

Figure 3: Expected behaviour of an energy unstable mode for $(m=0, k=0)$: a perturbation at $t=0$ (a) is advected by the suction and speeds up (b). When it reaches the boundary layer the fluid loses its angular momentum and the perturbation is swept away (c).

4.2 Stability of a given velocity profile

Another method to get an upper bound on the energy stability limit is to specify completely the structure of a mode (i.e. specify m, k, $u(r)$, $v(r)$) and look for its energy stability limit. The quadratic form can be developed in cylindrical coordinates as :

$$\mathcal{H}\{\overrightarrow{v}\} = \int_\tau \left[\nu|\overrightarrow{\nabla}\overrightarrow{v}|^2 + (r\Gamma_r)uv - \frac{\psi}{r^2}(v^2-u^2)\right] d\tau \tag{15}$$

The first term in this integral is the damping due to viscous dissipation. The second term is the only one which depends on the azimuthal velocity profile of the laminar solution. The last term is proportional to ψ and is responsible for the upper bound we found in the last paragraph (the azimuthal velocity profile of the laminar solution did not play any role in the derivation of this bound since there is no dependance in V in equation 13). In this paragraph we would like to study specifically the effect of the azimuthal velocity profile of the laminar solution on the energy stability of the flow. We thus choose :

$$u(r) = -v(r)$$

which causes the last term of $\mathcal{H}$ to vanish. As we are going to evaluate some quadratic quantities we do not want to use complex notations. Let us write :

$$\overrightarrow{v} = \left| \begin{array}{ll} -v & \cos(m\theta)\cos(kz) \\ v & \cos(m\theta)\cos(kz) \\ w & \cos(m\theta+\phi_\theta)\cos(kz+\phi_z) \end{array} \right.$$

This decomposition leads to :

$$\frac{1}{2\pi L_z}\int_{\theta=0}^{\theta=2\pi}\int_{z=0}^{z=L_z} |\overrightarrow{\nabla}\overrightarrow{v}|^2 d\theta dz = \frac{(v_r)^2}{2} + \frac{(w_r)^2}{4} + \left(k^2+\frac{(m+1)^2}{r^2}\right)\frac{v^2}{2} + \left(k^2+\frac{m^2}{2r^2}\right)\frac{w^2}{2} \tag{16}$$

and w can be computed in terms of v using the incompressibility constraint $\overrightarrow{\nabla}.\overrightarrow{v}=0$:

$$-\frac{1}{r}(rv)_r\cos(m\theta)\cos(kz) - \frac{m}{r}v\sin(m\theta)\cos(kz) - kw\cos(m\theta+\phi_\theta)\sin(kz+\phi_z) = 0$$

Hence $\phi_z = \frac{\pi}{2}$, and :

$$w^2 = \frac{1}{k^2r^2}(r^2v_r^2 + 2rvv_r + (m^2+1)v)$$

Moreover we can notice that $(w_r)^2 = \frac{((w^2)_r)^2}{4w^2}$, with :

$$(w^2)_r = \frac{2}{k^2r^2}\left[-(m^2+1)\frac{v^2}{r} + r(v_r)^2 + m^2vv_r + rvv_{rr} + r^2v_rv_{rr}\right]$$

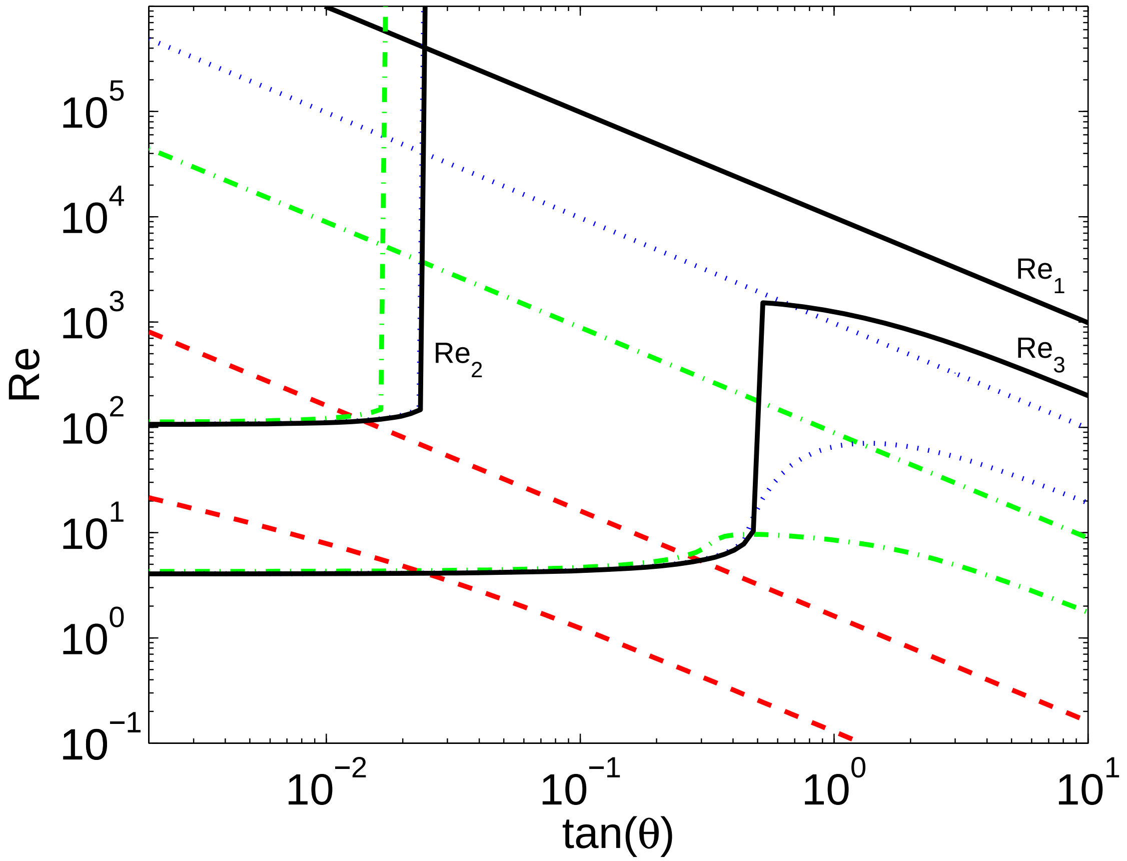

Figure 4: The three bounds on the energy stability limit. Re_1 is a straight line which decreases like $\tan(\Theta)^{-1}$. The bound Re_2 is out of the picture for $\eta = 0.02$, and makes the right angle shape in the upper left corner for η close to 1. The lower bound Re_3 is the lowest curve for every value of η. (dashed line : $\eta = 0.02$, dash-dotted line : $\eta = 0.9$, dotted line : $\eta = 0.99$, solid line : $\eta = 0.999$)

The energy stability limit of this mode is reached when $\mathcal{H}\{\overrightarrow{v}\} = 0$. Using equation 16, this energy stability limit becomes :

$$\int_{r=R_1}^{r=R_2} \left[(v_r)^2 + \frac{(w_r)^2}{2} + (1+m)^2 \frac{v^2}{r^2} + \frac{m^2}{2}\frac{w^2}{r^2} + k^2 v^2 + k^2 \frac{w^2}{2} - \frac{Re}{1-\eta}\frac{r\Gamma_r}{2R_2^2\Omega} v^2 \right] r dr = 0$$

where every term can be expressed in terms of v, v_r and v_{rr}. We chose $v(r)$ to be the simplest velocity profile that satisfies the boundary conditions on both u and v (since $u = -v$) :

$$v(r) = A(r-R_1)^2(r-R_2)^2$$

All the integrals in equation 17 can be computed and we are left with an implicit equation in Re, $\tan(\Theta)$ and η which can be solved numerically. The best upper bound that we find with this method is for ($k = \frac{\pi}{R_2 - R_1}, m = 0$). This mode corresponds to the well-known Taylor vortices. It is interesting to see that although the flow without suction is a stable configuration of the Taylor-Couette flow, a little bit of suction allows Taylor vortices to grow (they will at least have a transcient growth). The corresponding upper bound on the energy stability limit is called $Re_2(\tan(\Theta))$ and has been drawn for several values of η on figure 4. This bound goes to infinity for a finite value of the injection angle Θ. Around this value of Θ the quantity Γ_r becomes negative in a large region of the gap, so that all the terms in equation 17 are positive and the equation does not admit a solution anymore.

4.3 Lower bound on the energy stability limit

Let us define :

$$\mathcal{F}\{\overrightarrow{v}\} = \int_\tau (r\Gamma_r)uv - \frac{\psi}{r^2}(v^2 - u^2)d\tau$$

To find a lower bound on $\mathcal{H}$ one has to consider the fact that $\overrightarrow{v}$ cannot be arbitrarily large and match the homogeneous boundary conditions without having large gradients too. We will thus try to find a lower bound on $\mathcal{F}$ (which can be negative!) in terms of $||\overrightarrow{\nabla}\overrightarrow{v}||^2$. First of all we can get rid of the positive term $\frac{\psi}{r^2}u^2$ in $\mathcal{F}$. Using the inequality $|uv| \leq \frac{1}{2}[\frac{1}{c}u^2 + cv^2]$ which is valid for any $c > 0$, we get:

$$\mathcal{F}\{\overrightarrow{v}\} \geq -\int_\tau \frac{|r\Gamma_r|}{2}\left(\frac{1}{c(r)}u^2 + c(r)v^2\right) + \frac{\psi}{r^2}v^2 d\tau = -\int_\tau u^2\left(\frac{|r\Gamma_r|}{2c}\right) + v^2\left(\frac{\psi}{r^2} + c\frac{|r\Gamma_r|}{2}\right)d\tau$$

$c(r)$ is chosen in such a way that the coefficients of u^2 and v^2 are equal :

$$\frac{|r\Gamma_r|}{2c} = \frac{\psi}{r^2} + c\frac{|r\Gamma_r|}{2} \Rightarrow c^2 + \frac{2\psi}{r^3|\Gamma_r|}c - 1 = 0$$

$$\Rightarrow \begin{cases} c(r) = \frac{\zeta}{2}\left(\sqrt{1+\frac{4}{\zeta^2}} - 1\right) \\ \text{with } \zeta = \frac{2\psi}{r^3|\Gamma_r|} \end{cases}$$

This choice of c leads to :

$$\mathcal{F}\{\overrightarrow{v}\} \geq -\int_\tau \frac{|r\Gamma_r|}{2c}(u^2+v^2)d\tau = -\int_\tau \frac{\psi}{2r^2}\left(\sqrt{1+\frac{4}{\zeta^2}} + 1\right)(u^2+v^2)d\tau \tag{17}$$

We now use the fundamental theorem of calculus and the Schwartz inequality to get :

$$|v(r)| = \left|\int_{R_1}^r \frac{1}{\sqrt{\tilde{r}}}\sqrt{\tilde{r}}v_r(\tilde{r})d\tilde{r}\right| \leq \sqrt{\int_{R_1}^r \frac{1}{\tilde{r}}d\tilde{r}}\sqrt{\int_{R_1}^r |v_r(\tilde{r})|^2\tilde{r}d\tilde{r}}$$

The same technique can be applied to u and yields :

$$\begin{cases} |u| \leq \sqrt{\ln\left(\frac{r}{R_1}\right)}\sqrt{\int_{R_1}^r |u_r(\tilde{r})|^2\tilde{r}d\tilde{r}} \\ |v| \leq \sqrt{\ln\left(\frac{r}{R_1}\right)}\sqrt{\int_{R_1}^r |v_r(\tilde{r})|^2\tilde{r}d\tilde{r}} \end{cases}$$

Finally :

$$u^2 + v^2 \leq \ln\left(\frac{r}{R_1}\right)\int_{R_1}^r \left(|u_r(\tilde{r})|^2 + |v_r(\tilde{r})|^2\right)\tilde{r}d\tilde{r} \tag{18}$$

If we use this inequality in 17 the integrals separate and we find :

$$\mathcal{F}\{\overrightarrow{v}\} \geq -\int_{R_1}^{R_2} \frac{\psi}{2r}\ln\left(\frac{\tilde{r}}{R_1}\right)\left(\sqrt{1+\frac{4}{\zeta^2}} + 1\right)d\tilde{r}\int_\theta\int_z\int_{R_1}^r \left(|u_r(\tilde{r})|^2 + |v_r(\tilde{r})|^2\right)\tilde{r}d\tilde{r}d\theta dz$$

hence :

$$\mathcal{F}\{\overrightarrow{v}\} \geq -\int_{R_1}^{R_2} \frac{\psi}{2r}\ln\left(\frac{\tilde{r}}{R_1}\right)\left(\sqrt{1+\frac{4}{\zeta^2}} + 1\right)d\tilde{r} \quad ||\overrightarrow{\nabla}\overrightarrow{v}||^2$$

The lower bound on $\mathcal{H}$ is finally :

$$\mathcal{H}\{\overrightarrow{v}\} = \nu||\overrightarrow{\nabla}\overrightarrow{v}||^2 + \mathcal{F}\{\overrightarrow{v}\} \geq \left[\nu - \int_{R_1}^{R_2} \frac{\psi}{2r}\ln\left(\frac{\tilde{r}}{R_1}\right)\left(\sqrt{1+\frac{4}{\zeta^2}} + 1\right)d\tilde{r}\right] \quad ||\overrightarrow{\nabla}\overrightarrow{v}||^2$$

So that $\mathcal{H}$ is necessarily positive if :

$$\nu - \int_{R_1}^{R_2} \frac{\psi}{2r} \ln\left(\frac{\tilde{r}}{R_1}\right)\left(\sqrt{1+\frac{4}{\zeta^2}}+1\right) d\tilde{r} \geq 0$$

If we define $r = R_2 x$ and compute $\zeta(x)$ for the laminar azimuthal velocity profile found in section 2.3, the lower bound on the energy stability limit becomes :

$$\frac{\alpha}{2}\int_{\eta}^{1} \frac{\ln\left(\frac{x}{\eta}\right)}{x}\left(\sqrt{1+\frac{4}{\zeta^2}}+1\right) dx = 1 \tag{19}$$

$$\text{with } \zeta(x) = 2\tan\Theta \frac{|\eta^{2+\alpha}-1|}{|\alpha x^{2+\alpha}+2\eta^{2+\alpha}|} \tag{20}$$

To this lower bound corresponds a line $Re_3(\tan(\Theta))$ which has been drawn for several values of η on figure 4. Under this line the flow is absolutely stable.

5 Numerical computation of the energy stability limit

In a study on the plane Couette flow with suction, Doering Spiegel and Worthing [1] found that the flow was absolutely stable if the injection angle was above a critical value $\Theta_c \simeq 3^o$. At this value of the entry angle the energy stability limit goes to infinity. In the cylindrical problem, the upper bound found in 4.1 clearly discards the possibility of such a behaviour. One may wonder how the shape of the energy stability limit will evolve from the plane Couette limit ($\eta \rightarrow 1$) to a cylindrical geometry. To answer this question, we solved numerically the eigenvalue problem in 3.3 to compute the actual energy stability limit.

5.1 Simplification of the system of equations

As a first step we can reduce as much as possible the number of variables and equations in the system. Taking the divergence of the vectorial form of the Euler-Lagrange equation and using the incompressibility constraint we get :

$$\Delta p = -\frac{1}{2r}(r^2\Gamma_r v)_r - \frac{im}{2r}(r\Gamma_r)u + \frac{\psi}{r^2}\left[-u_r + \frac{u}{r} + \frac{imv}{r}\right] \tag{21}$$

We can apply the operator Δ to equation 9 and use the relation :

$$\Delta(p_r) = (\Delta p)_r + \frac{p_r}{r^2} - \frac{2m^2}{r^3}p$$

to remove $\Delta(p_r)$. the remaining terms in p are $(\Delta p)_r$, p_r and p. They can be expressed in terms of u, v and their derivatives using equations 21, 9 and 10. This leads to the first differential equation of a system of two equations in u and v :

$$\begin{aligned}
\lambda\left[\frac{-2im}{r^2}v + u_{rr} + \frac{1}{r}u_r - (k^2 + \frac{m^2+1}{r^2})u\right] &= (-\nu)\,u_{rrrr} + \left(-\frac{2\nu}{r}\right)u_{rrr} + \left(2A + \frac{\nu}{r^2}\right)u_{rr} \\
&+ \left(\frac{2A}{r} - \frac{\nu}{r^3} + 2A_r - \frac{im\Gamma_r}{2}\right)u_r + \left(A_{rr} + \frac{A_r}{r} - A(k^2 + \frac{m^2+1}{r^2}) - \frac{im\Gamma_{rr}}{2} - \frac{2im}{r^2}Z^*\right)u + \left(\frac{4im\nu}{r^2}\right)v_{rr} \\
&+ \left(-\frac{4im\nu}{r^3}\right)v_r + \left(\frac{6im\nu}{r^4} - Z(k^2 + \frac{m^2}{r^2}) - \frac{2imA}{r^2}\right)v + \psi\left[-\left(\frac{k^2}{r^2} + \frac{m^2}{r^4}\right)u + \frac{im}{r^3}v_r - \frac{im}{r^4}v\right]
\end{aligned} \tag{22}$$

To get the second equation of the system w is expressed in terms of u and v using the mass conservation equation 12. Inserting w in equation 11 we get p, which can be replaced in equation 10. This leads to the equation :

$$\begin{aligned}
&\lambda\left[-\frac{im}{r}u_r-\frac{im}{r^2}u+(k^2+\frac{m^2}{r^2})v\right]=\left(\frac{im\nu}{r}\right)u_{rrr}+\left(\frac{2im\nu}{r^2}\right)u_{rr}+\left(-\frac{im}{r}A\right)u_r \qquad (23)\\
&+\left(k^2Z^*-\frac{im}{r^2}A+\frac{2im\nu}{r^4}\right)u+\left(-\nu(k^2+\frac{m^2}{r^2})\right)v_{rr}+\left(\frac{\nu}{r}(-k^2+\frac{m^2}{r^2})\right)v_r\\
&+\left(A(k^2+\frac{m^2}{r^2})-\frac{2\nu m^2}{r^4}+\frac{k^2\psi}{r^2}\right)v
\end{aligned}$$

This system has derivatives up to the fourth order in u and to the second order in v. We have four boundary conditions on u and two on v, which is enough to solve it.

5.2 Numerical resolution of the eigenvalue problem

The system of equation was solved using a finite-difference method. If N is the resolution, the functions u and v are discretized on the domain $[R_1, R_2]$ as :

$$\begin{aligned}
u&=(u_1,u_2,...,u_{N-1})\\
v&=(v_1,v_2,...,v_{N-1})
\end{aligned}$$

with $u_n = u(r = R_1 + nh)$ and $h = \frac{R_2-R_1}{N}$. The eigenvalue problem is then replaced by a difference equation using the central difference approximations to the derivatives. Each derivative can be written as a matrix which coefficients can be determined from the four following Taylor developments :

$$\begin{aligned}
f(x\pm h)&=f(x)\pm hf^{(1)}(x)+\frac{h^2}{2}f^{(2)}(x)\pm\frac{h^3}{6}f^{(3)}(x)+\frac{h^4}{24}f^{(4)}(x)+O(h^5)\\
f(x\pm 2h)&=f(x)\pm 2hf^{(1)}(x)+2h^2f^{(2)}(x)\pm\frac{4}{3}h^3f^{(3)}(x)+\frac{2}{3}h^4f^{(4)}(x)+O(h^5)
\end{aligned}$$

We get the approximations of the derivatives making linear combinations of these four equalities. For instance, we get for the first derivative :

$$\begin{aligned}
f'(R_1+nh)&=\frac{f(R_1+(n+1)h)-f(R_1+(n-1)h)}{2h}\text{ if }2\le n\le N-2\\
f'(R_1+h)&=\frac{f(R_1+2h)-f(R_1))}{2h}=\frac{f(R_1+2h)}{2h}\\
f'(R_1+(N-1)h)&=\frac{f(R_2)-f(R_1+(N-2)h)}{2h}=-\frac{f(R_1+(N-2)h)}{2h}
\end{aligned}$$

We used the boundary conditions to determine the extreme coefficients of the matrix. The computation of the matrices of the third and fourth order derivatives requires the use of 'ghost values' which are values of the functions on points out of the domain, such as $f(R_1 - h)$ or $f(R_2 + h)$. These quantities can be expressed in terms of values of the function inside the domain using the boundary conditions on the derivatives of f. For instance :

$$f'(R_1)=0=\frac{f(R1+h)-f(R_1-h)}{2h}\Rightarrow f(R_1-h)=f(R_1+h)$$

The matrices of the derivatives are tridiagonal and pentadiagonal :

$$D_r = \frac{1}{2h}\begin{pmatrix} 0 & 1 & & 0 \\ -1 & \ddots & \ddots & \\ & \ddots & \ddots & 1 \\ 0 & & -1 & 0 \end{pmatrix} \qquad D_{rr} = \frac{1}{h^2}\begin{pmatrix} -2 & 1 & & 0 \\ 1 & \ddots & \ddots & \\ & \ddots & \ddots & 1 \\ 0 & & 1 & -2 \end{pmatrix}$$

$$D_{rrr} = \frac{1}{2h^3}\begin{pmatrix} -1 & -2 & 1 & & 0 \\ 2 & 0 & \ddots & \ddots & \\ -1 & \ddots & \ddots & \ddots & 1 \\ & \ddots & \ddots & 0 & -2 \\ 0 & & -1 & 2 & 1 \end{pmatrix} \qquad D_{rrrr} = \frac{1}{h^4}\begin{pmatrix} 7 & -4 & 1 & & 0 \\ -4 & 6 & \ddots & \ddots & \\ 1 & \ddots & \ddots & \ddots & 1 \\ & \ddots & \ddots & 6 & -4 \\ 0 & & 1 & -4 & 7 \end{pmatrix}$$

Each equation of the system can be written as a linear combination of these matrices applied to u or v. The whole system can finally be written :

$$MX = \lambda NX$$

where $X = (u_1, \ldots, u_N, v_1, \ldots, v_N)$ and M and N are two 2x2 block matrices corresponding to the two sides of the equations. Each block represents the operator acting on one of the functions (u or v) in one of the two equations.

The eigenvalue problem $MX = \lambda NX$ can then be solved with the software MATLAB.

5.3 From plane Couette to cylindrical Couette

The energy stability limit has been drawn for several values of η on figure 5.3. When η is close to one and for very small values of the entry angle the energy stability limit remains constant at $Re \simeq 82$. This is the energy stability limit of the plane Couette flow. When $\theta \simeq 3^o$ the energy stability limit increases tremendously (several orders of magnitude), but cannot go to infinity as in the plane geometry. The cylindrical geometry allows some modes to grow. When $\tan(\Theta) \simeq 0.3$ the most unstable mode is $(m = 0, k = 0)$ and the energy stability limit coincides with the upper bound Re_1.

When η goes to zero, the behavior of the energy stability limit is totally different from the plane geometry. This limit corresponds to the situation where the outer radius goes to infinity while the inner radius is kept constant. The energy stability limit is then a monotonically decreasing function of the injection angle. The initial Reynolds number $Re(\Theta = 0)$ is higher in this case because we have chosen a definition of the Reynolds number based on the width of the gap. This definition is not relevant anymore when $\eta \to 0$ and should be replaced by $Re' = \frac{R_1^2\Omega}{\nu} = \frac{\eta^2}{1-\eta}Re$ since R_2 goes to infinity.

6 Bounds on the energy dissipation

The first bounds on turbulent quantities were introduced by Howard [2] to shed some light on Malkus assumption that turbulent convection would maximize the heat flux in turbulent convection [8]. Since then some related techniques have been developed such as the background method [6] [7]. Although the background method can be applied to any kind of geometry, people have mostly concentrated on shear layers and plane flows. Constantin [10] used the method to compute a bound on the energy dissipation for the Taylor-Couette flow without suction and Doering, Spiegel and Worthing successfully found a bound on the energy dissipation in a shear layer with suction. However, in the Taylor Couette problem with suction it appears a lot more challenging to find a bound, and we will show in this section that the background method in its usual formulation cannot be used.

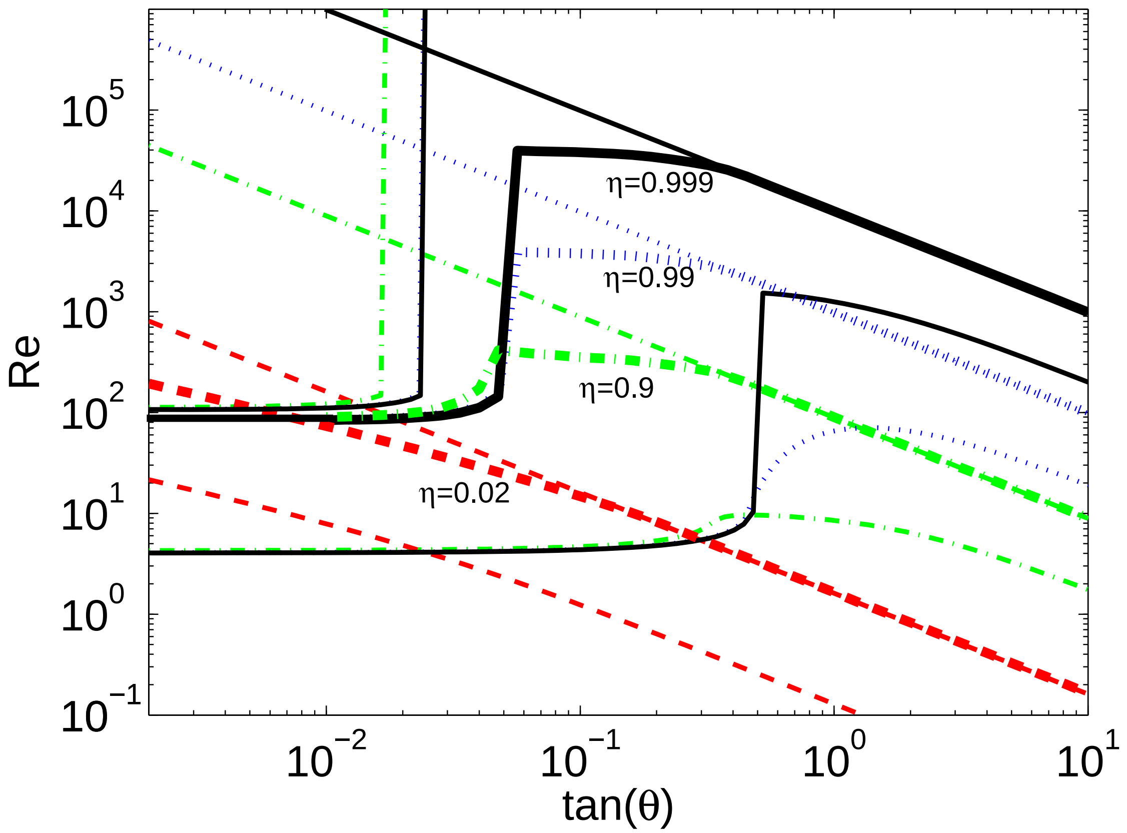

Figure 5: Energy stability limit of the Taylor-Couette flow with suction for different values of η.

6.1 The background method

The method uses a decomposition of the velocity field into a steady velocity profile and a time-dependant fluctuation field as in 3.1. The difference with the energy stability analysis is that the background profile remains to be chosen and is not necessarily the laminar solution. We can perform an integration by parts to write :

$$\int_\tau \overrightarrow{v}.\Delta\overrightarrow{V} d\tau = -\int_\tau (\overrightarrow{\nabla}\overrightarrow{V}).(\overrightarrow{\nabla}\overrightarrow{v})d\tau = -\frac{1}{2}\int_\tau |\overrightarrow{\nabla}\overrightarrow{u}|^2 - |\overrightarrow{\nabla}\overrightarrow{V}|^2 - |\overrightarrow{\nabla}\overrightarrow{v}|^2 d\tau$$

where the last equality comes from:

$$|\overrightarrow{\nabla}\overrightarrow{u}|^2 = |\overrightarrow{\nabla}\overrightarrow{V}|^2 + |\overrightarrow{\nabla}\overrightarrow{v}|^2 + 2(\overrightarrow{\nabla}\overrightarrow{v}).(\overrightarrow{\nabla}\overrightarrow{V})$$

Equation 6 can then be written as :

$$d_t\left(\frac{||\overrightarrow{v}||^2}{2}\right) + \frac{\nu}{2}||\overrightarrow{\nabla}\overrightarrow{u}||^2 = \frac{\nu}{2}||\overrightarrow{\nabla}\overrightarrow{V}||^2 - I \qquad (24)$$

$$\text{with } I = \int_\tau \frac{\nu}{2}|\overrightarrow{\nabla}\overrightarrow{v}|^2 + \overrightarrow{v}.(\overrightarrow{\nabla}\overrightarrow{V}).\overrightarrow{v} + \overrightarrow{v}.((\overrightarrow{V}.\overrightarrow{\nabla})\overrightarrow{V})d\tau \qquad (25)$$

The last term in I is linear in $\overrightarrow{v}$ which is not desirable in this procedure. To cancel this term we introduce another decomposition :

$$\overrightarrow{v} = \overrightarrow{W}(\overrightarrow{r}) + \overrightarrow{w}(\overrightarrow{r}, t)$$

where $\overrightarrow{W}$ and $\overrightarrow{w}$ are both divergence-free and verify the homogeneous boundary conditions. $\overrightarrow{W}$ is a steady flow whereas $\overrightarrow{w}$ is time dependant. This decomposition is inserted in I to find :

$$I = \mathcal{I}\{\overrightarrow{w}\} + \frac{\nu}{2}||\overrightarrow{\nabla}\overrightarrow{W}||^2 + \int_\tau \overrightarrow{W}.(\overrightarrow{\nabla}\overrightarrow{V}).\overrightarrow{W} + \overrightarrow{W}.((\overrightarrow{V}.\overrightarrow{\nabla})\overrightarrow{V})d\tau + \mathcal{L}\{\overrightarrow{w}\}$$

where :

$$\begin{aligned}\mathcal{I}\{\overrightarrow{w}\} &= \int_\tau \frac{\nu}{2}|\overrightarrow{\nabla}\overrightarrow{w}|^2 + \overrightarrow{w}.(\overrightarrow{\nabla}\overrightarrow{V}).\overrightarrow{w}\,d\tau \\ \mathcal{L}\{\overrightarrow{w}\} &= \int_\tau \overrightarrow{w}.\left[-\nu\Delta\overrightarrow{W} + (\overrightarrow{\nabla}\overrightarrow{V}).\overrightarrow{W} + (\overrightarrow{W}.\overrightarrow{\nabla})\overrightarrow{V} + (\overrightarrow{V}.\overrightarrow{\nabla})\overrightarrow{V}\right]d\tau\end{aligned}$$

$\overrightarrow{W}$ is then chosen to cancel the linear term in $\overrightarrow{w}$, that is $\mathcal{L}\{\overrightarrow{w}\} = 0$ for any vector field $\overrightarrow{w}$ that is divergence-free and satisfies the homogeneous boundary conditions (this does not necessarily imply that the bracket inside $\mathcal{L}$ has to be zero). If such a vector field $\overrightarrow{W}$ is chosen, it verifies $\mathcal{L}\{\overrightarrow{W}\} = 0$ which leads to:

$$\mathcal{I}\{\overrightarrow{W}\} = -\frac{1}{2}\int_\tau \overrightarrow{W}.((\overrightarrow{V}.\overrightarrow{\nabla})\overrightarrow{V})d\tau$$

The quantity I then becomes :

$$I = \mathcal{I}\{\overrightarrow{w}\} + \frac{1}{2}\int_\tau \overrightarrow{W}.((\overrightarrow{V}.\overrightarrow{\nabla})\overrightarrow{V})d\tau$$

This can be inserted in equation 24 to give :

$$d_t(||\overrightarrow{v}||^2) + \nu||\overrightarrow{\nabla}\overrightarrow{u}||^2 = \nu||\overrightarrow{\nabla}\overrightarrow{V}||^2 - \int_\tau \overrightarrow{W}.((\overrightarrow{V}.\overrightarrow{\nabla})\overrightarrow{V})d\tau - 2\mathcal{I}\{\overrightarrow{w}\}$$

where $\mathcal{I}\{\overrightarrow{w}\}$ is a quadratic form in $\overrightarrow{w}$. It is the same quadratic form as for the energy stability analysis with ν replaced by $\frac{\nu}{2}$. If we average this equation over a long time the left hand side becomes the average energy dissipation rate per unit mass (the time derivative averages to zero).

Here is the essence of the bounding procedure : If the background velocity profile is chosen so that $\mathcal{I}$ is a positive quadratic form, then this quadratic form can be dropped, which leads to the inequality :

$$\nu\overline{||\overrightarrow{\nabla}\overrightarrow{u}||^2} \leq \nu||\overrightarrow{\nabla}\overrightarrow{V}||^2 - \int_\tau \overrightarrow{W}.((\overrightarrow{V}.\overrightarrow{\nabla})\overrightarrow{V})d\tau$$

where the overline represents a long time average.

Usually the background profile is assumed to depend on the same coordinates as the laminar solution, and to verify the symmetries of the problem. For instance in a shear layer, the background is chosen as a function of the depth only. It seems natural to choose it independent of the horizontal coordinates since there is an invariance to any translation in these directions. For a cylindrical Couette flow we have an invariance to any translation in the θ and z directions. We are then tempted to chose an azimuthal background velocity profile which depends on r only, as for the laminar solution. This is a successful strategy for the classical Taylor Couette problem.

However, here is the problem that arises for the Taylor-Couette flow with suction : we find an upper bound on the energy stability limit of the flow studying the mode $(m = 0, k = 0)$. The derivation of this upper bound does not involve the azimuthal velocity profile. This means that for any injection angle Θ, and for any Reynolds number greater than $2Re_1(\Theta, \eta)$, the quadratic form $\mathcal{I}$ will not be a positive quadratic form, whatever function of r is chosen to be the background velocity profile. Therefore we cannot produce a bound on the energy dissipation with a background velocity depending only on r.

In studies on convection or shear layers [6] [7], the background velocity profiles happen to be very close to the average velocity profile of the flows at high Reynolds numbers, exhibiting very thin boundary layers near the walls and uniform profiles in the interior of the flow. This reinforces the common belief that the symmetries of the problem which are lost at relatively high Reynolds numbers through instabilities are recovered on average at even higher Reynolds numbers. The fact that we cannot choose a background velocity profile for the Taylor-Couette flow with suction which verifies the symmetries of the problem may raise the question of whether or not these symmetries are recovered at any Reynolds number.

7 Linear stability analysis

To understand how the symmetries of the system may be broken, as well as to complete the picture from the energy stability analysis, we shall now study the linear stability of the system.

7.1 Non-axisymmetric disturbances

Min and Lueptow [9] studied the linear stability of Taylor-Couette flow with suction, but their analysis includes only axisymmetric disturbances. They found that an inward flow has always a stabilizing effect and increases the critical Taylor number at which Taylor vortices appear. In the situation we are studying the inner cylinder remains steady. Without suction this configuration corresponds to a stable distribution of angular momentum and the Rayleigh criteria ensures that the flow is stable to axisymmetric perturbations. Since an inward flow has a stabilizing effect on these perturbations, we expect the flow to be linearly stable to any axisymmetric perturbation at any Reynolds number and any value of the entry angle Θ. For this reason our linear stability analysis focuses on non-axisymmetric perturbations. Such a perturbation breaks the invariance to translations in the θ direction.

In most instability mechanisms, one symmetry of the initial problem is broken at the onset of the primary instability whereas the other ones are broken through secondary instabilities. Since in our problem the most unstable perturbation has to break the invariance to translations in the θ direction, we expect it not to break the invariance to translations in the z direction. The most unstable mode would then have $(m \neq 0, k = 0)$. These are the modes of perturbation that we consider in the following linear stability analysis.

7.2 Linearization of the equations

We use the decomposition $\overrightarrow{u} = \overrightarrow{V_l} + \overrightarrow{v}$ and write a mode of perturbation as:

$$\overrightarrow{v} = (u(r), v(r), w(r))_{\{r,\theta,z\}} e^{-\lambda t} e^{im\theta}$$

where λ is now a complex number. We can set $w = 0$ and remove the vertical component of the Navier-Stokes equation without loss of generality. The linearization of the two other components leads to :

$$\begin{aligned} -\nu u_{rr} - \frac{\psi + \nu}{r} u_r + A_1 u - \lambda u + Z_1 v + p_r &= 0 \qquad (26) \\ -\nu v_{rr} - \frac{\psi + \nu}{r} v_r + A_2 v - \lambda v + Z_2 u + \frac{imp}{r} &= 0 \qquad (27) \end{aligned}$$

with :

$$\begin{aligned} A_1 &= im\frac{V}{r} + \frac{\psi}{r^2} + \nu\frac{m^2+1}{r^2} \\ A_2 &= im\frac{V}{r} - \frac{\psi}{r^2} + \nu\frac{m^2+1}{r^2} \\ Z_1 &= \frac{2im\nu}{r^2} - \frac{2V}{r} \\ Z_2 &= V_r + \frac{V}{r} - \frac{2im\nu}{r^2} \end{aligned}$$

The mass conservation equation becomes :

$$imv + (ru)_r = 0 \tag{28}$$

From equation 28 v can be expressed in terms of u. This expression of v is then inserted in equation 27 to get p in terms of u. p is differentiated with respect to r and injected into equation 26. This leads to a fourth order ODE in u :

$$\begin{aligned}
&\left[\nu r^2\right] u_{rrrr} + \left[(6\nu + \psi)r\right] u_{rrr} + \left[\nu(6 - m^2) + 3\psi - r^2 A_2\right] u_{rr} \\
&+ \left[-\frac{\psi + \nu}{r} m^2 + imrZ_1 + imrZ_2 - r^2 (A_2)_r - 3rA_2\right] u_r \\
&+ \left[m^2 A_1 + imZ_1 + imZ_2 + imr(Z_2)_r - r(A_2)_r - A_2\right] u = \lambda \left[-r^2 u_{rr} - 3ru_r + (m^2 - 1)u\right]
\end{aligned} \tag{29}$$

u and its first derivative must vanish at the 2 boundaries, which is enough boundary conditions to solve this equation.

7.3 Numerical computation of the linear stability limit

Equation 29 is an eigenvalue problem which can be solved numerically with the method described in 5.2. The linear stability limit is much higher than the energy stability limit in terms of Reynolds number and α. For this reason a very high resolution is needed to determine it. The finite resolution of the computation leads to a maximal value of α above which the linear stability limit cannot be easily determined.

The linear stability limit of different modes was represented on figures 6 and 7 for $\eta = 0.5$ and $\eta = 0.9$. The energy stability limit was added to the picture to make the comparison easier. There is a linear instability at small injection angles. The most unstable modes have $m \sim \frac{R_2}{R_2 - R_1} = \frac{1}{1-\eta}$, which corresponds to circular cells between the two cylinders.

At a certain value of the injection angle the linear stability limit seems to go to infinity. An analytical proof of this remains to be established. Comparing the limits obtained for the two values of η we see that the more cylindrical the geometry, the more linearly unstable the flow. From $\eta = 0.9$ to $\eta = 0.5$, the minimum value of the critical Reynolds number goes from approximately 10^4 to 2.10^3, and the maximum value of the injection angle that allows a linear instability increases by almost an order of magnitude. To emphasize the fact that this linear instability is found in the bulk of the flow (and not in the boundary layer as in the plane Couette flow with suction), a few pictures of the unstable mode at the onset of instability were added. For $\eta = 0.9$, the mode consists in only one row of rotating cells in the width of the gap if the injection angle is small. When the injection angle is closer to its critical value, this row splits into two rows of counter-rotating cells. For $\eta = 0.5$, we observe that the cells are closer to the outer boundary (the injection boundary) when the injection angle is far from the most unstable injection angle. At the most unstable value of the injection angle the cells occupy the whole width of the gap.

One should notice that in the limit of no suction and rotation only ($\tan(\Theta) \to 0$), the linear stability limit goes to infinity and the flow is stable. On the other hand, if there is only suction and no rotation ($Re \to 0, \alpha \to \infty$), we lose the instability too. This means that the linear instability exists only when both rotation and accretion are taken into account. It is lost if only one of these two ingredients is considered.

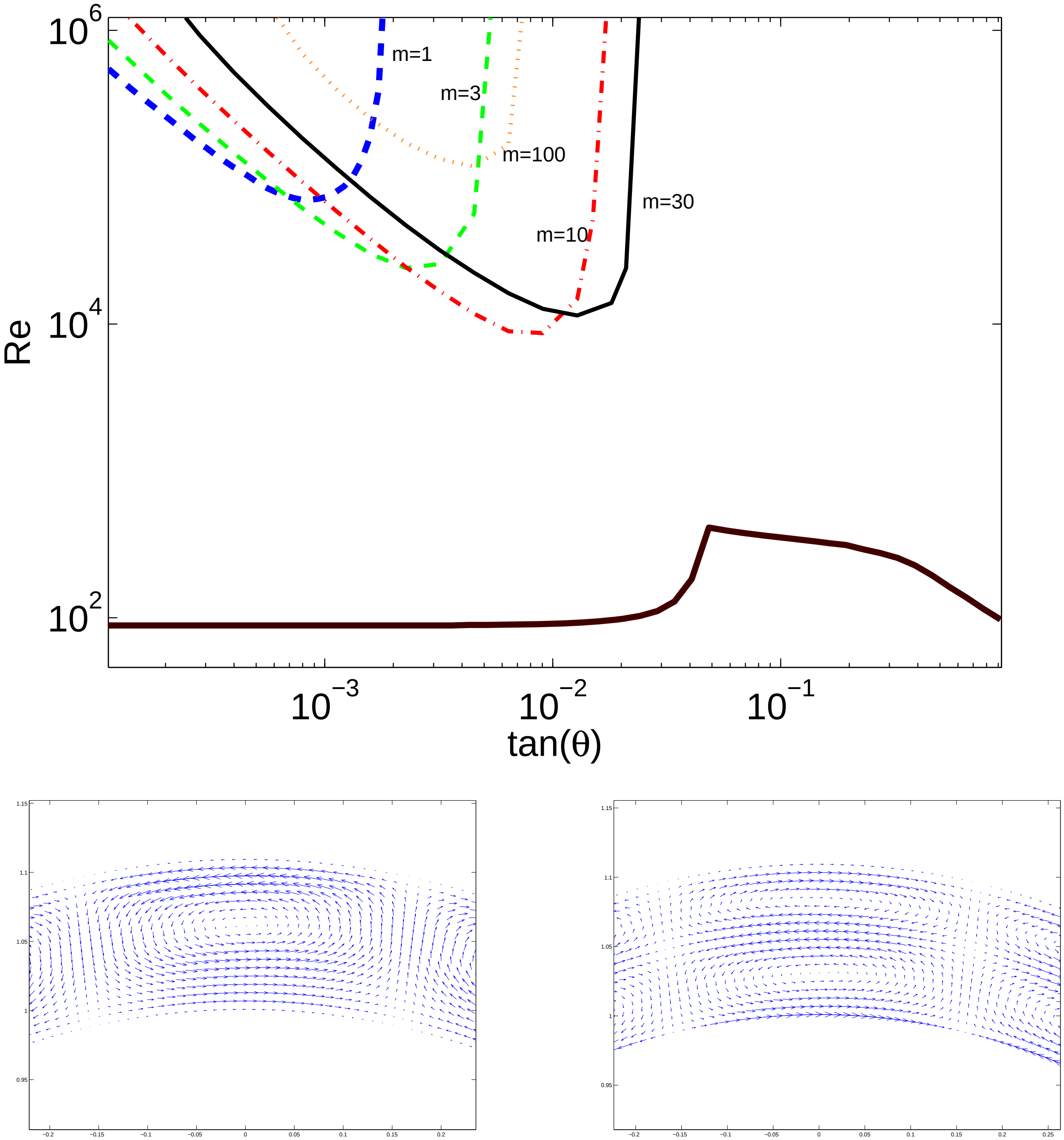

Figure 6: **Upper picture :** Linear stability limit of several modes for $\eta = 0.9$ (thick dashed line : $m = 1$, dashed line : $m = 3$, dash-dotted line : $m = 10$, solid line : $m = 30$, dotted line : $m = 100$). The energy stability limit has been added to make the comparison easier (thick solid line). **Lower left :** Unstable mode at the onset of instability for $m = 10$, $\tan(\Theta) = 0.003$, $\eta = 0.9$. One row of rotating cells can be seen in the width of the gap. **Lower right :** Unstable mode at the onset of instability for $m = 10$, $\tan(\Theta) = 0.01$, $\eta = 0.9$. Two rows of counter-rotating cells can be seen in the width of the gap.

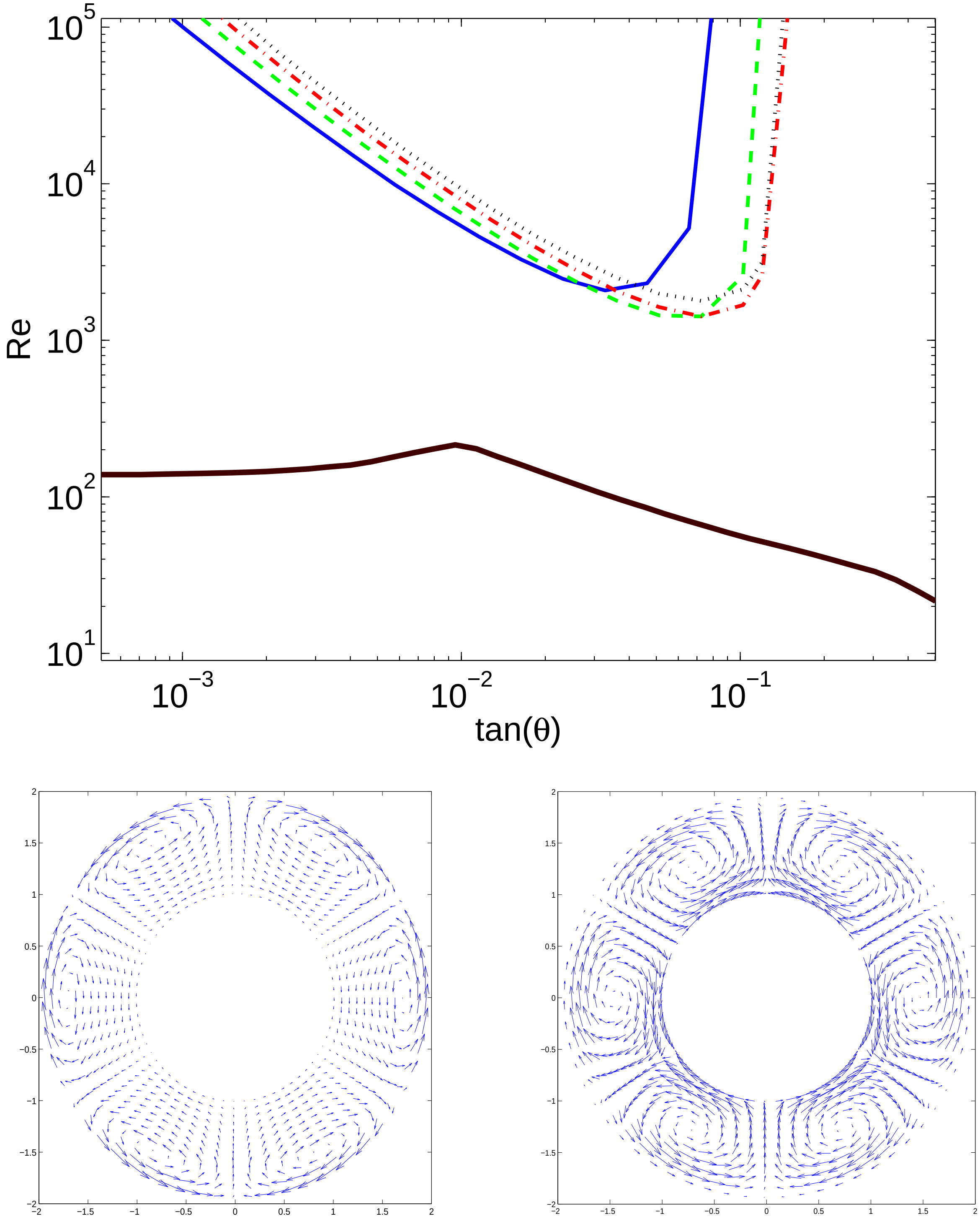

Figure 7: **Upper picture :** Linear stability limit of several modes for $\eta = 0.5$. In this more cylindrical geometry, linear instability is found for lower values of the Reynolds number and up to higher values of the injection angle. (solid line : $m = 1$, dashed line : $m = 2$, dash-dotted line : $m = 3$, dotted line : $m = 4$, thick solid line : energy stability limit). **Lower left :** Unstable mode at the onset of instability for $m = 3$, $\tan(\Theta) = 0.008$, $\eta = 0.5$. The cells are close to the injection boundary. **Lower right :** Unstable mode at the onset of instability for $m = 3$, $\tan(\Theta) = 0.08$, $\eta = 0.5$. The cells are in the whole width of the gap.

8 Conclusion

The actual energy stability limit has been computed for different configurations of the Taylor-Couette flow with suction : this flow is not energy stable provided that the Reynolds number is high enough, and we cannot rule out the possibility of a non-linear instability in such a flow. Moreover, this flow can be linearly unstable for certain values of the parameters : the combined efffects of rotation and accretion lead to a new linear instability which does not exist if only one of these ingredients is present.

This could lead to a scenario for a non-linear instability in an accretion disk : Let us consider a rotating disk without accretion. This disk is linearly stable but not energy stable. If it is subject to a perturbation, this perturbation could grow and carry out a little bit of angular momentum. This would drive accretion. Now that both rotation and accretion are present, the flow may not be linearly stable anymore and could become turbulent.

However, the flow we studied is very far from being a good model of an accretion disk and further work remains to be done to see if the results derived here could be applied to an actual accretion disk.

9 Acknowledgements

I would like to thank my supervisors C.Doering and E.Spiegel for their help during this summer. Thank you to all the GFD staff which gave me the great opportunity to come to the GFD program.

References

[1] C.R. Doering, E.A. Spiegel, R.A. Wothing *Energy dissipation in a shear layer with suction.* Physics of Fluids, 2000, volume 12, number 8.

[2] L.N. Howard. *Heat transport by turbulent convection.* Journal of Fluids Mechanics **17**, 405, (1963).

[3] S.A. Balbus, J.F. Hawley. *Instability, turbulence, and enhanced transport in accretion disks.* Review of modern physics volume 70, number 1 (1998).

[4] P. Drazin, W. Reid. *Hydrodynamic stability.* Cambridge University Press (1981)

[5] H.Ji, M.Burin, E.Schartman, J.Goodman. *Hydrodynamic turbulence cannot transport angular momentum effectively in astrophysical disks.* Nature, Volume 444 (2006)

[6] C.Doering, P.Constantin. *Variational bounds on energy dissipation in incompressible flows : III. Convection.* Phys. Rev. E **53**, 5957 (1996)

[7] C.Doering, P.Constantin. *Variational bounds on energy dissipation in incompressible flows : Shear flow.* Phys. Rev. E **49**, 4087 (1994)

[8] W.V.R. Malkus. *The heat transport and spectrum of thermal turbulence.* Proc. R. Soc. London, Ser. A **225**, 196 (1954).

[9] K. Min, R.M. Lueptow. *Hydrodynamic stability of viscous flow between rotating porous cylinders with radial flow.* Physics of Fluids, **6** (1) 1994.

[10] P. Constantin. *Geometric statistics in turbulence.* SIAM Review, Vol 36, No 1.

Nonlinear Ekman Dynamics for an Advective Flow

R.W.Dell, Supervised by J. Pedlosky

GFD Summer School, 2007

1 Introduction

Fridtjof Nansen, the famous Norwegian explorer, observed from the deck of his ship in the Arctic Ocean that icebergs mysteriously tended to drift at a 45° to the wind. The young graduate student Walfrid Ekman set out to explain this observation in his 1902 doctoral dissertation, and found it to be the combined effects of friction at the ocean's surface and the rotation of the Earth [2]. In explaining Nansen's observation, Ekman gave a general mathematical description of horizontal frictional boundary layers in rotating frames, now commonly called Ekman layers. These boundary layers are ubiquitous in geophysical fluid dynamics, at the bottom of the atmosphere, in the ocean surface layer, and probably at the ocean bottom. The critical feature of these boundary layers is that the combination of rotation and friction induces flow across lines of constant pressure, causing convergence in some regions and divergence in others. Where there is convergence, fluid is forced vertically out of the boundary layer, a phenomenon known as *Ekman pumping*. This small vertical velocity from the surface Ekman layer of the ocean is thought to drive much of the ocean circulation by compressing or stretching vertical vortex tubes and so inducing northward or southward flow.

Ekman derived his boundary layer solution for linear flows, neglecting the effects of momentum advection. Because the Ekman layer is so central to oceanic circulation, the details of its physics are of great interest to the fluid dynamics community, and several efforts have have been made to understand its nonlinear behavior. In 1964, Benton *et al* examined the nonlinear modifications to the Ekman layer for a flow with locally uniform shear far from the side boundaries, calculating the corrections numerically to a fifth order perturbation expansion [1]. Inspired by this example, Eliassen (1971) showed that nonlinear effects tended to suppress the pumping of fluid out of the boundary layer in the center of a cyclonic vortex [3]. This result was of considerable interest, as it has been observed on many occasions that the center of cyclones in the atmosphere, like the eyes of hurricanes, tend to be relatively cloud–free. If the Ekman layer was inducing downwelling—sucking fluid into the boundary layer instead of pumping it out—this might explain the clear–eyed cyclones. However, in 2000 Hart calculated analytically the nonlinear corrections to the Ekman pumping up to five orders of Rossby number, a small nondimensional parameter indicating the strength of rotation [4]. He was able to show that Eliasson's result was in fact an artifact of the assumption of locally uniform shear adopted from Benton *et al.* As a result, it was unlikely that Ekman dynamics explained the paucity of clouds in cyclone centers. However, Hart also restricted himself to unidirectional flows, that is flows that do not vary in the along–stream direction and where one of the velocity components is zero.

All of these authors restrict their discussion to a limited class of flows, usually unidirectional flows. This simplifies the computation significantly, but it excludes important physics: the effects of curvature of flows and the advection of material properties such as vorticity. We expect the lowest order nonlinear correction to the Ekman pumping velocity to be proportional to the advection of vorticity, so these authors may have excluded large effects even though they calculated very high–order corrections. To redress the oversight of previous studies, I will here calculate the weakly nonlinear form of the Ekman layer, and discuss the effect that including vorticity advection has on the structure of the boundary layer and the vertical velocity induced. I confine myself to discussing a case with a no–slip boundary condition, analogous to the ocean bottom. Though this is the less physically relevant case for ocean circulation, it is mathematically simpler and so a good starting point. I'll begin by reviewing the linear Ekman layer in Section 2, followed by the expansion in Rossby number in Section 3, including the weakly nonlinear solution for the Ekman pumping. Section 4 will discuss an illustrative example to help build intuition. Section 5 contains an alternative derivation of the weakly nonlinear solution for the illustrative example. I will conclude in Section 6.

2 The Linear Ekman Layer

We begin with the dimensionless Navier–Stokes equations for a homogeneous, steady flow:

$$\begin{aligned}
\epsilon\left(u\frac{\partial u}{\partial x}+v\frac{\partial u}{\partial y}+w\frac{\partial u}{\partial z}\right)-v &= -\frac{\partial p}{\partial x}+\frac{E}{2}\left(\frac{\partial^2 u}{\partial x^2}+\frac{\partial^2 u}{\partial y^2}+\frac{\partial^2 u}{\partial z^2}\right) && (1)\\
\epsilon\left(u\frac{\partial v}{\partial x}+v\frac{\partial v}{\partial y}+w\frac{\partial v}{\partial z}\right)+u &= -\frac{\partial p}{\partial y}+\frac{E}{2}\left(\frac{\partial^2 v}{\partial x^2}+\frac{\partial^2 v}{\partial y^2}+\frac{\partial^2 v}{\partial z^2}\right) && (2)\\
\epsilon\left(u\frac{\partial w}{\partial x}+v\frac{\partial w}{\partial y}+w\frac{\partial w}{\partial z}\right) &= -\frac{\partial p}{\partial z}+\frac{E}{2}\left(\frac{\partial^2 w}{\partial x^2}+\frac{\partial^2 w}{\partial y^2}+\frac{\partial^2 w}{\partial z^2}\right) && (3)\\
\frac{\partial u}{\partial x}+\frac{\partial v}{\partial y}+\frac{\partial w}{\partial z} &= 0 && (4)
\end{aligned}$$

In these equations, our dimensionless parameters are the Rossby number, $\epsilon=\frac{U_0}{2\Omega L}$, which gives the relative strength of advection and rotation, and the Ekman number, $E=\frac{\nu}{\Omega L^2}$, giving the relative strength of friction and rotation, where Ω is the rotation rate of the frame, ν is the frictional parameter, L is a length scale, and U_0 is a velocity scale taken from the flow far from the boundary. Far from the boundary, the flow is assumed to be inviscid, and both E and ϵ can be considered small. To lowest order, the above system of equations then becomes:

$$\begin{aligned}
-v &= -\frac{\partial p}{\partial x}\\
+u &= -\frac{\partial p}{\partial y}\\
0 &= -\frac{\partial p}{\partial z}\\
\frac{\partial u}{\partial x}+\frac{\partial v}{\partial y}+\frac{\partial w}{\partial z} &= 0
\end{aligned}$$

These are the standard equations of *geostrophic balance*, where rotational and pressure effects balance each other in the horizontal. We will assume that the flow far from the boundary always satisfies these equations, and we will denote the geostrophically balanced far field velocities $U(x,y)$ and $V(x,y)$. The continuity equation (4) implies that $w_z=0$. If we imagine that somewhere there is a horizontal boundary that fluid cannot penetrate, we know that $w=0$ everywhere.

Though the far field is inviscid, there must be a region near the boundary in which the frictional terms are of the same order as the rotational terms. Therefore, we introduce a new stretched coordinate ζ, defined so that the region where friction is important—the boundary layer—is the region where ζ is $O(1)$:

$$z=\sqrt{E}\zeta \qquad (5)$$

Assume $z=\zeta=0$ on the bottom boundary. Therefore:

$$\frac{\partial}{\partial z}=\frac{1}{\sqrt{E}}\frac{\partial}{\partial\zeta} \qquad ; \qquad \frac{\partial^2}{\partial z^2}=\frac{1}{E}\frac{\partial^2}{\partial\zeta^2}$$

We similarly introduce a rescaled vertical velocity W so that:

$$\frac{\partial w}{\partial z}=\frac{\partial W}{\partial\zeta}$$

Our equations of motion (1) – (4) then become:

$$\begin{aligned}
\epsilon\left(u\frac{\partial u}{\partial x}+v\frac{\partial u}{\partial y}+W\frac{\partial u}{\partial \zeta}\right)-v &= -\frac{\partial p}{\partial x}+\frac{1}{2}\left(E\frac{\partial^2 u}{\partial x^2}+E\frac{\partial^2 u}{\partial y^2}+\frac{\partial^2 u}{\partial \zeta^2}\right)\\
\epsilon\left(u\frac{\partial v}{\partial x}+v\frac{\partial v}{\partial y}+W\frac{\partial v}{\partial \zeta}\right)+u &= -\frac{\partial p}{\partial y}+\frac{1}{2}\left(E\frac{\partial^2 v}{\partial x^2}+E\frac{\partial^2 v}{\partial y^2}+\frac{\partial^2 v}{\partial \zeta^2}\right)\\
\epsilon E\left(u\frac{\partial W}{\partial x}+v\frac{\partial W}{\partial y}+W\frac{\partial W}{\partial \zeta}\right) &= -\frac{\partial p}{\partial \zeta}+\frac{E}{2}\left(E\frac{\partial^2 W}{\partial x^2}+E\frac{\partial^2 W}{\partial y^2}+\frac{\partial^2 W}{\partial \zeta^2}\right)\\
\frac{\partial u}{\partial x}+\frac{\partial v}{\partial y}+\frac{\partial W}{\partial \zeta} &= 0
\end{aligned}$$

The scale over which frictional effects are important has now been included in our governing equations, so we can neglect all terms that are still of order E. This gives:

$$\epsilon\left(u\frac{\partial u}{\partial x}+v\frac{\partial u}{\partial y}+W\frac{\partial u}{\partial \zeta}\right)-v = -\frac{\partial p}{\partial x}+\frac{1}{2}\frac{\partial^2 u}{\partial \zeta^2} \tag{6}$$

$$\epsilon\left(u\frac{\partial v}{\partial x}+v\frac{\partial v}{\partial y}+W\frac{\partial v}{\partial \zeta}\right)+u = -\frac{\partial p}{\partial y}+\frac{1}{2}\frac{\partial^2 v}{\partial \zeta^2} \tag{7}$$

$$0 = -\frac{\partial p}{\partial \zeta} \tag{8}$$

$$\frac{\partial u}{\partial x}+\frac{\partial v}{\partial y}+\frac{\partial W}{\partial \zeta} = 0 \tag{9}$$

To solve these equations, we assume that the Rossby number ϵ is small and expand all of our physical quantities in it:

$$\begin{aligned}
u &= u_0+\epsilon u_1+\epsilon^2 u_2+\ldots\\
p &= p_0+\epsilon p_1+\epsilon^2 p_2+\ldots\\
&\vdots
\end{aligned}$$

To $O(1)$, equations (6) – (9) are:

$$-v_0 = -\frac{\partial p_0}{\partial x}+\frac{1}{2}\frac{\partial^2 u_0}{\partial \zeta^2} \tag{10}$$

$$u_0 = -\frac{\partial p_0}{\partial y}+\frac{1}{2}\frac{\partial^2 v_0}{\partial \zeta^2} \tag{11}$$

$$0 = -\frac{\partial p_0}{\partial \zeta} \tag{12}$$

$$\frac{\partial u_0}{\partial x}+\frac{\partial v_0}{\partial y}+\frac{\partial W_0}{\partial \zeta} = 0 \tag{13}$$

These equations describe the linear Ekman layer problem. To solve it, we recall first that:

$$\begin{aligned}
U &= -\frac{\partial p_0}{\partial y}\\
V &= \frac{\partial p_0}{\partial x}
\end{aligned}$$

We can then define an auxiliary variable, Λ_0 such that:

$$\Lambda_0 = (u_0-U)+i(v_0-V)$$

The x– and y–momentum equations (10) — (11) then can be compactly expressed:

$$\frac{\partial^2 \Lambda_0}{\partial \zeta^2} - 2i\Lambda_0 = 0$$

This second–order equation has two solutions, but we are only interested in the solution that is bounded as $\zeta \to \infty$, that is the solution that does not modify the flow far from the boundary:

$$\Lambda_0 = -\lambda e^{-\zeta(1+i)} \tag{14}$$

Applying the no slip boundary condition and converting back into real velocities, we find $\lambda = U + iV$, and:

$$\begin{aligned} u_0 &= U + e^{-\zeta}\left(-U\cos\zeta - V\sin\zeta\right) && (15) \\ v_0 &= V + e^{-\zeta}\left(U\sin\zeta - V\cos\zeta\right) && (16) \end{aligned}$$

We can find W_0 using the continuity equation (13):

$$\begin{aligned} W_0 &= \frac{1}{2}\left(\frac{\partial U}{\partial y} \underbrace{- \frac{\partial V}{\partial y} - \frac{\partial U}{\partial x}}_{=0} - \frac{\partial V}{\partial x}\right) e^{-\zeta}\cos\zeta \\ &\quad + \frac{1}{2}\left(\frac{\partial U}{\partial y} + \underbrace{\frac{\partial V}{\partial y} + \frac{\partial U}{\partial x}}_{=0} - \frac{\partial V}{\partial x}\right) e^{-\zeta}\sin\zeta + C(x,y) \\ W_0 &= -\frac{1}{2}\omega e^{-\zeta}\left(\cos\zeta + \sin\zeta\right) + \frac{1}{2}\omega && (17) \end{aligned}$$

We find the constant of integration by applying a no normal flow boundary condition at the bottom boundary. In this, $\omega = \frac{\partial V}{\partial x} - \frac{\partial U}{\partial y}$ is the relative vorticity of the far field flow. We see that even infinitely far from the boundary, friction has induced a vertical velocity $W_0 = \frac{1}{2}\omega$ that is proportional to ω, the vorticity of the flow.

We have now completed the linear Ekman layer problem. We can see why it is worth pressing on to a weakly nonlinear solution by taking a look at the vorticity equation, found by taking the curl of the momentum equations (1) —(3):

$$\epsilon\left(u\frac{\partial \omega}{\partial x} + v\frac{\partial \omega}{\partial y} + w\frac{\partial \omega}{\partial z}\right) - \frac{\partial w}{\partial z} = \frac{E}{2}\left(\frac{\partial^2 \omega}{\partial x^2} + \frac{\partial^2 \omega}{\partial y^2}\right) + \frac{\partial^2 \omega}{\partial z^2})$$

Far from the boundary, where the effects of friction given by the right hand side of the equation are small, the vertical velocity gradient is balanced by the advection of vorticity. This strongly suggests that advective effects will play an important role in the weakly nonlinear solution. Let's calculate it.

3 Rossby Number Expansion

To find the weakly nonlinear correction, we examine our governing equations (6) to (9) to $O(\epsilon)$:

$$\begin{aligned} \left(u_0\frac{\partial u_0}{\partial x} + v_0\frac{\partial u_0}{\partial y} + W_0\frac{\partial u_0}{\partial \zeta}\right) - v_1 &= -\frac{\partial p_1}{\partial x} + \frac{1}{2}\frac{\partial^2 u_1}{\partial \zeta^2} && (18) \\ \left(u_0\frac{\partial v_0}{\partial x} + v_0\frac{\partial v_0}{\partial y} + W_0\frac{\partial v_0}{\partial \zeta}\right) + u_1 &= -\frac{\partial p_1}{\partial y} + \frac{1}{2}\frac{\partial^2 v_1}{\partial \zeta^2} && (19) \\ 0 &= -\frac{\partial p_1}{\partial \zeta} && (20) \\ \frac{\partial u_1}{\partial x} + \frac{\partial v_1}{\partial y} + \frac{\partial W_1}{\partial \zeta} &= 0 && (21) \end{aligned}$$

As in the linear problem, we can define an auxiliary variable $\Lambda_1 = u_1 + iv_1$, and express the x– and y–momentum equations in terms of it:

$$\begin{aligned}\frac{\partial^2 \Lambda_1}{\partial \zeta^2} - 2i\Lambda_1 \quad = \quad & 2\Big[\frac{\partial p_1}{\partial x} + i\frac{\partial p_1}{\partial y} + u_0\frac{\partial u_0}{\partial x} + v_0\frac{\partial u_0}{\partial y} + W_0\frac{\partial u_0}{\partial \zeta} + \\ & \qquad iu_0\frac{\partial v_0}{\partial x} + iv_0\frac{\partial v_0}{\partial y} + iW_0\frac{\partial v_0}{\partial \zeta}\Big]\end{aligned} \tag{22}$$

Advection by the first–order velocity field becomes the forcing we apply to the order ϵ velocities. Note that we include the pressure p_1 with the forcing terms because it does not induce any cross-isobar flow, and so will not induce any change in the Ekman pumping or boundary layer structure. We assume that the pressure terms balance with the advection terms that do not decay to zero far from the boundary. After much algebra, we find that these forcing terms can be expressed:

$$\frac{\partial^2 \Lambda_1}{\partial \zeta^2} - 2i\Lambda_1 = ae^{-\zeta(1-i)} + be^{-\zeta(1+i)} + ce^{-2\zeta} \tag{23}$$

where

$$\begin{aligned} a &= i\lambda\omega - 2U\frac{\partial \lambda}{\partial x} - 2V\frac{\partial \lambda}{\partial y} \\ b &= \lambda\omega - 2U\frac{\partial \lambda}{\partial x} - 2V\frac{\partial \lambda}{\partial y} \\ c &= -\lambda\omega + (U - iV)\left(\frac{\partial \lambda}{\partial x} + i\frac{\partial \lambda}{\partial y}\right)\end{aligned}$$

In equation (23) the second forcing term is of the same form as the homogeneous solution, proportional to $\exp[-\zeta(1+i)]$. This forcing term is dangerous, because it yields solutions proportional to $\zeta\exp[-\zeta(1+i)]$, giving terms like $(1+\epsilon\zeta)\exp[\zeta(1+i)]$ in the final expression for velocity. When you get far enough from the boundary that $\epsilon\zeta$ is $O(1)$ our expansion becomes disordered, that is terms of $O(\epsilon)$ are not smaller than those of $O(1)$, and our solution becomes invalid. Terms with this disturbing property are called *secular*, and one such term is found below in the solution for Λ_1. The solution for equation (23), once again applying the no–slip boundary condition $\Lambda_0 = 0$ at $\zeta = 0$, is:

$$\Lambda_1 = \frac{i}{4}ae^{-\zeta(1-i)} - \underbrace{\frac{b}{2(1+i)}\zeta e^{-\zeta(1+i)}}_{\text{secular}} + \frac{c}{4-2i}e^{-2\zeta} - \underbrace{\left(\frac{i}{4}a + \frac{c}{4-2i}\right)e^{-\zeta(1+i)}}_{\text{homogeneous}} \tag{24}$$

To deal with the secular term, we can use the approximation $e^x \approx (1+x)$ to combine it with the homogeneous solution, also indicated above, and interpret it as a modification to the structure of the boundary layer. While this may seem presumptuous, it yields the same boundary layer thickness as approaching this problem with a multiple–scale expansion, so it is probably true. The multiple–scale approach is shown in Section 5. With this approximation, we find for the total velocity field of the fluid to order ϵ:

$$\begin{aligned}\Lambda \quad &= \quad (u-U) + i(v-V) = \Lambda_0 + \epsilon\Lambda_1 + O(\epsilon^2) \\ &= \quad -\left(\lambda + \epsilon\big(\frac{i}{4}a + \frac{c}{4-2i}\big)\right)\underbrace{\exp\left[-\zeta\big(1 + i + \epsilon\frac{b}{2\lambda(1+i)}\big)\right]}_{} + \epsilon\frac{i}{4}ae^{-\zeta(1-i)} + \epsilon\frac{c}{4-2i}e^{-2\zeta}\end{aligned} \tag{25}$$

This is admittedly difficult to interpret. However, we can see that the thickness of the boundary layer, given by the exponential term indicated with an underbrace, is modified in a way that is involves to the vorticity and the advection of the geostrophic flow. We can also use Λ and the continuity equation to calculate the

Ekman pumping out of the boundary layer for an arbitrary geostrophic flow. Continuity (9) tell us:

$$\begin{aligned} W &= -\int \left[\frac{\partial u}{\partial x} + \frac{\partial v}{\partial y}\right] d\zeta \\ &= -\frac{\partial}{\partial x}\left(\Re\left[\int \Lambda d\zeta\right]\right) - \frac{\partial}{\partial y}\left(\Im\left[\int \Lambda d\zeta\right]\right) \end{aligned}$$

We are interested in the value of W as we move far away from the boundary—the amount of fluid that is actually pumped out of the boundary layer and into the far field fluid. We can see from equation (25) that we will find a solution of the form:

$$\Lambda = -\left(\lambda + \epsilon(\alpha + \gamma)\right) e^{-\zeta(1+i+\epsilon\beta)} + \epsilon\alpha e^{-\zeta(1-i)} + \epsilon\gamma e^{-2\zeta} \tag{26}$$

In this, $\alpha = ia/4$, $\beta = b/(2\lambda(1+i))$, and $\gamma = c/(4-2i)$. This integrates very easily to give:

$$\int \Lambda d\zeta = \frac{\lambda + \epsilon(\alpha+\gamma)}{1+i+\epsilon\beta} e^{-\zeta(1+i+\epsilon\beta)} - \epsilon\frac{\alpha(1+i)}{2} e^{-\zeta(1-i)} - \epsilon\frac{\gamma}{2} e^{-2\zeta} + C(x,y) \tag{27}$$

We find the constant of integration $C(x,y)$ by applying the boundary condition $W(\zeta = 0) = 0$. Since all of the terms in Λ decay with increasing ζ, $W(\zeta \to \infty) = C(x,y)$. Evaluating this by hand is not anyone's idea of fun, so I use a computer algebra program, Maple 11, to find:

$$\begin{aligned} W_\infty = {} & \frac{1}{2}\omega - \epsilon\frac{7}{40}\left(\left(\frac{\partial U}{\partial y}\right)^2 + U\frac{\partial^2 U}{\partial y^2}\right) + \epsilon\frac{1}{10}\left(U\frac{\partial^2 V}{\partial y^2} - \frac{\partial U}{\partial x}\frac{\partial V}{\partial y} - V\frac{\partial^2 U}{\partial x^2}\right) + \\ & +\epsilon\frac{13}{40}\left(V\frac{\partial^2 U}{\partial y^2} - U\frac{\partial^2 U}{\partial x\partial y} + V\frac{\partial^2 V}{\partial x\partial y} + \frac{\partial U}{\partial x}\frac{\partial V}{\partial x} + \frac{\partial V}{\partial x}\frac{\partial V}{\partial y} - \frac{\partial U}{\partial x}\frac{\partial U}{\partial y} + -\frac{\partial U}{\partial y}\frac{\partial V}{\partial y}\right) \\ & -\epsilon\frac{9}{20}\frac{\partial V}{\partial x}\frac{\partial U}{\partial y} + \epsilon\frac{17}{40}\left(U\frac{\partial^2 V}{\partial x^2} - \left(\frac{\partial V}{\partial x}\right)^2 - V\frac{\partial^2 V}{\partial x^2}\right) \\ & -\epsilon\frac{7}{10}\left(\left(\frac{\partial U}{\partial x}\right)^2 + U\frac{\partial^2 U}{\partial x^2} + \left(\frac{\partial V}{\partial y}\right)^2 + V\frac{\partial^2 V}{\partial Y^2}\right) \\ & -\epsilon\frac{11}{40}\left(U\frac{\partial^2 V}{\partial x\partial y} + V\frac{\partial^2 U}{\partial x\partial y}\right) \end{aligned} \tag{28}$$

This is the weakly non-linear solution for the Ekman pumping induced by a no–slip boundary in a rotating frame. As with many of the things I have presented in this essay, it is rather difficult to interpret on its own. We notice that that there is no direct dependence on vorticity advection, though all the terms of the vorticity advection enter the above expression. Therefore, we will now turn to a simplified example to build intuition about the effects of nonlinearity on the Ekman layer.

4 An Illustrative Example

We can gain great insight into the effect of advection on the boundary layer by exploring the simplest test flow in which advection is present:

$$\begin{aligned} U &= U(y) \\ V &= \text{constant} \end{aligned}$$

This is the unidirectional flow examined by Hart, Pedlosky, and others, modified by a constant cross–stream velocity. The thickness of the boundary layer is controlled by the decaying exponential in Λ. It is the real part of the exponential designated by an underbrace in equation (25):

$$\Lambda \propto \exp\left[-\zeta + \epsilon\zeta\frac{1}{4}\omega\left(1 - \frac{2V^2}{U^2+V^2}\right)\right] \tag{29}$$

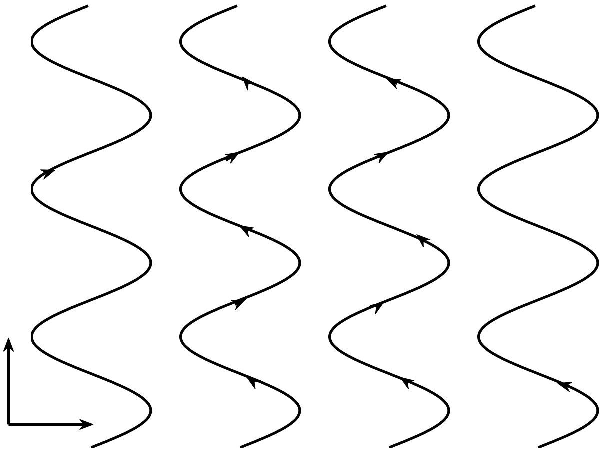

Figure 1: Streamlines for the Illustrative Example. Plan View.

In this flow, the relative vorticity $\omega = -\frac{\partial U}{\partial y}$. If the cross–flow velocity V goes to zero, this reduces to the solution for a unidirectional flow derived by Hart [4] and by Pedlosky [5] in the invited lectures of this year's summer school. That is, we find that the thickness of the Ekman layer is modified proportionally to the vorticity of the flow: where the vorticity is positive the Ekman layer is thicker, and where the vorticity is negative the Ekman layer is thinner. If, on the other hand, the cross–flow velocity V is very large, the thickness of the Ekman layer is modified in the opposite direction, thicker where the vorticity is negative and thinner where the vorticity is positive.

For this flow field, we find a solution of the form given in (26), with:

$$\beta = -\frac{1}{4\lambda}\left((i-1)U\frac{\partial U}{\partial y} + (i-3)V\frac{\partial U}{\partial y}\right) \tag{30}$$

$$\alpha = \frac{1}{4}\left(U\frac{\partial U}{\partial y} - iV\frac{\partial U}{\partial y}\right) \tag{31}$$

$$\gamma = \frac{3i+1}{10}\left(U\frac{\partial U}{\partial y} + V\frac{\partial U}{\partial y}\right) \tag{32}$$

Integrating, and taking the limit as $\zeta \to \infty$, we find

$$W_\infty = -\frac{1}{2}\frac{\partial U}{\partial y} - \epsilon\frac{7}{40}\left(\left(\frac{\partial U}{\partial y}\right)^2 + U\frac{\partial^2 U}{\partial y^2}\right) + \epsilon\frac{13}{40}V\frac{\partial^2 U}{\partial y^2} \tag{33}$$

The final term looks like the advection of vorticity. However, it is unclear if that is the appropriate physical interpretation because the general solution given in equation (28) is not directly proportional to vorticity advection.

To better understand the quantities we've derived, let's examine a specific flow:

$$\begin{aligned} U &= \cos ky \\ V &= \text{constant} \end{aligned}$$

The streamlines of this flow are shown in Figure 1. This flow makes an ideal test case because it is not computationally demanding, but has the physical characteristics we are interested in investigating: regions of positive and negative vorticity and fluid advected between them. The boundary layer thickness is:

$$\Lambda \propto \exp\left[-\zeta + \epsilon\zeta\frac{1}{4}k\sin ky\left(1 - \frac{2V^2}{\cos^2 ky + V^2}\right)\right]$$

This is shown in Figure 2 for three cases: no advection, weak advection, and strong advection. One immediately sees the importance of considering advection because the even the *sign* of the lowest order nonlinear effect depends on it. Previously published higher order solutions might not even correctly predict if the boundary layer should be thicker or thinner. Figures 3 and 4 show the vertical velocity profiles for this test case, and one can see that for some advection strengths the boundary layer is thickened and for some it is compressed, as suggested by Figure 2. The Ekman pumping shown in Figure 5 is given by:

$$W_\infty = \frac{k}{2}\sin ky - \epsilon\frac{7}{40}k^2 - \epsilon\frac{13}{40}Vk^2\cos ky$$

Increasing the cross-flow velocity affects both the phase and the magnitude of the Ekman pumping. The phase of the Ekman pumping shifts from being in phase with the vorticity of the flow to being $\frac{\pi}{2}$ out of phase with it. The weakly nonlinear correction is also proportional to the curvature of the sinusoidal flow—as k increases and the length scale of the oscillations decrease, the fluctuations in vorticity become more pronounced and the Ekman pumping stronger. Note that the nonlinear correction to the Ekman pumping can be asymmetrical as the vertical velocity induced by the vorticity can either reinforce or suppress it.

5 Multiple Scale Expansion

Another way to derive a weakly nonlinear solution to the Ekman layer is by assuming the vertical scales of the boundary layer, the far–field flow, and the transition region between them are all well separated and performing a multiple scale expansion. As in the Rossby number expansion, we start with the boundary layer coordinate $\zeta = z/\sqrt{E}$, as defined in equation (5). We also define a coordinate that is of order one in the transition region between the boundary layer and the interior flow:

$$\eta = \epsilon\zeta = \frac{\epsilon}{\sqrt{E}}z$$

We assume that the scale of ζ and η are so widely separated that we can treat them as independent variables. Therefore:

$$\frac{\partial}{\partial z} = \frac{1}{\sqrt{E}}\frac{\partial}{\partial\zeta} + \frac{\epsilon}{\sqrt{E}}\frac{\partial}{\partial\eta} \quad ; \quad \frac{\partial^2}{\partial z^2} = \frac{1}{E}\frac{\partial^2}{\partial\zeta^2} + 2\frac{\epsilon}{E}\frac{\partial^2}{\partial\zeta\partial\eta} + \frac{\epsilon^2}{E}\frac{\partial^2}{\partial\eta^2}$$

Our equations of motion (1) – (4) then become:

$$\begin{aligned}
\epsilon\left(u\frac{\partial u}{\partial x} + v\frac{\partial u}{\partial y} + W\frac{\partial u}{\partial\zeta} + \epsilon W\frac{\partial u}{\partial\eta}\right) - v &= -\frac{\partial p}{\partial x} + \frac{1}{2}\left(E\frac{\partial^2 u}{\partial x^2} + E\frac{\partial^2 u}{\partial y^2} + \frac{\partial^2 u}{\partial\zeta^2} + 2\epsilon\frac{\partial^2 u}{\partial\zeta\partial\eta} + \epsilon^2\frac{\partial^2 u}{\partial\eta^2}\right) && (34)\\
\epsilon\left(u\frac{\partial v}{\partial x} + v\frac{\partial v}{\partial y} + W\frac{\partial v}{\partial\zeta} + \epsilon W\frac{\partial v}{\partial\eta}\right) + u &= -\frac{\partial p}{\partial y} + \frac{1}{2}\left(E\frac{\partial^2 v}{\partial x^2} + E\frac{\partial^2 v}{\partial y^2} + \frac{\partial^2 v}{\partial\zeta^2} + 2\epsilon\frac{\partial^2 v}{\partial\zeta\partial\eta} + \epsilon^2\frac{\partial^2 v}{\partial\eta^2}\right) && (35)\\
\epsilon E\left(u\frac{\partial W}{\partial x} + v\frac{\partial W}{\partial y} + W\frac{\partial W}{\partial\zeta} + \epsilon W\frac{\partial W}{\partial\eta}\right) &= -\frac{\partial p}{\partial\zeta} + \frac{E}{2}\left(E\frac{\partial^2 W}{\partial x^2} + E\frac{\partial^2 W}{\partial y^2} + \frac{\partial^2 W}{\partial\zeta^2} + 2\epsilon\frac{\partial^2 W}{\partial\zeta\partial\eta} + \epsilon^2\frac{\partial^2 W}{\partial\eta^2}\right)\\
\frac{\partial u}{\partial x} + \frac{\partial v}{\partial y} + \frac{\partial W}{\partial\zeta} + \epsilon\frac{\partial W}{\partial\eta} &= 0
\end{aligned}$$

To $O(1)$, we recover the same linear Ekman layer discussed previously. Its solution from equation (14) is:

$$\Lambda_0 = -\lambda e^{-\zeta(1+i)} \tag{36}$$

However, instead of saying that the coefficient λ varies only in x and y, we allow it to vary in the transitional vertical coordinate η, as well. This coordinate is so dilated with respect to the boundary layer that variations in η seem constant within the boundary layer. If we let the coefficient $\lambda = A + iB$, the no slip boundary condition gives us $A(\zeta = 0) = -U$ and $B(\zeta = 0) = -V$. The Ekman pumping becomes:

$$\begin{aligned}
W_0 &= C(x,y,\eta) + \frac{1}{2}\left(\frac{\partial B}{\partial x} - \frac{\partial A}{\partial y} + \frac{\partial B}{\partial y} + \frac{\partial A}{\partial x}\right)e^{-\zeta}\cos\zeta\\
&\quad + \frac{1}{2}\left(\frac{\partial B}{\partial x} - \frac{\partial A}{\partial y} - \frac{\partial B}{\partial y} - \frac{\partial A}{\partial x}\right)e^{-\zeta}\sin\zeta && (37)
\end{aligned}$$

Since A and B now are considered to vary vertically, we can not assume that $\frac{\partial A}{\partial x} + \frac{\partial B}{\partial y} = 0$. To determine A and B we must solve the next higher order problem, which has governing equations:

$$\begin{aligned}
\left(u_0\frac{\partial u_0}{\partial x} + v_0\frac{\partial u_0}{\partial y} + W_0\frac{\partial u_0}{\partial \zeta}\right) - v_1 &= -\frac{\partial p_1}{\partial x} + \frac{1}{2}\left(\frac{\partial^2 u_1}{\partial \zeta^2} + 2\frac{\partial^2 u_0}{\partial \zeta \partial \eta}\right) \\
\left(u_0\frac{\partial v_0}{\partial x} + v_0\frac{\partial v_0}{\partial y} + W_0\frac{\partial v_0}{\partial \zeta}\right) + u_1 &= -\frac{\partial p_1}{\partial y} + \frac{1}{2}\left(\frac{\partial^2 v_1}{\partial \zeta^2} + 2\frac{\partial^2 v_0}{\partial \zeta \partial \eta}\right) \\
0 &= -\frac{\partial p_1}{\partial \zeta} - \frac{\partial p_0}{\partial \eta} \\
\frac{\partial u_1}{\partial x} + \frac{\partial v_1}{\partial y} + \frac{\partial W_1}{\partial \zeta} + \frac{\partial W_0}{\partial \eta} &= 0
\end{aligned}$$

We can again combine the $x-$ and y–momentum equations to find an inhomogeneous differential equation for $\Lambda_1 = u_1 + iv_1$, analogous to equation (22):

$$\begin{aligned}
\frac{\partial^2 \Lambda_1}{\partial \zeta^2} - 2i\Lambda_1 &= 2\Big[\frac{\partial p_1}{\partial x} + i\frac{\partial p_1}{\partial y} + u_0\frac{\partial u_0}{\partial x} + v_0\frac{\partial u_0}{\partial y} + W_0\frac{\partial u_0}{\partial \zeta} - \frac{\partial^2 u_0}{\partial \zeta \partial \eta} + \\
&\qquad + iu_0\frac{\partial v_0}{\partial x} + iv_0\frac{\partial v_0}{\partial y} + iW_0\frac{\partial v_0}{\partial \zeta} - \frac{\partial^2 v_0}{\partial \zeta \partial \eta}\Big]
\end{aligned} \tag{38}$$

As in the single–scale expansion, we find secular forcing terms in this equation that resonate with the homogeneous solution, proportional to $\exp[-\zeta(1+i)]$. In order to ensure that our perturbation expansion in ϵ does not become disordered, we insist that all secular terms sum to zero. This is the condition for the existence of a well–behaved expansion in Rossby number, so it is called the *solvability condition.* It is:

$$\frac{\partial \lambda}{\partial \eta} + \frac{1}{1+i}\left(U\frac{\partial \lambda}{\partial x} + V\frac{\partial \lambda}{\partial y}\right) - \lambda\left(C(x,y,\eta) + \frac{\omega}{2i(1+i)}\right) = 0 \tag{39}$$

In this, $C(x, y, \eta)$ is our constant of integration from equation (37) for the linear Ekman pumping. We find $C(x, y, \eta)$ by forming a vorticity equation from our $x-$ and y–momentum equations (34) and (35). We are interested in the transitional region between the boundary layer and the far field, which is far enough from the boundary that things are no longer changing over scales of ζ. The $O(\epsilon)$ vorticity equation is:

$$u_0\frac{\partial \omega_0}{\partial x} + v_0\frac{\partial \omega_0}{\partial y} - \frac{\partial W_0}{\partial \eta} = 0$$

Since we are looking outside of the boundary layer, $u_0 = U$ and $v_0 = V$, and we can integrate to find that:

$$W_0(x,y,\eta)\Big|_{\zeta\to\infty} = C(x,y,\eta) = \left(U\frac{\partial \omega}{\partial x} + V\frac{\partial \omega}{\partial y}\right)\eta + C'(x,y) \tag{40}$$

As before, we use the no normal flow boundary condition at the bottom boundary to find $C'(x, y) = -\frac{1}{2}\omega$. We see very clearly from this method that the Ekman pumping to $O(\epsilon)$ should be proportional to the *vorticity advection* in the interior.

We can now use the method of characteristics to convert the solvability condition, a partial differential equation, to a group of ordinary differential equations. We define a characteristic parameter s such that:

$$\frac{\partial x}{\partial s} = U \tag{41}$$

$$\frac{\partial y}{\partial s} = V \tag{42}$$

$$\frac{\partial \eta}{\partial s} = 1 + i \tag{43}$$

Our solvability condition (39) now reduces to:

$$\frac{\mathrm{d}\lambda}{\mathrm{d}s} - \lambda\left((1+i)C(x,y,\eta) - i\frac{1}{2}\omega\right) = 0 \tag{44}$$

It is straightforward to integrate an equation of this form and find λ, but in order to do so we need an expression for $C(x, y, \eta)$, which requires that we know the specific form of the far field velocities U and V. Unfortunately, this is as far as it is possible to go in the general case. To see how this method would work for known velocities, let's consider the same flow that we discussed in Section 4: $U = \cos ky$ and $V =$ constant. Equations (41) and (43) give $y = Vx + y_0$ and $\eta = (1+i)s$. Putting these into $C(x, y, \eta)$ from equation (40), we can solve equation (44) by direct integration in s. One finds eventually that:

$$\begin{aligned}\lambda \quad = \quad & \lambda_0 \exp\Big[-(1+i)Uk\eta \sin ky - \frac{U}{V}(2i - \frac{1}{2})\cos ky + \\ & + \frac{U}{V}(2i - \frac{1}{2})(\cos(ky - \frac{Vk\eta}{2})\cosh\frac{Vk\eta}{2} + +i\sin(ky - \frac{Vk\eta}{2})\sinh\frac{Vk\eta}{2}\Big]\end{aligned}$$

This solution is only accurate to order ϵ, so we approximate all of the functions containing an $\eta = \epsilon\zeta$ to order ϵ, for example $\sinh x \approx x$. To find the changes induced by advection in the thickness of the boundary layer, we apply our boundary conditions at $\zeta = \eta = 0$ to find λ_0 and take the real part of the exponential above, giving:

$$\Lambda \propto \exp\left[-\zeta + \epsilon\zeta\frac{1}{4}\omega\left(1 - \frac{2V^2}{U^2 + V^2}\right)\right] \tag{45}$$

This is exactly the same boundary layer thickness that we calculated using the single–scale expansion, shown in equation (29). The fact that one can calculate it in two different ways substantially reinforces one's confidence that it might be correct.

Unfortunately, the two–scale method proved to be both less general and more complicated than a simple single–scale expansion. However, it was useful for confirming our previous efforts. Moreover, it provided us with an intuitive understanding of why the Ekman pumping should be proportional to the vorticity advection in the interior flow.

6 Conclusions

In this study, we found the weakly nonlinear correction to the Ekman boundary layer of an arbitrary horizontal flow over a plate. Previous studies had concentrated on unidirectional flows of the form $U = U(y)$, $V = 0$. Guided by the intuition that the Ekman pumping out of the boundary layer should be related to the advection of vorticity, a quantitiy that goes to zero in the case of unidirectional flow, we performed an expansion in Rossby number. We found that both the structure of the boundary layer and the Ekman pumping were strongly effected to order ϵ by advection. We derived a general expression for the weakly nonlinear Ekman pumping for an arbitrary far–field flow, and studied a simple example in detail. In our example, both the Ekman pumping and the modification to the thickness of the boundary layer were shifted in phase by the introduction of vorticity.

There are a number of interesting applications for continued research in this area. Repeating these calculations for a stress boundary condition, analgous to the surface of the ocean, should be straight–forward mathematically. Once that is done, there are a number of high–resolution data sets already collected that might allow us to see if the non–linear corrections derived here are important in oceanographic contexts. In areas of very high wind stress, such as storms, or in areas where there is a strong and narrow current like the Gulf Stream, these corrections may prove to be significant.

I would like to acknowledge the help of my advisor Joe Pedlosky, for his advice and assistance, and for the stimulating principle lectures; the rest of the GFD faculty, and the GFD fellows for the wonderful atmosphere of Walsh Cottage. Finally, I would like to thank Claudia Cenedese and John Whitehead for all their efforts organizing the summer school.

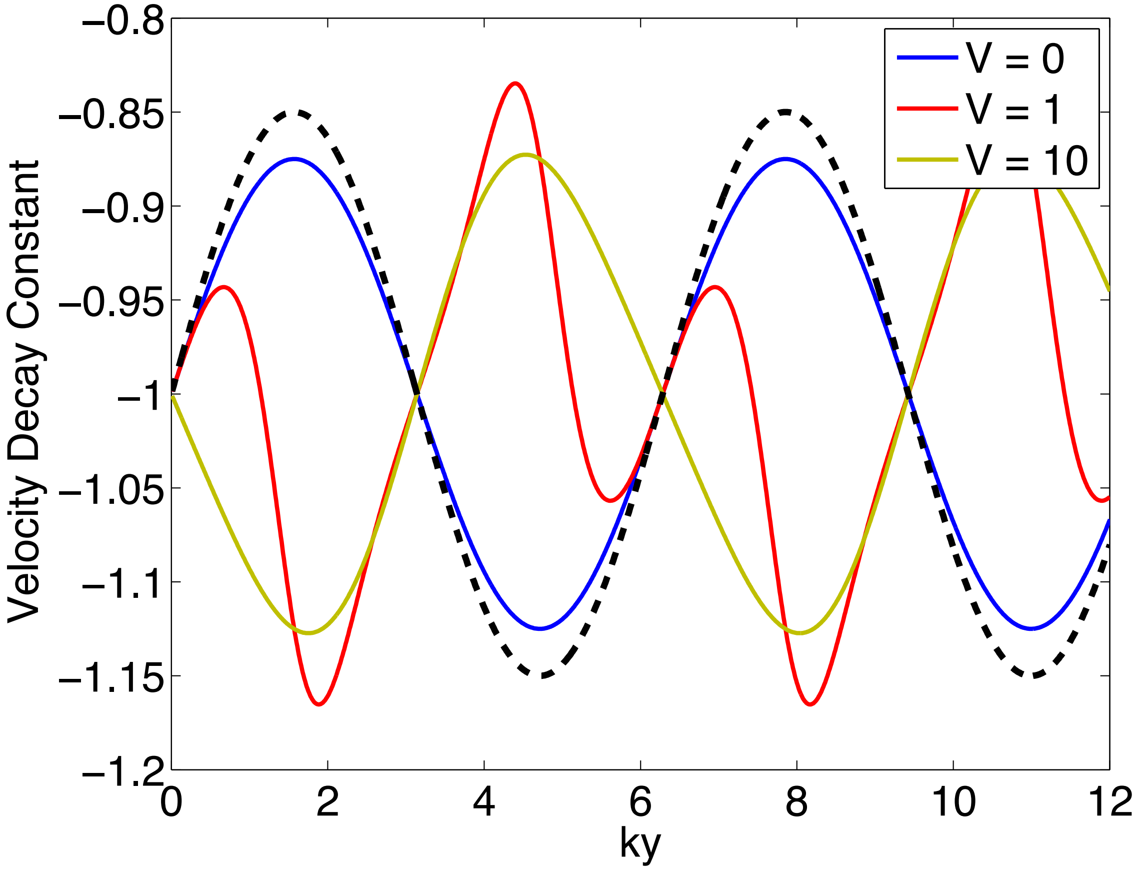

Figure 2: Modification of the boundary layer thickness for varying advection strength. The base flow in this figure is $U = \cos ky$, $V = \text{constant}$. Notice how for low cross–stream velocities, shown in blue, the modification boundary layer thickness is proportional to the vorticity, shown in the dashed line. For high cross–stream velocities, shown in yellow, the modification of the boundary layer thickness is opposite to the vorticity.

Bibliography

[1] G.S.Benton, F.B.Lipps, and S.-Y. Tuann. The Structure of the Ekman Layer for Geostrophic Flows with Lateral Shear. *Tellus*, 1964.

[2] V.W.Ekman. On the influence of the Earth's rotation on ocean-currents. *Arkiv for Matematic, astronomi, och fysik*, (11), 1905.

[3] A. Eliassen. On the Ekman layer in a circular vortex. *Journal of the Meteorological Society of Japan*, 1971.

[4] J.E.Hart. A note on the nonlinear correction to the Ekman layer pumping velocity. *Physics of Fluids*, 12(1):131-135, 2000.

[5] J.Pedlosky. GFD Summer School Lectures — Boundary Layers. This volume, 2007.

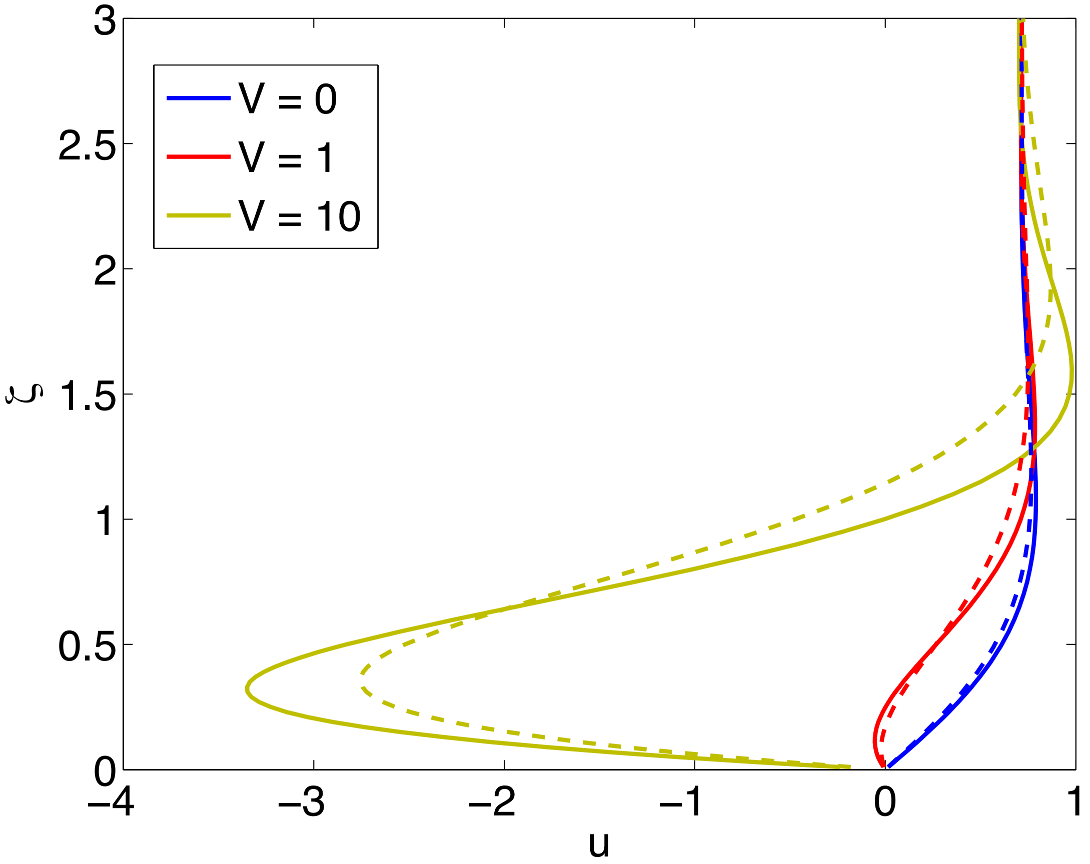

Figure 3: x–velocity in the boundary layer for varying strengths of advection for $ky = \frac{\pi}{4}$ in out example velocity field of $U = \cos ky$, $V =$ constant. Dashed lines indicate the linear Ekman solution, and solid lines indicate weakly nonlinear solution. All of the velocities have been rescaled by the maximum far–field velocity. Note that nonlinear effects may thicken or thin the boundary layer at a given location, depending on the strength of the advection.

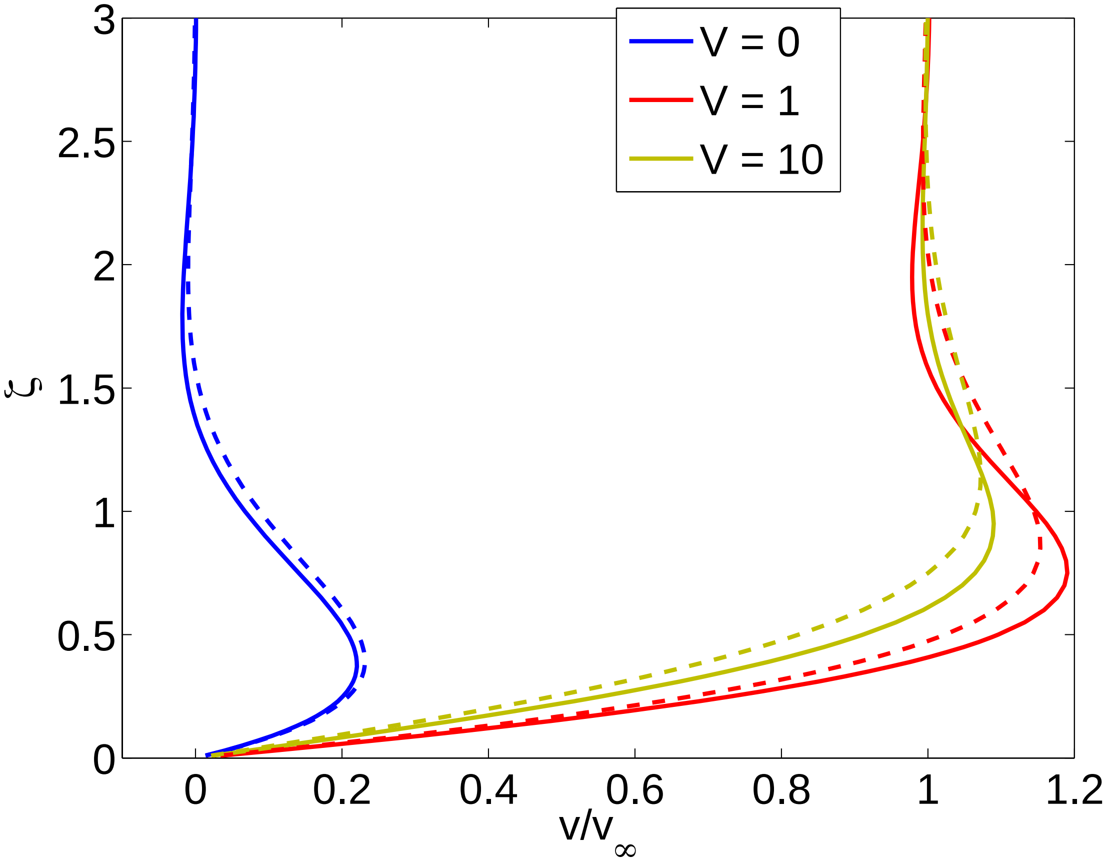

Figure 4: Advection velocity in the boundary layer for varying strengths of advection for $ky = \frac{\pi}{4}$ in out example velocity field of $U = \cos ky$, $V =$ constant. As in Figure 3, dashed lines give the linear solution and solid lines give the weakly non-linear solution. For the strong advection case of $V = 10$, the velocities have been rescaled by V.

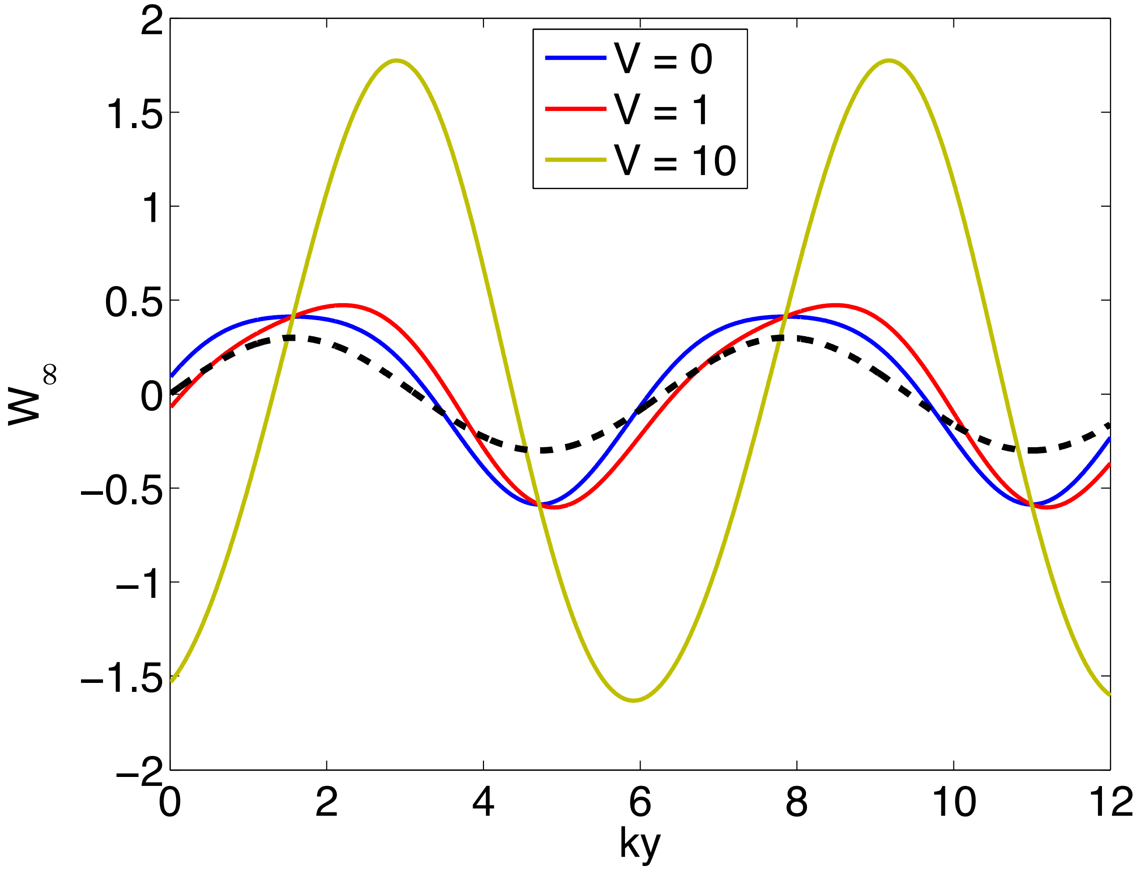

Figure 5: Ekman pumping, W_∞. The dashed black line gives the vorticity of the far–field flow. The introduction of vorticity advection shifts the phase of the Ekman pumping by $\pi/2$. Note also that there is a weak asymmetry in the Ekman pumping between areas of positive and negative vorticity.

An experimental study of the circular internal hydraulic jump

Iva Kavčič[1]

University of Zagreb, Croatia

Advisor: Steve Thorpe

Bangor University, Wales, UK

Abstract. The results of an experimental investigation of the circular internal hydraulic jump in two-layer fluid are presented, with focus on the dependence on the flow rates and density differences between fresh and salty water used. For the lower flow rates the stable circular patterns, consisted of three or four well-formed stationary waves, were observed, while for the higher flow rates their axial symmetry was lost by deformation of entire wave pattern in cusp-like features. This stable, laminar regime lasted 4-5 minutes, after which instabilities started to develop, finally breaking the wave patterns in turbulent motion. The radii of stationary waves were measured, and the depths of the fluid inside and outside the jump were calculated in order to find the critical values of jump radius, fluid depth and Froude number just before the onset of instabilities. While the values of jump radius, fluid depth and Froude number inside the jump (reaching values of up to 12-14) strongly depend on variations in flow rate and density difference, this dependence does not seem to be so strong for the Froude number outside the jump. Their values are below 1, due to dispersion relation for the internal waves in two-layer fluid used to calculate the fluid depth outside the jump. Comparison of results with the analytic Watson's (1964) model for the jump in the single-layer flow indicates the existence of similar functional dependence for the two-layer fluid. Finally, the experiments where the sharp density difference was smoothed by diffusion indicate that the stationary, laminar waves cannot occur in a continuously stratified fluid.

Keywords: Hydraulic jump; Stationary waves; Stratified fluid

1. Introduction

The circular hydraulic jump may arise when a fluid jet falling vertically at moderate Reynolds number strikes a horizontal plate (a usual fluid dynamics phenomenon, for instance often observed in a kitchen sink). Fluid is spread radially in a thin layer, until reaching a radius at which the layer depth increases

---

[1] E-mail: ivakavc@gfz.hr

abruptly. Theoretical predictions for the jump radius based on inviscid theory were first presented by Rayleigh (1914) in a paper on hydraulic jumps and bores. The dominant influence of fluid viscosity on the jump radius was elucidated by Watson (1964), who developed an appropriate description of the boundary layer on the impact plate. Watson (1964), however, has not accounted for another important influence on the jump radius in single-layer flow: the surface tension. Bush and Aristoff (2003) reviewed Watson's study of the circular hydraulic jump, and later illustrated the influence of surface tension on the jump radius in their experimental study (Bush et al., 2006). Subsequent studies of the circular jump have focused principally on describing the boundary layer separation and closed circulation cells ("rotors"), which may cause the changes of surface slopes and stable shapes other than circular, especially when fluids other than water are used (Watson, 1964; Craik et al., 1981; Bowles and Smith 1992; Bohr et al., 1993; Higuera, 1994; Bush and Aristoff, 2003; Bush et al., 2006).

The surface tension, however important it may be in the single-layer jumps, is negligible at the interface between the layers in the internal circular hydraulic jumps. These are produced when a denser fluid falls vertically onto a horizontal surface submerged beneath a deep layer of less dense, miscible fluid, radially spreading from the point of impact, at the typical distance of a few centimetres from it. Recent theoretical and numerical studies of internal hydraulic jumps in stably stratified two-layer miscible flows have been focused on the entrainment and mass transfer between the layers (Holland et al., 2002), and development of the proper parameterizations for description of energy dissipation in turbulent flows (Hassid et al., 2007). As seen from above, continuously stratified fluids are often represented as being in two layers. The subject of whether the stationary internal hydraulic jumps can occur in a stratified flow beneath of an unstratified stationary layer may be of some importance in relation to the jumps of much greater size that are postulated to occur in flows through channels on the flanks of mid-ocean ridges and through passages connecting the deep ocean basins (Thurnherr et al., 2005; Thorpe, 2007), although there are as yet no observations with sufficient resolution to establish the presence or otherwise of such transitions. Another example of what is described as the stationary internal hydraulic jump in the lee of The Sierra Nevada can be found in the book of Lighthill (1978; his Fig. 117).

This experimental study of the circular internal hydraulic jump attempts to gain insight in this interesting problem and to answer to some of the above questions, extending experimental work with two-layer fluid conducted by S. A. Thorpe. The report is organized as follows: first, a description of the experimental apparatus, with the details of representative experiments and observed jump patterns is given in Section 2. The calculated quantitative parameters are described in Section 3, followed by the conclusions and recommendations for future experiments in Section 4.

2. Experiments and observations

2.1. Experimental set-up

The simplified sketch of apparatus is given in Fig. 1. Salty water of density ρ_2 was pumped (Fig. 1, 5) from the bucket (Fig. 1, 6) through the nozzle of radius $a_{noz} = 0.113$ cm (Fig. 1, 3) into the square glass tank (Fig. 1, 1; tank dimensions were 58.4×58.4 cm). Prior to the start of experiment it was necessary to establish the uniform flow of salty water by removing the bubbles of air. For that purpose an additional plastic tube with the T-junction (Fig. 1, 4) was used, directing the salty water in another bucket until the bubbles went out of the plastic tube. After that the flow was redirected to the nozzle for a few moments to push out the air from it. The nozzle was elevated to the height of about 0.3 cm from the tank bottom (to minimize any mixing between the descending with the surrounding fluid). Then, the tank was filled with fresh water of density ρ_1 to a depth of 3 cm, and left undisturbed for 15-20 minutes so the water could come to rest.

The pump was calibrated for the range of flow rates (Q) from 0.95-8.8 cm^3s^{-1} (pump settings 0-999). However, it was observed that their values were somewhat smaller with the full experimental setup. Apparently, the small nozzle radius, rather than the higher density of salty water used in experiments mostly affected the flow rate. The density of fresh water was almost constant through all experiments ($\rho_1 \approx 0.99825$ gcm^{-3}). A plastic plate (Fig. 1, 2), covered with paper, was used both as support for the nozzle (in order to ensure that the impinging fluid was perpendicular to the tank bottom) and as the shadowgraph screen for observing and recording the observed patterns. They were made visible by the parallel light beam projected (Fig. 1, 9) onto (and reflected from) the mirror (Fig. 1, 7) below the tank, angled at $\alpha = 45°$ from the horizontal, and recorded with the Nikon digital photo camera (Fig. 1, 8) placed on the ladder above the tank. The photo of experimental setup is given in Figure 2 (camera not shown).

The range of flow rates used (also measured), and the corresponding speeds (v_{noz}) and Reynolds number (Re_{noz}) of flow in the nozzle are shown in Table 1. Here the Reynolds number is calculated as

$$Re_{noz} = \frac{v_{noz} a_{noz}}{\upsilon}, \tag{1}$$

where

$$v_{noz} = \frac{Q}{a_{noz}^2 \pi}, \tag{2}$$

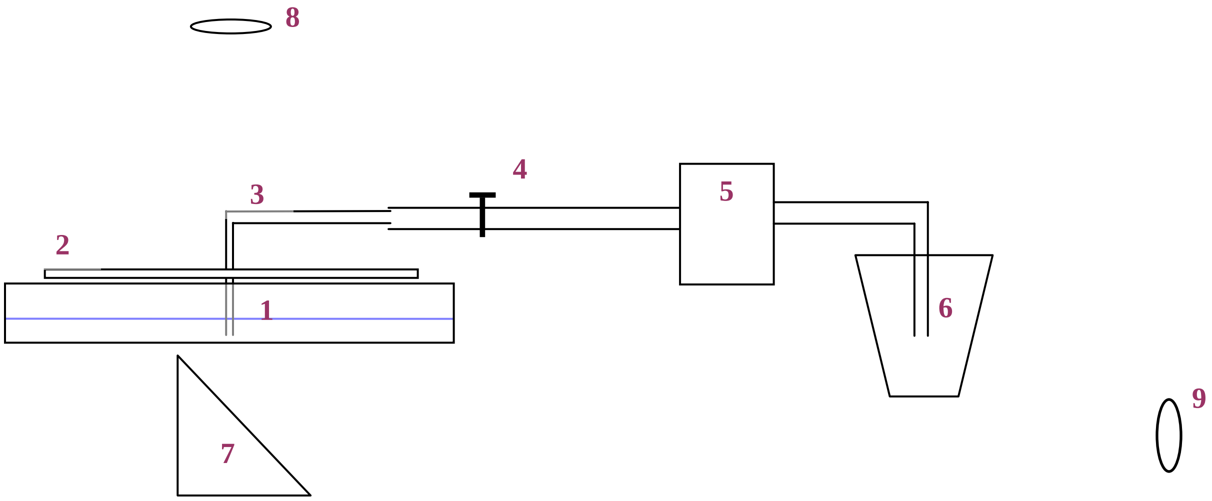

Figure 1. The simplified sketch of experimental apparatus: 1. Square tank: a_t = 58.4 cm, h_t = 5 cm, filled with fresh water (ρ_1); 2. Screen; 3. Nozzle (a_{noz} = 0.113 cm), at d_a = 0.3 cm; 4. Plastic tube with T-junction; 5. Pump; 6. Bucket with salty water (ρ_2, $\rho_2 > \rho_1$); 7. Mirror, α = 45°; 8. Camera; 9. Projector

Setting	**Q (cm^3s^{-1})**	**v_{noz} (cms^{-1})**	**Re_{noz}**
50	0.398	9.917	111.64
100	0.828	20.625	232.20
150	1.258	31.332	352.73
200	1.675	41.720	469.68
250	2.101	52.343	589.27
300	2.520	62.790	706.89

Table 1. Flow rates, flow speeds in the nozzle and Reynolds number of the flow in nozzle.

a)

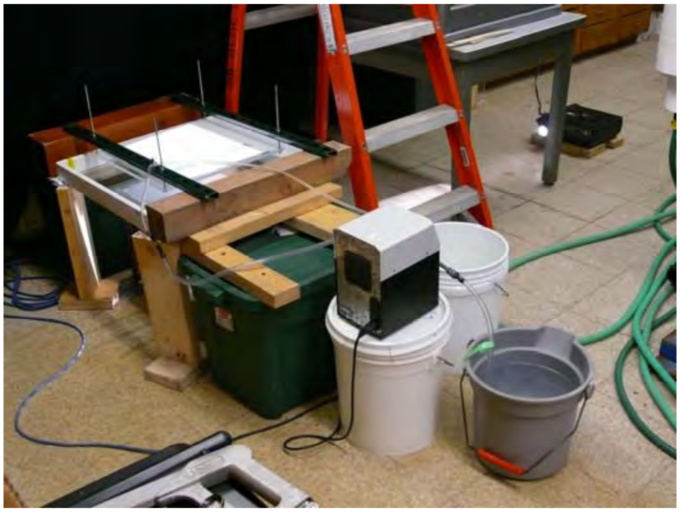

b)

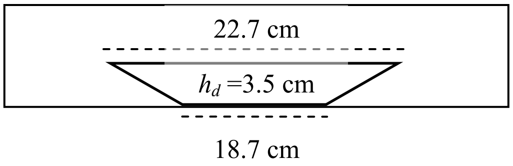

Figure 2. (a) The photo of experimental setup; (b) Pie dish used to simulate the circular geometry, with h_d denoting its height.

and $\nu = 1.004\times10^{-6}$ m^{2}s^{-1} is the value of kinematic viscosity of fresh water at 20 °C. Since the range of temperature of both fresh and salty water used in these experiments was approximately 18–23 °C, and the salty water was on average about 5-10 % denser than fresh, the above value of kinematic viscosity can be used with reasonable accuracy.

Two sets of experiments were made: the first with the higher density of salty water ($\rho_2 \approx 1.10544$ gcm^{-3}) for all flow rates in Table 1, and second using $\rho_2 \approx 1.05044$ gcm^{-3}, for pump settings 100 and 200. Each of them (apart from the one with the highest flow rate, 300), was performed at least twice: once in the square tank, and the other time with the Pyrex glass pie dish (put into the tank, dimensions and geometry shown in Fig. 2a) needed to simulate the radially symmetric boundaries. When conducting experiments with the pie dish, the initial height of fresh water was set at about 4 cm (≈ 5 mm deeper than the height of the pie dish) so that the fresh water covered its edge. When emptying the tank at the end of the experiment, it was observed that in the case of lower flow rates (settings 50-200) almost all of the salt water remained in the pie dish. Fresh water was effectively pushed out by salty water without the return circulation over the dish edge. At the higher flow rates (settings 250–300) filling of the dish with salty water was quick, initializing relatively fast overflow over the dish edge and corresponding inflow of the fresh water.

2.2. Development of the circular jump

As can be seen from Table 1, the experiments were conducted in the range of moderate Reynolds numbers (order 10^2 - 10^3). After the preparations, described in Section 2.1, the flow of salty water was switched on. It produced a radially spreading density current that eventually reached the side walls and in which, at a few centimetres from the impinging jet, stationary circular waves were formed. Due to the difference in refractive indices of fresh and salty water it was possible to distinguish between the crests (bright bands) and troughs (dark bands) of stationary waves that formed the transition region between the interior and exterior flow. The time evolution of typical observed wave patterns is shown in Figs. 3 (an example for the square tank) and 4 (an example for the pie dish). In the square tank stationary waves were formed within first 10 s after the start , with radii from 0.8 to 3.5 cm (Fig. 3a, shown after ≈ 3 min after the start of experiment). When the pie dish was used, the wave patterns were formed ≈ 30 s after the start of experiment (Fig. 4a), with the similar range of wave radii.

In the first set of experiments ($\rho_2 \approx 1.10544$ gcm^{-3}), for both square tank and pie dish, the observed waves were circular for the pump settings 50-200 (see Table 1 for the corresponding Q and Re_{noz}) and formed of three (settings 50-150) or four bright rings (setting 200). The same was observed in the second set when the lower density ($\rho_2 \approx 1.05044$ gcm^{-3}) was used for flow rate Q_{100} (Fig. 3a). When the flow rate was increased to $Q_{250} = 2.101$ cm^{3}s^{-1} in the first, or to $Q_{200} = 1.675$ cm^{3}s^{-1} in the second set of experiments, the axial symmetry was lost in the cusp-like deformations (Fig. 4a). The higher flow rates (Q_{300} and Q_{250}, for the first and second set of experiments, respectively) lead to wave breaking almost instantly after the flow of salty water started. Since they could not produce stable laminar wave patterns in the experiments presented, they are not discussed in this report. Also, the symmetry of waves was, even at the lower flow rates, extremely sensitive to any variations from horizontal; consequently, great care was taken in levelling the system. The white spot in Figs. 3 and 4 is a hole drilled in the plastic plate, through which potassium permanganate was added in most of the experiments in order to detect a possible appearance of boundary layer separation and rotors. Although we did not observe any clear indication of rotors, potassium permanganate was very useful in determining the general circulation patterns in the tank or the pie dish.

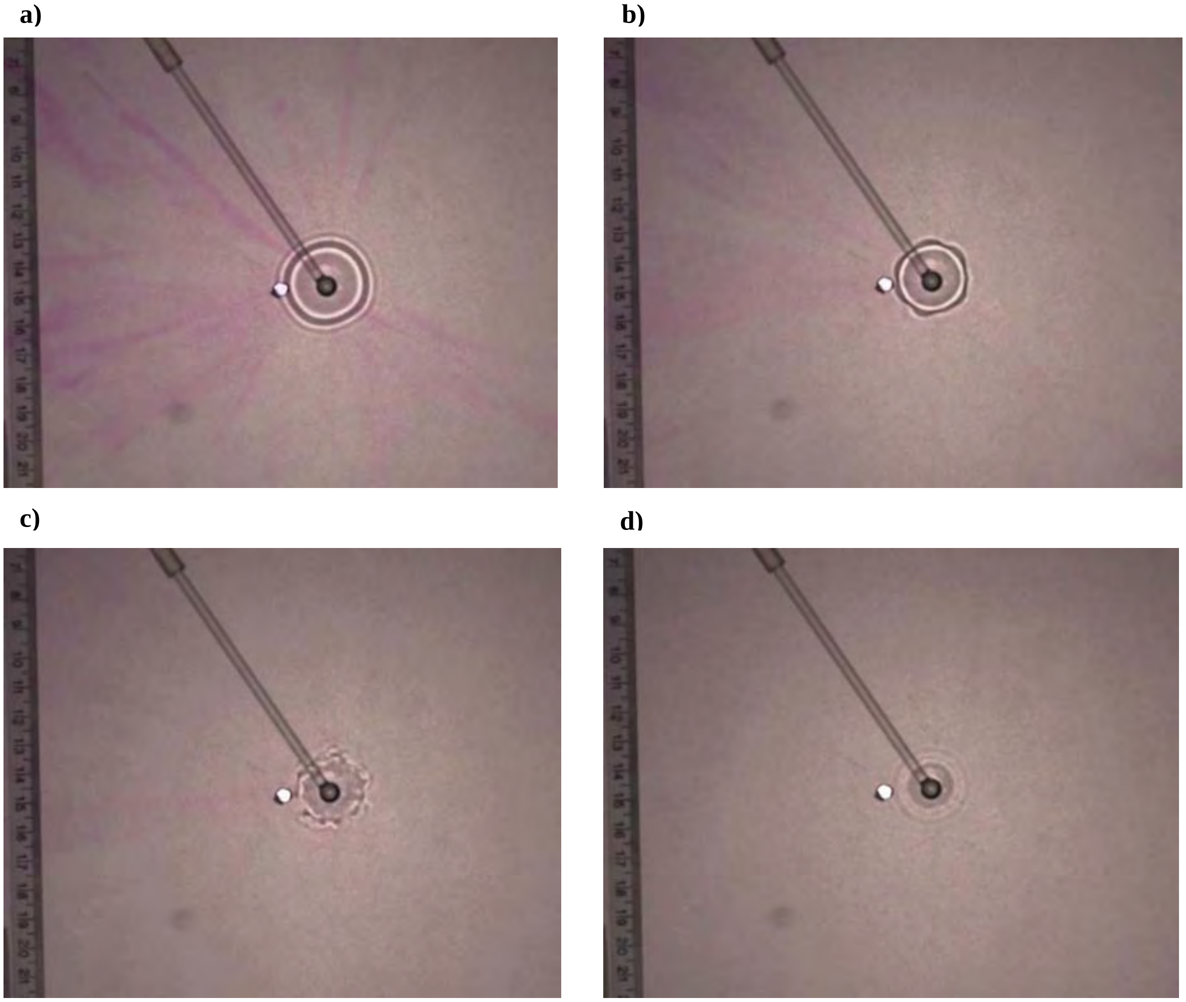

Figure 3. Observed jump patterns in the square tank at (a) 3 min 10 s, (b) 6 min, (c) 9 min 50 s and (d) 21 min 58 s after the start of experiment. Here $Q_{100} = 0.828$ cm^{3}s^{-1}, $Re_{noz} = 232.20$ and $\rho_2 = 1.05058$ gcm^{-3}.

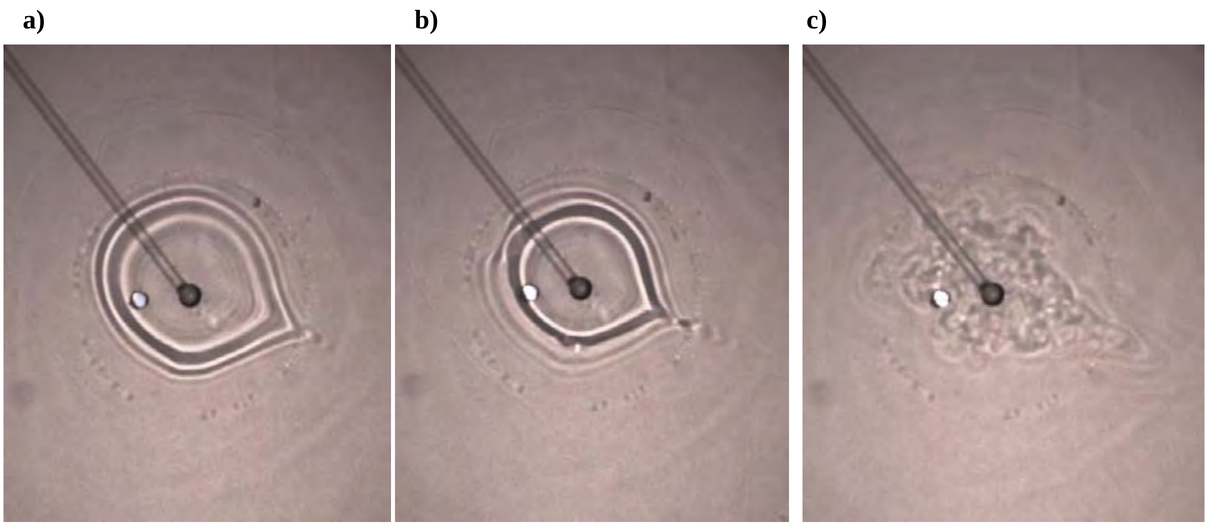

Figure 4. Observed jump patterns in the pie dish (a) 36 s, (b) 40 s and (c) 1 min after the start of experiment. Here Q_{250} = 2.101 cm^{3}s^{-1}, Re_{noz} = 589.27 and ρ_2 = 1.10511 gcm^{-3}. The size of photos is ≈ 10 cm×14 cm

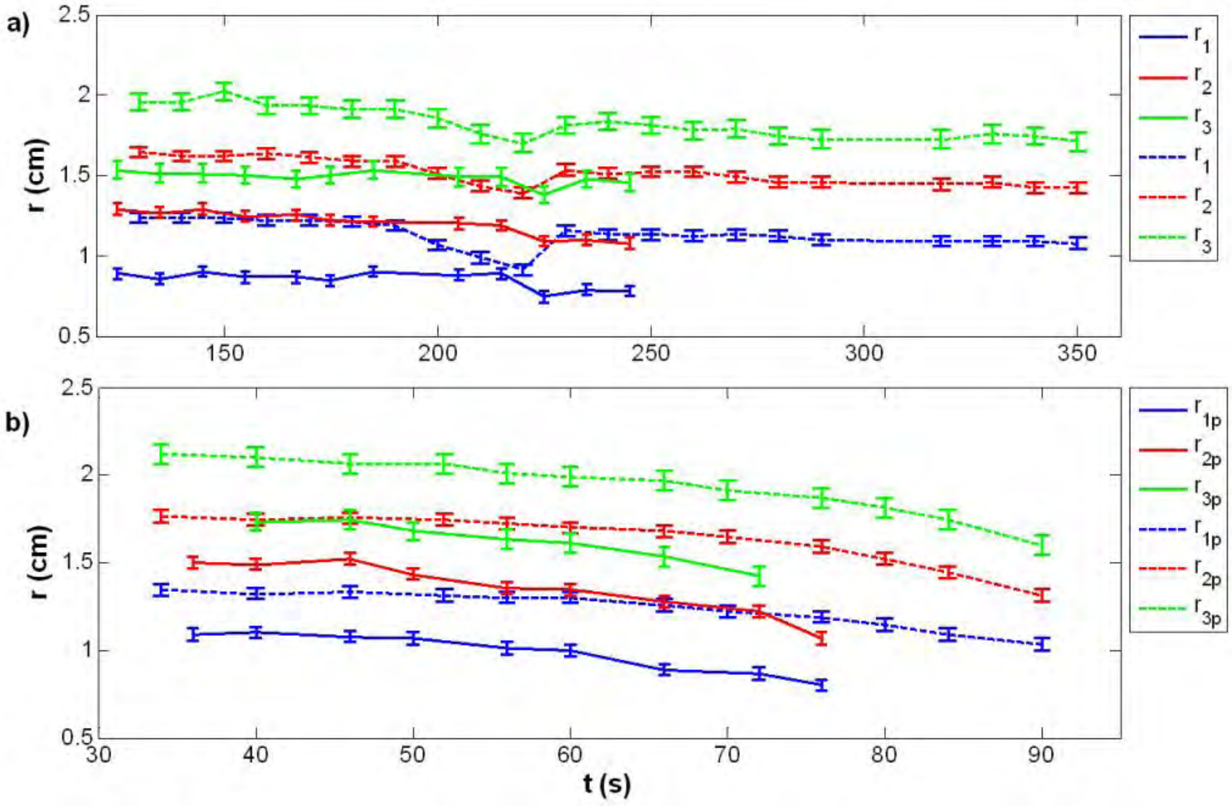

Figure 5. Time evolution of the standing wave radii (with error bars) for the pump setting 100: (a) without, and (b) with the pie dish for ρ_2 = 1.10527 gcm^{-3} (solid) and ρ_2 = 1.05058 gcm^{-3} (dashed). Here Q_{100} = 0.828 cms^{-1} and Re_{noz} = 232.20; r_1 and r_3 are the radii of the innermost and outermost waves, respectively.

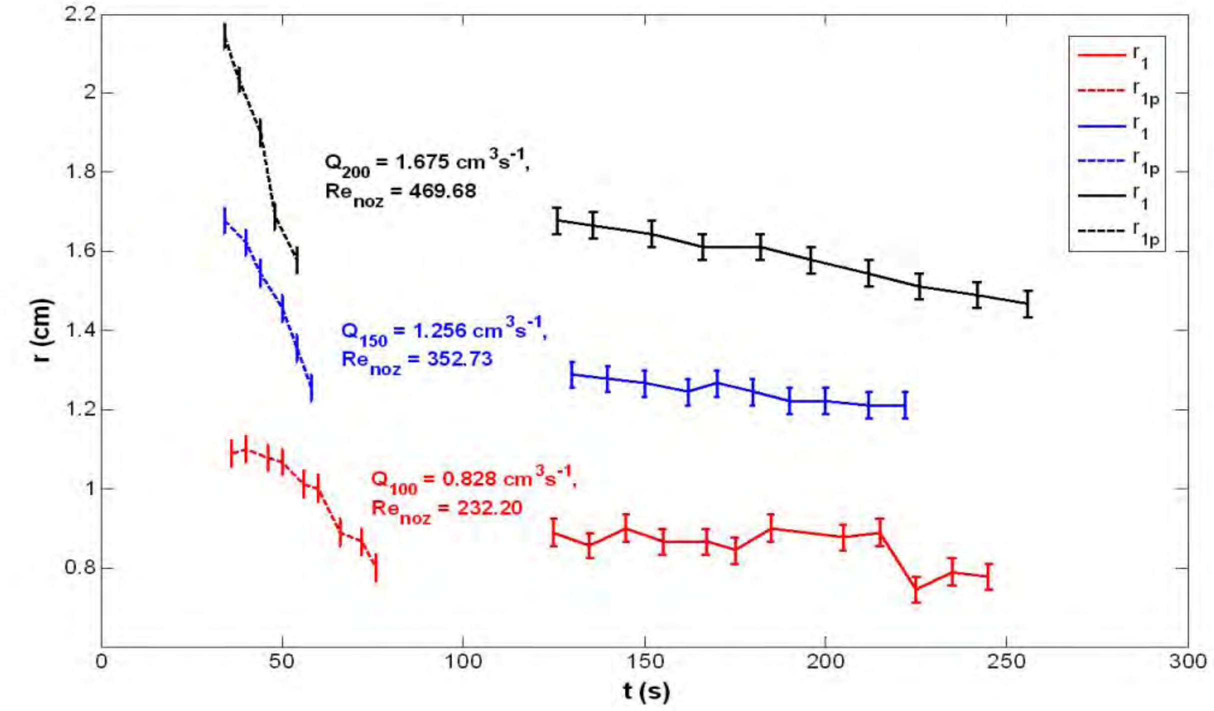

Figure 6. Time evolution of the innermost wave radius (with error bars), r_1, for the pump settings 100 (red, ρ_2 = 1.10527 gcm^{-3}), 150 (blue, ρ_2 = 1.10552 gcm^{-3}) and 200 (black, ρ_2 = 1.10507 gcm^{-3}), for the experiments without (solid) and with the pie dish (dashed).

The photos were processed by digitally extracting the cross-sections of wave patterns and detecting the positions of light maxima (in pixels), which then gave the estimates of the wave crests radii. To convert the radii from pixels to centimetres the translucent plastic ruler attached on top of the plastic plate (Fig. 1, 2, and Fig. 3) was used as the scale (at the resolution of photos used in experiments, 1 cm ≈ 45 pixels). Figure 5 shows the time evolution of wave crests radii (r_1, r_2, and r_3, respectively) for the flow rate Q_{100}, for both the higher (solid) and lower (dashed) density of salty water. In this, and all following plots as well, the results are shown after the time needed for the salty water to completely cover the bottom of the tank (≈ 2 min, Fig. 5a) or the pie dish (≈ 30 s, Fig. 5b), so the waves could be considered as quasi-stationary. The error bars (vertical ticks in plots) were calculated from the estimated uncertainties in determining the crests radii (± 2 pixels ≈ ± 0.04 cm for the inner waves, due to the stronger and thus better resolved light maxima, and ± 3 pixels ≈ ± 0.07 cm for the outer waves). It can be seen (Fig. 5) that the distance between the rings decreases as their radii increase, independently of the density difference, flow rate or geometry used. Also, the decreased density difference between fresh and salty water is responsible for increasing the wave radii for the same flow rate (Fig. 5, dashed lines). In Figure 6 a similar comparison is given for the various flow rates at the same density difference (only the innermost radius, r_1, is shown), showing that increasing the flow rate (from Q_{100} to Q_{200}) results in increase of wave crests radii (red, blue and black lines, respectively). Both Figures 5 and 6 show the main difference between the experiments without and with the pie dish, i.e. when the pie dish was used, the greater wave radii were observed, but their decreasing with time was faster (due to the faster filling with salty water). This rapidity of changes brings into question the assumption of waves being stationary in the pie dish, although the same assumption is valid in the square tank.

2.3. Transition from steady wavelike to turbulent flow

The stable wave patterns, described in Section 2.2, lasted for approximately 4 min for the salt solution of higher, and 5 min for the solution of lower density (Fig. 3a). After that time the outer band was deformed by the irregular undular instabilities moving around it, while the inner waves were still visible (Fig. 3b). After ≈ 1 min for the solution of higher, i.e. ≈ 1.5 – 2 min for the solution of lower density (Fig. 3c) the inner waves also collapsed and the motion became turbulent. This motion appeared to be organized in the forms looking alike the flower petals that were moving in groups around, and bursting in and out of the deformed outer band (Fig. 3c). As the turbulent mixing decreased the density differences, the flow eventually calmed (Fig. 3d). Experiments with the tank only therefore lasted from 30-50 min (depending on the flow rate) and the photos were taken initially every 10 s, and after that every 15-30 s as the flow became steadier. When the pie dish was used, the onset of instabilities was after ≈ 1 min after the start of experiment (Fig. 4b). Also, the transition between the laminar and turbulent regime happened almost instantly (within a few seconds), leading to the well developed turbulent forms (Fig. 4c). Because of the faster dynamics photos were initially taken every 5 s, and later every 10-15 s, and experiments lasted approximately 5 min.

The last values of wave crests radii in Figs. 5 and 6 are those estimated just before the onset of undular instabilities deformed the outermost wave (Figs. 3b and 4b). They, and all the parameters that will later be derived from them, will be referred as the "critical values". Besides increasing the wave radii for the same flow rate, it can be seen that the decreased density difference between fresh and salty water also postpones the onset of instabilities. For the flow rate Q_{100} (Re_{noz} = 232.20), in the square tank the radii of last undisturbed waves were estimated 240 s after the start of experiment for $\rho_2 \approx 1.10544$ gcm^{-3} (Fig. 5a, solid), and 350 s for $\rho_2 \approx 1.05044$ gcm^{-3} (Fig. 5a, dashed). As commented in Section 2.2, the duration of stable regime is shorter when the pie dish is used in experiments (Fig. 5b; ≈ 76 s for $\rho_2 \approx$ 1.10544 gcm^{-3}, solid, and 90 s for $\rho_2 \approx 1.05044$ gcm^{-3}, dashed). Interestingly, the onset of instabilities does not seem to depend on the increase of flow rates, and therefore the Reynolds numbers of the flow (Fig. 6).

2.4. Experiments with continuous stratification

The experiments in two-layer fluid, described above, were later modified in order to investigate whether the internal hydraulic jump can occur in a continuously stratified fluid. Two such experiments were made (only in the pie dish, at Q_{150} = 1.258 cm^{3}s^{-1} and Re_{noz} = 352.73), one for each mean density of salty water used ($\rho_2 \approx$ 1.10544 gcm^{-3} and $\rho_2 \approx$ 1.05044 gcm^{-3}). To cover the distance between the nozzle and the pie dish bottom (about 3 mm of depth), the pie dish was initially filled with the salty water for approximately 85 s. This layer of salty water was then let to diffuse for at least two hours so the continuous density gradient between it (below) and fresh water (above) could be established. Since the above layer of fresh water was ≈ 3 cm thick, it could be considered as being of uniform density. After that, the experiment was conducted as usual, and the observations were compared to the former ones with the same flow rate and sharp density interface. In both of these experiments, independently of density difference or flow rate used, no stable laminar wave patterns as in previous experiments were observed. Instead, the diverging flow instantly became turbulent with no appearance of a stationary, laminar, circular jump surrounding the point of impact of the jet on the horizontal plane. Figure 7 shows the comparison of experiments with sharp density discontinuity (two-layer fluid, Fig. 7a), and with the continuous stratification in the lower layer (Fig. 7b), both at ≈ 45 s after the start of experiment. According to these observations, the stationary, laminar hydraulic jump cannot be sustained in a continuously stratified layer in motion beneath a stationary layer of uniform density.

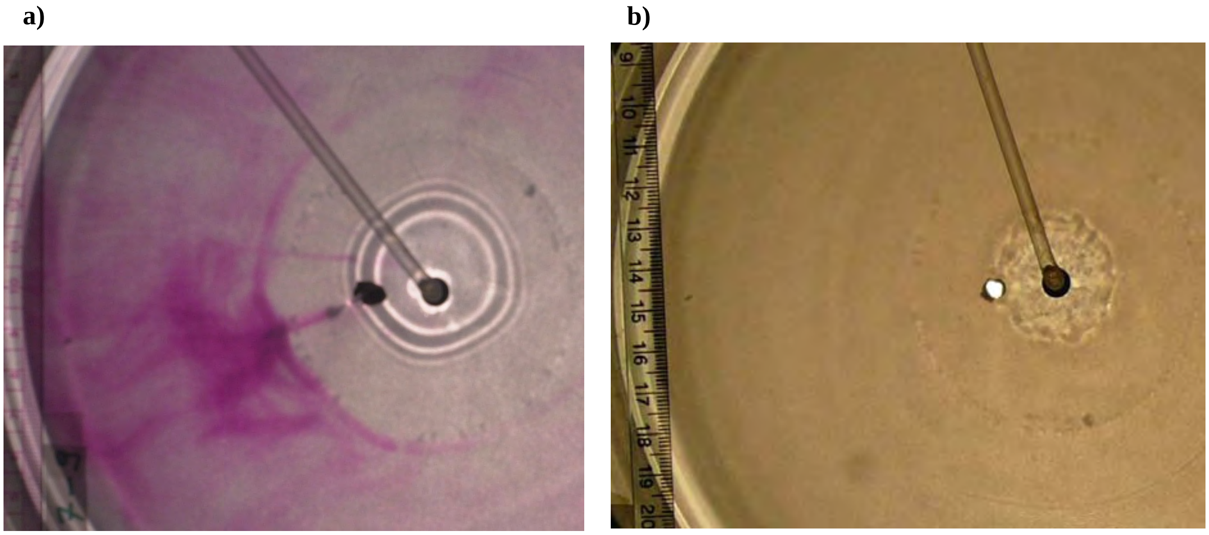

Figure 7. Observed jump patterns in the pie dish (a) in two layer fluid, and (b) with continuous stratification in the upper layer, both at ≈ 45 s after the start of experiment. Here Q_{150} = 1.258 cm^{3}s^{-1}, Re_{noz} = 352.73 and $\rho_2 \approx$ 1.10544 gcm^{-3}.

3. Parameter study

In this section we try to describe the observations in terms of some common parameters, which may also lead us to the conditions necessary for the development of instabilities in wave patterns. Furthermore, in Sec. 2 we saw that the difference in geometry of the problem (i.e. using the pie dish in experiments) affects the dynamics of observed waves. That brings us to the question: which are the common characteristics of these two types of experiments? As in Sec. 2, we will carry out this analysis first for the fixed density difference and different flow rates, and then we will compare results for the chosen flow rate, but with different densities of salty water. The main parameters we will use to describe the flow are:

1. Froude number inside (upstream), Fr_1, and outside (downstream) the jump, Fr_2. Here they are defined as

$$Fr_{1,2} = \frac{U_{1,2}^2}{g' H_{1,2}}. \tag{3}$$

U_1 and U_2 are the flow speeds inside and outside the jump, respectively, H_1 and H_2 are the corresponding depths of salty water, and g' is the reduced density. $U_{1,2}$ and g' can be calculated as:

$$U_{1,2} = \frac{Q}{2\pi R_{1,2} H_{1,2}}, \tag{4}$$

$$g' = g\delta_\rho, \ \ \delta_\rho = \frac{\rho_2 - \rho_1}{\rho_2}. \tag{5}$$

Here R_1 and R_2 are the radii within, and just outside the jump, determined from the estimated radii of wave crests as:

$$R_1 = r_1 - \frac{r_2 - r_1}{2}, \tag{6a}$$

$$R_2 = r_{3,4} + \frac{r_{3,4} - r_{2,3}}{2}, \tag{6b}$$

where the value of R_2 depends on the number of waves observed (3 for flow rates 50-150 and 4 for higher ones). In the first set of experiments ($\rho_2 \approx 1.10544$ gcm^{-3}) $\delta_\rho \approx 0.097$, and in the second ($\rho_2 \approx 1.05044$ gcm^{-3}) $\delta_\rho \approx 0.05$ for all flow rates. According to Eqs. 4 and 6, the flow speed is inversely proportional to the wave radii. When relating this to the distances between the rings (Section 2.2, Fig. 5), it can be seen that as the wave radii increase from the inner to outer wave, the flow slows down.

Since the direct measurements of H_1 and H_2 were not available, they had to be estimated. The mean thickness of the layer below the interface along which the waves were propagating against the flow, *h*, was calculated in two ways. One was to use the flow rate, *Q*, the time, *t*, and the surface of the tank or pie dish covered with salty water, $(A_1)_{T,P}$. The latter was estimated from the total surface, $(A)_{T,P}$, and R_1 as

$$h = \frac{Qt}{(A_1)_{T,P}}, \quad (A_1)_{T,P} = (A)_{T,P} - (R_1^2)_{T,P}\pi. \tag{7}$$

The another one, used further in this report, was to numerically estimate *h* from the dispersion relation for the phase speed (*c*) in two-layer, inviscid fluid (Thorpe, 2005) as

$$c^2 = \frac{g'}{k} tanh[kh], \quad k = \frac{2\pi}{\lambda}, \tag{8a}$$

where λ is the wavelength (estimated as the difference in successive wave radii), and *k* is the corresponding wave number. This relation is derived taking into consideration the assumptions of small amplitudes of internal waves (i.e. linear displacements), and no velocity shear between the layers (see Eq. 3.4, Thorpe, 2005). Since the observed waves were stationary, the phase speed had to be equal to the flow speed, *U*, given with (4). Then, (8a) becomes:

$$\frac{2\pi Q^2}{g' r^2 \lambda^3} = (kh)^2 \, tanh(kh). \tag{8b}$$

Rewriting Eq. 8 gives $Fr_2 = tanh(kh)/(kh),$ so the values of Fr_2 thus obtained are between 0 and 1 (corresponding to the limits for subcritical flow in 2D case). The depth outside the jump, H_2, was then taken as $H_2 = h(r = R_2)$. For the depth inside the jump, H_1, we took the value of H_2 at the first moment when the waves were well-formed, so their radii could have been measured from the photos. This was usually 10 s after the start of experiment in the tank, and 30-35 s in the pie dish (see Section 2.2). Furthermore, it was assumed that H_1 remained constant and was never greater than H_2.

2. The ratio of outer (H_2) and inner (H_1) depth of the salty fluid, *q*

$$q = H_2 / H_1 \tag{9}$$

Some of the calculated parameters for $\delta_p \approx 0.097$ are plotted in Figures 8-11. The dependence of R_2 on H_2 (and therefore on λ) is given in Fig. 8. It can be seen that, independently of the geometry of experiment used (Fig. 8; values in the tank, circles, or in the pie dish, asterisks), we find almost the same values of R_2 at the same H_2 (i.e. the same wavelengths at the same jump radii) for the given flow rate.

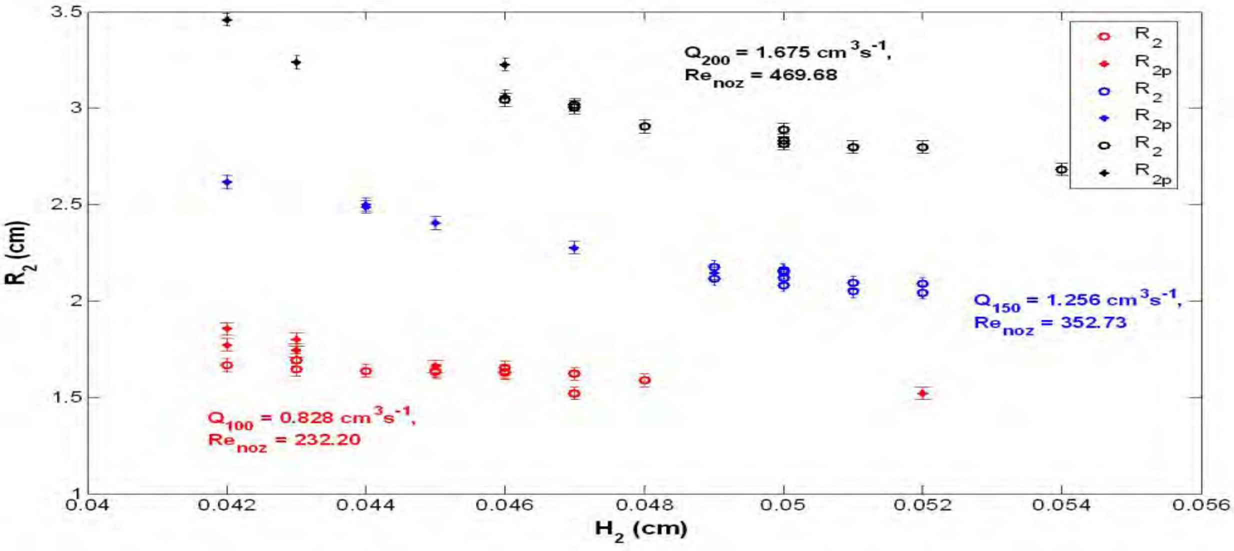

Figure 8. Dependence of outer jump radius, R_2 (with error bars), on H_2 for the pump settings 100 (red), 150 (blue) and 200 (black), for the experiments without (circles) and with the pie dish (asterisks). The rest as in Figure 6.

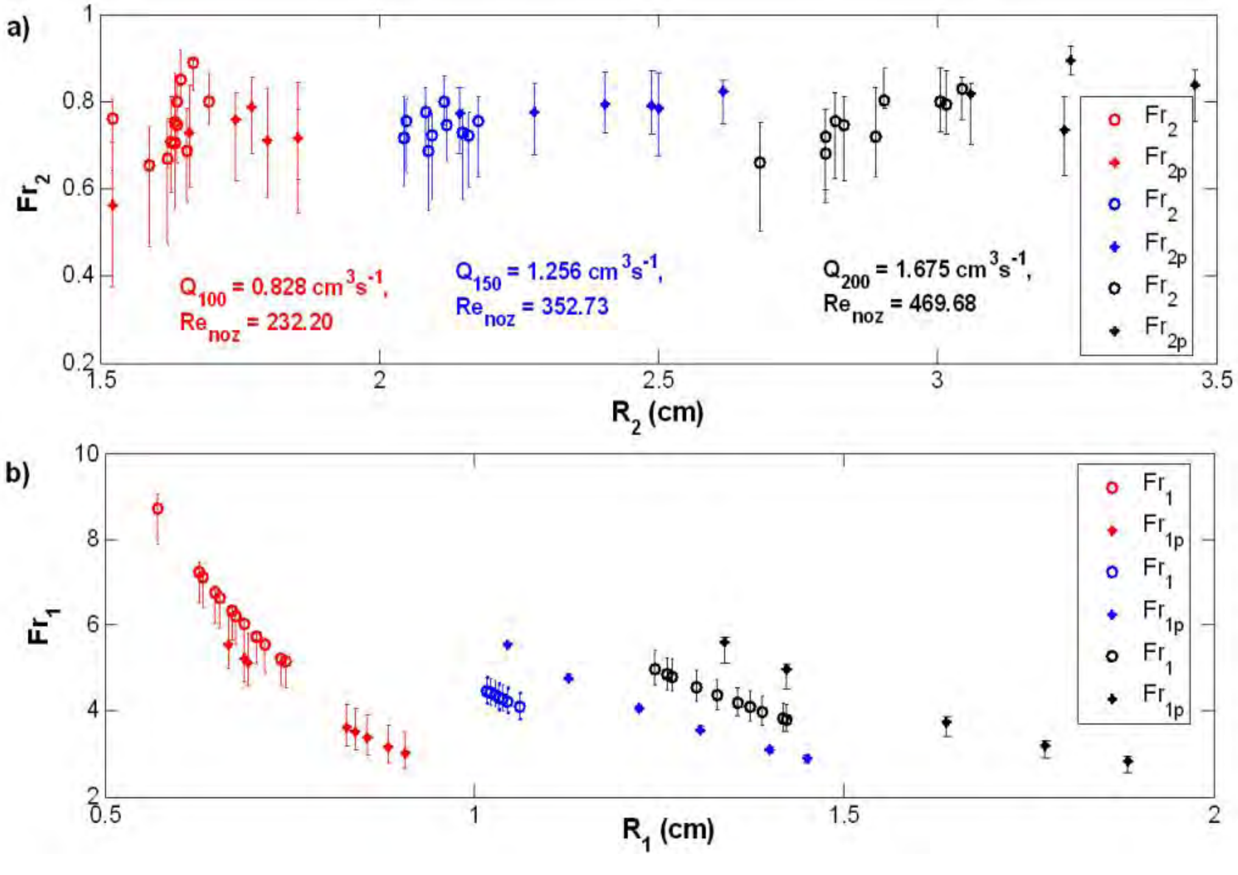

Figure 9. a) Downstream Froude number, Fr_2 (with error bars), versus outer jump radius, R_2; b) upstream Froude number, Fr_1 (with error bars), versus inner jump radius, R_1. The rest as in Figure 7.

Furthermore, as discussed in Section 2.2, the number of waves does not depend on the experimental geometry. From now on, we will refer to this behaviour of the observed waves as the "dynamical similarity" of wave patterns in the tank and the pie dish. The values of R_2 decrease with time (see also Figs. 5 and 6) and H_2 increases. The critical values of both R_2 and H_2, i.e. the values just before the onset of instabilities, seem to grow as the flow rate is increased.

According to Eq. 8, the values of downstream Froude number (Fr_2, Fig. 9a) are below 1, and there is no significant correlation with R_2. However, the upstream Froude number (Fr_1, Fig. 9b) clearly increases as R_1 decreases (the jump becoming narrower with time), achieving the maximal values of ≈ 8-10 for the lowest flow rate depicted (Q_{100}, red), and ≈ 5-6 for the higher flow rates (Q_{150}, blue; Q_{200}, black) just before the onset of instabilities (smallest R_1).

The time evolution of the depth ratio, q, is shown in Fig. 9. This increase of the fluid depth at the jump is more evident in the pie dish (asterisks, dashed lines), reaching values of ≈ 1.1-1.25 before transition to turbulent regime. Also, the values of q are smaller when only the tank is used due to the slower filling. However, these results have to be taken with some caution, since they are calculated from H_2, the estimate of which is mostly subject to uncertainties in determining the outer ring radii from photos.

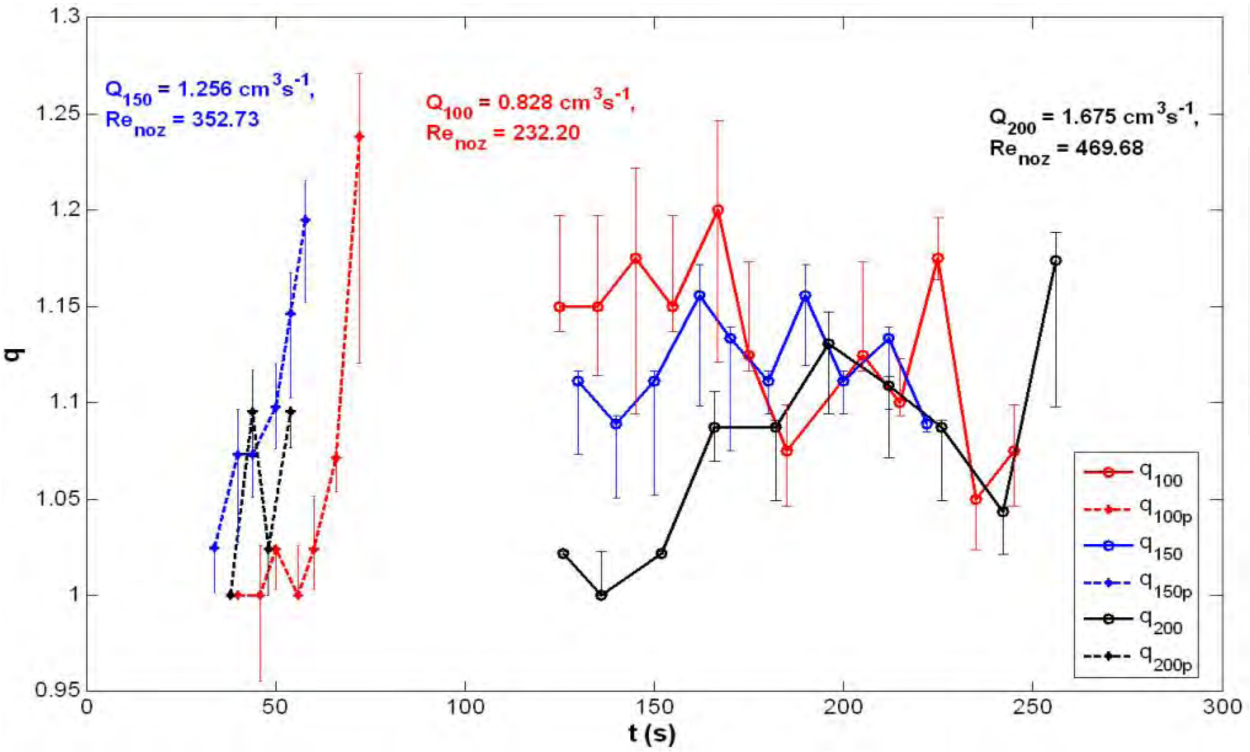

Figure 10. Evolution of q (Eq. 9), with error bars, in time. The rest as in Figure 7.

Watson (1964) derived the theoretical prediction of the jump position (R_1) in the single-layer, viscous fluid, for both the laminar and turbulent flows. He determined R_1 by equating the rate of loss of momentum to the thrust of pressure, not taking into account the surface tension (significant factor in the single-layer fluid but not present here), and assuming that $H_1 << H_2$. He also assumed that the radial width of the jump can be ignored, which may not be the case here (see Fig. 5 for comparison of r_3 and r_1). His comparison of theory and experiments is repeated here in Fig. 11, i.e. Watson's (1964) Fig. 4, with a being the nozzle radius (here a_{noz}), Re the Reynolds number of flow in the nozzle (here Re_{noz}), r_1 position of the jump (here R_1), and d the depth outside the jump (here H_2). In two-layer fluid experiments his theoretical relations can be written as (see his Eqs. 41 and 42):

$$A = \frac{R_1}{a_{noz}} Re_{noz}^{-1/3}, \tag{10a}$$

$$B = \frac{R_1 H_2^2 g' a_{noz}^2}{Q^2} + \frac{a_{noz}^2}{2\pi^2 R_1 H_2}. \tag{10b}$$

From Table 1 it can be seen that Reynolds numbers in our experiments are of order of magnitude less than his, due to the lower flow rates used. The observed R_1 are here from 0.5 to 2 cm (Fig. 9a), while in his experiments their range is ≈ 2.5-18 cm (1-7 in.). Measurements of d in his experiments gave results of ≈ 0.33-1.65 cm (0.13-0.65 in.), and here H_2 was estimated as ≈ 0.04-0.06 cm. The differences between his and our measurements result mainly in shifting our calculated values given in Eq. 9a to the right (Fig. 12) of his theoretical curve (Fig. 11). As for the values of B, their range (-1.55 to -2) is close to his values ($\bar{2}.5 - \bar{2}$, Fig. 11, equivalent to the span of -1.5 to -2 in Fig. 12), and also with similar, but slower, linear decay. These results indicate that the analogous theoretical relation might also hold for the jump radius of the problem studied here.

Figures 13 and 14 show some of the parameters already calculated using the density $\rho_2 \approx 1.10544$ gcm^{-3} ($\delta_\rho \approx 0.097$) for flow rate Q_{100}, but now compared with the results for reduced density of salty water, $\rho_2 \approx 1.05044$ gcm^{-3} ($\delta_\rho \approx 0.05$). We see that the functional dependence of R_2 on H_2 remains the same, i.e. there is "dynamical similarity" of experiments with and without the pie dish (Fig. 13a, asterisks and circles, respectively). However, the critical values of both R_2 and H_2 are greater for the lower density of salty water (Fig. 13a, black). There is also clear dependence of upstream Froude number, Fr_1, on density difference between salty and fresh water (Fig. 13b). As can be expected from theory (Eqs. 3 and 5), decreasing ρ_2 results in increase of critical Fr_1 from 8-10 for $\delta_\rho \approx 0.097$ (Fig. 13b, red) to 12-14 for $\delta_\rho \approx 0.05$ (Fig. 13b, black). As before, the values of Fr_2 are below 1 and without significant correlation with R_2 (not shown).

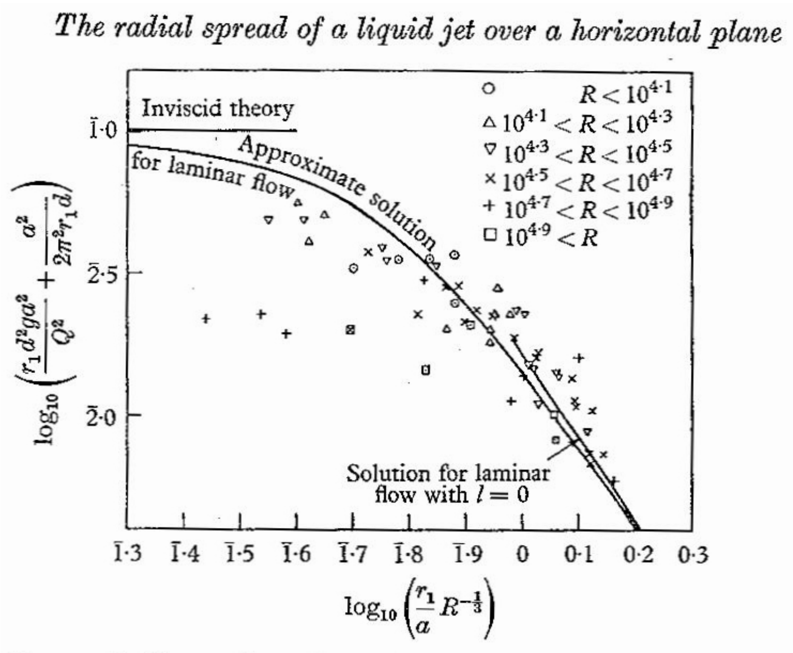

Figure 11. Watson's (1964, Fig. 4) comparison of experiment and theory for jump relation (single layer, laminar flow). Here a is the nozzle radius (≈ 0.3 cm), R is the Reynolds number, g is gravity and d is the depth of fluid outside the jump (here corresponding to H_2).

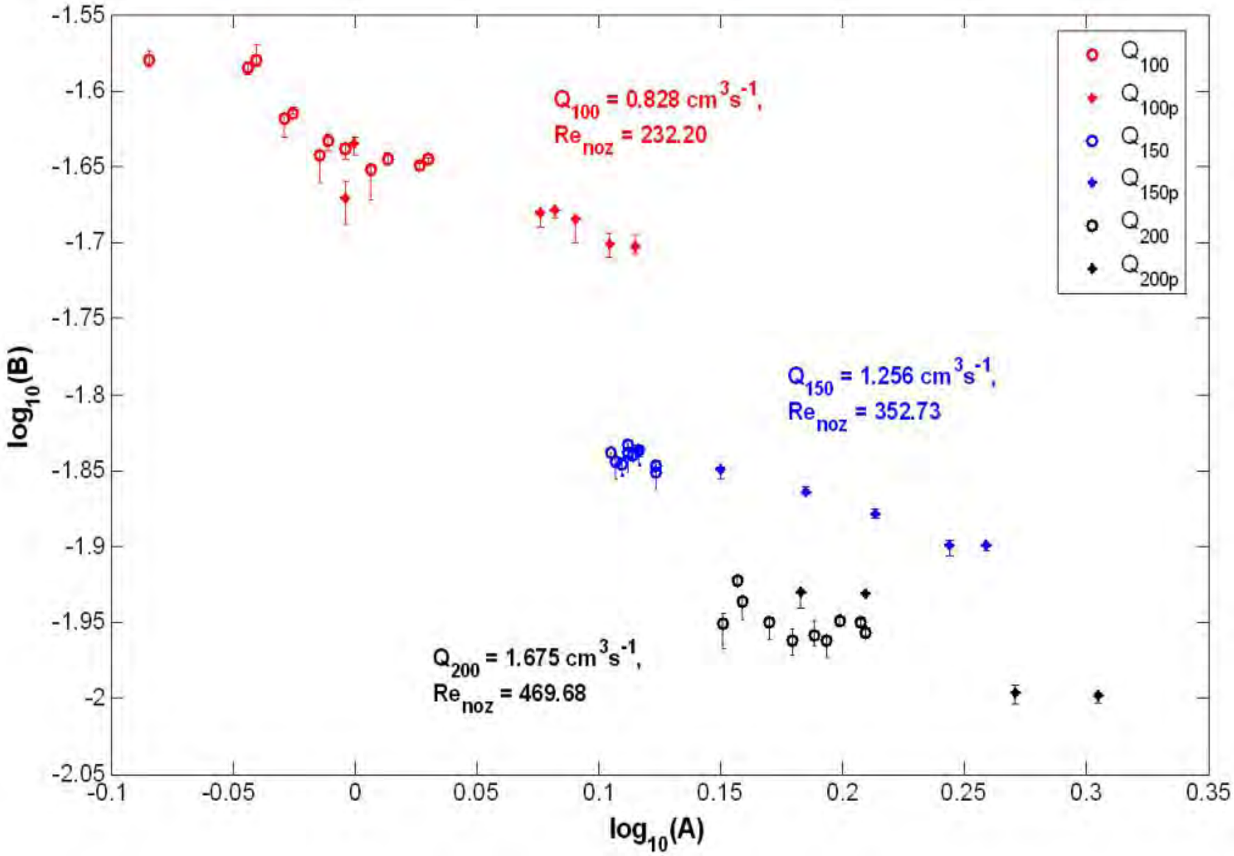

Figure 12. Comparison with Watson's results, with error bars (see Fig. 11). The rest as in Figure 6.

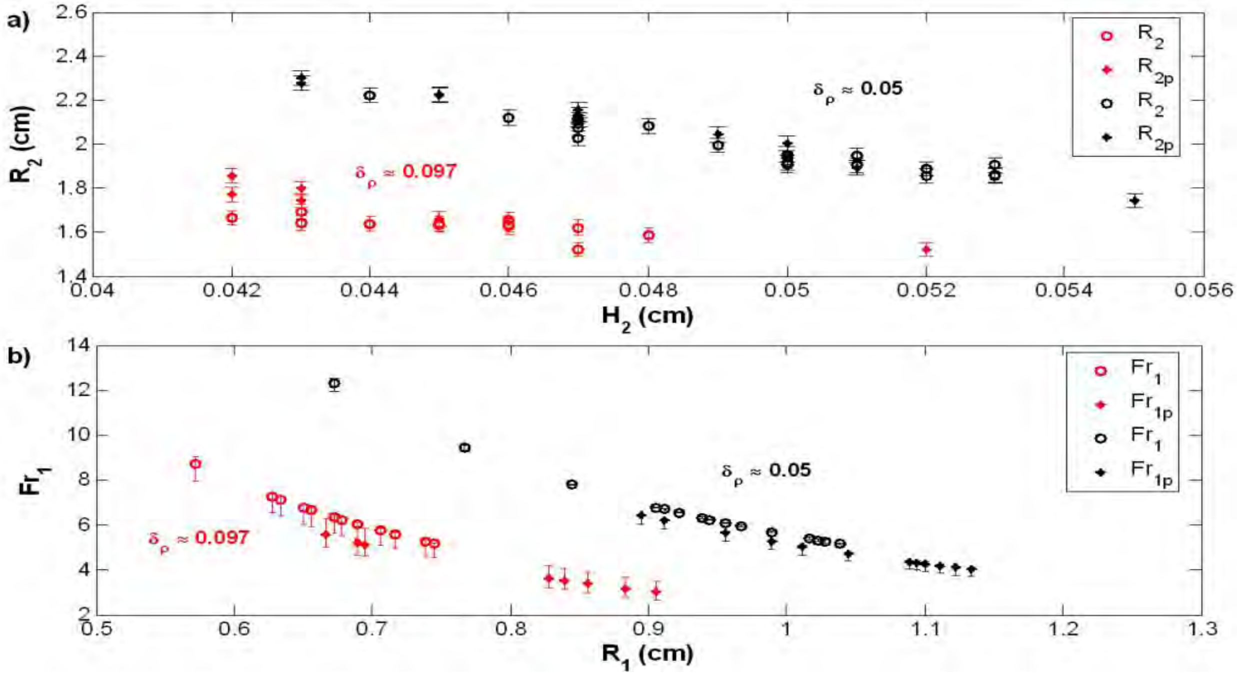

Figure 13. a) Dependence of outer jump radius, R_2 (with error bars), on H_2; b) upstream Froude number, Fr_1 (with error bars), versus inner jump radius, R_1. Pump setting in both plots is 100 ($Q_{100} = 0.828\text{cm}^3\text{s}^{-1}$, $Re_{noz} = 232.20$), for the experiments without (circles) and with the pie dish (asterisks). Results for $\rho_2 \approx 1.10544$ gcm^{-3} ($\delta_\rho \approx 0.097$) are in red, and for $\rho_2 \approx 1.05044$ gcm^{-3} ($\delta_\rho \approx 0.05$) are in black.

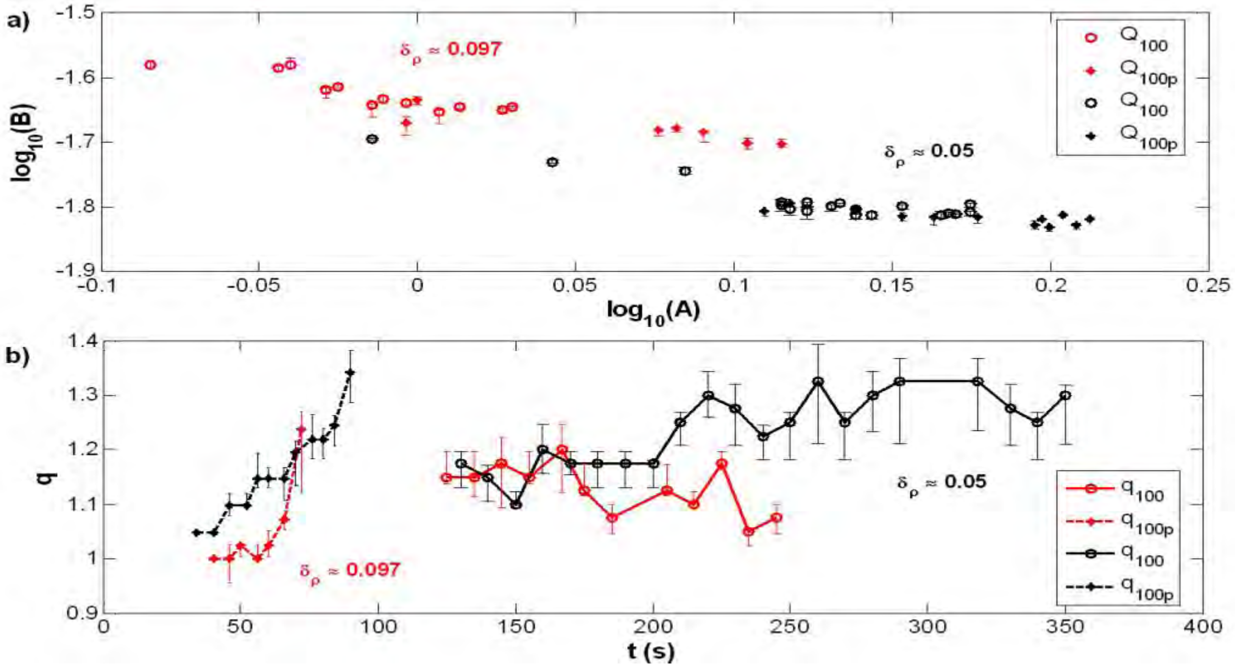

*Figure 14.*a) Comparison with Watson's results, with error bars (see Fig. 11); b) evolution of q (Eq. 9), with error bars, in time. The rest as in Figure 13.

Not only the critical values of R_2 (and R_1, Fig. 13a) are greater when the density difference is decreased; it is also the case for q (Fig. 14b, black), with values of ≈ 1.3-1.4 for both the pie dish (asterisks, dashed line) and the square tank only (circles, solid line). These increased values affect the theoretical predictions based on Watson's (1964) relations (Eq. 9) by placing the results for $\delta_\rho \approx 0.05$ (Fig. 14a, black) below the ones for $\delta_\rho \approx 0.097$ (Fig. 14a, red).

4. Conclusions and recommendations for future experiments

The circular hydraulic jump has been the subject of many theoretical, experimental, and lately numerical studies. Still, many facets of it remain unexplained or unexplored. In this experimental study we tried to describe some of the features of the circular internal jumps in two-layer fluid, and explore the possibility of their occurrence in fluid with continuous stratification.

In the two-layer case, both qualitative behaviour and calculated parameters show dependence on the flow rates and density differences used. Increasing Reynolds number in the nozzle (for the same density difference) or decreasing the density difference between fresh and salty water results in destabilizations of the flow, which can be seen as the cusp-like deformations and narrow, quickly varying, waves within the internal ring of the jump (Fig. 4a and 4b). The onset of instabilities seems to depend more on the density difference than on Reynolds number. Results for upstream Froude numbers (Figs. 9b and 13b) seem to confirm those observations. Although there are differences in values of R and H (and consequently Fr_1, Eq. 3) when the pie dish is used in experiments, the overall dynamic behaviour also seems to be similar (Figs. 8 and 13a). The time evolution of jump amplitude q (Eq. 9), although not completely precise because of uncertainties in determining the outer wave radii, still indicates that the maximal values are reached just before the transition into turbulent regime (≈ 1.1-1.4). In all experiments, no clear indication of rotor formation has been observed.

The experiments where the sharp density difference was smoothed by diffusion show no observational evidence of stationary waves (Fig. 7), implying that the stationary, laminar waves cannot occur in continuously stratified fluid. Still, it would be recommendable to further verify these observations by repeating the experiments in fluid with the known (prescribed or measured) density gradient.

The above conclusions for two-layer fluid, however, have to be taken with some caution, because their derivation is based not on measured values of fluid depth, but their estimates from the dispersion relation for inviscid fluid (Eq. 8). The direct measurements of the depth of salty fluid would therefore be very useful for investigating the role of viscosity, and revealing the jump structure itself. Craik et al. (1981), in their experiments for single-layer fluid, used a laser dye absorption for measurements of the height profile and thus the jump radius. Bloom and Burns (1997) also recommended this method in their experimental report. The method works by scanning a laser perpendicular to the tank bottom, and reading the intensity of transmitted light. The presence of dye in the fluid then makes the amount of light absorbed directly proportional to the fluid height. For the two-layer fluid, the laser should perhaps be aimed through side walls of the tank, and due to differences of refractive indices for salty and fresh water the dye might not be necessary at all.

Ideally, the experiments would have to be conducted in a circular tank, large enough so the circulation caused by the side walls would not significantly affect the jump patterns. Also, the great sensitivity of experiment on disturbances from its surroundings makes it necessary that the support base for the tank is stable, and attenuating vibrations. In this experimental study we have only explored moderate Reynolds numbers (of order 10^2); it would be worth to explore the behaviour for the higher Reynolds numbers by increasing the radii of nozzles used. Further experimental investigation, as well as the developed theoretical model to verify the observations against, would be very useful in revealing the dynamics of this interesting phenomenon.

Acknowledgements

I wish to thank to Steve Thorpe for his guidance and supervision, and especially for his great patience. Keith Bradley is thanked for the help with the experiment. Thanks to the GFD Staff, especially Claudia Cenedese, Jack Whitehead, Jeannie Fleming and Penny Foster for taking such a good care of us.

Thanks to Joe Pedlosky for his interesting lectures, and the esteemed audience (particularly Joe Keller and Ed Spiegel) whose comments made me doubt the things I thought I knew well.

Daphne Thorpe is very much thanked for knowing the importance of good chocolate cakes in times of crisis. George, I doubt I will ever be good in softball, but thank you for trying to teach me.

Finally, to all my fellow Fellows: I hope our paths will cross again some day.

References

Bloom C., 1997, *The circular hydraulic jump-pursuit of analytic predictions*, PhD Thesis (University of Texas)

Bloom C. and E. Burns, 1997, *The hydraulic jump-experimental analysis*, Laboratory report (University of Texas)

Bohr, T., P. Dimon and V. Putkaradze, 1993, Shallow-water approach to the circular hydraulic jump, *J. Fluid Mech.* **254**: 635-648.

Bowles, R. I. and F. T. Smith, 1992, The standing hydraulic jump: theory, computations and comparison with experiments, *J. Fluid Mech.* **242**: 145-168.

Bush, J. and J. Aristoff, 2003, The influence of surface tension on the circular hydraulic jump, *J. Fluid Mech.* **489**: 229–238.

Bush, J., J. Aristoff and A. Hosoi, 2006, An experimental investigation of the stability of the circular hydraulic jump, *J. Fluid Mech.* **558**: 33–52.

Craik, A., R. Latham, M. Fawkes and P. Gibbon, 1981, The circular hydraulic jump, *J. Fluid Mech.* **112**: 347–362.

Hassid, S., A. Regev and M. Poreh, 2007, Turbulent energy dissipation in density jumps, *J. Fluid Mech.* **572**: 1–12.

Higuera, F. J., 1994, The hydraulic jump in a viscous laminar flow, *J. Fluid Mech.* **274**: 69-92.

Holland, D. M., R. R. Rosales, D. Stefanica and E. G. Tabak, 2002, Internal hydraulic jumps and mixing in two-layer flows, *J. Fluid Mech.* **470**: 63–83.

Lighthill J., 1978, *Waves in fluids*, Cambridge University Press, 504 pp.

Lord Rayleigh, 1914, On the theory of long waves and bores, *Proc. Roy. Soc. Lond.* **A 90**: 324-328.

Thorpe, S. A., 2005, *The turbulent ocean*, Cambridge University Press, 439 pp.

Thorpe, S. A., 2007, Dissipation in hydraulic transitions in flows through abyssal channels, *J. Mar. Res.* **65 (1)**: 147-168.

Thurnherr, A. M., L. C. St. Laurent, K. G. Speer, J. M. Toole and J. R. Ledwell, 2005, Mixing associated with sills in a canyon on the mid-ocean ridge flank, *J. Phys. Oceanogr.* **35 (8)**: 1370–1381.

Watson, E.J., 1964**,** The radial spread of a liquid jet over a horizontal plane, *J. Fluid Mech.* **20**: 481-499.

Length and Shape of a Lava Tube

Miranda Holmes

Summer 2007

Abstract

We study a model of a viscous melted substance flowing in a cold circular tube. As the fluid flows, it cools and solidifies at the tube radius, and we investigate the question 'how far can the fluid flow and remain liquid?' A theoretical solution is derived for the radius of the liquid tube and the temperature profiles in the liquid and the solid. It is shown that if the fluid is maintained at constant flux, the tube can be infinitely long, but if it is maintained at constant pressure difference across the length of the tube, then there is a maximum length which depends on the Peclet number and a dimensionless temperature. The stability of the steady-state profiles are investigated, and it is shown that the linear stability of the tube radius can be determined from the functional relationship between pressure and flux. Numerical simulations are performed to test these predictions.

1 Introduction

Lava tubes are a common feature in basaltic lava flows. When a long, slow eruption supplies a steady stream of low-viscosity lava, the flow tends to concentrate in channels. If the channels roof over and become encased in solid material, then the tube of fluid is thermally insulated and can transport hot lava a long way with little loss of heat. An insulated tube such as this can also form in pahoehoe (sheet) flows, without first flowing in a channel, when the sheet cools and gradually restricts the fluid to narrow regions in the interior. These lava tubes can feed flows that are far away from their source, making the extent of a volcanic flow much greater than if the lava were to flow as a slab. [10]

It is common to find lava tubes with lengths of 10-30km, but some tubes are much longer. The Mauna Loa flow tube, in Hawaii, is over 50km long, and the Toomba and Undara flows in Queensland, Australia are 123km and 160km long respectively. The longest known tube is over 200km long, on the volcanic region of Alba Patera, Mars.

We would like to address the question: how long can a lava tube be? If the geometry of the environment were not a factor, how far could a flow of liquid, which is embedded in a solid of the same material, transport hot fluid before cooling and solidification arrests the flow? Previous studies have looked at the temperature distribution within a tube of constant radius ([13], [4]), the velocity profile of flow in a constant-width channel ([11]), the driving pressure required to keep open a short, constant radius tube of pillow lava ([7]), the cooling processes operating along the length of a tube ([6]), the effect of temperature-dependent viscosity on flow localization ([16], [5], [17]), and the time-dependent melting or solidification of flow through a two-dimensional slot with cooling at infinity ([2], [3], [9]). We will expand on these studies by allowing the radius of the tube to vary, and by providing the appropriate boundary conditions so that we can look at the problem in steady-state. We will ignore the temperature dependence of viscosity, so as to isolate the effect of melting and solidification processes at the boundary of the tube, and their relationship to the heat advected through the tube and conducted radially outward.

We will construct an idealized model of a tube, find a solution for the shape of the tube and conditions for its existence, investigate the stability of the tube, explain the results of our numerical simulations, and finally discuss extensions of the model and ideas for further research.

2 The Model

2.1 Setup and equations

We will model a lava tube as a tube of a fixed length L with a perfectly circular cross-section, whose radius $a(x)$ may depend on the distance down the tube. Liquid enters the tube at a uniform initial hot temperature T_i and it flows through the tube with a velocity profile $\vec{u}$, to be determined. We suppose that the tube is embedded in a solid, made of the same material as the liquid, which is a large cylinder of radius r_0. The boundary of this cylinder is maintained at a constant temperature T_0, which is colder than the melting temperature. The temperature varies continuously from $T = T(0, x) > T_m$ at the center of the tube, which is liquid, to T_0 at the edge of the cylinder, which is solid. The radius of the liquid tube is exactly the isotherm $T = T_m$. (See Figure 1).

Some justification needs to be made for our assumptions and choice of boundary conditions. On the tube boundary, we have chosen to have a clear distinction between solid material and liquid material, rather than to vary the viscosity and so to have a transition region. While we acknowledge that the viscosity change with temperature may be a factor, particularly in the formation of a tube or channel, we assume that once the tube has been formed, the increase in viscosity from its solid-like state to its liquid-like state is rapid enough that the fluid can be modelled as a two-state material with a simple cutoff solidification temperature. ([9]). The melting temperature is chosen to be the temperature at which the amount of crystallization in the lava exceeds 55%. This is based on observations that the lava behaves as a fluid until the amount of crystallization exceeds a threshhold, at which point its crystalline network is strong enough that it behaves as a brittle solid, and is not susceptible to erosion by the shear forces in the flow. ([13])

L = length of tube
r_0 = radius of cylinder
T_s = melting temperature
T_i = temperature of fluid entering tube
T_0 = temperature of outer boundary
ΔP = pressure difference across tube
Q = flux through tube
μ = viscosity of fluid
κ = thermal diffusivity of material (assumed equal for solid and liquid)
ρ = density of liquid
c_p = heat capacity of liquid
L_H = latent heat of fusion

Table 1: Parameters used in the model

The boundary condition on the edge of the cylinder of constant temperature was chosen for two reasons: (i) The difference between the eruption temperature T_i and the melting temperature T_m is an order of magnitude smaller than the difference between T_m and the ambient conditions, represented by T_0. ([13]). This implies that it is the processes within the tube, and not the environment, which are limiting the cooling, so any heat lost to the walls of the cylinder can be conducted away as fast as it is generated; and (ii) It corresponds to the experiment set up by Jack Whitehead. It is not intended to reproduce the conditions of a real tube, which lives in a much more inhomogeneous environment, and it generates a singularity when combined with the constant temperature boundary condition at the entrance, but it allows us to investigate the properties of such an ideal tube before adding in the complications of a more detailed heat flux function or a model of the source of lava.

We choose the lava tube to have a fixed length L, rather than to vary it dynamically, because often the length of a lava tube is set by factors external to the flow. For example, the slope of the terrain may increase abruptly, causing the lava to pour out of the tube and begin a new sheet flow, or the tube may reach the ocean and drain as a pillow lava flow.

We now introduce the equations of the model.

The variables in the system are:

$\vec{u}(x,r)$ = velocity field in tube
$T(x,r)$ = temperature profile in liquid
$T_e(x,r)$ = temperature profile in solid
$a(x)$ = radius of tube

The parameters used in the model are shown in Table 1.

When solving for these variables, we are looking for steady-state, axisymmetric solutions, so time derivatives and azimuthal derivatives will be ignored.

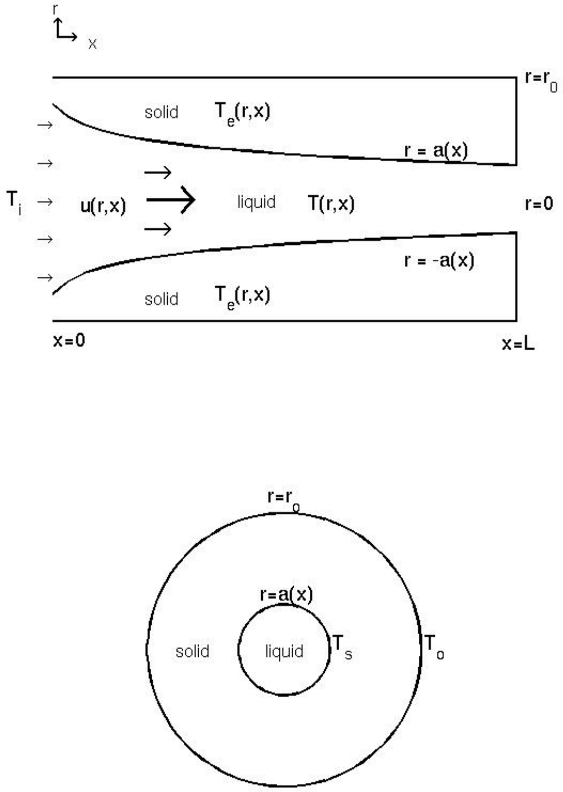

Figure 1: Top: Cross-section of the lava tube through its center line. Bottom: Cross section of the tube at constant x

We will also assume that changes in the radial direction are much greater than changes in the axial direction, so x-derivatives are ignored when they are of the same order as r-derivatives. In particular, we will ignore conduction in the x-direction.

We solve the equations for each of the velocity, temperatures, and radius in turn.

Velocity The viscosity of lava is high enough that we expect to be able to neglect the nonlinear terms in the Navier-Stokes equations. We also expect laminar flow because the Reynolds number of lava flowing in a tube is order 100, much less than the transition to turbulence in a circular pipe, which occurs at $Re = 2000$ to 4000. ([13],[7]) Indeed, the velocity of lava in a channel has been shown to conform very well to the parabolic profile predicted by assuming a laminar Newtonian fluid ([11]), and we expect the same to hold true for a tube.

Thus, the along-tube component of velocity satisfies

$$P_x = \mu \frac{1}{r}\frac{\partial}{\partial r}(r\frac{\partial u}{\partial r}) \ , \qquad u = 0 \text{ at } r = \pm a(x) \tag{1}$$

Solving this gives

$$u = \frac{-P_x}{4\mu}(a^2(x) - r^2)$$

Integrating u from $r = 0$ to $r = a(x)$ gives a relationship between the flux and the pressure:

$$P_x = -\frac{8\mu Q}{\pi a^4(x)} \tag{2}$$

We can use this to express u as

$$u = \frac{2Q}{\pi a^2}(1 - (r/a)^2) \tag{3}$$

The radial component of velocity can be solved for using the condition of non-divergence:

$$v = \frac{2Qa'r}{\pi a^3}(1 - (r/a)^2)$$

In non-dimensional form (see (9)), u is

$$u = \frac{Pe\kappa L}{a_0^2 a^2}(1 - h^2) \tag{4}$$

External Temperature Field The temperature field in the solid, neglecting x-derivatives, satisfies a diffusion equation:

$$\kappa \frac{1}{r}\frac{\partial}{\partial r}(r\frac{\partial T_e}{\partial r}) = 0 \ , \qquad T_e|_{r=r_0} = T_0 \ , \quad T_e|_{r=a(x)} = T_s \tag{5}$$

This can be solved to give

$$T_e = \frac{T_0 - T_s}{\ln \frac{r_0}{a(x)}} \ln \frac{r}{a(x)} + T_s \tag{6}$$

Or, in non-dimensional form (see (9)),

$$T_e = \frac{K}{\ln \frac{r_0}{a(x)}} \ln \frac{r}{a(x)} \tag{7}$$

where $K = \frac{T_0 - T_s}{T_i - T_s}$ is a non-dimensional constant relating the amount of cooling by the boundary condition to the amount of heating from the incoming lava.

Internal Temperature Field The internal temperature field is given by a balance between advection and diffusion:

$$u\frac{\partial T}{\partial x} + v\frac{\partial T}{\partial r} = \kappa\frac{1}{r}\frac{\partial}{\partial r}(r\frac{\partial T}{\partial r})$$

$$T|_{r=a(x)} = T_s \ , \quad T|_{x=0} = T_i \ , \quad \frac{\partial T}{\partial r}|_{r=0} = 0 \tag{8}$$

Before solving for $T(x,r)$, we first do a change of variables:

$$h = \frac{r}{a(x)}$$

This will prove to be very convenient, as the streamlines of the flow are lines of constant h, so we will end up with only one partial derivative in the advection term. After the change of variables, and substituting $u = \frac{2Q}{\pi a^2}(1-h^2)$, the equation becomes

$$\frac{2Q}{\kappa\pi a(x)^2}(1-h^2)\frac{\partial T}{\partial x} = \frac{1}{a(x)^2}\frac{1}{h}\frac{\partial}{\partial h}(h\frac{\partial T}{\partial h})$$

We will non-dimensionalize with the following:

$$\begin{aligned} x &= Lx' \\ a(x) &= a_0 a'(x) \\ \frac{T-T_s}{T_i-T_s} &= T' \\ Q &= Pe\frac{\kappa L\pi}{2}q' \\ P &= \Delta P P' \end{aligned} \tag{9}$$

Here, a_0 is a typical scale for $a(x)$, usually chosen to be r_0. The pressure was non-dimensionalized with a typical pressure difference across the length of the tube, and the flux was non-dimensionalized so that it has a nice form when related to P - the scale is likely not representative. The non-dimensional parameter Pe is a modified Peclet number, which we will simply call the Peclet number, and is defined to be

$$Pe = \frac{\Delta P a_0^4}{4\kappa\mu L^2} \tag{10}$$

After dropping the primes, we can write the equations in terms of either P or q as

$$\frac{PeP}{\int_0^1 \frac{1}{a^4}}(1-h^2)\frac{\partial T}{\partial x} = \frac{1}{h}\frac{\partial}{\partial h}(h\frac{\partial T}{\partial h}) \tag{11}$$

$$q(1-h^2)\frac{\partial T}{\partial x} = \frac{1}{h}\frac{\partial}{\partial h}(h\frac{\partial T}{\partial h}) \tag{12}$$

with boundary conditions

$$T|_{h=1} = 0\ , \quad \frac{\partial T}{\partial h}|_{h=0} = 0\ , \quad T|_{x=0} = 1\ .$$

The pressure difference across the tube, P, is related to the flux by

$$P = \frac{q}{Pe}\int_0^1 \frac{1}{a^4} dx \tag{13}$$

We can solve (11) or (12) by separation of variables. We show the solution for (12) because it is simpler; to obtain the solution for (11) we simply substitute $PeP/\int_0^1 \frac{1}{a^4}$ for q.

The temperature field that solves the equation is

$$T(x,h) = \sum_n A_n e^{-\lambda_n^2 x/q}\phi_n(h) \tag{14}$$

where λ_n, ϕ_n are the eigenvalues and eigenvectors of the problem and A_n are constants that are determined from the initial temperature distribution. See the Appendix for a discussion of the eigenfunctions.

Radius of Tube The rate of change of the radius of the tube is proportional to the difference in heat flux at the boundary of the tube. This heat flux should be the heat flux in the normal direction, but using our slowly-varying-in-x assumption, we take it to be the flux in the radial direction only. The time-dependent equation for the radius is a standard Stefan equation (see [15]):

$$\frac{L_H}{c_p}\frac{da}{dt} = \kappa\left(\frac{\partial T_e}{\partial r}|_{r=a(x)} - \frac{\partial T}{\partial r}|_{r=a(x)}\right)$$

where L_H is the latent heat of solidification, and c_p is the heat capacity.

In steady-state, and with our change of variables and non-dimensionalization, this becomes

$$\frac{\partial T}{\partial h}|_{h=1} = \frac{\partial T_e}{\partial h}|_{h=1} \tag{15}$$

From (6) and (14), we can calculate

$$\begin{aligned}
\frac{\partial T}{\partial h}|_{h=1} &= \sum_n G_n e^{-\lambda_n^2 x/q}\ , \qquad G_n = A_n\phi_n'(1) \\
\frac{\partial T_e}{\partial h}|_{h=1} &= \frac{K}{\ln r_0/a(x)} = \frac{-K}{\ln a(x)}
\end{aligned}$$

Substituting into (15) and solving for $a(x)$ gives

$$
\begin{aligned}
a(x) &= \exp\left(\frac{-K}{\frac{\partial T}{\partial h}|_{h=1}}\right) \\
&= \exp\left(\frac{-K}{\sum G_n e^{-\lambda_n^2 x/q}}\right) \qquad (16)
\end{aligned}
$$

Before proceeding, we remark that our steady-state model, defined by (4), (7), (11), and (15), depends on only two non-dimensional parameters:

$$Pe = \frac{\Delta P a_0^4}{4\kappa\mu L^2}\ , \qquad K = \frac{T_0 - T_s}{T_i - T_s}$$

The first, the Peclet number, gives the ratio of the horizontal advection of temperature to the vertical conduction of heat. The greater the Peclet number, the more heat is being advected through the tube, so we expect the tube to be more open. The second, which we will call the temperature constant, gives the ratio between the amount of cooling and the amount of heating. A greater $|K|$ means stronger cooling, so we expect the tube to be more closed.

2.2 Existence of a Solution

Notice from (16) that $a(x)$ depends on q. If we set q, then we can solve explicitly for $a(x)$. However, if we choose to set P instead, then $q = PeP/\int \frac{1}{a^4}$, so we must solve a transcendental equation for a. This may or may not have a solution. We will show that if we choose to hold ΔP constant, so that $P = 1$, then the existence of a solution depends on our choice of Peclet number.

Claim There exists a critical number depending on K, call it $Pe_c(K)$, such that

$$
\begin{array}{rclcl}
Pe & > & Pe_c(K) & \Rightarrow & \text{There are 2 solutions for } a(x) \\
Pe & = & Pe_c(K) & \Rightarrow & \text{There is 1 solution for } a(x) \\
Pe & < & Pe_c(K) & \Rightarrow & \text{There are no solutions for } a(x)
\end{array} \qquad (17)
$$

Proof Consider K to be fixed. We consider the solution (16) to (12), and use this to plot P as a function of q. We define

$$f(q) \equiv q \int_0^1 \frac{1}{a^4(x,q)} dx$$

so that

$$P(q) = \frac{1}{Pe} f(q) \qquad (18)$$

We must find a q that solves (18) for $p = 1$.

By calculating $f'(q)$, it is possible to show (see Appendix) that there is a value of q, call it q_c, such that $f(q)$ has a minimum at q_c, is monotone decreasing for $q < q_c$ and monotone increasing for $q > q_c$. (See Figure 2 for an example.)

This implies that (18) has two solutions whenever $Pe > f(q_c)$ and no solutions if $Pe < f(q_c)$. Defining $Pe_c(K) = f(q_c)$ implies the result.

A plot of the critical Peclet number versus K is shown in figure 3. As expected, when $|K|$ increases the critical Peclet number does too, because there is stronger cooling.

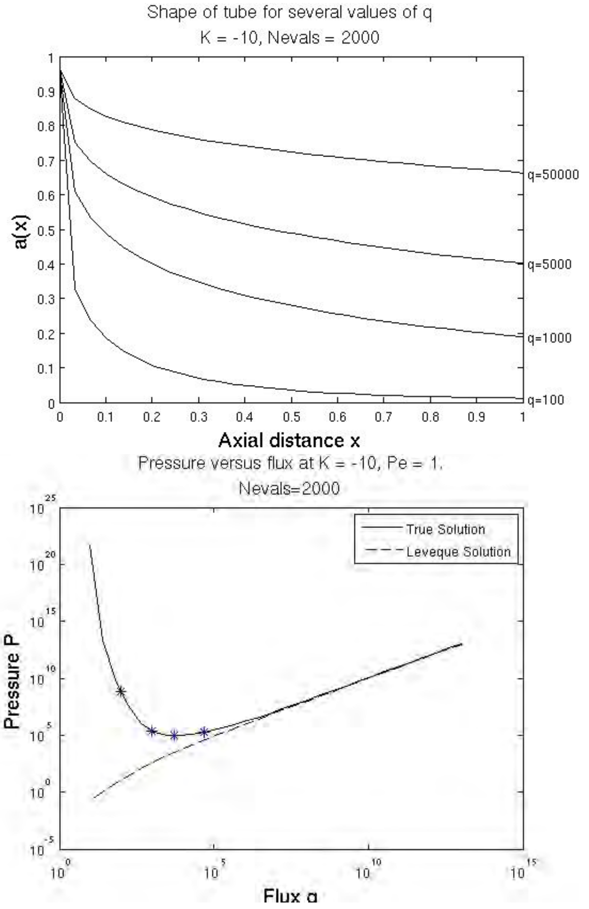

Figure 2: Top: Steady-state $a(x)$ calculated for several different values of q. Bottom: Pressure difference across the tube as a function of flux. The pressure differences for the tubes shown on the left are plotted as starred points. The pressure calculated from the Leveque approximation is shown with a dashed line.

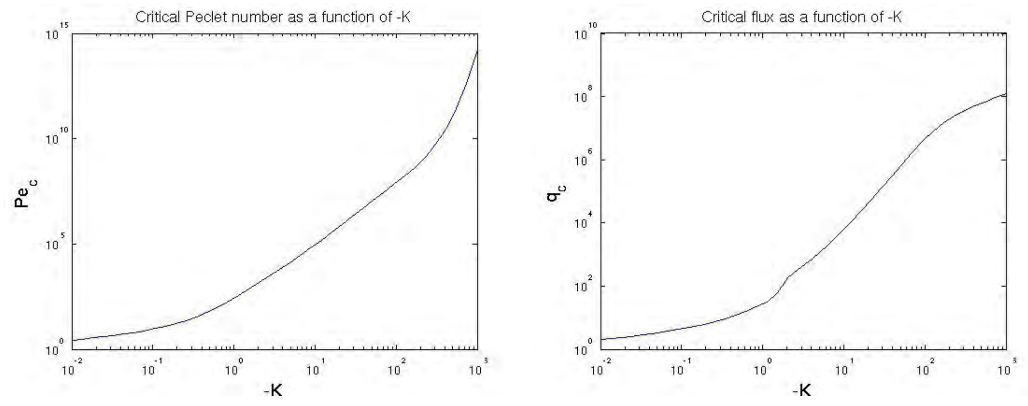

Figure 3: Left: Critical Peclet number versus K. Right: Critical flux versus K.

2.3 Implication for length of a lava tube

From (17), we can calculate the maximum possible length of a lava tube. We must have

$$L_{\max} < \sqrt{\frac{\Delta P a_0^4}{4\kappa\mu Pe_c(K)}} \tag{19}$$

We try to estimate this maximum length in two ways:

1. Assuming the flow is gravity-driven
2. Assuming the flow is pressurized at its source

Variable	Range in Literature	Value Used
κ	1e-7 - 1e-6 m^2/s	1e-7m^2/s
μ	30 - 200 Pa·s	100 Pa·s
ρ	1560-2600kg/m^3	2600 kg/m^3
a_0	1-100m	10m
T_i	$1150 - 1180°\mathrm{C}$	
T_s	1077-1130°C	
T_0	30-100°C	
K	-10 to -40	
$Pe_c(k)$	9.2e4 to 6.4e6	

Table 2: Values of some parameters for basaltic lava, and the values used in our calculations. K is calculated from the temperature data, and Pe_c is calculated from K.

Gravity-Driven flow If the flow is gravity-driven, then the pressure difference is given by the hydrostatic pressure difference calculated from the change in height H:

$$\Delta P = \rho g H$$

We use the parameters shown in Table 2, and take the radius of the tube to be 10m. This may be slightly larger than tubes that are most commonly observed, but many of the longest tubes also have very large radii, sometimes exceeding 50m ([12]). For a flow that drops 1km, with an initial radius of 10m, we find that for $K = -10$ to -40,

$$L \approx 30 - 250\text{km}$$

This is certainly in the range expected, although it varies a lot with a change in the parameters. It is therefore likely that a flow is not entirely gravity-driven.

Pressure-Driven Flow There is much evidence that the flow along a lava tube has a pressure-driven component, particularly in very long tubes over shallow slopes. Features along the tube such as tumuli, and dome-shaped fountaining at tube breakout points, are commonly found along long tubes and indicate that such tubes are probably fed by a source under high pressure. ([12]) The source could become pressurized in many ways; for example, if there is a thick layer of heavy, solid material floating on top of the lava source, or if the lava originates from an elastic chamber.

It therefore makes sense to consider the pressure to be limited by a certain value, which is the maximum value that the source can sustsain. We suppose that our source is surrounded by solid basalt, and choose this value to be the tensile failure strength of solid basalt:

$$\Delta P_{\text{crit}} = 0.1 - 2.5\text{MPa}$$

If $\Delta P > \Delta P_{\text{crit}}$, we expect the magma at the source to break out of its solid chamber and to develop a new system of tubes and flows.

Using ΔP_{crit} as the value of ΔP in our calculation of Pe and using the given range of K gives an upper bound on the length of a tube of initial radius 10m as

$$L_{\max} \leq 200 - 900\text{km}$$

These values are slightly larger than the longest observed lava flow (of ∼200 km, on Mars), and an order of magnitude larger than a typical lava tube. However, real lava tubes have much more complicated cooling terms and geometry, have time-dependent parameters, and are likely not operating at their maximal capacity, so this shows that our theory is a candidate for a model of the processes important in restricting the length of a tube. To properly evaluate the accuracy of the length predictions, however, one would need to look at data and values of the parameters for a particular tube.

2.4 Shape of a(x)

It is interesting to examine a plot of $P(q)$ and compare it to plots of $a(x)$. Figure 2 shows plots of $a(x)$ for several values of q. When q is on the branch where $\frac{dP}{dq} > 0$, the tube is quite large and has radius comparable to the radius of the cylinder. As $q \to q_c$, the tube gets much smaller, and when q is on the branch $\frac{dP}{dq} < 0$, the tube becomes tiny very quickly. In this regime, the pressure difference required to maintain such a flux increases very rapidly with a small decrease in flux.

This feature is analogous to that of a fluid whose viscosity changes with temperature. The size of the tube determines its resistance to the flow, and can be thought of as its 'viscosity'. The smaller the tube, the higher its viscosity. In a high flux regime, the tube's size, or viscosity, changes little with flux, so the pressure is determined mainly from the shear forces induced by the flux. As the flux decreases, a point is reached where the 'viscosity' starts to increase rapidly, dominating the contribution from the flux, so the pressure begins to rise.

Whitehead and Helfrich ([16]) found a curve similar to ours, relating the flux through a fissure to the pressure drop across it, for a fluid whose viscosity changes with temperature. Their curve had the same shape except for very small fluxes, where the pressure reached a maximum and then came back down to 0 at $q = 0$.

2.5 Leveque Approximation

When q is large, x/q is small, so we will need to sum up a large number of eigenfunctions to get a good approximation of the temperature field and tube radius. Leveque ([8]) found an approximate solution of (12) that is valid when x/q is very small. He assumed that the change in temperature happened only within a thin boundary layer of size $\delta(x/q)$ near the edge of the tube. He neglected the curvature term, approximating the flow in this boundary layer as planar, and used a linear approximation for the velocity field. After introducing a similarity variable $\eta = (1-h)/\delta(x/q)$, he found a similarity solution $F(\eta) = T(x/q, h)$ for the temperature in the boundary layer:

$$T(x/q,h) = F(\eta) = \frac{1}{\Gamma(4/3)} \int_0^{\eta} e^{-\gamma^3} d\gamma \,, \qquad \eta = \frac{1-h}{\delta(x/q)} \tag{20}$$

$$\delta(x/q) = \left(\frac{9}{2}h\right)^{1/3} \tag{21}$$

We can combine this with (16) to obtain an approximation for $a(x)$ near $x = 0$. Since $a(x) = r_0 \exp(-K/\frac{\partial T}{\partial h}|_{h=1})$, we find that

$$a(x) \doteq r_0 e^{K\Gamma(\frac{4}{3})\left(\frac{9x}{2q}\right)^{1/3}} \,, \qquad x/q \ll 1 \,. \tag{22}$$

When q is large enough, this gives almost perfect agreement with the exact solution. Even when q is not so large, the shape still agrees quite well. The pressure, however, is not so easily approximated with the Leveque solution. When q is large, the pressure agrees very well (see Figure 2), but it starts to diverge as q approaches the critical q_c, and fails completely when $q < q_c$ as the Leveque pressure is monotonically increasing.

3 Stability

Once we know the radius of the tube, we would like to know whether this shape is stable. If we perturb it a little, will it return to steady-state or will it continue to melt back the walls or to solidify until it plugs up?

To answer these questions we must reintroduce time into the equations. Let us assume that the velocity field and external temperature adjust instantly to the radius, and introduce time only into the equations for internal temperature and radius. If we non-dimensionalize time with the diffusive timescale, so that

$$t = \frac{a_0^2}{\kappa} t'$$

then the equations become

$$T_t + q(1-h^2)\frac{\partial T}{\partial x} - a a_t h T_h = \frac{1}{h}\frac{\partial}{\partial h}(h\frac{\partial T}{\partial h}) \tag{23}$$

$$S\frac{da}{dt} = \frac{1}{a}\left(\frac{\partial T_e}{\partial h}|_{h=1} - \frac{\partial T}{\partial h}|_{h=1}\right) \tag{24}$$

with the same boundary conditions as before.

The non-dimensional Stefan number is

$$S = \frac{L_H}{c_p(T_i - T_s)}$$

Let us assume that S is large, so we can ignore a_t in (23), and also that q is large enough that T_t becomes negligible. Then we only have one time-dependent equation, (24).

Suppose we start with the radius $a(x)$ that solves the steady problem, and then we change it a little bit. Will it go back to the original radius? If we maintain a constant flux q through the tube, then we see that the answer must be yes. If we increase $a(x)$, then we decrease $\frac{\partial T_e}{\partial h}$ and we increase $\frac{\partial T}{\partial h}$, (which are both negative), so $\frac{da}{dt} < 0$ and $a(x)$ relaxes to its original value. If we decrease $a(x)$, the signs of the fluxes are reversed and the walls melt back to their original configuration. This argument is valid at each point x since the heat fluxes in (24) are local, for constant flux.

However, if we keep the pressure difference across the tube constant, then a heuristic argument shows that there is a potential for instabilities. Suppose we increase the radius of the tube a little bit. The conductive heat flux acts to resolidify it. However, since the pressure difference is fixed, the flux through the tube also increases, by (2). Thus, more heat is being advected through the tube, and this might cause enough melting to offset the conduction terms.

We now investigate the linear stability quantitatively. Let $\tilde{a}(x) = a(x) + \epsilon a_1(x)$, where $a(x)$ is the steady profile for a given q and ϵ is small. We expand all relevant terms and variables up to $O(\epsilon)$. Thus

$$\begin{aligned} \frac{\partial T_e}{\partial h} &= \frac{K}{\ln r_0/a} + \epsilon \left(\frac{K a_1}{a \ln^2 r_0/a} \right) \\ \tilde{q} &= q + \epsilon q \frac{4 \int \frac{a_1}{a^5}}{\int \frac{1}{a^4}} \\ \frac{\partial T}{\partial h}|_{h=1} &= \sum G_n e^{-\frac{\lambda_n^2}{q} x} \left(1 + \epsilon \lambda_n^2 \frac{x}{q} \frac{4 \int \frac{a_1}{a^5}}{\int \frac{1}{a^4}} \right) \end{aligned}$$

Keeping terms of $O(\epsilon)$ in (24) (and ignoring S, or re-defining time by it) gives

$$a \frac{da_1}{dt} = \frac{K a_1}{a \ln^2 r_0/a} - \frac{x}{q} \frac{\int \frac{4a_1}{a^5}}{\int \frac{1}{a^4}} \sum \lambda_n^2 G_n e^{-\frac{\lambda_n^2}{q} x} \tag{25}$$

Using

$$\sum \lambda_n^2 G_n e^{-\frac{\lambda_n^2}{q} x} = -q \frac{\partial}{\partial x} \left(\frac{\partial T}{\partial h}|_{h=1} \right) = -q \frac{K a'}{a \ln^2 1/a}$$

we can write this as

$$\frac{da_1}{dt} = \frac{K}{a^2 \ln^2 1/a} \left(a_1 + x a'(x) \frac{\int \frac{4a_1}{a^5}}{\int \frac{1}{a^4}} \right) \tag{26}$$

This has the form

$$\frac{da_1}{dt} = c(x) a_1 + k(x) \int_0^1 j(y) a_1(y) dy \tag{27}$$

where $c(x) = \frac{K}{a^2 \ln^2 a} < 0$, $k(x) = x a'(x) c(x) > 0$, $j(x) = 4/a^5(x) > 0$.

The RHS can be turned into a self-adjoint operator by a simple change of variables. Let

$$v(x) = \sqrt{\frac{j(x)}{k(x)}} a_1(x)$$

Then the equation becomes

$$\frac{dv}{dt} = Lv \equiv c(x) v + h(x) \int_0^1 h(y) v(y) dy \tag{28}$$

where $h(x) = \sqrt{k(x) j(x)}$.

We note the following:

- Range$(c(x)) = (-\infty, c_m]$, where $c_m = \sup(c(x)) < 0$. This is because $a^2 \ln^2 a = 0$ at $a = 0, 1$ so it has a maximum on $a \in (0, 1]$, and $K < 0$.
- $0 < h(x) \leq h_m$. This still needs to be proved - we must show that $\lim_{x\to 0} h(x) < \infty$. Numerical solutions indicate that it should be true.

Thus, although L is an unbounded operator on $L_2(\mathbb{R})$, the Fredholm component $h(x) \int h(y)v$ is bounded. We could truncate $c(x)$ at some finite value to obtain a bounded operator, and then we could apply the spectral theorem to represent the solution in spectral space. We won't need the boundedness of L to calculate its spectrum, however, so we leave it in its unbounded form for now.

We make the following claims about the spectrum of L.

Claim

- The point spectrum of L consists of one eigenvalue λ_0, with corresponding eigenfunction $\frac{h(x)}{\lambda_0 - c(x)}$. λ_0 is the solution to $\int \frac{h^2(y)}{\lambda - c(y)} = 1$, and $\lambda_0 > c_m$.
- The continuous spectrum is equal to Range$(c(x))$.
- There are no other points in the spectrum.

Proof To see that $\frac{h(x)}{\lambda_0 - c(x)}$ is an eigenfunction, simply calculate: $Lv = \frac{c(x)h(x)}{\lambda_0 - c(x)} + h(x) \int \frac{h^2(y)}{\lambda_0 - c(y)} = \frac{\lambda_0 h(x)}{\lambda_0 - c(x)}$.

To see that there is only one such $\lambda_0 > c_m$ solving $f(\lambda) = \int \frac{h^2(y)}{\lambda - c(y)} = 1$, note that $\lim_{\lambda\to c_m} f(\lambda) = \infty$, $\lim_{\lambda\to\infty} = 0$, and $f'(\lambda) = -\int \frac{h^2(y)}{(\lambda - c(y))^2} < 0$.

To show that $\lambda = c(x_0)$ is in the continuous spectrum, we show that $\lambda - L$ cannot have a bounded inverse. We do this by providing a sequence $\{v_n\} \in L_2$ such that $\|v_n\| = 1$ and $\|(\lambda - L)v_n\| \to 0$. Letting $v_n = b_n 1_{(x_0 - \delta_n, x_0 + \delta_n)}$, where $2\delta_n b_n = 1$, $\delta_n \to 0$, and using the continuity of $c(x)$ does the job.

To show that this is the entire spectrum, we show that if $\lambda \notin \{c(x)\} \cup \{\lambda_0\}$, then $\lambda - L$ has a bounded inverse.

Let

$$Tv \equiv \frac{v + \int \frac{h(y)v}{\lambda - c(y)} / \left(1 - \int \frac{h^2(y)}{\lambda - c(y)}\right)}{\lambda - c(x)}$$

Then $(\lambda - L)T = T(\lambda - L) = I$, and

$$\|Tv\| \leq \frac{2\|v\|}{(\lambda - c_m)^2} \left(1 + \frac{h_m^2/(\lambda - c_m)^2}{1 - \int \frac{h^2(y)}{\lambda - c(y)}}\right)$$

Thus, appealing to the spectral theorem for unbounded operators, we can express the solution to (28) as

$$v(x,t) = A_0 e^{\lambda_0 t} \frac{h(x)}{\lambda_0 - c(x)} + \int_{\lambda \in Range(c(x))} A_\lambda e^{\lambda t} \phi(\lambda, x) d\lambda \tag{29}$$

where $\phi(\lambda, x)$ are the distributions corresponding to the continuous spectrum.

Since the continuous spectrum is always negative, the stability of the problem is determined entirely by the sign of the largest eigenvalue, λ_0. It is possible to show that

Claim

$$\begin{aligned} \frac{dP}{dq} > 0 \quad &\Rightarrow \quad \lambda_0 < 0 \qquad \text{(stable)} \\ \frac{dP}{dq} < 0 \quad &\Rightarrow \quad \lambda_0 > 0 \qquad \text{(unstable)} \end{aligned}$$

Proof See Section 8.3 in the Appendix for a proof given general heat flux and pressure relationships.

It is helpful to change back to our original variables to see the structure of the discrete eigenfunction. In the original variables, it becomes

$$xa'(x) \frac{c(x)}{\lambda_0 - c(x)}$$

Since $xa_x + qa_q = 0$, it is also proportional to

$$a_q \frac{c(x)}{\lambda_0 - c(x)} = \frac{a_q}{\frac{\lambda_0}{c(x)} - 1}$$

Thus, if $\lambda_0 / c(x) \approx$ const, which can happen if $\lambda_0 \gg c_m$, for example, (since $c(x)$ changes slowly over most of its range), then the most slowly-decaying perturbation is almost in the direction of the nearest steady profile.

4 Numerical Simulations

Numerical simulations were performed to test the stability predictions. The pressure difference was kept constant, and the tube radius was stepped forward in time using (24). Time derivatives were calculated using forward Euler, the trapezoidal rule was used for integration, and 1000 eigenfunctions were used to calculate the heat flux and steady profiles. 40 points were used to represent the tube in the horizontal. The simulations were stopped if the tube ‘plugged up’ - defined to be when $a(x) = 0$ for some x.

The numerical simulations confirm the theoretical predictions. If we start with a profile that is linearly stable and perturb it a little, it returns to its original state. We can even perturb it a lot, provided the perturbation is not too negative, and it will return to the steady state. If the perturbation is too much in the direction towards 0, however, then the tube plugs up - this seems to happen when $\int \frac{1}{a^4}$ for the perturbed profile is too large. It is hypothesized, though not shown, that if the initial flux q_0, calculated from $q_0 = P/\int \frac{1}{a_0^4}$, where a_0 is the initial profile, is smaller than the flux q_{unstable} corresponding to the unstable profile for a given P, then the tube will plug up.

If we start with a profile that is predicted to be linearly unstable and perturb it a little, it moves away from the unstable state. Which way it moves depends on how we perturb it. If the perturbation is mostly positive, in the direction of the stable profile corresponding to the same value of P, then it opens up, and moves to the stable profile. If the perturbation is mostly negative, away from the stable profile, then the tube plugs up.

As the tube moves from one profile to another, its shape is always close to that of a steady profile. Any localized disturbances to the profile are rapidly ironed out. This is consistent with the linear theory, which predicts large negative eigenvalues in the continuous spectrum, which appears to be associated with highly localized eigenfunctions.

5 Extensions of the model

5.1 Chamber Dynamics

We can introduce more dynamics into the problem by allowing the pressure to change. One simple modification is to assume the pressure is given by the height of lava in a lake, which is fed by a fixed flux q_0, or that the lava fills an elastic chamber whose pressure depends on how much lava is inside. In both cases, we can write the equation for the change in pressure as

$$\gamma \frac{dP}{dt} = q_0 - q(t) \tag{30}$$

where γ is a non-dimensional constant related to the characteristics of the magma chamber, such as the area of the lake or the elasticity of the chamber. The ratio S/γ tells us the rate of change of pressure compared to the rate of change of the radius.

Numerical simulations show that if the lake is fed with a flux q_0 that is in the stable regime, $q_0 > q_c$, then the tube converges to a tube with a radius $a(x, q_0)$, as long as it starts off with a great enough radius. If the lake is fed with a flux that is too small, $q_0 < q_c$, then every tube plugs up no matter how great its initial radius. Although the system showed growing or decaying oscillations for certain choices of γ/S, no limit cycles were observed, as was the case in the simulations performed by Whitehead and Helfrich ([16]). This is probably because, unlike their pressure-flux relationship, which had an extra stable regime near $q = 0$, our pressure-flux relationship lacks a second stable branch that can help to sustain oscillations.

We also tried setting $q = 0$ to see how fast a lake can be drained by a lava tube. It was never possible to drain the lake; the tube plugged up rapidly as soon as the pressure dropped below the critical value.

5.2 Branching Tubes

Whitehead and Helfrich ([16]) performed an experiment in which they let hot paraffin flow radially outward from a source. After a certain time, the paraffin was cool and viscous enough to be considered a solid, except in a few locations where it flowed rapidly in channels. Initially there were several channels, but as time progressed they all closed up except for one, which continued to flow indefinitely.

Wylie et al ([17]) performed a similar experiment, in which they showed that flow of liquid wax tends to concentrate in a single, narrow finger, with the rest of the flow almost stagnant.

In real lava flows, networks of tubes are occasionally observed instead of a single tube. We are interested in the processes that allow or inhibit several tubes to exist simultaneously. Under which combinations of parameters is it more favourable to feed a flow with several tubes, rather than a single big one? Is there an optimal density of tubes that we should expect? Answers to these questions would help us not only to understand the size and emplacement of lava tubes, but also the location and spacings of volcanoes themselves, as these are formed when a localized tube of lava flows up a fissure in a dike.

We have constructed a simple model in an attempt to answer these questions. Since this work is in its beginning phases, we outline the ideas only briefly so that they can be pursued later in more depth.

We suppose we have a series of n identical tubes, all parallel to the x-direction, which are located at points $\{y_i\}$ along the y-axis. We can non-dimensionalize y so that the points lie between 0 and 1. The tubes are fed by flow through a pipe which lies along the y-axis. There is a uniform flux per unit length q_0 into the pipe. The pressure difference across each tube is given by the pressure P_i at its corresponding point on the pipe. The flux through each tube q_i is determined by the pressure through some relationship, $P_i = f_i(q_i)$, such as (13). This in turn determines the flow through the pipe, which determines the pressure in the pipe.

We need a relationship between the pressure in the pipe and the flux through the pipe. Let us assume the flow in the pipe is Poiseuille flow. We then have

$$P_y = -\gamma q(y)$$

where γ is a non-dimensional parameter related to the size of the pipe compared to the sizes of the tubes.

We can calculate that the flux in the pipe is given by

$$q(y) = q_0 y - \sum q_i 1_{y>y_i}$$

(assuming that r_0 is small enough that we can neglect the modification to q near the entrance of a pipe).

Thus

$$P(y) = P_0 - \gamma \left(q_0 \frac{y^2}{2} + \sum q_i (y - y_i) 1_{y > y_i} \right)$$

where P_0 is the pressure at 0. Let P_f be the pressure at $y = 1$. Our full set of variables to solve for are

$$P_0\ , \quad \{P_i\}_{i=1..n}\ , \quad P_f\ , \quad \{q_i\}_{i=1..n}$$

The equations we have to solve for them are

$$\begin{aligned} \{P_i &= P_0 - \gamma \left(q_0 \frac{y_i^2}{2} + \sum q_k (y_i - y_k) 1_{y_i > y_k} \right) \} \\ P_f &= P_0 - \frac{q_0}{2} + \sum q_k (y_i - y_k) \\ \{P_i &= f_i(q_i)\} \end{aligned}$$

We can add one more equation, so we add conservation of mass:

$$\sum q_i = q_0$$

These equations were modelled on Matlab, and a solution can be found given the locations of the tubes $\{y_i\}$.

We next want to add time into the system. One way to do this is to let the relationship $P_i = f_i(q_i)$ depend on time, so that $f_i = f_i(q_i, t)$. In our simulations, we included time in the pressure-flux relationship by simulating the dynamics of each individual tube, and calculating the pressure as $P_i = q_i \int 1/a_i^4(x, q_i, t) dx$. Our procedure was to solve the system given initial tube profiles, use the calculated values of pressure to step the tube radii forward in time, and repeat using the new radii.

Figure (4) shows some of our results for $\gamma = 1$. We started with 50 identical tubes at locations chosen randomly from a uniform distribution in $(0, 1)$, and provided a flux per unit length that was enough to sustain 6 tubes in a stable configuration. Most of the tubes plugged up, and we ended up with 5, or occasionally 4, tubes in a steady flow. The model showed strong localization: almost all of the time the 5 tubes were sequential points, and only in a very small number of runs did they split into 2 groups.

5.3 2D Planar Flow

There are several situations in which we may be interested in a type of lava transport which could be modelled as a 2-dimensional ‘tube’. One is when lava flows down a slope as a sheet, and is homogeneous in the cross-sheet direction. Another is when a volcano erupts and send lava up a long, narrow fissure. The shape and thermal properties of the 2-dimensional system should be susceptible to an analysis similar to the 3-D case. We looked at the equations for the 2D system in the hopes that they would have similar results to the 3-D. We were surprised to find that they were actually harder to analyze than the 3-D equations, but preliminary calculations suggest that they may share the same qualitative characteristics.

The 2-D equations use the same non-dimensionalization, except for a slight change. The Peclet number is modified to be

$$Pe = \frac{2\Delta P a_0^4}{3\kappa\mu L^2}$$

The external temperature equation solves $\frac{\partial^2 T_e}{\partial h^2} = 0$, $T_e|_{h=r_0/a} = K$, $T_e|_{h=1} = 0$, and has solution and consequent flux

$$T_e = \frac{Ka(x)(h-1)}{r_0 - a(x)} \ , \qquad \frac{\partial T_e}{\partial h} = \frac{Ka(x)}{r_0 - a(x)}$$

The internal temperature equation and the relationship between P and q are

$$\begin{aligned} a(x)q(1-h^2)T_x &= \frac{\partial^2 T}{\partial h^2} \\ q &= \frac{PeP}{\int \frac{1}{a^3}dx} \end{aligned}$$

The internal temperature is thus

$$T(x,h) = \sum_n A_n \exp\left(-\frac{\lambda_n^2}{q}\int^x \frac{1}{a(s)}ds\right)\phi_n(h) \tag{31}$$

where λ_n, ϕ_n are the eigenvalues and eigenvectors of the problem, solving

$$\phi'' - \lambda^2(1-h^2)\phi = 0 \ , \qquad \phi(1) = 0 \ , \quad \phi'(0) = 0$$

and A_n are determined from the temperature distribution at $x = 0$. These eigenfunctions are discussed in Shah and London ([14]).

Unfortunately, $a(x)$ appears in the solution for T. This means that even if we are given the flux, we may not be able to solve for $a(x)$. We find that

$$\begin{aligned} \frac{Ka(x)}{r_0 - a(x)} &= \sum_n G_n \exp\left(-\frac{\lambda_n^2}{q}\int^x \frac{1}{a(s)}ds\right) \ , \\ & \quad G_n = A_n\phi_n'(1) \\ \Rightarrow \quad a(x) &= \frac{r_0 \sum A_n R_n \exp\left(-\frac{\lambda_n^2}{q}\int^x \frac{1}{a(s)}ds\right)}{Kr_0 + \sum A_n R_n \exp\left(-\frac{\lambda_n^2}{q}\int^x \frac{1}{a(s)}ds\right)} \end{aligned} \tag{32}$$

This is a transcendental equation that defines $a(x)$. It may or may not have a solution, and the solution may or may not be unique. A simple argument shows that it probably does not have a solution in all of parameter space.

Suppose the initial temperature distribution is such that it is made up of only one eigenfunction. (This would also be the case if we start the experiment far down the tube, where the other eigenfunctions have decayed exponentially.)

We must solve

$$G_1 \exp\left(-\lambda_1^2 \int_0^x \frac{1}{qa(s)} ds\right) = \frac{Ka(x)}{r_0 - a(x)} \tag{33}$$

for $a(x)$. Taking the derivative of both sides and substituting for the exponential gives

$$\frac{da}{dx} - \frac{\lambda_1^2}{qr_0} a = -\frac{\lambda_1^2}{q}$$

Solving and using initial condition $a(0) = \frac{G_1}{K+G_1}\bar{r}$, obtained by setting $x = 0$ in (33), gives

$$a(x) = r_0 \left(1 - \frac{K}{K + G_1} e^{\frac{\lambda_1^2}{q} x}\right)$$

In order for this to be greater than 0, we need

$$\frac{G_1}{K} > e^{\frac{\lambda_1^2}{qr_0}}$$

.

Thus, if q is too small or $|K|$ is too large, we expect there to be no solution.

6 Conclusions

We have created a simplified model of the heat transport in a lava tube, and used this to investigate the existence, shape, and maximal possible length of a lava tube. This model predicts a functional relationship between the pressure difference across the length of the tube, and the flux of fluid through the tube in steady-state, such that for large values of the flux, $\frac{dP}{dq}$ is positive, for small values it is negative, and P has a minimum at $q = q_c$, which depends on a non-dimensional temperature constant. This curve tells us whether or not, for a given non-dimensional Peclet number, a steady-state lava tube can exist. It further tells us when such a solution is stable to small linear perturbations: when $q > q_c$ the tube is stable and when $q < q_c$ the tube is unstable. These linear stability predictions were confirmed with numerical simulations. Unstable tube shapes either went to the stable state corresponding to the same pressure difference, or plugged up and ceased to exist. The maximal length of a lava tube was estimated for typical values of the parameters, and was found to be approximately 30-900km, depending on the assumptions.

7 Acknowledgements

Thank you to Jack Whitehead, for supervising this project, as well as to Lou Howard, Norman Lebovitz, and Ted Johnson for many helpful suggestions and discussions. Many thanks also to WHOI and the GFD program for the opportunity to participate in this program.

8 Appendix

8.1 Eigenvalues of the temperature problem

The eigenfuctions are solutions of

$$\phi'' + \frac{1}{h}\phi' + \lambda^2(1-h^2)\phi = 0\ , \qquad \phi(1) = 0\ , \quad \phi'(0) = 0\ .$$

They are given by

$$\phi_n = e^{-\lambda_n^2 h^2/2} M(\frac{1}{2} - \frac{\lambda_n}{4}, 1, \lambda_n h^2)$$

where $M(a, b, z)$ is the confluent hypergeometric function:

$$\begin{aligned} M(a,b,z) &= 1 + \frac{a}{b}z + \frac{(a)_2}{(b)_2}\frac{z^2}{2!} + \ldots + \frac{(a)_n}{(b)_n}\frac{z^n}{n!} + \ldots \\ & \quad (a)_n = a(a+1)(a+2)\ldots(a+n-1)\ , (a)_0 = 1 \end{aligned}$$

and λ_n are solutions of the transcendental equation

$$M(\frac{1}{2} - \frac{\lambda}{4}, 1, \lambda) = 0\ .$$

It can be shown that

$$M(a,b,z) = \frac{\Gamma(b)}{\Gamma(a)} e^z z^{a-b} \left(1 + O(|z|^{-1})\right)$$

so

$$\phi_n(h) = \frac{e^{\lambda_n/2}}{\lambda_n \Gamma(\frac{1}{2} - \frac{\lambda_n}{4})} \frac{e^{-\frac{\lambda_n}{2}(h-1)^2}}{h^{(1+\frac{\lambda_n}{2})}} \left(1 + O(\frac{1}{\lambda_n h^2})\right)$$

The eigenfunctions are orthogonal with respect to weighting function $h(1-h^2)$.

See Chapter 13 of Abramowitz and Stegun for more information about the confluent hypergeometric function. [1]

Shah and London ([14]) show that the eigenvalues and initial conditions G_n can be approximated as

$$\begin{aligned}
\lambda_n &= \lambda + S_1\lambda^{-4/3} + S_2\lambda^{-8/3} + S_3\lambda^{-10/3} + S_4\lambda^{-11/3} + O(\lambda^{-14/3}) \\
G_n &= \frac{C}{\lambda_n^{1/3}}\left(1 + B_1\lambda^{-4/3} + B_2\lambda^{-6/3} + B_3\lambda^{-7/3} + B_4\lambda^{-10/3} + B_5\lambda^{-11/3} + O(\lambda^{-4})\right)
\end{aligned}$$

where

$$\begin{aligned}
\lambda &= 4n + 8/3 \\
S_1 &= 0.159152288 \\
S_2 &= 0.011486354 \\
S_3 &= -0.224731440 \\
S_4 &= -0.033772601 \\
C &= 1.012787288 \\
B_1 &= 0.144335160 \\
B_2 &= 0.115555556 \\
B_3 &= -0.21220305 \\
B_4 &= -0.187130142 \\
B_5 &= 0.0918850832
\end{aligned}$$

They also list more accurate values of these numbers for the first few eigenvalues.

8.2 Calculation of $f'(q)$

We have that

$$f(q) = q\int_0^1 \frac{1}{a^4(x,q)}$$

Thus

$$\begin{aligned}
f'(q) &= \int_0^1 \frac{1}{a^4}\left[1 - 4q\frac{\partial(\ln a)}{\partial q}\right] \\
&= \int_0^{1/q} \frac{1}{a^4}\left[1 - 4K\frac{\sum G_n\lambda_n^2 s e^{-\lambda_n^2 s}}{(\sum G_n e^{-\lambda_n^2 s})^2}\right] ds
\end{aligned}$$

after change of variables $s = x/q$. Now the only dependence of $f'(q)$ on q is in the limit of the integral.

Let

$$g(s) \equiv \frac{K\sum G_n\lambda_n^2 s e^{-\lambda_n^2 s}}{(\sum G_n e^{-\lambda_n^2 s})^2}$$

Then

$$g'(s) = \frac{(\sum G_n e^{\lambda_n^2 s})(\sum -KG_n\lambda_n^2(1-\lambda_n^2)se^{-\lambda_n^2 s}) + 2K(\sum G_n\lambda_n^2 e^{-\lambda_n^2 s})(\sum G_n\lambda_n^2 s e^{-\lambda_n^2 s})}{(\sum G_n e^{-\lambda_n^2 s})^3}$$

Using $K, G_n < 0$ we find that $g(0) = 0$, $g'(s) > 0$ $(s > 0)$, $g(s) \to \infty$ as $s \to \infty$. Thus, we are integrating a quantity which is positive for small s and negative, going to $-\infty$, for large s, and changes sign only once, so $\exists\ q_c$ s.t. $f'(q) < 0$ for $q < q_c$, $f'(q) > 0$ for $q > q_c$.

8.3 Derivation of the linear stability equation - general case

We derive the linear stability problem for a general external heat flux, internal heat flux, and pressure relationship. We show that if these functions have a particular form, then the tube radius is linearly stable whenever $\frac{dP}{dq} > 0$ and linearly unstable whenever $\frac{dP}{dq} < 0$.

Let us have the following functions:

$$\begin{array}{rcll} a(x,q): & \mathbf{R}\times\mathbf{R}\to\mathbf{R} & = & \text{tube radius} \\ P(q,a): & \mathbf{R}\times C(\mathbf{R})\to\mathbf{R} & = & \text{Pressure} \\ E(a): & \mathbf{R}\to\mathbf{R} & = & \text{External heat flux} \\ I(x,q): & \mathbf{R}\times\mathbf{R}\to\mathbf{R} & = & \text{Internal heat flux} \end{array}$$

We make the following assumptions:

- $\frac{\delta P}{\delta a}$ is a linear, positive definite operator from $C(\mathbf{R}) \to \mathbf{R}$.
- $E'a < 0$
- $\frac{\partial a}{\partial q} > 0$.

We also suppose that any arbitrary profile evolves in time according to

$$\frac{da}{dt} = E(a) - I(x,q)\ , \qquad \frac{dP}{dt} = 0\ .$$

Suppose we start with a steady profile a, with corresponding flux q, and perturb it by ϵa_1. Let the flux change by an amount ϵq_1. We derive the $O(\epsilon)$ equation for the evolution of a_1. We have that

$$\begin{aligned} \frac{dP}{dt} = 0 \quad &\Rightarrow \quad \frac{\partial}{\partial \epsilon}|_{\epsilon=0} P(q_0 + \epsilon q_1, a + \epsilon a_1) = 0 \\ &\Rightarrow \quad q_1 \frac{\partial P}{\partial q} + \frac{\delta P}{\delta a}[a_1] = 0 \\ &\Rightarrow \quad q_1 = \frac{-\frac{\delta P}{\delta a}[a_1]}{\frac{\partial P}{\partial q}} \end{aligned}$$

Thus, a_1 evolves according to

$$\begin{aligned} \frac{da_1}{dt} &= \frac{\partial}{\partial \epsilon}|_{\epsilon=0} \left(E(a + \epsilon a_1) - I(x, q + \epsilon q_1)\right) \\ &= a_1 \frac{\partial E}{\partial a} - q_1 \frac{\partial I}{\partial q} \\ &= a_1 \frac{\partial E}{\partial a} + \frac{\frac{\delta P}{\delta a}[a_1]}{\frac{\partial P}{\partial q}} \frac{\partial I}{\partial q} \end{aligned}$$

Since a satisfies $E(a) = I(x,q)$, we can take the q-derivative of this to get $\frac{dE}{da}\frac{\partial a}{\partial q} = \frac{\partial I}{\partial q}$. We also know that $\frac{\partial P}{\partial q} = \frac{dP}{dq} - \frac{\delta P}{\delta a}[\frac{\partial a}{\partial q}]$. Substituting these into the last equation gives

$$\frac{da_1}{dt} = \frac{dE}{da}\left(a_1 + \frac{\frac{\partial a}{\partial q}\frac{\delta P}{\delta a}[a_1]}{\frac{dP}{dq} - \frac{\delta P}{\delta a}[\frac{\partial a}{\partial q}]}\right) \tag{34}$$

Set the RHS equal to λa_1 and solve for a_1 to get

$$a_1 = \frac{\frac{dE}{da}\frac{\delta P}{\delta a}[a_1]\frac{\partial a}{\partial q}}{(\frac{dP}{dq} - \frac{\delta P}{\delta a}[\frac{\partial a}{\partial q}])(\lambda - \frac{dE}{da})}$$

Let $\frac{\delta P}{\delta a}[a_1] = D$. Take $\frac{\delta P}{\delta a}$ of the above equation to get

$$\frac{\delta P}{\delta a}\left[\frac{-\frac{dE}{da}\frac{\partial a}{\partial q}}{(\frac{dp}{dq} - \frac{\delta P}{\delta a}[\frac{\partial a}{\partial q}])(\lambda - \frac{\partial E}{\partial a})}\right] = 1 \tag{35}$$

If $\frac{dP}{dq} = 0$ and $\lambda = 0$, then LHS $= 1$. If $\frac{dP}{dq} \uparrow$ or $\lambda \uparrow$, then LHS $\downarrow$, and if $\frac{dP}{dq} \downarrow$ or $\lambda \downarrow$, then LHS $\uparrow$. Therefore

$$\begin{aligned} \frac{dP}{dq} > 0 \quad &\Rightarrow \quad \lambda < 0 \qquad \text{(stable)} \\ \frac{dP}{dq} < 0 \quad &\Rightarrow \quad \lambda > 0 \qquad \text{(unstable)} \end{aligned}$$

References

[1] Abramowitz and Stegun. *Handbook of Mathematical Functions*. Dover, 1972.

[2] Bruce and Huppert. Thermal control of basaltic fissure eruptions. *Nature*, 342:665–667, 1989.

[3] Bruce and Huppert. *Magma Transport and Storage*, chapter Solidification and melting in dykes by the laminar flow of basaltic magma, pages 87–102. Wiley, 1990.

[4] Dragoni, D'Onza, and Tallarico. Temperature distribution inside and around a lava tube. *Journal of Volcanology and Geothermal Research*, 115:43–51, 2002.

[5] Karl. Helfrich. Thermo-viscous fingering of flow in a thin gap: a model of magma flow in dikes and fissures. *Journal of Fluid Mechanics*, 305:219–238, 1995.

[6] Keszthelyi. A preliminary thermal budget for lava tubes on the earth and planets. *Journal of Geophysical Research*, 100:20411–20420, 1995.

[7] Klingelhofer, Hort, Kumpel, and Schmincke. Constraints on the formation of submarine lava flows from numerical model calculations. *Journal of Volcanology and Geothermal Research*, 92:215–229, 1999.

[8] Leveque. Les lois de la transmission de chaleur par convection. *Annales des Mines, Memoires, Series 12*, 13:201–299,305–362,381–415, 1928.

[9] Lister and Dellar. Solidification of pressure-driven flow in a finite rigid channel with application to volcanic eruptions. *Journal of Fluid Mechanics*, 323:267–283, 1996.

[10] Peterson, Holcomb, Tilling, and Christiansen. Development of lava tubes in the light of observations at mauna ulu, kilauea volcano, hawaii. *Bulletin of Volcanology*, 56:343–360, 1994.

[11] Saimoto and Gregg. Channeled flow: Analytic solutions, laboratory experiments, and applications to lava flows. *Journal of Geophysical Research*, 106:8629–8644, 2001.

[12] Sakimoto, Crisp, and Baloga. Eruption constraints on tube-fed planetary lava flows. *Journal of Geophysical Research*, 102:6597–6613, 1997.

[13] Sakimoto and Zuber. Flow and convective cooling lava tubes. *Journal of Geophysical Research*, 103:27465–27487, 1998.

[14] Shah and London. *Advances in Heat Transfer.* Academic Press, 1978.

[15] Turcotte and Schubert. *Geodynamics.* Cambridge University Press, 2002.

[16] Whitehead and Helfrich. Instability of flow with temperature-dependent viscosity: A model of magma dynamics. *Journal of Geophysical Research*, 96:4145–455, 1991.

[17] Wylie, Helfrich, Dade, Lister, and Salzig. Flow localization in fissure eruptions. *Bulletin of Volcanology*, 60:432–440, 1999.

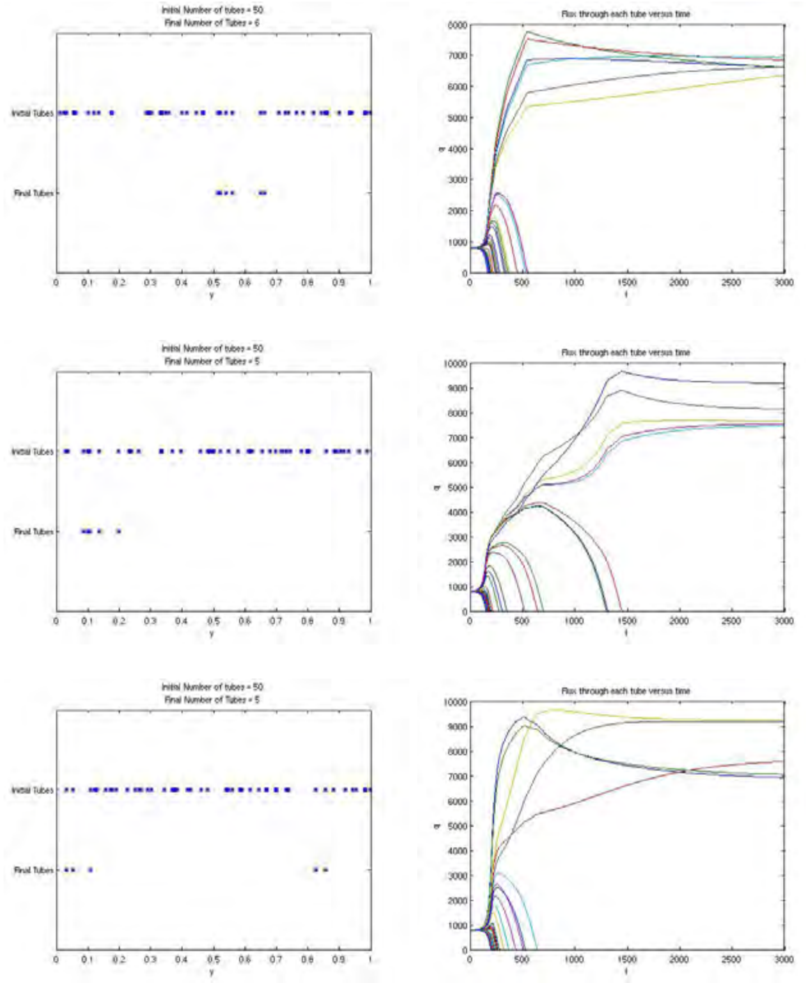

Figure 4: Simulations of systems of tubes. Left: Plot showing initial location of tubes (top row) and tubes that remained open after a long time (bottom row). Right: Flux through each tube as a function of time.

Simultaneous Differential Diffusion under Weak Turbulence

A. RUIZ-ANGULO[1]

[1]Department of Mechanical Engineering, California Institute of Technology, Pasadena, CA 91106, USA

We present the results from experimental measurements of simultaneous fluxes of heat and salt across an interface of a diffusively stable bi-layer system. Turbulence was generated inside each of the layers by oscillating grids. Time series of temperature and salinity were taken until both properties came to equilibrium.

1. Introduction

The density of sea-water, ρ_{sw}, is a function of temperature, T, and salinity, S. In the ocean, when mixing of density surfaces occur (diapycnal), temperature and salinity mix as well. The two properties could either mix at the same rate or at a different rates. In the presence of turbulence, the larger molecular diffusivity of T might create a preferential turbulent transfer relative to S. However, the usual formulas used in numerical models of the ocean specify a transfer independent of diffusivity. If diffusion is incorporated, this process is often called *differential diffusion*.

The more familiar *double diffusion* convection has two important regimes based on the density ratio (R_ρ): $R_\rho = \alpha \partial T \partial z / \beta \partial S z > 1$ corresponding to the *finger regime* and $R_\rho = \beta \frac{\partial S}{\partial z} / \alpha \frac{\partial T}{\partial z} > 1$ for the *diffusive regime* (Turner (1979)). The *diffusive* and *finger* regimes lead to differential diffusion by imposing 'ordinary' turbulence, i.e., the kinetic energy driving the the double diffusion is supplied. Turner (1968) and Linden (1971) found that the convective finger regime could be accelerated and both properties, temperature and salinity mixed at the same rate for small Ri. The experiments showed that the action of the turbulence could overcome the heat flux due to the fingers.

Numerical simulations of turbulent mixing models ignore the fact that temperature and salinity might transport differentially, arguing that for low Richardson number, Ri, heat and salt fluxes produce an effective coefficient of eddy diffusivity $\kappa \sim 1$. On the other hand, for weakly turbulent flows –low to moderate Ri– the diffusivity ratio, κ_T/κ_S (where κ_T and κ_S are the eddy diffusivities for salt and heat) is less than 1 (Jackson & Rehmann (2003*b*), Gargett *et al.* (2003)). It has been show as well (Jackson & Rehmann (2003*a*)) that the mixing efficiency is sensitive to the eddy diffusivity; therefore, considering $\kappa = 1$ would represent an error on calculations were the mixing regime is not strenuously turbulent, i.e., $Ri > 1$.

Recent work has led to a greatly improved understanding of this phenomenon. Zellouf *et al.* (2005) presented experiments on single density stratified interface configurations, where salt and heat fluxes are calculated separately. By finding an effective Richardson number, Ri, based on the turbulence generated by two grids oscillating on each of the stable layers they showed that the heat and salt buoyancy fluxes in stratified fluid grid turbulence possessed two different responses to the mixing. This is similar to that in a double-diffusive convection system.

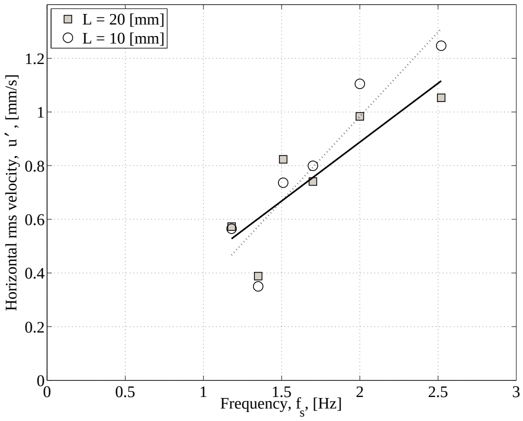

Figure 1. Horizontal rms velocity as a function of the grids frequency. The zero reference corresponds to the initial location of the stratified interface. The length L is measured symmetrically from the zero reference

Even for configurations where T and S are stable, there is potential for differential transport of T and S (Merryfield *et al.* (1998)). The objective of the present work is to document wether the buoyancy fluxes of heat and salt under mild turbulence are the same or are different.

2. Experimental setup and technique

Induced mixing experiments were carried out for a diffusively stable bi-layer system. Before each experiment, half of an insulated tank was filled up with *cold* and *salty* water. On top of that layer, *fresh* and relatively *warm* water was slowly poured over a floating sponge, producing a sharp interface between the two layers. Two grids previously located in the middle of each layer were oscillated to produce turbulence. The turbulence intensity is a linear function of the oscillating frequency (see Figure 1).

2.1. *Experimental apparatus*

All the experiments were conducted in an insulated container made out of styrofoam, the inner dimensions of the tank were 300 × 300 × 300 [mm], the thickness of the walls were 25.7 [mm].

For this experiment, the heavier *cold and salty* fluid was poured into the tank first and then the lighter *warm and fresh* fluid was carefully poured on top of the first layer. The lighter fluid was slowly pumped onto a floating sponge in order to minimize the mixing at the interface. Figure 3 sketches a typical interface between the two layers. In every case both layers were of equal depth, 150 [mm]. In these experiments the interface between the two fluids remained sharp and stable before any oscillations commenced. For all the analysis the molecular diffusion was neglected. The main goal of this work was to look at the mixing driven by weak turbulence. Although in the absence of turbulence the mixing thickness for such a stable configuration grows as $O(1/\sqrt{t})$, all the experiments started soon after the top layer was completed.

The two grids that generated the turbulence were machined out of a Plexiglas plate, of thickness 6.43 [mm] and dimensions 100 × 100 [mm]. Figure 2 shows a sketch of the grid geometry, 16 holes of 12.7 [mm] in diameter were equally distributed on the plate,

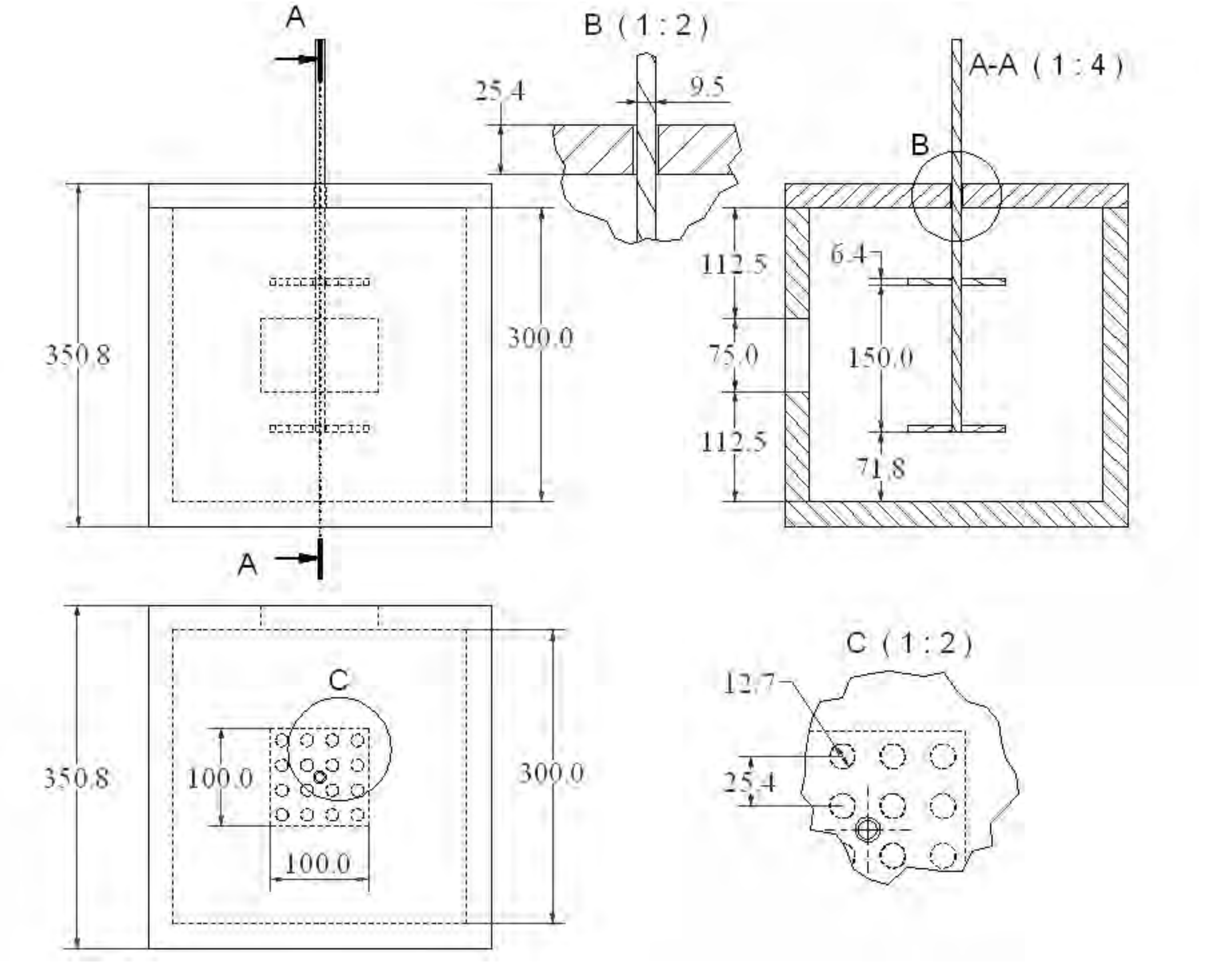

FIGURE 2. Experimental apparatus. The upper left panel corresponds to one side view of the experiment, the section AA' represents a cut right in the centre of the apparatus. The thickness of the walls is uniform, 25.4 [mm]. The location of the grids correspond to the centre of each layer. The two grids are identical and a detailed picture with the distribution of the holes is shown. The detail B shows the top cover of tank and the rod which was coupled to an electric motor. The lower left panel is the top view of the apparatus.

the separation between centers was 25.7 [mm]. The two grids were connected from the center by a long rod with 9.52 [mm] in diameter. The location of the grids was at the centre of each stratified layer where they simultaneously oscillated. Note that both grids were 75 [mm] away from the interface.

The rod was coupled to a mechanism which converted the rotational motion from an electric motor into a periodic linear vertical displacement. The displacement length, the stroke, was set to 10 [mm] for all the experiments. The motor was connected to a variable speed device which allowed us to adjust the grid oscillating frequency. For all the experiments the oscillating frequency ranged from $1 - 3$ [Hz]. The precision of this controlling device combined with the friction of the mechanism produced errors in the frequency around 10%. For each experiment, the oscillating frequency was measured by recording the sound produced by the mechanism every cycle. The sound signal was recorded, filtered and a simple spectral analysis was performed resulting on the oscillating

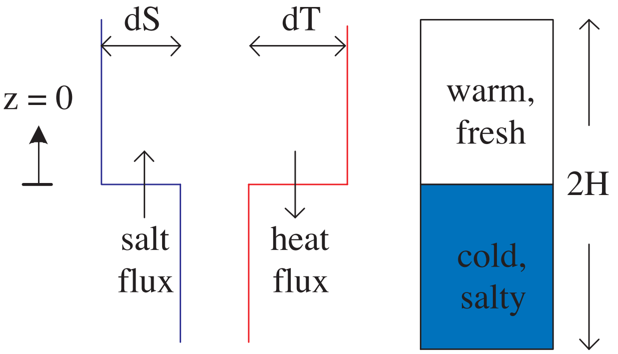

FIGURE 3. Initial temperature and salinity profiles. The configuration presented is diffusively stable. The interface is set to be the zero reference, the total depth of the tank is 2H.

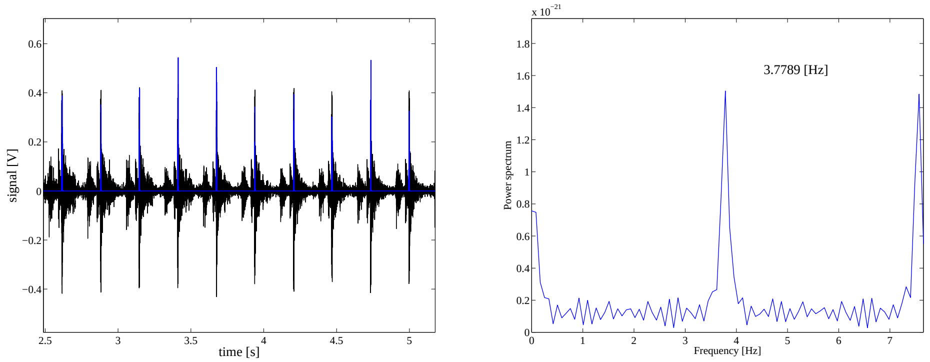

FIGURE 4. Recorded sound signal and the resulting filtered one (left panel), the corresponding characteristic frequency obtained by using a typical Fast Fourier Transform (FFT).

frequency. This procedure was repeated several times within every single experiment, the average of those measurements corresponded to the grids frequency.

The fluid properties were measured from two fixed points located symmetrically about the interface. Two syringes were placed at the hypothetical centre of each layer, 150 [mm] apart. Similarly, two thermometers were placed at the same height as the syringes, sharing the same $x-y$ plane.Time series of temperature and density were simultaneously taken at those two fixed locations.

The temperature changes of each layer were tracked by using a HOBO temperature logger accurate up to 0.01 [^{o} C] . For all the experiments, the sampling rate was 2 [samples/s]. Both thermistors were programed to start at the same time, their internal watch corresponded to real time. The evolution of the density with time was tracked by taking samples of water from the two syringes placed at the centre of each layer. In order to compare density and temperature time series, an external watch was synchronized with the internal watch of the thermistors. The sampling rate for the density varied for all the experiments, approximately $1-2$ samples every 10 [min]. The sampled fluid was then analyzed separately with the Anton-paar density meter. The experiment was constantly running at the same rate for several hours until the quantities approached equilibrium, those times ranged from $1-3.5$ [hrs]. The heat losses through the wall were neglected.

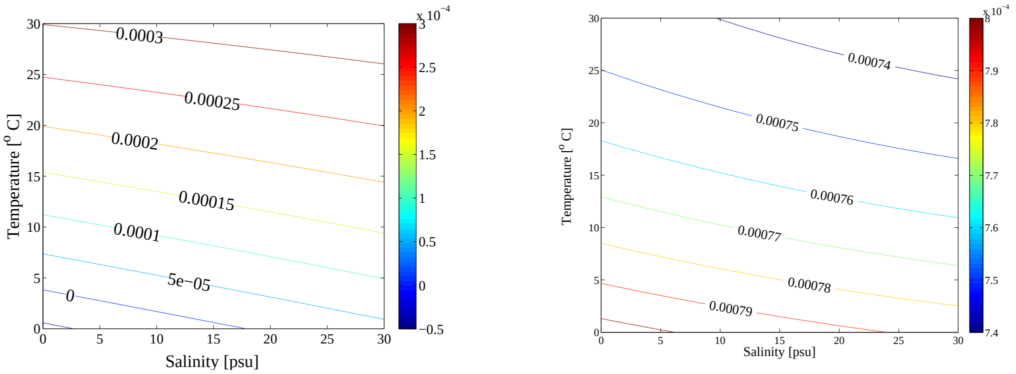

FIGURE 5. Variations of α (left) and β (rigth) with of temperature and salinity at a constant pressure (atmospheric). The range of values for T and S spans the experiments presented in this work

.

The insulation quality of the tank was tested . Therefore, the heat flux with the exterior was ignored within each experiment.

3. Experimental observations

The initially stable layer, represented in Figure 3, gradually changed once the grids started oscillating, small incursions of fluid from the lower and upper layer crossed the interface and transport of heat and salt began. The experiment was designed to be symmetric; therefore, the flux of heat and salt through the interface was assumed to be the same for the upper and lower layer.

In order to compare the contribution of density due to temperature and salinity, the quantities were expressed in buoyancy units. The linear relation for density, ρ, as a function of temperature, T, and salt concentration, S, is given by Equation 3.1

$$\frac{\rho(S,T)-\rho_0}{\rho_0} = -\alpha(T-T_0)+\beta(S-S_0) \tag{3.1}$$

The coefficients α, thermal expansion, and β, saline contraction, are functions of P, T, and S. The coefficient α was pretty sensitive to the changes in T and S, whereas β barley changed within the experimental range. Those variations are shown in figure 5.

The initial conditions for all the experiments are shown in Table 1. The density ratio, R_ρ[†], is defined by the ratio of the magnitude of density due to the temperature difference

---

[†] In order to obtain positive ratio of densities, a minus sign was added since $\Delta\rho < 0$ and $\Delta T > 0$

Experiment number	R_ρ	N, [1/s]	f_s, [1/s]
DD01	0.67	0.72	1.18
DD02	0.49	0.83	2.28
DD03	0.34	0.87	1.76
DD04	0.29	1.69	1.58
DD05	0.29	1.04	1.85
DD06	0.23	1.01	1.72
DD07	0.16	1.36	1.66

TABLE 1. Initial conditions for different experiments. The experiments are sorted by their density ratio, R_ρ. The initial buoyancy frequency, N, and the average oscillating frequency, f_s, are tabulated as well.

across the interface to the density change due to temperature difference,

$$R_\rho = -\frac{\alpha \Delta T}{\beta \Delta S} \tag{3.2}$$

where ΔT and ΔS are the initial temperature and salinity jumps across the interface.

Since the coefficient of thermal expansion is a function of T and S, the density difference due to temperature is defined by $\alpha\Delta T = (\alpha_w T_w - \alpha_c T_c)$. From figure 5 it is possible to observe that the changes in β within the experimental range of T and S are small.

The buoyancy frequency, N^2, is defined by $-(g\Delta\rho)/(\rho_0 H)$, where H is the distance from the interface to the point where the samples are taken, $\Delta\rho$ is the difference in density between the two layers, ρ_0 is the average density and g is the acceleration due to gravity.

The heat flux, F_T across the interface is defined by

$$A\frac{d}{dt}\int_{H/2}^{0} \rho_c c_p T_c dz = F_T A \ = \ -A\frac{d}{dt}\int_{0}^{H/2} \rho_w c_p T_w dz = F_T A \tag{3.3}$$

where A is the area of the interface, c_p is the specific heat at constant pressure, ρ_c and T_c are the density and temperature of the 'cold' layer. Similarly, ρ_w and T_w are the the density and temperature of the 'warm' layer. Due to the symmetry of the experiment, the heat and salt fluxes across the interface should have the same magnitude.

$$A\frac{d}{dt}\int_{H/2}^{0} \rho_0 S_c dz = F_S A \ = \ -A\frac{d}{dt}\int_{0}^{H/2} \rho_0 S_w dz = F_S A \tag{3.4}$$

where S is the salt concentration and the subindices c and w correspond to the cold and warm layers.

3.1. *Differential equilibrium*

The state of equilibrium is defined as the absence of fluctuations on the buoyancy quantities, which corresponds to a fully mixed state. For the combinations presented in this work the equilibrium is reached differently for temperature and salinity.

For a relatively weak stratification and a relatively strong turbulence, the equilibrium is reached at the same time for temperature and salinity (See Figure 6). On the other hand, for relatively strong stratification and weak turbulence, differential diffusion occurs. In Figure 7 it is possible to observe that the buoyancy temperature has reached equilibrium

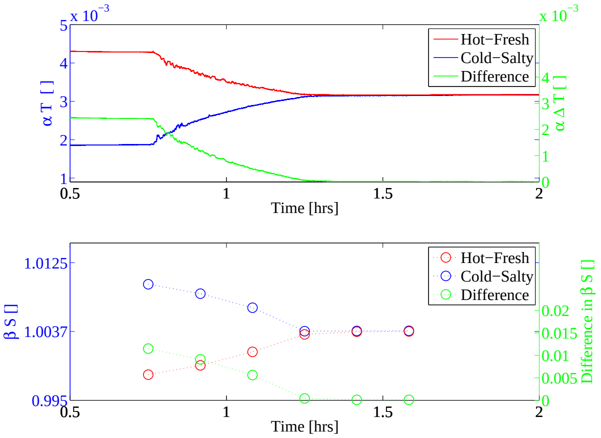

FIGURE 6. Experiment DD03. The upper panel shows the temperature decaying with time and in the lower layer, the corresponding decay of salinity – both in buoyancy units –. The final equilibrium state is about the same for both quantities.

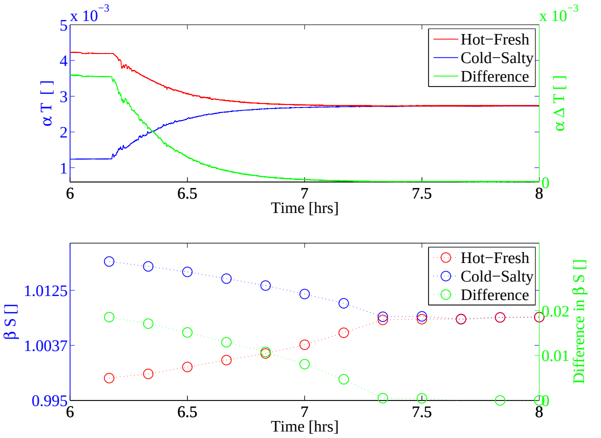

FIGURE 7. Experiment DD06. The upper panel shows the temperature decaying with time and in the lower layer, the corresponding decay of salinity – both in buoyancy units –. The final equilibrium state is different for both quantities.

but the salinity requires more time to become fully mixed. In this case, the differential transport of the properties is clear.

3.1.1. *Constant oscillating frequency*

To isolate the effect of the stratification on the experiments, we carried an experiment where we changed the initial stratification and on average the oscillating frequency remained constant. From Table 1 the experiments taken were: $DD03$, $DD06$ and $DD07$. The $T - S$ evolution is shown in Figure 8 where the blue symbols correspond to the cold and salty layer and the red symbols correspond to the warm and fresh layer. The ordinate corresponds to the temperature in Celsius and the abscissa corresponds to the salinity in *psu* units. The contour lines correspond to iso-density (isopycnals) surfaces.

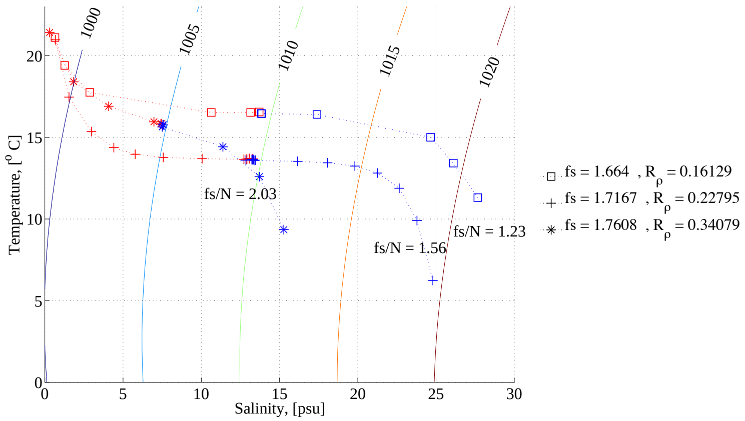

FIGURE 8. $T - S$ diagram for relatively constant oscillating frequencies

.

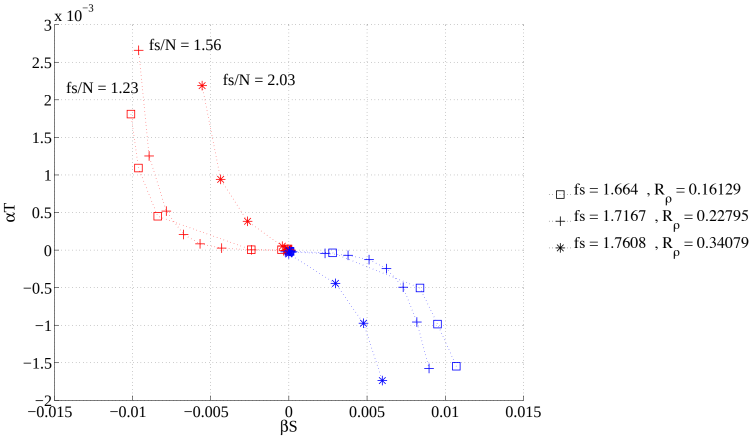

FIGURE 9. $T - S$ diagram in buoyancy units for relatively constant oscillating frequencies

.

Figure 9 shows a similar plot as Figure 8 representing a $T - S$ diagram in buoyancy units. For convenience the origin corresponds to the equilibrium point form both sides, salinity and temperature. The direction of time travels from the extreme on the curves towards the equilibrium point.

For relatively high density ratios (Eq. 3.2) and similar oscillating frequency the temperature and salinity reach equilibrium at similar times. The lower the density ratio, the slower the salinity reaches equilibrium. The ratio of oscillating frequency, f_s, to the initial buoyancy frequency, N, was estimated. The ratio of frequencies is a measurement of the inertia to the stratification strength; therefore, the larger the frequency ratio, the faster the quantities come to equilibrium.

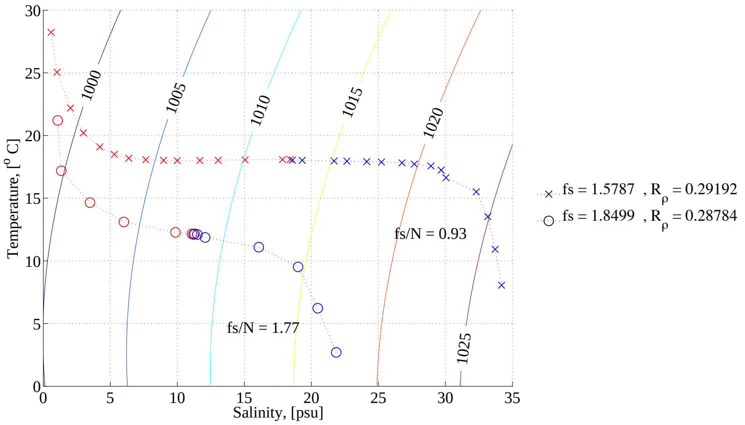

FIGURE 10. $T - S$ diagram for relatively constant density ratios.

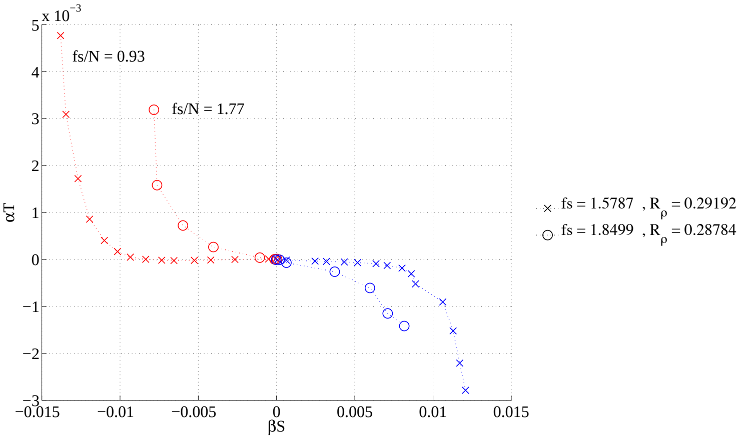

FIGURE 11. $T - S$ diagram in buoyancy units for relatively constant density ratios.

3.1.2. *Constant density ratio*

We now look at the influence of the frequency. Note that for the density ratio to be equal does not mean that the initial conditions are exactly the same. The variations on the oscillating frequency produced the two expected regimes: differential equilibrium and non differential equilibrium. In Figure 11 two different experiments, $DD04$ and $DD05$, are shown. The ratio of densities was constant for the two experiments and the oscillating frequencies were 1.58 and 1.85 Hz. Figure 10 shows the dimensional $T - S$ diagram, $iso - density$ surfaces were superimposed to show that the mixing process crosses those lines until it reaches equilibrium. Similarly to the previous section the larger the ratio of frequencies, the slower the equilibrium is reached.

4. Summary

This study presented controlled laboratory experiments that allowed to observe simultaneously the evolution of the heat and salt fluxes across the interface between two layers. The diffusively stable layers presented for all the experiments were perturbed by symmetrically oscillating two grids in the range of $1.2 < f_s < 2.2$ Hz. The density ratios spanned the range of $0.16 < R_\rho < 0.67$.

We separated the effects in frequency perturbed and density ratio perturbed and we found that for both cases there is a mismatch on reaching the equilibrium for the temperature and for the salinity. We also found that the heat flux decreases monotonically for all the cases, regardless of the value of f_s or R_ρ. On the other hand, the flux of salt tends to be constant for low oscillating frequencies ($DD01$ and $DD04$), for the rest of the experiments the flux of salt increases reaching a maximum approximately at the same time as the heat flux begins to asymptote.

In the absence of a proper Richardson number, the ratio of frequencies seemed to be the right parameter to characterize the differential equilibrium

Combined results from numerical simulations, laboratory experiments and geophysical measurements indicate that, at low (but non-zero) turbulence levels (small Reb), there is a strong tendency for incomplete mixing of salinity when temperature is completely mixed (small d). If this is widespread in the deep ocean, models that mix both constituents at the same rate must be reconsidered.

5. Acknowledgments

Thanks to all the fellows and staff from the GFD program, specially to Jack Whitehead for his guidance and Keith F. Bradley for his help on building and putting together the experiment. Special thanks to George Veronins and Louis Howard for their helpful discussions.

REFERENCES

GARGETT, ANN E., MERRYFIELD, WILLIAM J. & HOLLOWAY, GREG 2003 Direct numerical simulation of differential scalar diffusion in three-dimensional stratified flow. *Journal of Physical Oceanography* **33**, 1758–1782.

JACKSON, P. RYAN & REHMANN, CHRIS R. 2003*a* Kinematic effects of differential transport on mixing efficiency in a diffusively stable, turbulent flow. *Journal of Physical Oceanography* **33**, 299–304.

JACKSON, P. RYAN & REHMANN, CHRIS R. 2003*b* Laboratory measurements of differential diffusion in a diffusively stable, turbulent flow. *Journal of Physical Oceanography* **33**, 1592–1603.

LINDEN, P. F. 1971 Salt fingers in the presence of grid generated turbulence. *Journal of Fluid Mechanics* **49**, 611–624.

MERRYFIELD, W.J., HOLLOWAY, GREG & GARGETT, ANN E. 1998 Differential vertical transport of heat and salt by weak stratified turbulence. *Geophysical Research Letters* **25** (15), 2773–2776.

TURNER, J.S. 1968 The influence of molecular diffusivity on turbulent entrainment across a density interface. *Journal of Fluid Mechanics* **33**, 639–656.

TURNER, J. STEWART 1979 *Buoyancy Effects in Fluids*. Cambridge University Press.

ZELLOUF, Y., DUPONT, P. & PEERHOSSAINI, H . 2005 Heat and mass fluxes acress density interfaces in a grid-generated turbulence. *International Journal of Heant and Mass Transfer* **48**, 3722–3735.

50272-101

REPORT DOCUMENTATION PAGE

1. REPORT NO. WHOI-2008-05

2.

3. Recipient's Accession No.

4. Title and Subtitle
2007 Program of Studies: Boundary Layers

5. Report Date
June 2008

6.

7. Author(s) Claudia Cenedese and John A. Whitehead, Co-Directors;
Joseph Pedlosky and Steven Lentz, Co-Principal Lecturers

8. Performing Organization Rept. No.

9. Performing Organization Name and Address

Woods Hole Oceanographic Institution
Woods Hole, Massachusetts 02543

10. Project/Task/Work Unit No.

11. Contract(C) or Grant(G) No.
(C)OCE-0325296
(G)N00014-07-10776

12. Sponsoring Organization Name and Address
National Science Foundation and Office of Naval Research

13. Type of Report & Period Covered
Technical Report

14.

15. Supplementary Notes
This report should be cited as: Woods Hole Oceanog. Inst. Tech. Rept., WHOI-2008-05.

16. Abstract (Limit: 200 words)

The topic of the Principal Lectures for the forty-ninth year of the program was ‘Boundary Layers”. The subject centers around those problems in which the boundary conditions lead to a large gradient near the boundary. Nine of this year’s principal lectures were given by Joe Pedlosky and the tenth was given by Steve Lentz. The fluid mechanics of boundary layers was reviewed, first starting from its classical roots and then extending the concepts to the sides, bottoms, and tops of the oceans. During week four, a mini-symposium on “Ocean Bottom and Surface Boundary Layers” gathered a number of oceanographers and meteorologists together to report recent advances. And finally, Kerry Emanuel of MIT delivered the Sears Public Lecture to a packed hall in Clark 507. The title was “Divine Wind: The History and Sciences of Hurricanes.” The ten student projects continue to constitute the heart of the summer GFD experience. These are studies of new, original, and tractable problems by our fellows, who are in the midst of their graduate work. Some of the studies are already continuing to grow to full projects to be published in due course. Whatever the results of this summer’s experience are for each fellow, be it a fully finished work, new ideas, fearless and honest inquiry, or simply experience working with a staff member in our craft, we wish our fellows well in their future studies and research. Special thanks go to a number of people who served to make the program flow smoothly. Jeanne Fleming and Penny Foster ran the office and performed administrative work for the many visits and lectures. Their work in preparation during the “slack” season (completely misnamed) is especially appreciated. Janet Fields helps with all aspects of the academic programs for the fellows and, as usual, did a superb job. Keith Bradley created apparatus for a number of laboratory experiments, plus helped with odd tasks such as repairing old bicycles. George Veronis ran the world-class softball team that counted a number of wins in the season, including a victory over the staff, who, although never wiser, never seem to age. We extend our sincere thanks to the National Science Foundation for support for this program under OCE-0325296. Support was also provided by the Office of Naval Research, Processes and Prediction Division, Physical Oceanography Program, under grant N00014-07-10776.

17. Document Analysis a. Descriptors

boundary layers
stratified fluids
ocean circulation

b. Identifiers/Open-Ended Terms

c. COSATI Field/Group

18. Availability Statement
Approved for public release; distribution unlimited.

19. Security Class (This Report)
UNCLASSIFIED

20. Security Class (This Page)

21. No. of Pages
316

22. Price

(See ANSI-Z39.18) *See Instructions on Reverse* **OPTIONAL FORM 272 (4-77)**
(Formerly NTIS-35)
Department of Commerce